Adams, Lauren (2024) *A holistic study of the effect of the murine microbiome on metabolism and systemic inflammation using integrated molecular imaging technologies.* PhD thesis.

https://theses.gla.ac.uk/84322/

A holistic study of the effect of the murine microbiome on metabolism and systemic inflammation using integrated molecular imaging technologies

Lauren Adams

BSc, MSc

A thesis submitted to the University of Glasgow for the degree of
Doctor of Philosophy (PhD)

School of infection and immunity

College of Medical, Veterinary and Life Sciences

University of Glasgow

Glasgow

G12 8QQ

December, 2023

Abstract

Inflammatory bowel disease (IBD) is a multifactorial disease involving genetic susceptibility, impaired barrier function, alterations in the microbiome, and a dysfunctional immune response. Current therapeutic treatments are aimed at controlling symptoms; however, symptoms recur, and patients can become susceptible to infection, increasing the need for new treatments. There has been a growing interest in the role host-microbe interactions play in the development of IBD and many studies have uncovered distinct shifts in small molecule classes in patients compared to healthy controls. Microbial and host small molecules are able to interact with host immune cells and polarize them towards either a pro- or anti-inflammatory phenotype. This immunometabolism/ immunomodulation is an emerging concept that plays an important role in human health and disease. Furthermore, IBD patients frequently experience extraintestinal manifestations, commonly affecting organs such as the liver, lung, eyes, kidney, and spleen, and often results in a loss of proper function. The cause of systemic inflammation is still poorly understood; however, studies have suggested that small molecules originating from the intestinal bacterial community may play a role.

Firstly, we aimed to discover small molecular changes in the intestine (ileum and colon) and systemic sites (liver and eye) in a mouse model after infection with an IBD associated pathobiont, adherent-invasive *Escherichia coli* (AIEC). We applied a powerful analytical technique known as mass spectrometry imaging (MSI) to map the spatial distribution and relative abundance of molecules across a sample surface in a label-free manner. This allows the distribution of known and unknown molecules including proteins, metabolites, and lipids to be determined. Our infectious mouse model revealed specific molecular changes across the different organs that were either microbial or host derived, and many play a role in the onset or perpetuation of inflammation. Despite, producing informative host-microbe interaction data, results of this proof-of-concept study were not fully reflective of human IBD.

Therefore, we investigated metabolomic adaptation in intestinal and systemic sites in a dextran sodium sulphate (DSS) mouse model. This model has been shown to reflect human disease, including disrupted barrier function, microbial dysbiosis and immune cell dysregulation. MSI revealed 30 molecules in the colon, 88 molecules in the ileum, 239 molecules in the liver, 65 molecules in the spleen and 16 molecules in the kidney differed in abundance between DSS colitis and uninflamed control mice. This study confirmed the identity of some intestinal molecules including creatine, docosahexaenoic acid (DHA), and 1-methylnicotinamide (1-MNA). However, identifying the location and abundance of specific molecules does not provide an overall assessment of the tissue environment that may lead to inflammation. Therefore, we applied imaging mass cytometry (IMC) to tissue regions of interest (ROI), where molecules of interest had been located. IMC found markers such as CD4 and major histocompatibility complex class II (MHCII) were decreased in the inflamed ileum, whereas CD4 and others (e.g. NKp46, granzyme B) were increased in the inflamed colon compared to the control. Hence, our study combined two imaging technologies to gain a better understanding of how region-specific molecules may be influencing the immunological profile in the ileum, colon, and liver.

Rheumatoid arthritis (RA) is another inflammatory condition with a poorly understood aetiology and has been linked to IBD. We applied MSI and IMC to investigate metabolomic and immunological changes in a mouse model of RA, collagen induced arthritis (CIA). We found 9 molecules in the lung, 3 molecules in the kidney, 2 molecules in the liver, and 16 molecules in the spleen could differentiate between diseased and non-diseased mice. In the lung, only one molecule was increased in the diseased group compared to the control groups and was identified as lysophosphatidylcholine 18:0 (LysoPC 18:0). IMC revealed cells expressing the markers B220 and CD19 (B cells) were increased in the lung of CIA mice compared to controls. Therefore, LysoPC (18:0) may promote the recruitment of B cells in the lung.

As microbes play an important role in immune priming and homeostasis, this study wanted to identify metabolomic and immune profile differences in mice with (specific pathogen free) and without (germ-free) a microbiome. MSI

revealed 9 molecules in the colon, 1 molecule in the ileum, 255 molecules in the liver, 5 molecules in the spleen and kidney, and 6 molecules in the lung that discriminate between germ-free (GF) and specific pathogen free (SPF) mice. We were able to confirm the identity of two polyamine molecules, spermidine and spermine, that were decreased in the SPF liver compared to GF liver. *In vitro* experimentation showed that spermidine reduced the percentage of macrophages expressing MHCII in a dose dependent manner. Impaired macrophage MHCII expression has been linked to dysfunctional adaptive immune activation; thus, reducing spermidine might be a microbial adaptation to support the development of the adaptive immune response.

This study highlights the usefulness of MSI and IMC as metabolomic and immunological discovery tools that can be used together to identify how molecules and cells within an environment may be interacting under different conditions. This allows us to hypothesise and test various host-microbe and immunometabolism mechanisms that may be implicated in inflammatory processes during IBD and RA.

Table of Contents

List of Tables

List of Figures

Acknowledgement

Author's Declaration

I hereby declare that this thesis is the result of my own work and has been composed for the degree of PhD at the University of Glasgow. This work has not been submitted for any other degree at this or any other institution. All work presented was performed by myself unless otherwise stated. All sources of information and contributions to the work have been specifically acknowledged in the text.

Lauren Adams

December 2023

Abbreviations

°C	Degrees Celsius
µg	Microgram
µl	Microlitre
µM	Micromolar
µm	Micrometre
1-MNA	1-methylnicotinsmide
3M-4-TMAB	3-methyl-4-(trimethylammonio)butanoate
4-TMAP	4-(trimethylammonio)pentanoate
5-AVAB	5-amino valeric acid betaine
AA	Arachidonic acid
AIEC	Adherent invasive Escherichia coli
APC	Antigen presenting cell
ATCC	American Type Culture Collection
ATP	Adenosine triphosphate
AUC	Area under the curve
BA	Bile acid
BCA	Bicinchoninic acid
CCL20	Chemokine (C-C motif) ligand 20
CD	Crohn's disease
CFA	Complete Freud's Adjuvant
cfu	Colony forming units
CIA	Collagen induced arthritis
CID	Collision induced dissociation
CO_2	Carbon dioxide
COX	Cyclooxygenase
DAI	Disease activity index
DC	Dendritic cells
DESI	Desorption electrospray mass spectrometry
DG	Diglyceride
DHA	Docosahexaenoic acid
DNA	Deoxyribonucleic acid
DSS	Dextran sodium sulphate
EIM	Extraintestinal manifestation
ELISA	Enzyme linked immunosorbent assay
FBS	Fetal bovine serum
FDR	False discovery rate
GF	Germ-free
GWAS	Genome wide association studies
h	hour
H&E	Haematoxylin and eosin
HIF	Hypoxia inducible factors
HMDB	Human metabolome database
IBD	Inflammatory bowel disease
IEC	intestinal epithelial cell
IFN-γ	Interferon-gamma

IL	interleukin
IMC	Imaging mass cytometry
kDa	Kilo Dalton
KEGG	Kyto Encyclopedia of Genes and Genomes
kHz	Kilohertz
KO	Knockout
Kv	Kilovolts
LB	Luria bertani media
LDH	Lactate dehydrogenase
LPS	Lipopolysaccahride
LysoPC	Lysophosphatidylcholine
M	Molar
m/z	Mass-to-charge
MALDI	Matrix assisted laser desorption ionisation
MFI	Mean fluorescence Intensity
mg	Milligram
MG	Monoglyceride
MHCII	histocompatibility complex class II
ml	Millilitre
mM	Millimolar
MOI	Multiplicity of infection
ms	millisecond
MS	Mass spectrometry
MSI	Mass spectrometry imaging
MSMS	Tandem mass spectrometry
MVA	Multivariate analysis
NAFLD	Non-alcoholic fatty liver disease
NCE	Normalised collision energy
NF-κB	nuclear factor kappa B
NK	Natural killer
nm	nanometers
NMR	Nuclear magnetic resonance
NOD	Nucleotide oligomerisation domain
OD_{600}	Optical density at 600 nm
PA	Propionic acid
PBS	Phosphate buffered saline
PCA	Principle component analysis
PCR	Polymerase chain reaction
PFA	Paraformaldehyde
PG	Prostaglandins
PI3K	phosphatidylinositide 3-kinase
PLS-DA	Partial least square discriminant analysis
PMN	Polymorphonuclear
ppm	parts per million
PRR	Pattern recognition receptor
RA	Rheumatoid arthritis
RFU	Relative fluorescence unit
RMS	Root mean squared
RNA	Ribonucleic acid
RNS	Reactive nitrogen species

ROC	Receiver operating characteristic
ROI	Region of interest
ROS	Reactive oxygen species
RT	Room temperature
SCFA	Short chain fatty acid
SFB	Segmented filamentous bacteria
SPF	Specific pathogen free
TEER	Transepithelial electrical resistance
Tfh	T follicular helper cells
Th	T helper
TIC	Total ion current
TJ	Tight junction
TLR	Toll like receptors
TMA	Trimethylamine
TMRE	Tetramethyl rhodamine ethyl ester
TNF-α	Tumour necrosis factor alpha
TOF	Time-of-flight
UC	Ulcerative colitis
V	Volts
v/v	Volume per volume
VIP	Variable importance in projections
ZO	Zonula occludens
Ω	ohms

Chapter 1 Introduction

1.1 Inflammatory bowel disease

Inflammatory bowel disease (IBD) is a relapsing idiopathic inflammatory condition that includes two subtypes: ulcerative colitis (UC) and Crohn's disease (CD) [1]. UC is localised to the large intestine whereas CD can affect any part of the gastrointestinal (GI) tract but mostly affects the terminal ileum and proximal colon [2,3]. IBD presents with symptoms such as severe abdominal pain, diarrhoea, excessive fatigue, weight loss and fever and most patients are diagnosed before the age of thirty [4]. IBD is also a progressive condition that can lead to intestinal complications such as abscesses, fistulas, and strictures which can require surgical intervention [5]. IBD can also cause significant morbidity as 26% of patients die prematurely and has been associated with the development of cancer [6]. IBD affects more than four million people across the United States and Europe and cases were steadily increasing throughout the 21st century [7]. However, over the last 10 years the prevalence of IBD has plateaued in Western countries but disability in patients has increased to 71% [8,9]. Despite plateauing in Western countries, IBD has emerged and is steeply increasing in newly industrialised countries across Asia, South America, and the Middle East; thus, IBD is a global disease with prevalence in every continent [7,10]. There is currently no cure for the disease and the aetiology remains unclear; hence, there is no preventative measure to reduce occurrence [11,12]. As a result, therapeutic intervention strategies have focused on mitigating symptoms which includes an immunosuppression approach (Standard care outlined in Table 1) [4,11]. Due to increasing prevalence and lack of cure, IBD is a major public health burden leading to substantial healthcare and socioeconomic costs [13,14].

Table 1.1 Standard care options for IBD patients

Drug Class	Example of drugs	Basic mechanism of action
Aminosalicylates	Mesalamine, Sulfasalazine	Suppress inflammation in the lining of the intestine

Corticosteroids	Prednisone, Budesonide	Reduce inflammation by suppressing the immune system response
Immunomodulator	Azathioprine, Methotrexate	Suppress the immune system to reduce inflammation
Biologics	Infliximab, Adalimumab	Target specific proteins involved in the inflammatory process
Janus Kinase (JAK) Inhibitors	Tofacitinib	Block JAK enzymes to reduce inflammation and immune response

1.1.1 Genetic and environmental factors in IBD pathogenesis

The aetiology of IBD remains relatively unknown, but it has been described as a multifactorial condition that involves a dynamic interplay between host genetic susceptibility, environmental factors, and microbiota [15,16]. Advances in DNA analysis and sequencing have allowed for the emergence of many genome-wide association studies (GWAS) which can reveal single nucleotide polymorphisms (SNPs) factors [17]. Research has identified approximately 163 IBD-associated gene loci, of which 110 are associated with both CD and UC, and mostly belong to specific pathways essential for antimicrobial immune responses [17,18]. The first susceptibility gene of CD was identified as nucleotide-binding oligomerization domain-containing 2 (NOD2) in 2001 [19]. NOD2 is an intracellular pattern recognition receptor (PRR) that is expressed by intestinal epithelial cells (IECs), Paneth cells and monocyte-derived cells [20]. NOD2 can recognise the muramyl dipeptide (MDP), a conserved motif present in bacterial peptidoglycan, resulting in the induction of autophagy to modulate both innate and adaptive immune responses [21,22]. Further genetic analysis revealed CD-associated polymorphisms in other autophagy-related genes, *ATG16L1* and *IRGM* [23,24]. Autophagy is essential for intracellular homeostasis, degradation of cytosolic contents and provides resistance and removal of invading intracellular microbes [25,26]. Therefore, IECs and immune cells that display *ATG16L1* and NOD2 variants have defective antibacterial autophagy [27]. Moreover, GWAS have identified a significant association between IBD and the *IL23R* gene, which encodes a subunit of the

receptor for the proinflammatory cytokine IL-23 [28]. IL-23 participates in the generation of Th17 cells, which have been implicated in the pathogenesis of IBD [29]. Other susceptibility genes that have been found to regulate immune function include *CARD9*, *IL1R2* and *SMAD3* amongst others [17,18]. Despite the expanding number of susceptibility gene loci associated with the development of IBD, only 20%-25% account for heritability and only 8%-14% IBD patients report a family history [30,31]. Furthermore, the concordance for homozygous twins does not reach higher than 50%, indicating that gene-gene interactions, gene-pathway interactions, and gene-environment interactions play an important role in IBD pathogenesis [32,33].

In addition to genetic susceptibility, a large number of environmental factors have been described as risk factors for IBD [34]. Cigarette smoking is a well-recognised risk factor in CD as it thought to influence epigenetic changes related to immune responses, autophagy and immunosuppression and is also associated with a higher rates of postoperative complications; however, smoking is not considered a risk factor in UC [34,35]. However, the role of smoking is strongly influenced by genetic factors and ethnicity as the association is only observed in non-Jewish white individuals [36]. Furthermore, exposure to prescription drugs including, hormonal medications, oral contraceptives, and long-term use of nonsteroidal anti-inflammatory drugs have been associated with increased incidence of IBD [37]. The exact mechanism behind these associations has not been fully defined but is biologically plausible due to anti-inflammatory and immune mediator properties [34,37]. A study conducted in a Swiss IBD cohort also found that being underweight in childhood and adulthood, as well as being less physically activity increased the risk of developing IBD [38]. Another study described that sporting activity influences immunological balance by dampening the secretion of pro-inflammatory cytokines such as IL-1, IL-2, and IL-6, while anti-inflammatory cytokines including IL-10 are increased [39]. Moreover, stress has long been proposed to play a role in the pathogenesis of IBD [40]. Mood components of stress, such as depression and anxiety, may play a strong role in exacerbating IBD as studies have found antidepressants beneficially impact IBD progression [41,42]. More recently, ecological, and epidemiologic evidence has suggested that air pollution, linked to the development of industrialisation, increased the risk of IBD and the rates of hospitalisation [43,44]. Therefore, a

variety of risk factors have been associated with the onset and exacerbation of IBD [41,43,44].

Moreover, diet plays a crucial role in shaping the composition of the microbiota and can control IBD symptoms [45]. Excusive enteral nutrition (EEN) is a basic diet that does not contain solid food and has been shown to induce remission within paediatric patients, without any significant side effects [46]. EEN rapidly changes the composition of microbiota, promoting the growth of beneficial bacteria and effectively reduces inflammation [45,46]. The varying success of treatments that involve microbial alterations strongly supports evidence that dysbiosis is an important factor in IBD pathology.

1.1.2 Immunological factors in IBD pathogenesis

Intestinal epithelial cells

The GI mucosa acts as a semi-permeable barrier that allows the absorption of nutrients and immune regulation, while protecting against harmful antigens and invading microorganisms [47]. The mucosa is comprised of several elements including mechanical, chemical, and immune barriers that function as a defence mechanism[48]. These elements include a central single cell layer consisting of specialised IECs, the inner lamina propria where innate and adaptive immune cells reside, and an outer mucus layer that contains commensal microbes, antimicrobial proteins (AMPs) and secretory immunoglobulin A (IgA) molecules [47-49]. The mucus layer is the first line of physical defence against external stimuli and prevents pathogens from directly interacting with IECs [50]. Underneath the mucus layer, IECs such as absorptive enterocytes, goblet cells, enteroendocrine cells, Paneth cells and microfold cells provide the most integral part of the mucosal barrier[47,50]. Together these cells form a continuous and polarised monolayer, linked by a series of dynamic junctional complexes, that separates the lumen from the lamina propria, restricting the passage of molecules [51,52]. The three most important complexes are tight junctions (TJs), adherens junctions (AJs) and desmosomes[53]. TJs are the most adhesive complexes that seal the intercellular space forming a barrier, and consist of transmembrane proteins (e.g. occludin, claudin), peripheral membrane proteins (e.g. zonula occludens (ZO)), and regulatory proteins [47,54]. Therefore, in a healthy gut, the

microbiota does not come into contact with IECs, and is separated from underlying immune cells resulting in immune tolerance [55]. As well as forming a physical barrier, IECs maintain mucosal defence by expressing a wide range of pattern-recognition receptors (PRRs) [56,57]. PRRs such as Toll-like receptors (TLRs) form the backbone of the innate immune system by mediating a rapid response and recognition of conserved microbial components, initiating an inflammatory response for microbial clearance [58,59]. However, the intestinal barrier is not static but is highly dynamic and responsive to internal and exogenous stimuli such as cytokines, bacteria, and dietary factors [60]. A dysfunctional intestinal barrier is a characteristic feature of IBD and the different levels of protective mechanisms (e.g. PRRs, AMPs, TJs) are disturbed [61]. This allows more microbes to come into contact with the epithelium and mucosal immune mechanisms [62]. Consequently, excessive immune reactions are triggered, resulting in chronic intestinal inflammation [63].

T cell response

T cells are part of the adaptive immune response, they are thymus-derived and proliferate and differentiate in the periphery after stimulation with specific antigens [64]. CD4+ T helper cells have been implicated as major initiators in IBD as they are enriched in inflamed tissue and lesions [65]. Furthermore, blocking, or depleting CD4+ T helper cells has been proven as an effective treatment in IBD, suggesting a prominent role in disease pathology [66]. CD4+ T helper cells are subtyped based on their relevant immune functions and include Th1, Th2 and Th17 [64]. Th1 cells are essential for protecting against pathogens and primarily produce interferon (IFN)-γ and tumour necrosis factor (TNF)-α [67]. These proinflammatory mediators can activate innate immune cells such as macrophages, allowing for the removal of pathogenic organisms [68]. However, during IBD, IL-12 is secreted by antigen presenting cells (APCs) and acts via signal transducer and activator of transcription factor (STAT)4 to promote the differentiation of naïve T cells into Th1 cells [69]. STAT4 also signals the upregulation of the IL-12 receptor and IFN-γ expression, resulting in further expansion of Th1 population [67,69]. Moreover, IFN-γ has been described as an important factor in IBD development as studies have found IBD patients secreted higher levels of the cytokine and inhibition of IFN-γ correlated with a reduction

in inflammation and tissue damage [70]. TNF-α has also been implicated as playing an important role in disease pathology, linked to the dysregulation of the intestinal barrier and proinflammatory affects; hence, anti-TNF therapy is currently used to treat IBD [71]. Other proinflammatory cytokines that are secreted by Th1 cells include IL-1, IL-2, IL-6, and IL-8, which have all been implicated in driving inflammatory responses during IBD [72,73]. Moreover, Th1 cells increase the expression of Major Histocompatibility Complex II (MHCII) in APCs allowing for antigen presentation, which activates macrophages as well as CD4+ T cell immune response [74]. Furthermore, human GWAS studies have also identified several SNPs associated with the development of IBD, lead to altered gene expression of a number of Th1 related factors (*IL18RAP and TRIB1*)[75]. Therefore, current evidence suggests that Th1 cells and their mediators play an important role in IBD pathology.

More recently, IL-17 producing Th17 cells were discovered and play an important role in maintaining commensal microbiota populations at important barrier sites to ensure immune homeostasis [76]. Th17 cells express the chemokine receptor 6 (CCR6) on the surface which allows the cells to migrate to specific intestinal tissue targets in the presence of the CCR6 ligand chemokine ligand 20 (CCL20) [77]. Under homeostasis conditions IL-17 secreted by Th17 cells promotes IEC proliferation, IgA secretion and AMPs, thereby enhancing the intestinal barrier function [78]. Moreover, IL-17 can bind Th1 cell surface receptors which inhibits the secretion of proinflammatory factors such as IFN-γ, resulting in immune regulation [79]. However, hyperproliferation and activation of Th17 cells has been shown to lead to various autoimmune diseases and IBD [80]. In particular, Th17 cells are more abundant in the mucosa of IBD patients and animal models, compared to IBD patients in remission and also have upregulated IL-17 expression [81]. Studies have found that IL-17 can act alone or synergistically with other proinflammatory mediators, chemokines, and proteases (e.g. IL-6, IL-8) to induce inflammation via the activation of nuclear factor kappa light chain enhancer of activated B cells (NF-κB) signalling pathways [82,83]. This promotes the expression of the Th17 chemokine ligand 20 (CCL20) in IECs, promoting the recruitment and further activation of Th17 cells which aggravates the inflammatory response [84,85].

Macrophages and dendritic cells

The gut-associated lymphoid tissue (GALT) includes an arrangement of innate intestinal mononuclear cells, such as macrophages and dendritic cells (DCs) within the lamina propria [64]. These cells are positioned within a close proximity to the enteric luminal compartment, separated by an epithelial cell monolayer [86,87]. Macrophages and DCs are responsible for maintaining gut homeostasis by sampling luminal antigens that gain access to the lamina propria to maintain tolerance and efficiently clearing microbes and stimuli [88]. Macrophages are a highly heterogeneous population of cells and are often simply classified based on their phenotypes into two functional groups: M1 inflammatory (high IL-12; low IL-10) and M2 wound healing (low IL-12; high IL-10) [89]. These two classes can be further subclassed based on specific function; for example, M2c macrophages are a subtype of M2 macrophages that are characterised by IL-10 and glucocorticoids and lack of CD68 and MHCII [90]. The phenotype of macrophages is induced by the microenvironment and the presence of specific cytokines [87,89]. M1 macrophages are polarized by IFN-γ produced by NK and Th1 cells, TNF-α produced by other antigen presenting cells (APCs) and engagement of PRRs such as NOD and TLRs with PAMPS [91]. After polarisation towards an M1 phenotype, macrophages produce a variety of proinflammatory cytokines such as IL-12, IL-6 and TNF-α as well as reactive oxygen (ROS) and nitrogen species (RNS) [92]. These proinflammatory mediators can then promote the differentiation and activation of Th1 and Th17 cells, which in turn supports the clearance of intracellular pathogens [93]. However, while M1 macrophages are essential for the clearance of invading pathogens, the production of proinflammatory mediators and adaptive immune cell activation has been implicated in IBD pathogenesis [92,94]. Moreover, an increase in M1 macrophage populations and activity can result in tissue damage, predisposing the host to the development of inflammation and lesions [87,89].

DCs are professional APCs and have the ability to initiate adaptive immune responses against pathogens [95]. This interaction can be mediated via DCs ability to produce IL-23 after PRR stimulation, which is an important component of anti-microbial defence [96]. Therefore, DC IL-23 production links the innate and adaptive immune responses; however, excessive, or inappropriate DC IL-23

production favours a proinflammatory Th17-cell response including the emergence of IL-17 and IFN-γ-producing cells associated with chronic intestinal inflammation [97]. Moreover, DC processes linked to IBD genetic susceptibility have been identified as potential targets for therapeutic intervention [95]. This includes blocking the interaction between DCs and T cells to reduce the activity of the IL-23/IL-17 proinflammatory pathway that is important in IBD pathogenesis [97,98]. During IBD, DCs accumulate at sites of inflammation and express higher levels of activation markers and increased TLR responsiveness; thus, DCs are likely to contribute to disease pathology [98,99]. Moreover, both macrophages and DCs actively promote the return to homeostasis after immune activation and inflammation [100]. Studies have found that the cells are able to respond to pro-resolving mediators such as prostaglandin D_2 (PGD_2) and adenosine that are produced during inflammation [100,101]. This results in the inhibition of proinflammatory cytokine production and induction of T-cell proliferation as well as clearance of apoptotic cells and production of anti-inflammatory cytokine IL-10 [101]. However, patients with active IBD exhibit higher levels of M1 macrophages and activated DCs, suggesting that immune cell polarisation is skewed, and resolution cannot be achieved [102]. Therefore, innate immune cells can initiate IBD development by inappropriately clearing microbes and failing to switch to an inflammation-resolving anti-inflammatory response [89,91,95].

B cells

Intestinal B cells are primarily located in the lymphoid follicles and as plasma cells in the lamina propria[103]. B cells can become activated in lymphoid follicles, followed by migration to the lamina propria and differentiation into IgA secreting cells [103,104]. Studies have found that B cells are increased in the inflamed mucosa of IBD patients, implicating them in disease pathology [105]. Firstly, B cells are able to secrete immunoglobulins such as IgA that can activate pathogenic macrophages [106]. However, B cells are also able to condition the activity of effector memory T cells that have already been primed by APCs such as DCs [107]. Studies have shown that B cell marker CD40 interacts with gp39 on effector T cells; however, when these markers are overexpressed the secretion of IFN-γ is elevated and spontaneous colitis develops [108]. B cells are also cytokine-producing cells and can secrete proinflammatory cytokines such as IL-4,

IFN-γ, IL-2, and TNF-α; hence, B cells might contribute the inflammatory environment in IBD [103,109]. Moreover, B cells are capable of controlling colitis via MHC class I mediated antigen presentation that induces regulatory CD8$^+$ T cells that can dampen the inflammatory response [110]. Autophagy is involved in this MHC-dependant antigen presentation, making it an important aspect in B cell function; however, autophagy is associated with the development of CD, and may involve dysfunctional B cells [110-112]. Therefore, B cells have the potential to suppress as well as exacerbate intestinal colitis which is likely to be dependent on location and inflammatory state [113].

1.1.3 Role of the intestinal microbiome

The gut microbiome, comprising collective genomes of symbiotic, commensal and pathobiont microorganisms, is of increasing interest due the importance of microbes in health and disease [114]. In the gut, the dominant bacteria phyla are *Firmicutes* and *Bacteroides* [115]. These bacteria play a fundamental role in several aspects of host homeostasis including immune cell development and homeostasis, food digestion, enteric nerve regulation and promote angiogenesis [116]. This symbiotic relationship can trigger specific biological responses; thus, microbes have the potential to significantly impact host physiology [117]. In addition to the IBD associated risk factors described, other risk factors of IBD include antibiotic use, diet, mode of birth such as caesarean section and bacterial infection [35,118]. Whilst the exact mechanism behind these factors may be different, they share a commonality which is adaptation to the gut microbiome [119]. Therefore, microbial perturbations in IBD are considered a critical factor in IBD pathogenesis; however, it is not clear how the process occurs and whether microbes play a central cause or are a consequence of disease [120,121]

Microbial composition in IBD

Shotgun metagenomic sequencing has revealed that the microbial composition and diversity in the gut is a key factor in the development of IBD [121,122]. Studies have found that IBD patients have greater fluctuations in microbial composition compared to healthy individuals, resulting in bacterial dysbiosis [123]. Dysbiosis in IBD patients has been characterised by an increase in the abundance of

Bacteroidetes and Proteobacteria, and a decrease in Firmicutes [124]. This shift in bacterial colonisation results in the reduction in beneficial bacteria such as *Faecalibacterium prausnitzii* and *Roseburia intestinalis,* while the growth of pathogenic and pathobiont bacteria, such as *Bacteroides fragilis* are increased [125]. The two types of IBD, CD and UC, show substantial overlap in their gut microbial signatures, suggesting that dysbiosis is a general indicator of inflammation [125,126]. However, CD patients exhibit a higher degree of dysbiosis compared to UC patients, which has been linked to inflammation in the ileum [127]. Moreover, ileal CD is associated with a more significant decrease in alpha diversity compared to colonic CD [127,128]. Therefore, location and degree of intestinal inflammation underpins bacterial dysbiosis signature [127,128]. As a consequence of dysbiosis in IBD, the host-microbe beneficial interactions are reduced resulting in a loss of key functions required for gut homeostasis [129].

Microbial interaction with intestinal barrier

Commensal microbes present in the mucus layer ensure resistance to pathogens by producing antimicrobial substances, modulating the luminal pH, and compete for nutrients [54]. Moreover, studies using germ-free animals have shown that commensal bacteria promote angiogenesis, the development of gut-associated lymphoid tissue and the epithelium [56]. Therefore, commensal bacteria not only exert protection against pathogens, but are essential in forming a functional intestinal mucosal barrier [51,56]. Studies have shown that IBD patients have an increased gut permeability, particularly during active disease; however, whether an impaired barrier function is the result or cause of IBD is still unclear [130,131]. The disruption in the mucosal barrier can result in the translocation of intestinal microbiota and potentiation of the immune system [132]. During intestinal inflammation there are distinct changes in the mucus layer environment which includes decreased mucin production via goblet cells, decreased glycosylation products and a reduction in antimicrobial factors, weakening the protective functionality [55,133]. Members of the IBD-associated microbiota are able to use mucus as an energy source and tightly control its production, and it has been suggested that mucus changes during IBD are a result and cause of dysbiosis [134]. Moreover, TJ proteins are disrupted during IBD pathogenesis, impairing barrier integrity and allowing the translocation of microbes [135]. Studies have

demonstrated that colonising germ-free mice with specific gut microbiota such as *Bacteroides thetaiotaomicron*, increases the expression of genes that encode proteins such as ZO-1 [136]. Moreover, other microbes such as commensal Escherichia coli C25 have been found to alter the localisation of claudin-1 and activate the secretion of IL-8 in epithelial cells [137]. Studies have also shown that hydrogen sulphide producing bacteria, such as *Atopobium parvulum,* are increased in CD patients with severe inflammation, resulting in IECs mitochondrial damage leading to dysfunction and inflammation [138]. Therefore, it has been suggested that dysbiosis in the inflamed intestine may exacerbate increased permeability via a variety of mechanisms [136,137].

Microbial interactions with immune cells

During IBD, a dysfunctional interaction between intestinal microbiota and the mucosal immune system occurs, leading to a loss of immune tolerance and inflammation [139]. A large number of abundant Proteobacteria pass through the mucosal barrier and pathogen-associated molecular patterns (PAMPs), lipopolysaccharide (LPS) and flagellin on the bacterial surface are recognised by TLRs of the innate immune response [140]. When the intestinal barrier is disrupted, macrophages and DCs sense PAMPs with PRRs, signalling a downstream activation of central immune response pathways: NF-κB, mitogen activated protein kinases (MAPKs), and interferon regulatory factors (IRFs) [87]. The activation of these pathways resulting in the production of proinflammatory cytokines (e.g. IL-1, IL-6 and TNF-α), chemokines, and AMPs [87,88]. These chemical signals are then responsible for the recruitment of neutrophils, activation of macrophages, and the maturation of DCs, promoting the induction of the adaptive immune response [141,142]. IBD patients have elevated levels of many proinflammatory cytokines in serum and mucosal tissue; thus, it has been postulated that this elevation is primarily due to the uncontrolled immune response to bacterial antigens [143]. Therefore, the innate immune system can contribute to the IBD pathogenesis by inappropriately responding to commensal and pathogenic microbes, leading to a proinflammatory response.

Moreover, T-cell responses to microbial antigens are common in IBD patients [144]. Studies have shown that the gut microbiota such as adherent invasive *Escherichia coli* (AIEC) can induce the differentiation of T cells into Th17 cells

[145]. The bacterial activation of Th17 cells has also been shown to exacerbate inflammatory responses in IBD [146,147]. For example, segmented filamentous bacteria (SFB) stimulate the production of ROS and use microbial adhesion-trigger endocytosis to transfer antigenic proteins into IECs [148]. This increases the secretion of cytokines IL-23 and IL-1ß and induces Th17 cell differentiation resulting in IL-17 expression that can aggravate intestinal inflammation [81,148]. Furthermore, *Actinobacterium Eggerthella lenta* is enriched in IBD patients and expresses the cardiac glycoside reductase 2 (Cgr2) enzyme, which in turn upregulates IL-17A expression in intestinal Th17 cells [149]. Moreover, the pathobiont, *Bilophila wadsworthia* is increased in IBD patients and has been found to promote Th1 immune responses and susceptibility to colitis in *IL10$^{-/-}$* mice [150,151]. Therefore, there is growing evidence to suggest the proliferation and activation of Th17 and Th1 cells during IBD involves microbial stimuli. IBD patients and colitis models also have higher levels of B cell produced antibodies reactive to microbial antigens [152]. For example, in an IL-4-mediated spontaneous colitis in T-cell receptor α knockout mice, B cells are expanded with an increase in the production of antibodies such as anti-neutrophilic cytoplasmic antibodies (ANCA) [153]. Studies have also found that microbes directly activate B cells to express IL-6 and IgG1, resulting in Th17 cell differentiation and activation [154]. Therefore, microbes can alter B cell function which can lead to T-cell activation and inflammation. Hence, gut microbiota dysbiosis, cytokine imbalance and immune activation, and destruction of the mucosal barrier contribute to IBD pathogenesis.

Microbiota targeted IBD treatment approaches

As there is a complex dynamic link between microbes and the development of IBD, various microbial targeted therapies have been developed [155]. Supplementation with probiotics, such as *E. coli Nissle* 1917, has been shown to inhibit the growth of pathogenic bacteria as the H1 flagella forms a tight network structure preventing the adhesion and invasion of pathogenic bacteria to IECs [156]. In addition, the probiotic is also able to secrete bacteriocins to outcompete pathogens for nutrients in the intestine [155,156]. Clinical trial studies indicate that the probiotic is efficient in maintaining remission in IBD patients and animal colitis models also show it can promote mucosal wound healing

[157,158]. Faecal microbiota transplantation (FMT) involves supplementation with microbes isolated from healthy individuals and has been found to restore intestinal mucosal immune homeostasis in IBD patients [159]. The treatment has been found to be particularly useful for improving recurrent *Clostridium difficile* infection and clinical trials indicate that intensive FMT doses can induce remission [160,161]. [454645,46]

1.2 Metabolomics

Metabolomics is a term that refers to the analysis of patterns of small molecular metabolites in biological samples, allowing the metabolic status to be determined [162]. This analysis is performed using analytical chemistry techniques such as mass spectrometry (MS) [163]. These techniques allow for qualitative and quantitative identification of potentially thousands of metabolites in a variety of biological materials such as tissue, blood, or cell extract [164]. The data generated by such techniques are typically large and complex and often multivariate pattern-recognition data processing methods, including principle component (PCA) and partial least square discriminant analysis (PLS-DA), are used for data interpretation [165]. PCA is an unsupervised approach that reduces the dimensionality of data by elucidating the biggest contributors to variations within the dataset [166]. Unsupervised PCA, is often followed by supervised approaches such as PLS-DA, which can relate experimental groups (e.g. control vs disease) to metabolic features [167]. Multivariate analysis also produces graphical visualisation of trends within the data, allowing the identification of metabolic features responsible for differences between experimental groups [165-167]. Therefore, multivariate analysis often precedes metabolite annotation, allowing for the identification of metabolites of interest that could be biomarkers of biological outcomes including disease [165,168].

Univariate statistical tests are widely used in MSI data analysis to identify significant differences between two or more groups of mass spectra across spatial locations [169,170]. These tests can compare *m/z* relative intensities between two or more groups and include: students t-test (assess whether mean intensity between two groups is significantly different, analysis of variance (ANOVA extends the t-test to more than two groups), Welch's t-test (variation of t-test that accounts for unequal variances), and Kruskal-Wallis test (non-

parametric analogue of ANOVA) [170-172]. As MSI generates large datasets, it is common to perform multiple hypothesis testing comparing many *m/z* values simultaneously [171]. This requires the incorporation of a false discovery rate (FDR) correction such as Benjamini-Hochberg procedure, which controls for the expected proportion of false positive discoveries [173]. While univariate statistical tests on MSI data can reveal significant changes between groups, they do not capture complex interactions between *m/z* values and might miss important features [170,171]. Therefore, multivariate, and univariate techniques should be used together in order to provide a more comprehensive understanding of the relationships within MSI datasets [169,173].

1.2.1 Microbial metabolites and IBD

The mechanistic basis of host-microbe interaction involves the microbial production of primary metabolites and conversion of small molecules into secondary metabolites such as polysaccharides, nucleic acids, and structural proteins [174]. The crosstalk between microbial and human metabolites influences a variety of essential processes such as nutrient and xenobiotic metabolism, immune regulation, and complex neurological behaviours [175,176]. Therefore, metabolic pathways operating in the human body are the result of the collective human genome and microbiome activities [177]. Shifts in microbial composition during IBD translate to alterations in metabolic profiles which has been linked to pathological outcomes [114,178]. Current studies have identified several metabolite classes associated with inflammation in the tissue, faeces, urine, and serum of patients [179]. These classes include but are not limited to bile acids, short chain fatty acids, tryptophan metabolism and trimethylamines that are described below.

Bile acids

Bile acids (BAs) are produced in the liver via enzymatic processing of cholesterol [180]. These primary BAs are then conjugated with taurine or glycine prior to secretion, followed by absorption into the small intestine via the blood stream [181]. BAs in the intestine play an important role in maintaining homeostasis by facilitating the absorption of dietary triglycerides, fat soluble vitamins and cholesterol [182]. In the intestine, 95% BAs are cycled back to the liver via active

transport, known as the enterohepatic circulation of BAs [180]. However, the remaining 5% of BAs in the intestine undergo microbial processing, resulting in the generation of secondary BAs such as deoxycholic acid (DCA) and ursodeoxycholic acid (UDCA) [183]. It has been suggested that different secondary BAs including UDCA can protect barrier function, regulate the microbiome, and dampen inflammation [184]. However, some evidence has suggested that DCA can be cytotoxic to IECs by inducing oxidative stress, membrane damage and impairing DNA repair which can lead to mucosal inflammation [185]. Studies have shown that there is an altered gut BA composition in CD patients and that the severity of inflammation is negatively correlated with BA levels [186]. Therefore, it has been suggested that BAs play a role in CD aetiology and further work is needed to characterise the consequences of specific BAs on the regulation of intestinal immune response [187].

Short chain fatty acids

Microbial shirt chain fatty acids (SCFAs) are significantly reduced in the intestine of IBD patients [188]. Acetate, propionate, and butyrate are the SCFAs produced by anaerobic microbial enzymatic hydrolysis of accessible carbohydrates in undigested food residues [189]. These molecules play an important role in maintaining host homeostasis; in particular, butyrate protects barrier function by providing an energy source to IECs [190]. IBD patients have a reduction in the butyrate-producing bacterial species such as *Faecalibacterium prausnitzzi*, *Roseburia inulinivorans* and *Clostridium lavalense*, resulting in decreased butyrate production [191]. This is thought to play a role in CD progression as butyrate confers strong anti-inflammatory effects by activating anti-inflammatory cells such as T regulatory cells and M2 macrophages [192]. Furthermore, butyrate can prevent macrophages from releasing proinflammatory nitric acid, IL-6 and IL-12; thus, making macrophages hyporesponsive to gut commensals [193]. Furthermore, butyrate has been found to indirectly down-regulate inflammation by increasing cellular processes that require oxygen consumption, thereby inhibiting the growth of pathobionts [194].

Tryptophan

Studies in IBD patients have found that tryptophan metabolism is increased and that tryptophan levels are negatively correlated with disease activity [195]. Tryptophan is an essential amino acid that enters different host and microbial metabolic pathways, resulting in the production of bioactive molecules [196]. Tryptophan can be metabolised via the kynurenine pathway (KP) by the enzyme indoleamine 2,3-dioxygenase 1 (IDO1) [197]. This results in the production of bioactive molecule kynurenine; both IDO1 and kynurenine are positively correlate with disease severity and are described as having an immunomodulatory effect [196,197]. Furthermore, microbial metabolism of tryptophan results in the production of indole and indole derivates such as indole-3-propionate [198]. These molecules modulate the integrity of the gut barrier by supporting TJ protein expression on the apical site of IEC membranes which protects against colitis [199]. During intestinal inflammation, the concentration of indole is reduced which can act as a signal for enteric pathogenic *E. coli* to switch on gene expression at the locus of the enterocyte effacement (LEE) pathogenicity island, supporting attachment [200]. Therefore, a reduction in tryptophan catabolism to indole may support bacterial dysbiosis, impair barrier function and result in inflammation [198,200].

Trimethylamine (TMA)

TMA is a microbially derived polyamine by-product from the metabolism of dietary compounds such as carnitine, choline, and betaine [201]. TMA production mostly occurs in the colon due to the high abundance of Gammaproteobacteria, Firmicutes and Actinobacteria [202]. TMA enters the bloodstream via passive diffusion and is circulated to the liver where is it enzymatically converted into trimethylamine-N-oxide (TMAO) and excreted in urine [203]. TMAO has been implicated in different health conditions including cardiovascular disease and has been described as a biomarker of IBD [204,205]. Studies have highlighted that TMAO may play a role in IBD pathogenesis via different mechanisms such as altering autophagy, inducing pathogenic gene expression, and reducing mitochondrial transmembrane potential [206,207]. However, the role of the precursor TMA plays in disease pathology has been largely overlooked, despite a toxic effect being described over a decade [208]. More recently, studies have shown that TMA is toxic in the colon by inducing oxidative stress, cell death, cell

cycle arrest and decreasing intracellular ATP levels [201]. Therefore, more research is needed to elucidate the role TMA plays in exacerbating IBD pathology such as impairing IEC barrier function and proinflammatory cytokine release. In addition, two novel microbial metabolites identified as 3-methyl-4-(trimethylammonio)butanoate (3M-4-TMAB) and 4-(trimethylammonio)pentanoate (4-TMAP) have been found to colocalise with carnitine in the brain and inhibit carnitine fatty acid oxidation, impairing brain function [209]. The molecules 3M-4-TMAB and 4-TMAP inhibit fatty acid oxidation by preventing the linking of carnitine to a fatty acid and impairing enzymes involved in transporting fatty acids into the mitochondria, respectively [209,210]. As these molecules originate from gut microbes in the intestine, it is important to evaluate the effect they may have on intestinal immune cells in relation to IBD pathology.

Benzoate

Benzoate is a simple carboxylic acid produced in the intestine by the microbial breakdown of dietary compounds including amino acids and purines [211]. Benzoate has strong antimicrobial properties and is widely used as a food preservative in a range of products including soft drinks and jams [212]. However, studies have shown that benzoate has immunomodulatory activity resulting in the suppression of Th1-type responses and increasing the Th2-type responses, which in turn reduces the ability to clear pathogens and promotes allergenic responses [213]. Benzoate has also been found to reduce the number of infiltrating macrophages and TNF-α expression in chronic kidney disease models, suggesting that the molecule could be a useful anti-inflammatory mediator [214]. However, benzoate and benzoate metabolism derivatives have been associated with the severity of IBD by promoting the growth and virulence of *Enterobacteriaceae*, resulting in microbial dysbiosis [215]. In addition, patients suffering with orofacial granulomatosis, an extraintestinal disease associated with CD, showed significant signs of improvement when treated with a benzoate-free diet [216]. Therefore, a combination of different bacterial species or a dynamic interplay between individual species and their metabolites may be implicated as a driving factor in IBD pathogenesis [126].

1.3 Systemic complications associated with IBD

Inflammatory insult and an imbalanced gut microbiota during IBD result in the loss of mucosal barrier function in the small and large intestine [217]. Luminal contents, including commensal bacteria and their metabolites, then gain access to extraintestinal tissues via the bloodstream [218]. In response, the extraintestinal immune system must deal with the resulting influx, increasing the likelihood of an aberrant response and systemic inflammation [219]. IBD patients frequently experience one or more extraintestinal manifestations (EIM), mostly affecting the joints, skin, and eyes as well as lungs, spleen, kidney, and pancreas [220]. Hepatobiliary manifestations are fairly common and occur in approximately 30% of IBD patients with 5% developing chronic liver disease [221]. Patients can experience a wide range of liver complications from asymptomatic abnormal liver tests to severe life-threatening liver failure [222]. The exact aetiology of IBD related liver disease is still poorly understood but the conditions are described as sharing common autoimmune backgrounds as well as metabolic dysfunction [223,224]. For example, primary sclerosing cholangitis (PSC) is a chronic and progressive bile duct disorder that can result in cirrhosis and end-stage liver disease and occurs in up to 3% IBD patients [225]. Moreover, IBD patients have higher susceptibility to non-alcoholic fatty liver disease (NAFLD), affecting approximately 40% of patients [226,227]. NAFLD patients also experience gut microbial dysbiosis and the severity of the disease has been shown to be altered by bacterial metabolites [228]. Studies have reported that patients experience disturbed BA metabolism resulting in increased macrophage activity, decrease in butyrate resulting in increased gut permeability and also excessive lipid accumulation [226,228]. Therefore, microbes and their metabolites have been implicated in the development of IBD liver complications.

IBD-related arthropathy, a type of inflammatory arthritides, is the most common EIM affecting up to 30-40% of patients, and includes diseases such as ankylosing spondylitis, psoriatic arthritis, and reactive arthritis [229]. Arthritic conditions are more frequent in CD patients compared to UC patients [230]. Studies have suggested that arthritis associated with IBD involves a dysregulated gut bacterial community as disease models in germ-free environments do not develop gut or joint disease [231]. Moreover, the migration of gut lymphocytes and proinflammatory macrophages have been implicated in joint inflammation

resulting from an impaired barrier function [232,233]. However, neither aspect in disease pathology has been fully developed [230,234]. Rheumatoid arthritis (RA) is a chronic synovitis-based systemic disease of unknown aetiology and is characterised by symmetrical invasive inflammation of joints [235]. While RA is not considered as a EIM of IBD, epidemiological studies suggest that RA does tend to cluster with IBD as IBD patients are more likely to develop RA compared to healthy controls [235,236]. The exact mechanism behind this association is not definitive but both diseases share similar immunological signatures that will be discussed in the coming chapters [237,238]. Other manifestations that affect less patients include ocular conditions such as uveitis, scleritis and episcleritis lesions, affecting approximately 12% CD patients [239].

1.3.1 Systemic complications and the metabolome

In parallel with research on how host-microbiota interactions drive IBD pathogenesis in the intestine, evidence has suggested that these interactions are associated with systemic inflammatory disease [240]. The link between IBD and systemic inflammatory diseases has not been fully demonstrated, however, microbial dysbiosis in the gut arising from genetic or environmental perturbations has been described as a potential cause [217]. Therefore, dysbiosis in the IBD gut, may underlie or perpetuate the course of systemic inflammatory diseases (Figure 1.3.1) [114,240].
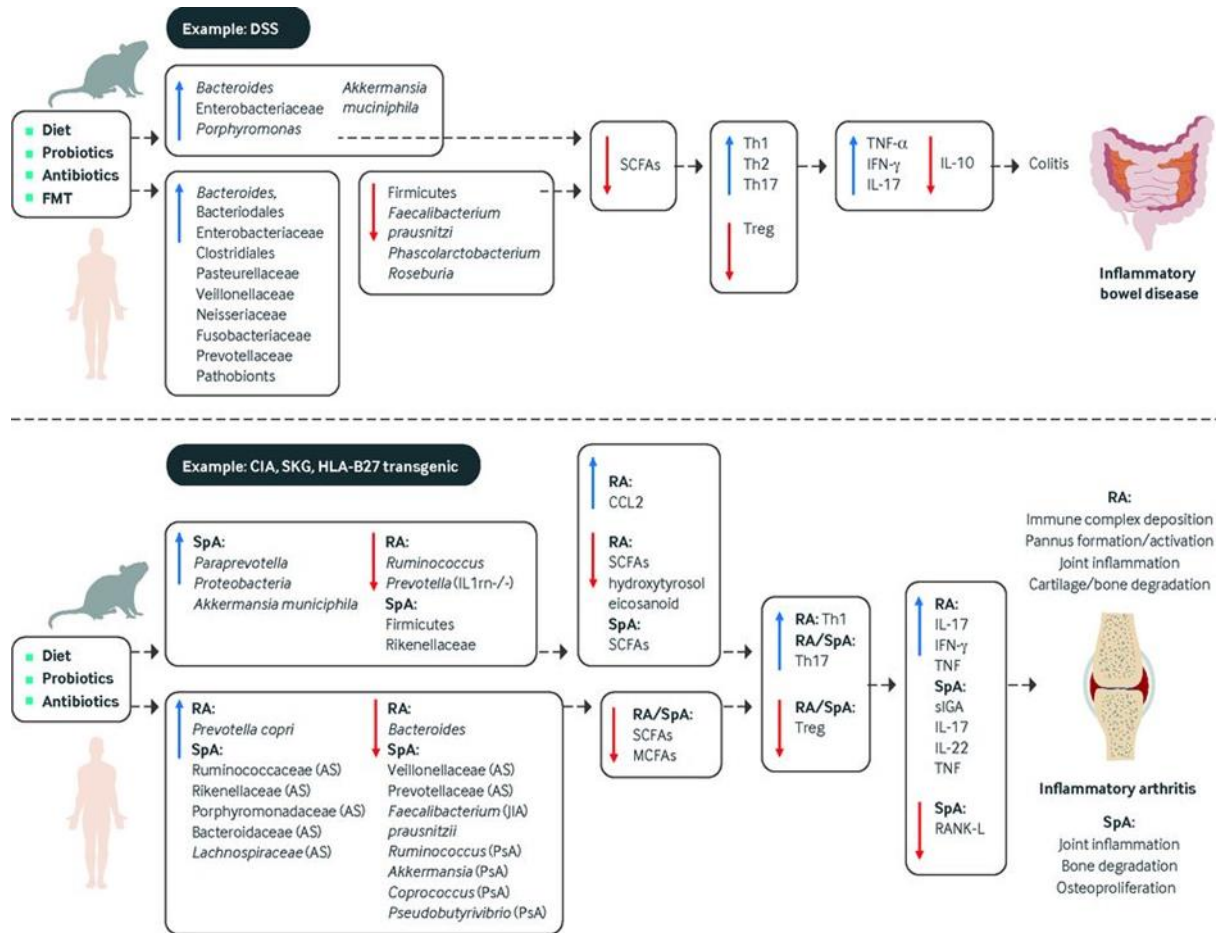
Figure 1.3.1. Influence of perturbed microbiome on metabolite production, immunomodulation, and development of systemic inflammatory disease in mice and human models. As an example, dextran sodium sulphate (DSS) induces IBD like symptoms alongside an increase in Bacteroides, decrease in Firmicutes and decrease in SCFAs. This has been associated with an increase in Th1, Th2 and Th17 cells and a decrease in Tregs. Evidence suggests the microbiome and its metabolites have an important role in IBD and systemic inflammatory diseases, including arthritis [114]

Animal models have suggested that gut commensal microbes play a role in systemic inflammatory disease and involves two, non-mutually exclusive immunomodulation mechanisms: bystander effects (antigen-nonspecific) and molecular mimicry (antigen-specific) [241]. Germ-free mice expressing the KRN T cell receptor transgene and the MHC class II molecule A(g7) (K/BxN) are resistant to the development of arthritis due to the reduced systemic germinal centre formation which subsequently reduces autoantibody production [242]. However, recolonisation with segmented filamentous bacteria (SFB) activates Th17 and follicular helper T cells (Tfh) cells in the intestine which are trafficked to the spleen, enhancing germinal centre formation and production of autoantibodies [242,243]. Autoantibodies were found to aggregate in the joints of K/BxN mice, triggering the activation of the complement cascade and recruitment of pro-inflammatory cells including neutrophils and macrophages which induced the

development of arthritis [242]. Furthermore, Horai *et al* found that in models of autoimmune uveitis, interphotoreceptor retinoid-binding protein (IRBP)-specific CD4^{+} T cells that migrate to the eye and drive the pathogenesis are first activated in the gut (239). This activation is thought to occur due to the cross-reactivity of adaptive immune responses to structurally related gut microbial peptides [244]. Therefore, microbes and alterations in metabolite production in IBD patients may result in bystander effects and molecular mimicry, inducing pro-inflammatory and immunoregulatory pathway activation [245]. This disturbance in microbe-host interaction mechanisms causes a loss of self-tolerance, initiating systemic inflammation in extraintestinal sites [246]. Despite the link between commensal bacteria and systemic inflammation, no single causative agent or consortia of bacteria have been specifically identified to cause disease in humans [126]. Hence, additional research is warranted to identify bacteria and mechanisms of immunoregulation in extraintestinal inflammatory disease settings. Therefore, finding metabolites that are altered in the gut and systemic tissue, and determining their role in altering the host immunological phenotype would provide a better understanding of host-microbe molecular interactions involved in IBD and systemic inflammation.

1.4 Spatial imaging technology

1.4.1 Mass spectrometry imaging overview

Mass spectrometry imaging (MSI) is a powerful technique that enables the spatial distribution of molecules within a sample to be visualised based on their mass-to-charge ratio (*m/z*) value. The technology combines the principles of mass spectrometry with spatial information, allowing researchers to map the distribution of various molecules, such as metabolites, lipids, peptides, and small molecules, across a samples surface including biological tissues [247,248]. This technique does not require the use of labels, allowing for both targeted and untargeted metabolomic investigation. Therefore, MSI has been applied in biological research to explore the identification of novel molecules and disease related molecular changes [249]. Other applications of MSI include clinical diagnostics, monitoring drug distribution in tissues and quality control of pharmaceutical products [250].

Sample preparation

The basic workflow of any MSI experiment begins with careful sample preparation [251]. After dissection or collection, biological tissue samples are typically flash-frozen to prevent enzymatic tissue degradation and delocalisation of molecules [252]. This step is crucial as even subtle changes in sample integrity can impair *m/z* signal intensity and the types of molecules being detected [252]. Samples are then usually embedded into an MSI compatible media, and thinly sectioned (usually between 5–20 μm), before being thaw-mounted onto appropriate microscope slides [253]. For optimal sample preparation, slides are dried to remove moisture, vacuum sealed and stored at -80˚C until use [252,253].
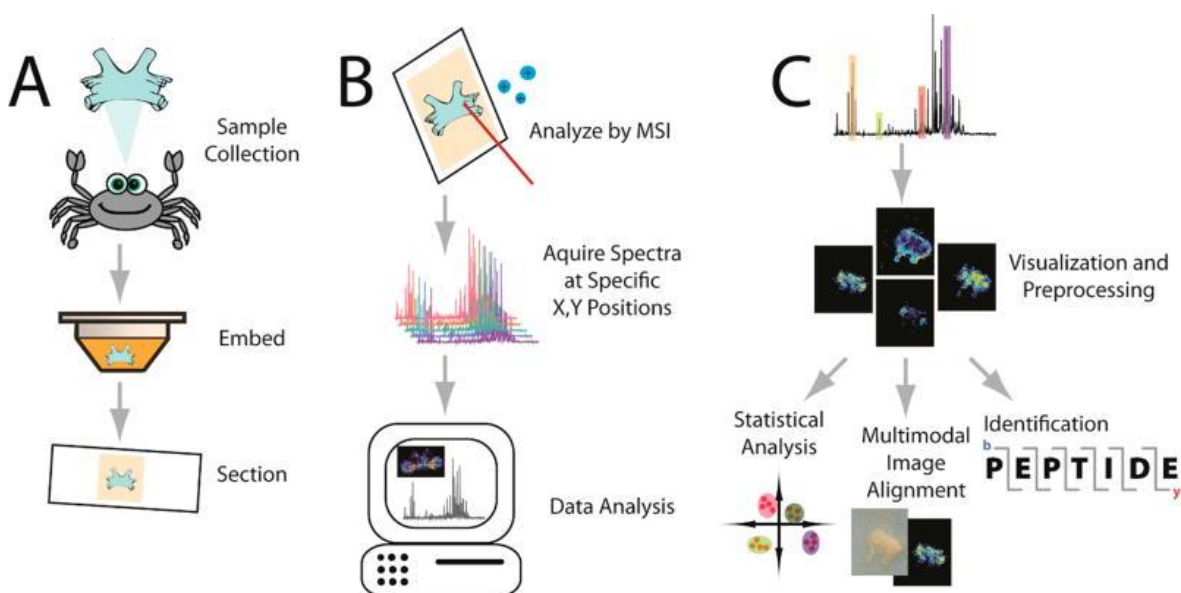
Figure 1.4.1. Visual generic workflow for MSI experimentation and analysis. A) Tissue sample is collected and embedded into a supportive media compatible with MSI. Embedded sample is then sectioned and thaw-mounted onto slides. B) The sample is ionised in a (*x, y*) grid and mass analysers detect ions and determine their mass-to-charge ratio (*m/z*). The intensities of *m/z* are quantified within a pixel, generating a mass spectrum. Software tools are then used to process and visualise the data. C) The data generated undergoes various preprocessing stages such as normalisation, followed by statistical analysis and molecular identification [172].

Sample ionisation

The setup of an MSI experiments involves defining the area of interest by creating an (*x, y*) grid, which directs how the ionisation source travels across the sample surface. A mass spectrometer then ionises the molecules and collects a mass spectrum at each pixel, resulting in the spatial resolution which is defined

by the pixel size (µm) [254,255]. There are several different ionisation techniques that are compatible with MSI and may require specific preparation to preserve the sample and molecules. The most commonly used ionisation technique for MSI is matrix-assisted laser desorption ionisation (MALDI) as it can image a wide range of molecular weights and species including metabolites and proteins. This ionisation method requires a low molecular weight matrix to be applied on the sample surface, allowing for the ionisation of singly charged ions with an enhanced signal [256-258]. A laser beam can then be directed over the sample surface, which causes the matrix to vaporise and desorb analyte molecules; desorbed ions are then accelerated into the mass spectrometers mass analyser which will be discussed in later sections [259]. This technique allows for a high spatial resolution as most metabolomics papers using MALDI conduct experiments at less than 10 µm. However, as spatial resolution is refined, the ion yield often decreases; thus, MSI experiments often require a balance between finer spatial resolution and obtaining enough signal intensities [260]. Different varieties of MALDI-MSI exist such as scanning microprobe MALDI (SMALDI) and infrared (IR) IR-matrix-assisted laser desorption electrospray ionisation (MALDI-ESI) [261]. Secondary ion mass spectrometry (SIMS) is another ionisation technique commonly used in MSI. It involves a primary ion beam, typically composed of positive ions, being directly ejected onto the sample surface [262]. The primary ions then collide with molecules on the samples surface and the energy created is sufficient enough to overcome the binding energies holding molecules in place [263]. This results in the molecules being releases as secondary ions which travel to the mass analyser [262,263].

Desorption electrospray ionisation (DESI) is newer advanced analytical technique that can be combined with imaging [264]. DESI-MSI does not require any sample pretreatment and involves spraying a samples surface with a charged solvent spray, typically a mixture of methanol and water, at a shallow angle [264,265]. The charged droplets then impact the sample, causing the desorption of analyte molecules from the surface and helps transfer these molecules into the gas phase. The molecules that are desorbed into the gas phase are then ionised by the charged solvent droplets and directed towards the mass spectrometer for analysis via a capillary inlet [266]. This technique can be employed to image a wide variety of biomolecules, especially smaller molecules [267]. Moreover, unlike

MALDI, DESI-MSI causes little damage to the morphology of tissue as it does not use a high energy laser; thus, making it more compatible with post-MSI tissue staining for histological analysis [264]. However, compared to MALDI-MSI, the spatial resolution achieved with DESI-MSI is reduced as most studies achieve 50-200 μm [260]. This decrease in spatial resolution has been attributed to different factors such as solvent composition, capillary size, and gas flow rate [268]. Therefore, MSI experiments will require the use of different ionisation techniques depending on experimental aims.

Mass analysis

Typically, ions generated by MALDI and SIMS are analysed using a time-of-flight (TOF) mass analyser; operates on the principle that ions of different m/z will travel at different speeds, allowing the separation of ions [269]. TOF mass analysis begins with the acceleration of ions into a drift region, the ions then travel through this region without any significant forces acting on them. Once the ions have travelled through, they reach a detector and the time taken by the ions to travel from the ion source to the detector is measured [270,271]. The ions arriving at the detector are counted, and their arrival times are recorded with precision. The recorded flight times are converted into m/z values using the relationship between ion kinetic energy and m/z [272]. Lighter ions reach the detector faster than heavier ions, allowing for their separation and accurate determination of their m/z values [271,272]. This technique has a range of advantages which includes its quick speed making it suitable for high-throughput applications as well as its ability to handle a broad range of m/z values. However, compared to other analysers, TOF mass analysers have limited resolving power (less ability to distinguish between closely spaced ions) and lower mass accuracy in parts-per million (ppm) [273,274]. Moreover, DESI-MSI is often coupled with an Orbitrap mass analyser; high resolution mass analyser for accurate determination of m/z of ions, known for its exceptional resolving power and mass accuracy [275]. The Orbitrap analyser operates based on the principles of harmonic oscillation and Fourier transform to determine the m/z of ions [275]. In the orbitrap, ions are trapped between two sets of electrodes (a central spindle electrode and an outer barrel-like electrode). The spindle electrode has a central metal spindle surrounded by an insulating material, creating an electrostatic trap [276,277]. A

voltage is then applied to the spindle electrode to create an electric field. The trapped ions experience a combination of radial and axial oscillations in response, which creates a current in the outer electrodes [277,278]. This current is a function of ion density and position and is converted into a signal that is subjected to a Fourier transformation, which is then converted into m/z [279]. Despite Orbitrap analysers being high resolving and accurate, they have a much slower scan speed compared to most TOF analysers [277]. Therefore, TOF analysers are more commonly used for high throughput omics studies, whereas Orbitrap analysers are commonly used for quantitative analysis and biomarker discovery [273,277].

Spatial mapping and compatibility with histological techniques

The information generated by mass analysers can then be used to generate mass spectra from each pixel [277,279]. Computational software such as SCiLS (available commercially from Bruker) are able to select an individual m/z value and the intensity of the m/z from each pixels spectrum [280]. The intensities from each pixel are the combined to produce a heat map image depicting the relative distribution of the m/z across the samples surface [281]. Therefore, studies are able to provide localisation information to their metabolomic, proteomic, or lipidomic research. This spatial information has been of particular use when comparing the metabolic signature of tumours to surrounding healthy tissue [282]. MSI can also be used to aid pathologists and clinicians in the diagnosis and management of diseases such as cancer, especially when combined with histological staining [283]. Haematoxylin and eosin (H&E) staining can distinguish nucleic acids from proteins with blue and red colouring, respectively [284]. This allows the visualisation of differences between cells, providing information on tissue morphology and cell structure which pathologists can use to determine different disease states [285]. As some MSI techniques are non-destructive, H&E staining can be carried out on the same slide and software including SCiLS allows the H&E stain to be co-registered with the MSI image. This allows studies to focus their research on specific regions of interest (e.g. tumour vs healthy) and make direct metabolic comparisons between the regions [172,286].

Identification of molecules

The identity of *m/z* values can be putatively determined based on their intact mass by matching the accurate mass to a database of known molecules within a certain mass error range [287]. However, to fully identify a specific *m/z* value, tandem MS (MSMS) must be used. This technique provides more detailed structural information about a molecule compared to MS [288]. A sample undergoes two successive stages of mass analysis: the first stage requires the selection of a precursor ion which is then fragmented into smaller fragments using mechanisms such as collision-induced dissociation (CID) [289]. The second stage involves the resulting fragment ions being directed into a mass analyser, producing a pattern of fragment ions that are highly informative and can be used to deduce the structure of the molecule [290,291]. Specialised software and databases can then be used to match the experimental fragment ions to known or predicted molecular structures, allowing for a more accurate identification [291,292]. Therefore, the identification of molecules in MSI experiments can be time consuming and difficult, especially when identifying novel molecules [290].

1.4.2 MSI analysis

Untargeted and targeted MSI approaches can result in the generation of large data files with a high degree of dimensionality, due to the acquisition of complex information including spatial and relative abundance [172]. As the technology continues to improve spatial resolution, the size of data files continues to increase, making analysis more complex and challenging [293]. Therefore, software and analysis pipelines have advanced to efficiently analyse data without losing valuable information [172,293].

Data preprocessing

Before MSI data is analysed, it is essential that the data is processed to ensure accurate and efficient analysis [172]. The intensity peaks in mass spectra can be influenced by numerous technical factors such as sample preparation, matrix application and instrument sensitivity; thus, a crucial and expected preprocessing step is normalisation [294]. Normalisation removes systemic artifacts that can affect the mass spectra, which improves variance allowing for more reliable comparisons [295]. The most commonly applied normalisation technique is total ion current (TIC); intensity of all *m/z* values present in spectrum are

summed (TIC) and then original intensity value is divided by the TIC [172,293]. This means that analytes are scaled up or down using a well-matched reference ion, by assuming that that there are a comparable number of signals in each spectrum, allowing for signal variability correction [296]. This method has successfully been used to conduct relative quantification between control and disease tissue sections by correcting the signal of endogenous molecules [297]. However, this method does have limitations and is prone to bias as additional tissue microenvironment factors such as protein binding of target molecules and differences within cell densities are not considered [294]. TIC normalisation is also impractical for untargeted analysis as analytes with different chemical structures have different ablation and ionisation efficiencies; thus, normalising to an internal standard is not accurate [294,298]. In circumstances where comparisons between spectra with a different number of data points are made, root mean squared (RMS) normalisation is used instead of TIC [299]. RMS calculates the squared intensity value for each analyte, followed by determining the square root of the mean squared intensity value and finally dividing the original intensity value by the mean square root [300]. Therefore, each intensity is divided by a consistent measure of the data's variability and adjusts the data to reduce variations in signal intensity that are unrelated to the biological question being investigated [296,300]. Another method for normalisation includes normalisation to an endogenous molecule that is expected to be homogenously expressed throughout the tissue and between experimental conditions [301]. Therefore, it is important to consider the characteristics of the experiment and data before choosing the appropriate normalisation method required before further analysis [172,300].

Biomarker identification

A receiver operator characteristic (ROC) curve analysis is a graphical representation that assesses the performance of a binary classification model by plotting the true positive rate (sensitivity) (y-axis) against the false positive rate (specificity) (x-axis) at various thresholds [302]. This plot generates a ROC curve, and the area under the curve (AUC) quantifies the overall performance of a classifier [303]. The AUC ranges from 0 to 1, indicating accuracy; AUC of 0.5 indicated random performance, while AUC between 0.7-0.8 are generally

considered acceptable, and 0.9 and above are considered to be good discrimination [304]. Therefore, classifiers with a higher AUC generally perform better at distinguishing between two class (e.g. disease vs control) [304]. Hence, ROC analysis is common in MSI as it can be used to discriminate the ability of a specific m/z to classify groups of interest, making it a useful tool in biomarker discovery [302,304]. However, it is rare that a single biomarker is able to correctly classify groups with a high enough AUC acceptable for clinical diagnostics [305]. [165–167]

1.4.3 Imaging mass cytometry overview

Imaging mass cytometry (IMC) is a powerful multiplex tool for studying complex tissue morphology and function and was developed by Bernd Bodenmiller's group in 2014. The development of the technique was based on suspension-based single-cell mass cytometry (cytometry time of flight (CyTOF) and combines ultraviolet ablation of antibody-stained tissue on slides (Hyperion Tissue Imager, Standard BioTools) [306]. In conventional CyTOF, staining antibodies are coupled with fluorophores allowing for detection and quantification; however, antibodies used for IMC are coupled with stable metal isotopes, mostly from the lanthanide series [307]. Therefore, studies have successfully stained tissue with up to 40 different antibodies without interference from autofluorescence or management of spectral overlap [308]. After staining, the tissue is ablated with a laser over a selected region of interest (ROI) to create 1 µm spot size, resulting in plumes of aerosolised, atomised, and ionised tissue which is carried by helium gas into the TOF mass spectrometer to analyse the m/z of isotopes [307,308]. The tissue is analysed spot-by-spot as the tissue section moves under the laser at an acquisition speed of approximately 100 minutes per 1 mm² of tissue [309]. The isotope abundance gathered from each 1 µm spot can then be mapped to the original co-ordinates as image pixels to produce a high dimensional image [310].
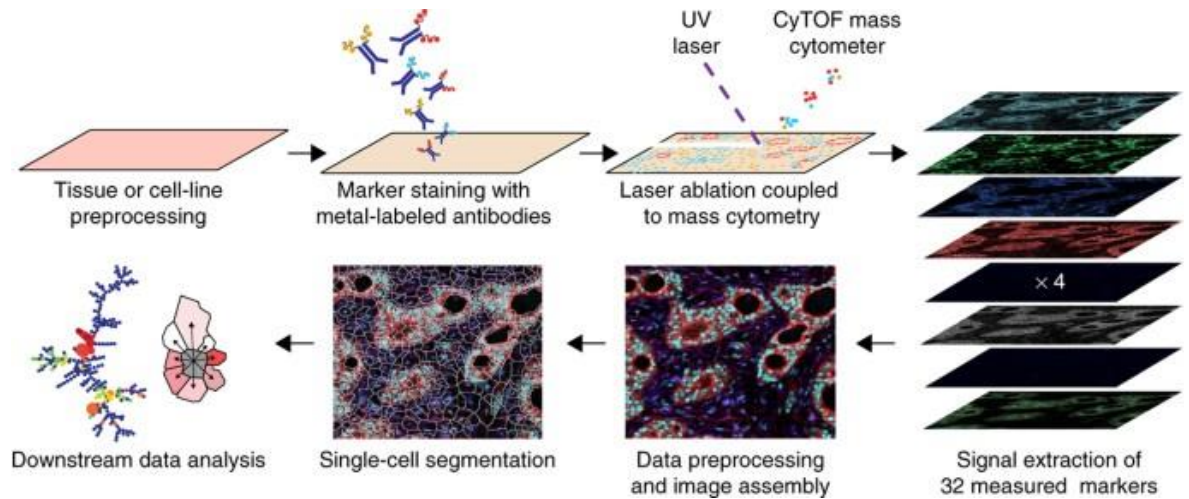
Figure 1.4.2. Visual generic workflow for IMC experimentation and analysis. Tissue sectioned on slide and stained with up to 40 different antibodies conjugated to stable metal isotopes. Region of interest ablated with laser and plumes of ionised isotopes detected by time-of-flight mass spectrometer. Isotope abundance mapped back to original co-ordinates to produce high dimensional image. Multiplex information used for cell segmentation, annotation, and downstream analysis [309].

This allows for the localisation of proteins within various cell compartments (e.g nucleus, cytoplasm) and has been applied to various biological research settings allowing the discovery of novel cell phenotypes, cell-cell interactions, and immune cell infiltration [311]. This multiplexed spatial information also enables a variety of distinct cell types to be simultaneously analysed within their native microenvironment. The microenvironment consists of a complex matrix of fluids, proteins and cells which provide signals that influence cell-specific phenotypes and function (e.g. subsets of T cells) within an organ, resulting in either health or disease [312,313]. Research has highlighted the role of the tumour microenvironment in disease pathogenesis and tumour function. For example, IMC uncovered tumours from melanoma patients respond differently to anti-programmed cell death-1 (anti-PD-1) therapy, depending on tumour microenvironment archetypes [314]. Thus, IMC has been used to further our understanding of disease pathology, including cancer, by providing spatial data for a large number of cell-based parameters at a subcellular resolution [311,315].

1.4.4 Image processing and data analysis

Due to its wide applications and usefulness in clinical research, IMC is increasing in popularity; however, a key bottleneck in IMC is the complex nature of analysing up to 40 parameters with added spatial information [307,308]. Data

analysis can be performed from a morphological point of view as software such as MCD viewer (Standard BioTools) allow image pixel coordinates and signal intensities from the different metal isotope markers to be visualised [307]. The raw data files observed in MCD viewer can then be converted into multichannel .tiff files, suitable for downstream bioinformatics analysis but requires careful processing and efficient pipelines [316]. One of the first and potentially the most crucial step in IMC analysis is single-cell segmentation: tissue is stained with a DNA intercalator dye prior to imaging, allowing the identification of nuclei which helps identify the boundary of individual cells [317]. Software such as CellProfiler and HALO (Indica Labs) are often used for single-cell segmentation, with the users being able to adjust inputs such as size filters, smoothing and thresholding [318]. However, this can often lead to errors, especially when segmenting tightly packed cells. For more accurate single-cell segmentation, supervised classifiers such as random forest classifier have been developed: humans outline single-cells to produce a set of annotated cells that can then be used to train machine learning algorithms [317,319]. Machine learning algorithms can also be used to segment certain areas and pixels in the image as defined objects, cells, subcellular compartments, or morphological regions (e.g tumour vs non-tumour) [320]. This aspect of IMC is useful when exploring the role of specific tissue structures in the context of disease pathology [309].

As discussed, immune cells such as DCs, macrophages, T cells and B cells, as well as their subsets are differentially regulated in health and disease. Therefore, accurate and high throughput methods for annotating cell types, within the tissue compartments in which they reside, may improve our understanding of disease manifestations [321]. IMC allows cells and their subsets to be assigned a phenotype based on the expression of specific markers (stained by antibodies), individual cell types can then be quantified and typically presented as 'percentage positive cells' [322]. This quantitative data can then be further analysed using multivariate and univariate methods, providing information on the immunological status of a sample[320,322]. As spatial information is also available many studies perform cellular neighbourhood analysis (localise regions with specific cell type composition), spatial context analysis (specific regions in the tissue where defined cell neighbourhoods interact), patch detection (detection of interconnected groups of similar cell classes), and cell-cell

interaction analysis [322-325]. Hence, cell segmentation and annotation provide a detailed map of cell populations, their spatial distribution, and molecular characteristics within a tissue sample. This information contributes to a deeper understanding of tissue biology, disease mechanisms and potential therapeutic targets; thus, IMC can answer key clinical and biological questions based on cellular dynamics involved in disease pathology [318,323,324].

1.5 Research aims

As evidenced above, microbes interact with the host and play an important role in IBD aetiology. Further studies have demonstrated microbe-host interactions involved in disease pathology are underpinned by small molecules. Metabolomics has helped identify molecules changed in IBD patients, however, their specific role in pathogenesis remains to be fully elucidated. Therefore, this study will investigate the effect specific microbial small molecules have on macrophages in the context of infection, as well as their effect on IECs function. This study will also aim to employ MSI to investigate molecular changes in the intestine as well as systemic tissue of mice, following infection with a pathobiont implicated in IBD. As this infection model is not a well-established model of IBD, MSI will also be used to investigate metabolic changes in the intestine and systemic sites in a reliable IBD model. This technique will also be coupled with IMC to determine the effect the metabolic microenvironment may have on immune cell phenotype and function. By combining these two spatial imaging technologies, this study aims to improve our understanding of the inflammatory pathways in the intestine as well as systemic sites, indicating potential biomarkers and therapeutic targets.

RA tends to cluster with IBD and both diseases share similar systemic complications such as NAFLD [236,326]. Therefore, this study will also combine MSI and IMC to investigate the impact intestinal and systemic metabolic shifts have on immune cell phenotype and function in an animal model of RA. This will help provide a better understanding of disease mechanisms, providing new insight into novel biomarkers and therapeutic targets that could be shared between the inflammatory conditions. Moreover, the technologies will also be applied to germ-free and specific pathogen free models to assesses metabolic and immune cell function, highlighting new mechanisms in microbe-host mediated physiology.

Revealing new microbial mechanisms may also be harnessed for therapeutic intervention strategies. Overall, identifying similarly changed molecules between different tissue types and diseases, may elucidate mechanistic connections between microbes, the host, and inflammatory responses.

Chapter 2 Materials and methods

2.1 *In vitro* experiments

2.1.1 Adherent-invasive *Escherichia coli* strain LF82 infection mouse model

Six to eight-week-old male C57BL/6 mice were orally administered 20mg of streptomycin in 100 µl of sterile water 24 hours (h) prior to infection. Mice were infected with $5×10^7$ colony-forming units (cfu) per millilitre (ml) of *E. coli* strain LF82lux (Wall group, University of Glasgow) in 100 µl of sterile phosphate buffered saline (PBS) by oral gavage or 100µl of sterile PBS for uninfected control mice. Mice were fed water that contained 20 mM of sodium propionate which was replaced daily or sterile water. Mice were euthanized fourteen days post infection, as previously described. Tissue was collected, processed, and used for DESI-MSI (full method described in Chapter 2.6). Approval for these procedures was given prior to their initiation by an internal University of Glasgow ethics committee and all procedures were carried out in accordance with the relevant guidelines and regulations as outlined by the U.K. Home Office (PPL 7008584).

2.1.2 Bacterial strains, molecules, and cell maintenance

Molecules used in this study were dissolved in water to make stocks and stored as aliquots at -20°C. Molecules were fully defrosted before use and diluted to reach desired working concentrations. The concentrations and purchasing information can be view in Table 2.1.1.

Table 2.1.1. Molecules used in study

Molecule	Low concentration	High concentration	Catalog	Company
L-Tryptophan	10 µm	30 µm	T0254	Sigma-Aldrich
Sodium butyrate	0.5 mM	2 mM	B5887	Sigma-Aldrich
Trimethylamine hydrochloride (TMA)	10 µm	30 µm	T72761	Sigma-Aldrich
3-methyl-4-(trimethylammonio)butanoate (3, 4-TMAB)	20 µm	1 mM	custom made	AstraZeneca
4-(trimethylammonio)pentanoate (4-TMAP)	20 µm	1 mM	custom made	AstraZeneca
Ursodeoxycholic acid (UDCA)	10 µm	30 µm	U5127	Sigma-Aldrich
Glycocholic acid hydrate (GCA)	250 nM	500 nM	G2878	Sigma-Aldrich
Sodium benzoate	10 µm	50 µm	B3420	Sigma-Aldrich

AIEC strain LF82 and intestinal commensal strain *E. coli* K-12 used *in vitro* were cultivated in lysogeny broth (LB) or on LB agar. Strains for infection were back-diluted 1:10 after overnight growth into RPMI-1640 (Sigma) supplemented with 3% foetal bovine serum (FBS) and 1% L-glutamine. Cultures were then grown at 37°C in a shaking incubator at 180 revolutions per minute (rpm) until an OD_{600} of 0.6 before further diluting to give a final multiplicity of infection (MOI) of 100. Bacterial supernatants used in this study were cultivated as described for infection but after reaching an OD_{600} of 0.6, cultures were incubated statically for a further 6 hours at 37°C. Cultures were then centrifuged at 400 g for 5 minutes before supernatants were collected and filter sterilised.

RAW 264.7 macrophages and human intestinal epithelial HCT-8 cells were purchased from the American Type Culture Collection (ATCC). RAW 264.7 macrophages were cultured in RPMI-1640 (Sigma) that was supplemented with 10% FBS, 1% L-glutamine, 1% penicillin/ streptomycin (P/S). HCT-8 cells were cultured in RPMI supplemented with 10% horse serum (HS), 1% P/S, 1% L-glutamine and 5 mM sodium pyruvate. Cells were incubated at 37°C, 5% CO_2 and passaged every 2-3 days up to a maximum of 30 times.

2.1.3 AIEC strain LF82 growth and survival in RAW 264.7 macrophages and TNF-α production

RAW 264.7 macrophages were seeded at a density of $2x10^5$ in RPMI-1640 (Sigma Aldrich) supplemented with 3% FBS and 1% L-glutamine, and incubated at 37°C, 5% CO_2 for 5-6 hours. The macrophages were then activated with 100 ng/ml of LPS and supplemented with the appropriate metabolite concentration before incubating for 18 hours. Cells were then inoculated (MOI 100) and infection left

to proceed for 1 h at 37°C, 5% CO_2. To determine bacterial invasion, extracellular bacteria were washed away, and 50 µg/ml gentamycin sulphate was added for 1 h to kill any remaining cell-associated bacteria. Media was then replaced with RPMI supplemented with 3% FBS, 1% L-glutamine and the appropriate metabolite. Cells were then incubated for a further 24, 48 and 72 h. After infection, cells were harvested with 2% Triton X-100. Total bacteria were enumerated by counting colony forming units (CFUs) after overnight incubation at 37°C on agar plates. TNF-α production was then quantified in the supernatant using a sandwich ELISA Max Deluxe Set Mouse TNF-α (Biolegend, San Diego, CA), according to the manufacturers protocol. Absorbance was read at 450 nm and 570 nm using Fluostar Optima plate reader. The protein concentration of the cell lysate was also determined using a BCA assay (Thermo Scientific) according to manufacturer's protocol.

2.1.4 Transepithelial electrical resistance (TEER) and the production of pro-inflammatory cytokines in apical and basolateral regions

The surface of 0.3 cm^2, 3.0 µm pore sized Transwell™ inserts (Corning Incorporated Cell Culture Inserts) were coated with 50 µg/ml rat tail collagen (Invitrogen). After collagen coating, 1 ml of culture media was added to the basolateral side of a 24-well tissue culture plate and HCT-8 cells were seeded at a density of $2x10^5$ in 200 µl of media per insert. The cells were then cultured at 37°C, 5% CO_2. TEER was measured using a voltmeter (EVOM2) in triplicate for each well. Cells were grown until a monolayer had been achieved represented by TEER value above 300 Ω. TEER was calculated by multiplying the surface area of the transwell (in cm^2) by the NET resistance (which is the resistance measured minus the resistance of a blank transwell covered by cell culture media. The selected bacterial metabolites were then added at the chosen concentrations and TEER was measured over a time course up to 24 hours. The apical and basolateral supernatants were then collected and stored at -20°C for further use. The transwell inserts were transferred into a 24-well plate containing 0.1% TritonX-100 for lysis of HCT-8 monolayers. The concentration of IL-6, 1L-8 and IL-15 were quantified using individual ELISA kits from Biolegend (San Diego, CA), following manufacturer's protocol.

2.1.5 Quantification of epithelial barrier protein using Western blot

HCT-8 cells were seeded at a density of $2x10^5$ cells/ml into a 24-well cell culture plate and the appropriate metabolites were added. Cells were incubated at 37°C, 5% CO_2 for 48 h. Cells were then infected with LF82 at an MOI 100 for 3 h. Cells were washed with ice cold PBS twice and subsequently lysed for 10 minutes with radioimmunoprecipitation assay lysis buffer (RIPA) (ThermoFisher), supplemented with cOmplete™, Mini, EDTA-free Protease Inhibitor Cocktail (11836170001, Roche) and PhoSTOP™ (4906845001, Roche). Lysates were frozen at -80°C prior to use. Samples were defrosted, centrifuged at 15,000 RPM for 20 min and supernatants collected. Protein concentration in supernatants was measured using the BCA protein assay kit (ThermoFisher). Samples were then adjusted to 1 µg/µl by adding an appropriate volume of lysis buffer. NuPAGE™ LDS Sample Buffer (4X) (NP0007, ThermoFisher) was added, followed by heating at 95°C for 10 min and running on a 4-12% bis-tris protein gel (NP0321BOX, Invitrogen). The gel was transferred onto a nitrocellulose membrane via electrophoretic wet transfer. The membrane was then blocked in 5% Bovine serum albumin (BSA) (A9418, Sigma-Aldrich) in 0.1% PBS-Tween for 1 h at room temperature (RT). Blocking was followed by incubating membrane with 1:1000 dilution of primary antibody (ZO-1, ThermoFisher) and loading control (GAPDH, Cell Signalling Technology), overnight at 4°C. Membranes were washed and incubated with 1:10,000 dilution of HRP-conjugated secondary antibody at RT for 1 h. Membranes were developed by applying enhanced chemiluminescence (Pierce™ ECL 32106, ThermoFisher) and imaged with a C-DiGit blot scammer (LI-COR). Blots were set up into biological triplicates and bands were analysed using ImageJ software before Ordinary one-way ANOVA was performed on Graphpad prism. Antibodies used for Western blotting are listed in Table 2.1.2.

Table 2.1.2. Antibodies used for Western Blot

Antibody	Species	Catalog number	Company
ZO-1	Mouse monoclonal	339100	ThermoFisher Scientific
GAPDH	Rabbit monoclonal	2118	Cell Signalling Technology
Rabbit IgG (H+L) Secondary Antibody, HRP	Goat polyclonal	31460	ThermoFisher Scientific

2.1.6 Quantification of caspase-3/7 activity in HCT-8 cells

HCT-8 cells were seeded at a density of $2x10^5$ cells/ml into a 24-well cell culture plate and the appropriate metabolites were added. Cells were incubated at 37°C, 5% CO_2 for 24 h before supernatants were collected. Cells were then lysed using 0.1% TritonX-100 and stored at -20°C. Caspase 3/7 was then quantified as described in Chapter 2.9.

2.1.7 TMRE-Mitochondrial membrane potential analysis

Mitochondrial membrane potential was measured with a TMRE (tetramethylrhodamine ethyl ester) assay (abcam, 113852). HCT-8 cells were seeded at a density of $2x10^5$ cells/ml into a 96-well cell culture plate and the appropriate metabolites were added. Cells were the incubated for 24 h at 37°C, 5% CO_2. The positive control carbonyl cyanide-p-trifluoromethoxyphenylhydrazone (FCCP), an uncoupler of mitochondrial oxidative phosphorylation, was applied at a final concentration of 20 μM for 10 min before TMRE treatment. The cells were incubated with 1 μM TMRE for 30 min at 37°C, 5% CO_2, followed by washing twice with 100 μl of PBS containing 0.2% bovine serum albumin (BSA). A volume of 100μl of PBS containing 0.2% BSA was added to each well, and the fluorescence was measured in the FLUOstar Galaxy plate reader (BMG Labtechnologies GmbH, Offenburg, Germany) with excitation/emission: 544/590 nm. PBS containing 0.2% BSA was then removed from cells and replaced with 20 μl 0.1% TritonX-100 and cells were kept on ice before storing at -20°C. The protein concentration of the cell lysate was then determined using a BCA assay (Thermo Scientific) according to manufacturer's protocol. Data was normalised using sample protein concentration and shown as

TMRE fluorescence percentage of untreated cells. One-way ANOVA was performed using Graphpad prism (*p<0.05, **p<0.005 versus the control condition (cells without metabolites).

2.1.8 Quantification of LDH release as a feature of apoptosis

HCT-8 cells were seeded at a density of $2x10^5$ cells/ml into a 24-well cell culture plate and the appropriate metabolites were added. Cells were incubated at 37°C, 5% CO_2 for 24 h before supernatants were collected. Cells were then lysed using 0.1% TritonX-100 and stored at -20°C until use. LDH levels were then determined in cell supernatants using ab65393 LDH-Cytotoxicity Assay Kit following manufacturers' protocol (abcam, United Kingdom) described in Chapter 2.8.

2.2 Animal number, euthanasia and sample preparation

Animals throughout this study were euthanized by exposure to rising concentrations of CO_2 and death was confirmed using cervical dislocation. Specific mouse strains and disease model setup will be described in the appropriate forthcoming chapters. Sample collection and preparation was the same for each model used in this study. The entire colon was removed, and length was recorded, without stretching. Colon and ileum contents were gently removed, cut longitudinally along the mesenteric line and swissed rolled before embedding into hydropropyl-methylcellulose/ polyvinylpyrrolidone hydrogel (Sigma-Aldrich). Tissue was then snap frozen in a slurry of dry ice and isopropanol (Sigma-Aldrich) then rinsed in a slurry of dry ice and isopentane (Sigma-Aldrich) for 30 seconds. Frozen blocks were then left on dry ice to allow alcohol to evaporate before storing at -80°C. Other tissue types including liver, kidney, spleen, and lung were removed, frozen and stored as described. Ten micrometre (µM) thick sections were cut from frozen tissue blocks using a cryostat microtome (Thermo Scientific). Consecutive cutting of sections was repeated until enough sections were obtained, and thaw mounted onto superfrost non-conductive microscope slides for DESI-orbitrap-MSI. All slides were dried, vacuum packed and stored at −80°C following sectioning.

Power calculations were not used to determine the number of animals used in the studies. Power calculations need to have a biological change that can be used to determine a measure of significance. Mass spectrometry imaging measures at the cellular level that may not result in a measurable physiological change in the mice for weeks-months. Therefore, when imaging we only need enough mice to ensure we can do statistical analysis on our imaging, usual a minimum of 5. This reduces the number of animals needed and also their suffering as they don't undergo weeks-months of treatment.

2.3 Dextran Sodium Sulphate model

2.3.1 Reagents and animals

Dextran sodium sulphate (DSS) with a molecular weight of 40kDa was purchased from Alfa Aesar by Thermo Fisher Scientific. Male C57BL/6 mice (7-8 weeks old) were purchased from Envigo and housed in sterile cages. Mice received a standard laboratory chow diet. Approval for these procedures was given prior to their initiation by an internal University of Glasgow ethics committee and all procedures were carried out in accordance with the relevant guidelines and regulations as outlined by the U.K. Home Office (PPL P64BCA712).

2.3.2 Induction of colitis and evaluation of colitis clinical scores

Following a 7-day adaptation period, mice were randomly assigned to groups (5 mice per group), consisting of normal drinking water control, and drinking water supplemented with either 2% or 3% weight over volume (w/v) DSS for 7 days. The individual body weight of each animal was recorded daily during the experiment to monitor weight loss. Mice were observed daily for clinical symptoms of colitis, including stool consistency and gross bleeding. To evaluate colitis severity, the Disease Activity Index (DAI) was calculated as the sum of the scores for weight loss, stool consistency and gross bleeding (Table 2.3.1). Immediately before and at the end of the experiment, fresh faeces were sampled from each mouse for gut microbiota compositional analysis.

Table 2.3.1. Evaluation of disease activity index (DAI)

Score	Weight loss	Stool consistency	Blood
0	None	Normal	Negative

Score	Weight loss	Stool consistency	Blood
1	1–5%	Soft	Negative
2	6–10%	Soft	Positive
3	11–18%	Very soft; wet	Blood traces in stool visible
4	>18%	Watery diarrhoea	Gross rectal bleeding

2.3.3 Molecules and cells used for *in vitro* experiments

Human intestinal epithelial HCT-8 cells were purchased from the American Type Culture Collection (ATCC) and cultured in RPMI supplemented with 10% horse serum (HS), 1% P/S, 1% L-glutamine and 5 mM sodium pyruvate. Cells were incubated at 37°C, 5% CO_2 and passaged every 2-3 days up to a maximum of 30 times. HS was reduced to 3% during experimentation. HCT-8 cells were seeded at $2x10^5$ in 24-well plates and treated with the appropriate metabolites (Table 2.4). All molecules used in this study were prepared by dissolving in water, filter sterilised and diluted to the appropriate concentration in cell culture media. After treatment, cells were incubated at 37°C, 5% CO_2 for 72h. Supernatants and lysates were collected and stored followed by the quantification of LDH, caspase-3/7, and cytokine secretion, described in Chapter 2.8-2.10.

Table 2.4. Molecules of interest used in HCT-8 in vitro assays

Molecule	Low concentration	High concentration	Catalog	Company
cis-4,7,10,13,16,19-Docosahexaenoic acid	50 μM	100 μM	53171	Sigma-Aldrich
Creatine	50 μM	100 μM	C0780	Sigma-Aldrich
1-Methylnicotinamide	50 μM	100 μM	SML0704	Sigma-Aldrich

2.4 Collagen Induced Arthritis model

2.4.1 Animals and ethics

Male DBA/1 mice were purchased from Envigo, housed following institutional guidelines, and had to have a starting weight of at least 20 g. Approval for these procedures was given prior to the initiation by an internal University of Glasgow ethics committee and all procedures were carried out in accordance with the

relevant guidelines and regulations as outlined by the UK Home Office. Animal model was set up under Home Office Project Licensee, P8C60C865.

2.4.2 Induction and evaluation of CIA

CIA animal model used in this study was set up by Dr Miguel Pineda at the University of Glasgow. Mice were intradermally injected at the base of the tail with 100 μg of bovine type II collagen (CII) purchased from MD biosciences (in 0.05 M glacial acetic acid). Before injection CII was emulsified in complete Freund's adjuvant (CFA) purchased from MD Biosciences at a ratio of 1:1. Mice were re-immunized with 200 μg CII diluted in sterile PBS after 21 days. Mice were monitored for clinical symptoms of arthritis until the day of sacrifice (Day 35). Clinical severity was graded as follows: 0 = no inflammation; 1 = mild inflammation (one toe); 2 = medium inflammation (more than one toe); 3 = severe inflammation (entire joint inflamed); 4 = deformation leading to loss of limb function. Individual mouse arthritic score was then calculated by summing the scores recorded for each limb. The size of foot pads was measured (mm) using callipers and the length of the small intestine and colon (cm) was measured following dissection.

2.4.3 MSI, IMC and microbiome sequencing

The liver, lung, kidney, and spleen were collected from five CIA mice. The liver was collected for five naïve mice, while lung, kidney and spleen were collected from four naïve mice. The liver, spleen and lung were collected from four CFA mice, while the kidney was collected from three CFA mice.

2.4.4 Molecules and cells used for *in vitro* experiments

Human epithelial-like lung, A549 cells were purchased from the American Type Culture Collection (ATCC) and cultured in RPMI supplemented with 10% Fetal Bovine Serum (FBS), 1% P/S and 1% L-glutamine. Cells were incubated at 37°C, 5% CO_2 and passaged every 2-3 days up to a maximum of 30 times. FBS was reduced to 3% during experimentation. A549 cells were seeded at 2×10^5 in 24-well cell culture plates and left to adhere overnight, followed by treatment with increasing concentrations of LysoPC (18:0), which was dissolved in water and diluted in cell culture media (Table 2.5). Cells were then incubated at 37°C, 5%

CO_2 for 72h. Supernatants and lysates were collected and stored followed by the quantification of LDH, caspase-3/7, and cytokine secretion, described in Chapter 2.8-2.10.

Table 2.5. LysoPC (18:0) used to determine function in vitro

Molecule	Lowest concentration	Highest concentration	Catalog	Company
1-stearoyl-2-hydroxy-sn-glycero-3-phosphocholine (18:0 LysoPC)	100 nM	50 µM	855775P	Avanti

2.5 Germ free and Specific pathogen free model

2.5.1 Animals

6–8-week-old germ-free and specific pathogen free C57BL/6 mice were obtained from BSF Aquatics, Germ-free & Farm, Biological Service Facilities, University of Manchester. Germ free mice were of mixed population (n=4 female, n=2 male) and specific pathogen free were all female (n=6). During tissue preparation one SPF liver and lung sample was damaged, hence SPF group has 5 samples instead of 6.

2.5.2 Molecules and cells used for *in vitro* experiments

Human epithelial-like liver, HepG2 cells were purchased from the American Type Culture Collection (ATCC) and cultured in Eagle's Minimum Essential Medium (EMEM) (Sigma Aldrich) supplemented with 10% FBS, 1% P/S and 1% L-glutamine. Cells were incubated at 37°C, 5% CO_2 and passaged once a week up to a maximum of 20 times. FBS was reduced to 3% during experimentation. HepG2 cells were seeded at $2x10^5$ per well in 24-well plate and left to adhere overnight, followed by treatment with increasing concentrations of spermine and spermidine that were dissolved in water and diluted in cell culture media (Table 2.6). A liver cell line was used as both spermine, and spermidine were found in the liver. Supernatants and lysates were collected and stored followed by the quantification of LDH, caspase 3/7, and cytokine secretion, described in Chapter 2.8-2.10.

Table 2.6. Molecules used to determine function using in vitro assays

Molecule	Low concentration	High concentration	Catalog	Company

| Spermine | 50 µM | 100 µM | S3256 | Sigma-Aldrich |
| Spermidine | 50 µM | 100 µM | S0266 | Sigma-Aldrich |

2.6 Mass spectrometry imaging

2.6.1 DESI-MSI

Vacuum sealed slides were brought to room temperature (RT) before opening and all DESI-MSI experiments were set up as follows. DESI-MSI was performed on a Thermo Scientific Q-Exactive mass spectrometer equipped with an automated Prosolia 2D DESI source. A home-built DESI sprayer assembly was used with the spray tip positioned at 1.5 mm above the sample surface and at an angle of 75°. The distance between the sprayer to mass spectrometer inlet was 7 mm with a collection angle of 10°. The spray solvent was methanol/water (95:5 v/v), delivered at 1.5 µL/ min using a Dionex Ultimate 3000 pump (Thermo Scientific) at a spray voltage of 4.5 kV. Nitrogen was used as the nebulisation gas at a pressure of 7 bars. The Q-Exactive mass spectrometer was operated in positive ion and negative ion mode for all analysis using an S-Lens setting of 75 V. To acquire full mass spectra in the mass range of m/z 100–1000 a mass resolution of 70000, AGC) target of 5000000 and injection time of 150 ms was used. The .raw files were converted into mzML files using ProteoWizard msConvert and compiled into. imzML format using imzML converter version 1. Data sets were then converted into .slx files and analysed using SCiLS Lab MVS (version 2020b Premium 3D). All DESI data analysis is performed on root mean square (RMS) normalised data. Relative operating characteristic (ROC) curve analysis was performed to visualize the discrimination capability of an *m/z* value between two conditions. Area under the curve (AUC) values were generated by ROC analysis and cut off ranges were set at AUC>0.75 and AUC<0.25 to produce a list of *m/z* that might discriminate between conditions.

2.6.2 Multivariate and univariate analysis

Following ROC analysis, unsupervised and supervised multiclass classification and correlation were performed to visualise data and highlight molecules of interest. This multivariate analysis (MVA) was performed using SIMCA 17 software package

(Sartorius Stedim Biotech). Unsupervised principal component analysis (PCA) was applied to obtain on overview of data and detect any potential outliers. Subsequently, supervised partial least squares-discriminate analysis (PLS-DA) was used to identify specific changes amongst the groups. In PLS-DA, the *Y* variable was assigned to a defined class and corresponded to *X* variable. The model was generated after the data was autofitted according to R^2, Q^2, and classification performance. The quality of the model was validated using two parameters: R2Ycum (goodness of fit) and Q2cum (goodness of prediction). A threshold of >0.5 is widely accepted as good model classification to assure reliable predictive capabilities. Group separation is presented as score plots. Variable importance in projections (VIP) was used as a readout from PLS-DA that reflects the metabolites contribution to the model. VIP>1 indicates a higher percent variation in the model when a metabolite is included, whereas VIP<0.5 indicates that a metabolite plays a less important role. Following multivariate analysis, univariate analysis was performed in Graphpad prism (8.4.3). The measurement data were expressed as mean relative abundance ± SD. One-way ANOVA was used for comparing more than two groups and nonparametric t-test with 5% false discovery rate (FDR) correction was used for comparing two groups. Statistical significance was established as $p < 0.05$. Molecules with a VIP>1 and/ or a *p* value <0.05 were selected for further analysis.

2.6.3 Histological Staining

After DESI-MSI, tissue sections were fixed by submerging in 4% paraformaldehyde (PFA) for 10 minutes. Sections were then stained with Mayer's haematoxylin for 1 minute, before rinsing with tap water and submerging in acid alcohol. Tissue was then stained with eosin for 20 seconds, followed by rinsing with tap water and washed 3 times with absolute ethanol. Tissue sections were then submerged in xylene for 1 minute and cover slips applied using DPX mountant. Haematoxylin and eosin (H&E) stained tissue were imaged with an Aperio CS2 digital pathology scanner (Aperio Tech, Oxford, UK) at 40x and observed in ImageScope software (Aperio Tech).

2.7 Identification of metabolites

Molecules that were significantly altered in model organs were putatively identified using the Human Metabolome Database (HMDB) based on the mass accuracy provided by DESI MSI analysis. Searches were focused to mass (M) +/- most common adducts- negative mode included M-Hydrogen (H) and M+Chlorine (Cl), positive mode included M+H, M+Potassium (K) and M+Sodium (Na). To further identify molecules, DESI-Tandem MS (MSMS) was performed on tissue sections using Thermo Scientific Q-Exactive Orbitrap mass spectrometer. The data was acquired in either positive or negative mode with a spray voltage of 4.5kV, 70,000 resolution, maximum injection time of 1000 ms, and S-lens settings of 75 V. Precursor ion mass was set with a mass tolerance of 0.5 m/z and the mass range acquired was optimised for each analyte. Higher energy collision dissociation (HCD) with normalised collision energy (NCE) was used for fragmentation of ions during MSMS measurements ranging from 10 to 50 NCE. The identities of the ions were established based on the product ion spectra after comparing to spectra from previously published data using online platforms, HMDB and mzCloud (https://www.mzcloud.org/). Spectra of standards listed in table below was also acquired using DESI-MSMS and was compared to spectra from tissue, before using *in vitro* experimentation.

2.8 Metabolite enrichment analysis

Significantly changed molecules are shown as clustered heatmaps generated by the online MetaboAnalyst 5.0 platform (https://www.metaboanalyst.ca/). All available metabolite identities were used in MetaboAnalyst metabolite set enrichment analysis (MSEA). This tool detects major pathways that are associated with the metabolites present in the study. The applied library was the KEGG human metabolic pathways, comprising of 84 metabolite sets. The enrichment ratio was defined as the ratio of observed hits (detected metabolite) per pathway to the count expected by chance [327]. One-tailed p values were provided after adjusting for multiple testing, enrichment was considered significant when $p<0.05$.

2.9 Imaging mass cytometry

Tissue sections were fixed using 4% paraformaldehyde for 10 minutes at room temperature (RT). This was followed by tissue permeabilization with 1 x casein solution containing 0.1% Triton X-100 for 5 minutes at RT. Tissue were then incubated with blocking buffer (1x casein solution) for 30 minutes at RT inside a humidifier chamber. An antibody cocktail was prepared with the appropriate dilution of antibodies (Table 2.7) Tissues were the fully covered with antibody solution and incubated overnight in the humidifier chamber at 4°C. DNA Ir-Intercalator (Fluidgm) was diluted 1:400 using PBS and pipetted onto tissue, followed by a 30-minute incubation at RT. Tissue was washed in PBS for 5 minutes and repeated three times after each step of the protocol. After the final PBS wash, tissue was rinsed for 30 seconds in deionised water and left to dry at room temperature. Slides were then stored at RT before imaging.

Table 2.7 Immune cell marker antibodies, clone and tags used for all IMC staining.

Marker	Tag	Cell type	Clone	Tag2	Species	Dilution
ATPase	141	Membrane	EP1845Y	141Pr	Rabbit	V; 1:100
Cleaved caspase 3	142	Apoptosis	D3E9	142Nd	Rabbit	V; 1:25
Vimentin	143	Mesenchymal cells	D21H3	143Nd	Rabbit	V; 1:400
B220	144	B cells	RA3-6B2	144Nd	Rat	V; 1:25
CD68	145	Macrophages	FA-11	145Nd	Rat	V; 1:100
CD31	146			146Nd		V; 1:50
CD45	147	Myeloid cells	30-F11	147Sm	Rat	V; 1:100
PanCK	148	Epithelial cells	C11	148Nd	Mouse	V; 1:200
CD19	149	B cells	6D5	149Sm	Rat	V; 1:50
CD103	150	Dendritic cells	AF1990	150Nd	Goat	V; 1:25
Ly6G	151		1A8	151Eu	Rat	V; 1:50
PAKT	152		D9E	152Sm		V; 1:25
CD11c	153	Dendritic cells	D1V9Y	153Sm	Rabbit	V; 1:50
CD11b	154	Macrophage subset	M1/70	154Sm	Rat	V; 1:50
F4/80	155	Macrophages	CI:A3-1	155Gd	Rat	V; 1:50
CD163	156	M2 Macrophages	TNKUPJ	156Gd	Rat	V; 1:50
e cadherin	158	Epithelial cells	2.40E+11	158Gd	Rabbit	V; 1:100
Collagen 1	159		Poly	159 Tb		V; 1:200
glut1	160	Hypoxia	EPR3915	160Gd	Rabbit	V; 1:100
CD69	161		Poly	161Dy		V; 1:400
Ki67	162	Proliferation	B56	168Er	Mouse	V; 1:100
a-SMA	163	Fibroblast and pericyte phenotype	Polyclonal	163Dy	Rabbit	V; 1:400
lyve1	164	lymphatic vessels	poly	164Dy	Rabbit	V; 1:300

FOXP3	165	Treg	FJK-16s	165Ho	Rat	V; 1:25
epcam	166	Epithelial cells	G8.8	166Er	Rat	V; 1:900
NKp46	167	NK cells	Polyclonal	147Sm	Goat	V; 1:25
CD8	168	T cells (CD8+)	53-6.7	146Nd	Rat	V; 1:50
CD206	169	M2 Macrophages	CD68C2	169Tm	Rat	V; 1:50
arg1	170	M2 Macrophages	Poly	170Er	Sheep	V; 1:100
CD4	172	T cells (CD4+)	RM4-5	172Yb	Rat	V; 1:50
MHCII	174	Immune cells	M5/114.15.2	174Yb	Rat	V; 1:200
Granzyme B	176	Activated T cells	Polyclonal	176Yb	Goat	V; 1:300
Collagen IV	209	ECM	Polyclonal	209Bi	Rabbit	V; 1:100

Tissue was imaged using the Hyperion Imaging System (Fluidigm), rasterizing at 200Hz with an ablation energy of 5 dB. Laser was frequently tuned between imaging runs to ensure tissue was fully ablated without leaving scratches on the glass. Once acquisition was complete images were exported from MCDviewer as a 32-bit TIFF an imported into HALO image analysis platform (Indica Laboratories) for analysis. Using random forest machine learning tissue classifier module, colon and ileum were segmented into muscularis and mucosa, whilst liver and lung were analysed as whole tissue and vessels based on morphology and blood vessel cell marker, CD31. The Hiplex module was firstly used to segment the DNA intercalator from each cell with a proxy for the cytoplasm being 1 µM radius from the nucleus. Thresholds were then set to define positive cell staining for each marker. Phenotypes for cells of interest were defined using markers cited in current literature. Percentage positive cells and percentage positive phenotype cells were the defined within tissue regions. Statistical analysis was performed in Graphpad prism, comparisons made for the DSS and germ/ specific pathogen free model used T-tests and the CIA model used non parametric one-way ANOVA with Kruskal Wallis to compared groups to control (naïve). Differences between disease and control samples were considered significant when $p<0.05$.

Table 2.8. Immune cell phenotypes defined by specific markers in IMC analysis

Phenotype	Markers
Helper T cells	CD3 + CD4
Cytotoxic T cells	CD3 + CD8
Regulatory T cells (Tregs)	CD3 + CD4 + FOXP3
Activated Cytotoxic T cells	CD3 + CD8 + Granzyme B
Natural killer cell	NKp46

Activated natural killer cell	NKp46 + Granzyme B
B cells	B220 + CD19
Neutrophils	Ly6G + CD11b
Dendritic cells	CD11c + M1 MHCII
Antigen-presenting Dendritic cells	CD11c + MHCII + CD103
Macrophages	F4/80 + CD68 + CD11b (some overlap with dendritic cells)
M2c Macrophages	F4/80 + CD163
M2a/c Macrophages	F4/80 + Arg1
M2a Macrophages	F4/80 + CD206
M1 and M2b Macrophages	F4/80
M1 Macrophages	F4/80 + MHCII
Blood vessel	CD31
Pericyte (found around large blood vessels)	aSMA
Mesenchymal cell	Vimentin
Epithelial cell	E Cadherin + PanCK + EpCam
Proliferation	Ki67
PI3K signalling	pAKT
Hypoxia	GLUT1
Apoptosis	CC3

2.10   Microbiome sequencing and bioinformatic analysis

Fresh faecal samples were collected from the colon of individual mice after culling and immediately stored on dry ice in sterile Eppendorf's before storing at -80°C. DNA was extracted from samples using QIAamp PowerFecal Pro DNA Kit following manufacturer's protocol (Qiagen). Where possible, stool was collected at the beginning of the experiment and prepared as describe to determine how the microbiome changes over time. The quantity of extracted DNAs was measured using Qubit (Thermo Fisher Scientific) before storing at -20°C. Samples were analysed by Novogene for 16S rDNA Amplicon sequencing. PCR amplification of the bacterial 16s rRNA genes V3-V4 region was performed using a forward and reverse primer that were connected to barcodes for multiplexed sequencing. PCR products with the proper size were selected by 2% agarose gel electrophoresis. Equal amounts of PCR products were pooled, end-repaired, A-tailed, and further ligated with Illumina adapters. Libraries were then sequenced on a paired-end Illumina platform to generate 250bp paired-end raw reads.

Paired-end reads was assigned to samples based on their unique barcodes and truncated by cutting of the barcode and primer sequences. Paired-end reads were merged using FLASH (V1.2.7). Splicing sequences called raw tags were quality filtered under specific conditions according to Qiime (V1.7.0). Tags were compared with reference database (SILVA) using UCHIME algorithm to detect chimera sequences which were subsequently removed. Novogene performed analysis and plotted results using packages in R software (Version 2.15.3).

2.11 Quantification of LDH release as a feature of cell death

Cells were seeded at the appropriate density into 24-well cell culture plate and appropriate metabolites were added. Cells were incubated at 37°C, 5% CO_2 before supernatants were collected. Cells were then lysed using 0.1% TritonX-100 and stored at -20°C until use. LDH levels were then determined in cell supernatants using ab65393 LDH-Cytotoxicity Assay Kit following manufacturers' protocol (abcam, United Kingdom). Absorbance was read at 450 nm and at a reference wavelength of 650 nm using a Fluostar Optima plate reader. Cytotoxicity percentage was calculated by ((Test Sample – Low Control)/(High Control – Low Control) X 100). ANOVA was performed for each molecule versus the control condition (cells without treatment).

2.12 Quantification of caspase-3/7 activity as a feature of apoptosis

Cells were seeded into a 24-well cell culture plate and the appropriate metabolites were added (specific details found in relevant chapters). Cells were incubated at 37°C, 5% CO_2 and supernatants were collected. Cells were then lysed using 0.1% TritonX-100 and stored at -20°C. Caspase 3/7 was then quantified in the cell lysate using Apo-ONE® Homogeneous Caspase-3/7 Assay (Promega, Fisher scientific) according to manufacturer's protocol. The protein concentration of the cell lysate was also determined using a BCA protein assay kit (Thermo scientific), according to manufacturer's protocol. Assays were read on a FluoStar Optima plate reader (BMG Biotech). The data presented depicts caspase activity as relative fluorescence unit (RFU) per gram of protein. ANOVA

was performed for each molecule versus the control condition (cells without treatment).

2.13   Quantification of cytokine secretion

The secretion of TNF-α, IL-8, IL-6 and IL-15 was then quantified in cell supernatant using a sandwich ELISA Max Deluxe Set Human (Biolegend, San Diego, CA), according to the manufacturer's protocols. The secretion of IFN-γ was also quantified in cell supernatants using a sandwich mouse IFN- γ Duo Set ELISA (DY485-05, R&D systems). Standards and samples were diluted appropriately to obtain results within the stated detection levels. Absorbance was read at 450 nm and 570 nm using Fluostar Optima plate reader. The concentration of secreted cytokine was quantified based on kit standard calculations and results are shown as picogram (pg) per ml. The protein concentration of the cell lysate was also determined using a BCA assay (Thermo Scientific) according to manufacturer's protocol. ANOVA was performed for each molecule versus the control condition (cells without treatment).

2.14   Splenic analysis of immune cell activation and function

2.14.1   Cell preparation and culture

Spleens were collected from C5BL/6J mice and kept in in Hanks' Balanced Salt Solution (HBSS) on ice until further processing. Spleens were mechanically dissociated, homogenised, and passed through a 70 μM cell strained undergoing 2 washes (1400 rpm/ 400g, 4°C for 7 minutes) in MB (phosphate buffered saline (PBS) with 0.5% foetal calf serum (FCS) and 2 mM ethylenediaminetetraacetic acid (EDTA)). Red blood cells (RBC) were lysed with 1-2 ml of RBC lysis buffer for 3-5 minutes (Thermo). Following another washing step cells were counted and cultured in 96 well round-bottom plates at a final concentration of 2.5×10^6/ml in complete RPMI (RPMI with 10% FCS, 1% L-glutamine and 1% PenStrep). Cultured cell suspensions were stimulated with either recombinant mouse IL-12+IL-18 to activate innate and adaptive immune effector cells (both at 5ng/ml), IL-4 to activate humoral and adaptive immune cells (10ng/ml) or appropriately diluted metabolites (50 μM LysoPC (18:0), creatine and DHA, and 4 μM or 0.16 μM

spermidine). Cells were incubated overnight at 37°C, 5% CO_2. In the final 4 hours of culture brefeldin A and monensis (eBioscience) were added to block secretion of intracellular cytokines for detection by cytometry.

2.14.2   Generating isotypes and live/dead staining

Cell culture plates were centrifuged at 1400 rpm, 4°C for 7 minutes and supernatants were stored at -20°C until further use. Live/dead stain (eBioscience Fixable Viability Dye eF506) was diluted 1:1000 in clean PBS and incubated with cells for 20 minutes at 4°C. Cells were vortexed to resuspend pellet before adding 150 µL MB to each well. Isotypes were generated by taking equal volumes of each sample from 1 condition and pooling together in spare wells.

2.14.3   Surface and internuclear staining

Cells were stained with the following antibodies to CD69 (clone H1.2F3, Biolegend), CD19 (clone 6D5, Biolegend), NK-1.1 (clone PK136, Biolegend), granzyme B (clone GB11, Biolegend), IFN-γ (clone XMG1.2, Biolegend), CD3 (clone 17A2, Biolegend), CD40 (clone 5C3, Biolegend), MHCII (clone M5/114.15.2, Biolegend) and CD45 (clone HI30, Biolegend). Surface stain was performed for 45-60 minutes at 4°C. In the final 5 minutes of staining, intracellular fixation buffer was added and washed with MB. For intracellular cytokine staining cells were first with 1x Fix/Perm buffer (eBioscience Foxp3 kit) for 1 hour on ice to. Intracellular stain was performed overnight at 4°C. Following washing the cell preparations were filtered on 70um nylon mesh and samples were analysed on flow cytometers (BD Celesta). Data was analysed using FlowJo software (Tristar).

Chapter 3 The role of microbial molecules in Inflammatory bowel disease

3.1 Introduction

3.1.1 Adherent-invasive Escherichia coli in inflammatory bowel disease

Escherichia coli (E. coli) is a Gram-negative, facultative anaerobe symbiont that constitutes approximately 0.1% of the gut microbiome in humans [328]. Despite their low abundance, *E. coli* are among the first bacterial colonisers of the infant GI tract and often establish lifelong colonization in adults [329]. During early life, *E. coli* members contribute to health by providing a strong stimulus for B cell maturation as well as structuring the intestinal epithelium to allow for further microbial colonisation [329,330]. Commensal *E. coli* continue to support host health by producing essential vitamin K2 and B-complex vitamins and outcompeting enteric pathogens for nutrients and space [331]. However, *E. coli* strains can acquire genes that confer a virulent phenotype, resulting in a broad range of intestinal and extraintestinal diseases [332]. The intestinal pathogenic *E. coli* have been divided into 6 categories: enterohaemorrhagic *E. coli* (EHEC), enteropathogenic *E. coli* (EPEC), enterotoxigenic *E. coli* (ETEC), enteroaggregative *E. coli* (EAEC), enteroinvasive *E. coli* (EIEC) and diffusely adherent *E. coli* (DAEC) [333]. However, another potential pathotype called adherent-invasive *E. coli* (AIEC) has been associated with inflammatory bowel disease (IBD), particularly Crohn's disease (CD) [334]. AIEC have been isolated from the ileal lesions of 36% CD patients compared to only 6% healthy controls [335]. AIEC, including the reference strain *E. coli* LF82, are closely related to numerous pathogenic strains such as meningitis-associated strain S88 and urinary-isolate strain UTI89 [336]. However, AIEC including LF82 do not possess typical virulence factor-encoding genes found in other pathogenic strains [337]. Therefore, their pathotype can only be identified by their phenotypic traits [338].

The first phenotypic trait displayed by AIEC is the ability to adhere and invade intestinal epithelial cells (IECs)[339]. IECs provide the intestine with a selectively permeable physical barrier via the connection of transmembrane proteins [340]. Furthermore, IECs secrete cytokines to recruit immune cells to the mucosa to

prevent robust proinflammatory response against commensals whilst maintaining the ability to clear pathogens [341]. However, IECs in CD patients overexpress the host receptor carcinoembryonic antigen-related cell-adhesion molecule 6 (CEACAM6) which interacts with type 1 pili (FimH) expressed by AIEC to mediate adherence [342]. This overexpression can be attributed to altered gene expression, however, CEACAM6 on the apical membrane of IECs can also be regulated by proinflammatory cytokines such as interferon gamma (IFN-γ) and tumour necrosis factor alpha (TNF-α) [343]. When AIEC molecularly interacts with IECs, the cells release both IFN-γ and TNF-α, thus it can be suggested AIEC indirectly upregulate expression of CEACAM6, furthering their ability to adhere to IECs and persist within the environment [342,343]. Furthermore, AIEC adhesion to IEC activates signalling pathways that release downstream proinflammatory cytokines such as IL-6, IL-8, and IL-15 [344]. These cytokines can then directly or indirectly alter the epithelial barrier by disrupting transmembrane proteins including tight junction (TJs) proteins, zonula occludens (ZO) [344,345]. This in turn leaves gaps between cells, increasing the permeability of the intestinal barrier allowing for uncontrolled immune cell infiltration, bacterial colonisation, and inflammation [342,346]. Therefore, evidence strongly supports a role for AIEC in IBD pathology by inducing proinflammatory cytokine release and increasing barrier permeability [342,344,346].

The second phenotypic trait of the AIEC pathotype is the ability to overcome the immune response in order to survive and replicate within macrophages [342]. Macrophages are innate immune cells that are recruited by infected IECs via cytokine signalling to ingest and phagocytose AIEC [347]. However, AIEC survive within macrophages by encoding mechanisms that protect against high temperature stress, acid stress and reactive oxygen species (ROS) that form the oxidative response to phagocytosed pathogens [348]. The bacteria can also replicate in large vacuoles within the macrophage, without inducing cell death [349]. Studies have shown that bacterial survival and replication stimulates macrophage aggregation and fusion to form multinucleated giant cells that can progress to granulomas [350]. Furthermore, AIEC infected macrophages secrete higher levels of TNF-α which in turn can expand CEACAM6 expression resulting in elevated AIEC attachment [351,352]. TNF-α can also activate a T-cell mediated inflammatory response, a hallmark of CD pathology [353]. As a result, anti-TNF-α

agents such as Inflixmab have been used as treatments with improved response and remission in patients [354] . Therefore, AIEC can be described as a key player in the progression of CD [342,348-350].

3.1.2 *E. coli* LF82 response to propionic acid

AIEC have been found in the gut microbiome of a small proportion of the healthy population [355]. However, in the context of CD, the pathobiont can adapt to outcompete other gut microbiome members and express their pathotypic traits [356]. This adaptation has been linked to the utilisation of mucosal metabolites that are enriched in the inflamed environment, such as ethanolamine [357]. Ethanolamine metabolism produces toxic by-products that can damage bacterial cells, however, AIEC have genes that encode microcompartments (MCPs) that ensure safe ethanolamine (EA, *eut* operon) utilization for growth and energy [357,358] . Furthermore, studies have found that microbially produced short chain fatty acids (SCFAs) including propionic acid (PA) are reduced in the mucosa of IBD patients due to a reduction in SCFA producing bacteria [188]. PA has been shown to have strong anti-inflammatory and antimicrobial properties, thus is used globally in both agriculture and medicine [359]. However, studies have found PA increases the transcription of the *eut* operon in AIEC, suggesting that PA can act as a signal for the bacteria to adapt and thrive in inflamed niches [358]. AIEC are also able to use PA as a sole carbon source to support growth [360]. Additionally, the utilisation of PA as a carbon source has been found to heighten the virulence traits associated with IBD, which includes increasing AIEC LF82 adherence and invasion of Caco-2 IECs, biofilm formation and acid tolerance [361]. AIEC metabolism of PA has also been found to increase TNF-α release from macrophages [362]. Furthermore, *in vivo* models have observed a 40% decrease in PA in the stool of mice following AIEC LF82 infection, suggesting AIEC are catabolizing PA and outcompeting SCFA producing bacteria [357,362]. Therefore, metabolic carbon sources can act as signals for AIEC pathogenic adaptation to increase survival and expansion, resulting in a proinflammatory cascade [360,361,363].

3.1.3 *E. coli* LF82 infection as a model for IBD

Animal studies have been used to investigate CD pathogenesis, however due to the multifaceted nature of the disease no model to date fully represents human disease [364]. Studies have shown that prolonged infection with AIEC induces immunopathological changes that are common in CD patients [337]. The changes include an increase in CEACAM receptors, crypt loss in IECs, elevated levels of IFN-γ and TNF-α within lesions found in the lamina propria as well as strong T cell and macrophage infiltration [337,339,365]. However, many long-term AIEC colonization models do not promote CD-like disease markers without the use of colitogenic chemicals such as dextran sodium sulphate (DSS), resulting in physical damage to the epithelial lining of intestine and colitis [366]. In addition, studies that use AIEC infection to induce a disease phenotype often use transgenic mice including human CEACAMs expressing mice [367]. Therefore, current AIEC models do not accurately reflect the pathogenic capabilities of AIEC to induce inflammation that is pathognomonic of human CD [337,364,366].

3.1.4 The role of microbial and host small molecules in IBD

Microbes in the gut benefit the host by providing defence against pathogens, promote immune maturation and synthesise nutrients [329]. Furthermore, the microbiome interacts with the host via the production of proteins, lipids and small bioactive metabolites that are critical signalling molecules [368]. However, bacterial dysbiosis and inflammation in CD patients alters the microbe-host metabolome, yet the molecular mechanisms underlying aetiology is still poorly understood [369]. Therefore, researchers are beginning to use metabolomics to identify molecular biomarkers that can discriminate between healthy individuals and inflammatory disease states [370]. As previously described, microbial metabolites such as bile acids, SCFAs, tryptophan, TMA and benzoate have can discriminate between healthy controls and IBD patients. However, further investigation is required to elucidate their biological function in relation to immune homeostasis and IBD pathology.

As evidenced above AIEC plays an important role in CD aetiology and exposure to PA enhances the virulent phenotype [339,361]. Further studies have demonstrated microbe-host interactions involved in disease pathology are underpinned by

small molecules and metabolites [357]. Therefore, this chapter aimed to employ MSI to investigate molecular changes caused by infection of mice with the AIEC type strain LF82 in a novel colitis mouse model where intestinal PA levels were supplemented with dietary PA. This would help further the understanding behind microbe-host interactions and identify new biomarkers of disease. Furthermore, metabolomics has helped identify molecules changed in IBD patients, however, their specific role in pathogenesis remains to be elucidated. Therefore, this study also aimed to investigate the effect specific small molecules have on macrophages in the context of AIEC infection, as well as their effect on IECs function.

3.2 Results

3.2.1 Gastrointestinal infection with *E. coli* LF82 and exposure to propionic acid induced intestinal metabolic shifts

Receiver operating characteristic (ROC) analysis did not identify any peaks that could discriminate between infected and uninfected ilea samples when mice were fed normal drinking water. However, ROC analysis identified 36 peaks that were discriminative between infected and uninfected ilea samples when the drinking water was supplemented with sodium propionate. The 36 peaks were selected for univariate statistical analysis, but no peak was found to be significantly changed between the groups. ROC analysis identified 43 discriminative peaks between infected and uninfected colon samples (normal drinking water). Univariate analysis of the 43 peaks did not find any to be significantly changed.

Lastly, ROC analysis identified 41 peaks that were discriminative between infected and uninfected colon samples when mice were fed propionic acid. Univariate analysis confirmed that 16 peaks were significantly changed between the groups and results are shown as heatmap images that indicate the relative abundance of the molecules *in situ* (Figure 3.2.1). The *m/z* for each significantly changed molecule was searched on the Human metabolome database (HMDB) to assign putative identities (Table 3.1). However, identities could only be putatively assigned to nine of the molecules. The putative identities of *m/z* 131.03, 179.05, 195.05, 199.03, 238.04, 279.03, 282.04, 160.13 and 170.03 were glutaric acid, alpha-D-glucose, D-mannonic acid, L-rhamnulose, adipolyglycine, pseudouridine, N2-succinylglutamic acid, 5-amino valeric acid betaine (5-AVAB) and beta-guanidinopropionic acid, respectively. The following molecules were decreased in infected colons compared to uninfected colons; glutaric acid (4.12-fold; *p*=0.012), alpha-D-glucose (5.36-fold; *p*=0.0068), D-mannonic acid (4.9-fold; *p*=0.0271), L-rhamnulose (3.04-fold; *p*=0.0408), adipolyglycine (7.65-fold; *p*=0.0253), pseudouridine (7.47-fold; *p*=0.0128), N2-succinylglutamic acid (16.9-fold; *p*=0.0108), 5-AVAB (2.87-fold; *p*=0.0290) and beta-guanidinopropionic acid (2.48-fold; *p*=0.0467).
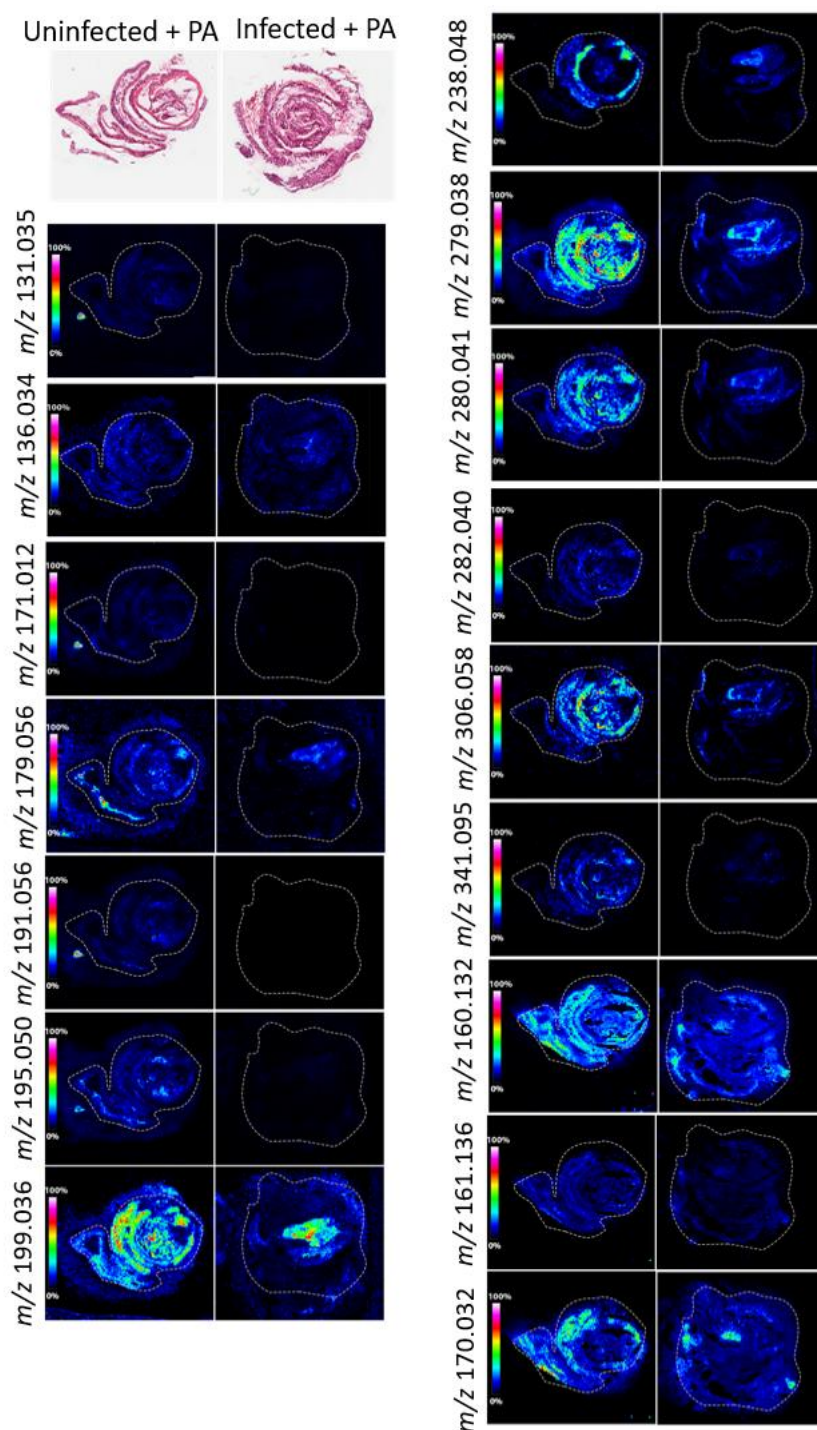
Figure 3.2.1 MSI heatmaps of small molecule changes in the colon during AIEC LF82 infection and propionic acid supplementation. MSI was performed on swiss rolled colon sections from uninfected and infected mice that had PA supplemented into the drinking water. SCiLS lab software was used to select tissue regions and ROC analysis picked peaks that are likely to discriminate between the two groups. MSI heatmaps show 16 molecules that univariate analysis (multiple T-test with FDR 5%) found to be significantly changed between the two groups and images are labelled with the *m/z*. The coloured scale bar shows the relative abundance of the molecule from 0% (dark blue) to 100% (pink).

Table 3.1. Putative identities or m/z of all significantly changed molecules found in the colon of uninfected and mice fed PA supplemented water
P-values were adjusted using false discovery rate (FDR) 5% to correct for multiple comparisons and molecules highlighted in grey are downregulated in infected compared to uninfected colons.

m/z	Putative compound name	adduct	adduct_type	delta(ppm)	Mean of uninfected (PA)	Mean of infected (PA)	p-value
131.0353	Glutaric acid	M-H	-	3	309.3	75.08	0.012064
136.0342			-		40.8	10.28	0.044782
171.012			-		528.9	3.052	0.038488
179.0566	alpha-D-Glucose	M-H	-	3	78.27	14.6	0.006836
191.0567			-		234.3	0.3009	0.010421
195.0508	D-Mannonic acid	M-H	-	1	236.9	48.33	0.027174
199.0361	L-Rhamnulose	M+Cl	-	9	259.9	85.38	0.040883
238.0486	Adipoylglycine	M+Cl	-	1	50.76	6.634	0.025325
279.0387	Pseudouridine	M+Cl	-	1	1578	211.1	0.01284
280.0416			-		99.74	9.57	0.012173
282.0404	N2-Succinylglutamic acid	M+Cl	-	7	27.25	1.609	0.010832
306.0581			-		83.61	8.115	0.024049
341.0958			-		33.46	1.379	0.004427
160.1325	5-amino valeric acid betaine	M+H	+	5	1793	624.3	0.021323
161.1365			+		137.3	34.37	0.029045
170.0324	Beta-Guanidinopropionic acid	M+K	+	1	1041	419.5	0.046788

3.2.2 Gastrointestinal infection with *E. coli* LF82 has a systemic metabolic effect

ROC analysis of the liver found 82 peaks to be discriminative between infected and uninfected groups. Univariate analysis found one of these peaks (*m/z* 574.4511) to be significantly changed (Fig. 3.3.2). The relative intensity of this molecule was reduced 1.73-fold (p=0.0027) in the liver of infected mice compared to uninfected mice. However, no putative identity can be made using the HMDB (Table 3.3.2). Moreover, supplementation with PA resulted in 66 discriminative peaks between infected and uninfected liver samples. Univariate analysis found two of these peaks to be significantly changed. The relative abundance of *m/z* 256.0596 and 258.05706 were increased 4.56-fold (p=0.00052) and 7.14-fold (p=0.0008) in the liver of infected mice compared to uninfected mice, respectively. These molecules were putatively identified as N-acetyl-D-glucosamine and 4-hydroxyphenylpropionylglycine, respectively (Figure 3.2.2).
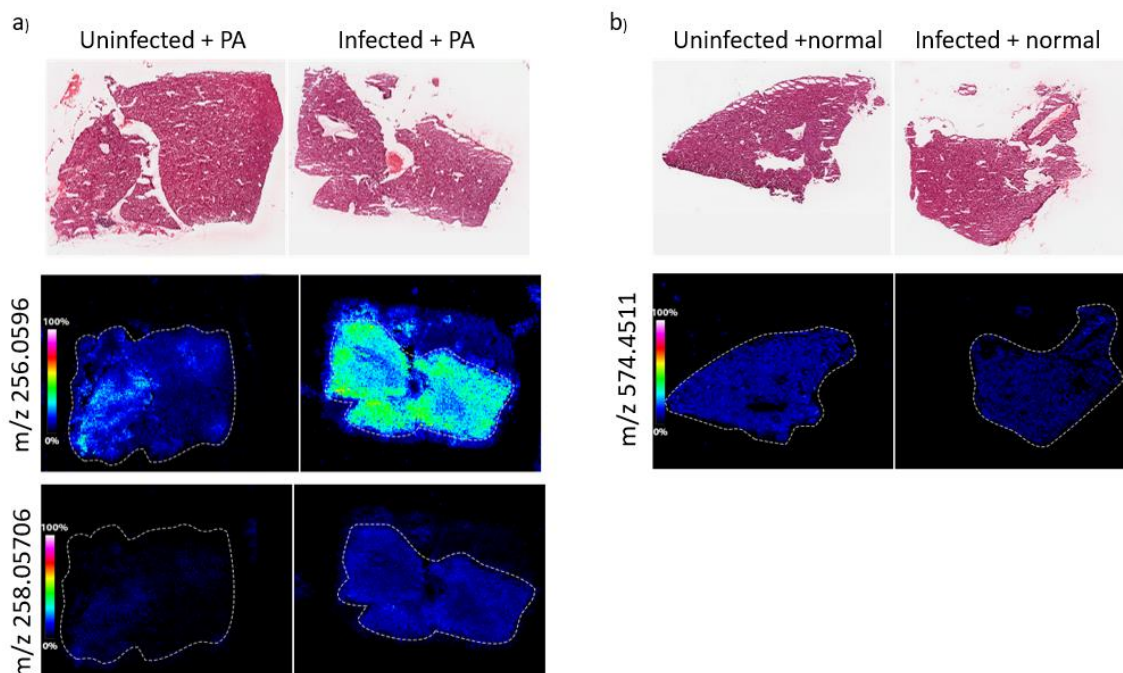
Figure 3.2.2 MSI heatmaps of small molecule changes in the liver during AIEC LF82 infection with a) propionic acid supplementation or b) normal drinking water.
MSI was performed on liver sections from uninfected and infected mice. SCiLS lab software was used to select tissue regions and ROC analysis picked peaks that are likely to discriminate between the groups. MSI heatmaps show 3 molecules that univariate analysis (multiple T-test with FDR 5%) found to be significantly changed between infected and uninfected groups and images are labelled with the *m/z*. The coloured scale bar shows the relative abundance of the molecule from 0% (dark blue) to 100% (pink).

Table 3.2.2. Putative identities or m/z of all significantly changes molecules found in the liver of uninfected and infected mice. Molecule *m/z* 574.45 was found in the normal drinking water model and *m/z* 256.06 and 258.05 were found in PA supplemented water model. *P*-values were adjusted using FDR 5% and molecules highlighted in grey are downregulated in infected compared to uninfected liver.

m/z	Putative compound name	adduct	adduct_type	delta(ppm)	Mean of uninfected	Mean of infected	p-value
574.45					37.05	21.34	0.0027
256.06	N-Acetyl-D-glucosamine	M+Cl	-	1	50.61	231.1	0.00052
258.06	4-hydroxyphenylpropionylglycine	M+Cl	-	12	19.87	142	0.000848

Furthermore, ROC analysis did not find any discriminative peaks in eye between infected and uninfected mice that were given normal drinking water. Supplementing the water with PA resulted in one peak discriminating between infected and uninfected eye tissue (Figure 3.2.3). The relative abundance of *m/z* 160.1342 was reduced 1.97-fold (*p*=0.0184) in the eye of infected compared to uninfected mice and was putatively identified as 5-amino valeric acid betaine (5-AVAB) using the HMDB (Figure 3.2.3).
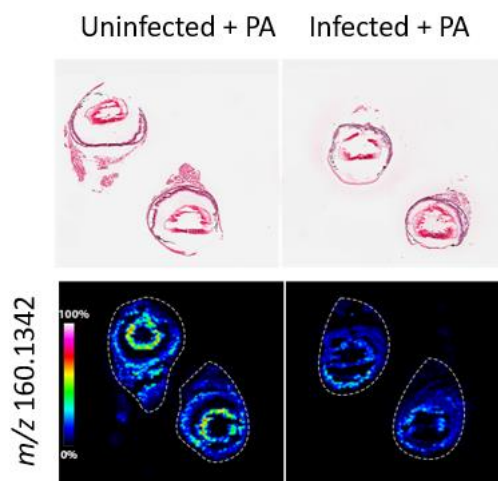
Uninfected + PA   Infected + PA

m/z 160.1342

m/z	Putative compound name	adduct	adduct_type	delta(ppm)	Mean of uninfected (PA)	Mean of infected (PA)	p-value
160.1343	5-amino valeric acid betaine	M+H	+	7	1913	970.7	0.0184

Figure 3.2.3 MSI heatmaps of small molecule changes in the liver during AIEC LF82 infection with propionic acid. MSI was performed on eye sections from uninfected and infected mice. SCiLS lab software was used to select tissue regions and ROC analysis picked peaks that are likely to discriminate between the groups. MSI heatmaps show 1 molecule that univariate analysis (multiple T-test with FDR 5%) found to be significantly changed between infected and uninfected groups and images are labelled with the *m/z*. The coloured scale bar shows the relative abundance of the molecule from 0% (dark blue) to 100% (pink). Putative identity of *m/z* 160.1342, mean of relative abundance and p-value shown as a table. *P*-value is highlighted in grey to indicated that the molecule is downregulated in infected compared to uninfected eyes.

3.2.3 Small molecules affect macrophage response to *E. coli* LF82 infection

This study investigated the effect that bacterial metabolites and small molecules have on RAW 264.7 macrophage function. Cells were stimulated with LPS and exposed to molecules at a range of concentrations prior to infection with *E. coli* LF82. Cells were lysed after infection for 24 h or 72 h (Fig. 1a-b & c-d, respectively) and colony forming units (CFU)/ml were measured. After 24-hour infection, treatment with molecules had no significant effect on macrophage bacterial clearance compared to cells without molecule exposure (Fig. 3.3.4a-b). However, 72-hour infection shows that treating macrophages with the lower concentration (250 nM) of GCA significantly increased CFU/ml, 3.3-fold, compared to infection alone (*p=0.0167) (Figure 3.2.4). To test whether GCA influences bacterial growth, a dose response growth curve was established under 5% CO_2 conditions. The results did not show any significant changes to LF82 growth in the presence of GCA (8.1.1). As GCA does not enhance bacterial

growth, it can be suggested that an increase in CFU/ml after 72h may be due to inhibited bacterial clearance by RAW 264.7 macrophages.
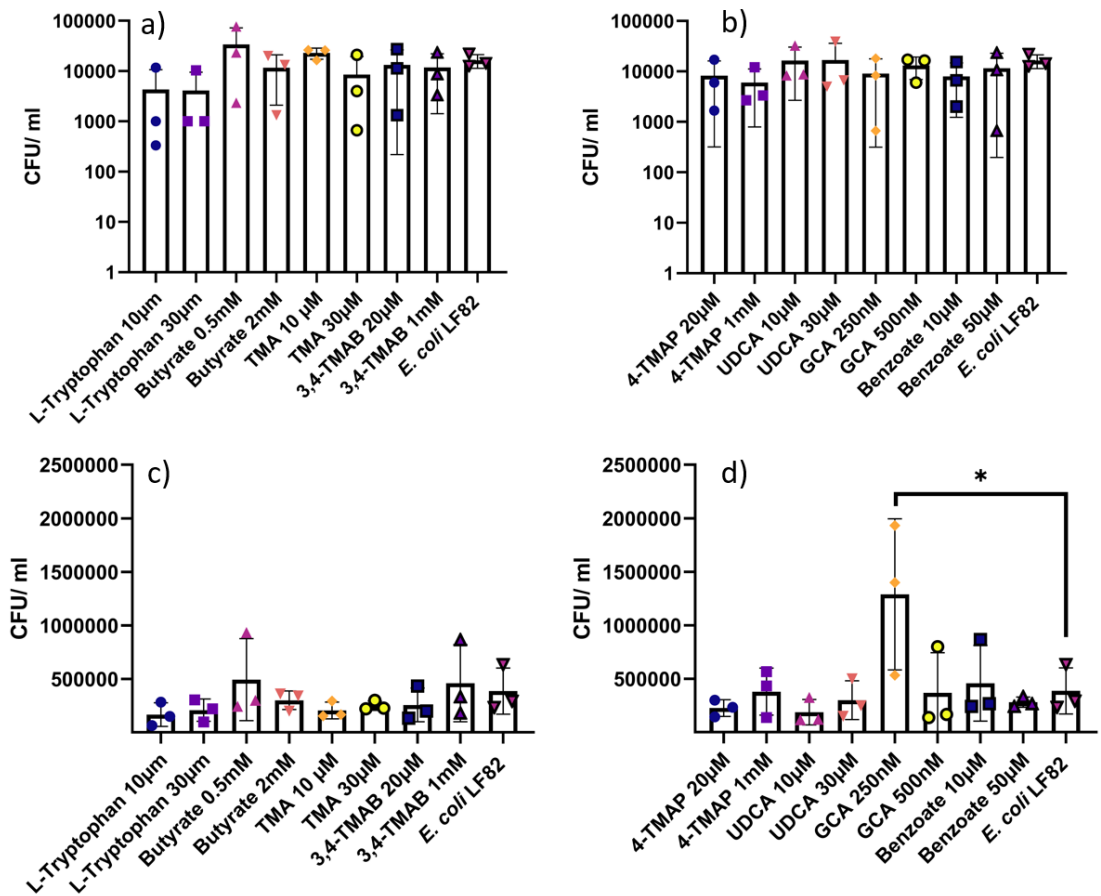
Figure 3.2.4 AIEC strain LF82 growth and survival in RAW 264.7 macrophages after a-b) 24h and c-d) 72h infection. Macrophages were exposed to various microbial metabolites at different physiologically relevant concentrations before infecting with *E. coli* LF82. Data are shown as the mean of three biological replicates ± standard deviation (SD) (error bars). One-way ANOVA was performed across all metabolites and *p<0.05 versus the control condition (infection without metabolites) was considered statistically significant.

The supernatants from this infection assay were collected and used to quantify the release of pro-inflammatory cytokine, TNF-α. It was hypothesised that only cells pre-treated with GCA would have altered levels of TNF-α since no other molecule affected bacterial clearance. However, after 24 h infection, treatment with 0.5 mM butyrate significantly increased TNF-α release, 1.5-fold (**p=0.0032), compared to infection without molecule exposure (Figure 3.2.5). Furthermore, 72 h infection resulted in TNF-α being significantly released into the supernatant when cells were treated with 2 mM butyrate (2.0-fold, *p*=0.0477), 20 µM 3M-4-TMAB (2.1-fold, *p*=0.0251), 250 & 500 nM GCA (2.3-fold, *p*=0.0049 & 0.0060 respectively) and 10 & 50 µM benzoate (2.4 & 2.1-fold,

p=0.0021 & 0.0204 respectively) (Figure 3.2.5). This indicates that RAW macrophages or LF82 respond specifically to individual molecules. Furthermore, an increase in TNF-α release suggests that small molecules have the potential to induce macrophages towards an inflammatory response.
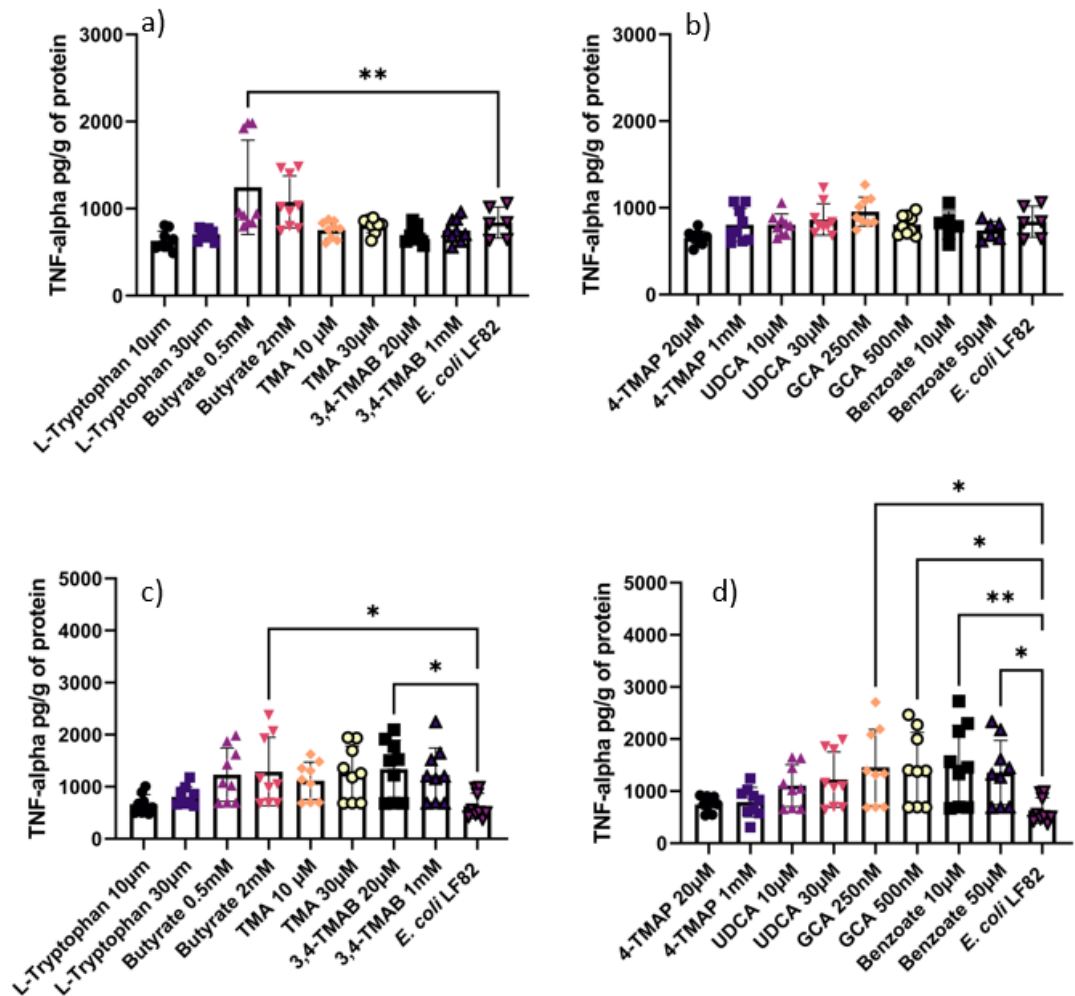
Figure 3.2.5 TNF-α released into supernatant of RAW 264.7 macrophages following exposure to metabolites and infection with AIEC strain LF82 for a-b) 24 h and c-d) 72 h. Macrophages were exposed to various microbial metabolites at different physiologically relevant concentrations before infecting with *E. coli* LF82. TNF-α was quantified in the cell supernatant and normalised to per gram of protein in cell lysate. Data is shown as the mean of 9 technical replicates ± standard deviation (SD) (error bars). One-way ANOVA was performed across all metabolites and *p<0.05, **p<0.01, ***p<0.001, ****p<0.0001 versus the control condition (infection without metabolites) was considered statistically significant.

3.2.4 Small molecules as cytotoxic stressors and inducers of apoptosis

This study also aimed to investigate the role specific small molecules have on human epithelial cells (HCT-8) *in vitro*. Firstly, an LDH assay was used to

determine whether the molecules were cytotoxic to HCT-8 cells. LDH is a stable cytoplasmic enzyme found in all cells and is released into the extracellular environment when the plasma membrane is damaged [371]. Therefore, the amount of LDH released can be used to calculate how cytotoxic exogenous stressors are in comparison to control cells. Figure 3.2.6 shows that most small molecules tested are not cytotoxic compared to the HCT-8 untreated control. The supernatant from an LF82 culture was also tested to investigate whether the pathobiont can produce small molecules that induce disease-like phenotypes *in vitro*. The supernatant of *E. coli* K-12 was also tested to investigate whether any changes induced by *E. coli* LF82 were specific to the strain or common across *E. coli* species. The results show that the supernatants from both *E. coli* strains are not cytotoxic to HCT-8 cells. However, compared to the control, 2 mM butyrate significantly increased the percentage cytotoxicity by 1.98-fold (*p=0.0320), whereas 1 mM of 4-TMAP significantly decreased percentage cytotoxicity 4.7-fold (*p=0.0456) (Figure 3.2.6).
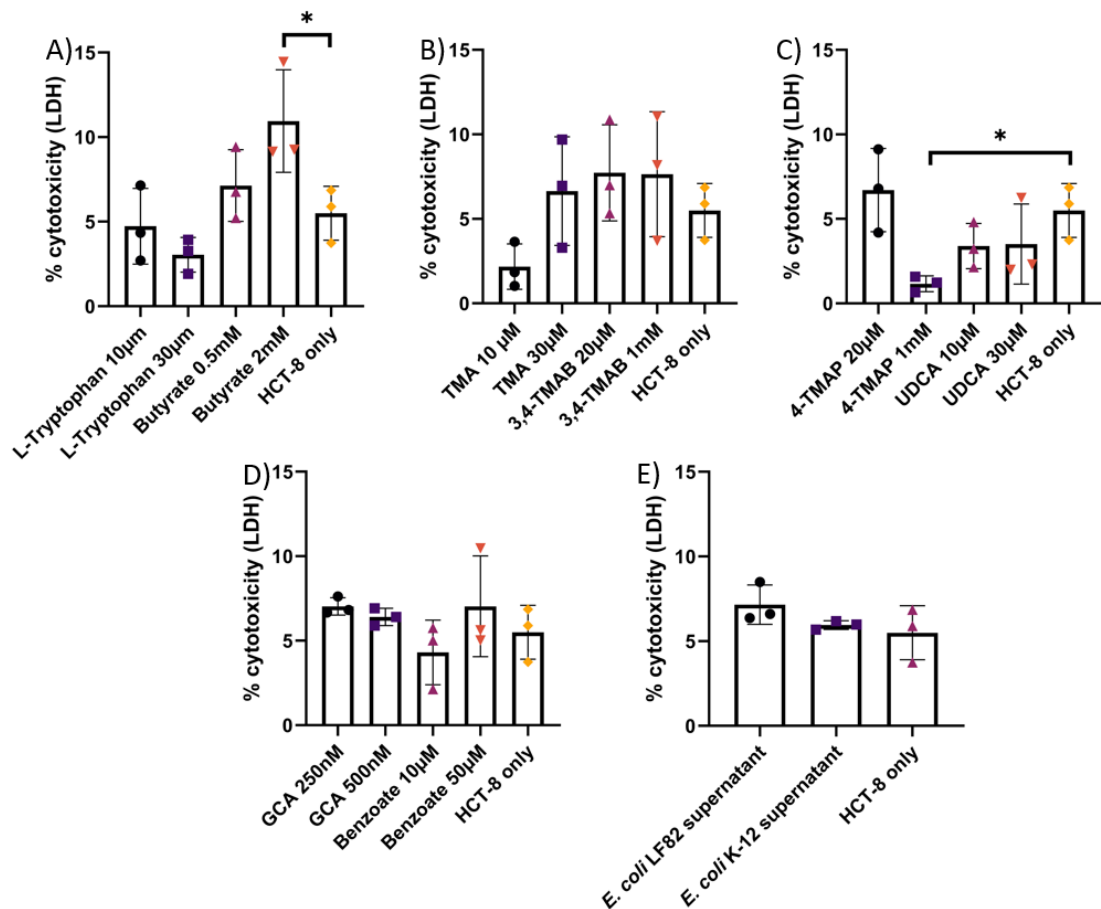
Figure 3.2.6 LDH release from treated HCT-8 cell indicates cytotoxic effect. HCT-8 cells were exposed to various microbial metabolites and the supernatants from *E. coli* LF82 and K-12 for 24 h. HCT-8 cells only and cells treated with 2% Triton-x were used as low and high LDH release

controls, respectively. The percentage of cytotoxicity was calculated as %=((measured absorbance of sample-low control)/(high control-low control))x100. Data are shown as the mean of three biological replicates ± standard deviation (SD) (error bars). One-way ANOVA was performed across all metabolites and *$p<0.05$, **$p<0.01$, ***$p<0.001$, ****$p<0.0001$ versus the control condition (cells without molecules) was considered statistically significant.

A caspase-3/7 assay was used to measure relative fluorescence unit (RFU) which is indicative of caspase levels. RFU were then normalised to gram of protein in samples to account for varying cell number. Figure 3.2.7 shows that most molecules, including bacterial supernatants do not significantly increase apoptosis. However, treating the cells with 2mM of butyrate significantly increased RFU/g of protein, 7.89-fold (****$p<0.0001$) indicating that the cells are undergoing an elevated level of apoptosis. Trypsin was included as a positive control and significantly increased RFU/g of protein 5.58-fold (****$p<0.0001$) (Figure 3.2.7). This indicates that butyrate may induce more cell apoptosis than trypsin, which supports the finding in Fig.3.2.6 that a higher concentration of butyrate is toxic to HCT-8 cells.
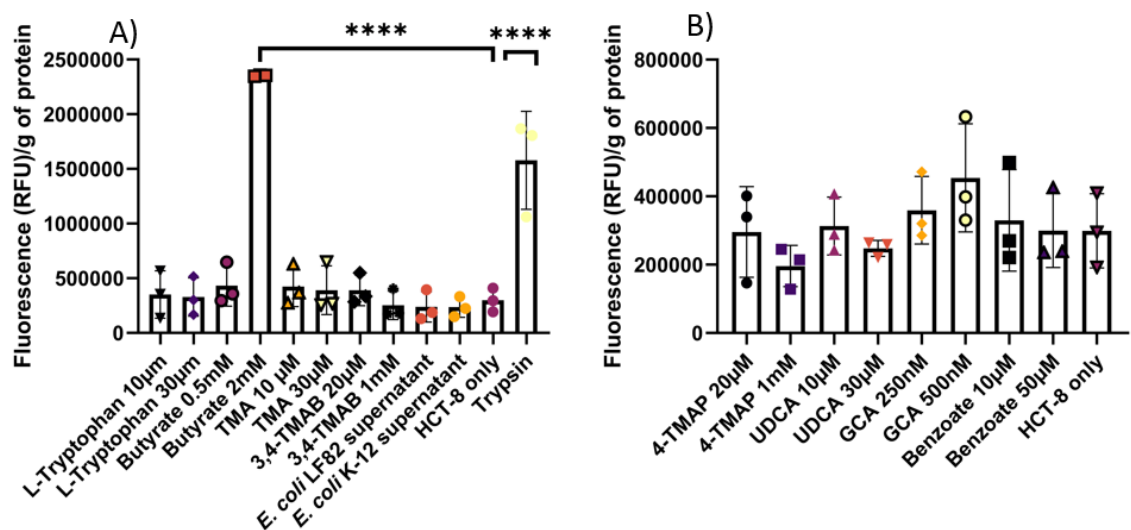
Figure 3.2.7 Caspase-3/7 release from HCT-8 cells. HCT-8 cells were exposed to various microbial metabolites and the supernatants from *E. coli* LF82 and K-12. Relative fluorescence units (RFU) were normalised to per gram of protein in the cell lysate. Data are shown as the mean of three biological replicates ± standard deviation (SD) (error bars). One-way ANOVA was performed across all metabolites and *$p<0.05$, **$p<0.01$, ***$p<0.001$, ****$p<0.0001$ versus the control condition (cells without molecules) was considered statistically significant.

3.2.5 Small molecules effect on intestinal barrier function

This study used Western blotting to quantify ZO-1 expression in HCT-8 cells, pre-treated with small molecules, followed by infection with *E. coli* LF82 (Figure 3.2.8). When compared to uninfected cells, infection without pre-treatment showed a significant decrease (2.21-fold) in ZO-1. However, the pre-treatment of cells with L-tryptophan, butyrate, TMA, UDCA, and benzoate significantly increased the expression of ZO-1 by up to 2.57-fold (p=0.0028), 3.10-fold (p=0.0007), 2.42-fold (p=0.0067) and 2.19-fold (p=0.0001), respectively, compared to infected cells without pre-treatment. There was no significant difference between expression level of HCT-8 control (non-treated, non-infected) and the test conditions previously stated, suggesting that these molecules may be able to enhance barrier function during infection.
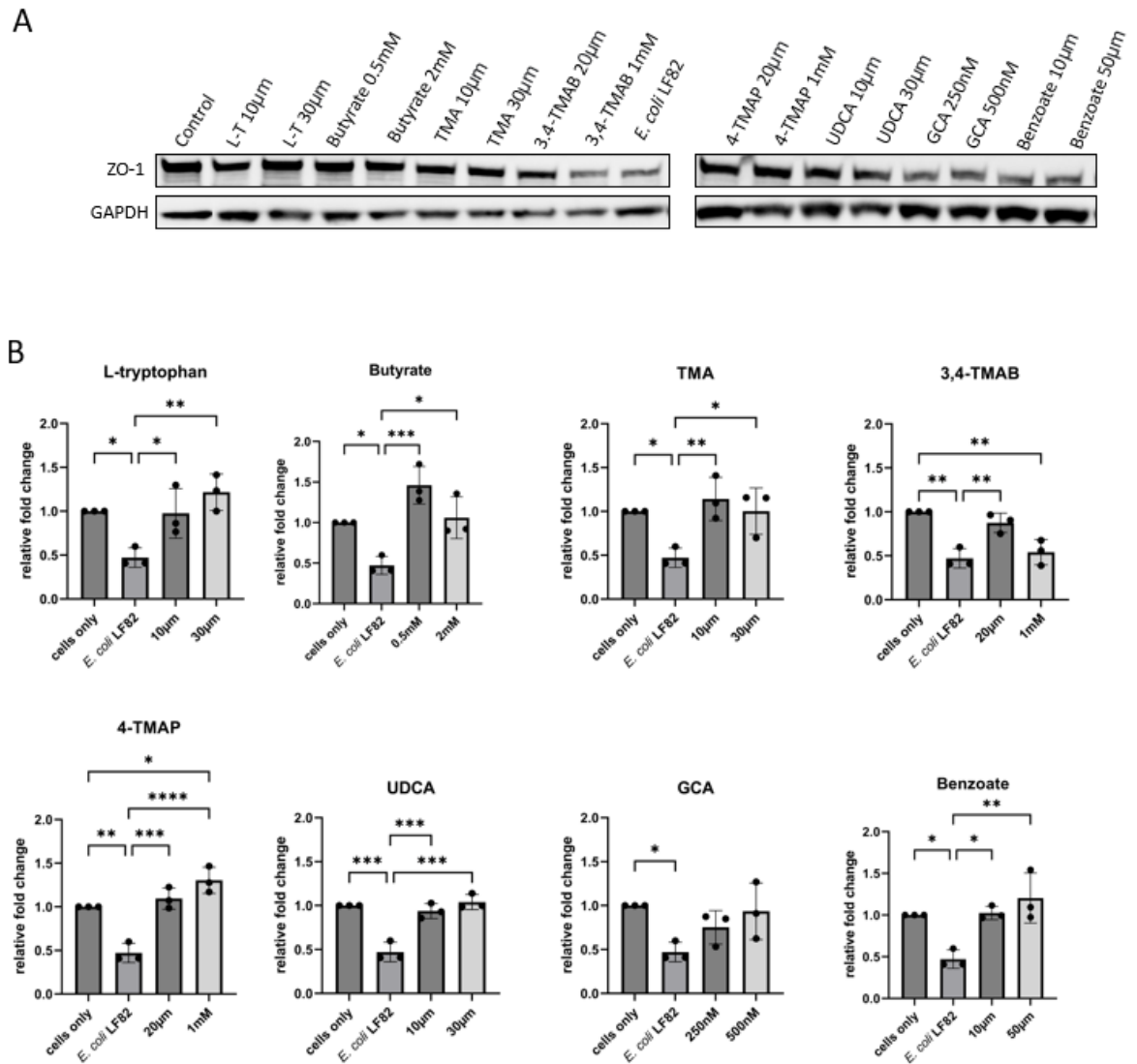
Figure 3.2.8 HCT-8 exposure to small molecules rescues ZO-1 expression following infection with E. coli LF82. A) Image shows ZO-1 and GAPDH expression (columns 1-18) in HCT-8 cells. Cells were pre-treated for 48 h with small molecules at different concentrations, followed by infection with *E. coli* LF82 for 3 h. Column 1 shows HCT-8 cells without pre-treatment or infection and column 10 shows infected HCT-8 without molecule pre-treatment. Immunoblotting was performed using anti-ZO1 (1:1000, ThermoFisher) and anti-GAPDH (1:1000, Cell Signalling). Blots were visualised with HRP-conjugated secondary antibodies (1:10,000) and developed using enhanced chemiluminescence (ECL). B) Graphs are labelled with the molecule that was used to pre-treat HCT-8 cells before infection and show the relative fold change in ZO-1 expression compared to control (HCT-8 cells without treatment or infection). Data shown represents three biological replicates and ImageJ was used for analysis. One-way ANOVA was performed to test significance by comparing all conditions using Graphpad Prism. $*p<0.05$, $**p<0.01$, $***p<0.001$, $****p<0.0001$ versus the control condition (infection without metabolites) was considered statistically significant.

Furthermore, pre-treatment of cells with 250 nM and 500 nM GCA, increased ZO-1 expression 1.4 ($p=0.3570$) and 1.9-fold ($p=0.0758$), respectively, compared to infection without pre-treatment. This increase was not statistically significant, however, there was also no significant change between pre-treatment infection

and HCT-8 control. Therefore, it can be suggested that GCA may protect barrier function but to a lesser extent than other test molecules. Exposing HCT-8 cells to 20 µM 3,4-TMAB significantly increased ZO-1 expression by 1.8-fold (p=0.0071), compared to infection alone. However, when the concentration of 3,4-TMAB is increased to 1 mM, expression is similar to infection without pre-treatment and reduced significantly by 2-fold compared to HCT-8 control (p=0.0033). This suggests that the molecule may be protective but only at low concentrations. The pre-treatment of cells with 4-TMAP significantly increases ZO-1 expression by up to 2.76-fold (p<0.0001) compared to infection alone. Additionally, when the concentration is increased to 1 mM, expression is also significantly increased 1.3-fold (p=0.0405), compared to HCT-8 control. This suggests that the molecule may enhance barrier function.

To investigate whether the changes in ZO-1 expression would translate to an enhanced or impaired barrier function, a transepithelial electrical resistance (TEER) *in vitro* model was developed. HCT-8 cells were grown in transwell inserts until a monolayer was formed (TEER value above 300 Ω). The selected molecules and *E. coli* supernatants were added into the apical compartment and the time-dependent dynamic changes of the barrier function was measured across a 24 h period. The results are shown as relative percentage TEER change compared to the control (0 h TEER reading). Figure 3.2.9 shows that most of the tested molecules do not significantly change barrier function across different time points, compared to control (HCT-8 cells only). However, the addition of 2 mM butyrate significantly increased barrier function 0.7-fold (p=0.0058) after 6 h, compared to HCT-8 only control (Fig. 3.2.9B). *E. coli* K-12 also significantly increased barrier function 0.77-fold (p=0.0376) and 0.74-fold (p=0.0223) after 3 h and 6 h, respectively, compared to the control (Fig. 3.3.9H). Trypsin was included as a positive control to strongly disrupt barrier function to ensure the model was working appropriately (data not shown).
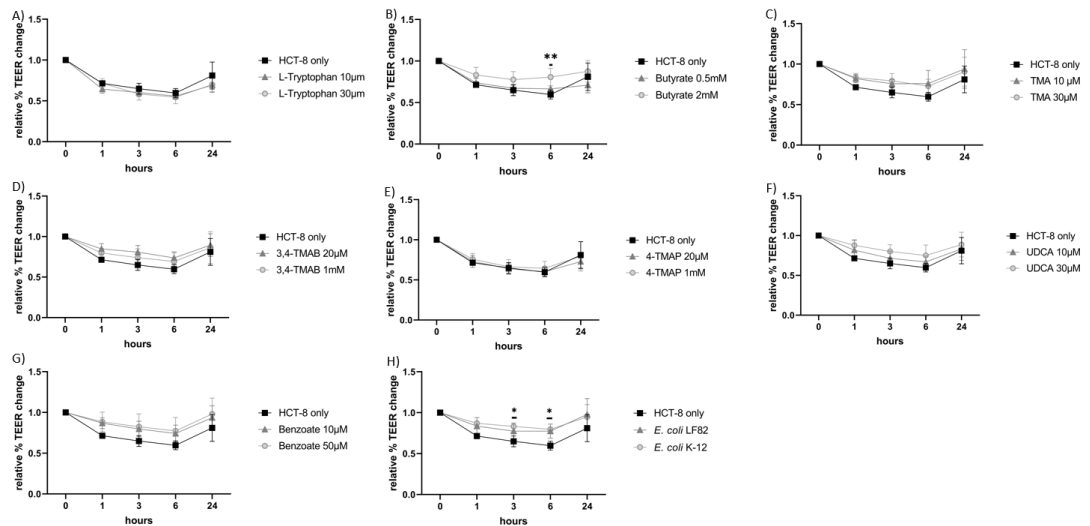
Figure 3.2.9 TEER as a model for HCT-8 barrier function in response to small molecules.
HCT-8 cells were cultured until sufficient monolayer was formed, indicated by a Ω above 300. Cells were treated with molecules and the supernatants from *E. coli* LF82 and K-12. TEER was measured over a 24 h period and results are shown as a relative percentage change compared to control (0 h TEER reading). Data shown is the mean of three biological replicates ± standard deviation (SD) (error bars). Two-way ANOVA was performed to test significance between HCT-8 only and different molecule concentrations at each time point. *$p<0.05$, **$p<0.01$, ***$p<0.001$, ****$p<0.0001$ versus the control condition (infection without metabolites) was considered statistically significant.

Supernatants collected from the basolateral and apical TEER compartments were screened for cytokine release using ELISA. Figure 3.2.10 shows the release of IL-6 pg/ml when cells were exposed to specific molecules at different concentrations. UDCA and 3,4-TMAB were the only molecules that increased IL-6 release into the basolateral compartment, compared to the control (8.2-fold $p=0.04$ and 8.6-fold $p=0.04$, respectively). IL-6 production in the apical compartment was significantly increased by up to 2.09-fold with L-tryptophan ($p=0.02$), 2.56-fold with butyrate ($p=0.002$), 2.41-fold with TMA ($p=0.0016$), 2.8-fold with 3,4-TMAB ($p=0.001$), 2-fold with 4-TMAP ($p=0.013$), 2.2-fold with UDCA ($p=0.0279$), 2.3-fold with GCA ($p=0.0457$) and 2.6-fold with benzoate ($p=0.0126$). However, the supernatants isolated from *E. coli* LF82 and K-12 did not increase IL-6 production in basolateral or apical compartments.
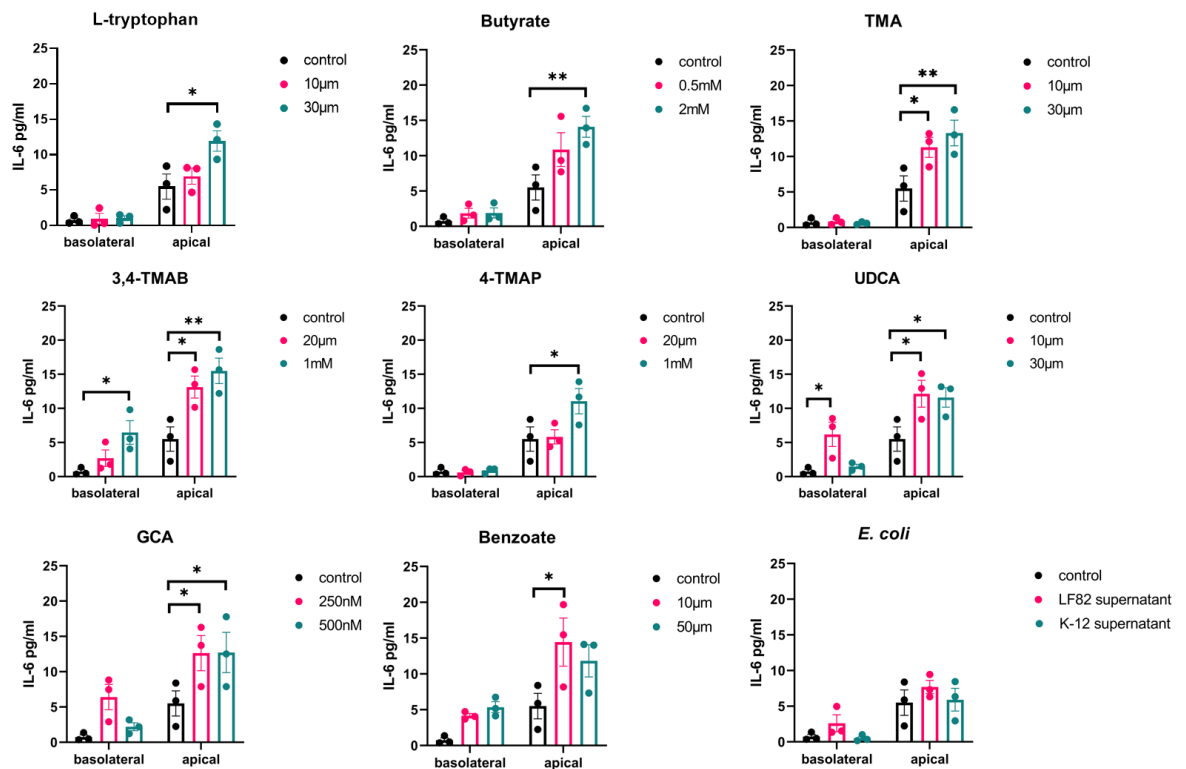
Figure 3.2.10 IL-6 release into apical and basolateral epithelial compartments. The apical side of the HCT-8 TEER barrier model was stimulated with either molecules or supernatant from *E. coli* strains LF82 and K-12 cultures. After 24 h the supernatants were collected from the apical and basolateral epithelial compartments, separately. IL-6 was quantified using ELISA and the data is shown as the mean of 3 biological replicates ± standard error of the mean (SEM) (error bars). Two-way ANOVA was performed for each molecule versus the control condition (cells without treatment). *$p<0.05$, **$p<0.01$, ***$p<0.001$, ****$p<0.0001$ is considered statistically significant.

Figure 3.2.11 shows the release of IL-15 pg/ml when cells were exposed to specific molecules at different concentrations. IL-15 production in the basolateral compartment was significantly increased by up to 3.2-fold with Butyrate ($p=0.02$), 2.27-fold with 3,4-TMAB ($P=0.0085$), 4.12-fold with Benzoate ($p=0.0003$) and 2.2-fold with *E. coli* LF82 supernatant ($p=0.0075$). However, exposing cells to 4-TMAP and *E. coli* K-12 supernatant, both significantly reduced basolateral production of IL-15 by approximately 9-fold ($p=0.0038$ and $p=0.0445$, respectively). IL-15 production in the apical compartment was significantly increased by up to 2.15-fold with L-tryptophan ($p=0.034$), 2.8-fold with 3,4-TMAB ($p=0.0437$), 4.11-fold with 4-TMAP (p<0.0001), 3.95-fold with UDCA ($p=0.0014$) and 4.3-fold with GCA (p<0.0001). Furthermore, Figure 3.3.12 shows the release of IL-8 pg/ml. The molecules selected in the study did not significantly change the production of IL-8 in either the apical or basolateral compartments. However, *E. coli* LF82 supernatant significantly increased IL-8

basolateral release 8.5-fold (*p*=0.0280) and apical release 13.1-fold (p<0.0001). *E. coli* K-12 supernatant did not elicit the same effect, suggesting the response is strain specific.
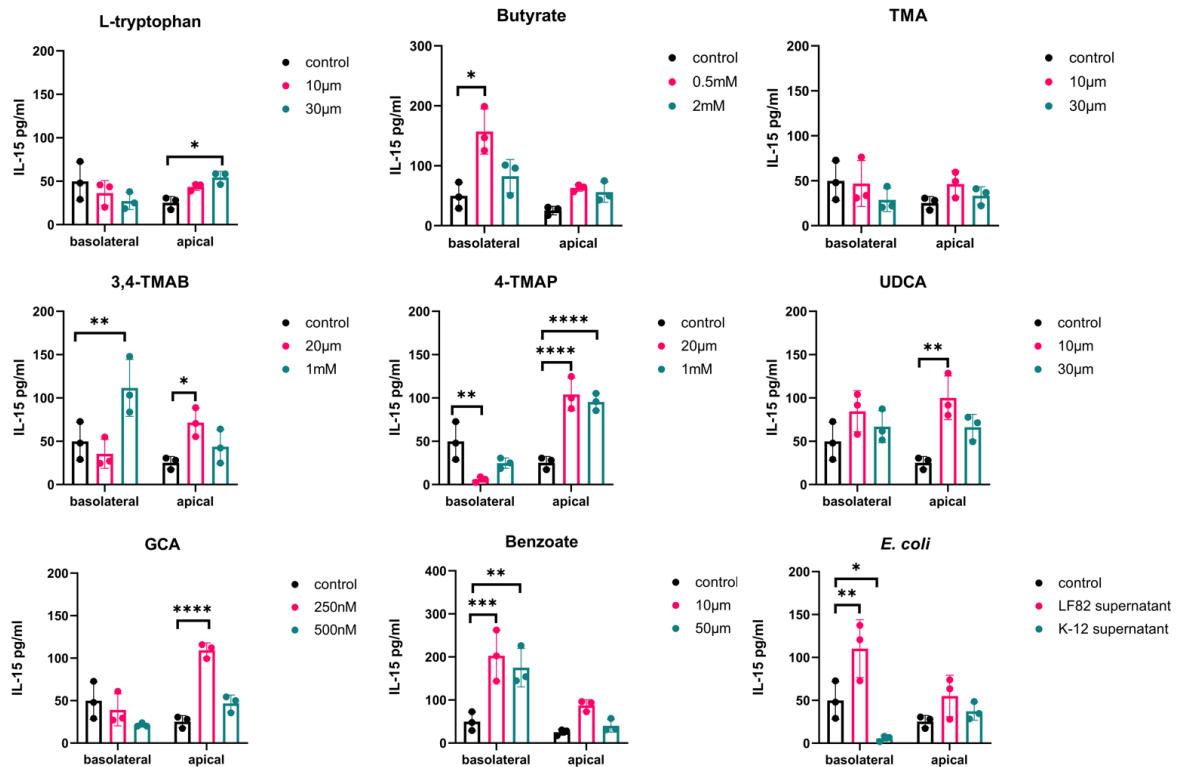
Figure 3.2.11 IL-15 release into apical and basolateral epithelial compartments. The apical side of the HCT-8 TEER barrier model was stimulated with either molecules or supernatant from *E. coli* strains LF82 and K-12 cultures. After 24 h the supernatants were collected from the apical and basolateral epithelial compartments, separately. IL-15 was quantified using ELISA and the data is shown as the mean of 3 biological replicates ± standard deviation (SD) (error bars). Two-way ANOVA was performed for each molecule versus the control condition (cells without treatment). *p<0.05, **p<0.01, ***p<0.001, ****p<0.0001 is considered statistically significant.
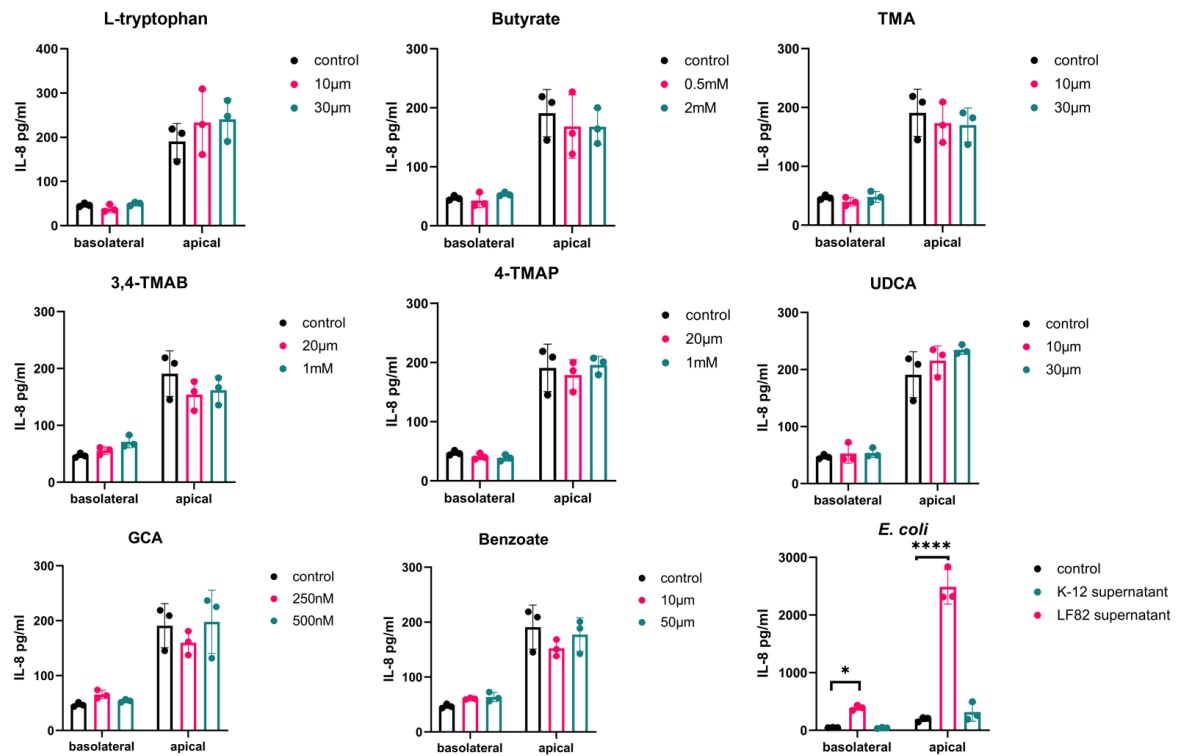
Figure 3.2.12. IL-15 release into apical and basolateral epithelial compartments. The apical side of the HCT-8 TEER barrier model was stimulated with either molecules or supernatant from *E. coli* strains LF82 and K-12 cultures. After 24 h the supernatants were collected from the apical and basolateral epithelial compartments, separately. IL-8 was quantified using ELISA and the data is shown as the mean of 3 biological replicates ± standard deviation (SD) (error bars). Two-way ANOVA was performed for each molecule versus the control condition (cells without treatment). *$p<0.05$, **$p<0.01$, ***$p<0.001$, ****$p<0.0001$ is considered statistically significant.

3.2.6 Small molecules affect epithelial cell mitochondrial function

This study investigated whether the selected molecules and *E. coli* supernatants can impair mitochondrial activity using a TMRE-mitochondrial membrane potential assay (Figure 3.2.13). HCT-8 cells were exposed to molecules for 24 h and membrane potential was measured as a percentage of the control (HCT-8 without treatment) per g protein. L-tryptophan, butyrate, 3,4-TMAB, UDCA and *E. coli* supernatants did not significantly impair mitochondrial activity, compared to the control. However, TMA, 4-TMAP, GCA and benzoate significantly impaired mitochondrial activity by up to 1.62-fold ($p=0.0018$), 1.6-fold ($p=0.0005$), 1.76-fold ($p=0.0011$) and 1.70-fold ($p=0.0127$), respectively. FCCP was included as a positive control and significantly reduced activity 2.08-fold. This indicates that specific small molecules can cause mitochondrial dysfunction in HCT-8 IECs.
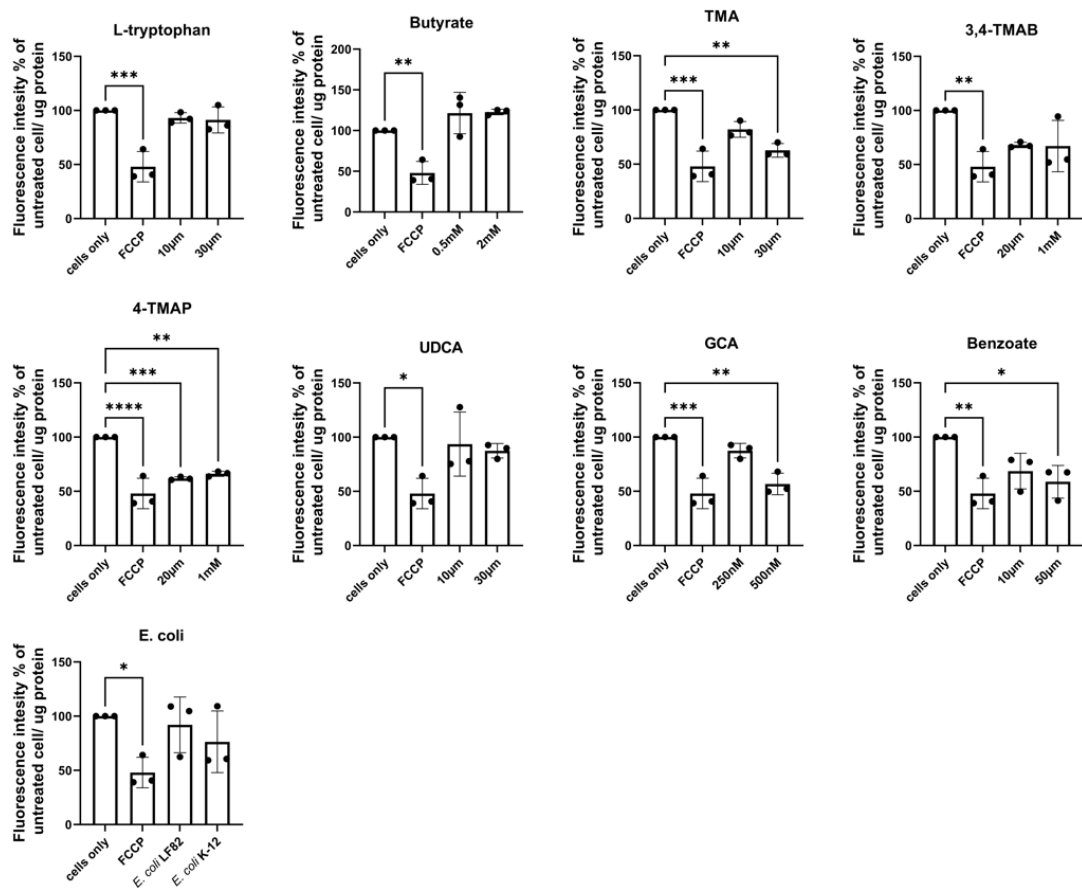
Figure 3.2.13 Mitochondrial membrane potential. HCT-8 cells were exposed to various microbial metabolites and the supernatants from *E. coli* LF82 and K-12 for 24 h. Cells only and FCCP were used as high and low mitochondrial membrane potential controls, respectively. Fluorescence was measured and calculated as a percentage of high control (cells only) then normalised to ug of protein in cell lysate. Data are shown as the mean of three biological replicates ± standard deviation (SD) (error bars). One-way ANOVA was performed to compare conditions to control (cells only) and *$p<0.05$, **$p<0.01$, ***$p<0.001$, ****$p<0.0001$ was considered statistically significant.

3.3 Discussion

It is evident that microbe-host molecular interactions play a role in CD onset and progression [215]. Discovering new biomarkers that can distinguish between healthy and disease states is vital for the development of therapeutic targets [204]. As previously described AIEC can adhere to and invade IECs, as well as survive within macrophages, resulting in a proinflammatory response implicating the bacteria as a driver of intestinal inflammation [339,350]. However, the AIEC-host metabolomic interactions that may contribute to disease pathology remain to be fully elucidated. Therefore, this study used MSI to identify both known and novel molecules altered during bacterial infection. Furthermore, the *in vivo* model of AIEC infection also involved supplementing the drinking water with PA, as it was shown to promote a virulent phenotype and in turn elicit a strong inflammatory response in the intestine [361]. The quantity of TNF-α in the ileum was significantly increased during infection (with and without PA), whereas a significant increase in the colon was only shown when infection was supplemented with PA (8.1.2). This indicated that the infection model did induce colitis. This study found that LF82 infection alongside normal drinking water and propionic acid supplemented drinking water did not significantly alter the microbe-host metabolome in the ileum. This was unexpected as AIEC are reportedly increased in the ileum of CD patients compared to controls, hence it was hypothesised that there would be a higher bacterial burden resulting in metabolomic shifts [335]. Furthermore, infection with normal drinking water did not result in any significant changes to the colonic metabolome. When the infection model was supplemented with PA, MSI identified 16 significantly changed molecules in the colon; 9 of these molecules were able to be putatively identified using the HMDB. However, shifts in the colonic metabolome when infection occurs alongside PA exposure supports the hypothesis that the model may be useful for identifying biomarkers of disease. Recovery of LF82*lux*, a luminescent strain of LF82 with an erythromycin cassette for recovery of LF82*lux* post-infection, was attempted using stool samples collected at the end of the experiment, however, no bacterial counts could be obtained suggesting that infection was cleared and that metabolic changes observed are long lasting (data not shown).

Glutaric acid was identified as one of the molecules significantly decreased in the infected colon when drinking water was supplemented with PA. Glutaric acid is a simple five carbon dicarboxylic acid that is produced during the metabolism of amino acids, including tryptophan [372]. As previously described, tryptophan metabolism is increased in IBD patients resulting in the production of bioactive molecules that have an immunomodulatory effect [197]. Furthermore, in IBD patients, less tryptophan is converted into the protective molecule, indole, which may result in a leaky intestinal barrier and inflammation [199]. Therefore, it can be suggested that the observed decrease in glutaric acid may involve increased alternative tryptophan metabolism that does not support gut homeostasis. To date, there is little evidence that glutaric acid is directly involved in intestinal inflammation; hence more research is needed to investigate the role it is playing in the infection model. Furthermore, N2-succinyl-L-glutamic acid was putatively identified as being downregulated in the colon of infected mice fed PA. This succinylated molecule is another carboxylic acid that can be produced endogenously by gut microbes; thus, it can be suggested that LF82 infection alters the gut microbiome resulting in the downregulation of its production [373]. Succinylation is a type of post-translation protein modification that involves transferring a succinyl group to a residue of the target protein [374]. This metabolic reprogramming has been associated with various health conditions such as cancer and metabolic disorders [375]. Unlike, other post-translational modifications, the prevalence and biological function of succinylation is largely unknown; however, studies have concluded that it plays a role energy metabolism within the mitochondria [376]. Therefore, N2-succinyl-L-glutamic acid may play a role as a biomarker of AIEC infection and be an indicator of disrupted cellular energy production [376,377].

In addition, the molecule putatively identified as alpha-D-glucose was decreased in the infected colon with PA supplementation. Alpha-D-glucose is an analogue of glucose that is used by the host and bacteria for energy; high levels of glucose metabolism have been found to increase inflammation by stimulating the release of pro-inflammatory mediators such as IL-6 and IL-12 [378]. Moreover, the release of TNF-α during colonic inflammation has been found to disrupt glucose metabolism by inhibiting insulin receptors leading to insulin resistance and the development of diabetes [379]. In the urinary tract of diabetes patients, high levels

of glucose metabolism have been found to impair epithelial barrier function and heighten *E. coli* burden during infection [380,381]. Therefore, a link is emerging between infection and glucose metabolism in the context of IBD and diabetes [379,382]. This study suggests that infection with LF82 increases the metabolism of available glucose, resulting in a decreased production of alpha-D-glucose in the colon and could be a useful biomarker of inflammation. Interestingly, the infection with PA supplementation showed a decrease in the molecule putatively identified as beta-guanidinopropionic acid (GPA), in the colon. GPA is produced endogenously via creatine synthesis and has been shown to modulate glucose metabolism and mitochondrial biogenesis [383]. Studies have shown that supplementation with GPA reduces glucose levels in hyperglycaemic mice and improves clinical outcomes [384,385]. Despite the protective effects in hyperglycaemia, the role GPA plays in the inflammatory process is still unclear. However, this study suggests that the downregulation of GPA is involved in supporting high levels of glucose metabolism which evokes an environment conducive to AIEC infection and inflammation [379,382,385]. Therefore, glucose and GPA may be useful biomarkers of infection induced colitis.

The colon of infected mice supplemented with PA also showed a decrease in a molecule putatively identified as pseudouridine. This molecule is derived from the post-translational modification of uridine in RNAs [386]. Pseudouridylation sites are widespread in RNAs which are critical for translational processes and aid the formation of stable protein structures that are involved in responding to environmental stress [387]. Studies have found that pseudouridine has a tumour suppressor effect in colon cancer; however, it's role in inflammation and infection remain to be fully elucidated [388,389]. Therefore, its usefulness as a biomarker for infection and inflammation is unknown. Lastly, the molecules D-mannonic acid, L-rhamnulose and adipoylglycine were putatively identified and downregulated in the colon of infected mice when supplemented with PA. These molecules are naturally occurring sugars and sugar acids that are metabolised by *E. coli* and other gut microbes [390-392]. Their role in infection and inflammation is unclear but it has been suggested that bacterial utilization can support growth [391]. Thus, it can be suggested the LF82 are metabolising these molecules as a mechanism of infection and persistence within the gut.

When the model was supplemented with PA, infection caused a decrease in a molecule in the colon that was putatively identified as 5 amino valeric acid betaine (5-AVAB) (*mz* 160.13). 5-AVAB is a trimethylated compound that has recently been described as a metabolically important and production is likely to be associated with specific members of the gut microbiome [393]. Increased levels have been associated with positive health effects such as brain development, insulin secretion and reduced risk of cancer [393,394]. The molecular mechanism that underpins the effect on the host involves the ability of 5-AVAB to influence lipid and energy metabolism by inhibiting ß-oxidation of fatty acids [393,395]. ß-oxidation of fatty acids occurs in the mitochondria of cells and releases acetyl coenzyme A for cellular energy [396]. However, studies have found inhibiting fatty acid oxidation forces cells to use glucose for energy metabolism, providing a protect effect for cardiac pathologies and diabetes [396,397]. 5-AVAB has also been shown to elicit an anti-inflammatory protective effect for endothelial damage caused by high glucose concentrations [398]. As the infection model showed reduced levels of alpha-D-glucose indicating high levels of glucose metabolism, it can be hypothesised that a reduction in 5-AVAB elevates the potential for damage and inflammation during infection. As 5-AVAB production involves the gut microbiome it can also be suggested that the downregulation in the colon is due to a dysbiosis created by the pathobiont, which in turn elicits a negative consequence for health [209,393,394]. However, the hydrophilic nature of trimethylated metabolites makes it hard to separate using liquid chromatography, often resulting in misidentification [399]. Identification becomes even harder when different trimethylated compounds have the same *m/z* and share many chemical properties [400]. A study using nuclear magnetic resonance (NMR) found a molecule with *m/z* 160.13 in the brain of specific pathogen free mice (SPF) was in fact two microbe-derived compounds, 3M,4-TMAB and 4-TMAP [209]. These molecules colocalised with carnitine and inhibited carnitine-mediated fatty acid oxidation; thus, impairing brain function [209]. Therefore, it is important to consider that these are putative identifications in this study and further confirmation is needed before future investigation into potential roles in inflammation.

IBD has been associated with the development of systemic inflammation and comorbidities that can affect a variety of organs [401]. Liver injury is a common

IBD associated complication and can range from being asymptomatic to life-threatening [402]. The exact mechanism behind IBD associated liver damage remains to be elucidated; however, studies have shown a link between gut dysbiosis and metabolic impairment in the liver [403,404]. Furthermore, it has been hypothesised that the leaky gut barrier during IBD allows toxic bacterial products to be disseminated to other organs, resulting in immunomodulatory dysfunction and organ damage [404,405]. This study used MSI to investigate the molecular link between the intestine and liver during AIEC infection. Infection without PA supplementation found that one molecule with *mz* 574.4511 was significantly down regulated in the liver, compared to uninfected control livers. To date, we have not been able to assign a putative identification to this molecule based on database and literature searches; thus, this potentially unknown molecule could be an interesting biomarker of systemic metabolic changes induced by infection. When the infection model was supplemented with PA, two molecules were significantly upregulated in the liver of infected mice compared to uninfected mice. The molecule with the *mz* 256.0596 was putatively identified as N-acteyl-D-glucosamine (GlcNAc). An elevated level of GlcNAc in the liver has previously been shown to increase insulin resistance by weakening insulin sensing receptors and prevents gluconeogenesis [406]. Studies have also demonstrated that a large amount of GlcNAc circulating in the blood is produced by the gut microbiome such as *Prevotella copri* [407,408]. CD patients have an abnormally high abundance of *Prevotella copri* in the faecal microbiome; thus, it can be suggested that GlcNAc in the liver might originate in the intestine as a result of AIEC induced dysbiosis and may have a negative consequence for liver function [401,408]. The second molecule to be significantly upregulated in the liver was putatively identified as 4-hydroxyphenylpropionylglycine, which belongs to a class of organic compounds called n-acyl-alpha amino acids [409]. These amino acids are endogenous signalling molecules can respond to stress conditions and belong to the complex lipid system known as endocannaboidome [409,410]. Studies have shown that distinct members of the endocannaboidome are upregulated in patients with CD and may provide protection against inflammation [411]. However, identification of all molecules involved in the endocannabinoid system is not complete and their mechanism of action is not fully understood [410,411]. Therefore, 4-hydroxyphenylpropionylglycine may be part of the lipid signalling response to provide protection to the liver during infection.

Ocular complications such as uveitis are infrequent in IBD patients but are associated with severe morbidity including blindness [412]. Research in autoimmune uveitis models has found that interphotoreceptor retinoid-binding protein (IRBP)-specific T cells that drive pathogenesis in the eye are first activated in the gut [413]. This activation is thought to occur due to cross-reactivity to structurally related gut microbial peptides, however, no single causative agent has been identified [413,414]. This study used MSI to investigate whether intestinal infection can alter the metabolome in the eye with the potential to induce inflammation or loss of function. During infection with PA supplementation, the molecule putatively identified as 5-AVAB was decreased in the eye of infected mice, compared to uninfected mice. As previously described, this molecule can inhibit β oxidation of fatty acids and was significantly reduced in the infected colon as a potential consequence of gut dysbiosis [393]. Therefore, it can be suggested that the molecule observed in the eye originated in the gut. Retinas use lipids to fuel mitochondrial function to meet their high metabolic demands and proteins involved in β oxidation are critical for photoreceptors and Muller glial cell function [415,416]. Defects in fatty acid β oxidation may cause lipid deficiency in the eye, resulting in damaged photoreceptors and retinal dysfunction, a hallmark of uveitis [416,417]. As 5-AVAB is reduced in the eye during infection, inhibition of β oxidation of fatty acids is theoretically lower which may provide more energy for photoreceptors. Therefore, it can be suggested that the down regulation of 5-AVAB is a metabolic adaptation to provide energy and restore function during infection [418].

As well as finding new potential biomarkers of AIEC induced colitis, this study investigated the role the specific small molecules have on macrophage function in relation to LF82 infection. GCA is a secondary bile acid produced by the colonic microbiome and is reported to be downregulated in IBD patients [419]. Previous studies have shown that GCA has an anti-inflammatory effect by inhibiting LPS-induced macrophage recruitment and proinflammatory cytokine secretion, warranting a potential use as an anti-inflammatory treatment [419,420]. This study has shown that exposing macrophages to a lower concentration (250 nM) GCA significantly increases the number of intracellular LF82 and stimulated the release of TNF-α after 72h infection. This finding was unexpected as literature suggested an anti-inflammatory and antimicrobial effect [420]. However,

studies have shown that bile acids can promote expression of AIEC virulence genes such as flagellin *fliC* allowing for persistence and growth in the gut [421]. Growth curves of LF82 did not show enhanced growth in the presence of GCA supplementation (8.1.1); thus, it can be suggested that the increased bacterial burden in macrophages is a fitness advantage that is only achieved during stress conditions which in turn may exacerbate inflammation [422]. The exact mechanism involved in increasing bacterial burden within macrophages during GCA exposure is still to be elucidated and warrants further investigation if GCA is to be used as an anti-inflammatory treatment for CD. The other molecules tested in this study did not affect bacterial burden within macrophages; however, butyrate, benzoate and 3,4-TMAB, did induce an upregulation of TNF-α. This was not expected as butyrate has previously been found to attenuate pathogenic bacterial induced hyperinflammatory responses in macrophages by decreasing mTOR kinase activity, resulting in downregulation of inflammatory cytokines including TNF-α [423]. Furthermore, benzoate has been found to decrease TNF-α release in kidney macrophages by inhibiting NF-κB activity [424]. However, both studies stimulated macrophages using lipopolysaccharide (LPS) [423,424]. Therefore, it can be suggested that LF82 macrophage stimulation is not dependent on LPS as TNF-α release is upregulated in the presence of anti-inflammatory agents shown to inhibit LPS induced activation. Furthermore, inflammatory macrophages (M1) rely on aerobic glycolysis for ATP production and the synthesis of inflammatory mediators, whereas anti-inflammatory macrophages (M2) switch metabolism to fatty acid oxidation and oxidative phosphorylation [425,426]. Inhibition of fatty acid oxidation consequently results in macrophage polarization being skewed towards an M1 phenotype resulting in the release of TNF-α [425-427]. Macrophages in this study were grown in a medium that contain various fatty acids such as palmitic acid, oleic acid and steric acid via the addition of foetal bovine serum (FBS), hence fatty acid oxidation is possible. As previously described, 3M,4-TMAB can impair fatty acid oxidation; thus, it can be suggested that the molecule is able to enhance macrophage pro-inflammatory response during infection [209].

This study also evaluated the impact small molecules may have on IECs considering their important role in proving a barrier to infection and regulating the immune response [343,428]. It has been well documented that there is a link

between IEC death and the development of IBD as patients have been found to have higher levels of cell apoptosis compared to healthy controls [429,430]. Therefore, it was important to confirm whether our molecules of interest were cytotoxic and induced apoptosis. The higher concentration of butyrate was the only molecule to show a cytotoxic effect and induce apoptosis. This finding was not unexpected as studies have reported butyrate induced apoptosis in Caco-2 cells via the mitochondrial pathway which involves upregulating the caspase cascade as well as mediating the release of ROS [431,432]. However, 4-TMAP significantly reduced LDH compared to the control, suggesting a protective effect. Studies have reported that IECs have decreased levels of ATP when high fat diets shift metabolism towards fatty acid β-oxidation, resulting in cellular death via necrosis [433,434]. It has been shown that 4-TMAP can inhibit fatty acid oxidation [209]; thus, it can be suggested that ATP levels are higher which prevents necrosis and other forms of cell death [434].

After determining that most molecules do not induce cell death, we aimed to assess whether the molecules could affect IEC barrier function which is largely controlled by tight junction proteins [435]. Studies have shown that IBD models have a loss of the tight junction protein zona occuldens-1 (ZO-1), which precedes disruption in barrier integrity and inflammation [340,435]. Furthermore, LF82 impairs barrier function by disruption the expression of tight junction protein, ZO-1 [436]; thus, it was important to evaluate the impact our molecules of interest have on ZO-1 expression during infection. The study found L-tryptophan, butyrate, TMA, 4-TMAP, UDCA and benzoate significantly increased ZO-1 expression in infected cells compared to untreated infected cells. These molecules were able to increase ZO-1 expression to a similar level as cells that had no molecular treatment or infection. As previously described L-tryptophan, butyrate and UDCA have been reported to protect barrier function, hence enhancing ZO-1 expression is not unexpected and could be a protective mechanism to overcome infection [190,199,437]. TMA and benzoate ability to increase ZO-1 expression was unexpected due to literature reporting potential cytotoxic effects linked to IBD pathology [208,213,216]. Both molecules can be anti-microbial towards E. coli [438,439]; IECs infection was extracellular, and bacteria were exposed to the molecules, hence it is possible that increased ZO-1 expression is linked to a lower microbial burden. ZO-1 expression level was increased in

infected cells pre-treated with GCA, compared to infected untreated cells. However, this increase was not found to be significant, hence the role this bile acid plays cannot be determined. Interestingly, a lower concentration (20 µm) of 3M-4-TMAB increased ZO-1 expression compared to untreated infected cells, however, increasing the concentration to 1 mM impaired the protective effect and ZO-1 expression was reduced. This downregulation might be a result of increased fatty acid oxidation inhibition causing a shift towards glycolysis resulting in hypoglycaemia, which has been shown to decrease ZO-1 levels [440,441]. However, 4-TMAP has similar mechanisms of action, but enhanced ZO-1 expression compared to the control; hence, the molecular-host interaction and response is highly specific.

After confirming that the molecules tested can have a protective or deleterious effect of ZO-1 expression, TEER was used to measure barrier function. TEER measurements fell across all test conditions including the control between the 0 h and 1 h timepoint, hence results were normalised and shown as a percentage change compared to the control. This is likely due to changes in oxygen levels and pH after cells are removed from incubator for measurements [442]. However, this decrease was not significant and monolayer integrity was maintained. Treating cells with 2 mM butyrate was the only metabolite condition that significantly increased barrier function compared to the control. This finding is supported by other studies that have found butyrate to increase production and regulate the assembly of tight junction proteins [423,443]. Therefore, it can be suggested that butyrate has the potential to protect barrier function during periods of environmental stress including changes in pH. Furthermore, exposing cells to commensal *E. coli* K-12 supernatant significantly increased TEER between 3 and 6h timepoints, compared to control. This non-pathogenic commensal strain has recently been indirectly implicated with the development of IBD due to its ability to induce inflammatory cascades in human IECs [444]. This pro-inflammatory phenotype is observed when *E. coli* K-12 interacts with human cells resulting in the expression of virulence associated genes and alters the gene expression of the host to impair intestinal functions [444,445]. This impairment includes disrupting the intestinal barrier function by supressing mRNA levels of *ZO-1* and other tight junctions including *claudin-1* [446]. As bacterial supernatants were collected from *E. coli* K-12 grown in the absence of human cells it can be

suggested that virulence factors were not expressed and that the supernatants do not contain mediators of microbe-cell damage but may in fact protect IEC barrier function.

IECs have two functionally and biochemically different surfaces that play specific roles in cellular function [447]. The apical surface faces the intestinal lumen and is mostly involved in absorption and secretion, whereas the basolateral surface mediates the interaction and attachment to underlying neighbouring cells via integrin proteins [448,449]. Furthermore, specific cytokines such as IL-6, IL-15 and IL-8 have been found to be overexpressed in the epithelium of the ileum and colon of CD patients [450]. These cytokines are pleotropic and have the potential to be proinflammatory under specific conditions [451]. Studies have shown that the apical or basolateral secretion of cell signalling molecules including cytokines have different outcomes for immune cell recruitment and activation [452]. In particular, the apical release of IL-6 and IL-8 has been associated with increasing neutrophil activation, overproduction of free radicals and skewing macrophage polarization towards a pro-inflammatory M1 phenotype [449,452]. This study found that metabolite treatment of cells did not change IL-8 release from apical or basolateral surfaces; however, LF82 supernatant significantly increased release from both surfaces but more so apically. Certain pathogenic *E. coli* strains have been shown to induce IL-8 secretion, resulting in reassembly of TJ proteins and increased permeability which allows the transmigration of polymorphonuclear leukocytes (PMNs) to cross epithelium into the lumen [453,454]. This effect has been shown after bacteria accumulate and attach to host cells via the pilus [454,455]. As this study used supernatant instead of bacterial infection, it can be suggested that LF82 can chemically signal IL-8 secretion without using virulence mechanisms which can potentially lead to recruiting PMNs to the intestinal lumen and skew activation towards a pro-inflammatory phenotype.

Furthermore, all tested metabolites increased the apical secretion of IL-6, whereas 3M-4-TMAB and UDCA increased basolateral secretion as well. It has been suggested that cells stimulated at the apical surface will only secrete IL-6 apically to ensure migrating immune cells are only activated once they have reached the lumen. Therefore, basolateral secretion induced by 3M-4-TMAB and

UDCA might be associated with the overactivation of immune cells within the intestinal tissue which might lead to inflammation and disease [447,449,456]. In addition, IL-15 can promote survival of IECs during infection and inflammation; however, overexpression on basolateral surfaces can induce apoptosis and T-cell activation leading to disease, depending on the stimulus [457,458]. Our results show that butyrate, 3,4-TMAB, 4-TMAP, benzoate and AIEC LF82 supernatant can increase IL-15 basolateral secretion, whereas L-tryptophan, 3, 4-TMAB, 4-TMAP, UDCA and GCA increase apical secretion. TMA was the only molecule that did not influence the level of IL-15 secretion. Therefore, it can be suggested that the tested molecules, except TMA, have the potential to induce tissue damage via IL-15 signalling. Furthermore, 3M-4-TMAB and 4-TMAP are the only molecules that increased secretion at apical and basolateral surfaces, hence they have the potential to induce extensive inflammation throughout the intestine by accessing the lumen and underlying neighbouring cell [449,452,458]. As this study measured the quantity of IL-8, IL-6, and IL-15 without observing the effects on immune cells, it cannot be confirmed whether the secretion of cytokines elicited a pro or anti-inflammatory effect. However, we can speculate that no molecule caused an overwhelming inflammatory cascade involving cytokines as the intestinal epithelial barrier function was not impaired [346,450]

Mitochondrial metabolism and function are known to play an important role in regulating immune cells and maintaining the intestinal epithelial barrier [459]. Furthermore, studies have linked dysregulated mitochondrial function in IECs to CD onset and disease severity [460]. This study measured mitochondrial membrane potential as an indicator of mitochondrial activity as it is an essential parameter involved in ATP synthesis, respiratory rate, and production of ROS [461]. Our study shows that TMA, 4-TMAP, GCA and benzoate can reduce mitochondrial membrane potential at specific concentrations. This finding supports the emerging evidence that microbiome derived small molecules including TMA and bile acids alter mitochondrial function [462]. As previously described, the role of TMA in disease has been overlooked due to a focus on the metabolised product, TMAO [208]. Therefore, the exact mechanism involved in TMA reduction of mitochondrial membrane potential remains to be fully elucidated and could be an interesting marker of microbial associated mitochondrial dysfunction in disease. Furthermore, 4-TMAP has been found to inhibit enzymes that are

involved in carnitine synthesis and fatty acid transportation into the mitochondria [209,210]. This inhibition can lead to a loss of mitochondria function which is observed in this study and may have negative consequences for health [463]. Furthermore, studies found specific secondary bile acids contribute to mitochondrial swelling and increase the permeability of the membrane after binding to specific membrane proteins and farnesoid X receptors [464]. This triggers mitochondrial fission and results in disordered energy metabolism and apoptosis [464,465]. Therefore, it can be suggested that GCA is another BA that impairs mitochondrial function. Currently, there is little evidence to suggest benzoate plays a role in mitochondrial dysfunction and studies have suggested it may even have a protective effect in neural cells by decreasing mitochondrial caspase-3/7 and ROS [466]. As this study shows benzoate impairs mitochondrial membrane potential, it can be suggested that the molecular effect is dependent upon cell type. Therefore, high benzoate levels in the intestine may result in cellular damage and inflammation [216,461,466].

This chapter shows that DESI MSI can be employed to discover molecules derived by the host and microbiome in response to AIEC, a potential driver of inflammation in CD. The study revealed that LF82 infection does not significantly alter the metabolome in the ileum or colon. Furthermore, one molecule was found to be altered in the liver as a consequence of infection; however, the identity of this molecule remains to be elucidated. When PA is supplemented into the drinking water, infection with LF82 results in more molecular changes within the colon, liver, and eye. The molecules that were putatively identified may have a role in mediating intestinal and systemic inflammation via different mechanisms; thus, PA supplementation in the infection model supports virulence and may be a useful model of colitis and systemic inflammation. Additionally, we evaluated the effect known molecules implicated in CD have on immune cell function in relation to AIEC. The results indicate that specific microbially derived small molecules can prime macrophages to be pro-inflammatory by enhancing bacterial burden and TNF-α. Furthermore, specific molecules can affect IECs function by altering ZO-1 expression, interleukin secretion and mitochondrial membrane potential. Thus, it is evident that microbial small molecules are important mediators of cellular function and may be involved in the inflammatory process observed in CD.

Chapter 4 Pathogenesis of dextran sodium sulphate colitis involves bacterial and host metabolites

4.1 Introduction

4.1.1 The use of animal models to decipher underlying mechanisms of IBD

Inflammatory bowel diseases (IBD) including Crohn's disease (CD) are complex multifactorial diseases characterised by chronic inflammation in a relapsing-remitting manner; however, the exact cause remains to be fully elucidated [467,468]. However, the understanding of the inflammatory process that underpins disease onset and therapeutic interventions have been advanced due to the development of numerous murine models of intestinal colitis [469]. The mouse models have been developed to characterise the complexity of IBD pathogenesis by reflecting underlying molecular mechanisms such as genetic mutations, impaired barrier function, and dysfunctional innate and adaptive immune responses [470]. IBD models fall into five main groups that include: 1) gene knockout (KO) models such as IL-10 KO mice [471]. The genetically engineered IL-10 KO mouse is one of the most used models to evaluate the pathophysiology of IBD [472]. IL-10 is a regulatory, anti-inflammatory cytokine and represents a key IBD susceptibility gene as mice spontaneously develop colitis around 3 months old [473,474]. This model has been characterised by the presence of proinflammatory infiltrates including lymphocytes, macrophages, and neutrophils [473,475]. However, the model can be highly variable in colitis development due to differences in the microbiome; thus, reproducibility has been an issue [472,474,475]. 2) Another genetically engineered model known as transgenic mouse models, involves overexpressing a gene of interest such as HLA B27 and IL-17, resulting in the interference of normal protein function and induction of inflammation [476]. 3) Spontaneous colitis models such as SAMP1/Yit mouse strain closely represents ileitis observed in CD patients without genetic, chemical, or immunological manipulation [477]. The model was developed by brother-sister mating of senescence accelerated mouse P1 (SAMP1) mice that displayed spontaneous skin lesions correlated with the presence of intestinal inflammation characterised by Th1 inflammatory infiltrates, crypt microabscesses and elongation, disruption of

the epithelium and tissue atrophy [478]. However, the exact cause of disease in this model is still unknown and it can take more than 30 weeks for the onset of disease, thus experiments can be time consuming and expensive [478-480]. 4) Adoptive transfer models can involve the transfer of CD4$^+$ T-cells (CD4$^+$CD45RB^{high} T-cells) from donor mice to severe combined immunodeficiency (SCID) mice that have deficient functional B and T lymphocytes [481]. Typically, after 5 to 10 weeks an aggravation of intestinal inflammation, specifically in the colon, is observed and studies were able to conclude that this model is mediated by Th1 responses associated with the production of proinflammatory IFN-γ and TNF-α [480,482]. However, the model uses immunodeficient mice to develop colitis; thus, a complete overview into the development of colitis is not possible [469,470,481]. 5) Chemically induced experimental models have been developed for use as a colitis model as they can be quick, reproducible, and controllable [483].

The most common chemically induced colitis model uses dextran sodium sulphate (DSS) which is sulphate polysaccharide that can have a molecular weight between 5 and 1400 kilodaltons (kDa) [484]. DSS between 36 to 50 kDa is optimal for penetrating the epithelial barrier and can enter the lamina propria, allowing interaction with and activation of immune cells; inducing similar clinical symptoms and histological features as human IBD [485]. Feeding mice with 1-5% DSS dissolved in water results in the development of colitis within one week and severity can be measured by weight loss, rectal bleeding, stool consistency and colonic shortening [486,487]. Furthermore, the model has been shown to respond positively to the anti-colitis drugs including sulfasalazine and mesalazine that have strong immunomodulatory functions; thus, the model is useful for IBD related research despite the mechanism of inflammation not being well understood [488]. DSS-induced acute inflammation is mostly affects, but is not limited to, the colonic mucosa as the negatively charged sulphate groups are thought to damage the intestinal mucosa and epithelial monolayer lining [484,489]. The damage to the epithelial cells involves loss of crypts and an altered immune response characterised by infiltration of granulocytes [490,491]. Damage to epithelial cells leads to increasing gut permeability, allowing commensal gut microorganisms to penetrate through the dysfunction epithelial tight junctions into the lamina propria [490-492]. This influx of microbiota can result in the activation of intestinal macrophages which secrete high levels of inflammatory

cytokines such as TNF-α, IL-1ß, and IL-6 [493]. These cytokines act as a chemoattractant signal to recruit immune cells such as dendritic cells, T cells, B cells and neutrophils into the colon which perpetuates the inflammatory environment [484,493]. Unlike human disease, DSS induced colitis does not require T and B cells as DSS has a direct toxic effect and studies have shown that inflammation can occur in immunodeficient mice such as SCID and *Rag1*$^{-/-}$ mice [494,495]. However, some studies have presented contradictory evidence and suggest that well established DSS-induced colitis involves polarized Th1/Th2 responses to achieve chronic inflammation [496,497]. Thus, most studies use DSS induced colitis to study the role of the innate immune response in IBD pathogenesis [494,496,497]

4.1.2 DSS induced colitis involves the gut microbiome and metabolome

In comparison to the dispute between whether specific immune cells play an important role in DSS induced colitis, studies have highlighted that intestinal bacteria are essential for the development of inflammation that is representative of human IBD [467,490]. Studies using germ-free (GF) mice showed that DSS induced only minimal inflammation represented by no colonic thickening or shortening, and low levels of proinflammatory cytokines IL-6, IL-17, TNF-α, and IFN-γ; however, mice had impaired barrier function [498]. The study also showed that conventional mice treated with antibiotics to perturb the intestinal microbiota had an increased inflammatory response but were less prone to epithelial injury which was correlated with an increase in IL-10 and other preservation barrier-related markers [498]. Furthermore, longitudinal microbiome analysis studies have indicated that DSS induced colitis results in dynamic fluctuations in microbial diversity, transitioning from a normal state to dysbiosis [499,500]. However, the microbiome in DSS induced colitis model can widely vary and be inconsistent among studies due to differences in environmental conditions, dose, and duration [501,502]. For example, at the genus level *Lactobacillus, Prevotella* and *Parabacteroides* have been shown to be increased and decreased across studies indicating discrepancy amongst the results [500,503]. Studies have also shown that mice deficient in NOD-like receptor family pyrin domain containing 6 (NLRP6), an epithelial cell derived inflammasome protein, develop more severe DSS induced colitis as NLRP6

induced IL-18 production controls the growth of *Prevotellaceae* species within the crypts [504]. Therefore, genetic susceptibility to IBD and progression of disease severity is underpinned by intestinal microbiota [504,505]. Furthermore, *Enterobacteriaceae* and *Bacteroides* show consistent expansion in the inflamed intestine [500]. This is thought to be due to an increasingly high oxygen level within the inflamed gut; thus, specific bacteria can outcompete strict anaerobes for nutrients and space [503,506]. Another possible reason to support dysbiosis is the release of lipocalin 2 (Lcn2) from epithelial cells which binds to iron-chelating siderophore enterobactin (Ent) to inhibit Ent-mediated iron acquisition, preventing bacterial iron utilisation and limits their growth [506,507]. In addition, some studies indicate a decrease in microbial diversity prior to observing inflammation, whilst other show dynamic shifts as inflammation proceeds [498,500,508]. Therefore, whether gut microbial dysbiosis is a cause or a consequence of DSS induced colitis has yet to be fully elucidated and warrants further investigation.
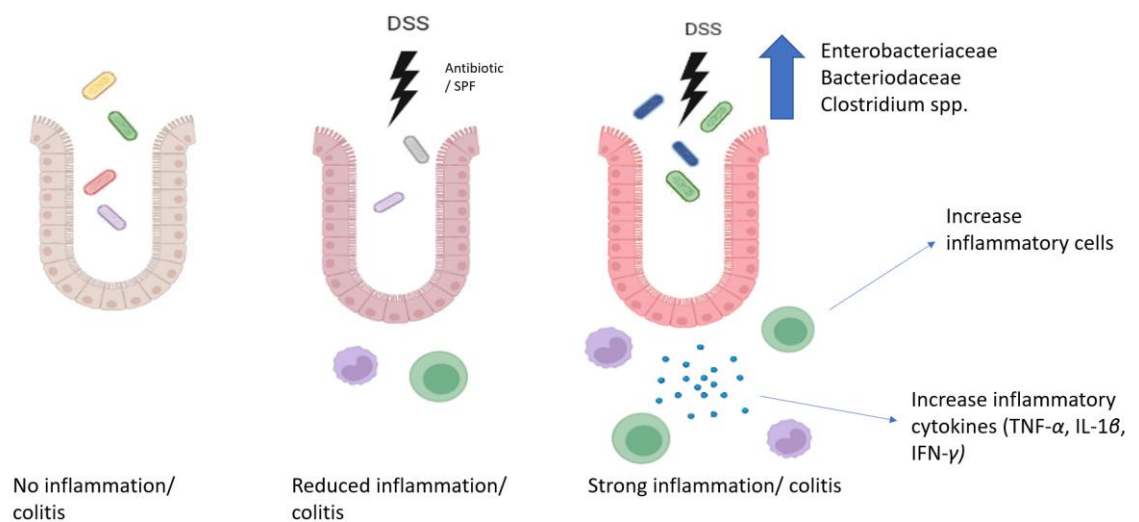
Figure 4.1.1 Mechanistic action of DSS in intestine. Intestinal cells and barrier integrity normal without DSS treatment and a healthy microbiome is likely (left). DSS enters the gut lumen and disrupts the integrity of the epithelial barrier, causing gaps between cells (right). Luminal contents, such as bacteria and microbial products, leak into the underlying tissue through the damaged epithelial barrier. Immune cells (depicted as purple and green cells) are recruited to the site of injury, triggering an inflammatory response characterised by cytokine release. Inflammatory mediators exacerbate tissue damage, perpetuating inflammation and further compromising the epithelial barrier. Studies have also shown that absence or reduction in the gut microbiome (GF, SPF or antibiotic treatment) before DSS exposure reduced epithelial damage.

The evidence suggests that DSS induced colitis involves the simultaneous interactions between the epithelial barrier, intestinal microbiota, and the host

immune response [494,496,500]. Bacterial metabolites can act as signals that affect immune homeostasis, host energy metabolism and the maintenance of mucosal integrity [509]. Studies have found that microbial metabolites such as ursodeoxycholic acid and its derivatives can reduce the severity of DSS induced colitis by inhibiting the expression of proinflammatory mucosal cytokines and apoptosis of epithelial cells [510,511]. Furthermore, tryptophan can be metabolised by intestinal bacteria into a series of indole-metabolites such as indole-3-propionic acid which has been shown to reduce intestinal permeability and protect mice from DSS-induced colitis [512]. Therefore, intestinal microbial dysbiosis during DSS colitis may result in the downregulation of specific metabolites involved in immune regulation; thus, promoting inflammatory processes [509,510,512]. Furthermore, multi-omic approaches have been implemented to gain a better understanding of the molecular basis of IBD pathogenesis [513]. Studies have found that DSS induced colitis significantly alters the metabolome and pathways such as amino acid and lipid metabolism are upregulated as severity of inflammation increases [514]. The activation of proinflammatory responses in DSS colitis model also involves altered host metabolites as PLS-DA metabolomic analysis has shown that succinic acid, glutamic acid, and glutamine are the main contributors of differentiation between colitis groups and controls [515,516]. Therefore, gaining a better understanding of the bacterial and host metabolites that interact with immune cells during DSS induced colitis might highlight new mechanisms of pathology [509,511,513,516].

4.1.3 Systemic alterations and extraintestinal diseases associated with DSS induced colitis

The microbiome has been shown to affect distal organs, for example, DSS induced colitis has been shown to activate the tryptophan (Trp) and kynurenine (Kyn) pathway in the brain due to skewed gut microbiota elevating the production of enzymes related to Trp-Kyn metabolism [517]. In the brain, Kyn pathway has been implicated in multiple pathologies such as Alzheimer's disease (AD), Parkison's disease (PD) and allergic encephalomyelitis [518-520]. Therefore, DSS colitis may impair brain function and cause neuropathologies due to changes in metabolism as a consequence of microbial dysbiosis [517,519]. During colonic inflammation, many IBD patients experience an extraintestinal manifestation (EIM) that can affect nearly any organ system including dermatological,

hepatopancreatobiliary, ocular, renal and pulmonary systems [521]. The liver is anatomically divided into lobes, however, each lobe does not have distinct functions meaning the metabolic function of the liver is uniform across the organ, and receives blood supply from the portal vein [522,523]. Complications such as non-alcoholic fatty liver disease (NAFLD) and gallstones have been associated with metabolite dysfunction [524,525]. Metabolomic studies revealed alterations in the liver in DSS induced colitis models including carnitine-related metabolism, one-carbon metabolism, and nucleotide synthesis [526]. Furthermore, liver host receptors are thought to activate and influence an inflammatory response after engaging with specific metabolites [527]. However, specific biomarkers of EIMs in the liver and their effects on liver inflammation still remains to be fully elucidated [523,527]. Furthermore, DSS induced colitis has been shown to cause splenomegaly and immune cell dysfunction in the spleen as well as metabolic changes in the kidney [528,529]. However, whether molecules are host or microbial derived and the role they may play in EIM onset is yet to be elucidated [528-530]. Furthermore, studies have shown that DSS induced colitis is sufficient to drive acute lung inflammation similar to asthma and chronic obstructive pulmonary disease (COPD); however, the exact mechanism that underpins inflammation is not known [531].

Therefore, this study uses the DSS induced colitis model to represent intestinal and systemic inflammation in order to study the effect microbial and host metabolites play in disease. The study aims to employ MSI and multivariate analysis to identify molecular changes in the colon and ileum during DSS induced colitis that may be potential biomarkers of disease. Furthermore, the study will investigate the systemic metabolic changes in the liver, kidney, spleen, and lung as a result of intestinal inflammation, that may have implications for health. IMC will also be employed to gain a better understanding of cellular changes within the colon, ileum and liver that may contribute to the onset or perpetuation of inflammation.

4.2 Results

4.2.1 DSS induced colitis alters the faecal microbiome and intestinal metabolome

Microbiome sequencing of faecal samples showed changes in the relative abundance of phyla between day 0 and day 7 of the experiment when mice were treated with 3% DSS (Figure 4.2.1). Firmicutes and Bacteroidota remained the most abundant phyla in the 3% DSS group after 7 days compared to the other groups, however, microbial diversity was reduced with an increase in the abundance of Proteobacteria. The heatmap also shows that the abundance of the top 35 genera present in faeces are changed after 7 days of 3% DSS treatment (Figure 4.2.1). *Clostridium, Mucispirillum, Turicibacter, Escherichia, Faecalibaculum, Lactobacillus, Dubosiella, Oscillibacter, Odoribacter, Parabacteroides, Bacteroides* and *Sutterella* are increased in 3% DSS treated mice, whereas others such as *Ruminococcus, Prevotella, Treponema, Lachnospiraceae, Faecalibacterium* and *Roseburia* are reduced.
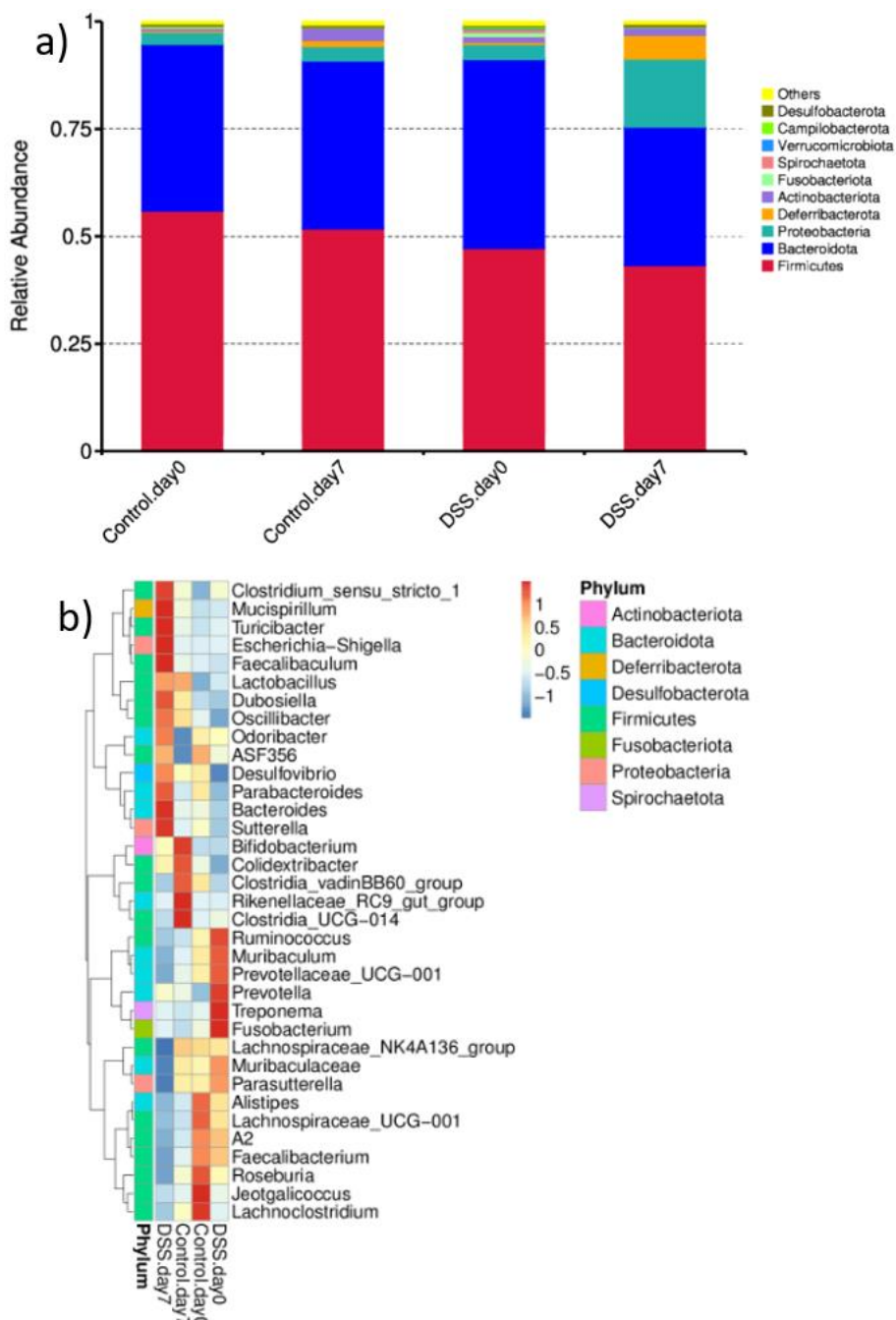
Figure 4.2.1 Relative abundance of bacterial phyla and heatmap of genera in DSS mice.
A) Histogram of relative abundance of the top 10 bacterial phyla in the faeces of control mice (0% DSS) and 3% DSS treated mice at the start (day 0) and end (day 7) of experiment. B) Heatmap of top 35 genera in control groups and 3% DSS treated mice on day 0 and day 7.

MSI was employed to elucidate intestinal molecular changes in the intestine during DSS induced colitis. The mass spectra were acquired in the range m/z 50-1000 to identify metabolites and lipids. In the ileum, ROC analysis performed in SCiLS Lab identified 176 peaks that were discriminative between 0% DSS and 3% DSS treated mice. The variation in the 176 metabolites detected were analysed to examine the clustering of groups using multivariate statistical analysis

including PCA (M1) & PLS-DA (M2). PCA score plots of the first (t [1]) and second (t [2]) principle component showed distinct clustering and clear separation between 0% DSS group from the 3% DSS treated group (parameters: R2X=0.857, Q2=0.754) (Fig. 4.3.2 M1). PLS-DA score plot (M2) was also able to separate the groups and clustered better than PCA (parameters: R2X=0.826, R2Y=0.907, Q2=0.788). The corresponding loadings plots indicated that variations in the levels of several metabolites were the main contributors to group separation. PLS-DA generated VIP scores above 1 highlight the molecules contributing the most to group separation (8.1.5). The peaks were then analysed using univariate tests and 88 were found to be significantly changed between the two groups ($p<0.05$). Out of 88 peaks only 49 molecules (55.6%) could be putatively identified using the HMDB. MSMS was used to confirm the molecular identities by matching spectra available online (data not shown). Only 6 molecules out of 88 (6.81%) had an identity confirmed by MSMS. The m/z and confirmed identity of these 6 molecules are as follows: 132.07-creatine, 162.11-carnitine, 259.24-arachidonic acid, 327.23-docosahexaenoic acid (DHA), 317.21-leukotriene A4 and 351.21-lipoxin A4. The 88 significantly changed molecules are shown as m/z, putative identity or confirmed identity in a heatmap (Figure 4.2.3) and full list of molecules changed are shown in 8.1.4.

Number	Model	Type	A	N	R2X(cum)	R2Y(cum)	Q2(cum)
1	M1	PCA-X	2	10	0.857		0.754
2	M2	PLS-DA	2	10	0.826	0.907	0.788
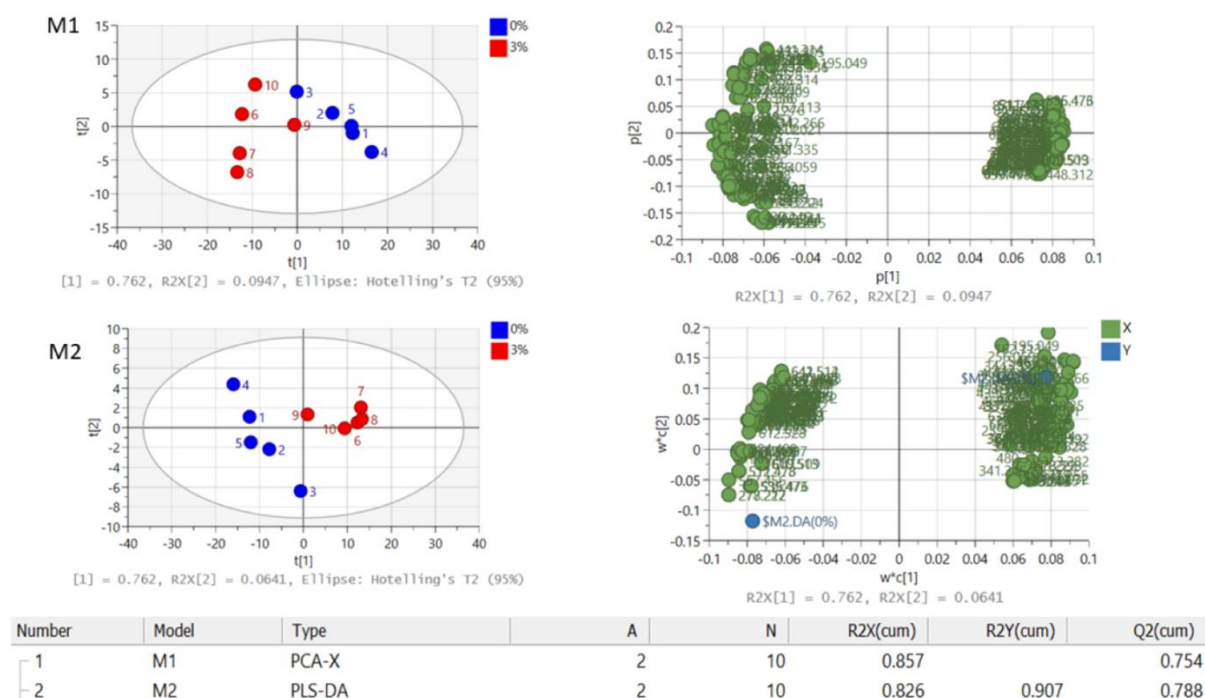
Figure 4.2.2 Unsupervised and supervised discriminant analysis.
M1) Unsupervised PCA analysis and M2) Supervised PLS-DA analysis show the molecules in the ileum of DSS colitis model can discriminant between the control (0% DSS-blue circles) and

diseased group (3% DSS-red circles). Analysis was performed using SIMCA 17 software. PLS-DA and PCA score plots consist of components 1 (t [1]) and 2 (t [2]). The ellipse represents the 95% confidence region for Hotelling's T2 statistic for the model.
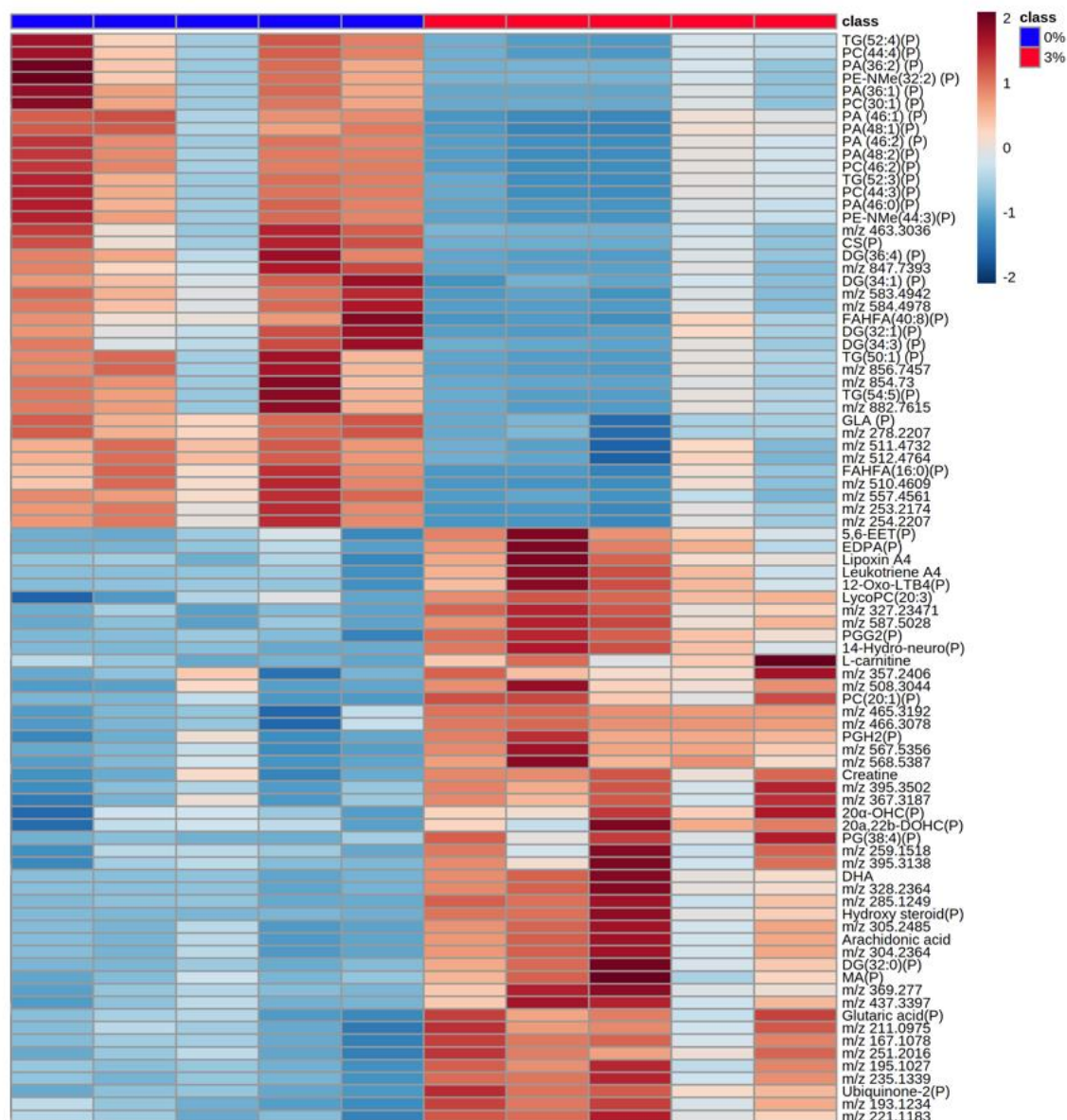
Figure 4.2.3 Heatmap of upregulated and downregulated molecules in ileum of DSS colitis model.
Heatmap shows *m/z* of molecules unable to be identified, putatively identified molecules (marked with a P) and molecules with an MSMS confirmed identification. Heatmap was created using Metaboanalyst 5.0. The colour of each sample is proportional to the significance of change in metabolite abundance indicated by the colour bar (red, up-regulated in DSS colitis group; blue, down-regulated in colitis group). Rows correspond to metabolites and columns correspond to samples.

KEGG pathway enrichment analysis showed that the molecules in the dataset are involved in at least 12 different pathways; Arachidonic acid metabolism, Steroid hormone biosynthesis, Primary bile acid biosynthesis, Biosynthesis of unsaturated fatty acids, alpha-Linolenic acid metabolism, fatty acid biosynthesis, Ether lipid

metabolism, Lysine degradation, Glycine, serine and threonine metabolism, fatty acid elongation, arginine and proline metabolism and fatty acid degradation. Arachidonic acid metabolism (p=1.50E-16), Steroid hormone biosynthesis (p=0.000103) and primary bile acid biosynthesis (p=0.000909) are the pathways that are significantly enriched in the ileum of the DSS colitis model and the molecules in our dataset that are involved in the pathway are listed (Figure 4.2.4).
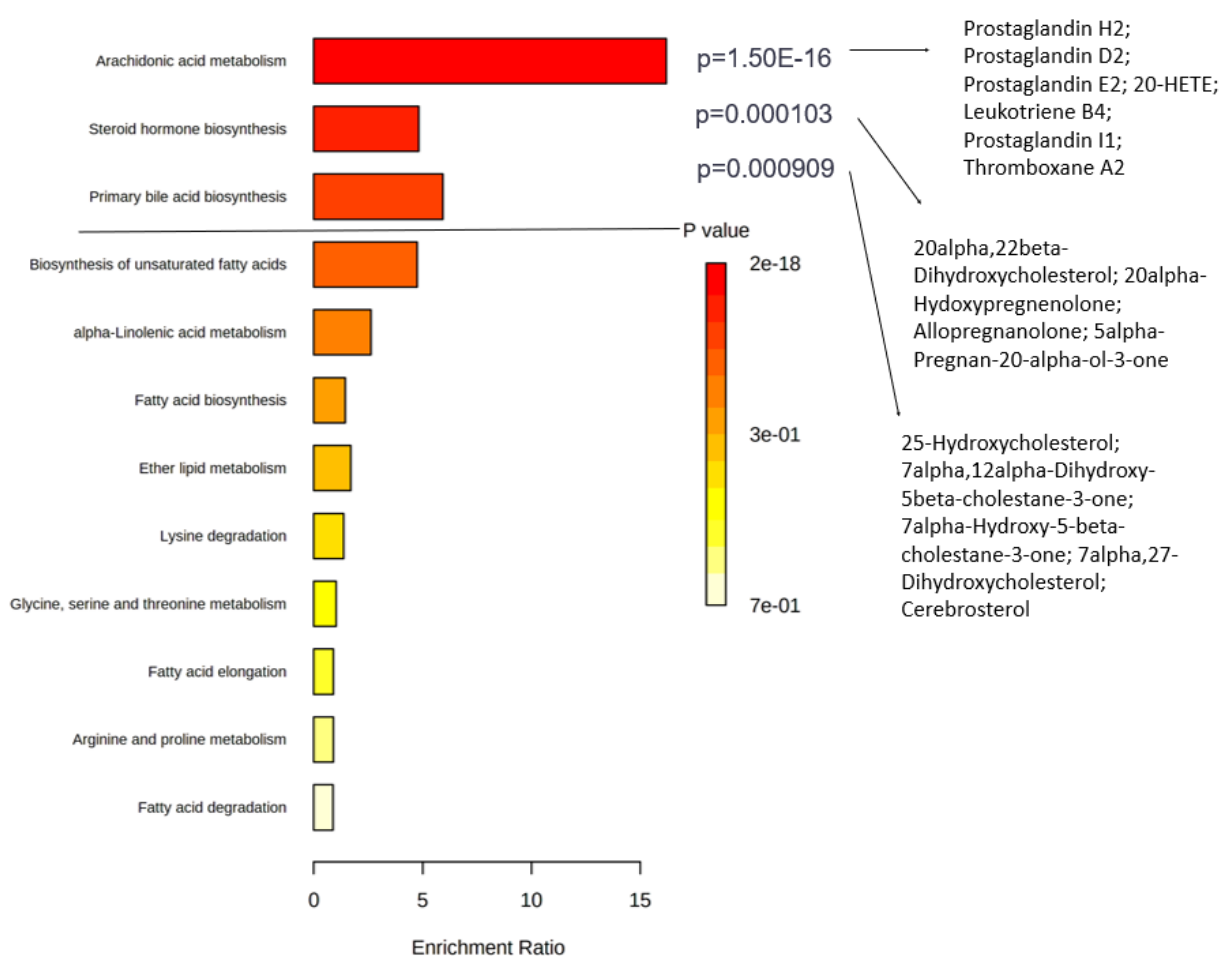
Figure 4.2.4 Enrichment of pathways in the ileum of DSS colitis model.
Enrichment pathway analysis using KEGG as reference found molecules involved in 12 different pathways: Arachidonic acid metabolism, Steroid hormone biosynthesis, Primary bile acid biosynthesis, Biosynthesis of unsaturated fatty acids, alpha-Linolenic acid metabolism, fatty acid biosynthesis, Ether lipid metabolism, Lysine degradation, Glycine, serine and threonine metabolism, fatty acid elongation, arginine and proline metabolism and fatty acid degradation. The top 3 pathways were significantly enriched, and the molecules involved in the pathway that are present in the dataset are listed.

ROC analysis of the colon identified 39 peaks that are potentially able to discriminate between the control and 3% DSS treated groups. The variation in the 39 metabolites detected were analysed to examine the clustering of groups using multivariate statistical analysis including PCA (M1) & PLS-DA (M2). PCA score plots of the first (t [1]) principle component did show distinct clustering and clear separation in the colon between 0% DSS group from the 3% DSS treated group (parameters: R2X=0.793, Q2=0.727) (Fig. 4.3.5 M1). PLS-DA score plot (M2) was also able to separate the groups and clustered better than PCA (parameters: R2X=0.946, R2Y=0.993, Q2=0.93). PLS-DA generated VIP scores above 1 highlight the molecules contributing the most to group separation (8.1.7). Univariate analysis indicated that 30 molecules were significantly changed (3 molecules downregulated and 27 molecules upregulated in 3% DSS group compared to the control). Using the HMDB, 20 of these molecules were assigned a putative identity (66.6%). However, MSMS fragmentation was only able to confirm the identity of one molecule, gamma-linolenic acid (GLA) (3% confirmed). The *m/z* and molecules with putative and confirmed identities are shown as a heatmap (Figure 4.2.6) and full list of molecules changed can be found in 8.1.6.

Model	Type	A	N	R2X(cum)	R2Y(cum)	Q2(cum)
M1	PCA-X	1	10	0.793		0.727
M2	PLS-DA	4	10	0.946	0.993	0.93
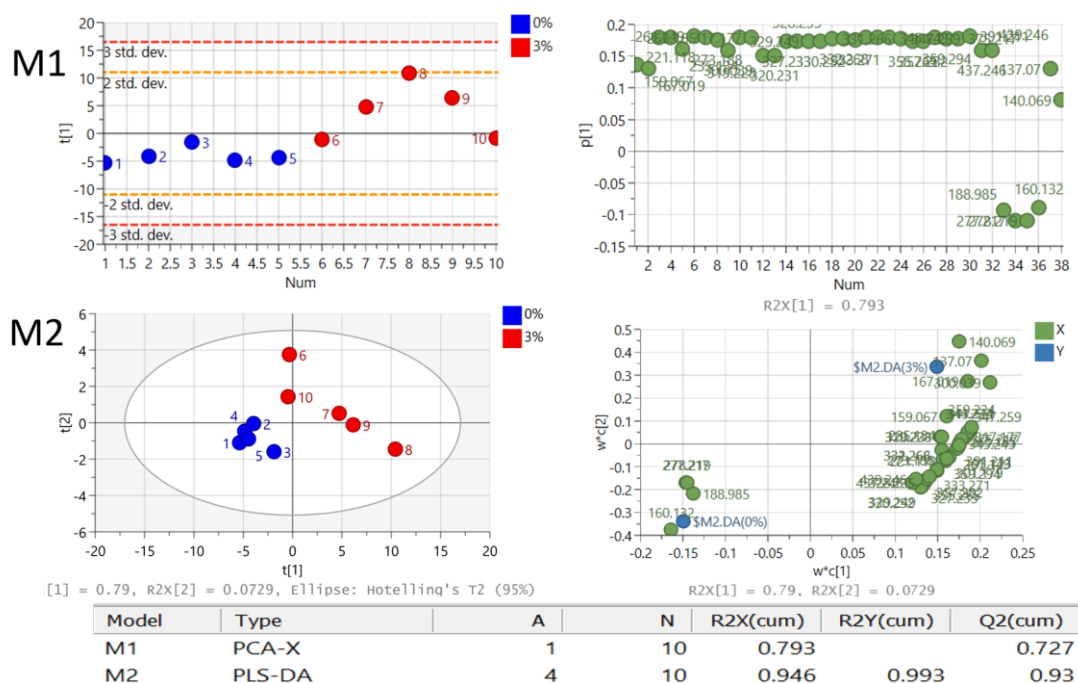
Figure 4.2.5 Unsupervised and supervised discriminant analysis.
M1) Unsupervised PCA analysis was able to discriminate between the groups using metabolite features. M2) Supervised PLS-DA analysis show the molecules in the colon of DSS colitis model can discriminant between the control (0% DSS, blue circles) and diseased group (3% DSS, red circles). Analysis was performed using SIMCA 17 software. Analysis was performed using SIMCA 17 software. PLS-DA and PCA score plots consist of components 1 (t [1]) and 2 (t [2]). The ellipse represents the 95% confidence region for Hotelling's T2 statistic for the model.
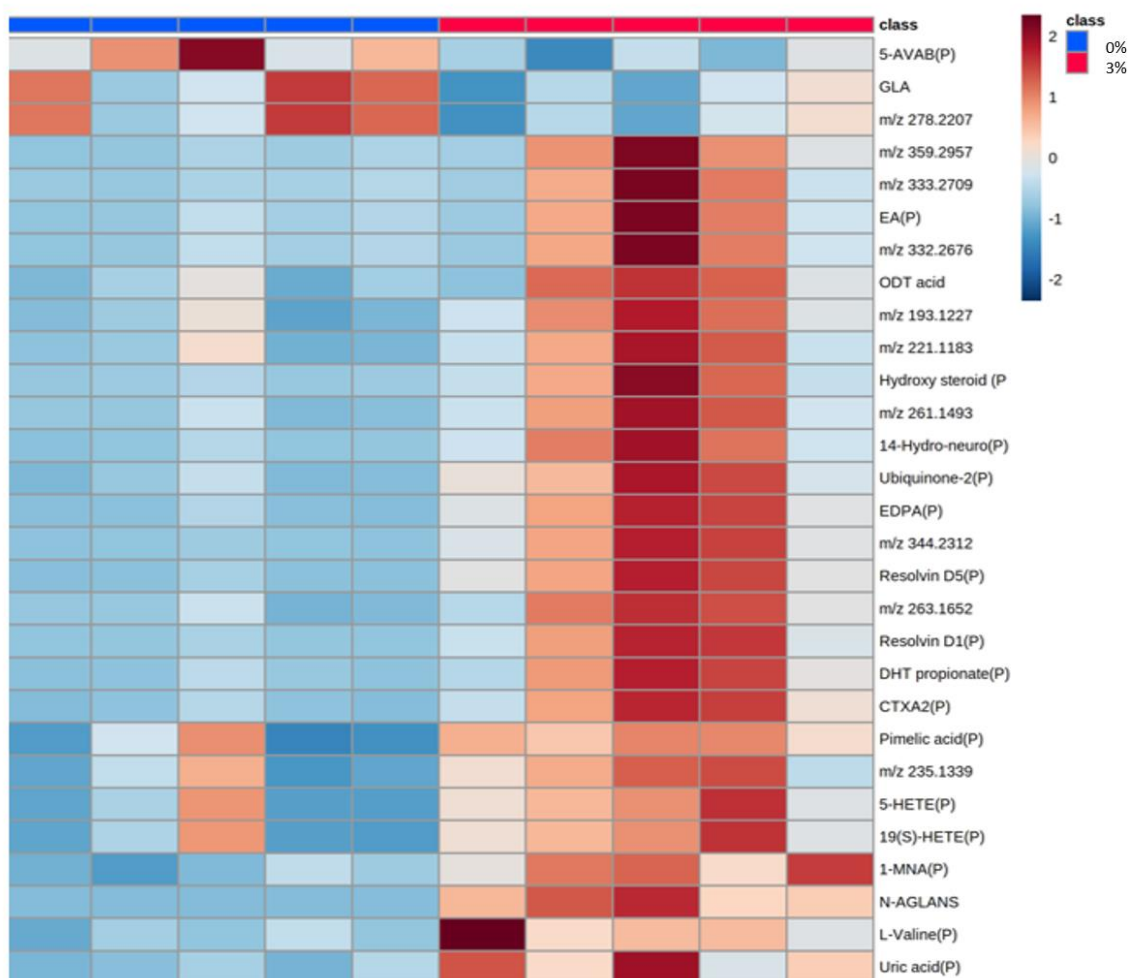
Figure 4.2.6 Heatmap of upregulated and downregulated molecules in colon of DSS colitis model.
Heatmap shows *m/z* of molecules unable to be identified, putatively identified molecules (marked with a P) and molecules with an MSMS confirmed identification. Heatmap was created using Metaboanalyst 5.0. The colour of each sample is proportional to the significance of change in metabolite abundance indicated by the colour bar (red, up-regulated in DSS colitis group; blue, down-regulated in colitis group). Rows correspond to metabolites and columns correspond to samples.

Furthermore, enrichment analysis using KEGG database indicated that the molecules found in the dataset are involved in at least 14 pathways: Arachidonic acid metabolism, Biosynthesis of unsaturated fatty acids, Steroid hormone biosynthesis, Valine, leucine and isoleucine biosynthesis, Fatty acid biosynthesis, Alpha-Linolenic acid metabolism, Nicotinate and nicotinamide metabolism, Pantothenate and CoA biosynthesis, Glycine, serine and threonine metabolism, Fatty acid elongation and degradation, Valine, leucine and isoleucine degradation, Aminoacyl-tRNA biosynthesis and Purine metabolism. Arachidonic acid metabolism was the only pathway to be significantly enriched (p=3.48e-7)

and molecules from the dataset that are involved in the pathway have been listed (Figure 4.2.7).
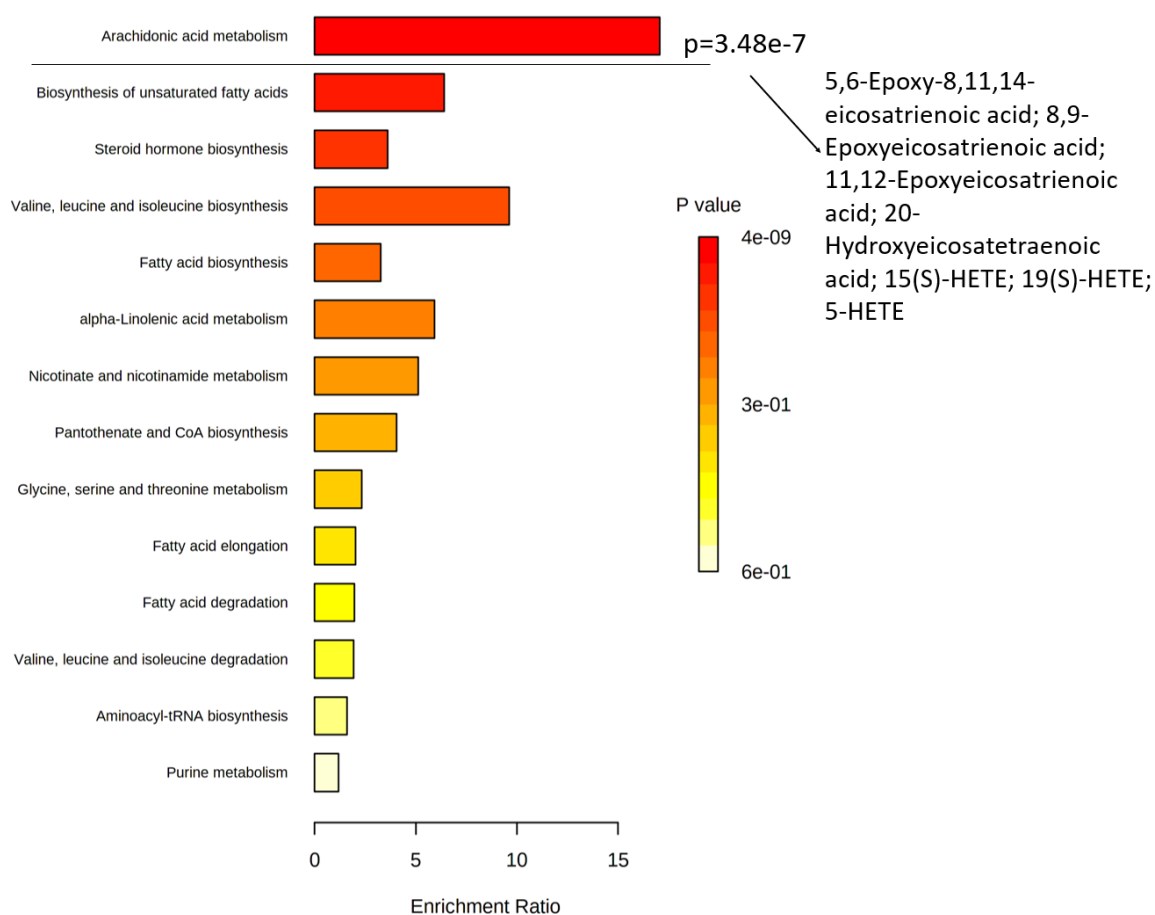
Figure 4.2.7 Enrichment of pathways in the colon of DSS colitis model.
Enrichment pathway analysis using KEGG as reference found molecules involved in 14 different pathways; Arachidonic acid metabolism, Biosynthesis of unsaturated fatty acids, Steroid hormone biosynthesis, Valine, leucine and isoleucine biosynthesis, Fatty acid biosynthesis, Alpha-Linolenic acid metabolism, Nicotinate and nicotinamide metabolism, Pantothenate and CoA biosynthesis, Glycine, serine and threonine metabolism, Fatty acid elongation and degradation, Valine, leucine and isoleucine degradation, Aminoacyl-tRNA biosynthesis and Purine metabolism. The top pathway was significantly enriched, and the molecules involved in the pathway that are present in the dataset are listed.

4.2.2 Specific intestinal metabolites potentially play a role in inflammation and cell function

As 128 molecules were found to be changed between the ileum and colon during colitis, this study selected molecules that had an interesting spatial distribution, a VIP>1, and/ or had their identities confirmed by matching online (mzCloud) spectra with ileum or colon tissue MSMS spectra (8.1.14) for further

investigation. A molecule of interest in the ileum had m/z 327.233 (VIP=1.057) and was identified as Docosahexaenoic acid (DHA). DHA was increased 2.66-fold (p=0.00197) in the colitis group compared to the control. The image suggests that the abundance of the molecule is higher in the muscularis, and submucosa compared to the mucosa; however, attempts to segment and classify the tissue into appropriate regions was not successful due to the complex heterogeneity of the intestine, thus bar graph data depicts relative abundance across entire tissue. The 'striped pattern' observed may also indicate sample preparation issues or instrumental artifacts, which might also contribute to lack of segmentation. The second molecule selected had m/z 132.0771 (VIP=1.050) and was identified as creatine. This molecule was increased 2.29-fold (p=0.0054) in the ileum of 3% DSS colitis group compared to controls. Lastly, a molecule with m/z 137.071 (VIP=1.605) was identified as 1-methylnicotinamide (1-MNA) and increased 2.59-fold (p=0.001162) in the colon of 3% DSS colitis group compared to the control group. The image indicates that 1-MNA is higher in the mucosa and submucosa; however, as previously described tissue could not be classified during analysis and data is shown as relative abundance across entire tissue (Figure 4.2.8).
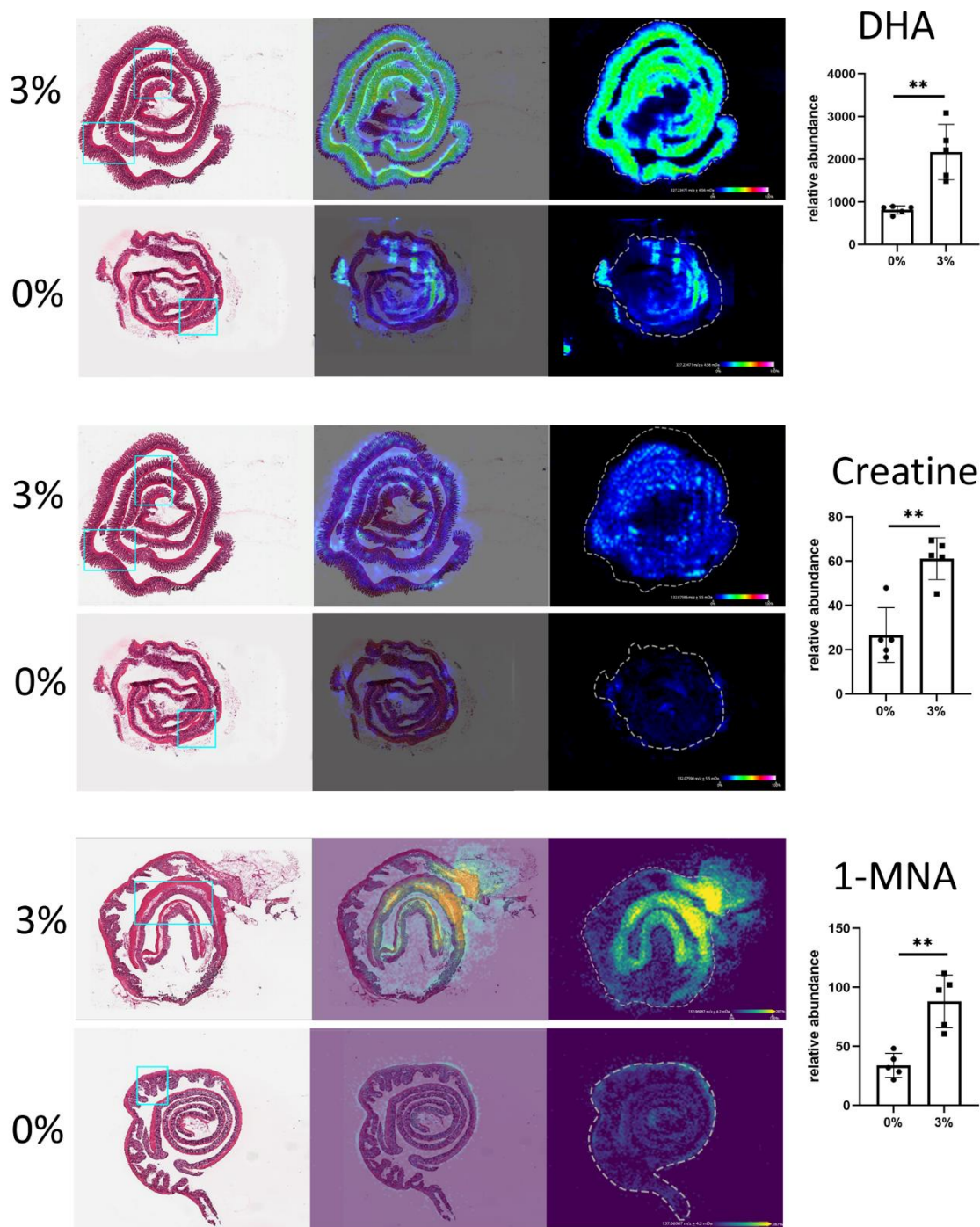
Figure 4.2.8 MSI image of DHA, Creatine and 1-MNA abundance in the intestine
From left to right; haematoxylin and eosin (H&E)-stained sections, overlayed image of H&E image and MSI of specific molecule, MSI heatmap of molecules (colour bar shows 0% to 100% relative abundance). Bar plot shows the relative abundance of DHA and Creatine in the ileum and 1-MNA in the colon. Data are shown as the mean of five biological replicates ± standard deviation (SD) (error bars). Multiple T-test was performed with FDR 5% adjustment to compare metabolite abundance between the groups (0% DSS and 3% DSS) *$p<0.05$, **$p<0.01$, ***$p<0.001$, ****$p<0.0001$ was considered statistically significant. Blue rectangular box shows the tissue region selected for imaging mass cytometry (IMC).

IMC was performed on tissue regions indicated by blue rectangular boxes in Figure 4.2.8. This technique revealed changes in structural and immune protein

markers, associated with IBD, at a 1 μM spatial resolution. A DNA intercalator was a generic marker used to determine the tissue organisation by highlighting the size and shape of the nucleus in individual cells and random forest machine learning tissue classifier module segmented the colon and ileum into mucosa and muscularis regions. In the ileal mucosa, the percentage of cells positive for markers F480, CD69, Ki67, CD4 and MHCII were downregulated 2.0-fold (p=0.0004), 1.96-fold (p=0.0176), 2.05-fold (p=0.0016), 1.77-fold (p=0.0252) and 1.86-fold (p=0.0105), respectively, in the 3% DSS group compared to the control (Figure 4.2.9).
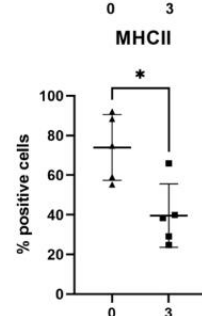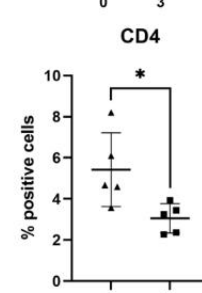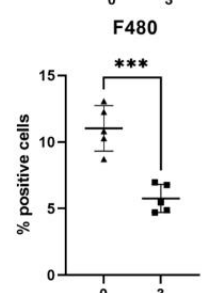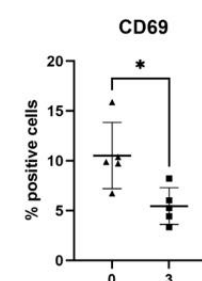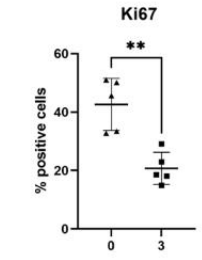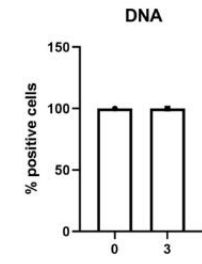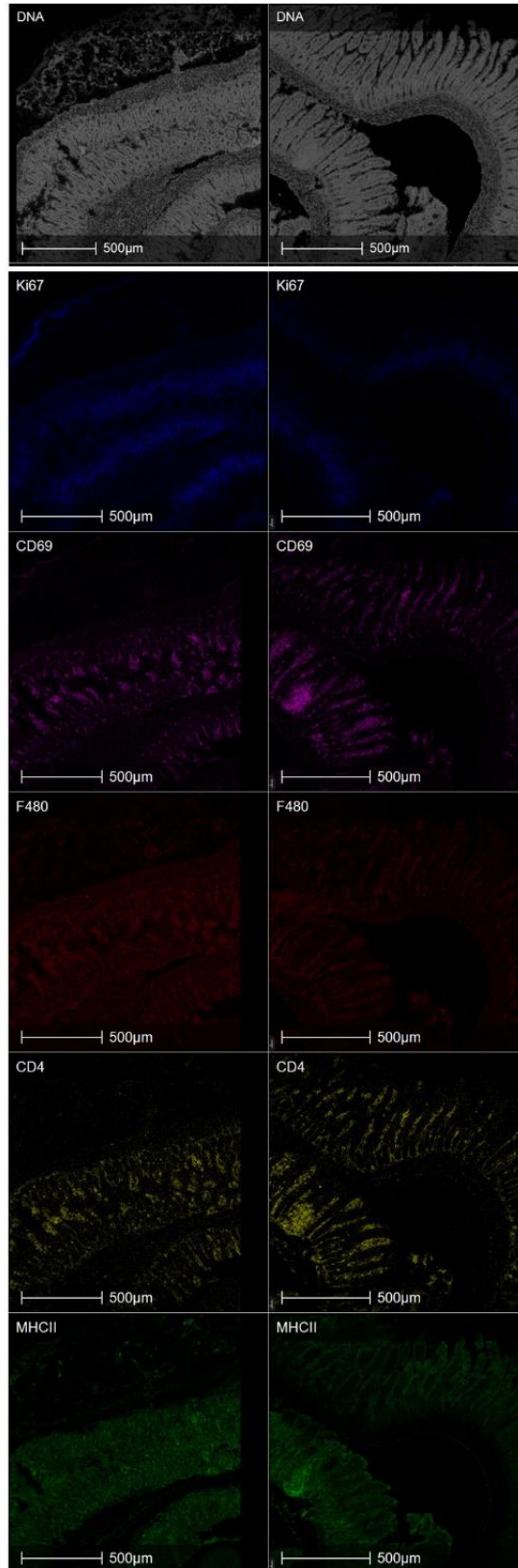
Figure 4.2.9 Representative IMC images of biological markers of cell function in the ileum of DSS colitis model
Image shown is the region indicated in Fig 4.3.8. From top to bottom, DNA intercalator identified single cells within the tissue section, markers for cell proliferation and immune cell function Ki67, CD69, F480, CD4 and MHCII. Percentage positive cells represented as bar graph showing five biological replicates. T-test performed to compare the two groups and *$p<0.05$, **$p<0.01$, ***$p<0.001$, ****$p<0.0001$ was considered statistically significant.

The markers observed in this study were then grouped to define single-cell phenotype and function such as proliferation, apoptosis, and activation. The study found that in the ileal mucosa of 3% DSS colitis mice, cells defined as Helper T cells (CD3$^+$, CD4$^+$), Dendritic cells (CD11c$^+$, MHCII$^+$), M2b and M1 macrophages (F480$^+$), and proliferation positive cells (Ki67$^+$) were decreased 1.78-fold ($p=0.0252$), 2.17-fold ($p=0.0136$), 1.91-fold ($p=0.0004$), 2.22-fold ($p=0.0043$) and 2.05-fold ($p=0.0016$), respectively, compared to the control (Figure 4.2.10). Furthermore, no individual markers were found to be significantly changed in the ileal muscularis of 3% DSS colitis mice compared to the control; however, M1 macrophages were found to be reduced 2.81-fold ($p=0.0319$) in the 3% group compared to control.
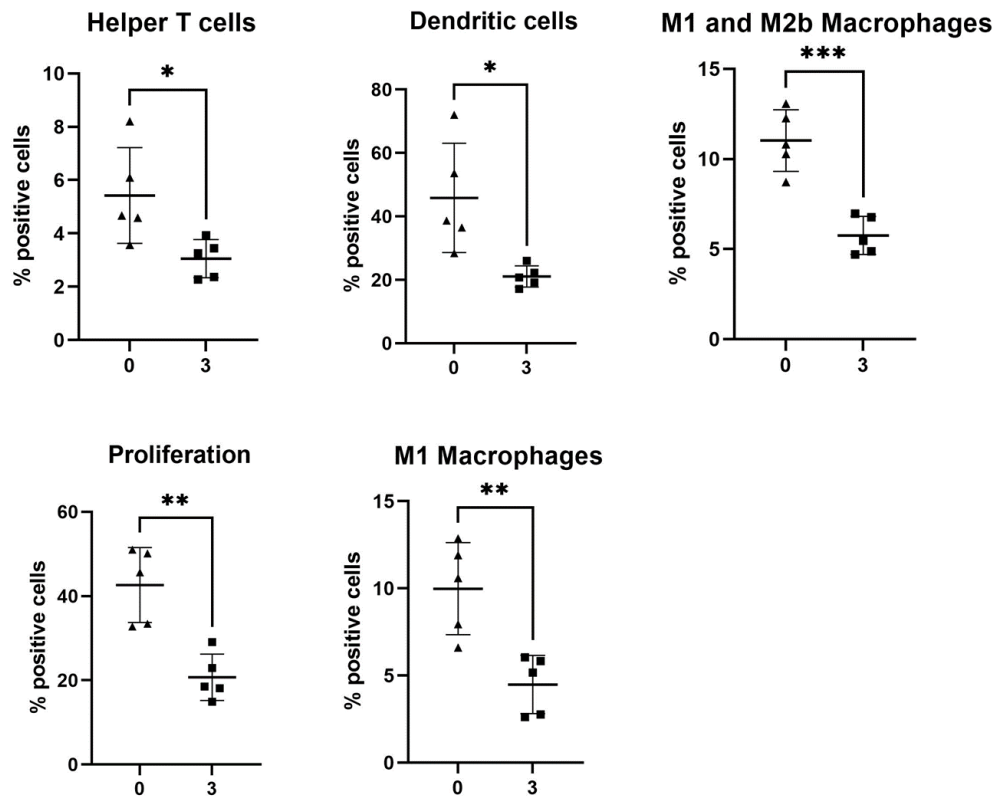
Figure 4.2.10 Bar graph of cell phenotype and function significantly changed in the ileal mucosa.
Percentage positive cells represented as bar graph showing five biological replicates and Helper T cells (CD3$^+$, CD4$^+$), Dendritic cells (CD11c$^+$, MHCII$^+$), M2b and M1 macrophages (F480$^+$), and proliferation positive cells (Ki67$^+$) were downregulated in 3% DSS colitis group compared to the control. T-test performed to compare the two groups and *$p<0.05$, **$p<0.01$, ***$p<0.001$, ****$p<0.0001$ was considered statistically significant.

In the colonic mucosa, 20 markers of cellular function, proliferation and structure were dysregulated between 3% DSS group and the control. Fig 4.3.11 shows the percentage of ATPase, Pan-CK, CD103, CD11c, E Cadherin, Glut1, Ki67 and EpCAM positive cells were decreased 5.01-fold ($p<0.0001$), 6.24-fold ($p=0.0246$), 2.62-fold ($p=0.0074$), 2.79-fold ($p=0.0030$), 8.07-fold ($p=0.0150$), 1.78-fold ($p=0.0177$), 3.30-fold ($p=0.0028$) and 8.57-fold ($p=0.0002$), respectively, in the 3% group compared to the control. The percentage of cells positive for the markers Vimentin, CD68, Ly6G, CD11b, F480, CD163, Collagen, Lyve1, FoxP3, NKp46, CD4 and Granzyme B significantly increased in the 3% group compared to the control by 2.39-fold ($p=0.0002$), 39.18-fold ($p=0.0019$), 22.13-fold ($p=0.0382$), 9.64-fold ($p<0.0001$), 8.30-fold ($p<0.0001$), 2.45-fold ($p=0.0018$), 2.28-fold ($p<0.0001$), 1.64-fold ($p=0.0342$), 9.50-fold ($p=0.0007$),

7.42-fold (p=0.0393), 4.88-fold (p=0.0025) and 2.72-fold (p=0.0402), respectively.
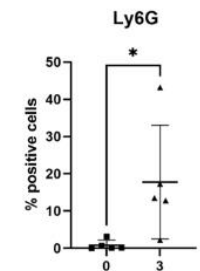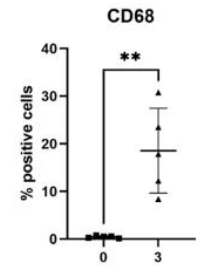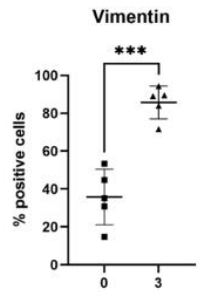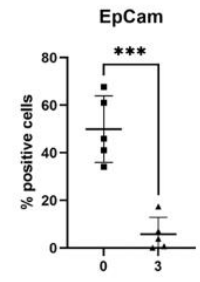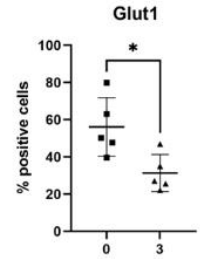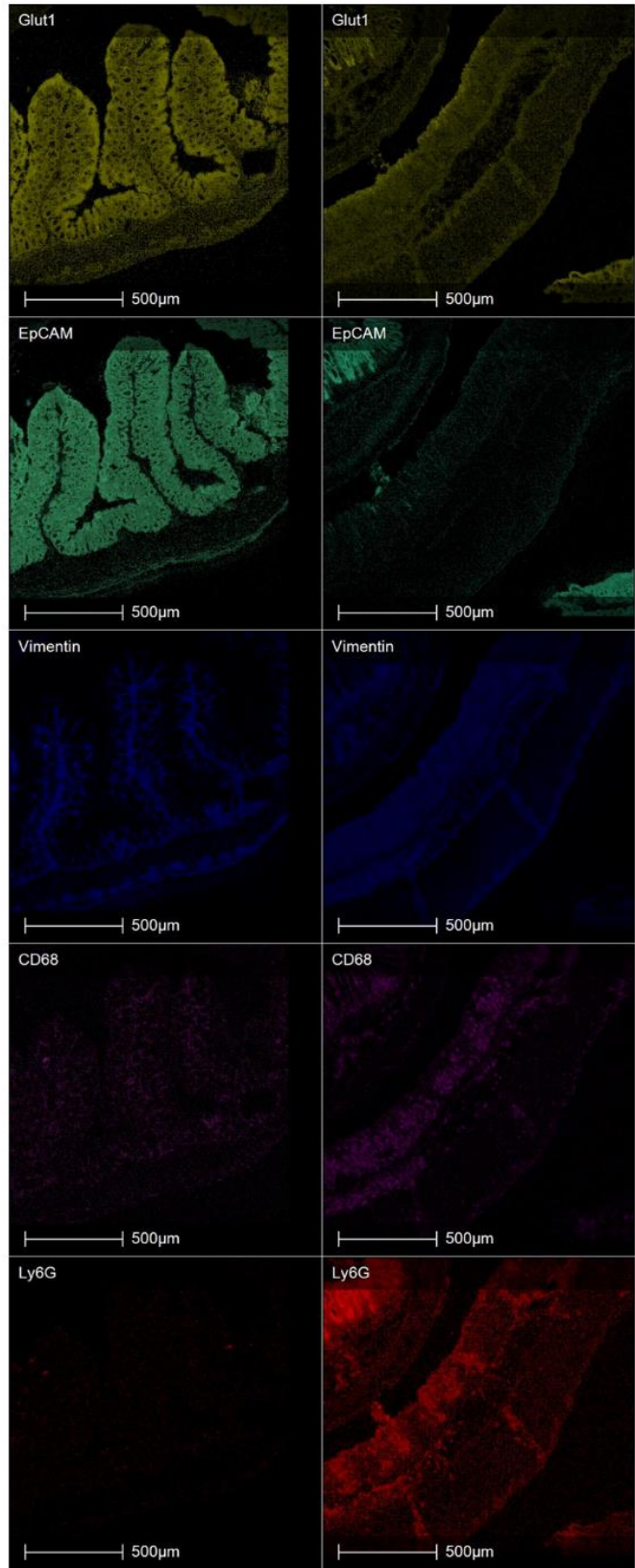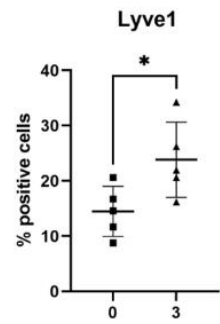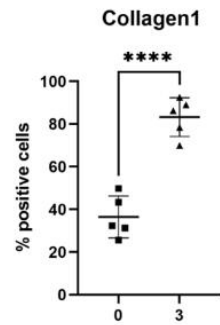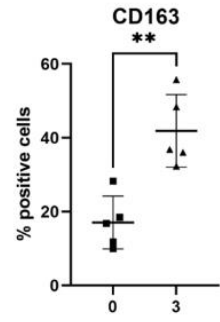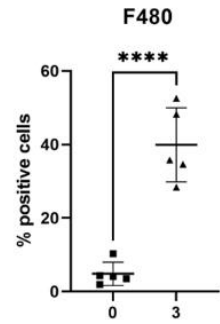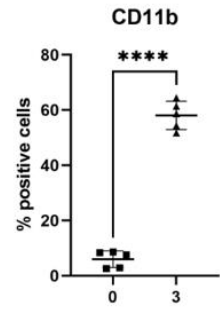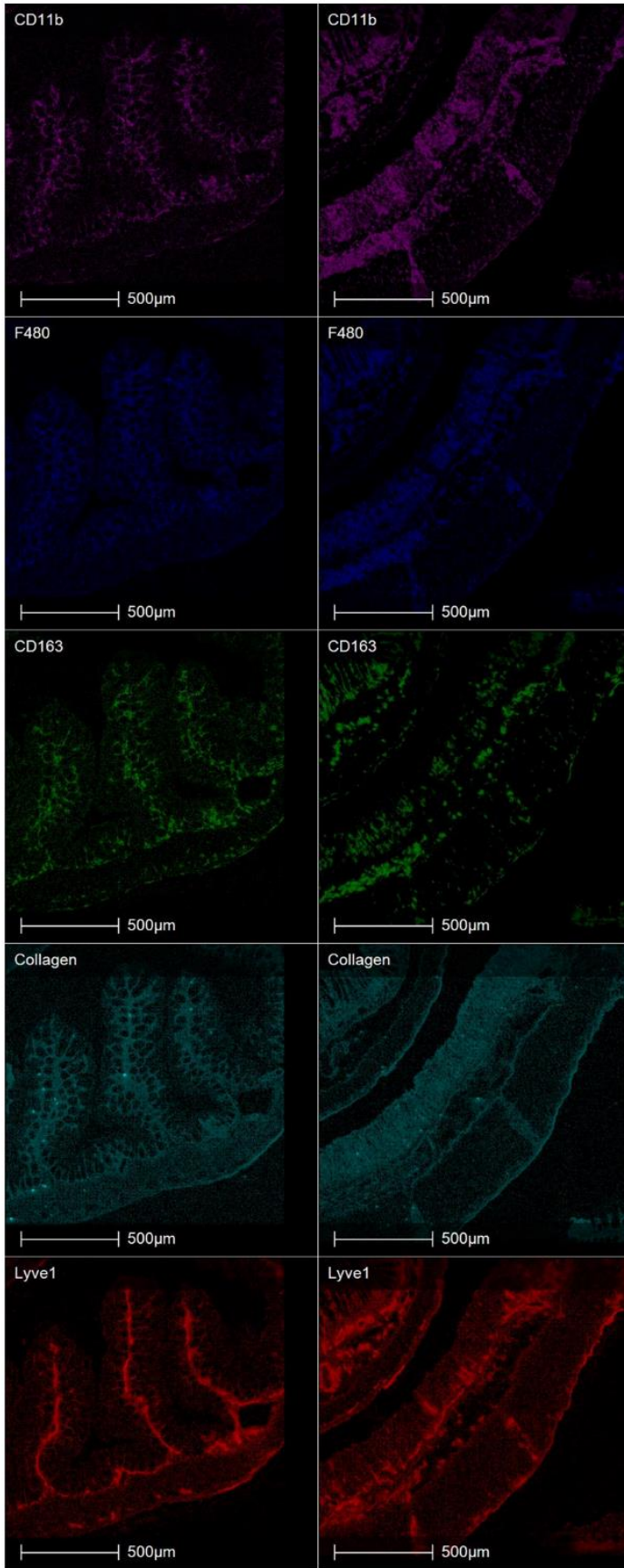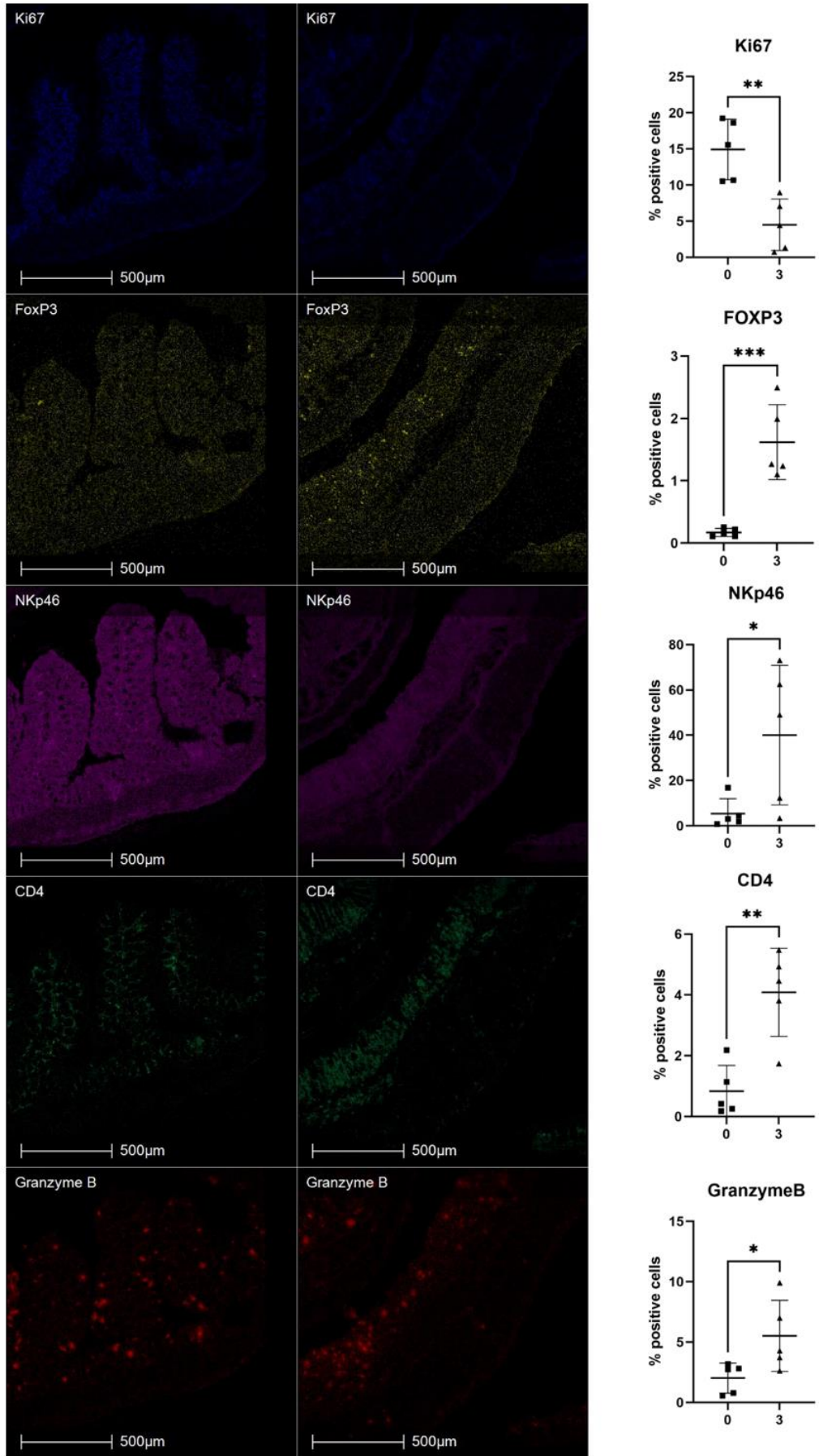
Figure 4.2.11 Representative IMC images of biological markers of cell function in the colon of DSS colitis model.
Image shown is the same region as in Fig 4.3.8. From top to bottom, DNA intercalator identified single cells within the tissue section, markers for cell proliferation and immune cell function ATPase, Pan-CK, CD103, CD11c, E Cadherin, Glut1, EpCAM, Vimentin, CD68, Ly6G, CD11b, F480, CD163, Collagen1, Lyve1, Ki67, FOXP3, NKp46, CD4 and Granzyme B. Ki67, CD69, F480, CD4 and MHCII. Percentage positive cells represented as bar graph showing five biological replicates. T-test performed to compare the two groups and *$p<0.05$, **$p<0.01$, ***$p<0.001$, ****$p<0.0001$ was considered statistically significant.

Furthermore, the markers were used to predict the dysregulation of 14 cellular phenotypes and functions between 3% DSS and control groups in the colon. Figure 4.2.12 shows the percentage of positive cells that were proliferative (Ki67$^+$), hypoxic (Glut1$^+$), or antigen-presenting dendritic cells (CD11c$^+$, MHCII$^+$, CD103$^+$) were significantly reduced in the colonic mucosa of 3% group by 3.3-fold ($p=0.0028$), 1.78-fold ($p=0.0177$) and 3.34-fold ($p=0.0078$), respectively, compared to the control. Furthermore, the percentage of helper T cells (CD3$^+$, CD4$^+$), regulatory T cells (CD3$^+$, CD4$^+$, FOXP3$^+$), natural killer (NK) cells (NKp46$^+$), neutrophils (Ly6G$^+$, CD11b$^+$), blood vessels (CD31$^+$) and mesenchymal cells (Vimentin$^+$) were significantly increased 4.92-fold ($p=0.0025$), 10.85-fold ($p=0.0071$), 7.43-fold ($p=0.0393$), 320-fold ($p=0.0110$), 2.85-fold ($p=0.0011$) and 2.39-fold ($p=0.0002$), respectively, compared to the control. The percentage of macrophages (F480$^+$, CD68$^+$, CD11b$^+$) and macrophage subsets including M2c (F480$^+$, CD163$^+$), M2a(F480$^+$, CD206$^+$), M2b (F480$^+$) and M1 (F480$^+$, MHCII$^+$) were also significantly increased in the 3% DSS colonic mucosa compared to the control 58.54-fold ($p=0.0014$), 12.39-fold ($p=0.0003$), 8.81-fold ($p=0.0397$), 8.30-fold ($p<0.0001$) and 4.72-fold ($p<0.0001$), respectively. The study also observed that in the colonic muscularis of the 3% DSS group, the percentage of CD11b$^+$, F480$^+$ and granzyme B$^+$ cells increased 8.24-fold ($p<0.0001$), 7.20-fold ($p=0.0008$) and 7.00-fold ($p=0.0234$), respectively, compared to the control. Furthermore, markers indicated that the percentage of M2c, M1 and M2 macrophages, and M1 macrophage positive cells significantly increased 6.15-fold ($p=0.0009$), 7.20-fold ($p=0.0008$) and 3.85-fold ($p=0.0419$), respectively, in the 3% group compared to the control.
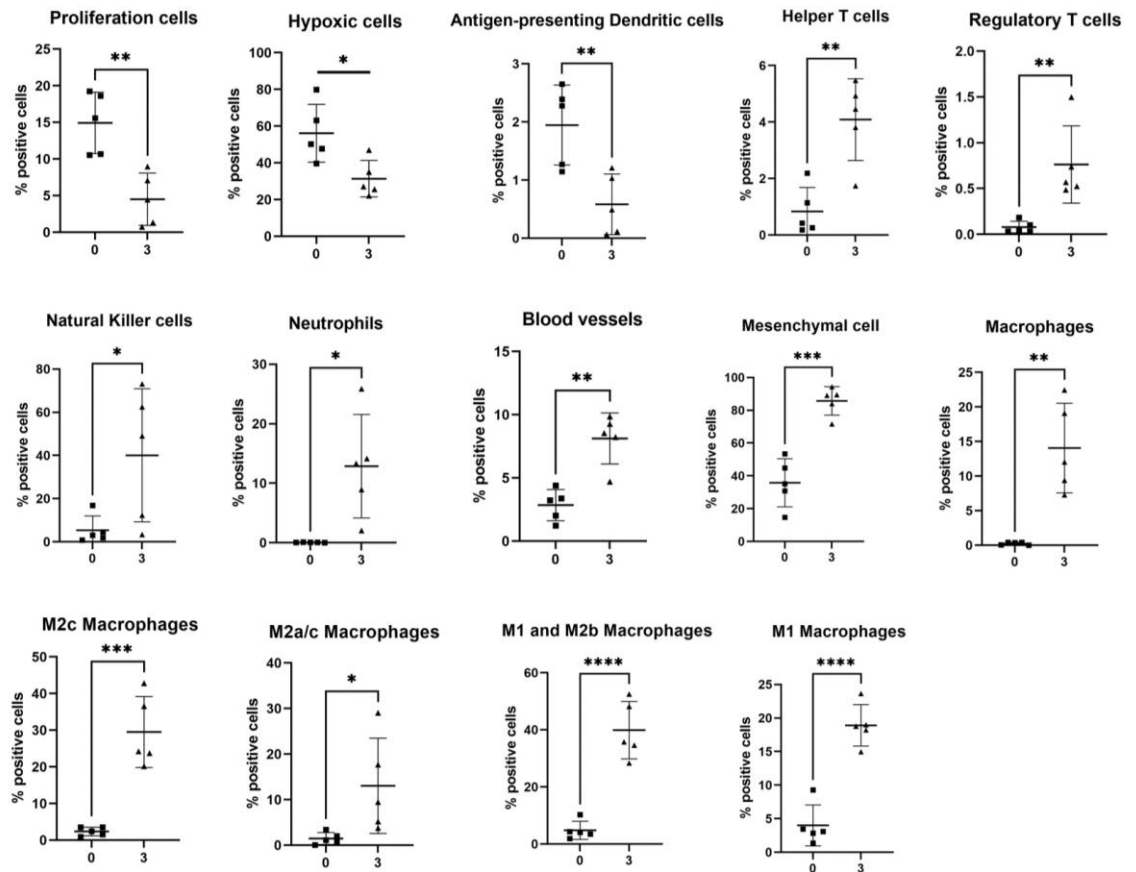
Figure 4.2.12 Bar graph of cell phenotype and function significantly changed in the colonic mucosa
Percentage positive cells represented as bar graph showing five biological replicates. Proliferative (Ki67^{+}), hypoxic (Glut1^{+}), and antigen-presenting dendritic cells (CD11c^{+}, MHCII^{+}, CD103^{+}) were reduced and Helper T cells (CD3^{+}, CD4^{+}), regulatory T cells (CD3^{+}, CD4^{+}, FOXP3^{+}), natural killer (NK) cells (NKp46^{+}), neutrophils (Ly6G^{+}, CD11b^{+}), blood vessels (CD31^{+}), mesenchymal cells (Vimentin^{+}), macrophages (F480^{+}, CD68^{+}, CD11b^{+}) and macrophage subsets including M2c (F480^{+}, CD163^{+}), M2a(F480^{+}, CD206^{+}), M2b (F480^{+}) and M1 (F480^{+}, MHCII^{+}) were increased in the 3% group compared to the control. T-test performed to compare the two groups and $*p<0.05$, $**p<0.01$, $***p<0.001$, $****p<0.0001$ was considered statistically significant.

To further elucidate how creatine, DHA and 1-MNA may be contributing to the altered immune profile observed by IMC, this study conducted a variety of *in vitro* tests using the HCT-8 intestinal epithelial cell line. Creatine, DHA and 1-MNA were purchased and MSMS spectra were collected alongside tissue spectra; creatine and 1-MNA tissue spectra closely match their standards as they share peaks at similar abundances, suggesting that they are the same molecule (8.1.14, 8.1.15). However, the spectra collected from the DHA chosen standard and tissue are not an accurate match; thus, the DHA molecule investigated in this study might not be representative of the molecule observed in the DSS induced colitis ileum (8.1.16). LDH assays indicated that creatine, DHA and 1-

MNA are cytotoxic to HCT-8 epithelial cells (Fig 4.3.13a). Creatine increased cytotoxicity by 19.6% (p=0.0001) and 21.3% (p<0.0001) compared to the control (no treatment) when exposed to 50 µM and 100 µM, respectively. HCT-8 treatment with 50 µM and 100 µM DHA also increased cytotoxicity by 26.8% (p<0.0001) and 21.15% (p<0.0001), respectively, compared to the control. Lastly, 1-MNA was also found to be cytotoxic to HCT-8 cells at 50 µM and 100 µM and increased cytotoxicity by 15.6% (p=0.0012) and 19.9% (p=0.0001), respectively. After establishing that the molecules are cytotoxic to HCT-8 cells, a caspase-3/7 assay was used to measure caspase levels as an indicator of cell apoptosis (Figure 4.2.13). Treating HCT-8 cells with 50 µM and 100 µM creatine significantly reduced RFU/g of protein 1.57-fold (p=0.0324) and 1.88-fold (p=0.0065), respectively, compared to the control. Furthermore, HCT-8 exposure to 50 µM of DHA significantly reduced RFU/g of protein 1.79-fold (p=0.0096) compared to the control. However, increasing the concentration of DHA to 100 µM has no significant effect on HCT-8 cell caspase-3/7 activation compared to the control. This suggests that creatine and DHA have the potential to reduce apoptosis in HCT-8 epithelial cells in a dose dependent manner. Moreover, exposing HCT-8 cells to 50 µM and 100 µM of 1-MNA did not significantly affect the RFU/g of protein compared to the control, suggesting that apoptosis is not triggered. Thus, the observed increased cytotoxic effect that occurs during molecule exposure must be due to an alternative pathway and may contribute to the cellular dysfunction observed in IMC data.
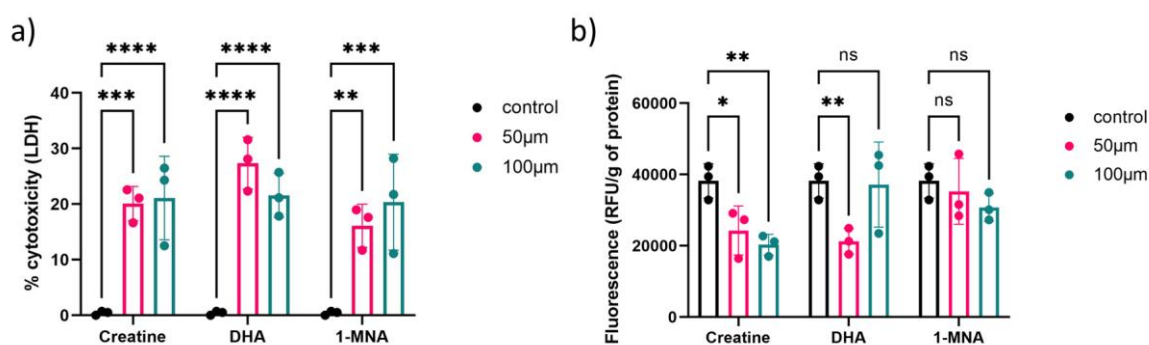
Figure 4.2.13 LDH and Caspase-3/7 release from treated HCT-8 cell indicates cytotoxic effect and apoptosis activity.
HCT-8 cells were exposed to creatine, DHA and 1-MNA for 72 h. a) LDH assay used HCT-8 cells only and cells treated with 2% triton-x as low and high LDH release controls, respectively. The percentage of cytotoxicity was calculated as %= (measured absorbance of sample-low control)/(high control-low control) x100. b) The caspase-3/7 assay calculated enzyme activity by measuring relative fluorescence units (RFU) of activity normalised to protein in cell lysates. Data

are shown as the mean of three biological replicates ± standard deviation (SD) (error bars). Two-way ANOVA was performed across to compared metabolite exposure to cell only controls *$p<0.05$, **$p<0.01$, ***$p<0.001$, ****$p<0.0001$ versus the control condition (cells without molecules) was considered statistically significant.

This study assessed whether the metabolites have the potential to be pro-inflammatory via the release of specifically selected cytokines. Fig 4.2.14a shows that creatine, DHA and 1-MNA used at 50 µM and 100 µM do not significantly alter HCT-8 secretion of IL-6, compared to control. Furthermore, 1-MNA does not affect HCT-8 IL-8 secretion compared to the control; however, exposing HCT-8 to 50 µM creatine or 100 µM DHA significantly reduced IL-8 release 1.41-fold ($p=0.0417$) and 1.40-fold ($p=0.0447$), respectively, compared to the control (Fig 4.3.14b). The study also found that exposing HCT-8 to 100 µM DHA significantly increased the release of TNF-α 3.22-fold ($p<0.0001$) compared to the control; however, creatine and 1-MNA did not affect the release of TNF-α (Fig 4.3.14c). The data also shows the 50 µM of creatine, DHA or 1-MNA does not after the release of IL-15 compared to controls (Fig 4.3.14d). However, increasing the concentration of creatine, DHA and 1-MNA to 100 µM resulted in HCT-8 increasing the release of IL-15 3.74-fold ($p=0.0009$), 3.66-fold ($p=0.0017$) and 3.55-fold ($p=0.0012$), respectively, compared to the control. Therefore, changes in specific cytokine profile are highly dependent on the molecule and increased concentrations are more likely to be pro-inflammatory. As MSI indicated that these molecules were increased *in vivo*, it is likely based on these results that they are contributing to the inflammatory process.
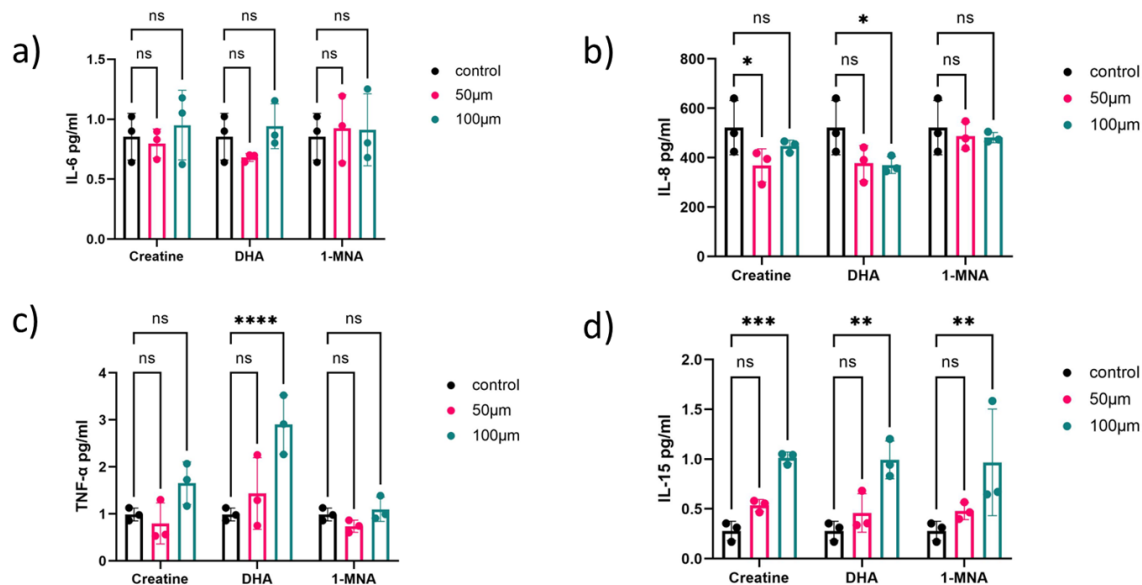
Figure 4.2.14 Cytokine release into cell supernatant after 72h exposure to metabolites.

HCT-8 cells were stimulated with creatine, DHA and 1-MNA for 72 h before supernatants were collected. ELISA was used to quantify the release of a) IL-6 pg/ml, b) IL-8 pg/ml, c) TNF-α pg/ml and d) IL-15 pg/ml. Data is shown as the mean of 3 biological replicates ± standard deviation (SD). Two-way ANOVA was performed for each molecule versus the control condition (cells without treatment). *$p < 0.05$, **$p < 0.01$, ***$p < 0.001$, ****$p < 0.0001$ is considered statistically significant.

After determining the modulatory effect creatine and DHA have on IECs, this study wanted to establish the effect on different immune cells. Immune cells were isolated from mouse spleens and stimulated with creatine, DHA, or a cytokine (IL-4 or IL-12+IL-18) as positive immune activating controls. Immune cells were gated and characterised as described in Appendix 8.2.15. Figure 4.2.15a shows that treating cells with DHA does not significantly change the percentage of NK cells, B cells, and macrophages positively expressing CD69, compared to the control. Stimulation with creatine also did not significantly change the percentage of B cells and macrophages positively expressing CD69, compared to the control. However, stimulating cells with creatine did increase the percentage of NK cells expressing CD69 2.67-fold (p=0.0007), compared to the control. Figure 4.2.15b shows the MFI of specific immune cells positively expressing markers. The results indicate that stimulation with creatine or DHA does not significantly affect the level at which macrophages express MHCII, or NK cell express granzyme B or B cells express MHCII compared to the control.
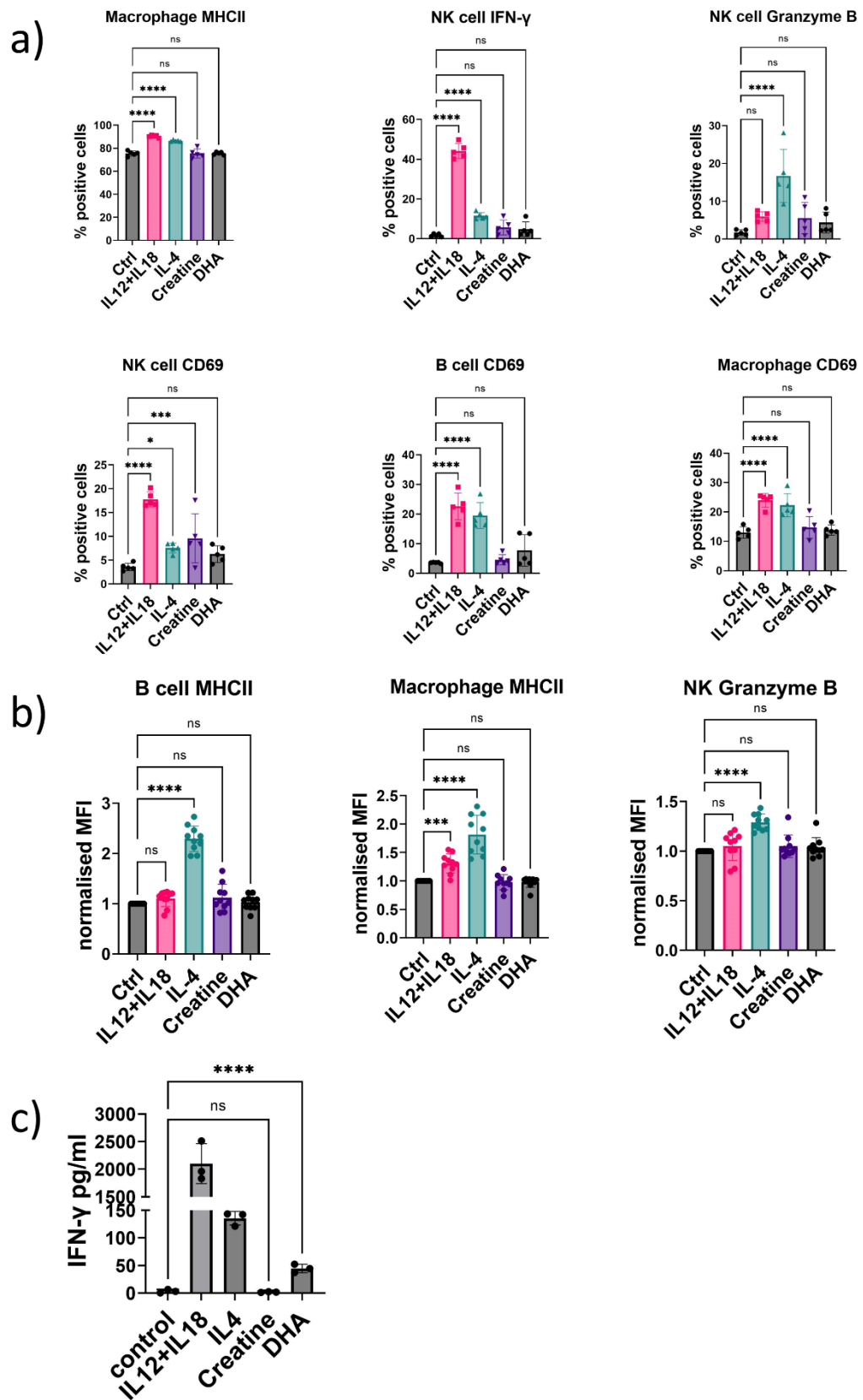
Figure 4.2.15 Flow cytometry and cytokine release analysis of splenic immune cells following stimulation with creatine and DHA. Immune cells were isolated from spleen tissue

and stimulated with 50 μM creatine or DHA as well as IL12+IL-18 and IL4 as positive immune activating controls. A) Percentage of immune cells (NK cells, B cells and macrophages) positively expressing specific markers (MHCII, IFN-γ, granzyme B and CD69). B) Mean fluorescence intensity (MFI) was normalised to control (no stimulation) and shows the relative amount of expressed marker within a positive population. A-B) One-way ANOVA was performed to compare stimulation versus the control condition (cells without treatment). C) ELISA was used to quantify the release of IFN-γ into immune cell supernatant and is shown as pg/ml. Unpaired T-test was performed to compared creatine or DHA stimulated groups to control and did not include positive controls (cytokine stimulations). Data is shown as the mean of 3 biological replicates ± standard deviation (SD). *$p<0.05$, **$p<0.01$, ***$p<0.001$, ****$p<0.0001$ is considered statistically significant.

Following flow cytometry analysis, this study wanted to quantify the release of specific cytokines into the supernatant. A proteome profiler mouse cytokine array (8.1.18) indicated that IFN-γ was increased in the cell supernatant following molecular exposure compared to the control and was selected for quantification using ELISA. Figure 4.3.15c shows that treating cells with creatine did not significantly alter IFN-γ release compared to the control ($p=0.9012$). However, treating cells with DHA increased the secretion of IFN-γ 13.29-fold ($p<0.0001$) compared to the control.

4.2.3 Intestinal colitis alters the metabolome in the liver

MSI was used to investigate the gut-liver metabolomic axis during severe intestinal colitis. ROC analysis identified 511 peaks in the liver that could discriminate between the control and disease group. The variation in the 511 metabolites detected was analysed to examine the clustering of groups using multivariate statistical analysis including PCA (M1) & PLS-DA (M2). PCA score plot of the first (t [1]) principle component did show clear separation in the colon between 0% DSS group from the 3% DSS treated group (parameters: R2X=0.703, Q2=0.605) (Fig. 4.3.16 M1). PLS-DA score plot (M2) was also able to separate the groups and clustered using the first and second principle components (parameters: R2X=0.0.767, R2Y=0.986, Q2=0.939). PLS-DA generated VIP scores above 1 highlight the molecules contributing the most to group separation (8.1.9). Univariate analysis indicated that 239 molecules were significantly changed between the groups (Appendix 88.1.8). This study could assign putative identities to 125 molecules (52.3%) and MSMS fragmentation confirmed the identity of one molecule as L-carnitine (0.41% identification rate).

Model	Type	A	N	R2X(cum)	R2Y(cum)	Q2(cum)
M1	PCA-X	1	10	0.703		0.605
M2	PLS-DA	2	10	0.767	0.986	0.939
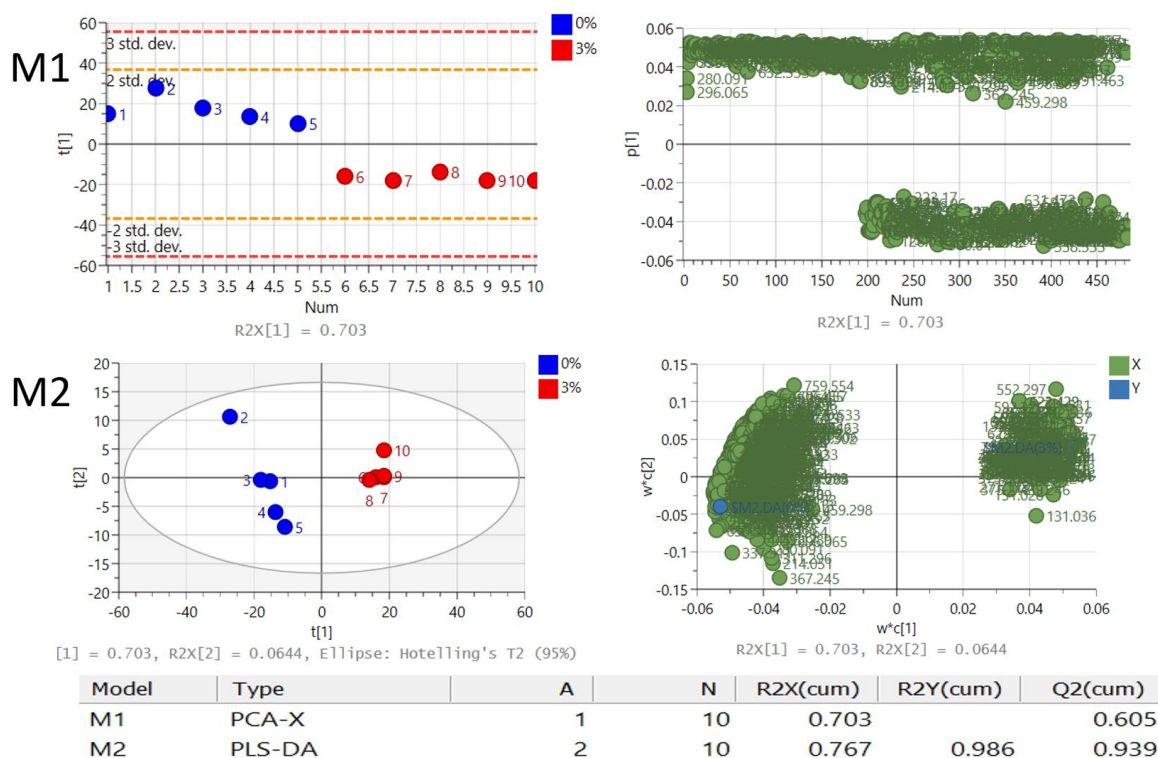
Figure 4.2.16 Unsupervised and supervised discriminant analysis
M1) Unsupervised PCA analysis was able to discriminate between the groups using metabolite features. M2) Supervised PLS-DA analysis show the molecules in the of DSS colitis model can discriminant between the control (0% DSS, blue circles) and diseased group (3% DSS, red circles). Analysis was performed using SIMCA 17 software. PLS-DA and PCA score plots consist of components 1 (t [1]) and 2 (t [2]). The ellipse represents the 95% confidence region for Hotelling'g T2 statistic for the model.

Furthermore, enrichment analysis using KEGG database indicated that the molecules found in the dataset are involved in at least 25 pathways (Figure 4.2.17): galactose metabolism (p=4.98E-04) and Biosynthesis of unsaturated fatty acids (p=1.46E-03) pathways were significantly enriched. Other metabolites in the liver that were identified are involved in Amino sugar and nucleotide sugar metabolism, Fructose and mannose metabolism, Caffeine metabolism, alpha-Linolenic acid metabolism, Neomycin, kanamycin and gentamicin biosynthesis, Starch and sucrose metabolism, Linoleic acid metabolism, Alanine, aspartate and glutamate metabolism, Ascorbate and aldarate metabolism, Arachidonic acid metabolism, Ubiquinone and other terpenoid-quinone biosynthesis, Arginine and proline metabolism, Tyrosine metabolism, Arginine biosynthesis, Nicotinate and nicotinamide metabolism, Histidine metabolism, Pantothenate and CoA biosynthesis, Ether lipid metabolism, beta-Alanine metabolism, Lysine degradation, Glycolysis / Gluconeogenesis, Glutathione metabolism, Phosphatidylinositol signalling system, Inositol phosphate

metabolism, Fatty acid elongation, Fatty acid degradation, Fatty acid biosynthesis, Aminoacyl-tRNA biosynthesis, Purine metabolism and Steroid hormone biosynthesis.
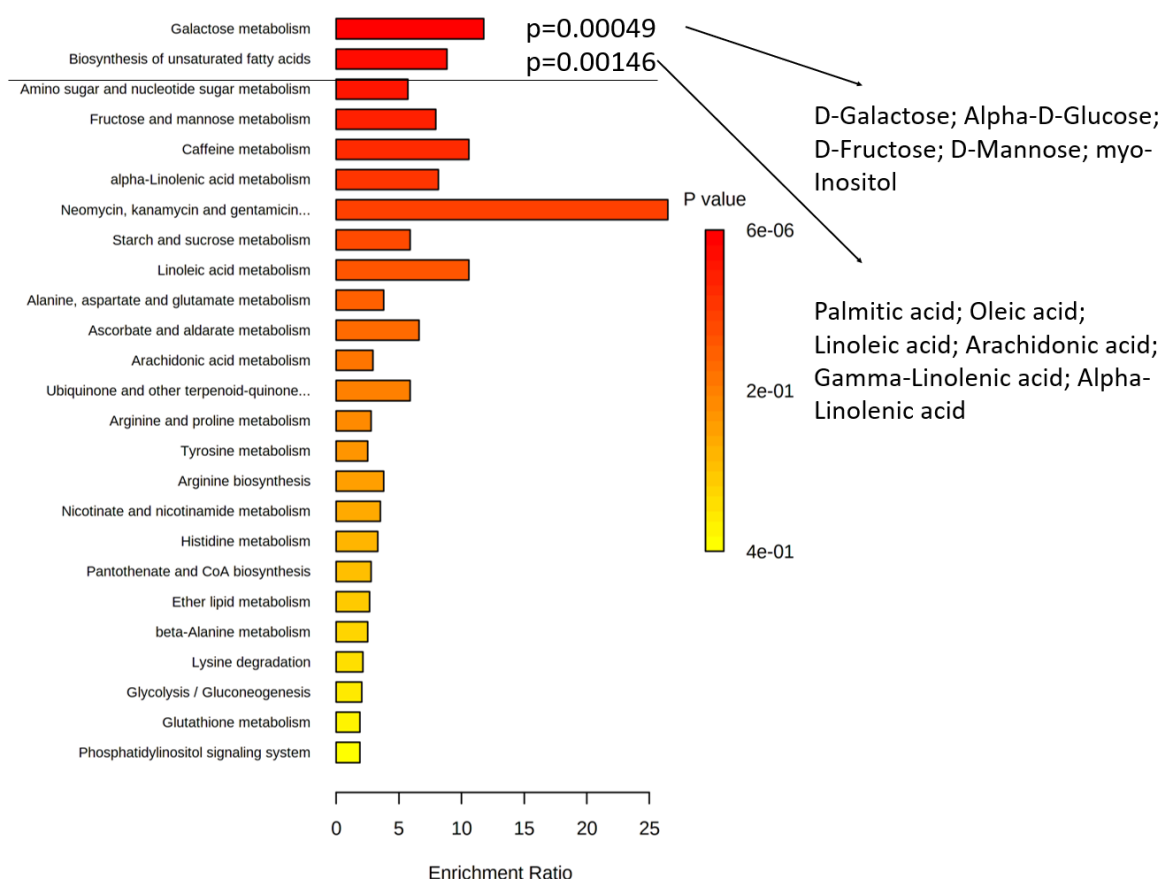
Figure 4.2.17 Enrichment of pathways in the liver of DSS colitis model
Enrichment pathway analysis using KEGG as reference found molecules involved in 25 different pathways. Galactose metabolism and biosynthesis of unsaturated fatty acids were significantly enriched, and the molecules involved in the pathway that are present in the dataset are listed.

This study aimed to identify molecular biomarkers of intestinal inflammation that were also altered in systemic sites that may contribute to disease development. We found 7 molecules to be similarly altered in the colon and ileum of the DSS colitis model. Molecules with the m/z 193.1234 and 221.1183 were significantly increased in both the ileum (1.78-fold, p=0.0019) and colon (2.32-fold, p=0.0239) during DSS induced colitis group compared to the controls; however, no putative identity was available. Four other molecules that were also upregulated in both tissues during colitis were m/z 301.1658 (ileum 15.8-fold, p=0.03; colon 4.84-fold, p=0.001), 317.1759 (ileum 3.06-fold, p=0.0012;

colon 7.9-fold, p=0.02), 343.228 (ileum 3.40-fold, p=0.0038; colon 7.1-fold, p=0.02) and 391.2126 (ileum 4.45-fold, p=0.0019; colon 12.64-fold, p=0.023). These molecules were putatively identified as 11b-Hydroxyandrost-4-ene-3,17-dione, ubiquinone-2, epoxydocosapentaenioc acid and 14-hydroperoxy-H4-neuroprostane, respectively. Lastly m/z 277.2172 was putatively identified as gamma-linolenic acid and was found to be significantly downregulated in the colon (2.09-fold, p=0.045) and ileum (2.11-fold, p=0.0012) of 3% DSS mice compared to the control.

Furthermore, the molecule upregulated in the colon and ileum that was putatively identified as ubiquinone-2 was also found to be upregulated 2.73-fold (p=0.00108) in the liver of colitis mice compared to the control. In addition, the molecule downregulated in the colon and ileum that was putatively identified as gamma-Linolenic acid was also downregulated 1.67-fold (p=0.0016) in the liver of colitis mice compared to the control. A further seven molecules were found to be similarly changed between the liver and ileum. The molecule with m/z 162.1138 was putatively identified as L-carnitine and found to be significantly upregulated 3.73-fold (p=0.0034) in the liver and 1.57-fold (p=0.0098) in the ileum of colitis group compared to the control. A further five molecules were found to be downregulated in both the ileum and liver of colitis group compared to the controls: m/z 509.4583 (ileum 3.91-fold, p=0.0019; liver 3.35-fold, p=0.00014), 511.4731 (ileum 1.98-fold, p=0.001; liver 1.50-fold, p=0.000435), 512.4757 (ileum 2.18-fold, p=0.0019; liver 1.53-fold, p=0.000405), 583.4945 (ileum 5.09, p=0.001; liver 8.88-fold, p=0.0001) and 607.4946 (ileum 3.18-fold, p=0.00233; liver 4.38-fold, p=0.00007). However, only m/z 509.4583 and 607.4946 could be assigned putative identities, fatty acyl esters of hydroxy fatty acid (FAHFA) and a diglyceride (DG(34:1)), respectively. Lastly, m/z 594.34087 was significantly downregulated 3.70-fold in ileum (p=0.00190) and upregulated 2.17-fold (p= 0.00235) in liver of 3% DSS mice compared to control and was putatively identified as a diglyceride (DG(18:0)) (Figure 4.2.18). Therefore, these molecules could be potential biomarkers of intestinal colitis and associated liver complications and warrant further investigation.

m/z	Identity
162.11389	L-carnitine
277.2172	gamma-Linolenic acid (P)
317.1759	Ubiquinone-2 (P)
509.45837	FAHFA(16:0/6-O-16:0) (P)
511.47317	
512.47578	
583.4945	
594.34087	DG(18:0)(P)
607.49468	DG(34:1)(P)

m/z	Identity
277.2172	gamma-Linolenic acid (P)
317.1759	Ubiquinone-2 (P)

m/z	Identity
277.2172	gamma-Linolenic acid (P)
317.1759	Ubiquinone-2 (P)

m/z	Identity
193.1234	
221.1183	
277.2172	gamma-Linolenic acid (P)
301.1658	11b-Hydroxyandrost-4-ene-3,17-dione
317.1759	Ubiquinone-2 (P)
343.228	Epoxydocosapentaenoic acid(P)
391.2126	14-Hydroperoxy-H4-neuroprostane(P)

Figure 4.2.18 Venn diagram of molecules altered in the ileum, colon, and liver in DSS colitis model

The top circle represents the 239 molecular changes in the liver, bottom-left circle represents 88 molecular changes in ileum and bottom-right represents 30 molecular changes in the colon. Overlapped segments indicate the number of molecules that are changed similarly between different tissue. The *m/z* and putative identities of the molecules commonly shared between tissue are highlighted in boxes.

4.2.4 Intestinal colitis results in a dysregulated immune cell profile in the liver

As MSI revealed hundreds of metabolite changes in the liver during colitis, IMC was employed for single-cell phenotyping to identify changes in function that could result in disease complications. As MSI heatmaps indicated that most molecules are homogenous throughout liver tissue, the sections were selected for IMC at random. The liver was segmented into regions, tissue and blood vessels based on tissue morphology. In the tissue of the 3% DSS group, the percentage of CD68^{+}, CD45^{+}, F480^{+}, CD163^{+}, E cadherin^{+}, collagen^{+}, Glut1^{+} and CD206^{+} cells increased 2.50-fold (p=0.0114), 1.96-fold (p=0.0465), 2.11-fold (p=0.0026), 2.49-fold (p=0.0113), 1.53-fold (p=0.00325), 2.09-fold (p=0.0422),

2.03-fold (*p*=0.0272) and 1.50-fold (*p*=0.0033), respectively, compared to control (Figure 4.2.19).
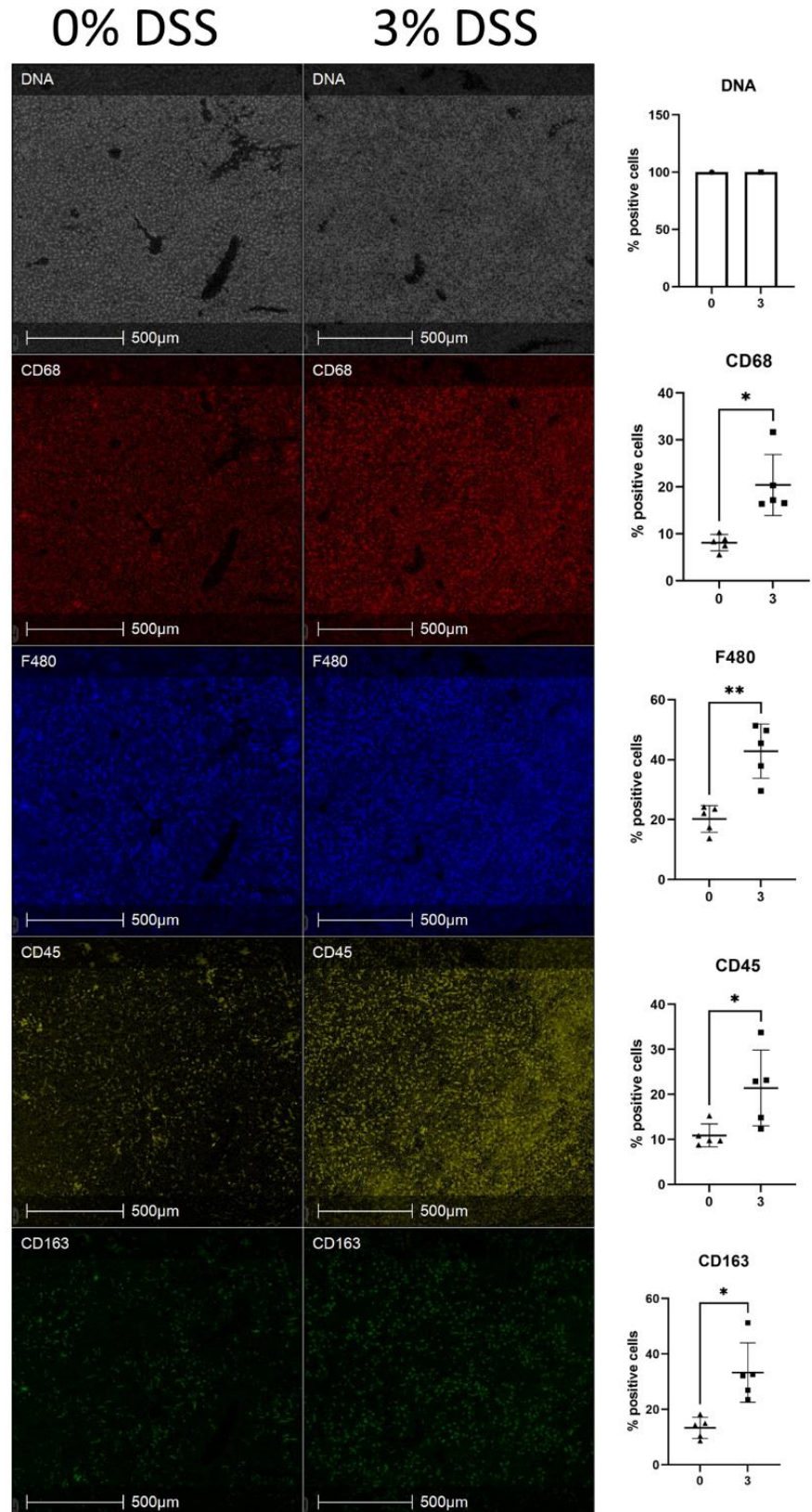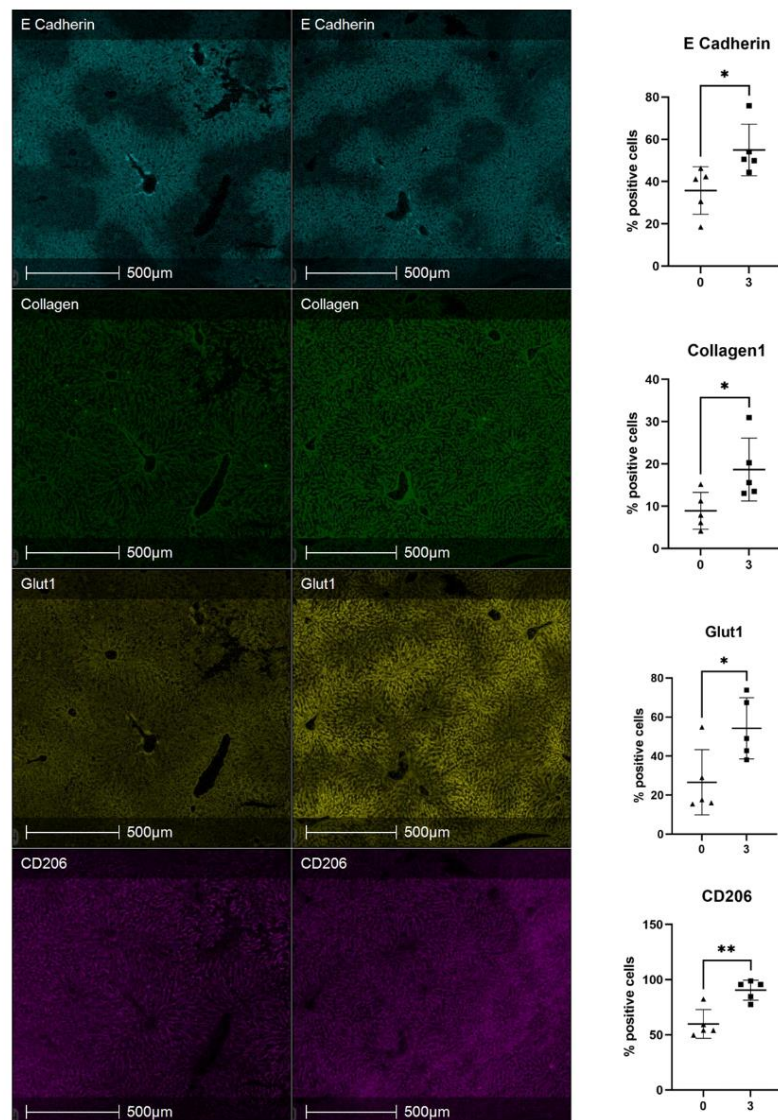
Figure 4.2.19 Representative IMC images of biological markers of cell function in the liver of DSS colitis model
From top to bottom, DNA intercalator identified single cells within the tissue section, markers for cell proliferation and immune cell function CD68, F480, CD45, CD163, E cadherin, collagen1, Glut1 and CD206. Percentage positive cells represented as bar graph showing five biological replicates. T-test performed to compare the two groups and $*p<0.05$, $**p<0.01$, $***p<0.001$, $****p<0.0001$ was considered statistically significant.

The markers selected for this study were used to predict changes in specific cell types and the results showed that in the 3% DSS group, the percentage of regulatory T cells (CD3$^+$, CD4$^+$, FOXP3$^+$) and activated cytotoxic T cells (CD3$^+$, CD8$^+$, granzyme B$^+$) was significantly reduced 2.44-fold ($p=0.0493$) and 14.42-fold ($p=0.0244$), respectively, compared to the control. However, the percentage of macrophage cells in the subclass M2c (F480$^+$, CD163$^+$) and M2a (F480$^+$, CD206$^+$) were significantly upregulated 2.42-fold ($p=0.0050$) and 2.32-fold ($p=0.0018$),

respectively, in the 3% DSS group. Lastly, the percentage of cells that were hypoxia (Glut1$^+$) positive increased 2.03-fold (p=0.0271) during 3% colitis compared to the control (Figure 4.2.20). Therefore, the metabolic and cellular environment in the liver during intestinal colitis may perpetuate disease complications.
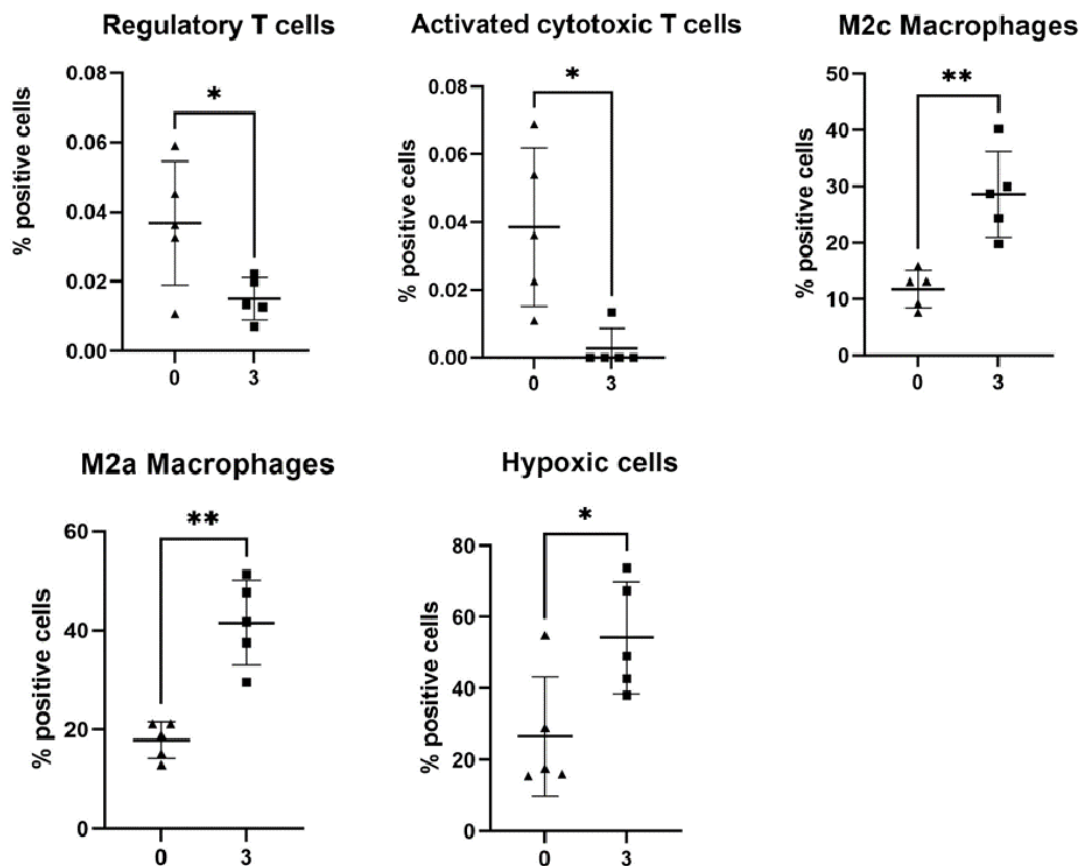
Figure 4.2.20 Bar graph of cell phenotype and function significantly changed in the liver. Percentage positive cells represented as bar graph showing five biological replicates and regulatory T cells (CD3$^+$, CD4$^+$, FOXP3$^+$) and activated cytotoxic T cells (CD3$^+$, CD8$^+$, granzyme B$^+$) significantly reduced; whereas, the percentage of macrophages in the subclass M2c (F480$^+$, CD163$^+$) and M2a (F480$^+$, CD206$^+$) and hypoxia (Glut1$^+$) were significantly upregulated in 3% group compared to the control. T-test performed to compare the two groups and *p<0.05, **p<0.01, ***p<0.001, ****p<0.0001 was considered statistically significant.

In liver vessels, the percentage of CD68$^+$, F480$^+$, CD11b$^+$, CD163$^+$, E Cadherin$^+$, Lyve1$^+$, NKp46$^+$, CD206$^+$, Glut1$^+$ and ATPase$^+$ cells increased in the 3% DSS group compared to control by 2.50-fold (p=0.0346), 2.25-fold (p=0.0005), 2.25-fold (p=0.0396), 2.98-fold (p=0.0169), 1.83-fold (p=0.0162), 2.29-fold (p=0.0179), 1.07-fold (p=0.0221), 1.51-fold (p=0.0092), 1.38-fold (p=0.0044) and 1.04-fold (p=0.0006), respectively. Furthermore, the percentage of M2c and M2a

macrophage positive cells significantly increased 3.26-fold (p=0.0081) and 2.73-fold (p=0.0005), respectively, in the 3% group compared to controls. Furthermore, the vessel in 3% groups had a 1.38-fold (p=0.0044) increase in the percentage of cells positive for hypoxia. This indicates that during intestinal colitis the liver undergoes injury via hypoxia.

4.2.5 Systemic shifts in spleen and kidney metabolome during intestinal colitis

MSI was used to investigate molecular changes in systemic sites including the spleen of mice with DSS induced intestinal colitis. ROC analysis found 69 peaks that could potentially discriminate between 0% and 3% DSS groups. The variation in the 69 metabolites detected were analysed to examine the clustering of groups using multivariate statistical analysis including PLS-DA (M1) and PCA (M2). PCA score plot of the first (t [1]) principle component did show distinct clustering and clear separation in the colon between 0% DSS group from the 3% DSS treated group (parameters: R2X=0.64, Q2=0.5) (Fig. 4.3.21 M2). However, PLS-DA score plot (M1) was able to separate the groups and clustered better than PCA using both the first and second principle component (parameters: R2X=0.0.733, R2Y=0.95, Q2=0.894). PLS-DA generated VIP scores above 1 highlight the molecules contributing the most to group separation (8.1.11).

Model	Type	A	N	R2X(cum)	R2Y(cum)	Q2(cum)
M1	PLS-DA	2	10	0.733	0.965	0.894
M2	PCA-X	1	10	0.64		0.5
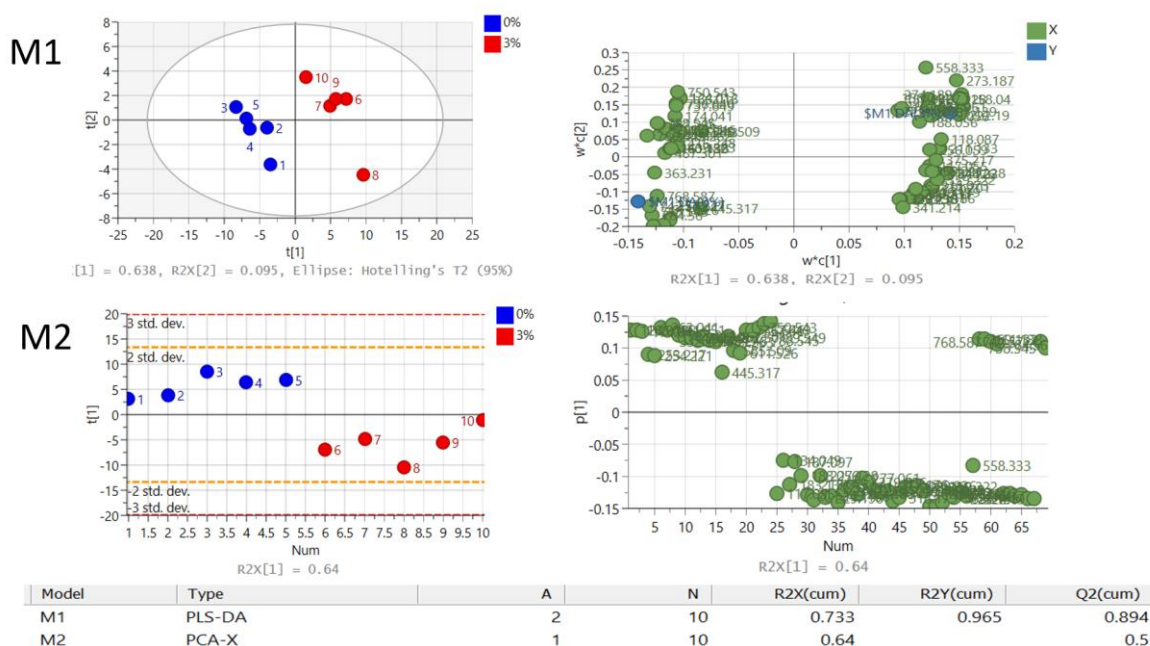
Figure 4.2.21 Unsupervised and supervised discriminant analysis.
M1) Supervised PLS-DA analysis show the molecules in the spleen of DSS colitis model can discriminant between the control (0% DSS, blue circles) and diseased group (3% DSS, red circles). M2) Unsupervised PCA analysis was not able to discriminate between the groups using metabolite features. Analysis was performed using SIMCA 17 software. PLS-DA and PCA score plots consist of components 1 (t [1]) and 2 (t [2]). The ellipse represents the 95% confidence region for Hotelling's T2 statistic for the model.

Univariate statistical analysis identified 65 peaks were significantly changed, however only 34 molecules (51.5%) were able to be assigned a putative identity. MSMS fragmentation was not able to confirm the identity of the molecules putatively identified. Molecules significantly changed are shown as a heatmap (Figure 4.2.22a) and further information can be found in Appendix 98.1.9. Enrichment analysis (Figure 4.2.22b) shows that the molecules identified in this study are involved in at least 18 different pathways such as Steroid hormone biosynthesis, Linoleic acid metabolism, Biosynthesis of unsaturated fatty acids, Amino sugar and nucleotide sugar metabolism, and Pyrimidine metabolism. However, none of the pathways identified were significantly enriched
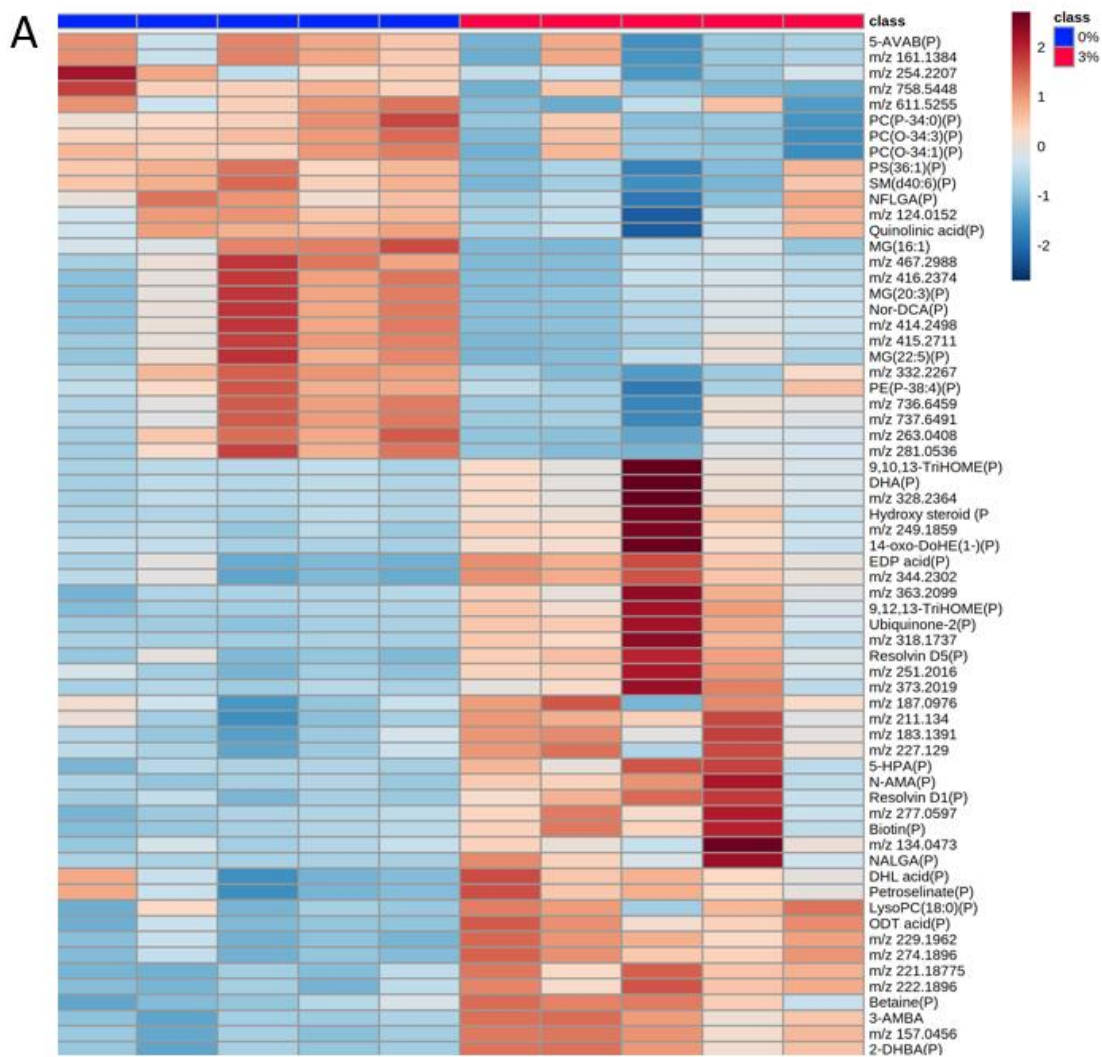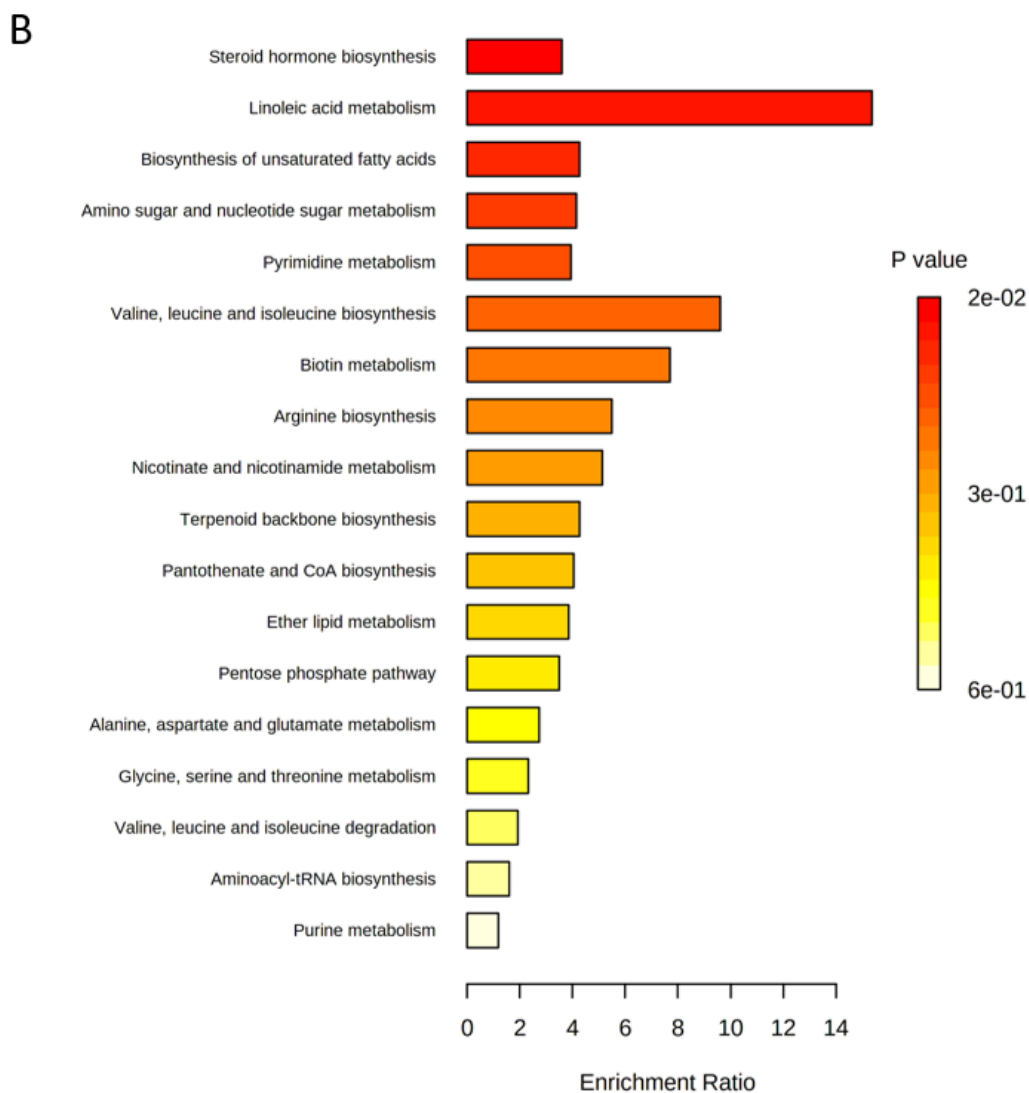
Figure 4.2.22 Molecules and pathways altered in spleen of DSS colitis model
A) Heatmap shows *m/z* of unidentified molecules, putatively identified molecules (marked with a P). Heatmap was created using Metaboanalyst 5.0. The colour of each sample is proportional to the significance of change in metabolite abundance indicated by the colour bar (red, up-regulated in DSS colitis group; blue, down-regulated in colitis group). Rows correspond to metabolites and columns correspond to samples. B) Enrichment pathway analysis performed using KEGG as reference and found molecules involved in 18 different pathways such as Steroid hormone biosynthesis, Linoleic acid metabolism, Biosynthesis of unsaturated fatty acids, Amino sugar and nucleotide sugar metabolism, and Pyrimidine metabolism. However, none of the pathways identified were significantly enriched.

Seven molecules were found to be similarly changed in the spleen and colon during DSS induced colitis. The molecule with *m/z* 160.1334 was putatively identified as 5-AVAB and was significantly downregulated 1.63-fold in the spleen (*p*=0.028) and 1.81-fold in the colon (*p*=0.02) of 3% DSS treated mice, compared to the control. Six other molecules were found to be significantly upregulated in both the spleen and colon of 3% DSS mice compared to controls. These molecules

were putatively identified as octadecatriencoic acid (2.04-fold colon (p=0.04); 1.54-fold spleen (p=0.0003)), 11b-hydroxyandrost-4-ene-3,17-dione (15.8-fold colon (p=0.03); 4.65-fold spleen (p=0.04)), ubiquinone-2 (7.9-fold colon (p=0.02); 3.38-fold spleen (p=0.005)), epoxydocosapentaenoic acid (7.1-fold colon (p=0.02); 2.37-fold spleen (p=0.0016)), resolvin D5 (19.0-fold colon (p=0.02); 2.28-fold spleen (p=0.0058)) and resolvin D1 (19.14-fold colon (p=0.02); 2.26-fold spleen (p=0.0062)). Five molecules were also found to be similarly altered in the ileum and spleen. Three of these molecules have been previously described as 11b-hydroxyandrost-4-ene-3-17-dione, ubiquinone-2 and epoxydocosapentaenoic acid; molecules were upregulated in the spleen 4.8-fold (p=0.0019), 3.06-fold (p=0.0012) and 3.4-fold (p=0.0038), respectively. The remaining two upregulated molecules, which could not be putatively identified, have m/z 251.2016 (2.13-fold ileum (p=0.0013); 1.58-fold spleen (p=0.0091) and m/z 328.2364 (2.66-fold ileum (p=0.0012); 2.62-fold (p=0.0391) (Figure 4.2.23).
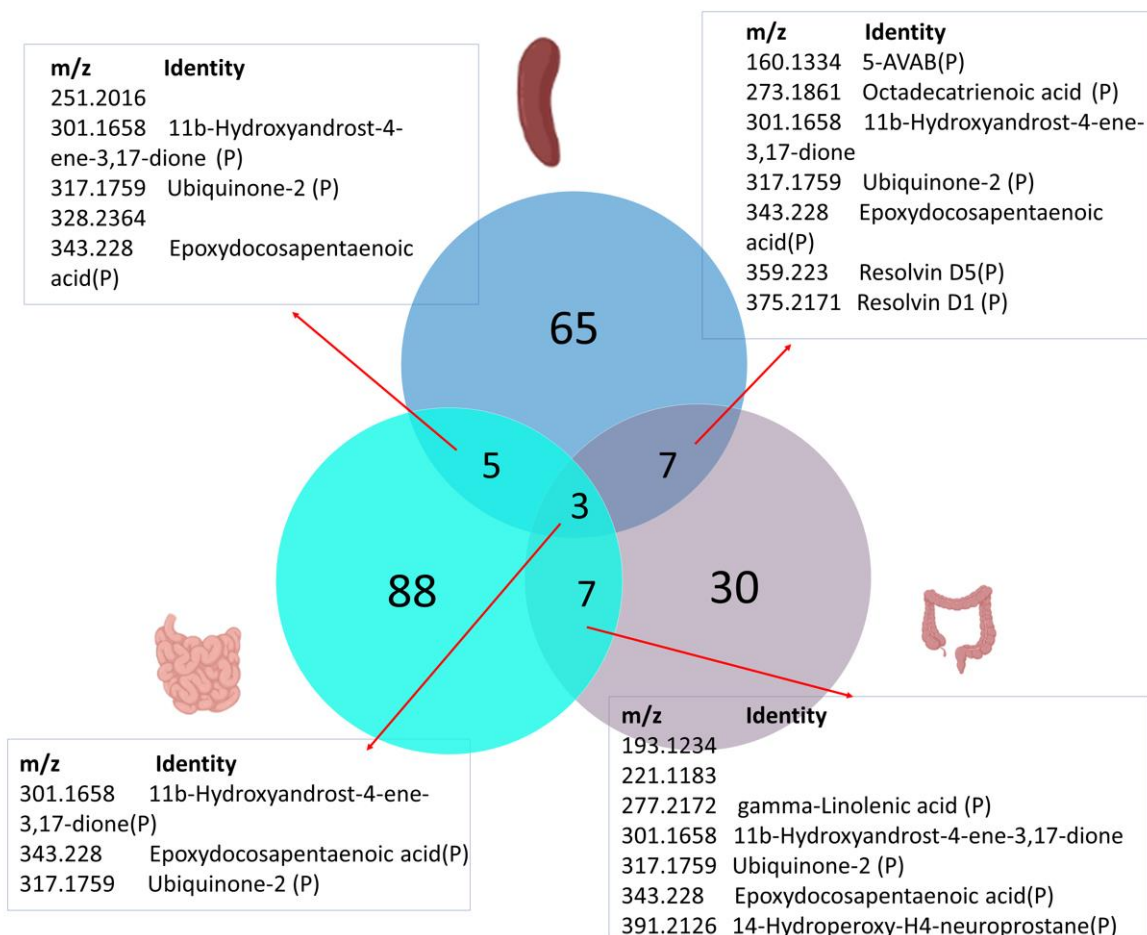
Figure 4.2.23 Venn diagram of molecules altered in the ileum, colon, and spleen in DSS colitis model.
The top circle represents the 65 molecular changes in the liver, bottom-left circle represents 88 molecular changes in ileum and bottom-right represents 30 molecular changes in the colon. Overlapped segments indicate the number of molecules that are changed similarly between different tissue. The *m/z* and putative identities of the molecules commonly shared between tissue are highlighted in boxes.

This study also investigated the molecular changes that occur in the kidney of the DSS colitis model and ROC analysis found 16 peaks that could be involved in discriminating between 3% DSS colitis mice and control mice. The variation in the 16 metabolites detected were analysed to examine the clustering of groups using multivariate statistical analysis including PLS-DA (M1) and PCA (M2). PCA score plots of the first (t [1]) and second (t [2]) principle component did show distinct clustering and clear separation in the colon between 0% DSS group from the 3% DSS treated group (parameters: R2X=0.904, Q2=0.685) (Fig. 4.3.24 M2). PLS-DA score plot (M1) was also able to separate the groups and clustered the groups but used only the first principle component (parameters: R2X=0.587, R2Y=0.729, Q2=0.625). PLS-DA generated VIP scores above 1 highlight the molecules contributing the most to group separation (8.1.13). All 16 molecules

were found to be significantly changed between the groups following univariate analysis and are shown in a heatmap (Figure 4.2.25a). This study could assign 11 putative identities to the molecules, but MS/MS could not accurately confirm identity based on fragmentation patterns. Furthermore, enrichment pathway analysis found that the molecules identified in this study contribute to at least 2 pathways; Ubiquinone and other terpenoid-quinone biosynthesis and phenylalanine metabolism; however, no pathway was significantly enriched (Figure 4.2.25b). MSI was also performed on lung tissue from the model; however, no significantly changed molecules were found (data not shown).

Model	Type	A	N	R2X(cum)	R2Y(cum)	Q2(cum)
M1	PLS-DA	1	8	0.587	0.729	0.625
M2	PCA-X	3	8	0.904		0.685
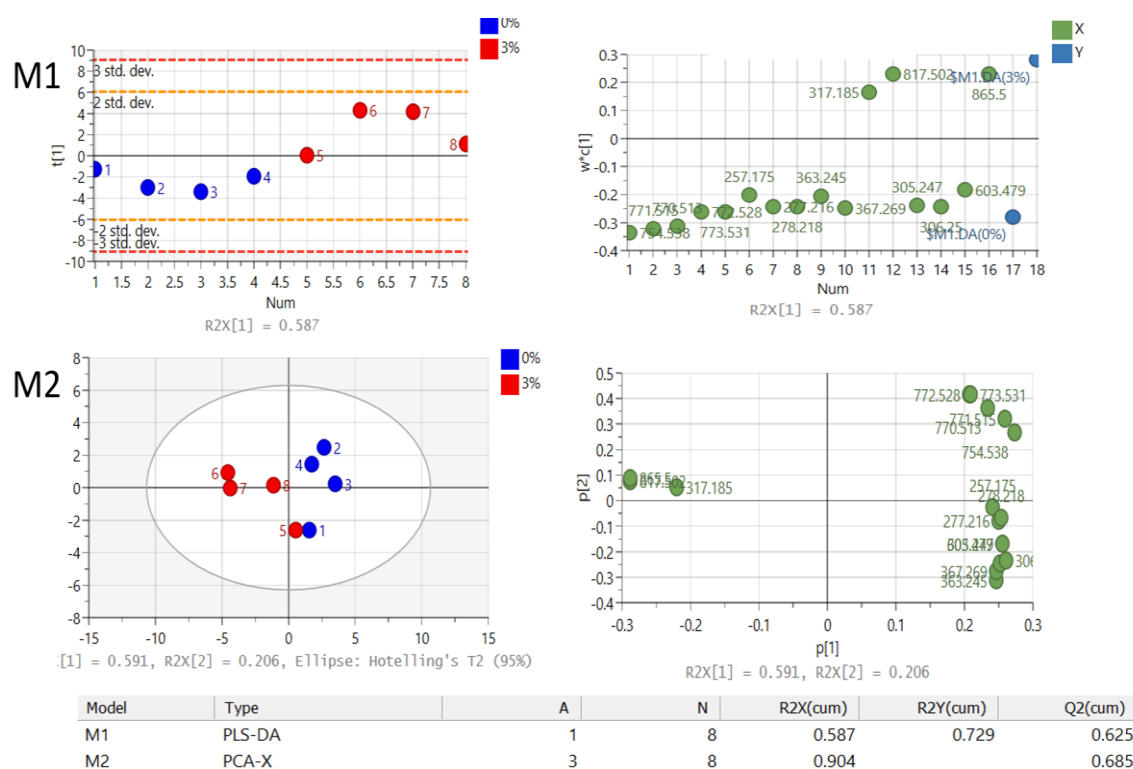
Figure 4.2.24 Unsupervised and supervised discriminant analysis
M1) Supervised PLS-DA analysis shows the molecules in the kidney of DSS colitis model can discriminant between the control (0% DSS, blue circles) and diseased group (3% DSS, red circles). M2) Unsupervised PCA analysis was able to discriminate between the groups using metabolite features. Analysis was performed using SIMCA 17 software. PLS-DA and PCA score plots consist of components 1 (t [1]) and 2 (t [2]). The ellipse represents the 95% confidence region for Hotelling's T2 statistic for the model.
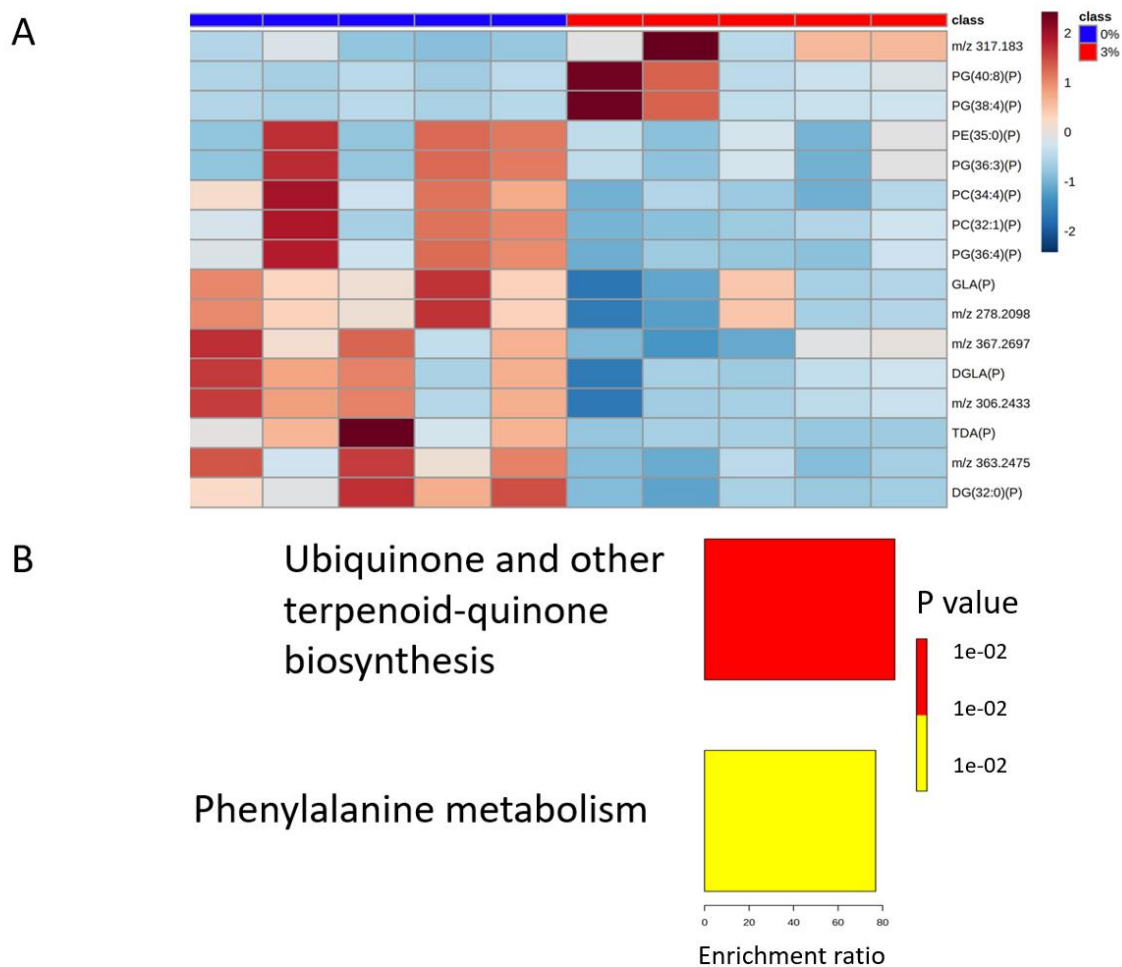
Figure 4.2.25 Molecule and pathways altered in kidney of DSS colitis model
A) Heatmap shows m/z of molecules unable to be identified, putatively identified molecules (marked with a P). Heatmap was created using Metaboanalyst 5.0. The colour of each sample is proportional to the significance of change in metabolite abundance indicated by the colour bar (red, up-regulated in DSS colitis group; blue, down-regulated in colitis group). Rows correspond to metabolites and columns correspond to samples. B) Enrichment pathway analysis used KEGG as reference and analysis found molecules involved in 2 different pathways; Ubiquinone and other terpenoid-quinone biosynthesis and phenylalanine metabolism; however, no pathway was significantly enriched.

As previously described, the molecule putatively identified as gamma-Linolenic acid was dysregulated in the ileum, colon, and liver in the colitis model. This molecule was also found to be significantly downregulated 2.03-fold (p=0.016) in the kidney of the colitis group compared to the control. The molecule with m/z 865.5019 was putatively identified as a phosphatidylglyceride (PG(38:4)) and was found to be upregulated in the ileum (4.52-fold, p=0.0028) and kidney (14.5-fold, p=0.0259) during DSS colitis compared to the control. Lastly, the molecule with m/z 305.2481 was putatively identified as Dihomo-gamma-linolenic acid. This molecule was significantly upregulated (1.96-fold, p=0.0019) in the ileum and downregulated in the kidney (1.71-fold, p=0.0156) in DSS colitis group

compared to the control (Figure 4.2.26). Therefore, some metabolites changed in the spleen and kidney may come from the inflamed and damaged intestine. Therefore, research into the role these molecules have on organ function may further our understanding of IBD and systemic complications.

m/z	Identity
277.2174	gamma-Linolenic acid (P)
305.2487	Dihomo-gamma-linolenic acid(P)
865.5019	PG(38:4)(P)

m/z	Identity
277.2174	gamma-Linolenic acid (P)

m/z	Identity
277.2174	gamma-Linolenic acid (P)

m/z	Identity
193.1234	
221.1183	
277.2172	gamma-Linolenic acid (P)
301.1658	11b-Hydroxyandrost-4-ene-3,17-dione
317.1759	Ubiquinone-2 (P)
343.228	Epoxydocosapentaenoic acid(P)
391.2126	4-Hydroperoxy-H4-neuroprostane(P)

Figure 4.2.26 Venn diagram of molecules altered in the ileum, colon, and kidney in DSS colitis model.
The top circle represents the 16 molecular changes in the kidney, bottom-left circle represents 88 molecular changes in ileum and bottom-right represents 30 molecular changes in the colon. Overlapped segments indicate the number of molecules that are changed similarly between different tissue. The *m/z* and putative identities of the molecules commonly shared between tissue are highlighted in boxes.

4.3 Discussion

Metabolomic pathways enriched in the colon and ileum

This study found that in the DSS colitis model the Arachidonic acid (AA) pathway was significantly enriched in the ileum and colon. AA is a polyunsaturated 20-carbon chain fatty acid that is incorporated into phospholipids in biological membranes; thus, plays an important role in cellular function [532]. Available AAs on the inner surface of cell membranes are hydrolysed by phospholipase A2 (PLA$_2$) into a free form which can be further metabolised in three different eicosanoid pathways to produce bioactive fatty acid mediators [533,534]. The first pathway involves AA cyclooxygenases (COXs) enzymes which are induced by inflammatory stimuli, hormones, and growth factors, resulting in the metabolism of AA into prostanoids such as prostaglandins (PGs) and thromboxanes (TXs) [535]. PGs bind to host cell receptors, such as PG EP1, to induce a signalling cascade resulting in changes to intracellular calcium, cyclic adenosine monophosphate (cAMP) and pro-inflammatory factors [536]. Furthermore, thromboxane's are potent vasoconstrictors and platelet aggregating agents that have been implicated in the pathophysiology of many cardiovascular diseases [537]. As studies have concluded that inflammatory prostaglandins exacerbate inflammation by dysregulating regulatory T cells, therapeutics have been developed to block COX enzymes [538]. However, eicosanoids also maintain integrity and defence in the epithelial and mucosal layer; thus, completely blocking production will have detrimental effects [538,539]. The second pathway involves Lipoxygenases (LOXs) enzymes that generate leukotrienes (LTs), such as LTB4, which is a potent chemoattractant and the main mediator in neutrophil recruitment and activation to initiate inflammation [540]. Thirdly cytochrome P450 (CYP) enzymes covert AA into epoxyeicosatrienoic acids (EETs), hydroxyeicosatetraenoic acid (HETEs) and eicosatetraenoic acids (ETEs) [534,541]. These mediators possess potent anti-inflammatory properties by preventing leukocytes migrating into tissue via the inhibition of cellular adhesion receptors and inhibiting the activity of COX enzymes; thus, reduces the production of pro-inflammatory prostaglandins and inhibit platelet aggregation [542,543]. As AA pathway mediators were upregulated in the inflamed colon and ileum, it was expected that mucosal cells would show similar trends in immunometabolism related cellular function. However, this was

not the case as the ileum showed a down-regulation of Ki67[+,] CD69^{+} , F480^{+}, CD4^{+} and MHCII^{+} cells in the inflamed mucosa; whereas, ATPase^{+}, Pan-CK^{+}, CD103^{+}, CD11c^{+}, E- cadherin^{+}, Glut1^{+}, Ki67^{+} and EpCAM^{+} cells were decreased and vimentin, CD68, Ly6G, CD11b, F480, CD163, collagen, Lyve1, FoxP3, NKp46, CD4 and granzyme B cells were increased in the colonic mucosa. These markers were used to phenotype cells and the study suggests in the ileal mucosa of 3% DSS colitis mice, helper T cells (CD3^{+}, CD4^{+}), dendritic cells (CD11c^{+}, MHCII^{+}), M2b and M1 macrophages (F480^{+}), and proliferation positive cells (Ki67^{+}) were downregulated. This suggests that ileal mucosa in the DSS colitis mouse is in an anti-inflammatory state, as studies have shown an increase in these cell subsets during active inflammation [544,545]. Furthermore, our study showed an increase in AA derivative, lipoxin A4, which is a pro-resolving and anti-inflammatory eicosanoid mediator with the ability to promote phagocytosis of apoptotic cells [546,547]. Lipoxin is produced instead of LTB4 after neutrophils are exposed to prostaglandins via the induction of 15-LOX, which acts as a signal to stop further neutrophil recruitment [548]. Therefore, the presence of this molecule indicates that the ileum is in a resolution phase and that specific derivatives of the AA pathway might be contributing to the anti-inflammatory environment and clearance of immune cells via immunometabolism [533,535,546,547].

However, the inflamed colonic mucosa cells that were proliferative (Ki67^{+}), hypoxic (Glut1^{+}), and antigen-presenting dendritic cells (CD11c^{+}, MHCII^{+}, CD103^{+}) were significantly reduced; whereas, helper T cells (CD3^{+}, CD4^{+}), regulatory T cells (CD3^{+}, CD4^{+}, FOXP3^{+}), natural killer (NK) cells (NKp46^{+}), neutrophils (Ly6G^{+}, CD11b^{+}), blood vessels (CD31^{+}), mesenchymal cells (Vimentin^{+}), macrophages (F480^{+}, CD68^{+}, CD11b^{+}) and macrophage subsets including M2c (F480^{+}, CD163^{+}), M2a(F480^{+}, CD206^{+}), M2b (F480^{+}) and M1 (F480^{+}, MHCII^{+}) were increased. Studies have shown that NK cells, macrophages and neutrophils might play a role in CD progression by producing large quantities of proinflammatory cytokines including TNF-α, IL-6 and IL-8 [549,550]. Moreover, antigen-presenting dendritic cells are pivotal in the balance between tolerance and active immunity towards commensal; thus, a decrease in the inflamed mucosa may be responsible for microbial exacerbation of DSS induced inflammation [551]. Despite AA pathway being enriched in the ileum and colon, there are some differences in the metabolites contributing to the pathway: AA pathway in ileum involved

upregulation of AA and derivates such as 20(S)-HETE, prostaglandin G2 (PGG2), thromboxane B2 and leukotriene B4 (LTXB4) in colitis groups; whereas derivatives such as 11,12-EET, 15S-HETE and 5(S)-HETE were up-regulated in the colon. It is likely that differences in this metabolic profile could be a cause of difference in cellular profile [552]. For example, 5(S)-HETE can be made by stimulated neutrophils in response to infection but under specific conditions can elicit a strong pro-inflammatory response by increasing neutrophil chemotaxis through the epithelial barrier [553]. After neutrophils have migrated, 5(S)-HETE increases degranulation resulting in the release of anti-bacterial products and ROS that cause bacterial dysbiosis, tissue injury and inflammation [554]. Furthermore, lipopolysaccharide (LPS) from gram-negative bacteria have been shown to significantly increase the production of 5(S)-HETE in neutrophils [555]. In this study, microbiome analysis showed that Proteobacteria (which are largely gram-negative) and *E. coli* are increased during DSS induced colitis [556]. Therefore, it can be suggested that microbial dysbiosis skews the AA pathway towards 5(S)-HETE production, which in turn recruits' neutrophils to the mucosa to elicit an inflammatory response [553,555,557]. As previously described, completely blocking eicosanoid production is detrimental to the intestinal barrier and mucosa; thus, the study suggests that blocking specific derivates such as 5(S)-HETE could alter the mucosal immune response and dampen inflammation [538,539,553,557].

Furthermore, steroid hormone biosynthesis and primary bile acid biosynthesis pathways were enriched in the ileum. In addition to hormonally active steroids such as estrogens, bile acids are steroid compounds derived from cholesterol; thus, the pathways are directly linked [558]. Both pathways involve the molecules putatively identified as 25-hydroxycholesterol and dihydroxy-cholesterols, which were upregulated in the 3% DSS treated group, compared to the control. Studies have previously reported that 25-hydroxycholesterol can have dual functionality by promoting pro- and anti-inflammatory effects [559]. 25-hydroxycholesterol can enhance B cell expression of IL-8 and Il-6, and LPS treated macrophages upregulate 25-hydroxycholesterol production, correlated with an increase in cytokine C-C motif chemokine ligand 5 (CCL5) [559,560]. Increased expression of these cytokines and CCL5, promotes immune cell infiltration to injured sites and exacerbates inflammation [559-561]. However, our IMC data does not suggest the

ileal mucosa was overcome with immune cell infiltrate and it is more likely that 25-hydroxycholerol is having an anti-inflammatory effect. 25-hydroxycholererol has been found to block sterol regulatory enhancer binding protein (SREBP), which decreases inflammasome activity and downregulates the production of potent proinflammatory cytokine, IL-1β [562,563]. IL-1β is known to promote the recruitment and retention of macrophages; thus, it can be suggested that the significant downregulation of macrophage subsets in the ileal mucosa is due to 25-hydroxycholesterol associated inhibition [561,562,564]. Hydroxycholerol can be hydrolysed to dihydroxycholesterols which have also been shown to have immunomodulatory effects [565]. In particular, 7β,27-dihydroxycholesterol has been described as a potent ligand agonist, promoting the migration of CD4+ T cells to inflamed sites and increased the secretion of proinflammatory cytokines, implicating a role in inflammatory conditions [566,567]. As the putatively identified dihydroxycholersterol molecules in this study are not 7β,27-dihydroxycholesterol and CD4+ T cells are downregulated in the 3% DSS ileal mucosa, it can be suggested that they are competing agonists with different outcomes for immunometabolism and immunomodulation [568,569]. Therefore, this study suggests that the differences in cellular function between in colon and ileum during DSS induced colitis is heavily influenced by metabolic pathways and targeting specific metabolites within the pathways are likely to have an impact as potential therapeutic targets [539,546,560,564].

Effect of creatine and DHA in vitro

To further characterise novel biomarkers of disease, this study focused its investigation on molecules that were shown to contribute to PLS-DA clustering of separated groups. In the ileum, creatine and DHA were found to be significantly upregulated in the 3% DSS group compared to the control and were involved in the clustering of groups; thus, they may play an important role in either immune cell homeostasis or inflammatory response. DHA is a long-chain omega-3 polyunsaturated fatty acid (PUFA) endogenously derived from alpha-linolenic acid (ALA), and has anti-inflammatory properties, resulting in the downregulation of pro-inflammatory AA-derived prostaglandins and leukotrienes [570]. More recently, studies have found that DHA not only dampens inflammation by reducing pro-inflammatory molecules but actively promotes resolution [571].

DHA is enzymatically oxidised by COXs and LOXs into mono-, di-, and tri-hydroxyDHA (HDHAs) which are anti-inflammatory docasanoids, known as resolvins (Rv), protectins (PD) and maresins (Ma) [572]. These molecules are structurally distinct from other anti-inflammatory AA-derived molecules such as lipoxins and have potent immunomodulatory effects [571,572]. Resolvins produced from DHA are known as D-series resolvins (RvDs) and molecules such as RvD1 and RvD5 can decrease the infiltration of PMN leukocytes into injured or infected tissue by inhibiting the expression of pro-inflammatory IL-1ß [573,574]. Furthermore, PD1 stimulates the phagocytosis of apoptotic macrophages, reduces cytokine production in T-cells and protects epithelial cells from oxidative stress [575,576]. Studies have also found that DHA supplementation can protect the epithelial barrier during *E. coli* infection by upregulating the expression of tight junction proteins, including occludin and claudin-1 [577]. Due to the anti-inflammatory and protective effects, DHA has been considered as a molecular target for treating IBD and other inflammatory conditions [571]. As an increase in DHA in the ileum is corresponded with a downregulation of helper T cells (CD3$^+$, CD4$^+$), dendritic cells (CD11c$^+$, MHCII$^+$), M2b and M1 macrophages (F480$^+$), it can be suggested DHA increased abundance is a protective mechanism against DSS induced colitis [578].

Endogenous production of DHA constitutes a low level of abundance in the intestine and the vast majority is absorbed from the diet [579]. DSS induced colitis mice and IBD patients both exhibit malabsorption of proteins, fats, and vitamins as well as a loss of appetite, resulting in weight loss [580]. However, gastrointestinal bacterial composition affects host fatty acid metabolism and studies have shown that administration of *Bifidobacterium* species in combination with ALA results in higher DHA levels in tissue [580,581]. Therefore, it can be suggested that despite reduced nutritional absorption during 3% DSS induced colitis, the level of DHA remains high in the ileum as bacterial dysbiosis, involving the overgrowth of specific bacteria maintains ALA metabolism [581]. Despite DHA being increased in the ileum, this study could not putatively identify the upregulation of HDHAs in the ileum. However, as the identification of pro-resolving mediators is relatively new, it is possible that some of the unidentified molecules in this study might be anti-inflammatory DHA-derived molecules and warrants further investigation [582]. Furthermore, inflammation in

the ileum is likely to be resolved; hence, there is reduced need for anti-inflammatory docasanoids, and DHA metabolism might be 'switched off', resulting in the highly accumulated DHA level [582,583]. Moreover, resolvins were putatively identified as being higher in the colon of mice with DSS induced colitis, in the absence of increased DHA abundance. Resolvins can be produced from other omega-3 fatty acids such as eicosapentaenoic acid (EPA); thus, it could be proposed that the resolvins observed in the colon were derived from an alternative substrate [583]. However, the putatively identities provided by the HMDB were D-series resolvins (RvDs), RvD1 and RvD5; thus, DHA is the more likely substrate [578,583]. Therefore, it can be suggested that exogenous ALA is being metabolised to DHA by microbes in the colon, similar to the ileum. However, as the inflamed colonic mucosa has an increased immune cell infiltration, including neutrophil-like phenotypic cells (Ly6G$^+$, CD11b$^+$), COX and LOX enzymes might metabolise high levels of DHA to produce docasanoids in an attempt to stop infiltration and resolve inflammation [547,576,583]. Therefore, DHA supplementation might be a useful IBD therapeutic.

Our study showed that DHA does not induce apoptosis in HCT-8 cell and can even lower apoptosis at low concentrations. However, DHA was cytotoxic towards HCT-8 cells at the tested concentrations. The exact mechanism behind this toxic effect is not known; however, studies have found that DHA is oxidised by ROS to produce electrophilic compounds that form damaged DNA adducts, initiating caspase-8-dependent apoptosis in specific cancer cells [584,585]. Furthermore, in colon cancer HT-29 cells, DHA caused mitochondrial malfunction and cell cycle arrest [586]. This effect in cancer cells is based on the high level of ROS oxidising DHA to cause damage; however, during IBD epithelial cells produce higher quantities of ROS, hence DHA might exacerbate cell death and inflammation resulting in the cytotoxic effect [587,588]. Furthermore, supplementing wild-type C57BL/6 and colitis-prone SMAD$^{-/-}$ mice with DHA increased LPS-induced B cell secretion of IL-6 and TNF-α [589]. Our study found that stimulating HCT-8 cells with DHA did not affect IL-6 production but increased the release of TNF-α. This pro-inflammatory cytokine can recruit macrophages and skew towards an M1 phenotype, induce epithelial cell death and impair barrier function by downregulating the expression of tight junction proteins [590]. Furthermore, our study revealed that DHA also increase IL-15 release, whereas IL-8 release is

decreased. The downregulation of IL-8 was expected as previous studies found that DHA treatment reduced keratinocyte IL-8 secretion in response to TNF-α stimulation [591]. IL-8 plays an important role in the accumulation and activation of neutrophils and T cells in the intestinal mucosa, leading to tissue disruption and inflammation; thus, DHAs potential inhibition of IL-8 production might dampen inflammation effectively [592]. Furthermore, IL-15 plays an important role in the mucosal barrier and regulates gut homeostasis by controlling the development and proliferation of both innate and adaptive immune cells [593]. On the contrary, IL-15 has pleiotropic functionality and can worsen colitis due to the stimulation of macrophages, NK cells and DCs cytotoxic activity [594]. Therefore, the release of IL-15 from HCT-8 cells during DHA exposure might have conflicting outcomes for intestinal inflammation that are underpinned by the microenvironment. Hence, if DHA accumulates in the intestine without being adequately metabolised to anti-inflammatory derivatives, there could be negative outcome for inflammation which needs to be fully considered before it can be used as a therapeutic. This study also found that DHA can increase splenic immune cell secretion of IFN-γ *in vitro*. Aberrant production of IFN-γ is considered a major driver of IBD as it contributes to an excessive immune response resulting in mucosal infiltration and damage; thus, DHA activation of IFN-γ production might be a molecular mechanism involved in pathology [595,596].

Creatine, also known as methylguanidine-acetic acid, is consumed exogenously in food products, and can be endogenously produced via the metabolism of the amino acids: arginine, glycine, and methionine [597,598]. Creatine plays an important role in cellular metabolism; phosphocreatine is degraded and used to synthesize adenosine diphosphate (ADP) and inorganic phosphate (Pi) into adenosine triphosphate (ATP) for cellular energy during exercise [599,600]. Creatine also shuttles Pi into the cytosol from the mitochondria, known as the creatine phosphate shuttle, allowing for the maintenance of ATP cellular needs [601]. Therefore, creatine can provide a critical source of energy during stress or injury such as impaired mitochondrial function [599,602]. Studies have shown that the creatine phosphate shuttle is enhanced in epithelial cells undergoing DSS induced metabolic stress, hence the observed increase in creatine in the 3% DSS treated ileum might be a metabolic response to restore cellular energy [603]. Furthermore, a loss of creatine *in vivo* has been correlated with increased

epithelial cell death as it is a protective factor in numerous cell types via regulation of mitochondrial oxidative phosphorylation [603,604]. Furthermore, creatine supplementation in DSS colitis models reduces the severity of disease and improves barrier function; thus, the use of creatine as a therapeutic for IBD patients is under consideration [604,605]. Our *in vitro* data supports the evidence that creatine prevents cell death as HCT-8 epithelial cells treated with creatine show significantly reduced rates of apoptosis in a dose dependent manner. However, the data also shows that creatine is cytotoxic to HCT-8 cells; the exact mechanism involved in this cytotoxicity is unknown and warrants further investigation if creatine is to be used as a therapeutic.

Furthermore, studies have suggested that creatine supports barrier function in colitis models by replenishing cytoplasmic ATP using the creatine kinase/phosphocreatine system to enhance cell proliferation [603,606]. Whilst our study cannot directly link creatine with cell proliferation, IMC revealed that 3% DSS ileal tissue had reduced percentage of Ki67$^+$ proliferative cells in the presence of increased creatine levels. Furthermore, studies have shown than creatine can have an anti-proliferative effect on primary tumours; thus, the hypothesis that creatine supplementation will improve proliferation to improve barrier function might not be fully accurate and further investigation is needed to elucidate the exact mechanism behind creatine associated anti-proliferation. This study also found that HCT-8 cells upregulate secretion of IL-15 in the presence of creatine. As IL-15 plays an important role in protecting or exacerbating the inflammatory environment in IBD, the impact of creatine induced IL-15 secretion cannot be elucidated in this study [593,594]. Moreover, studies have shown that creatine supplementation can reduce the secretion of TNF-α from macrophages, dampening the M1 inflammatory response [607]. Our data loosely supports this as IMC revealed a reduction in cells with a macrophage-like phenotype in the ileum, whilst creatine was increased. Furthermore, *in vitro* analysis revealed that TNF-α secretion was not affected in creatine treated HCT-8 epithelial cells, suggesting that the creatine will not induce inflammation via TNF-α pathway.

Our data also revealed that a lower dose of creatine significantly reduces the secretion of IL-8 from HCT-8 cells. As previously described, IL-8 plays an important role in the immune system; thus, creatines potential inhibition of IL-8

production might dampen inflammation effectively [592]. However, IL-8 production is mediated through toll-like receptors (TLRs) which recognise microbial particles; hence in the context of disease, where microbes are present, the effect of creatine on IL-8 inhibition might not be as pronounced [592,608]. Furthermore, microbes such as *Bacillus*, *Clostridia* and *Escherichia* strains can use creatine as a carbon and nitrogen source to support their expansion and growth [609]. *Clostridia* and *Escherichia* were enriched in this study's faecal microbiome during 3% DSS induced colitis, hence an increase in creatine might support this dysbiosis and have an impact on immunometabolism.

This study also found that stimulating splenic immune cells with creatine increased the percentage of NK cells expressing CD69. NK cells express CD69 after being activated by specific stimuli such as IL-2 [610]. In addition to activation, CD69 is an important regulator of immune responses in the intestine a expression is increased at sites of mucosal inflammation [611]. Studies have described CD69 as a proinflammatory molecule as it induces Ca^{2+} influx, lymphocyte proliferation as well as the production of potent inflammatory mediators such as TNF-α [611,612]. CD69 also plays a role in cell-cell dependent stimulation and migration of macrophages by T cells [613]. Moreover, IBD studies using the DSS model showed that CD69 expression is essential to the onset of disease [614]. Therefore, it can be suggested that an increase in creatine will increase NK cell CD69 expression, resulting in proinflammatory effects contributing towards DSS induced colitis [615]. However, IMC analysis indicated that CD69 expression was decreased in the inflamed ileum compared to the control and that macrophage presence was also decreased. Commensal microorganisms play a critical role in CD69 expression by intestinal lymphocytes as mice depleted of microflora have reduced CD69 levels [616]. Therefore, it can be suggested that the decrease in CD69 in the inflamed ileum is linked to a change in the gut microbiome [614,615]. As intestinal lymphocytes are exposed to a higher antigen load derived by microorganisms, a higher proportion of intestinal lymphocytes express CD69 compared to lymphocytes isolated from the spleen [616,617]. As creatine increased CD69 expression in splenic NK cell population, it can be suggested that cells have not encountered microbial stimuli and the response to creatine might not be indictive of intestinal responses in the context of IBD [616,617]. Therefore, more investigation into the link between specific cell types

and creatine, in a context that is reflective of active inflammation is needed to assess its usefulness as an IBD therapeutic [618].

Effect of 1-MNA in vitro

In the colon, 1-MNA was identified as being increased in the inflamed mucosa and was an important factor in separating the groups. 1-MNA is endogenously produced when nicotinamide (NA), a water-soluble form of vitamin B3, is N-methylated by the enzyme N-methyltransferase (NNMT) [619]. NNMT is predominantly expressed in the liver and studies have shown that conversion to 1-MNA is increased in the cirrhotic liver [620]. This increase has been described as hepatoprotective in liver inflammation as 1-MNA can exert an anti-inflammatory effect observed as supressed IL-4 and TNF-α immune cell signalling [621,622]. The anti-inflammatory activity of 1-MNA involves the activation of prostaglandin I2 (PGI$_2$) release from membrane phospholipids via COX-2 activity upon proinflammatory stimulation, such as cytokines and growth factors [623]. PGI$_2$ is the most potent natural inhibitor of platelet aggregation which prevents thrombotic occlusions and is becoming increasingly important as an immune cell regulator [624]. In addition, NNMT expression has been reported in other cells and organs, such as human oral cancer cells and the brain of PD patients; thus, implicating the mechanism in disease [625,626]. This disease mechanism might involve 1-MNA immune modulation of T cells [625]. Studies have shown that 1-MNA can accumulate within activated T-cells due to the absence of aldehyde oxidase 1 (AOX1), which degrades 1-MNA, leading to reduced population doubling and increased CD4$^+$ and CD8$^+$ T cells production of TNF-α [627]. As TNF-α is a potent mediator in the recruitment of immune cells, DNA damage and cell death, 1-MNA may be acting as a proinflammatory metabolite [628]. Therefore, the IMC results showing a high infiltration on immune cells in the inflamed colonic mucosa could be linked to higher 1-MNA levels. However, our *in vitro* cytokine assays showed that 1-MNA does not affect the secretion of IL-6, IL-8 or TNF-α in HCT-8 cells, hence the immunomodulatory effect must be cell specific. The data did show 1-MNA increased HCT-8 secretion of IL-15 which can have a pleotropic effect to either dampen or exacerbate inflammation; hence, 1-MNA may signal an inflammatory response [593]. Furthermore, 1-MNA did not induce apoptosis but was cytotoxic to HCT-8 cells and may lead to an impaired barrier function. To

our knowledge, there is no mechanistic evidence to support this effect. 1-MNA also reduces the expression of intracellular IFN-γ in CD4^{+} T cells [627]. CD4^{+} T cells production of IFN-γ is essential for bactericidal activity against many microbes [629,630]. Therefore, this study suggests that 1-MNA suppression of IFN-γ may result in impaired bacterial clearance, allowing for dysbiosis and microbial colonisation that exacerbates mucosal inflammation. In the context of IBD, 1-MNA may exacerbate inflammation by promoting bacterial dysbiosis and immune cell infiltration; thus, 1-MNA could be a target for therapeutic intervention.

Metabolomic and immunological changes in the liver during intestinal inflammation

During IBD, the intestinal epithelial barrier is impaired and resident microbiota and their derivates can gain access to the liver via the portal vein [631]. The intestinal products can then activate toll-like receptor ligands in the liver, inducing the secretion of proinflammatory mediators, resulting in hepatic inflammation and injury which has been associated with the development of cirrhosis and NAFLD [632]. The proinflammatory cytokines and other liver derived factors such as bile acids can then enter the intestine via systemic circulation and the biliary tract [632,633]. Therefore, the bidirectional crosstalk between the gut and liver influences microbial composition, immune regulation, and the inflammatory environment [632,634]. Furthermore, the gut-liver axis has been implicated in the onset of metabolic disturbances related to lipid and glucose homeostasis [635]. Hence, gaining a better understanding of how metabolic pathways and specific molecules change liver immunology during DSS induced colitis, might lead to intervention possibilities [634]. As primary bile acid biosynthesis was enriched in the ileum of the DSS induced colitis model, it was expected that bile acid pathways would be significantly altered in the liver due to the gut-liver axis; however, this was not the case, and the most significantly enriched pathway was galactose metabolism. Galactose is hydrolysed from ingested lactose in the intestine and travels to the liver where it is exclusively metabolised [636]. The pathway in this study involves a reduction of D-galactose in the liver of DSS induced colitis mice compared to the control. The enzymes, galactokinase and uridylyltransferase, metabolise D-galactose into glucose, which then enters the glycolysis pathway for energy production or stored in the

liver as glycogen [637]. The IMC data shows that the cellular marker, glucose transporter 1 (Glut1), was significantly increased in the liver of mice with colitis, compared to the control. Glut1 is translocated to hepatic cell membranes, to increase glucose uptake during stress, such as bacterial infection [638]. Therefore, it can be suggested that glucose availability in the liver during DSS induced colitis is impaired, resulting in increased D-galactose metabolism and Glut1 expression, in an attempt to salvage an energy supply [637,639,640].

However, Glut1 is also a marker of hypoxia which in a state of reduced oxygen supply and has been associated with the development of liver dysfunction and disease [638,640]. In particular, hypoxia-inducible factors (HIFs), HIF-1 and HIF-2 target *Glut1* to induce expression and have been shown to contribute to the development of hepatic steatosis by regulating lipid metabolism [641]. HIF-2 impairs fatty acid ß-oxidation by reducing the expression of associated genes, induces lipid accumulation and promotes lipid droplet formation via inducing the protein, perilipin-2 [642]. Furthermore, HIF-1 aggravates hepatic steatosis by inducing monocyte chemoattractant protein 1 (MCP1), resulting in immune cell infiltration [643]. This study found different lipid molecules such as diglycerides, triglycerides and ceramides were altered and that M2-like macrophages (M2c; F480$^+$, CD163$^+$, and M2a; F480$^+$, CD206$^+$) were increased in the liver of DSS induced colitis mice. M2a and M2c macrophages have been shown to protect against NAFLD by producing anti-inflammatory cytokines such as IL-10, decreasing the circulation of CD4$^+$ T cells and lessening necrosis [644,645]. Therefore, it can be suggested HIF-1 and HIF-2 are enhancing Glut1 protein expression and altering lipid metabolism, resulting in liver dysfunction during colitis. We can also speculate that HIF-1 induction of MCP-1 is attracting macrophages into the liver; however, the microenvironment in this study is skewing the macrophages towards an anti-inflammatory, protective phenotype. Therefore, further investigation to identify molecules in this study that skew macrophage polarization towards M2 may provide new therapeutic targets for protecting the liver from hypoxia and dyslipidaemia [640,642,645].

Biosynthesis of unsaturated fatty acids pathway was also enriched in the liver. The pathway included a decrease in the abundance of gamma-linolenic acid (GLA) in the liver, ileum, colon, and kidney of colitis mice. GLA is an omega-6,

18 carbon PUFA, that is consumed in the diet [646]. GLA is rapidly enzymatically converted into dihomo-gamma-linolenic acid (DGLA) in different cells and tissues [647]. Due to continuous conversion, GLA is naturally found at low levels with a corresponding increase in DGLA [648]. DGLA is enzymatically converted by COX and LOX into several metabolites such as 15-(S)-hydroxy-8,11,13-eicosatrienoic acid (15-HETrE) and PGE1 [648,649]. These DGLA metabolites have been shown to elicit an anti-inflammatory effect by inhibiting neutrophil production of LTB4, promoting vasodilation, and lowering blood pressure [650,651]. However, this study reported that both GLA and DGLA were decreased in the kidney following colitis. This decrease in abundance could be attributed to loss of appetite and weight loss in DSS induced colitis model, resulting in less GLA being absorbed from the diet [648]. However, *in vitro* studies have revealed that cells, including liver HepG2 cells, have the capacity to desaturate DGLA to form AA [652]. This increases the production of proinflammatory eicosanoids such as PGs, TXs and LTs which have been described above [554,650]. Studies have also shown that increased levels of AA correspond to reduced levels of DGLA [653]. Furthermore, this study found that AA was increased in the liver of colitis mice and is part of the same pathway as GLA. Therefore, it can be suggested that during colitis, GLA and DGLA are used as a substate for AA production, which skews the DGLA/ AA balance to support inflammation [648,650]. Furthermore, this study putatively identified prostaglandin G2 (PGG2), an AA derivative, as being increased in the colitis liver and has been implicated as a pathophysiological factor in liver cirrhosis by promoting platelet aggregation and thrombosis [654]. Therefore, the bidirectional liver-gut axis may exacerbate inflammation and tissue damage in both organs via Arachidonic acid metabolism; thus, GLA could be a biomarker of disease activity in the intestine, liver, and kidney [652,655].

Metabolomic changes that occurred in multiple tissue types during inflammation

Other molecules were putatively identified and similarly altered between tissue types that could potentially be biomarkers of disease and warrant further investigation. In particular, ubiquinone-2 was increased in the ileum, colon, liver, and spleen of DSS induced colitis mice, hence could be an important biomarker in intestinal and systemic inflammation. Ubiquinone-2, also known as

coenzyme Q2 (COQ2), is the second of at least ten functional proteins involved in the biosynthesis of endogenous coenzyme Q10 (CoQ10) [656]. Ubiquinone-2 is present in the cytosol and is responsible for the condensation of an isoprenoid chain with a benzoquinone ring, followed by a sequence of enzymatic reactions including methylation, decarboxylation, hydroxylation, and deamination [657]. Lastly, proteins direct the localisation of CoQ10 to the mitochondrial membrane [658]. Within the mitochondria, CoQ10 acts as an electron carrier that increases the generation of ATP via oxidative phosphorylation [659]. In addition, CoQ10 can be reduced to ubiquinol, which has been shown to have strong antioxidant and anti-inflammatory properties [660]. During LPS induced stress, ubiquinol treatment blocks protein kinase C (PKC) activity and improves mitochondrial function, preventing ROS generation and cellular damage [661]. Furthermore, in response to LPS, ubiquinol can downregulate the expression of inflammatory microRNAs that regulate the expression of IL-1 receptor (IL-1R) and associated kinase (IRAK-1) [662]. As both oxidative stress and proinflammatory IL-1 are increased in IBD patients, it can be suggested that the increase in ubiquinone-2 supports elevated CoQ10 biosynthesis to protect against LPS induced damage [663,664]. Furthermore, clinical studies indicate that CoQ10 supplementation in UC patients, decrease the severity of inflammation and blood pressure [665]. As ubiquinone-2 was increased in the intestine, liver, and spleen, it can be suggested that increasing biosynthesis or supplementation would not only reduce inflammation in the intestine but could have a systemic protective effect, increasing its usefulness as a therapeutic target [661,663,665].

Furthermore, the molecule putatively identified as epoxydocosapentaenoic acid (EDP) was increased in the ileum, colon, and spleen of colitis mice. This is a naturally occurring bioactive metabolite of DHA, derived via cytochrome P450 epoxygenses [666]. To our knowledge, research has largely overlooked this molecule as focus has been on DHA, however, EDP also has anti-inflammatory potential [666,667]. Studies have shown that EDP is increased in circulation of breast cancer patients, following DHA supplementation and has a positive effect on patients' prognosis [668,669]. This has been attributed to EDPs ability to inhibit angiogenesis, suppress endothelial cell migration, and primary tumour growth [670]. Furthermore, EDP can reduce the expression of TNF-α and TNF-α induced leukocyte adhesion in Müller cells and retinal endothelial cells; thus, may be

useful in treating inflammatory eye conditions [667]. Therefore, the increased EDP in the intestine and spleen might be an anti-inflammatory protective effect and warrants further investigation as an intestinal and systemic inflammatory therapeutic target.

In conclusion, this chapter shows that DESI MSI can be employed to discover molecules derived by the host and microbiome that could play a role in the onset and progression of DSS induced colitis. The study revealed numerous molecular pathways and specific molecules, such as creatine, DHA and 1-MNA, have immunomodulatory effects and have the potential to perpetuate inflammation within the intestinal mucosa. Furthermore, the study shows that specific metabolites are altered in the liver, spleen and kidney during inflammation and have the potential to drive pro and anti-inflammatory mechanisms. Some of these molecules such as GLA may result in systemic disease manifestations and may be new targets for therapeutic intervention. Lastly, some molecules such as ubiquinone-2 and EDP are present in multiple tissue including the intestine during colitis; thus, if used as therapeutic target could dampen both intestinal and systemic inflammation.

Chapter 5 Collagen induced arthritis (CIA) model exhibits systemic changes in metabolic and immune profiles

5.1 Introduction

5.1.1 Epidemiology and diagnosis of Rheumatoid arthritis (RA)

Rheumatoid arthritis (RA) is a chronic systemic autoimmune condition that primarily affects the lining of synovial joints in the hands and feet [671]. Clinical manifestations of the disease in joints include arthralgia, swelling, redness, and limited movement due to irreversible cartilage degradation and bone erosion [672]. In Western counties, RA affects between 0.5-1% of the population, and women are 2-3 times more likely to develop the condition [673]. The onset of disease can start in late childhood but mostly develops in those over the age of 60 [674]. Treating RA costs the UK National Health Service (NHS) an estimated £560 million each year and an economic burden over £1.8 billion a year due to sick leave and work-related disability [675]. However, the socioeconomic burden of RA is likely to continue increasing as a result of an ageing population [676].

Table 5.1 Standard of care for RA patients (671)

Drug Class	Example of current drugs	Mechanism of Actions
Nonsteroidal Anti-inflammatory Drugs (NSAIDs)	Ibuprofen, Naproxen	Inhibit cyclooxygenase (COX) enzymes, reducing prostaglandin synthesis, leading to pain and inflammation relief.

Disease-Modifying Antirheumatic Drugs (DMARDs)	Methotrexate, Hydroxychloroquine	Suppress the immune system, reducing inflammation and slowing the progression of rheumatoid arthritis.
Biologic Response Modifiers (Biologics)	Etanercept, Adalimumab	Target specific components of the immune system involved in inflammation, such as tumour necrosis factor (TNF), interleukin-6 (IL-6), or B cells, to reduce inflammation and joint damage.
Janus Kinase (JAK) Inhibitors	Tofacitinib, Baricitinib	Inhibit Janus kinases, which are enzymes involved in signaling pathways that contribute to inflammation, reducing inflammation and joint damage.

Growth and differentiation factors	Denosumab, Mavrilimumab	Involved in the activation, differentiation and survival of macrophages, dendritic cells, neutrophils and T helper cells; reduces inflammation and pain

The exact aetiology of RA is still incompletely understood; however, studies have shown there is a strong genetic component [673,677]. It has been estimated that 60% of RA cases are likely to be hereditary and approximately 100 loci have been identified across genomes that harbour RA susceptibility variants [678,679]. These RA risk loci usually affect genes of known immune function such as *IL6ST* which encodes a protein product that acts as a receptor complex for the inflammatory cytokine IL-6 [680]. However, studies indicate that disease concordance of identical twins is between 12-15%; thus, other factors such as diet, lifestyle and environment also contribute to the onset of disease [681]. Diagnosing RA is based on the 2010 American College of Rheumatology (ACR)/European League Against Rheumatism (ELAR) classification criteria [682,683]. The criteria include scoring against joint pain, location of inflammation and reported swelling as well as serological testing for autoantibodies such as rheumatoid factor (RF) and anti-citrullinated protein antibody (ACPA) which precede the onset of disease [684]. Autoantibodies have been described as useful biomarkers for diagnosis and predicting severity; however, there is a lack of standardisation and specificity in available diagnostic tests [685,686]. It has been shown that intervention treatments are most effective at reducing joint destruction, lessening disability and radiological progression when taken in the first 12 weeks after early symptoms appear [684]. However, due to the lack of a single diagnostic test and complex nature of the disease, most patients are not

diagnosed within this optimal treatment time period [687]. Therefore, gaining a better understanding of disease aetiology and identifying biomarkers of disease may improve diagnostic ability and improve patient outcomes [682,687,688].

5.1.2 Immunological basis of RA

In addition to a genetic predisposition, an autoreactive immune system involving innate immune cells such as macrophages, DCs, NK cells, as well as T cells and B cells from the adaptive immune response are involved in RA onset and progression [689-691]. Amongst these cell types, a T-cell mediated immune response has been described as essential for disease occurrence [692]. The exact role of T-cells in RA remains unclear; however, activated CD4+ T-cells have been shown to interact with human leukocyte antigen (HLA), MHC-II molecules and co-stimulating molecules such as CD28 on the surface of antigen presenting cells (APC)[693]. This cell-to-cell interaction leads to downstream maturation of CD4+ T-cells and activates CD8+ T-cells (cytotoxic T-cells), resulting in tissue damage and inflammation [694]. Furthermore, CD4+ Th1 cells are highly activated in RA and contribute to disease development by secreting proinflammatory cytokines such as IFN-γ, IL-2 and TNF-α, resulting in the recruitment and activation of macrophages to present MHC-II to T-cells [695,696]. Other T-cell subsets play a role in RA pathogenesis; IL-17 secretion by circulating Th17 cells is positively correlated with RA severity and results in the production of proinflammatory cytokines, chemokines, and matrix metalloproteinases (MMPs) [697,698].

Moreover, T-cells play an important role in B-cell recruitment and activation [699]. B-cells contribute to the development of RA by presenting their own antigens to follicular helper cells (Tfh) and peripheral helper cells (Tph), increasing the secretion of C-X-C motif chemokine ligand 13 (CXCL13) and IL-21[700,701]. This interaction promotes B cell differentiation and maturation, leading to the production of autoantibodies such as RF and ACPA, as well as others including anti-modified citrullinated vimentin antibody [702]. These autoantibodies participate in RA pathogenesis via multiple mechanisms; for example, RF and ACPA can activate the complement pathway, resulting in the production of C5a and membrane attack complex [703]. Autoantibodies can also form immune complexes with autoantigens to induce osteoclast differentiation through Fcγ receptors (FcγR), causing joint destruction [704]. Macrophages are another

essential mediator in RA pathogenesis and are consistently found in higher levels within the synovial tissue of patients [705]. As previously described, T cells signal the recruitment and activation of macrophages in RA development [696,697]. However, in the inflamed joint, macrophages contribute to joint destruction by expressing HLA and leukocyte adhesion molecules to activate T-cells [706,707]. Macrophage-mediated T-cell activation results in the secretion of inflammatory mediators such as IL-1α and IL-1ß which supports RA development [707,708]. Therefore, RA development involves the activation of T cells and a subsequent inflammatory cascade mediated by signalling networks [699,702,707].

5.1.3 The gut-joint axis

In addition to cell-based T-cell activation, studies have suggested that an unknown antigenic agent is presented to CD4+T cells by MHC-II during RA onset [689,691,709]. However, studies have failed to identify a putative infectious agent or antigenic peptide common to the development of RA [689,690]. Instead, studies have highlighted a critical role of gut microbiota in RA pathogenesis. RA patients have been found to have altered gut microbiomes compared to healthy individuals; for example, *Collinsella aerofaciens* is overrepresented in RA patients and can reduce the expression of TJ proteins in IECs [710]. Furthermore, *Faecalibacterium prausnitzii* is reduced in RA patients and has been shown to sustain intestinal barrier function and maintain Th17/Treg balance, resulting in anti-inflammatory effects [711]. As the gut barrier function is impaired in RA patients, it can be suggested that bacterial dysbiosis may play a role in weakening integrity [712]. Due to impaired barrier function, intestinal microbes might translocate from the intestine to other sites via the circulatory system [711,712]. As a result, innate and adaptive autoreactive immune cells are recruited into tissue in response to microbiota, which furthers inflammation and destruction via the release of proinflammatory mediators [713]. In addition to microbiota impairing the integrity of the intestinal barrier and triggering the migration of autoreactive cells to joints, microbes may contribute to RA pathogenesis via molecular mimicry [712,714]. Molecular mimicry is a mechanism that involves pathogen-derived antigens that share sequence homology with host-peptides [715,716]. This can lead to cross-activation of autoreactive T and B cells, which causes autoimmunity and tissue damage [716,717]. For example, the molecule N-acetylglucosamine-6-sulfatase has been identified as a T and B-cell-targeted autoantigen in more than 50% of RA

patients and has marked sequence homology with epitopes from sulfatase proteins from *Prevotella* and *Parabacteroidetes* species [712,718]. Studies have found that the expansion of intestinal *Prevotella* is correlated with enhances susceptibility to RA; thus, it can be suggested that microbes and molecular mimicry are contributing to disease onset [719].

Furthermore, microbial and host derived metabolites have been speculated to be a contributing factor in RA prevention or development [720]. Microbial bile acid (BA) conjugates are elevated in the faeces on RA patients and have recently been associated with bone metabolism [720,721]. BA levels have been positively correlated with vitamin D levels in the blood, which plays an important role in calcium regulation and bone health [722]. BAs such as ursodeoxycholic acid and SCFAs also dampen inflammation and protect bone health by inhibiting proinflammatory cytokines [723,724]. Other host derived molecules identified as contributors to RA onset and progression include lipid derivates such as prostaglandins (PGs), leukotrienes (LTs), lipoxins (LXs), platelet activating factor (PAF) and lysophosphatidylcholines (LysoPCs) [725-727]. These molecules each play their own unique part in pro and anti-inflammatory pathways by modulating the inflammatory response and oxidative stress [727,728]. Therefore, identifying disease-relevant microbial or host molecules that may be involved in inducing pathogenic autoimmunity will help provide novel biomarkers for diagnostic and therapeutic intervention as well as improve our understanding of disease aetiology.

5.1.4 Systemic effects of RA and association with IBD

RA is also a systemic disease that can affect a multitude of organ systems such as the eye, skin, heart, nerves, and lungs [729]. Pulmonary diseases such as pleuritis, bronchiolitis, rheumatoid nodules, and interstitial lung disease (ILD) are amongst the most common complications and are associated with 10-20% of mortality in RA patients [730,731]. Current research has suggested that pulmonary complications are due to a combination of genetic susceptibility and environmental stressors such as smoking [732]. However, the exact pathophysiologic basis for development of RA pulmonary complications remains elusive, which is largely due to a lack of a research [733]. This is because studying lung complications in RA patients is complicated due to difficulty collecting lung tissue from patients [734]. Therefore,

most studies investigating lung complications heavily rely on collection of blood and serum which is not effective for uncovering disease mechanisms in the tissue [735,736]. Furthermore, lung complications in RA are often asymptomatic or a change in lung function is observed without being able to diagnosis lung disease due to an absence of histological and clinical evidence [734,737]. Therefore, animal models have been used to investigate RA associated lung disease with most focusing on RA-ILD [733,735]. However, despite reports of different models showing lung inflammation and fibrosis, no model has been selected as the gold standard [733,738]. Furthermore, surgical lung biopsies from RA-ILD patients have found significantly higher numbers of CD4+T cells present in the lungs [729,739]. This may indicate that a dysregulated inflammatory cascade involving a host of signalling molecules such as cytokines, chemokines and growth factors are recruiting immune cells which collectively promotes epithelial and endothelial cell damage [740].

Furthermore, abnormal liver tests have been reported in 18-50% RA patients, despite liver manifestations generally not being recognised as a feature of RA [741]. However, recent evidence is emerging to suggest RA liver manifestations commonly involve liver steatosis, nodular regenerative hyperplasia, portal fibrosis and intrahepatic small vessel arteritis [742,743]. Furthermore, RA patients are at a higher risk of developing kidney inflammation, leading to renal dysfunction [744,745]. A further 5-10% RA patients have enlarged spleens which is caused by Felty syndrome in 1-3% patients [746]. The cause of this condition is still unknown and results in a decreased white blood cell count, leaving patients susceptible to infection [747,748]. Furthermore, RA disease complications are difficult to diagnose due to a lack of specific diagnostic markers and tests [742,745,748]. Studies have also shown that RA tends to cluster with IBD as IBD patients are more likely to develop RA and *vice versa* [749]. However, other studies dispute this bidirectional relationship and suggest that RA plays a causal role in the pathogenesis of IBD, but IBD does not cause RA [750,751]. The pathophysiological mechanisms underlying the relationship between RA and IBD are not entirely clear [750,752]. However, the conditions both involve similar cytokine signalling, immunomodulation, and alterations in the gut microbiota; thus, it is reasonable to conclude that both diseases share common inflammatory pathways [750,753]. Therefore, identifying molecular biomarkers in RA systemic sites may help clarify disease pathogenesis and comparing molecular changes with those observed in models of IBD might reveal links between the diseases [730,754].

5.1.5 Collagen induced arthritis animal model

The collagen induced arthritic (CIA) mouse model is commonly used to study RA and involves immunising genetically susceptible mice with collagen-II emulsified in Complete Freund's Adjuvant (CFA) [755-757]. Collagen-II cross-reacts with serum antibodies and acts as a T-cell dependent antigen [758]. This induces an autoimmune response in T-cells and B-cells, resulting in the production of RF and ACPA, as well as higher articular levels of proinflammatory cytokines such as TNF-α [759]. Therefore, CIA is clinically, histologically, and immunologically similar to human RA, making it a standard and valuable model for RA research [760]. The CIA model has been used to study RA-ILD as the model induces anti-citrullinated protein antibodies that react with various citrullinated proteins in the joint and lung [734,738,761]. However, to our knowledge no study has addressed changes to the metabolic environment in the lung that may support the onset of disease and progression [732,740,762]. Furthermore, the systemic response in the CIA model has still not been well characterised within different organs [760,763]. CIA model is also most commonly used to investigate the role innate and adaptive immune cells play in joint inflammation and very few studies address the role small molecules may play in systemic complications [759,764,765]. Therefore, this study will use mass spectrometry imaging (MSI) to identify small molecules that are changed in the lung, liver, spleen, and kidney of CIA mice that could contribute to disease complications. Furthermore, IMC will be used to investigate *in situ* immunomodulatory effects in systemic sites of CIA model that may contribute to pathology.
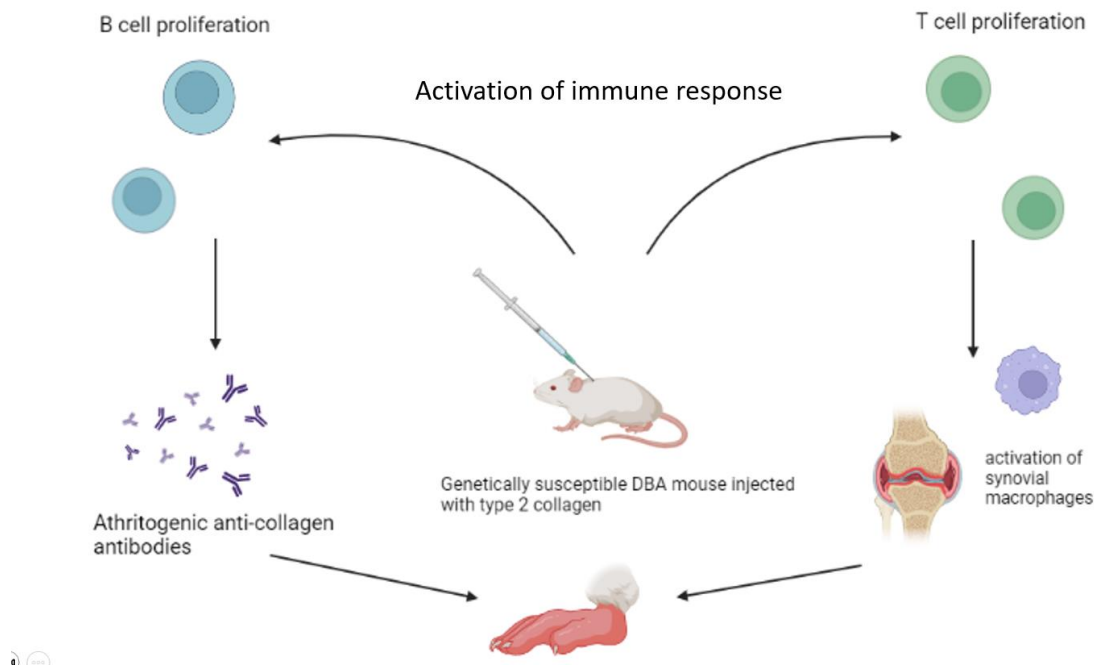
Figure 5.1.1 Collagen Induced Arthritis mechanism of action. Collagen is injected, typically type II collagen, into genetically susceptible mice. The injected collagen activates the immune system, leading to the initiation of an inflammatory response. 1) Production of Autoantibodies: B cells (blue cells) proliferate and produce autoantibodies against collagen, forming immune complexes, which trigger further immune responses. 2) Activation of T Lymphocytes (green cells): T lymphocytes are activated in response to the immune complexes, leading to the release of pro-inflammatory cytokines and activation of other immune cells such as synovial macrophages (purple cells). 3) Joint Destruction: Continued inflammation and immune response result in joint damage and destruction, leading to arthritis symptoms.

5.2 Results

5.2.1 CIA causes shifts in the faecal microbiome

Microbiome sequencing of faecal samples showed changes in the relative abundance of phyla between CIA mice and control groups at the end of the experiment (Figure 5.2.1a). Firmicutes and Bacteroidota were the most abundant phyla across all groups. However, Firmicutes were reduced and Bacteroidota were increased in CFA and CIA groups, compared to naïve control. The heatmap also shows that the abundance of the top 35 genera present in faeces are changed between naïve and CIA groups (Figure 5.2.1b). *Eubacterium, Odoribacter, Aerococcus, Paeniclostridium, Lactobacillus, Clostridium, Shigella*

and *Fusobacterium* are increased in CIA mice, compared to naïve group. Whereas others such as *Lachnospiraceae, Blautia, Prevotellaceae, Roseburia, Oscillibacter, Bacteroides, Lachnoclostridium, Colidextribacter, Anaerotruncus* and *Butyricicoccus* are reduced in CIA mice, compared to naïve control group.
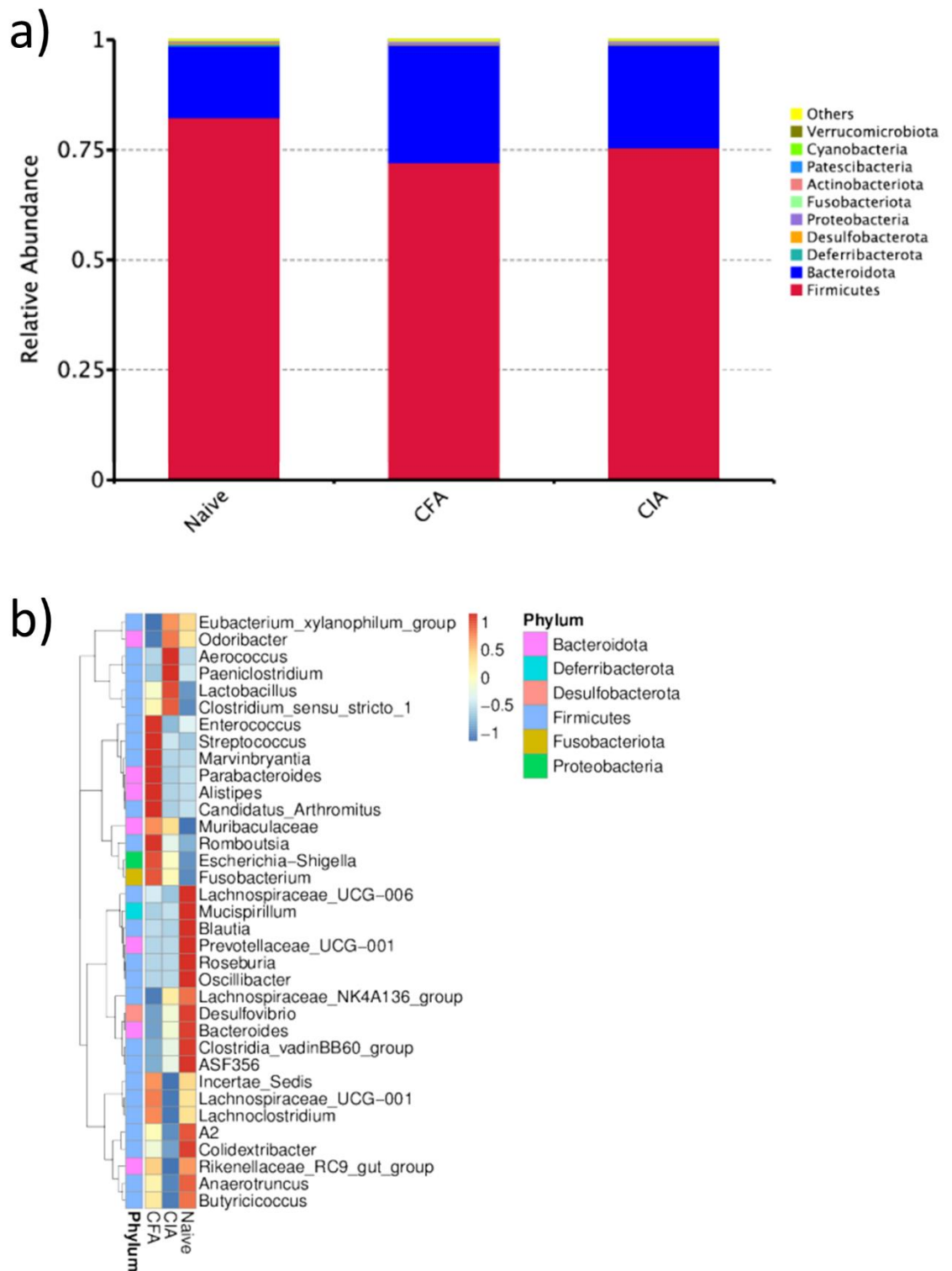
Figure 5.2.1 Relative abundance of bacterial phyla and heatmap of genera in CIA mice
A) Histogram of relative abundance of the top 10 bacterial phyla in the faeces of control mice (naïve and CFA) and CIA mice at the end of experiment (day 35). B) Heatmap of top 35 genera in faeces of control groups and CIA mice after experiment.

5.2.2 Metabolic changes in the spleen of CIA model

MSI was used to investigate the molecular changes in systemic sites including the spleen of CIA mice. ROC analysis found 78 peaks that could potentially discriminate between CIA and naïve groups. The variation in the 78 metabolites detected were analysed to examine the clustering of groups using multivariate statistical analysis including PCA (M1) and PLS-DA (M2). PCA score plots of the first (t [1]) and second (t [2]) principle component did show moderate clustering and clear separation in the spleen; CIA group clustered furthest from naïve (parameters: R2X=0.814, Q2=0.716) (Figure 5.2.2 M1). PLS-DA score plot (M2) was also able to separate and cluster the groups (parameters: R2X=0.663, R2Y=0.328, Q2=0.222) using the first (t [1]) principal component. As PCA had parameters above 0.5, the model is reliably predictive; however, PLS-DA is not accurately fitting or predicting results. The corresponding loadings plots indicated that variations in the levels of several metabolites were the main contributors to group separation.

Model	Type	A	N	R2X(cum)	R2Y(cum)	Q2(cum)
M1	PCA-X	2	13	0.814		0.716
M2	PLS-DA	1	13	0.663	0.328	0.222
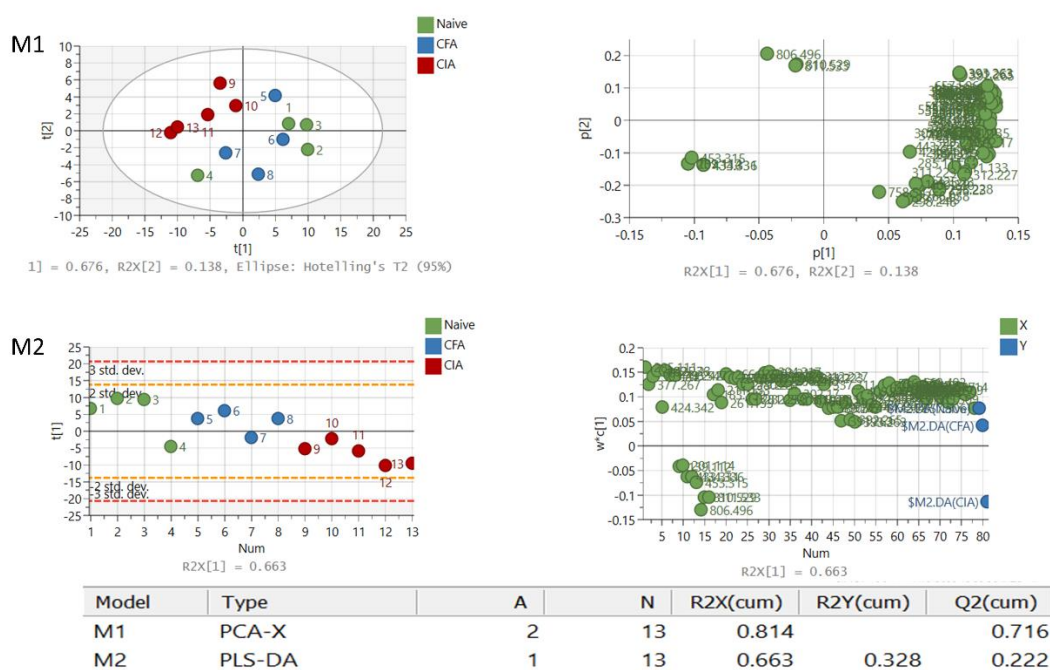
Figure 5.2.2 Unsupervised and supervised discriminant analysis of molecules in spleen.
M1) Unsupervised PCA analysis was able to discriminate between the groups using metabolite features. M2) Supervised PLS-DA analysis did discriminant between the controls (Naive, green circles; CFA, blue circles) and diseased group (CIA, red circles). Analysis was performed using SIMCA 17 software. PLS-DA and PCA score plots consist of components 1 (t [1]) and 2 (t [2]). The ellipse represents the 95% confidence region for Hotelling's T2 statistic for the model.

Univariate analysis indicated that 15 out of the 78 molecules were significantly decreased in the spleen of CIA mice, compared to the spleen of naïve control mice. The *m/z*, putative identity, and fold-decrease in CIA group of these molecules are as follows; 295.2264 (9,10-epoxy-12-octadecenoic acid (EOA); 1.72-fold (*p*=0.0126), 296.2306 (18-hydroxyoleate; 1.77-fold (*p*=0.0111), 266.0292 (unidentified; 43.46-fold (*p*=0.0066)), 297.2435 (10-oxooctadecanoic acid (OxoODE); 1.37-fold (*p*=0.0284)), 298.2469 (unidentified; 1.41-fold (*p*=0.0264)), 293.2123 (13-OxoODE; 2.21-fold (*p*=0.003)), 294.2155 (18-oxo-oleate; 2.42-fold (*p*=0.0025)), 312.2263 (unidentified; 1.70-fold (*p*=0.0086)), 285.11146 (unidentified; 2.10-fold (*p*=0.0004)), 377.26738 (monoglyceride (MG)(0:0/18:2(9Z,12Z)/0:0); 2.79-fold (*p*=0.0362)), 393.24 (cyclic phosphatidic acid (cPA)(16:0); 2.37-fold (*p*=0.0077)), 409.23636 (MG(0:0/18:1(9Z)-O(12,13)/0:0); 4.31-fold (*p*=0.0017)), 425.23034 (PA(8:0/8:0); 4.60-fold (*p*=0.0017)), 443.24227 (unidentified; 2.21-fold (*p*=0.0038)) and 758.54685 (unidentified; 1.44-fold (*p*=0.0062)). Furthermore, the molecule with *m/z* 806.4980 was significantly increased 2.19-fold (*p*=0.0085) in the CIA spleen, compared to naïve control. This molecule was putatively identified as phosphatidylserine (PS) (20:2(11Z,14Z)/18:4(6Z,9Z,12Z,15Z)) and the PCA loadings plot shows that it is contributing towards the separation of CIA group from naïve and CFA controls; thus, could be an important biomarker. Molecules above are shown in a heatmap (Figure 5.2.3a). No molecule was significantly changed between naïve and CFA groups; thus, changes in the CIA group are a result of disease onset and not the addition of the adjuvant. Enrichment analysis was performed in Metaboanalyst using all possible putative identities (Figure 5.2.3b). Linoleic acid metabolism (*p*=0.00213) was found to be enriched in the spleen due to the presence of 9,10-EOA and 12,13-epoxyoctadecenoic acid (EpOME); however, these identities relate to the same molecule with *m/z* 295.2264. Therefore, only one identity is likely to be correct, hence enrichment of this pathway is likely to be inaccurate. Glycerophospholipid metabolism was also identified as being enriched in the spleen due to the presence of phosphatidylglycerol in the dataset; however, enrichment was not significant (*p*=1.0)
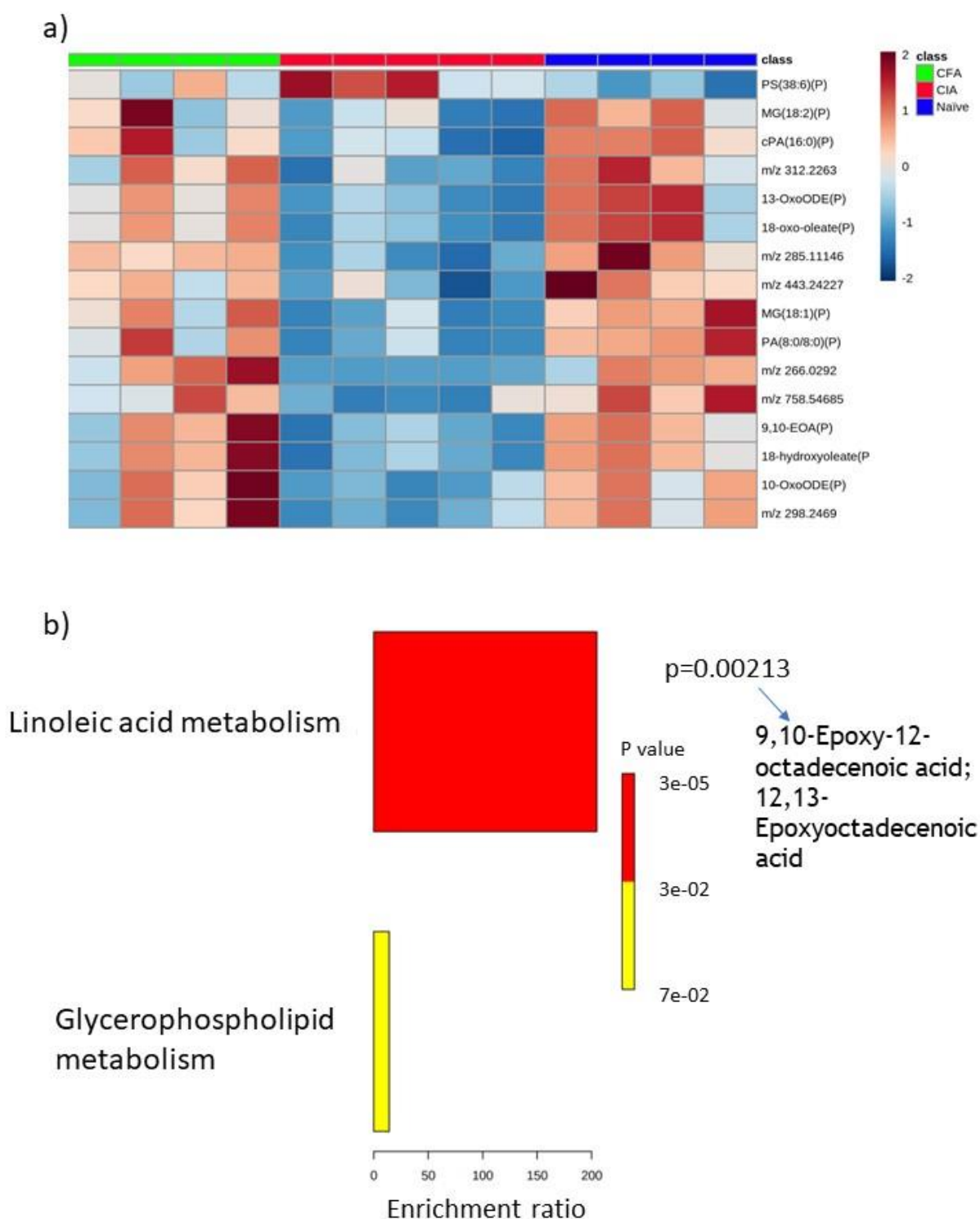
Figure 5.2.3 Heatmap of increased and decreased molecules in spleen of CIA model and enrichment of pathways.

a) Heatmap shows m/z of molecules unable to be identified, putatively identified molecules (marked with a P) and molecules with an MSMS confirmed identification. Heatmap was created using Metaboanalyst 5.0. The colour of each sample is proportional to the significance of change in metabolite abundance indicated by the colour bar (red, increased in CIA group; blue, decreased in CIA group). Rows correspond to metabolites and columns correspond to samples. b) Enrichment pathway analysis using KEGG as reference found molecules involved in two different pathways: linoleic acid metabolism and glycerophospholipid metabolism. Linoleic acid

metabolism pathway was significantly enriched, and the molecules involved in the pathway that are present in the dataset are listed.

5.2.3 Metabolic changes in the kidney of CIA model

In the kidney of the CIA model, ROC analysis found 3 peaks that could potentially discriminate between CIA and naïve groups. The variation in the 3 metabolites detected were analysed to examine the clustering of groups using multivariate statistical analysis including PCA (M1) and PLS-DA (M2). PCA score plots did show distinct clustering and clear separation in the kidney using the first (t [1]) principal component (parameters: R2X=0.922, Q2=0.808) (Figure 5.2.4). PLS-DA score plot (M2) was also able to separate and cluster the groups using the first (t [1]) principal component (parameters: R2X=0.922, R2Y=0.331, Q2=0.201). contributors to group separation.

Model	Type	A	N	R2X(cum)	R2Y(cum)	Q2(cum)
M1	PCA-X	1	12	0.922		0.808
M2	PLS-DA	1	12	0.922	0.331	0.201
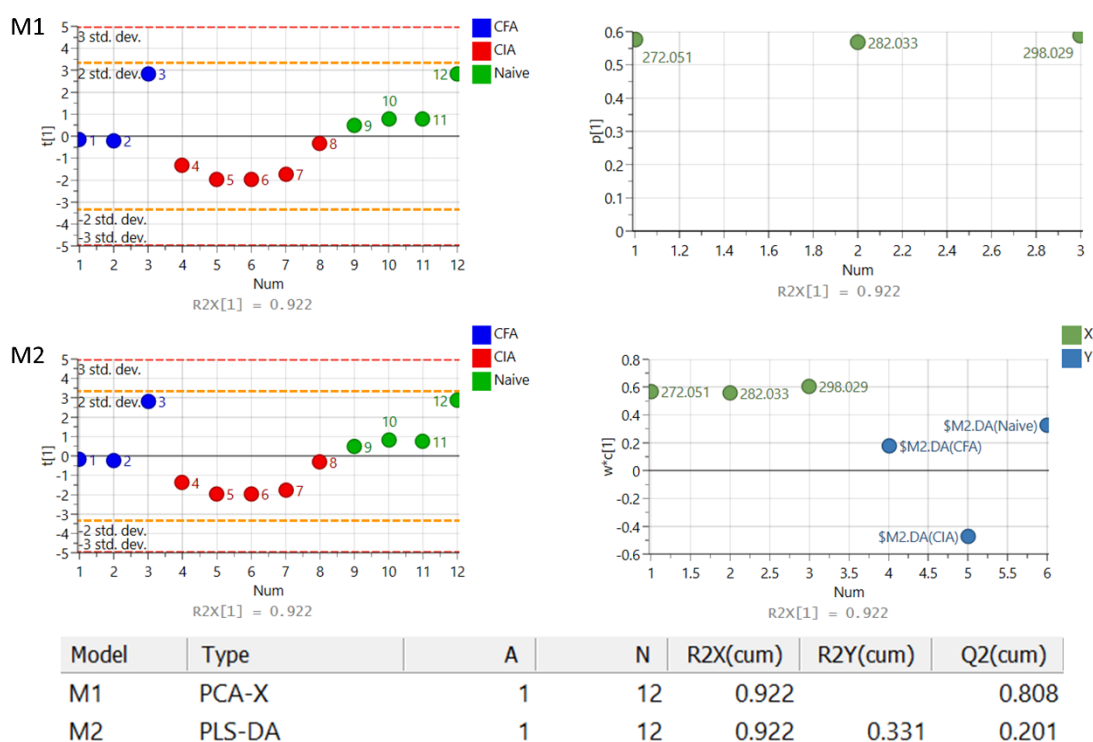
Figure 5.2.4 Unsupervised and supervised discriminant analysis of molecules in kidney
M1) Unsupervised PCA analysis was able to discriminate between the groups using metabolite features. M2) Supervised PLS-DA analysis discriminated between the controls (Naive, green circles; CFA, blue circles) and diseased group (CIA, red circles). Analysis was performed using SIMCA 17 software. PLS-DA and PCA score plots consist of components 1 (t [1]) and 2 (t [2]). The ellipse represents the 95% confidence region for Hotelling's T2 statistic for the model.

All 3 molecules identified by ROC analysis were found to be significantly deceased in the kidney of CIA mice, compared to naïve control mice (Figure 5.2.5). The molecule with *m/z* 272.0509 was putatively identified as fructoseglycine and was down 3.86-fold (*p*=0.0246). The molecule with *m/z* 298.0289 was putatively identified as creatinine citrate and was down 4.89-fold (*p*=0.0097). Lastly, the molecule with *m/z* 282.0328 could not be assigned a putative identity and was down 41.38-fold (*p*=0.0296). These molecules were not significantly changed between naïve and CFA groups, suggesting that the molecules are not decreased due to the adjuvant and may be useful biomarkers of disease. Due to the small number of changes, enrichment analysis could not be performed.
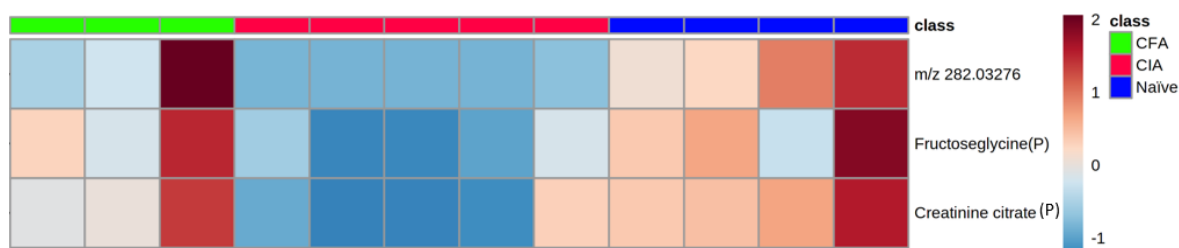
Figure 5.2.5 Heatmap of increased and decreased molecules in kidney of CIA model. Heatmap shows *m/z* of molecules unable to be identified and putatively identified molecules (marked with a P). Heatmap was created using Metaboanalyst 5.0. The colour of each sample is proportional to the significance of change in metabolite abundance indicated by the colour bar (red, increased in CIA group; blue, decreased in CIA group). Rows correspond to metabolites and columns correspond to samples.

5.2.4 Metabolic and cellular changes in the liver of CIA model

In the liver of the CIA model, ROC analysis found 20 peaks that could potentially discriminate between CIA and naïve groups. The variation in the 20 metabolites detected were analysed to examine the clustering of groups using multivariate statistical analysis including PLS-DA (M1) and PCA (M2). PCA score plots did show moderately distinct clustering and clear separation of groups in the liver using the first (t [1]) and second (t [2]) principal components (parameters: R2X=0.814, Q2=0.62) (Figure 5.2.6). PLS-DA score plot (M1) was also able to separate and cluster the groups using the first (t [1]) principal component only (parameters: R2X=0.695, R2Y=0.201, Q2=0.0448).
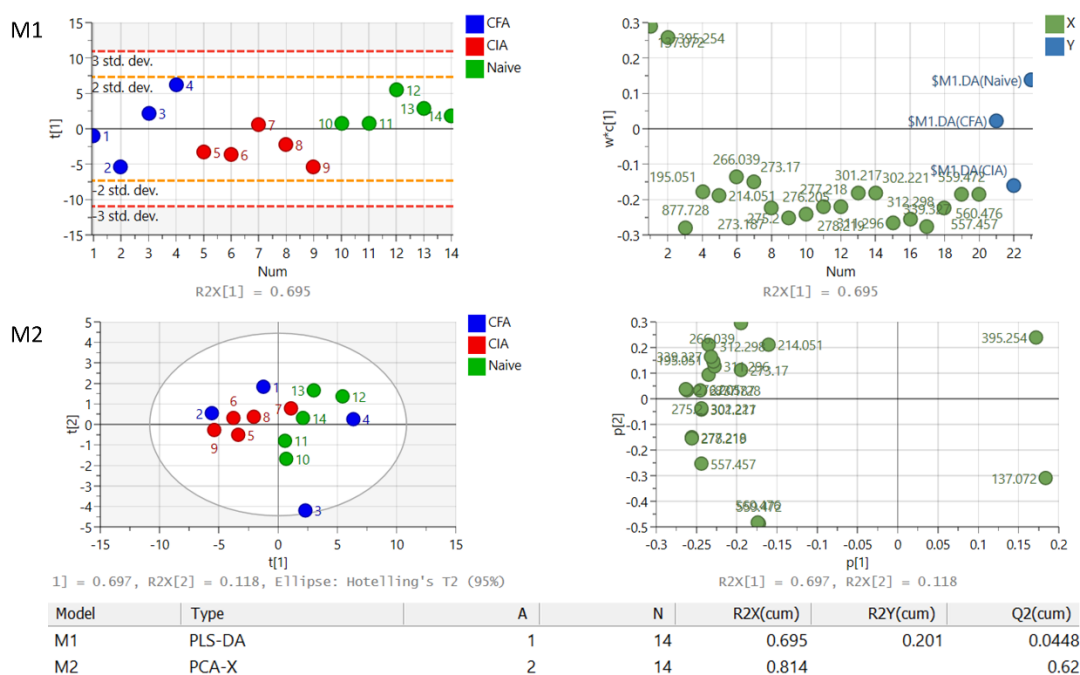
Figure 5.2.6 Unsupervised and supervised discriminant analysis of molecules in liver
M1) Supervised PLS-DA analysis did discriminant between the controls (Naive, green circles; CFA, blue circles) and diseased group (CIA, red circles). M2) Unsupervised PCA analysis was able to moderately discriminate between the groups using metabolite features. Analysis was performed using SIMCA 17 software. PLS-DA and PCA score plots consist of components 1 (t [1]) and 2 (t [2]). The ellipse represents the 95% confidence region for Hotelling's T2 statistic for the model.

Univariate analysis revealed that only 2 molecules were significantly changed in the liver of CIA mice, compared to naïve control mice (Figure 5.2.7). The molecule with m/z 877.7253 was putatively identified as triglyceride (TG) (54:7) and was increased 3.38-fold ($p=0.0375$) in the liver of CIA, compared to naïve mice. The molecule with m/z 137.072 was putatively identified as 1-MNA and was decreased 3.53-fold ($p=0.0229$) in the liver of CIA mice, compared to the control. There was no significant change in these molecules in the naïve group compared to the CFA group; thus, metabolite differences are likely to be due to disease onset and could be useful biomarkers. Furthermore, due to limited metabolite changes, enrichment pathway analysis could not be performed.
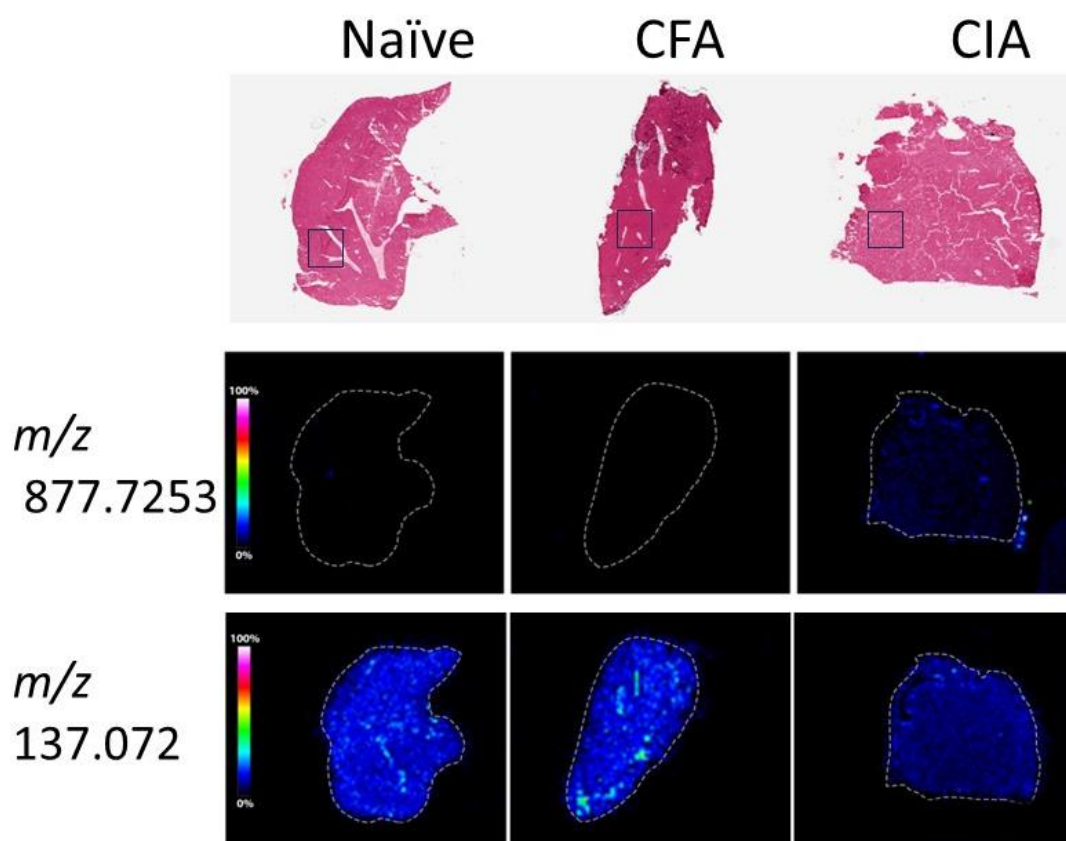
Figure 5.2.7 MSI image of m/z 877.7253 and 137.072 abundance in the liver.
From top to bottom: haematoxylin and eosin (H&E)-stained sections with rectangular boxes indicating region selected for IMC, MSI heatmap of *m/z* 877.7253 and 137.072 (colour bar shows 0% to 100% relative abundance).

IMC was used to quantify the percentage of cells that expressed specific markers of immune phenotype and function, at a 1 μM spatial resolution. Figure 5.3.8a shows in the tissue, the percentage of cells positively expressing the marker, cleaved caspase 3 (CC3), was reduced 2.94-fold (*p*=0.0103) in the CIA group compared to the naïve group. CC3^{+} cells were also phenotypically described as being apoptotic; thus, apoptosis is reduced in the liver of CIA mice, compared to naïve mice. Furthermore, the percentage of cells expressing the marker NKp46, was reduced 3.60-fold (*p*=0.0257), in the liver of CIA mice compared to naïve controls. Cells that are NKp46^{+} are described as natural killer (NK) cells; thus, NK cells are reduced in the liver of CIA mice, compared to naïve controls. Furthermore, cells that are NKp46^{+} and granzyme B[+] are described as being phenotypical of activated NK cells; this study found that the percentage of activated NK cells were decreased 2.28-fold (*p*=0.0478) in the liver of CIA mice compared to naïve controls (Fig.5.2.8b). In addition, cells that are F480[+] and MHCII[+] are phenotypical of M1 macrophages. The percentage of M1 macrophages

was also found to be reduced 2.34-fold (p=0.0382) in the liver of CIA mice compared to the control (Fig.5.2.8b).

a)

DNA

CC3/ Apoptosis

NKp46/ NK cells
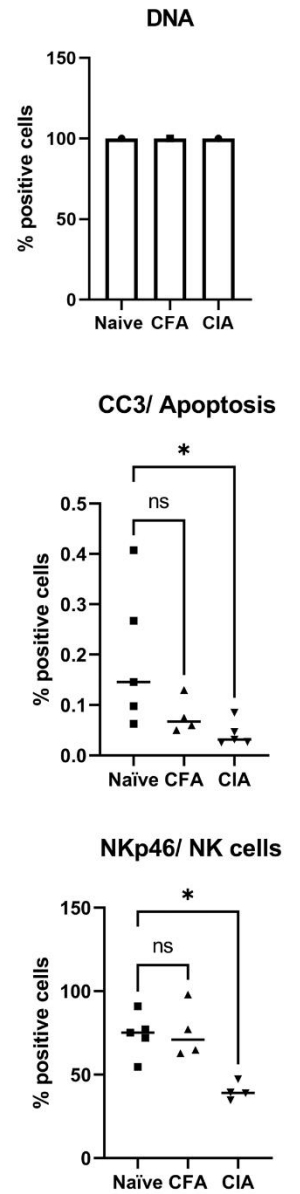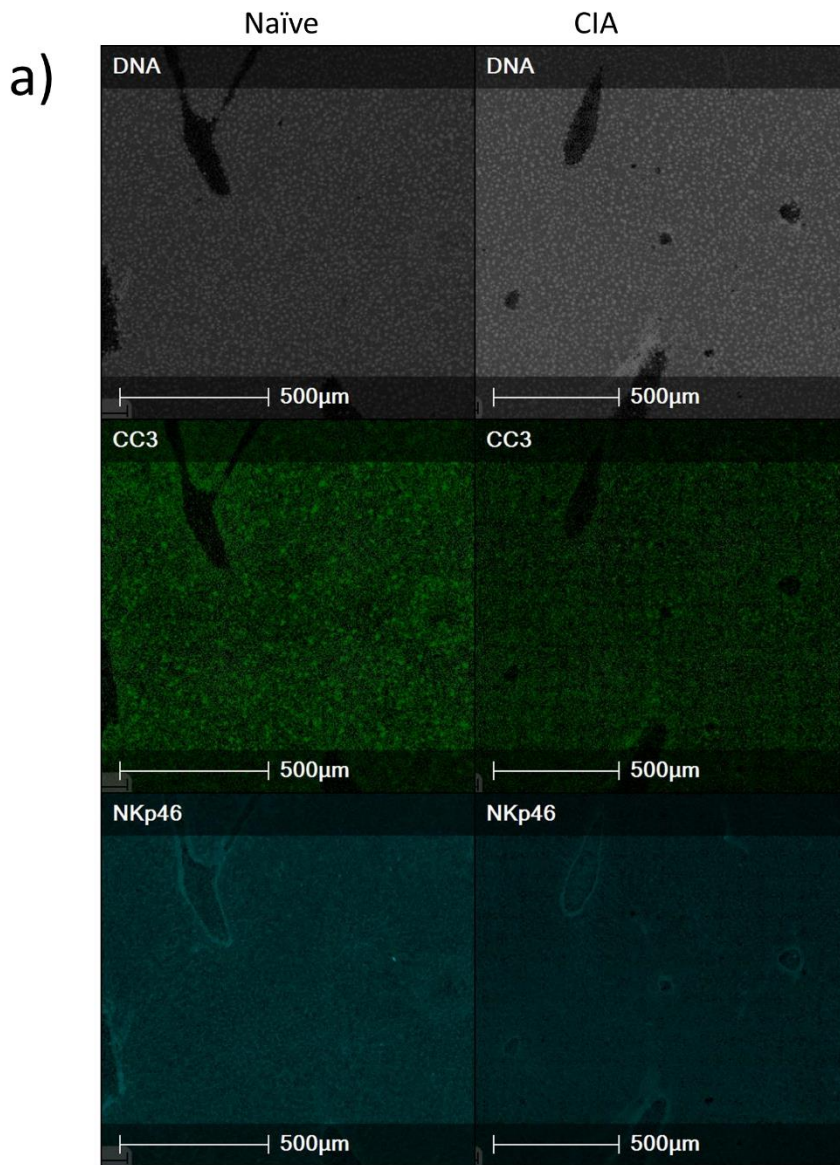
b)

Activated natural killer cell
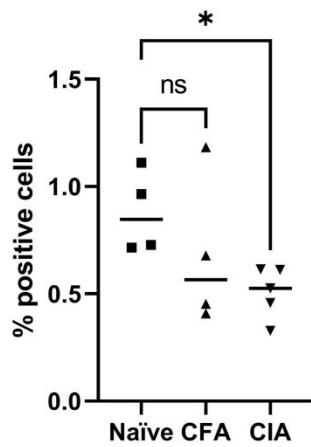
M1 macrophages
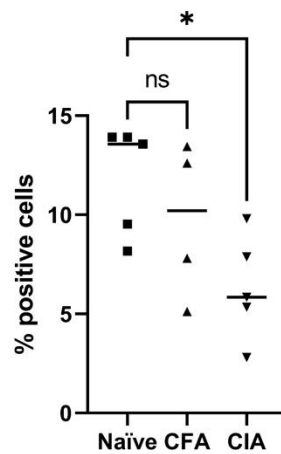
Figure 5.2.8 Representative IMC images of biological markers of cell function in the liver of CIA model.
Images shown are the region indicated in Figure 5.3.7 for naïve and CIA groups. a) Percentage of cells in the tissue expressing CC3 and NKp46. b) Percentage of cells expressing NKp46$^+$ and granzyme B$^+$ (activated NK cell phenotype) and F480$^+$ and MHCII$^+$ (M1 macrophage phenotype). Percentage positive cells represented as bar graph showing four or five biological replicates. One-way ANOVA performed to compare CFA and CIA groups to naïve control and *p<0.05, **p<0.01, ***p<0.001, ****p<0.0001 was considered statistically significant.

In the liver vessels (Figure 5.2.9), the percentage of cells expressing the markers CD31 and Glut1 were increased 2.15-fold (*p*=0.0467) and 3.29-fold (*p*=0.0064), respectively, in the CIA group compared to naïve controls. CD31 and Glut1 were used to phenotype cells as blood vessels and hypoxic cells, respectively; thus, this study indicates that blood vessels and hypoxia are increased in the liver vessel of CIA mice compared to the naïve group.
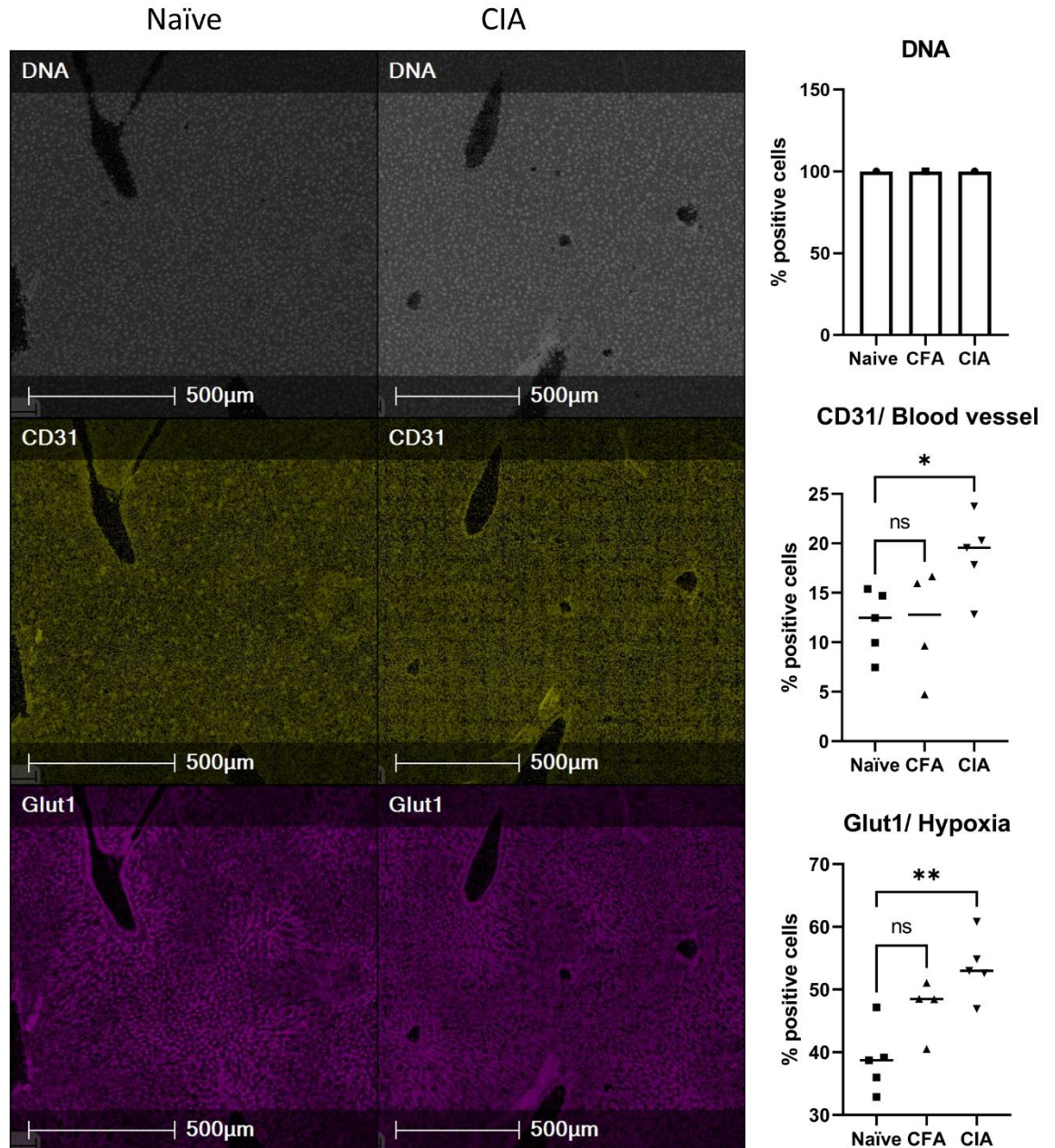
Figure 5.2.9 Representative IMC images of biological markers of cell function in the liver vessels of CIA model

Images shown are the region indicated in Fig 5.3.7 for naïve and CIA groups. From top to bottom, DNA intercalator identified single cells within the tissue section, markers for cell function CD31 (blood vessel marker) and Glut1 (Hypoxia marker). Percentage positive cells represented as bar graph showing four or five biological replicates. One-way ANOVA performed to compare CFA and CIA groups to naïve control and *$p<0.05$, **$p<0.01$, ***$p<0.001$, ****$p<0.0001$ was considered statistically significant.

5.2.5 Metabolic changes in the lung have immunomodulatory effects in the CIA model and cellular changes in the lung of CIA model

In the lung of the CIA model, ROC analysis found 12 peaks that could potentially discriminate between CIA and naïve groups. The variation in the 12 metabolites detected were analysed to examine the clustering of groups using multivariate statistical analysis including PLS-DA (M1) and PCA (M2). PCA score plots did show moderately distinct clustering and clear separation of groups in the lung; CIA clustered farthest from naïve group using t [1] and t [2] principal components (parameters: R2X=0.964, Q2=0.88) (Figure 5.2.10). PLS-DA score plot (M1) was also able to separate and cluster the groups but only used t [1] principal component (parameters: R2X=0.646, R2Y=0.41, Q2=0.31).

Model	Type	A	N	R2X(cum)	R2Y(cum)	Q2(cum)
M1	PLS-DA	1	13	0.646	0.41	0.31
M2	PCA-X	3	13	0.964		0.88
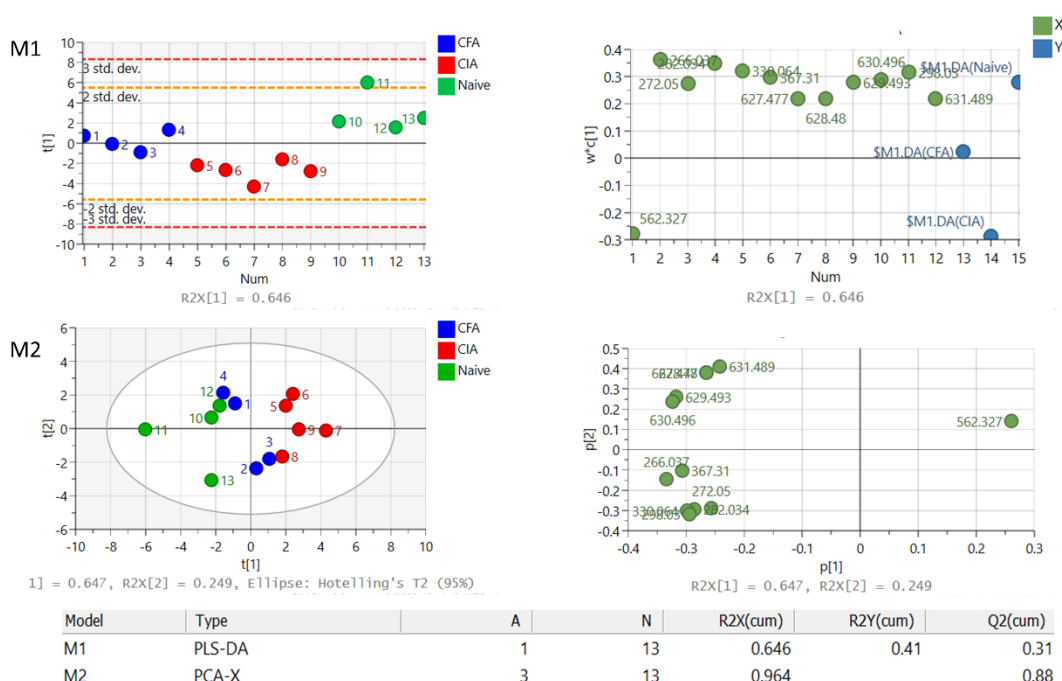
Figure 5.2.10 Unsupervised and supervised discriminant analysis of molecules in lung
M1) Supervised PLS-DA analysis also did not discriminant between the controls (Naive, green circles; CFA, blue circles) and diseased group (CIA, red circles). M2) Unsupervised PCA analysis was able to moderately discriminate between the groups using metabolite features. Analysis was performed using SIMCA 17 software. PLS-DA and PCA score plots consist of components 1 (t [1]) and 2 (t [2]). The ellipse represents the 95% confidence region for Hotelling's T2 statistic for the model.

The peaks were then analysed using one-way ANOVA and 9 were found to be significantly changed between the CIA and naïve groups (*p*<0.05) (Figure 5.2.11).

Pathway enrichment analysis was performed, and Ether lipid metabolism and Purine metabolism was identified as being enriched; however, the pathways were not significant (figure not shown). Therefore, this study will focus on individual molecules. Molecules with the following *m/z* were putatively identified and decreased in the CIA lung, compared to naïve control; 266.0391 (guanidine; 12.7-fold, *p*=0.0001), 272.0503 (fructoseglycine; 3.07-fold, *p*=0.0243), 282.035 (no identity; 20.84-fold, *p*=0.0005), 330.0628 (2'-deoxyadenosine 3'-monophosphate (dAMP); 8.50-fold, *p*=0.0034), 367.3105 (no identity; 9.28-fold, *p*=0.0063), 629.4926 (diglyceride (34:1); 1.61-fold, *p*=0.0187), 630.4956 (ceramide (t36:1); 1.61-fold, *p*=0.014) and 298.0294 (creatinine citrate; 6.99-fold, *p*=0.004).
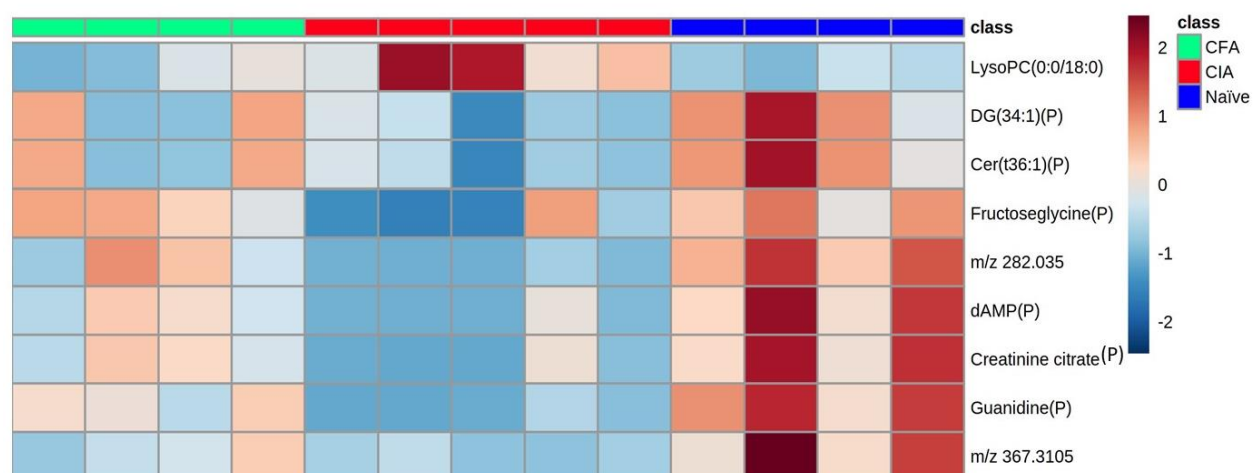
Figure 5.2.11 Heatmap of increased and decreased molecules in lung of CIA model
Heatmap shows *m/z* of molecules unable to be identified, putatively identified molecules (marked with a P) and molecular identities confirmed by MSMS. Heatmap was created using Metaboanalyst 5.0. The colour of each sample is proportional to the significance of change in metabolite abundance indicated by the colour bar (red, increased in CIA group; blue, decreased in CIA group). Rows correspond to metabolites and columns correspond to samples.

Molecules *m/z* 272.049 (fructoseglycine), 298.03 (creatinine citrate) and 282.034 (unidentified) were also found to be decreased in the kidney of CIA mice compared to naïve control. These are the only molecules found to be similarly altered in different organs in the CIA model; thus, could be useful biomarkers of systemic disease onset (Figure 5.2.12)
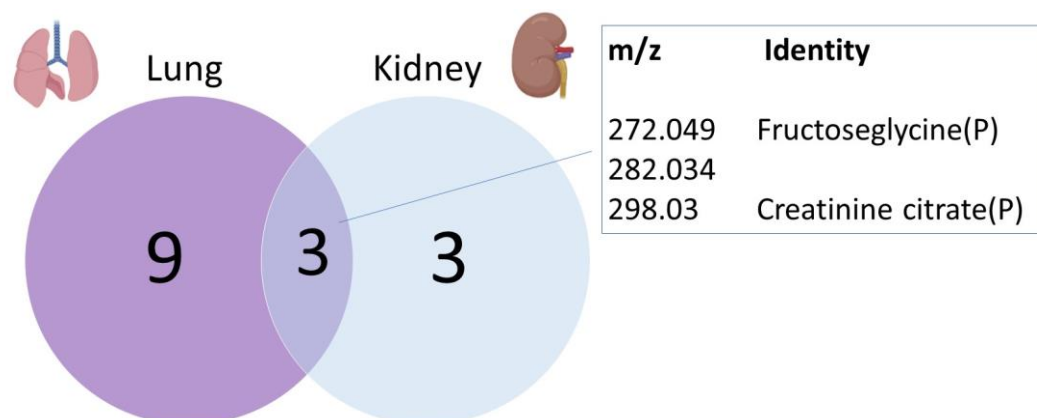
Figure 5.2.12 Venn diagram of molecules altered in the lung and kidney in CIA mouse model.
Left-circle represents the 9 molecular changes in the lung, right-circle represents 3 molecular changes in the kidney. Overlapped segment indicate the number of molecules that are changed similarly between different tissue. The *m/z* and putative identities of the molecules commonly shared between tissue are highlighted in boxes.

Furthermore, a molecule with *m/z* of 562.3272 was putatively identified as lysophosphatidylcholine (18:0) (LysoPC (18:0)) and was increased 2.50-fold (*p*=0.0275) in the lung of CIA mice, compared to naïve control mice (Figure 5.2.13). The PCA loadings plot also indicates that this molecule is contributing towards separating the CIA group from naïve and CFA groups; thus, the molecule might be involved in disease progression.
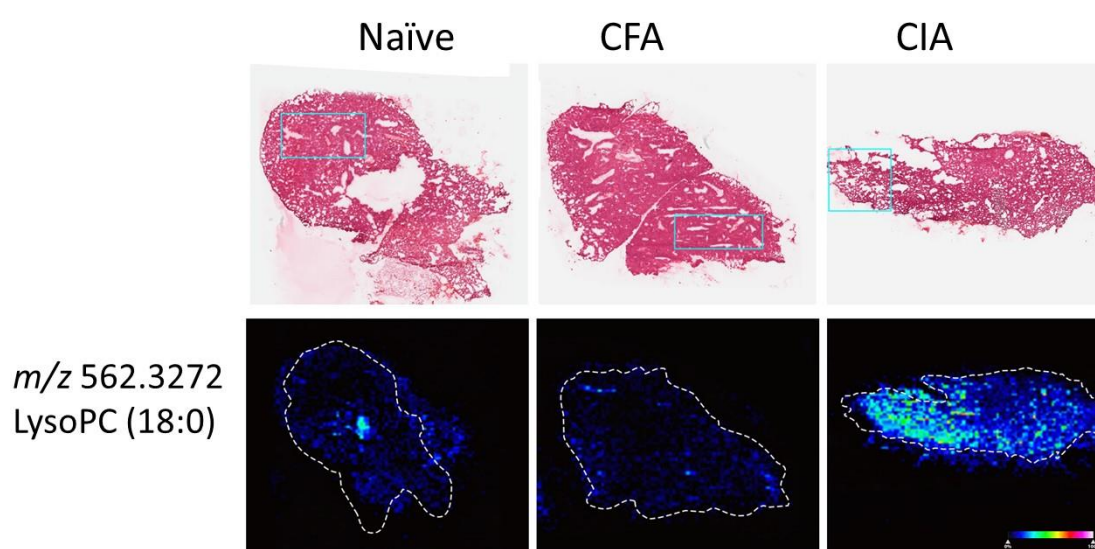
Figure 5.2.13 MSI image of m/z 562.3272 abundance in the lung.
From top to bottom: haematoxylin and eosin (H&E)-stained sections with rectangular boxes indicating region selected for IMC, MSI heatmap of *m/z* 562.3272 (colour bar shows 0% to 100% relative abundance).

A LysoPC (18:0) standard was spotted onto a slide and fragmented in the same run as the endogenous *m/z* 562.32 in lung tissue. The entire spectra were collected from *m/z* 50-562.32 and the fragmentation of the standard at NCE 20 and 30 are show in Figure 5.2.14. Compared to the spectra of endogenous 562.32 at NCE 30, fragmentation of the standard produced almost identical product ions at similar ratios. For example, the peak *m/z* 104.1 (choline ion) is present in the endogenous and standard fragmentation with a similar abundance. Furthermore, ions with *m/z* 86.09 and 503.2 are present with similar abundance in both the endogenous and standard fragmentation spectra. Therefore, this study can suggest with relative confidence that the endogenous molecule in the lung is LysoPC (18:0).
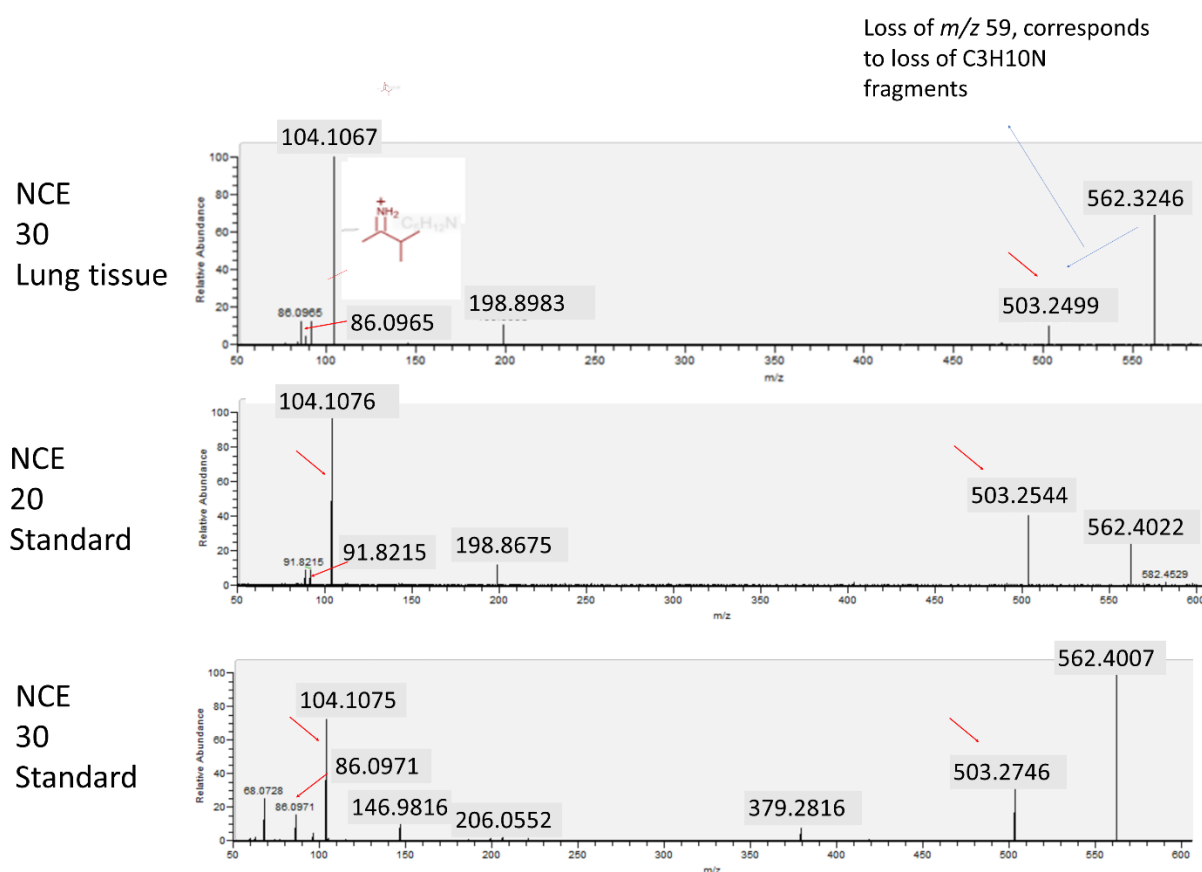
Figure 5.2.14 Comparison of MSMS fragmentation of m/z 562.32 in lung tissue and LysoPC (18:0) standard.
MSMS fragmentation spectra of the endogenous metabolite in the lung at *m/z* 562.32 and synthesised LysoPC (18:0) standard. Fragmentation was performed at increasing NCE energies and NCE 20 and 30 were selected for comparison. Spectra are shown as *m/z* (*x*-axis) plotted against relative abundance (*y*-axis). Similarity of peak presence and abundance suggests that *m/z* 562.32 in lung is likely to be LysoPC (18:0).

IMC was performed on tissue regions indicated by blue rectangular boxes in Figure 5.2.13.Figure 5.2.15 shows in the lung tissue, the percentage of cells positive for markers ATPase and Pan-CK decreased 2.92-fold (p=0.0285) and 2.76-fold (p=0.0207), respectively, in CIA group compared to naïve control. Furthermore, the percentage of Ly6G^{+} and NKp46^{+} cells increased 2.65-fold (p=0.0231) and 3.20-fold (p=0.0124), respectively, in CIA lung tissue compared to naïve group. Furthermore, the results indicate that there was no significant different in marker expression between naïve and CFA groups; thus, differences observed between naïve, and CIA are a result of disease onset.

Figure 5.2.15 Representative IMC images of biological markers of cell function in the lung of CIA model

Images shown are the region indicated in Figure 5.2.13 for naïve and CIA groups. From top to bottom, DNA intercalator identified single cells within the tissue section, markers for cell function ATPase, Pan-CK, Ly6G and NKp46. Percentage positive cells represented as bar graph showing four or five biological replicates. One-way ANOVA performed to compare CFA and CIA groups to naïve control and *$p<0.05$, **$p<0.01$, ***$p<0.001$, ****$p<0.0001$ was considered statistically significant.

Furthermore, the markers were used to predict the dysregulation of 5 cellular phenotypes and functions between CIA and naïve groups (Figure 5.2.16). Cells that are NKp46$^+$ are phenotypically NK cells and were increased 3.20-fold (p=0.0124) in the lung tissue of CIA mice compared to naïve group. Furthermore, cells expressing both CD3 and CD8 markers are phenotypical of cytotoxic T cells and were increased 2.91-fold (p=0.0140) in CIA lung compared to naïve group. Cells that are positive for the markers F480$^+$, CD68$^+$ and CD11b$^+$ are described as macrophages, which were also increased 3.26-fold (p=0.0097) in the CIA lung compared to naïve controls. Ly6G$^+$ and CD11b$^+$ cells are described as neutrophils, and B220$^+$ and CD19$^+$ cells are described as B cells. Ly6G$^+$ and CD11b$^+$ neutrophils increased 2.70-fold (p=0.0185), and B220$^+$ and CD19$^+$ B cells increased 2.71-fold (p=0.0314) in CIA lung compared to naïve group. The results also indicate that the immune profile is not significantly changed between the naïve group and CFA group; thus, changes in the lung immune profile are due to disease activity and not the adjuvant.
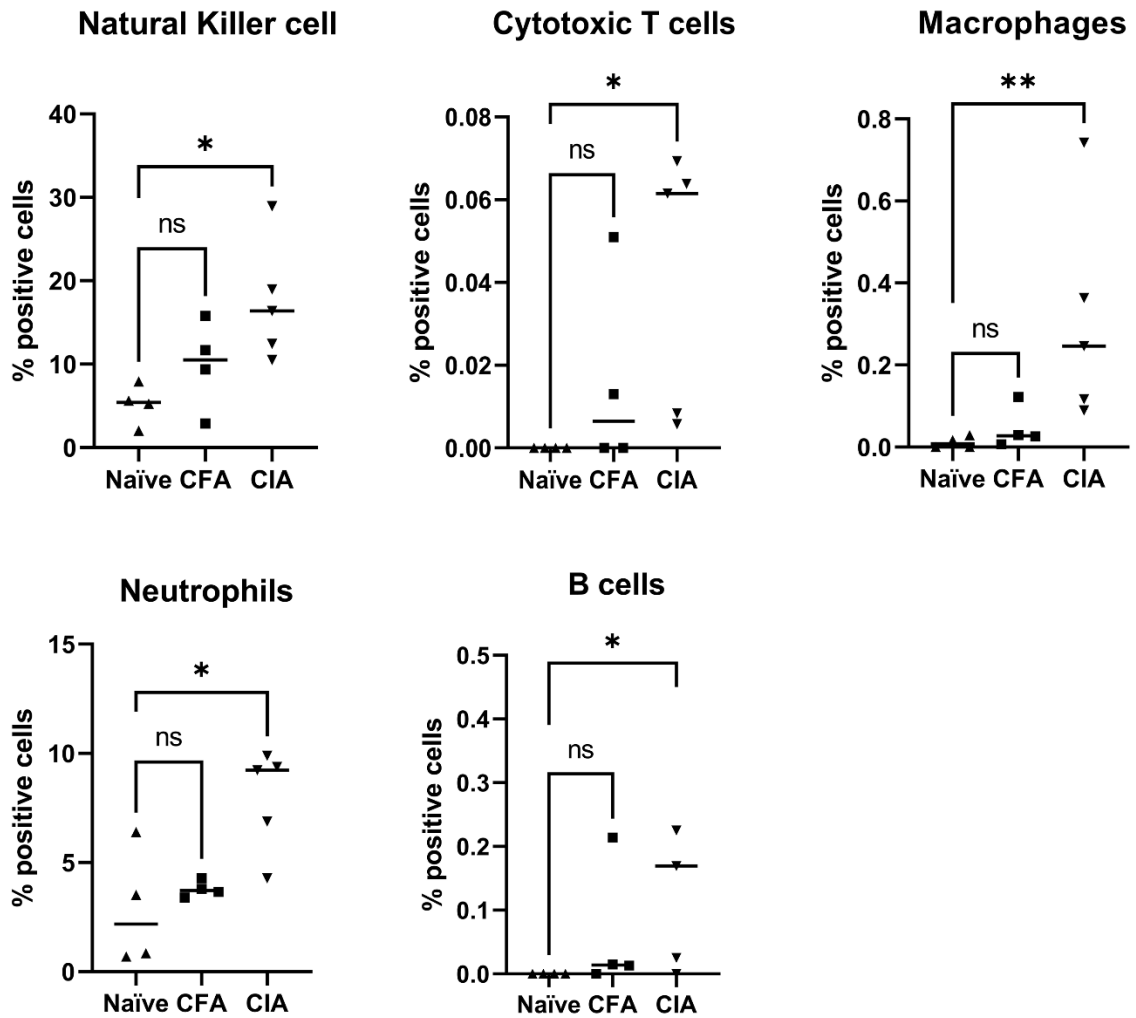
Figure 5.2.16 Bar graph of cell phenotype and function significantly changed in lung tissue.
Percentage positive cells represented as bar graph showing four or five biological replicates and natural killer cells (NKp46+), cytotoxic T cells (CD3+, CD8+), macrophages (F480+, CD68+, CD11b+), neutrophils (Ly6G+, CD11b +) and B cells (B220+, CD19+) were increased in CIA group compared to naïve control. Kruskal-Wallis One-way ANOVA performed to compare CIA and CFA groups to naïve group, and *p<0.05, **p<0.01, ***p<0.001, ****p<0.0001 was considered statistically significant.

Figure 5.2.17 shows in the lung vessels, the percentage of cells expressing CD163, CD206 and Glut1 were reduced 3.04-fold (p=0.0374), 3.38-fold (p=0.0039) and 2.64-fold (p=0.0482), respectively, in the CIA group compared to naïve. Cells positive for Glut1 are described as hypoxia positive; thus, hypoxia was also decreased in the lung vessel of CIA mice compared to naïve mice. Therefore, the immune profile of vessels is distinct from the rest of the lung tissue and may contribute to disease pathology.
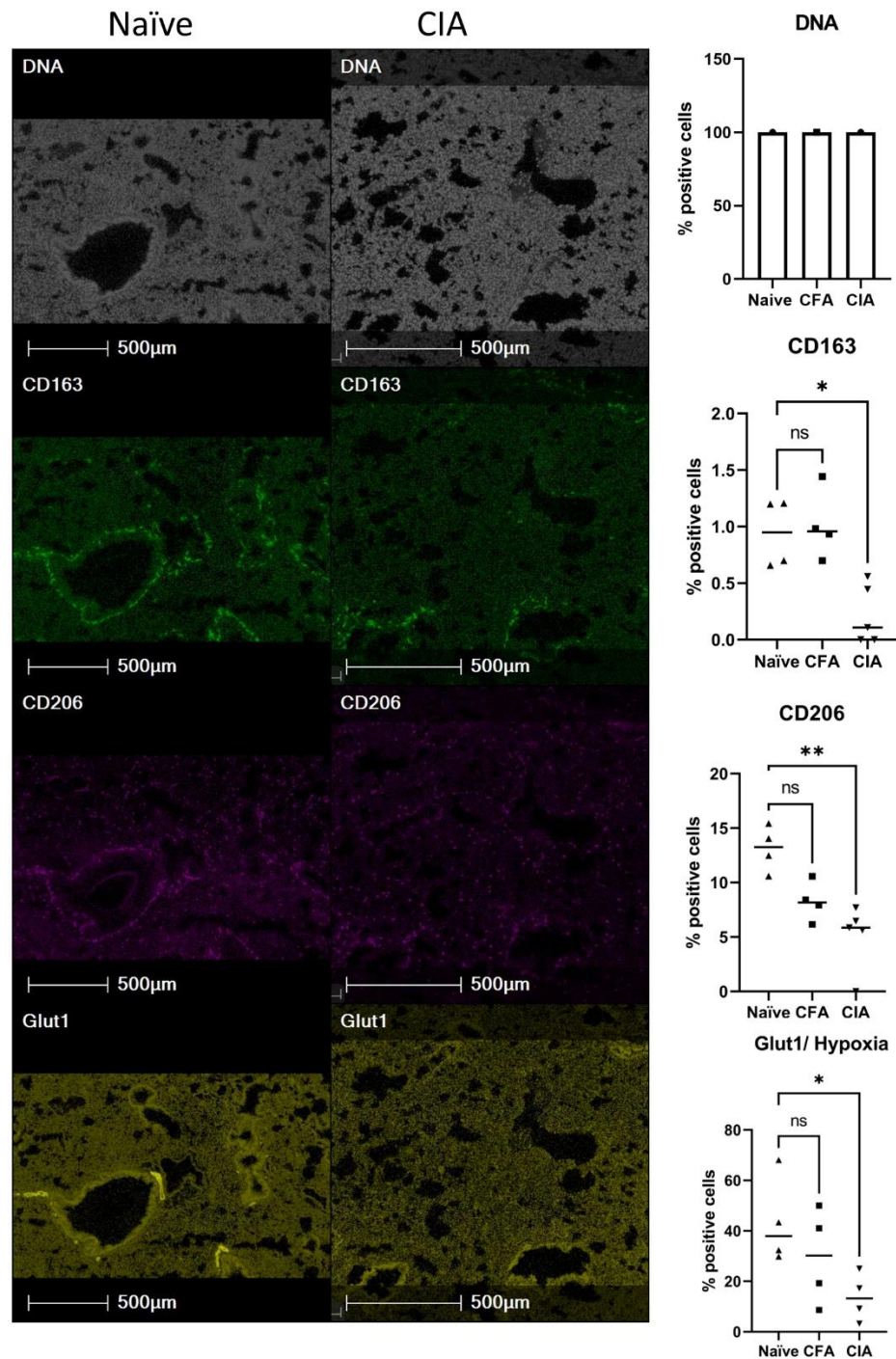
Figure 5.2.17 Representative IMC images of biological markers and phenotypes of cells in lung vessels of CIA model

Images shown are the region indicated in Fig 5.3.13 for naïve and CIA groups. From top to bottom, DNA intercalator identified single cells within the tissue section, markers for cell function CD163, CD206 and Glut 1 (hypoxia marker). Percentage positive cells represented as bar graph showing four or five biological replicates. One-way ANOVA performed to compare CFA and CIA groups to naïve control and *$p<0.05$, **$p<0.01$, ***$p<0.001$, ****$p<0.0001$ was considered statistically significant.

5.2.6 *In vitro* experiments reveal specific immunomodulatory effects induced by LysoPC (18:0)

As IMC indicates that CIA causes immunomodulation in the lung, this study aimed to assess whether the only increased metabolite, LysoPC (18:0), can affect lung cell function. Therefore, the LysoPC (18:0) standard was prepared at various concentrations and used to treat A549 lung epithelial cells (cancer cell line that has been used in research including respiratory, drug screening, inflammation and immunity). LDH assay indicates that LysoPC (18:0) is cytotoxic to A549 epithelial cells but only at higher concentrations (Figure 5.2.18a). LysoPC (18:0) at 25 µM and 50 µM increased the percentage of cytotoxicity 29.28-fold (p=0.0015) and 41.42-fold (p=0.0001), respectively, compared to the control. Furthermore, caspase-3/7 release was quantified as an indicator of cellular apoptosis (Figure 5.2.18b). LysoPC (18:0) at 25 µM increased caspase release (RFU/g of protein) 1.48-fold (p=0.3446), compared to the control; however, this increase was not significant, and it can be suggested that the significant increase in cytotoxicity involves mechanisms of cell death other than apoptosis. Furthermore, 50 µM LysoPC (18:0) increased caspase release 1.95-fold (p=0.0298), indicating that apoptosis is at least partly involved in the cytotoxic effect.
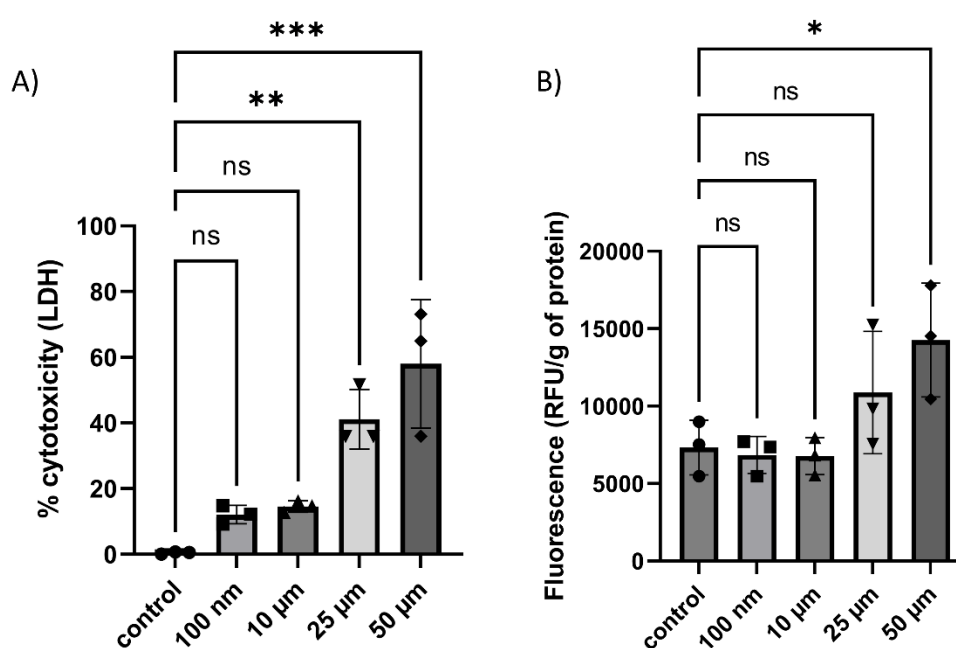
Figure 5.2.18 LDH and Caspase-3/7 release from treated A549 cell indicates cytotoxic effect and apoptosis activity.

A549 cells were exposed to LysoPC (18:0) at a range of concentrations for 72 h. a) LDH assay used A549 cells only and cells treated with 2% Triton-x as low and high LDH release controls, respectively. The percentage of cytotoxicity was calculated as %= (measured absorbance of sample-low control)/ (high control-low control) x100. b) The caspase-3/7 assay calculated enzyme activity by measuring relative fluorescence units (RFU) of activity normalised to protein in cell lysates. Data are shown as the mean of three biological replicates ± standard deviation (SD) (error bars). One-way ANOVA was performed across to compared metabolite exposure to cell only controls *$p<0.05$, **$p<0.01$, ***$p<0.001$, ****$p<0.0001$ versus the control condition (cells without molecules) was considered statistically significant.

This study also assessed whether LysoPC (18:0) had the potential to be to be pro-inflammatory to lung epithelial cells via the release of specifically selected cytokines. Figure 5.2.19 shows that exposing A549 cells to LysoPC (18:0) between 100 nM and 25 µM does not significantly increase the secretion of IL-6, IL-8 and TNF-α. However, 50 µM LysoPC (18:0) increases secretion of IL-6 12.90-fold ($p=0.0010$), IL-8 5.41-fold ($p=0.0056$) and TNF-α 21.42-fold ($p<0.0001$). Furthermore, IL-15 secretion was increased 21.88-fold ($p=0.0043$) and 30.15-fold ($p=0.0010$) after A549 exposure to 25 µM and 50 µM LysoPC (18:0), respectively, compared to the control. As IL-15 secretion was increased at a lower concentration, it can be suggested that LysoPC (18:0) has a specific immunomodulatory effect and that IL-15 activity is involved in LysoPC (18:0) induced inflammation.
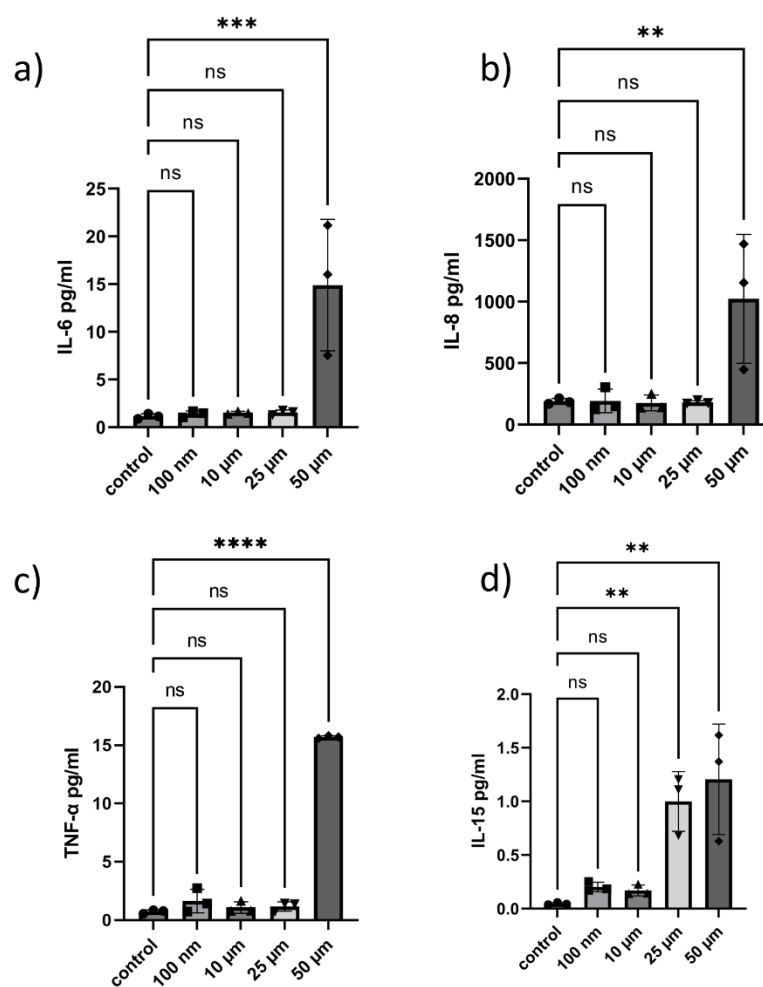
Figure 5.2.19 Cytokine release into cell supernatant after 72h exposure to LysoPC (18:0). A549 cells were stimulated with LysoPC (18:0) at a range of concentrations for 72 h before supernatants were collected. ELISA was used to quantify the release of a) IL-6 pg/ml, b) IL-8 pg/ml, c) TNF-α pg/ml and d) IL-15 pg/ml. Data is shown as the mean of 3 biological replicates ± standard deviation (SD). One-way ANOVA was performed for each molecule versus the control condition (cells without treatment). *$p<0.05$, **$p<0.01$, ***$p<0.001$, ****$p<0.0001$ is considered statistically significant.

After determining LysoPC (18:0) had a modulatory effect in lung epithelial cells, this study aimed to establish the effect on different immune cells. Immune cells were isolated from mouse spleens and stimulated with LysoPC (18:0) or a cytokine (IL-4 or IL-12+IL-18) as positive controls. Immune cells were gated and characterised as described in 8.1.17. Figure 5.2.20a shows that the percentage of NK cells B cells and macrophages positively expressing CD69, putative activation marker, is not significantly changed following stimulation with LysoPC (18:0) compared to the control. Stimulation with LysoPC (18:0) also did not significantly change the percentage of macrophages expressing MHCII or NK cells expressing IFN-γ and granzyme B. Figure 5.2.20b shows the MFI of specific immune cells positively expressing markers. The results indicate that stimulation

with LysoPC (18:0) does not significantly affect macrophage expression of MHCII or NK cell expression of granzyme B compared to the control. However, the results do show that the MFI of MHCII positive B cells increased 1.49-fold (p=0.0008) following LysoPC (18:0) stimulation, compared to the control.
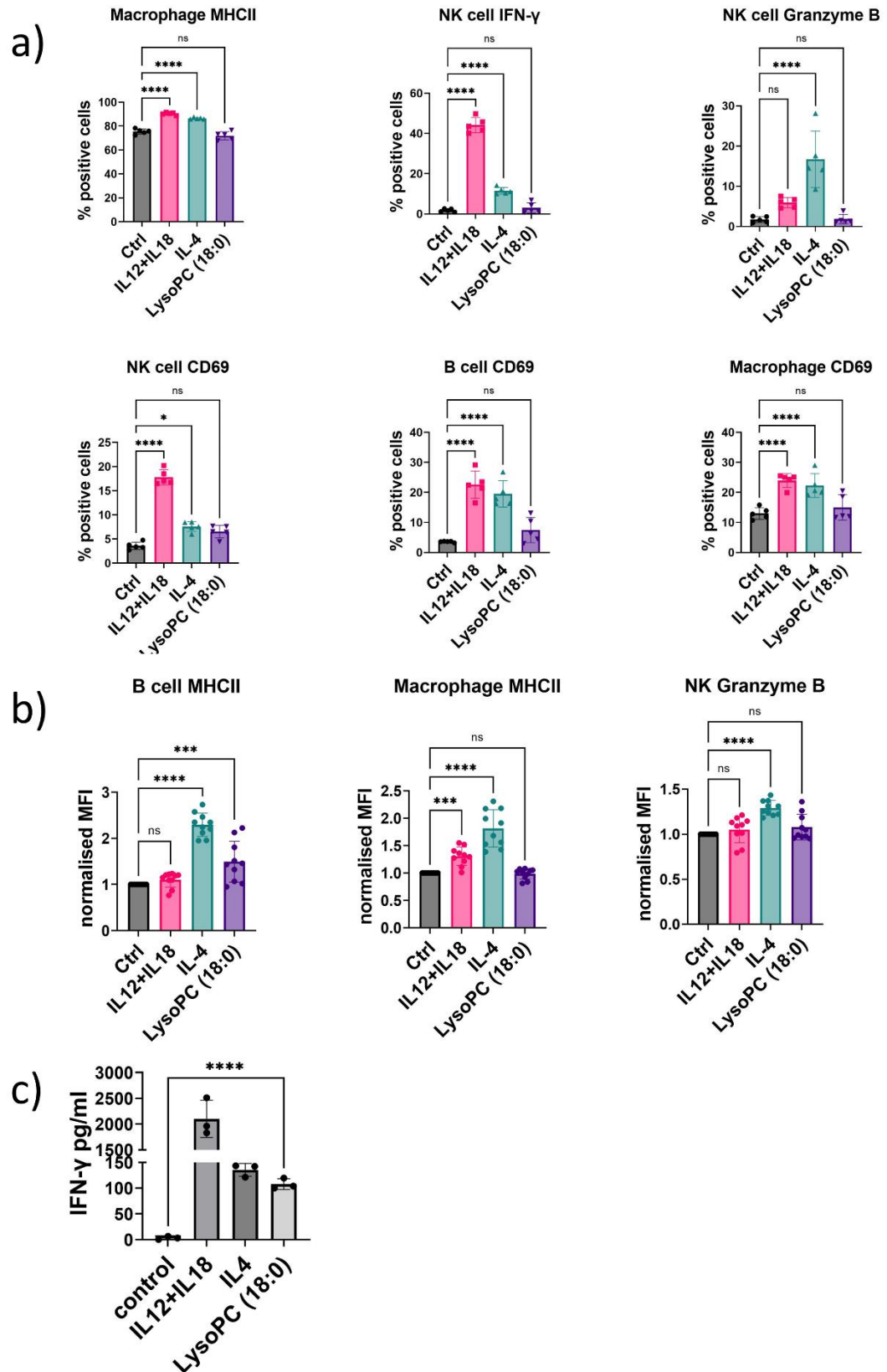
Figure 5.2.20 Flow cytometry and cytokine release analysis of splenic immune cells following stimulation with LysoPC (18:0). Immune cells were isolated from spleen tissue and stimulated with 50 µM LysoPC (18:0) as well as IL12+IL-18 and IL4 as positive immune activating controls. A) Percentage of immune cells (NK cells, B cells and macrophages) positively expressing specific markers (MHCII, IFN-γ, granzyme B and CD69). B) Mean fluorescence intensity (MFI) was normalised to control (no stimulation) and shows the relative amount of expressed marker within positive population. A-B) One-way ANOVA was performed to compare stimulation versus the

control condition (cells without treatment). C) ELISA was used to quantify the release of IFN-γ into immune cell supernatant and is shown as pg/ml. Unpaired T-test was performed to compared LysoPC (18:0) stimulated group to control and did not include positive controls (cytokine stimulations). Data is shown as the mean of 3 biological replicates ± standard deviation (SD). *p<0.05, **p<0.01, ***p<0.001, ****p<0.0001 is considered statistically significant.

Following flow cytometry analysis, this study aimed to quantify the release of specific cytokines into the supernatant. A proteome profiler mouse cytokine array (8.1.18) indicated that IFN-γ was increased in the cell supernatant compared to the control and was selected for quantification using ELISA. Figure 5.2.20c shows that IFN-γ release was increased 32.28-fold (*p<0.0001*) when cells were stimulated with LysoPC (18:0), compared to the control.

5.3 Discussion

The role of LysoPC(18:0) inflammation

PCA analysis showed that the metabolomic profile of the lung can be used to separate the naïve group from CIA group. The molecule *m/z* 562.3 identified as LysoPC (18:0) was significantly increased in the lung of CIA mice compared to control groups and may be a useful biomarker in lung complications associated with RA. LysoPCs are a class of lipid biomolecules derived by enzymatic cleavage of phosphatidylcholine (PC) by phospholipase A$_2$ (PLA$_2$) or by transferring fatty acids to free cholesterol via lecithin-cholesterol acyltransferase (LCAT)[766]. LysoPCs can be converted back to PCs by the intracellular enzyme lysophosphatidylcholine acyltransferase (LPCAT), which is found in numerous organs such as the lung, liver, and adipose tissue [767,768]. LPCAT has been shown to prefer LysoPC as a substrate over other lipids such as lysophosphatidic acid (LysoPA) and may play a critical role in regulating phospholipid biosynthesis [767,769]. However, LPCAT is unlikely to interact directly with extracellular circulating LysoPCs [768,770]. As this study shows an increase in LysoPC (18:0) without an observed increase in PC, it can be suggested that the molecule in the lung is extracellular and unavailable to LPCAT degradation [768-770]. The main biological function of PCs is to regulate the physical properties of the lipid bilayer in membranes, however, LysoPCs are distinct from their corresponding phospholipids and act as bioactive signalling molecules [771]. Furthermore, studies have shown that lipid metabolism alterations such as increased LysoPC (18:0) abundance in

the faeces of RA patients compared to healthy controls, participates in RA pathogenesis and severity [772,773]. LysoPCs have a broad spectrum of pro-inflammatory activities which has implicated them in the inflammatory injury of lungs and chronic diseases such as asthma [774,775]. Reports have indicated that different LysoPC species have varying levels of pro-inflammatory potential, and that LysoPC (16:0) and LysoPC (18:0) exert the strongest pro-inflammatory effect [774,776].

In particular, LysoPCs have been found to induce apoptosis by activating caspases, calcium influx, and mitochondrial pathways as well as increasing oxidative stress via the production of ROS [777]. Our study shows that LysoPC (18:0) was cytotoxic and increased caspase-3/7 release in A549 epithelial cells at the highest exposure concentration (50 µM) (Fig 5.3.18). Therefore, it can be suggested that LysoPC (18:0) may impair the lung epithelial barrier function in the CIA model due to increased levels of cell death [778]. LysoPCs can also increase the generation of cytokines such as IL-1ß, IL-8, IFN-γ, IL-6 and IL-5, resulting in the potent chemoattraction of inflammatory cells [779]. This study showed that the higher concentration of LysoPC (18:0) significantly increased the release of IL-6, IL-8, IL-15 and TNF-α from A549 cells (Fig 5.3.19). Therefore, it can be suggested that in the context of CIA, LysoPC (18:0) accumulation in the lung is likely to induce immune cell infiltration and inflammation via potent cell signalling [780]. In particular, LysoPCs have been shown to have a strong chemotactic effect on NK T cells, that is dependent on a signalling pathway mediated by G2A, a receptor widely expressed on the surface of lymphocytes [781]. LysoPCs can then alter the function of NK cells by inducing the expression of IFN-γ [782]. Our *in vitro* data showed that LysoPC (18:0) stimulation increased the secretion of IFN-γ, supporting current evidence (Fig 5.3.20c). Furthermore, IMC found that NKp46+ cells (NK T cells) were increased in the CIA lung compared to naïve controls; thus, it could be suggested that an increase in LysoPC (18:0) is resulting in the potent chemoattraction of NK T cells, dependent on IFN-γ signalling. Further investigation using flow cytometry analysis found that exposing immune cells to LysoPC (18:0) had no effect on the percentage of NK T cells expressing IFN-γ, Granzyme B or CD69; thus, it is likely that LysoPC (18:0) can attract NK T cells but does not affect function [781,782]. Furthermore, LysoPC species increase macrophage recruitment, enhance phagocytic function, induce the release of pro-

inflammatory cytokines, and promotes the M1 macrophage pathway [783,784]. IMC results showed that in the CIA lung, F480+, CD68+, CD11b+ cells (macrophages), were increased compared to naïve controls. However, our study showed LysoPC (18:0) had no effect on the percentage of macrophages expressing CD69 and MHCII; thus, the molecule may be able to promote recruitment but does not have an immunomodulatory effect in this context. IMC also found that CD3+, CD8+ cells (cytotoxic T cells), Ly6G+, CD11b + (neutrophils) and B220+, CD19+ (B cells) were increased in the lung of the CIA group compared to naïve controls. Our study also found that LysoPC (18:0) increased the relative expression of MHCII on positive B cells. MHCII molecules have been found to play a role in RA by interacting with CD4+ T-cells, resulting in the activation pro-inflammatory cytokines and autoantibodies, as previously described [700,701,785]. Therefore, it can be suggested that an increase in LysoPC (18:0) in the CIA lung will promote the recruitment of B cells and enhance their expression of MHCII, resulting in an inflammatory environment that can cause lung damage [783,785]. Thus, this study highlights a potential new molecular mechanism involved in RA associated lung complications.

Interplay between the gut microbiome and LysoPC

Studies have shown that butyrate producing bacteria are decreased in RA patients, whereas others such as *Fusobacterium nucleatum* are enriched in RA patients and positively associated with severity [786,787]. The microbiome analysis in this study showed that *Butyricicoccus* in reduced, whilst *Fusobacterium* is increased in the faeces of CIA mice compared to naïve controls; hence it is likely that the microbial and corresponding metabolite changes observed in the CIA model will be reflective of human RA [787,788]. In addition to LysoPCs being generated by PLA$_2$ cleavage and fatty acid transfer, Gram-negative bacteria produce apolipoprotein *N*-acyltransferase (Lnt) which can transfer a fatty acid moiety from PC to the LysoPC precursor [789,790]. Very few bacteria, such as *Pseudomonas aeruginosa* and *Borrelia burgdorferi,* can synthesise LysoPC, however many species such as *E. coli*, *Salmonella, Lactobacillus* and *Clostridia* can utilise host derived LysoPC [791]. Whilst the biological role of LysoPC in eukaryotes is known to involve immune cell signalling, the role in bacteria is still poorly understood [789,790]. However, studies have suggested the LysoPC regulates the activity of outer membrane proteins, acts as a signal to respond to osmotic challenges and is a nutritional resource to

remodel cell wall phospholipids [792,793]. Furthermore, environmental stress such as exposure to bile salts, acid and low oxygen conditions increases the amount of LysoPC in bacterial membranes, facilitating motility and survival [794,795]. This increase in LysoPC originating from the gut microbiota has been observed in IBD patients and may exacerbate colitis as it has been shown to impair tight junction proteins *in vitro* and *in vivo* [796]. Furthermore, LysoPC has bactericidal effects against Gram-positive bacteria by causing increased membrane permeability and can also have a more indirect antimicrobial effect towards Gram-negatives by inducing leakiness of bacterial membranes [797,798]. The analysis in this study indicates that specific Gram-positive bacteria such as *Roseburia* are reduced in the CIA group compared to the naïve group; thus, it can be speculated that CIA either causes or perpetuates an intestinal environment that supports the generation of LysoPC, which many be contributing towards bacterial dysbiosis [794,796,797]. Studies have also used Spearman correlation (does not assume specific distribution of data unlike Pearson correlation that assumes data follows a bivariate normal distribution) analysis to show that LysoPC (18:0) and other glycerophospholipid molecules such as PC (18:0) and PC [20:1(9Z)/0:0] are positively associated with *Alistipes* and *Lachnospiraceae*, and negatively correlated with *Blautia* [799]. *Blautia* spp are reduced in the faeces of RA patients and our study also found that *Blautia* was reduced in the CIA faecal microbiome compared to the naïve group [800]. Specific strains such as *Blautia coccoides* have been shown to improve the inflammatory state in patients with systemic lupus by promoting the production of immunosuppressive regulatory T cells [788]. Therefore, it can be suggested that the decrease in faecal *Blautia* in CIA mice, alters lipid metabolism in the host, resulting in an increase in pro-inflammatory LysoPC (18:0) and immunomodulation that contributes to RA and systemic inflammation [788,800]. As previously described, LysoPC can impair intestinal barrier function and it is possible that the molecule accumulated in the lung is not from an exogenous source [768,770,796]. Therefore, this study suggests that LysoPC (18:0) accumulation in the lung could be a result of increased bacterial generation in the intestine.

Metabolomic alterations in the lung

Molecules putatively identified as guanidine, fructoseglycine, dAMP, diglyceride (34:1), ceramide (t36:1) and creatinine citrate were decreased in the lung of CIA

mice compared to the control group. Guanidine is a decomposition product of the nucleobase guanine and is also proposedly generated by cells as part of the guanidine cycle [801,802]. However, guanidine is not considered a major cellular metabolite and no biological receptor in known to specifically recognise guanidine in humans [803]. More recently, studies have shown that guanidine is the natural ligand for the *ykkC* RNA motif in bacteria, which acts as a riboswitch to regulate genes encoding proteins such as urea carboxylases, arginases and creatininases[804,805]. These guanidine riboswitches also include genes for proteins that detoxify free guanidine via degradation and exportation [806,807]. Furthermore, bacteria may generate guanidine to use as an energy source when preferred sources such as glucose are in short supply [807]. Therefore, it can be suggested that bacterial dysbiosis in the CIA gut supports the generation of free and circulating guanidine, resulting in the activation of bacterial riboswitches and degradation of guanidine [804,805,807]. However, to our knowledge, the impact of this pathway in RA and lung diseases is unknown and warrants further investigation. In addition, Fructoseglycine is well-known biomarker that is increased during diabetes and is generated from mannitol, galactose, and glucose [808]. *E. coli* is able to breakdown the molecule using the enzymes fructoselysine-6-kinase and fructoselysine 6-phosphate deglycase into glucose-6-phosphate and lysine to be further processed via glycolysis and amino acid metabolism [809,810]. Therefore, it can be suggested that decreased levels of Fructoseglycine is associated with higher levels of bacterial degradation; thus, the metabolic profile in the lung might be linked to the gut microbiome. Fructoseglycine was also putatively identified and decreased in the kidney of CIA mice compared to naïve mice, hence the molecule might be a useful biomarker of systemic effects in RA. Moreover, patients with active RA show high levels of endogenous DNA damage which has been correlated with increased oxidative stress, defective DNA repair, and deregulated chromatin organisation [811]. DNA damage is increased in CD4+ T cells in RA patients, which has been linked to the insufficient production of mRNA transcripts and subsequent formation of the DNA repair kinase ataxia telangiectasia (AT) mutated (ATM) [812,813]. As dAMP is a nucleoside phosphate monomer, it is incorporated into DNA, allowing for the correct formation of the DNA template [814]. Therefore, dAMP can be used to study base interactions during DNA synthesis and DNA damage [815]. As this study found dAMP is reduced in the CIA lung compared to naïve controls, it can be suggested

the host cells including immune cells are undergoing DNA damage [812,815]. If untreated DNA damage can lead to apoptosis and a pro-inflammatory response in alveolar cells; thus, this mechanism may be involved in lung complications associated with RA [816,817].

Ceramides are a family of bioactive lipid molecules that are composed of sphingosine and a fatty acid [818]. Ceramides are essential precursors of all complex sphingolipids (SLs) which are localised in lipid bilayers to perform numerous structural functions and modulate the cellular response to stress [819]. Ceramides can be produced by the enzymatic hydrolysis of sphingomyelin by different sphingomyelinases, resulting in a variety of chemical structures with diverse pathophysiological functions [820,821]. Higher levels of circulating and accumulating ceramides have been associated with a variety of conditions such as atherosclerosis and type 2 diabetes due to a build-up of fatty deposits, stimulation of pro-apoptotic signals, and the generation of ROS [820,822]. Mouse models of RA have also implicated ceramides in the onset of disease as they induce apoptosis in rheumatoid synovial cells and are involved in the production of IL-1β and TNF-α as secondary lipid messengers that drive inflammation [823,824]. Therefore, studies are emerging that suggest the use of ceramides as therapeutic targets in RA and other conditions [819,821,823]. The gut microbiota has been shown to affect lipid metabolism and lipid levels in blood and tissues [825]. SLs can be derived from the host and gut bacteria of the phylum Bacteroidetes that constitutes genera including *Bacteroides* [826,827]. Bacteroidetes SLs are significantly decreased in the stool of IBD patients and are negatively correlated with gut inflammation, whilst host SLs are increased [828]. Studies have shown that reducing bacterial SLs in mice, increases the presence of macrophages which corresponds to an increase in MCP-1 secretion and provides an environment for inflammation [828,829]. In mouse models, *Bacteroides*-derived lipids transfer to host epithelial tissue and the portal vein, which affects host lipid metabolism [830,831]. This study found that *Bacteroides* are reduced in the CIA faecal microbiome compared to the control group; thus, it can be hypothesised that the ceramide found in the lung is a subunit of bacterial derived SLs, which is reduced due to bacterial dysbiosis. This altered lipid metabolism may result in recruitment of F480+, CD68+, CD11b+ cells (macrophages) into the CIA mouse lung, as previously described. Furthermore, studies have found that sphingomyelinases can also

activate the conversion of PCs to DGs [832]. As DG (34:1) was reduced in the lung of CIA mice alongside ceramide (t36:1), it can be suggested that the decrease is linked to impaired enzymatic activity and may have a negative impact on cellular function.

Creatinine is the end product of creatine metabolism in muscles and has been found to circulate in serum, followed by excretion in urine [833]. Creatinine can bind to citric acid to form creatinine citrate that is easily absorbed [834]. This study found that creatinine citrate was reduced in the lung and kidney of CIA mice, compared to the control group. Studies have suggested that a lower creatinine level in the kidney can be indicative of renal failure and that the citrate-to-creatinine ratio could be a marker in chronic kidney disease [835,836]. The exact link between low creatinine levels in serum and tissue and the onset of disease is unknown [835,836]. However, as creatinine production mostly occurs in muscles, studies suggest that a reduction is likely to be due to reduced muscle mass and poor nutritional state [837,838]. RA patients often experience changes in body composition, including reduced skeletal muscle mass and strength [839,840]. A study also found that treating RA patients with the drug Tofacitinib, an anti-inflammatory agent that blocks the action of Janus kinase enzymes resulting in reduced inflammatory cytokine cascade, increases serum creatinine levels [841,842]. The mechanism behind this increase is not fully understood; however, it can be suggested that creatinine levels and inflammation are linked [839-841]. Therefore, gaining a better understanding of reduced creatinine levels in the kidney and lung as well as other organs, in the context of RA, might highlight a useful intervention target. Two other molecules with the *m/z* 282.03 and 367.31 were found to be reduced in the CIA lung compared to naïve controls but could not be identified. These molecules may be unidentified due to a lack of available spectral libraries, especially for microbial metabolites [843,844]. These molecules might play an important role in immunomodulation and RA pathology. In particular, *m/z* 282.03 was also found in the kidney; thus, providing an identity and characterising phenotypic effect on cells could identify molecular mechanisms involved in RA associated systemic complications.

Hypoxic tissue environment role in RA

Glut1 is one of the most highly conserved and widely distributed glucose transporters [845,846]. Glut1 is strongly upregulated after innate and adaptive immune activation in a variety of inflammatory and autoimmune conditions, including RA [847]. Studies have shown that Glut1-dependent glycolysis is critical for parenchymal fibrosis in a bleomycin-induced lung injury model and inhibiting Glut1 significantly reduced lung inflammation [848]. Furthermore, during bacterial infection, Glut1-dependent glycolysis has been shown to activate absent in melanoma 2 (AIM2) inflammasome in the lung [849]. This results in the maturation and secretion of proinflammatory cytokines such as IL-18 and IL-1ß, exacerbating lung inflammation and injury [848,849]. Pulmonary atrial hypertension (PAH) patients also have upregulated Glut1 expression in the lung, which was linked to a dysregulated metabolic profile such as increased lipid accumulation [850,851]. Therefore, it was hypothesised that Glut1 would be upregulated in the lung of CIA mice and contribute to the development of lung injury. However, IMC data shows that the cellular marker, Glut1, was significantly reduced in the lung vessels of mice with CIA, compared to the control. As previously described, Glut1 is a marker of cell hypoxia which is a relevant feature in RA due to its involvement in synovial angiogenesis, apoptosis, oxidative damage, and cartilage degradation [848,852]. In the lung, short term hypoxia helps blood vessels constrict to direct blood to higher oxygen environments, which is turn helps deliver oxygen to tissues [853]. Therefore, it can be suggested that reduced hypoxia in the lung of CIA mice will result in poor blood oxygenation and impaired oxygen delivery to organs. This theory is supported as IMC revealed that Glut1 is increased in the liver vessels of CIA mice compared to the naïve group. Hence, it is likely that blood entering the liver from the lungs is less oxygenised, creating a hypoxic environment associated with the development of liver dysfunction [638,640]. Therefore, gaining a better understanding of LysoPC involvement in Glut1 regulation may provide a therapeutic intervention that protects RA patients from hypoxia induced organ damage [850,852,853].

Metabolomic changes in the liver

Moreover, in the liver of CIA mice the molecule putatively identified as triglyceride (TG) (54:7) was increased, compared to naïve mice. TG molecules represent the major form of storage and transport of fatty acids (FAs) within

cells and the liver is the central organ for fatty acid metabolism [854]. TGs are formed when three hydroxyl groups of a single glycerol molecule react with the carboxyl group of three fatty acids by forming ester bonds [855,856]. Despite the liver processing large quantities of FAs, only a small amount is stored as TGs in the form of cytoplasmic lipid droplets [857]. During chronic liver diseases such as NAFLD, TGs are accumulated to an excess extent in the liver and have been implicated as drivers of inflammation and steatosis; however, their specific contribution to disease is unclear [856,857]. Furthermore, RA patients have been reported to have changes in plasma lipid levels and increased TGs in synovial joints [858]. Therefore, the TG molecule increased in the liver of CIA mice might indicate a potential mechanism of systemic complications associated with RA. Furthermore, the molecule putatively identified as 1-MNA was decreased in the CIA liver compared to naïve controls. As previously described, 1-MNA is increased in the cirrhotic liver as a hepatoprotective mechanism to induce suppression of pro-inflammatory cytokines such as IL-4 and TNF-α [620,622]. Endogenous 1-MNA has also been found to modulate the cyclooxygenase-2/prostacyclin pathway to reduce thrombotic events, decrease mitochondrial ROS and support recovery during microbial infection [859,860]. Therefore, a reduction in the liver may lead to an environment that is supportive of inflammation. Furthermore, 1-MNA can be metabolised in the liver by aldehyde oxidase (AOX) to pyridones which results in the production of hydrogen peroxide, leading to oxidative stress, followed by IL-1β production and cell death [860,861]. Therefore, this study can suggest that a decrease in 1-MNA can be attributed to higher levels of metabolism in the liver, resulting in tissue damage. However, the IMC data shows that CC3+ cells (apoptotic cells) were reduced in the CIA liver, compared to naïve mice which suggests potential generation of ROS is not inducing apoptosis. A study has shown that 1-MNA reduced pyroptosis in macrophages by reducing IL-1β release and inhibiting NLRP3 inflammasome activity [861]. Pyroptosis is a form of inflammatory programmed cell death that is activated by caspase-1, caspase-4, and caspase 5, which elicits a proinflammatory effect to control pathogenic infection [862]. Furthermore, studies have found that mitochondrial ROS promotes pyroptosis in macrophages [862]. Therefore, it can be suggested that NKp46+ cells (NK cells), NKp46+ and Granzyme B+ cells (activated NK cells) and F480+ and MHCII+ cells (M1 macrophages) are being recruited to the liver and undergo pyroptosis due to 1-MNA reduction and metabolism. This immunodeficiency can

leave the liver susceptible to infection and has been associated with higher rates of mortality in liver diseases such as cirrhosis [862,863]. Hence, the 1-MNA pathway might provide a useful intervention target for the treatment of liver complications and immune dysfunction associated with RA [864].

In the spleen, unsupervised PCA analysis was able to show slight separation between CIA and naïve groups which suggests there are metabolic differences. Fifteen molecules were decreased in the spleen of CIA mice compared to the naïve group and may be useful biomarkers of RA associated spleen complications. In particular, the molecule m/z 295.2264 was putatively identified as 9,10-EOA or 12,13-EpOME, both of which are produced via COX and LOX enzymatic hydrolysis of linoleic acid [865]. These molecules exist in PMNs and possess strong anti-inflammatory properties; thus, a decrease in the spleen might lead to dysregulated immune function [866]. In addition to enzymatic production, EpOMEs can be further hydrolysed to DiHOMEs by bacteria, which have been shown to decrease the recruitment of dendritic and T_{reg} cells as well as impair function [865,867]. Therefore, it can be suggested that RA associated dysbiosis in this study supports the conversion of EpOME into DiHOME, indicated by low EpOME levels in the spleen, which in turn may encourage a proinflammatory response. Hence, confirmation of identity might highlight a mechanism of RA induced spleen injury. Furthermore, the molecule with m/z 806.4980 was the only molecule to be increased in the CIA mouse spleen compared to naïve controls and was putatively identified as phosphatidylserine (PS) (20:2(11Z,14Z)/18:4(6Z,9Z,12Z,15Z)). PS are minor membrane phospholipids that become externalised to the outer membrane when exposed to specific stimuli [868]. Furthermore, studies have found that apoptotic cells use PS as a surface lipid signal to encourage clearance via phagocytosis [869]. Phagocytotic cells that bind PS, have also been shown to have increased release of anti-inflammatory cytokines such as IL-10, as well as decreased release of proinflammatory cytokines including TNF-α and IL-1β [870]. PS has also been shown to induce phenotypic changes in dendritic cells and macrophages and can inhibit T-cell activation [870,871]. Thus, PS plays an important role in immune suppression to maintain homeostasis [871,872]. Therefore, this study suggests that an increase in PS in the spleen indicates that cells are undergoing apoptosis and signalling an immunosuppressive effect in response to RA[869,873].

In conclusion, this chapter shows that DESI MSI can be employed to discover molecules derived by the host and microbiome that could play a role in the onset and progression of RA associated systemic complications. The study revealed molecules, such as LysoPCs (18:0), have immunomodulatory effects and have the potential to perpetuate inflammation in the lung of CIA mice. Furthermore, the study shows that specific metabolites are also altered in the liver, spleen and kidney of the disease model compared to controls. Some of these molecules may contribute to the inflammatory process or be a biomarker of disease activity and may be new targets for therapeutic intervention. Lastly, some molecules such as fructoseglycine and creatinine citrate were found to be increased in the in the lung and kidney of CIA mice compared to naïve mice and may be useful therapeutic targets to treat or diagnose multiple systemic complication.

Chapter 6 Microbial metabolites associated with immunomodulation and host physiology

6.1 Introduction

6.1.1 Development of the gut microbiota

The human microbiota outnumbers host cells by at least a factor of ten and expresses approximately 10-fold more genes [874]. The complex community of microbes that colonise human hosts yield a huge capacity for enzymatic functionality which plays a fundamental role in host physiology [875]. In particular, microbial colonisation of the intestinal tract is essential for the maturation of the gut and immune system, digestion, and physical protection from pathogenic infection [875,876]. This colonisation begins at birth, or even prior, and the maternal vaginal, gut and skin microbiomes provide important bacterial inocula [876]. The gut microbiome in newborns has an uneven bacterial community, often transiently dominated by *Enterobacteriaceae* which is eventually outcompeted by *Bifidobacterium* and lactic acid bacteria before weaning [877]. The gut microbiota undergoes continuous compositional changes until children reach between 2 and 3 years of age [875,878]. By the age of 5, the gut microbiome reaches a sufficient level of diversity which is maintained into adulthood and is represented broadly by bacteria of the genera *Bacteroides*, *Prevotella*, *Ruminococcus* and *Clostridium* [877,879]. This diversity is heavily influenced by environmental factors such as birth weight, gestational age, diet, and antibiotic use [878,880]. As well as composition, the functionality of the early microbiota changes due to environmental conditions [879,881]. For example, before weaning the microbiota is enriched with bacteria that encode genes for lactate utilisation, whereas the introduction of solid food promotes the growth of bacteria enriched in genes that allow the utilisation of carbohydrates, vitamin synthesis and xenobiotic degradation [882]. Hence, a healthy and diverse gut microbiota has a myriad of positive functions.

6.1.2 The gut microbiota and the innate immune system

Alterations in intestinal microbiota during early infancy have been shown to increase the risk of childhood obesity, type 1 diabetes, NAFLD and autoimmune

conditions [883,884]. The link between a dysfunctional microbiota and the development of disease involves regulation of the immune system [885]. The mucosal surface of the intestine is comprised of innate immune cells and epithelial cells that encode receptor molecules for ligands of microbial origin such as LPS, flagellin and peptidoglycan [885,886]. Moreover, polysaccharide A (PSA) is produced by the commensal *Bacteriodes fragilis* and is recognised by the TLRs, TLR2/TLR1 heterodimer, leading to the activation of the phosphoinositide 3-kinase (PI3K) pathway, which in turn causes the expression of anti-inflammatory genes [887]. Furthermore, MyD88 is an adapter for multiple innate immune receptors that recognise microbial signals and effector molecules such as IL-1 and IL-18 [888]. MyD88 controls the expression of intestinal epithelial cells (IEC) secreted antimicrobial peptides, which restricts the growth of surface-associated gram-positive bacteria; thus, mice deficient in MyD88 display an altered gut microbiota composition [888,889]. After encountering a microbial signal, MyD88 has also been shown stimulate the production of the antibody IgA to protect the mucosal tissue for microbial invasion [889,890]. Furthermore, the commensal bacillus, *Clostridium butyricum*, has been shown to induce IL-10 producing macrophages that suppressed acute inflammation in experimental murine models [891]. Studies have also indicated that microbially derived molecules such as butyrate can drive monocyte-to-macrophage differentiation whilst others such as TMAO can drive macrophage polarisation in an NOD-like receptor family, pyrin domain containing 3 (NLRP3) inflammasome-dependent manner [889,892]. Therefore, it is clear that the microbiome and immune cells interact via receptors and molecular signals to maintain homeostasis.

6.1.3 The gut microbiota and the adaptive immune system

When innate immune cells encounter microbially derived ligands, cytokines are secreted to signal the differentiation of naïve T cells of the adaptive immune response into Tregs or different Th cells such as Th1, Th2 and Th17 [893]. Treg cells can be anti-inflammatory as they suppress the activation of mast cells, basophils, and eosinophils, whereas Th cells can direct and amplify inflammatory responses [893,894]. Therefore, the regulation and balance of T cells has been described as a critical factor for immune homeostasis and can prevent the development of inflammatory, autoimmune, and allergic diseases [895]. Studies have shown that a crosstalk between gut microbiota and the immune system is

essential for the generation of Tregs as mice lacking a microbiome have reduced levels [896]. Furthermore, the addition of specific bacteria such as *Lactobacillus*, *Bacteroides* and *Clostridium* can induce Treg differentiation *in vitro,* whereas *Bifidobacterium adolescentis* has been shown to induce the development of Th17 cells [897,898]. Th17 cells can strengthen the mucosal barrier and encourage IECs to produce antimicrobial peptides, ensuring local homeostasis in maintained [899]. These findings demonstrate how different commensal microbes can induce naïve T cell differentiation, resulting in a T cell population with diverse roles in immunity [896,897]. Additionally, DCs exposed to bacterial antigens can prime and activate T cells [900]. The CD40 ligand in activated T-cells can then stimulate the differentiation of naïve B cells into IgA$^+$ B cells, resulting in the production of large quantities of IgA [900,901]. As previously described, IgA plays an important role in shaping the gut microbial communities and protects against infection [890,901]. Therefore, the gut microbiome is required for innate and adaptive immune cell priming and activation, which in turn tightly controls microbial communities and maintains host physiology.

6.1.4 Microbiome associated gastrointestinal and systemic diseases

Previous chapters have highlighted the role that microbes and their metabolites play in IBD. This has been evidenced as germ-free and antibiotic treated animals have significant attenuation of colitis [902]. Moreover, IBD patients have lower biodiversity, particularly SCFA producers; thus, disease onset and progression has been linked to bacterial dysbiosis [903]. However, the gut microbiome does not only affect the intestine and has been shown to influence the immune status and function of distal organs [904]. The intestinal mucus barrier physically separates the microbiota from the epithelium, providing protection against an overactive inflammatory response [905,906]. Below the mucus layer, the gut barrier is formed of a monolayer of IEC which act to protect the gut from insult [907]. When the epithelium is breached by bacteria, they can enter the lamina propria and occasionally reach the mesenteric lymph nodes [906,908]. However, it is difficult for bacteria to disseminate systemically due to the existence of the gut vascular barrier (GVB) which prevents bacteria entering the portal circulation [909]. Therefore, the majority of microbes interact with the host in an indirect manner mediated by their metabolic products that can cross barriers [906,910]. In particular,

gut derived metabolites such as SCFAs, amino acids, and BAs can directly affect hepatic glucose and lipid metabolism [911]. This is because microbial metabolites are involved in the regulation of pathways related to lipid absorption, synthesis, and clearance [912]. Therefore, it is not surprising that depletion of the gut microbiota can result in dysfunctional hepatic lipid accumulation which in turn can impair organ function [911,912]. Hence, gut-liver communication mediated by microbial metabolites has been implicated in various liver diseases such as gallstones and NAFLD[913,914]. The dissemination of microbial metabolites might also affect the function and immune profile in other organs such as spleen, kidney, and lung. Therefore, this study aims to identify microbial molecules that are able to be systemically disseminated and evaluate their role in immune cell function.

6.1.5 Germ free and specific pathogen free mouse models to investigate importance of intestinal microbiome

Germ-free (GF) animal models are commonly used to study the effect a depleted microbiota has on host physiology, including organ function, cellular composition, and communication [915]. GF mice are bred in isolators to fully impair exposure to environmental microorganisms, keeping them free of detectable bacteria and viruses throughout their life [916]. Another model used to study microbe-host interactions is specific pathogen-free (SPF) mice that are free from known pathogens that can cause infection but are still colonised with commensal bacteria [917]. GF mice can be compared to SPF controls and have been found to have anatomical and physiological differences [918]. For example, GF mice have enlarged cecum's, underdeveloped small intestines with irregular villi and reduced IEC renewal compared to SPF counterparts [919,920]. These differences mean GF mice are less able to utilise nutrients obtained in the diet, hence weigh less compared to SPF mice [917,918]. Moreover, GF animals have been found to live longer and develop cancer less frequently but are more susceptible to infections than SPF mice [921]. The increase in susceptibility to infection is likely to be due to the role microbes play in priming and maturation of the immune system as previously described [903,908,910]. Studies have found distinct metabolic differences in the intestine of GF mice compared to SPF mice, suggesting the microbiome does cause distinct shifts to the host metabolome [922]. As previously described, metabolites play an important role in immune cell function, inflammation, and

cell signalling (Table 6.1. Microbial molecules discussed in chapter 1); thus, identifying metabolites that are altered due to microbial colonisation and evaluating their role in cell function might elucidate mechanisms involved in microbe-host mediate physiology [922,923]. Therefore, this chapter will use MSI and IMC to investigate the interactions between microbes and the host by identifying metabolomic and cellular differences between GF and SPF mice. Molecules that are altered and identified using MSMS will then be further characterised using *in vitro* assays to gain a better understanding of their role in health and disease.

Table 6.1 List of microbial metabolites details in Chapter 1 as a highlight summary

Microbial Metabolite	Molecular Function
Bile Acids	Regulation of lipid absorption and metabolism, modulation of gut microbiota, signaling molecules for host-microbe crosstalk
Short-Chain Fatty Acids (SCFA)	Energy source for colonocytes, regulation of gut barrier function, modulation of immune responses, anti-inflammatory effects
Tryptophan Metabolites	Precursors for neurotransmitters (e.g., serotonin, melatonin), modulation of immune responses, regulation of gut barrier function, influences mood and behaviour
Trimethylamine (TMA)	Precursor for trimethylamine N-oxide (TMAO), involved in host lipid metabolism, potential link to cardiovascular disease risk

6.2 Results

6.2.1 Metabolic and cellular alterations in the ileum associated with the microbiome

MSI was used to investigate the molecular changes in the ileum of SPF mice compared to GF mice. ROC analysis found one peak could discriminate between the two groups and had the *m/z* 160.1333 (Figure 6.3.1). This molecule was increased 14.73-fold (*p*<0.0001) in the SPF ileum, compared to the GF ileum. The molecule was putatively identified as 5-AVAB using the HMDB; however, MSMS was not able to accurately confirm this identity.
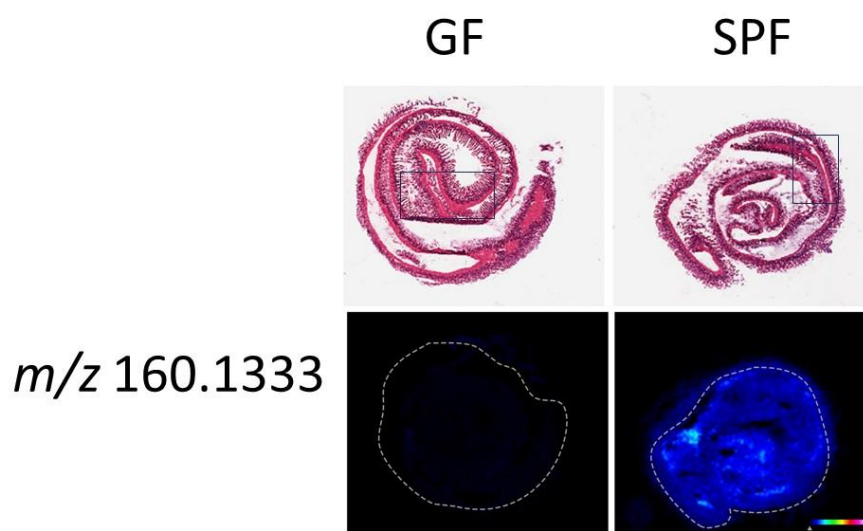
Figure 6.2.1 MSI image of m/z 160.1333 abundance in the ileum.
From top to bottom: haematoxylin and eosin (H&E)-stained sections with rectangular boxes indicating region selected for IMC, MSI heatmap of *m/z* 160.1333 (colour bar shows 0% to 100% relative abundance).

IMC was performed on tissue regions indicated by blue rectangular boxes in Figure 6.2.1. This technique revealed changes in structural and immune protein markers, at a 1 μM spatial resolution. A DNA intercalator was a generic marker used to determine the tissue organisation by highlighting the size and shape of the nucleus in individual cells. Random forest machine learning tissue classifier module segmented the ileum into mucosa and muscularis regions based on morphology and structure. In the mucosa, the percentage of ATPase^{+} cells decreased 1.07-fold (p=0.0256) in SPF mice, compared to GF mice. Whereas the percentage of Ki67^{+} expressing cells increased 1.21-fold (p=0.0394) in SPF mice,

compared to GF mice. Furthermore, F4/80$^+$ and CD163$^+$ cells are described as having a phenotype indicative of M2c macrophages, a subgroup of M2 macrophages. IMC results show that in the mucosa M2c macrophages are decreased 2.67-fold (p=0.0453) in SPF mice, compared to GF mice. In the muscularis, Pan-CK$^+$ and granzyme B$^+$ expressing cells are increased 6.09-fold (p=0.0297) and 9.78-fold (p=0.0400) in SPF mice, compared to GF mice. Whereas pAKT$^+$ expressing cells were decreased 4.31-fold (p=0.0477) in SPF mice, compared to GF mice. IMC analysis did not indicate significant changes in specific cell phenotypes in the muscularis between the two groups. Therefore, the addition of a gut microbiome results in immunomodulation in the ileal mucosa and muscularis.

A)

GF   SPF   DNA

mucosa: ATPase

mucosa: Ki67

muscularis: Pan-CK

muscularis: GranzymeB
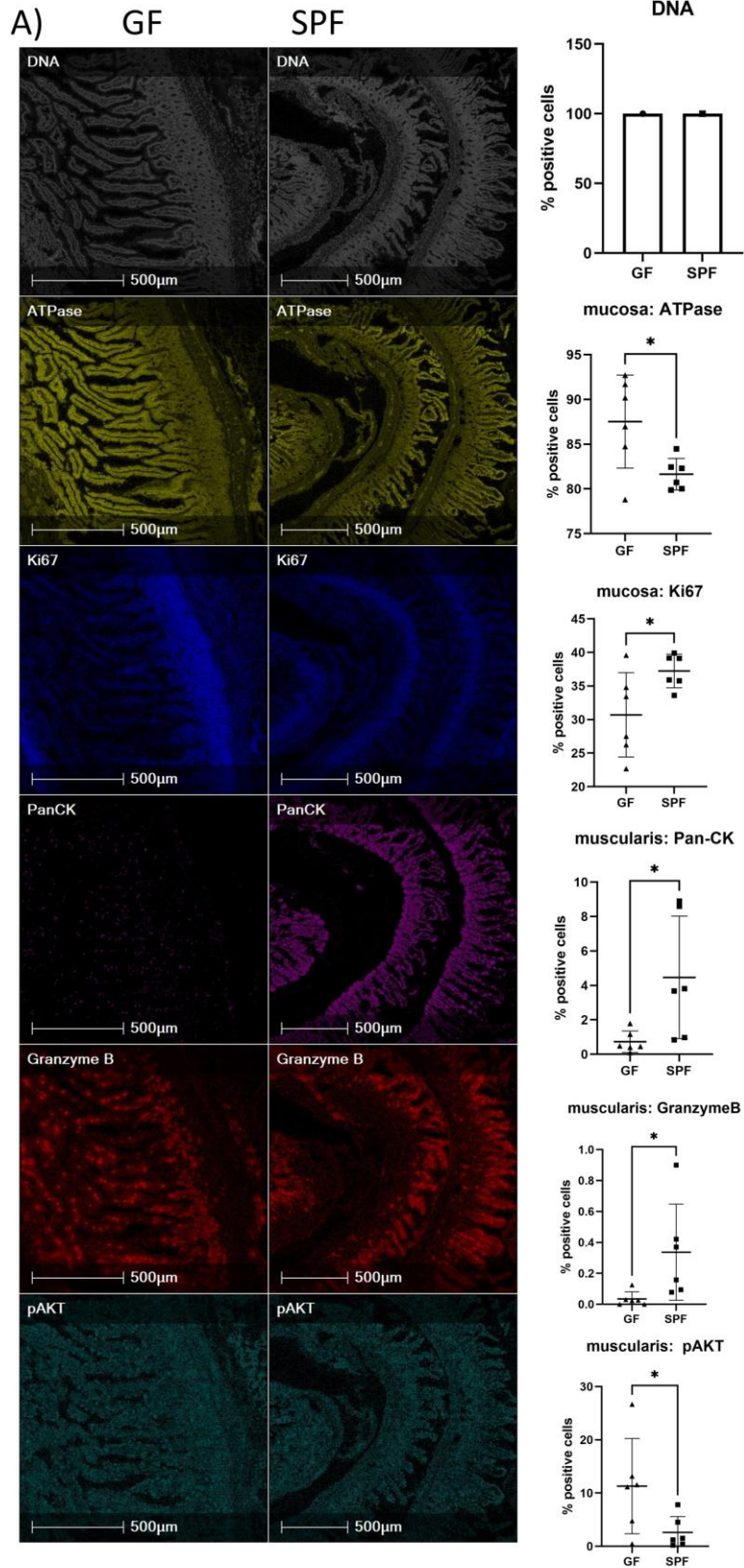
muscularis: pAKT

B)   M2c Macrophages
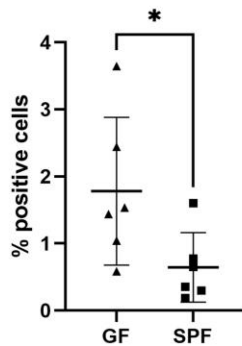
Figure 6.2.2 Representative IMC images of biological markers of cell function in the ilea mucosa and muscularis
Images shown are the region indicated in Figure 6.2.1 for GF and SPF groups. A) From top to bottom, DNA intercalator identified single cells within the tissue section, ATPase, Ki67, Pan-CK, granzyme B and pAKT. B) Bar graph showing the percentage of cells with a phenotype indicative of M2c macrophages. Percentage positive cells represented as bar graph showing four or five biological replicates. T-test performed to compare groups and *p<0.05, **p<0.01, ***p<0.001, ****p<0.0001 was considered statistically significant.

6.2.2 Metabolic and cellular alterations in the colon associated with the microbiome

MSI was also used to investigate the molecular changes in the colon of SPF mice compared to GF mice. ROC analysis identified 17 peaks could potentially discriminate between the two groups. The variation in the 17 metabolites detected were analysed to examine the clustering of groups using multivariate statistical analysis including PCA (M1) and PLS-DA (M2). PCA score plots of the first (t [1]) principal component did show clear separation in the colon between GF and SPF mice (parameters: R2X=0.67, Q2=0.563) (Figure 6.2.3). PLS-DA score plot (M2) was also able to separate the groups based on the colonic metabolomic profile (parameters: R2X=0.67, R2Y=0.975, Q2=0.959). Corresponding loadings plots show which metabolites might contribute to group separation.
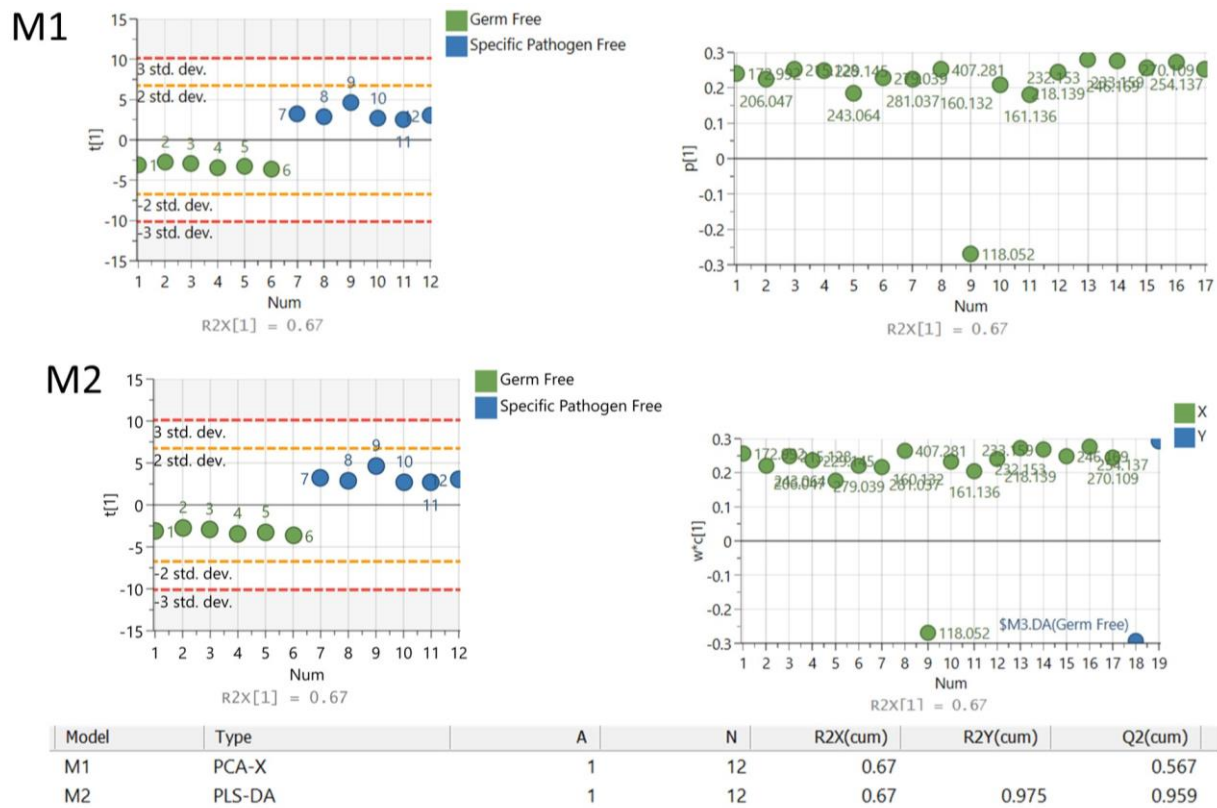
Figure 6.2.3 Unsupervised and supervised discriminant analysis.
M1) Unsupervised PCA analysis was able to discriminate between the groups using metabolite features found in the colon. M2) Supervised PLS-DA analysis also shows that the molecules in the colon can discriminate between groups (GF, green circles; SPF, blue circles). Analysis was performed using SIMCA 17 software. PLS-DA and PCA score plots consist of component 1 (t [1]).

Univariate analysis (T-test) performed indicated that 9 molecules out of the 17 were significantly changed between the groups (Figure 6.2.4). The molecules with the following m/z were increased in the colon of SPF mice compared to GF, and putatively identified using the HMDB; 172.9915 (280.85-fold, p=0.000373, phenol sulphate), 206.0493 (6.05-fold, p=0.0062, 4-(2-aminophenyl)-2,4-dioxobutanoic acid), 215.1283 (1.62-fold, p=0.000929, unidentified), 229.1445 (1.74-fold, p=0.002363, dodecanedioic acid), 243.0623 (1.58-fold, p=0.041662, pseudouridine), 279.0391 (2.03-fold, p=0.007065, uridine), 281.0359 (2.09-fold, p=0.008065, unidentified) and 407.2806 (22.42-fold, p=0.000179, cholic acid). The molecule m/z 118.0513 was also putatively identified as L-threonine and was decreased 3.03-fold (p=0.000061) in the colon of SPF compared to GF mice. This study attempted to perform pathway analysis using putative identities; however, enrichment was not significant (data not shown).
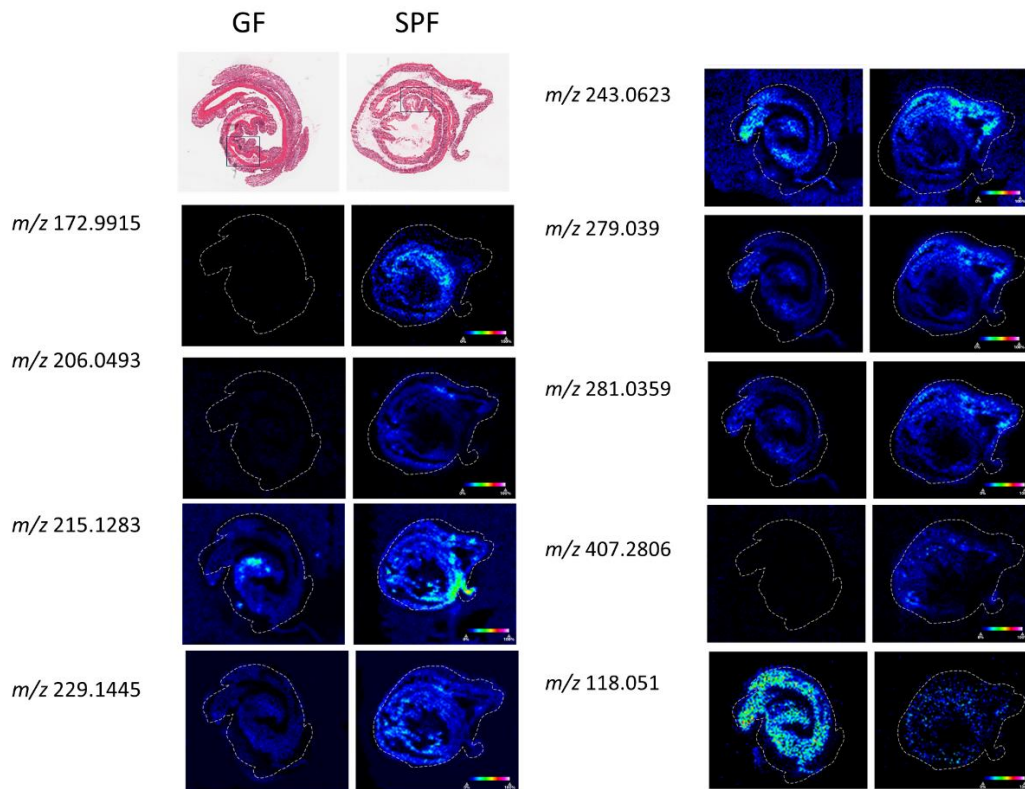
Figure 6.2.4 MSI image of m/z 172.9, 206.0, 215.1, 229.1, 243.0, 279.0, 281.0, 407.2, 118.5 abundance in the colon
From top to bottom: haematoxylin and eosin (H&E)-stained sections with rectangular boxes indicating region selected for IMC, MSI heatmap of *m/z* molecules (colour bar shows 0% to 100% relative abundance).

In the mucosa (Figure 6.2.5), the percentage of CD11b$^+$ and F480$^+$ expressing cells were increased 1.87-fold (p=0.0071) and 1.71-fold (*p*=0.0179), respectively, in SPF mice, compared to GF mice. Whereas E-cadherin$^+$ expressing cells were decreased 1.39-fold (*p*=0.0330) in SPF mice, compared to GF mice. Cells expressing both F480 and MHCII markers are phenotypically similar to M1 macrophages, whereas cells expressing Ly6G and CD11b markers are phenotypically similar to neutrophils. This study found, in the colonic mucosa, the percentage of positive cells with an M1 macrophage and neutrophil phenotype increased 1.95-fold (*p*=0.0496) and 4.15-fold (*p*=0.0095) in SPF mice compared to GF mice. This study did not find any significantly changed cell markers or phenotypes in the colonic muscularis, between GF and SPF mice. Therefore, the addition of a microbiome increases inflammatory cell populations and modifications to concentrations of several metabolites, suggesting an interplay between these two populations.

A) GF   SPF   DNA

DNA   DNA

CD11b   CD11b   mucosa: CD11b

F480   F480   mucosa: F480

E cadherin   E cadherin   mucosa: E Cadherin

B) M1 Macrophages   Neutrophils

Figure 6.2.5 Representative IMC images of biological markers of cell function in the colonic mucosa and muscularis.
Images shown are the region indicated in Fig 6.3.4 for GF and SPF groups. A) From top to bottom, DNA intercalator identified single cells within the tissue section, CD11b, F480 and E cadherin. B) Bar graph showing the percentage of cells with a phenotype indicative of M1 macrophages and neutrophils. Percentage positive cells represented as bar graph showing six biological replicates. T-test performed to compare groups and *$p<0.05$, **$p<0.01$, ***$p<0.001$, ****$p<0.0001$ was considered statistically significant.

6.2.3 Metabolic alterations in the liver associated with the microbiome

In the liver, ROC analysis found 711 peaks that could potentially discriminate between GF and SPF groups. Variation in the 711 molecules detected were analysed to examine the clustering of groups using multivariate statistical analysis including PCA (M1) and PLS-DA (M2). PCA score plots did show distinct clear separation in the liver (parameters: R2X=0.73, Q2=0.654) (Figure 6.2.6). PLS-DA score plot (M2) was also able to separate the groups using the first principle component (parameters: R2X=0.729, R2Y=0.918, Q2=0.897). Specific molecules are not labelled in the corresponding loadings plots due to the large number identified; however, molecules with a VIP>1 are listed in 8.1.31. Molecules with a VIP>1 were selected for univariate analysis (ANOVA) and 255 molecules were found to be significantly changed between GF and SPF groups. Out of 250 molecules, 159 molecules (63.6%) were assigned putative identities based on the HMDB. Heatmap in Figure 6.2.7 shows the molecules increased or decreased in the liver using negative mode DESI-MSI (identities listed in 8.1.29). The heatmap in Figure 6.2.8a shows molecules increased or decreased in the liver using positive mode DESI-MSI, and Figure 6.2.8b shows the lipids found to be changed in the liver (identities listed in 8.1.30). Out of the 250 molecules, none were found to be similarly changed in the ileum; however, *m/z* 172.9915 putatively identified as phenol sulphate was increased in the both the colon and liver of SPF, compared to GF mice. Therefore, it can be concluded that molecular differences in the liver do not directly come for the intestine but do involve microbial metabolism.

Model	Type	A	N	R2X(cum)	R2Y(cum)	Q2(cum)
M1	PCA-X	1	11	0.73		0.654
M2	PLS-DA	1	11	0.729	0.918	0.897
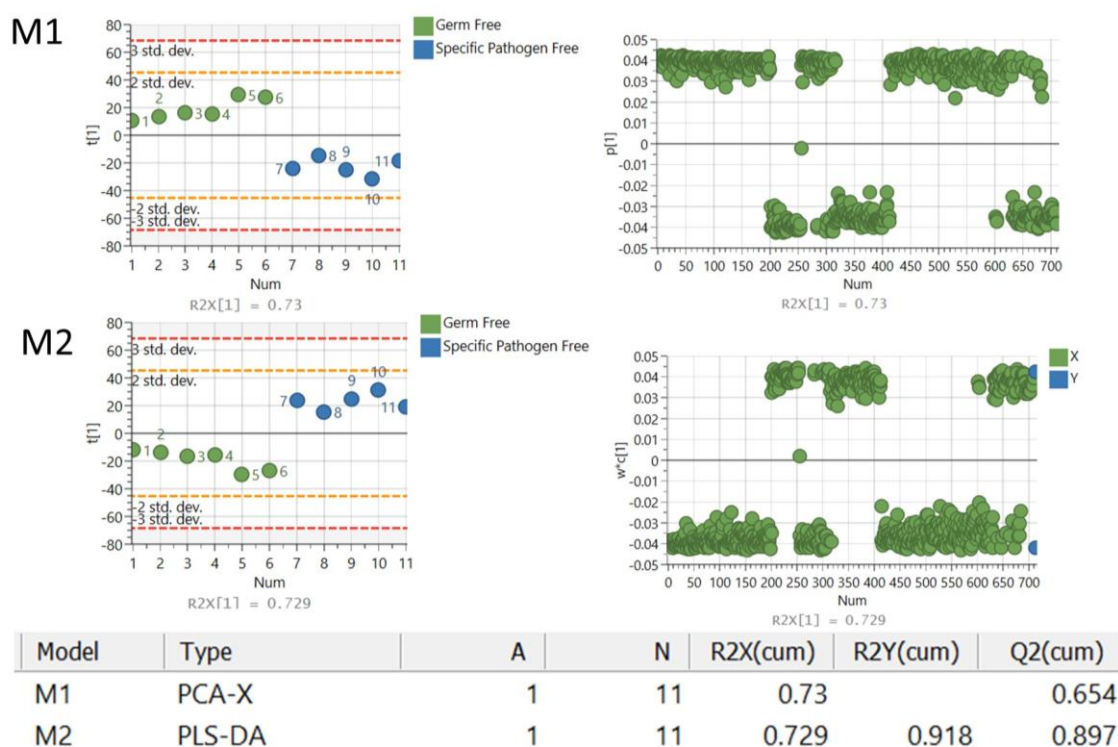
Figure 6.2.6 Unsupervised and supervised discriminant analysis.
M1) Unsupervised PCA analysis was able to discriminate between the groups using metabolite features found in the liver. M2) Supervised PLS-DA analysis also shows that the molecules in the liver can discriminate between groups (GF, green circles; SPF, blue circles). Analysis was performed using SIMCA 17 software. PLS-DA and PCA score plots consist of component 1 (t [1]).
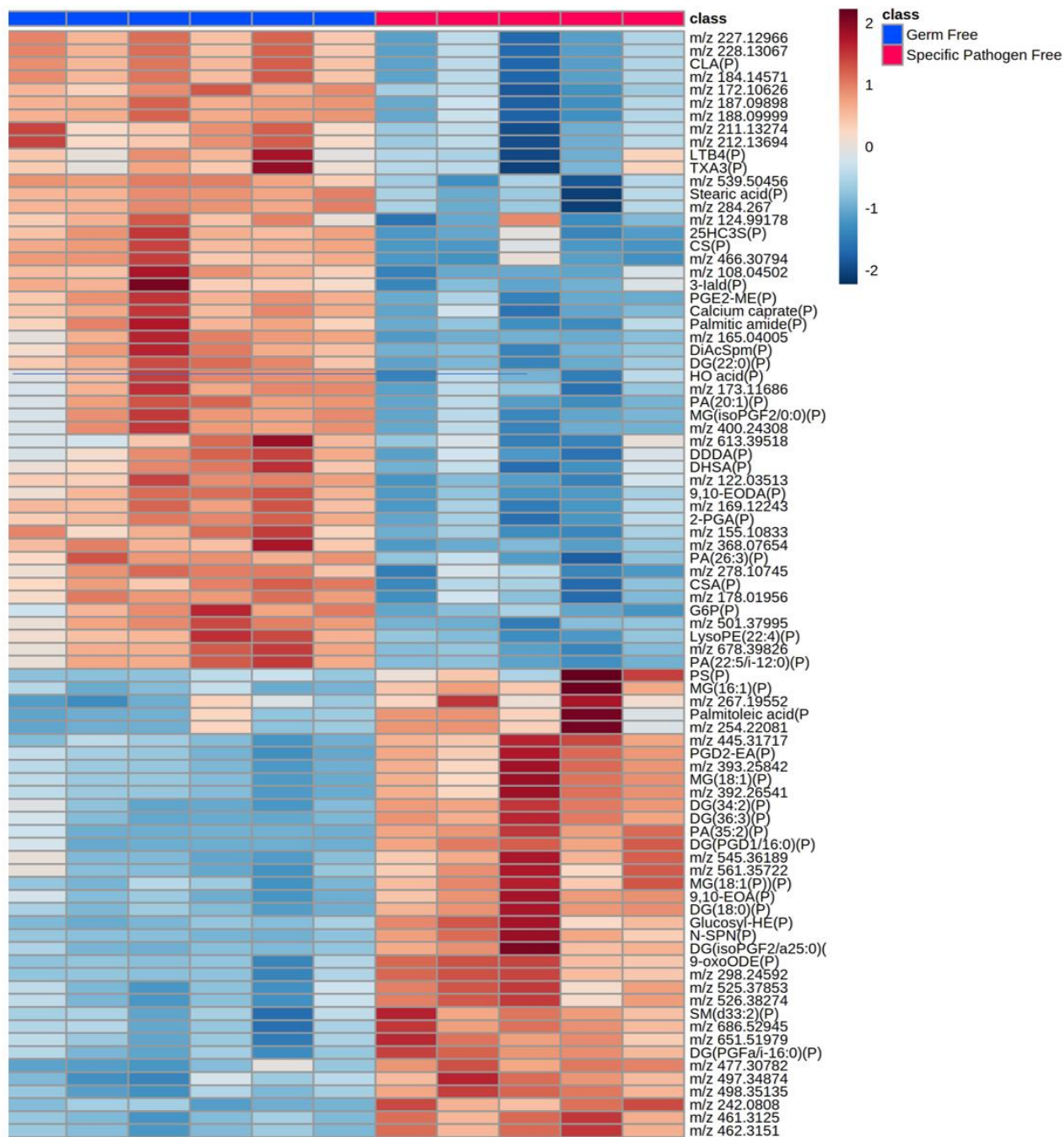
Figure 6.2.7 Heatmap of increased and decreased molecules in liver of GF and SPF mice using negative mode MSI.
Heatmap shows *m/z* of molecules unable to be identified, putatively identified molecules (marked with a P) and molecules with an MSMS confirmed identification. Heatmap was created using Metaboanalyst 5.0. The colour of each sample is proportional to the significance of change in metabolite abundance indicated by the colour bar (red, increased; blue, decreased). Rows correspond to metabolites and columns correspond to samples from individual mice (GF, blue, SPF, red).

A)

	class
	m/z 104.13534
	m/z 549.35466
	m/z 550.35928
	m/z 533.38071
	m/z 534.38533
	3-11oxo-12UO(P)
	m/z 505.35134
	m/z 521.32529
	m/z 522.32728
	MG(0:0/5isoPGF2)(P
	m/z 323.14731
	Fructose-lysine(P)
	m/z 325.16181
	m/z 439.23065
	3-HODE
	m/z 270.13925
	m/z 421.20013
	Glucopyranoside(P)
	PG(P)
	Threonyllysine(P)
	PGG2(P)
	DHAP(10:0)(P)
	2-oxoenterodiol(P)
	m/z 339.12126
	m/z 455.2046
	m/z 377.2757
	3b-oxoCholenoic (P
	m/z 300.26464
	Dec-l-carnitine(P)
	melatonin sulfate(
	m/z 402.13342
	m/z 301.10357
	indole-3-acty-glut
	m/z 401.12881
	Methionyl-Aspartat
	m/z 267.0991
	m/z 195.09534
	Methylsuberic acid
	Spermine
	m/z 365.27815
	Myristoylglycine(P
	m/z 129.14033
	Spermidine
	m/z 426.29159
	IDHP(P)
	NPA(P)
	10-oxoODE(P)
	m/z 385.15485
	m/z 130.16073
	m/z 329.35911
	Isonicotinamide
	3-oxo-carnitine(P)
	m/z 453.16907
	m/z 354.04326
	m/z 356.04197
	m/z 437.20564
	11-oxyandrosterone
	m/z 330.21119
	m/z 315.12089
	m/z 376.21849
	Valerenolic acid(P
	m/z 364.96256
	m/z 271.0939
	GPEA(P)
	m/z 317.11434

B)

Figure 6.2.8 Heatmap of increased and decreased molecules in liver of GF and SPF mice using positive mode MSI

A) Heatmap shows m/z of molecules unable to be identified, putatively identified molecules (marked with a P) and molecules with an MSMS confirmed identification. B) Heatmap shows m/z of molecules unable to be identified and putatively identified as lipid molecules. Heatmap was created using Metaboanalyst 5.0. The colour of each sample is proportional to the significance of change in metabolite abundance indicated by the colour bar (red, increased; blue, decreased). Rows correspond to metabolites and columns correspond to samples from individual mice (GF, blue, SPF, red).

Furthermore, enrichment analysis using KEGG database indicated that the molecules found in the dataset are involved in at least 25 pathways listed in Figure 6.2.9 Arachidonic acid metabolism (p=0.00000125) and amino sugar and nucleotide sugar metabolism (p=0.00189) were the only pathways to be

significantly enriched and molecules from the dataset that participate in the pathways have been listed.
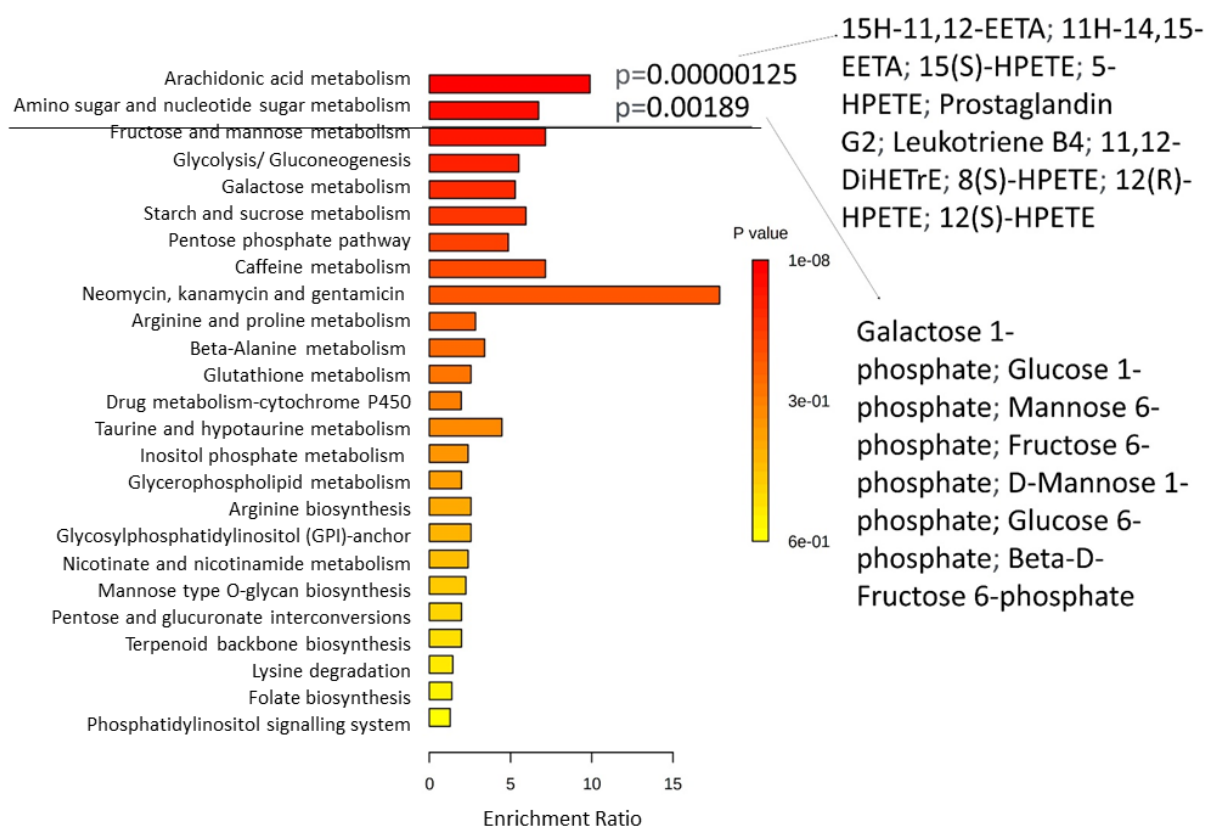
Figure 6.2.9 Enrichment of metabolic pathways in the liver
Enrichment pathway analysis using KEGG as reference found molecules involved in at 25 different pathways. The top 2 pathways were significantly enriched, and the molecules involved in the pathway that are present in the dataset are listed.

6.2.4 Metabolic alterations in the liver linked to immunological profile

Two molecules found in the liver were confirmed by MSMS fragmentation (0.8%) to be spermidine and spermine. A spermidine standard was spotted onto a slide and fragmented in the same run as the endogenous m/z 146.16 in liver tissue. The entire spectra were collected from m/z 50-146.2 and the fragmentation pattern at NCE 50 is shown. Compared to the spectra of endogenous m/z 146.16, fragmentation of the standard produced almost identical product ions at similar ratios. For example, the peaks at m/z 129.12, 112.11,75.09 and 72.08 show close similarities and also match the pattern available in m/zCloud. Hence, this study can suggest with relative confidence that the molecule m/z 146.16 is spermidine (Figure 6.2.10). Using the same MSMS method, a standard for

spermine was shown to have a similar fragmentation pattern as the reference from mzCloud and the endogenous m/z 203.05 from the liver. The peaks matched had m/z 129.12 and 112.11; thus, this study is confident that the endogenous m/z 203.05 is spermine (Figure 6.2.11). Spermidine and spermine were decreased 2.39-fold (p=0.00121) and 2.04-fold (p=0.000673), respectively, in the liver of SPF mice, compared to GF mice.
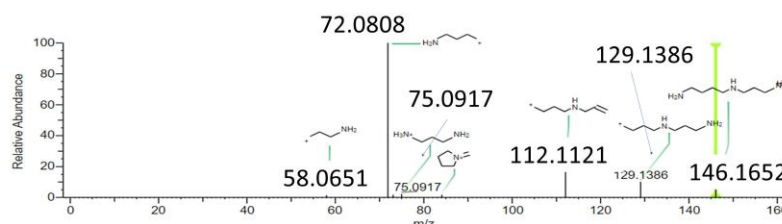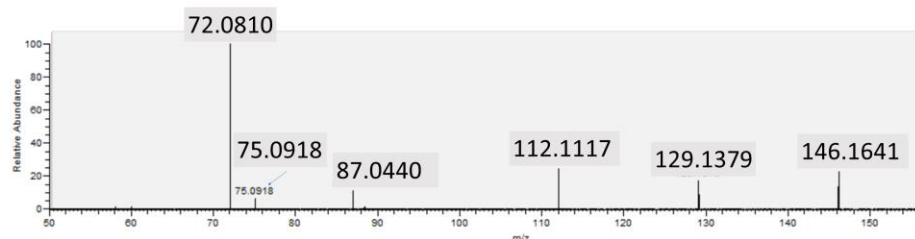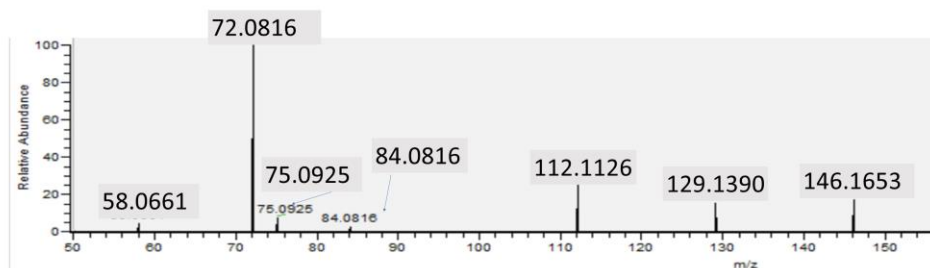
Figure 6.2.10 Comparison of MSMS fragmentation of m/z 146.16 in liver tissue and spermidine standard.
MSMS fragmentation spectra of the endogenous metabolite in the liver at m/z 146.16 and synthesised spermidine standard. Fragmentation was performed at increasing NCE energies and NCE 50 are shown for comparison. Spectra are shown as m/z (x-axis) plotted against relative abundance (y-axis). Similarity of peak presence and abundance suggests that m/z in liver is 146.16 likely to be spermidine.
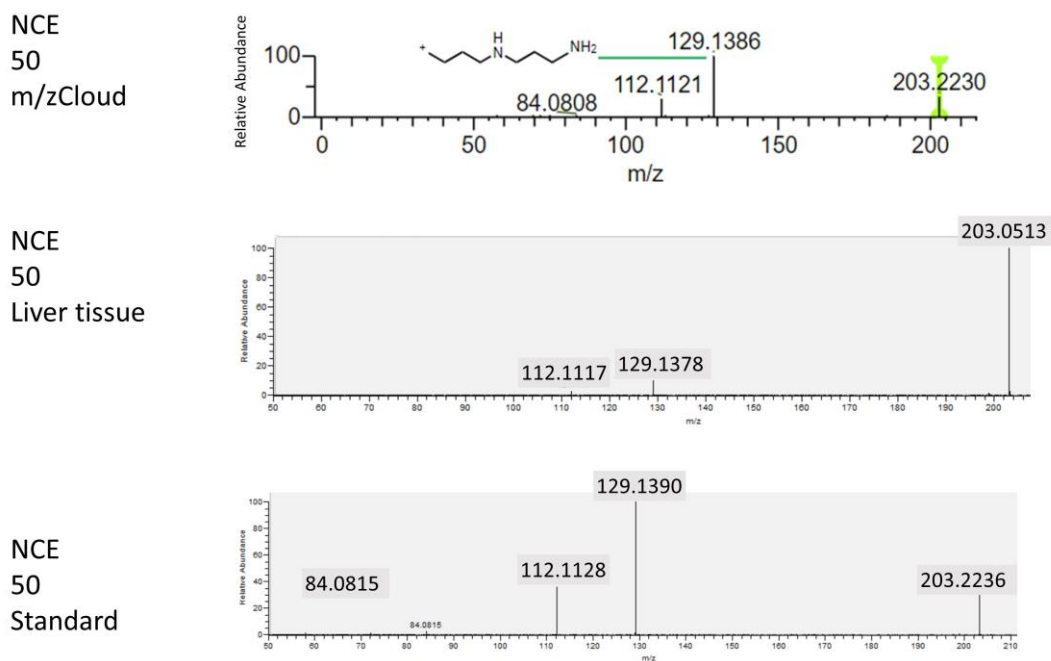
Figure 6.2.11 Comparison of MSMS fragmentation of m/z 203.05 in liver tissue and spermine standard.
MSMS fragmentation spectra of the endogenous metabolite in the liver at *m/z* 203.05 and synthesised spermine standard. Fragmentation was performed at increasing NCE energies and NCE 50 are shown for comparison. Spectra are shown as *m/z* (*x*-axis) plotted against relative abundance (*y*-axis). Similarity of peak presence and abundance suggests that *m/z* 203.05 in liver is likely to be spermine.
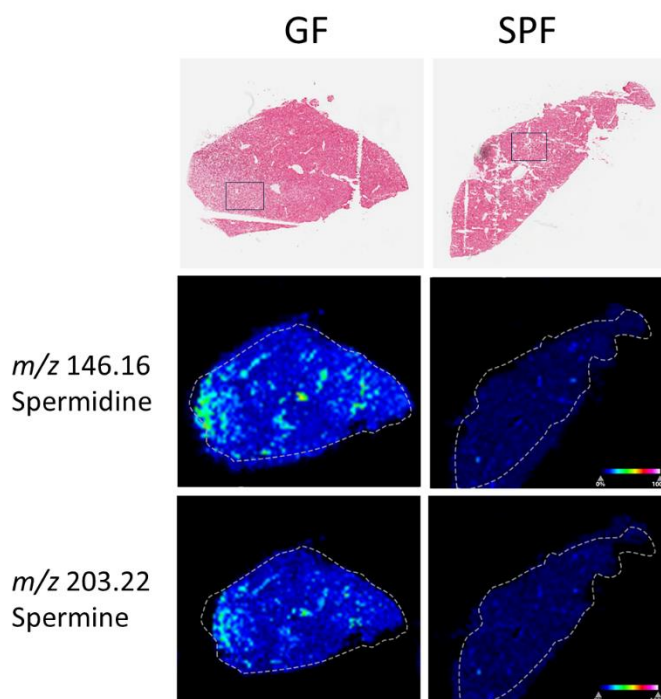
Figure 6.2.12 MSI image of m/z 146.16 and m/z 203.22 abundance in the liver.
From top to bottom: haematoxylin and eosin (H&E)-stained sections with rectangular boxes indicating region selected for IMC, MSI heatmap of m/z 160.1333 (colour bar shows 0% to 100% relative abundance).

To gain a better understanding of how spermidine and spermine might influence cell phenotype and function in the liver, IMC was performed on tissue regions indicated by blue rectangular boxes in Figure 6.2.12. In the liver tissue, the percentage of cells positive for the CD45 marker increased 1.38-fold (p=0.0222) in SPF mice, compared to GF mice (Figure 6.2.13). Furthermore, the results indicate that there was no significant different in marker expression between GF and SPF in liver vessels and phenotypical differences could not be determined.
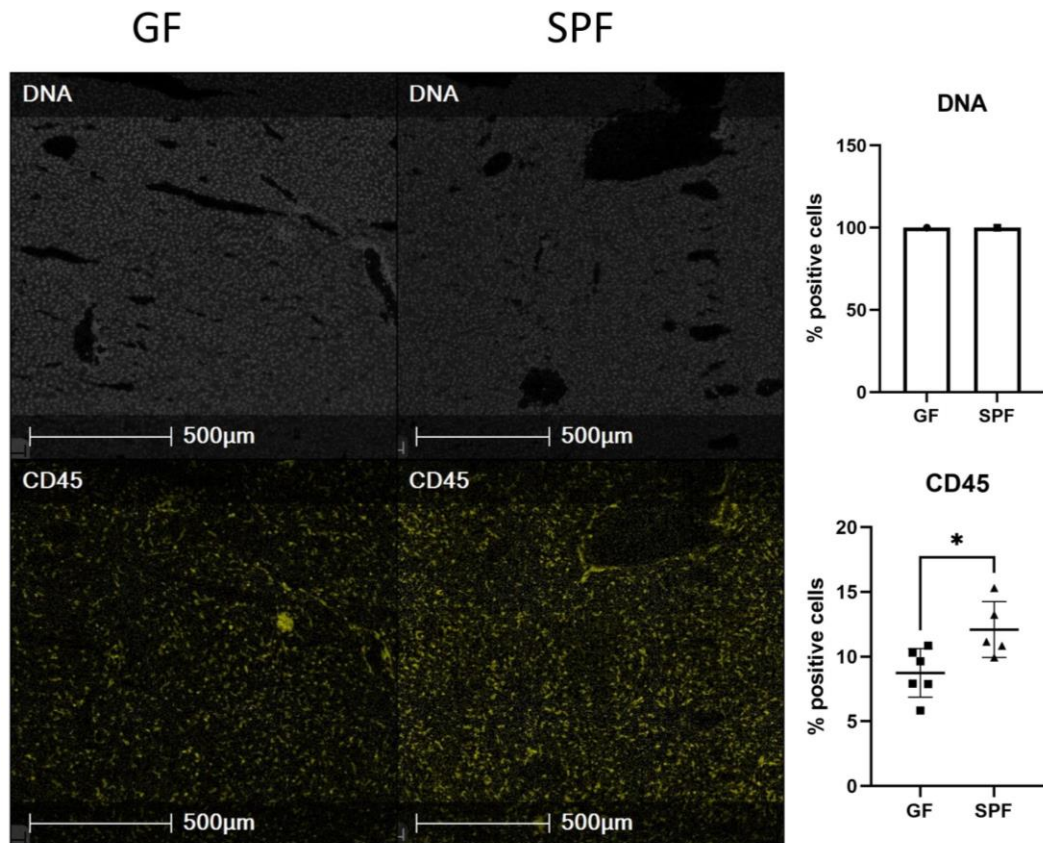
Figure 6.2.13 Representative IMC images of biological markers of cell function in the liver. Images shown are the region indicated in Fig 6.3.12 for GF and SPF groups. A) From top to bottom, DNA intercalator identified single cells within the tissue section and CD45. Percentage positive cells represented as bar graph showing six biological replicates. T-test performed to compare groups and *p<0.05, **p<0.01, ***p<0.001, ****p<0.0001 was considered statistically significant.

As IMC did not reveal specific cellular changes in regard to spermidine and spermine exposure, a variety of *in vitro* assays were performed to elucidate potential immunomodulatory mechanisms. Liver HepG2 cells were treated with an arbitrary concentration of 50 µM or 100 µM of spermidine or spermine as the concentration in liver tissue has not been confirmed and we wanted to see an effect without killing the cells. An LDH assay was used to determine cytotoxicity. Figure 6.2.14a indicates that spermidine is cytotoxic to HepG2 epithelial cells as treatment with 50 µM and 100 µM increase the percentage cytotoxicity 18.25-fold (*p*=0.0016) and 12.25-fold (*p*=0.0240), respectively, compared to the control. Furthermore, treatment with 50 µM spermine increased cytotoxicity 10.75-fold (*p*=0.0476), compared to the control. However, exposing HepG2 cells to 100 µM spermine increased cytotoxicity 9.5-fold (*p*=0.0893), which was not statistically significant. Furthermore, caspase-3/7

release was quantified as an indicator of cellular apoptosis (Figure 6.2.14b). Treating HepG2 cells with 25 µM and 50 µM spermidine decreased caspase release 1.88-fold (p=0.0055) and 1.58-fold (p=0.0225), respectively, compared to the control. Whereas, treating cells with 50 µM spermine decreased caspase release 1.67-fold (p=0.0146), compared to the control. However, increasing the concentration of spermine to 100 µM did not have any significant effect on caspase release, compared to the control. Therefore, it can be suggested that spermidine and spermine have a dose dependent effect of apoptosis, which is unlikely to be a mechanism of their cytotoxic effect.
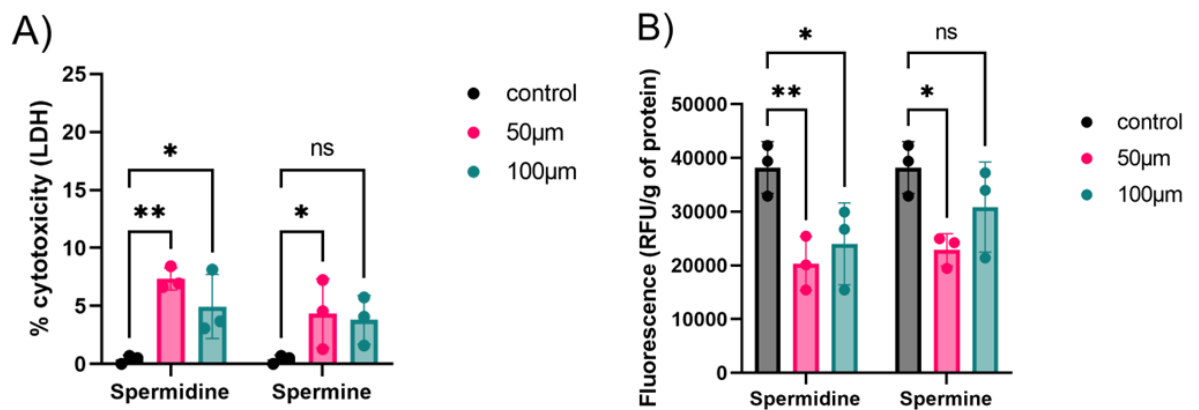
Figure 6.2.14 LDH and Caspase-3/7 release from treated HepG2 cells indicates cytotoxic effect and apoptosis activity.
HepG2 cells were exposed to 50 µM or 100 µM spermidine or spermine for 72 h. A) LDH assay used HepG2 cells only and cells treated with 2% triton-x as low and high LDH release controls, respectively. The percentage of cytotoxicity was calculated as %= (measured absorbance of sample-low control)/ (high control-low control) x100. B) The caspase-3/7 assay calculated enzyme activity by measuring relative fluorescence units (RFU) of activity normalised to protein in cell lysates. Data are shown as the mean of three biological replicates ± standard deviation (SD) (error bars). Two-way ANOVA was performed to compared metabolite exposure to cell only controls *p<0.05, **p<0.01, ***p<0.001, ****p<0.0001 versus the control condition (cells without molecules) was considered statistically significant.

This study also assessed whether spermidine and spermine had immunomodulatory effects in liver HepG2 epithelial cells via the release of specifically selected cytokines that are implicated in inflammatory processes, including IBD. Figure 6.2.15 shows that exposing HepG2 cells to 50 µM spermidine does not significantly change the secretion of IL-6, IL-8 or TNF-α; however, it reduced the secretion of IL-15 6.5-fold (p=0.0043), compared to the control. Furthermore, treatment with 100 µM spermidine did not significantly affect the secretion of IL-8, TNF-α or IL-15; however, it did increase the secretion of IL-6 1.86-fold (p=0.0209), compared to the control. Furthermore,

treatment with 50 μM or 100 μM spermine did not significantly affect the secretion of IL-6, IL-8 or TNF-α. However, treating cells with 50 μM spermine decreased IL-15 secretion 3.14-fold ($p=0.0140$), compared to the control. Whereas, treating cells with 100 μM spermine increased IL-15 secretion 2.29-fold ($p=0.0002$), compared to the control. Therefore, spermidine and spermine have a dose dependent, specific immunomodulatory effect *in vitro*.
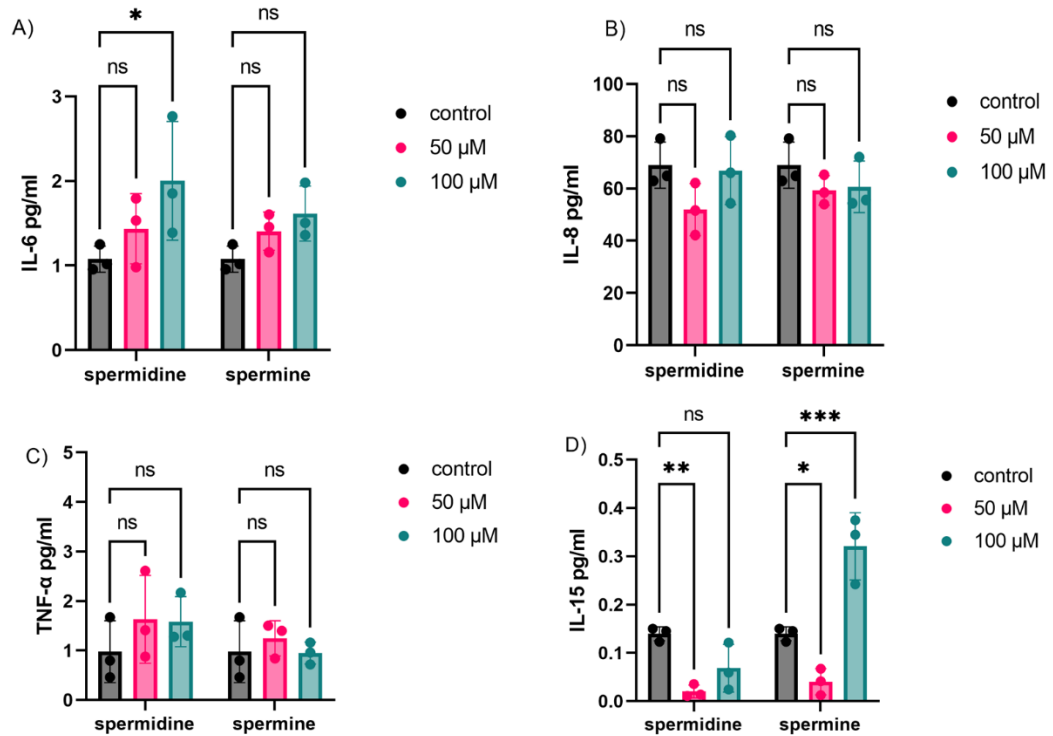
Figure 6.2.15 Cytokine release into cell supernatant after 72h exposure to spermidine or spermine. HepG2 cells were stimulated with 50 μM or 100 μM spermidine or spermine for 72 h before supernatants were collected. ELISA was used to quantify the release of a) IL-6 pg/ml, b) IL-8 pg/ml, c) TNF-α pg/ml and d) IL-15 pg/ml. Data is shown as the mean of 3 biological replicates ± standard deviation (SD). One-way ANOVA was performed for each molecule versus the control condition (cells without treatment). *$p<0.05$, **$p<0.01$, ***$p<0.001$, ****$p<0.0001$ is considered statistically significant.

After determining the modulatory effect spermidine has on liver epithelial cells, this study wanted to establish the effect on different immune cells. Immune cells were isolated from mouse spleens and stimulated with 4 μM or 0.16 μM spermidine or a cytokine (IL-4 or IL-12+IL-18) as positive controls of immune activation. Immune cells were gated and characterised as described in 8.1.17. Figure 6.2.16a shows that treating cells with 4 μM or 0.16 μM spermidine does not significantly change the percentage of NK cells, B cells, and macrophages positively expressing CD69, compared to the control. Treating cells with 4 μM or 0.16 μM spermidine also did not significantly change the percentage of NK cells

positively expressing granzyme B or IFN-γ compared to the control. However, treating cells with 4 µM or 0.16 µM spermidine significantly decreased the percentage of MHCII expressing macrophages 1.31-fold ($p<0.0001$) and 1.12-fold ($p=0.0002$), respectively, compared to the control. Figure 6.2.16b shows the MFI of specific immune cells positively expressing markers. The results indicate that stimulation with 4 µM or 0.16 µM spermidine does not significantly affect the level at which NK cell express granzyme B ($p=0.9961$ and 0.9999, respectively) or B cells express MHCII ($p=0.9999$ and 0.9995, respectively) compared to the control. Treating cells with 0.16 µM spermidine also did not significantly affect the level at which MHCII positive macrophages express MHCII ($p=0.1968$), compared to the control. However, increasing the concentration to 4 µM spermidine decreased the MFI of MHCII positive macrophages 1.38-fold ($p=0.0027$), compared to the control.
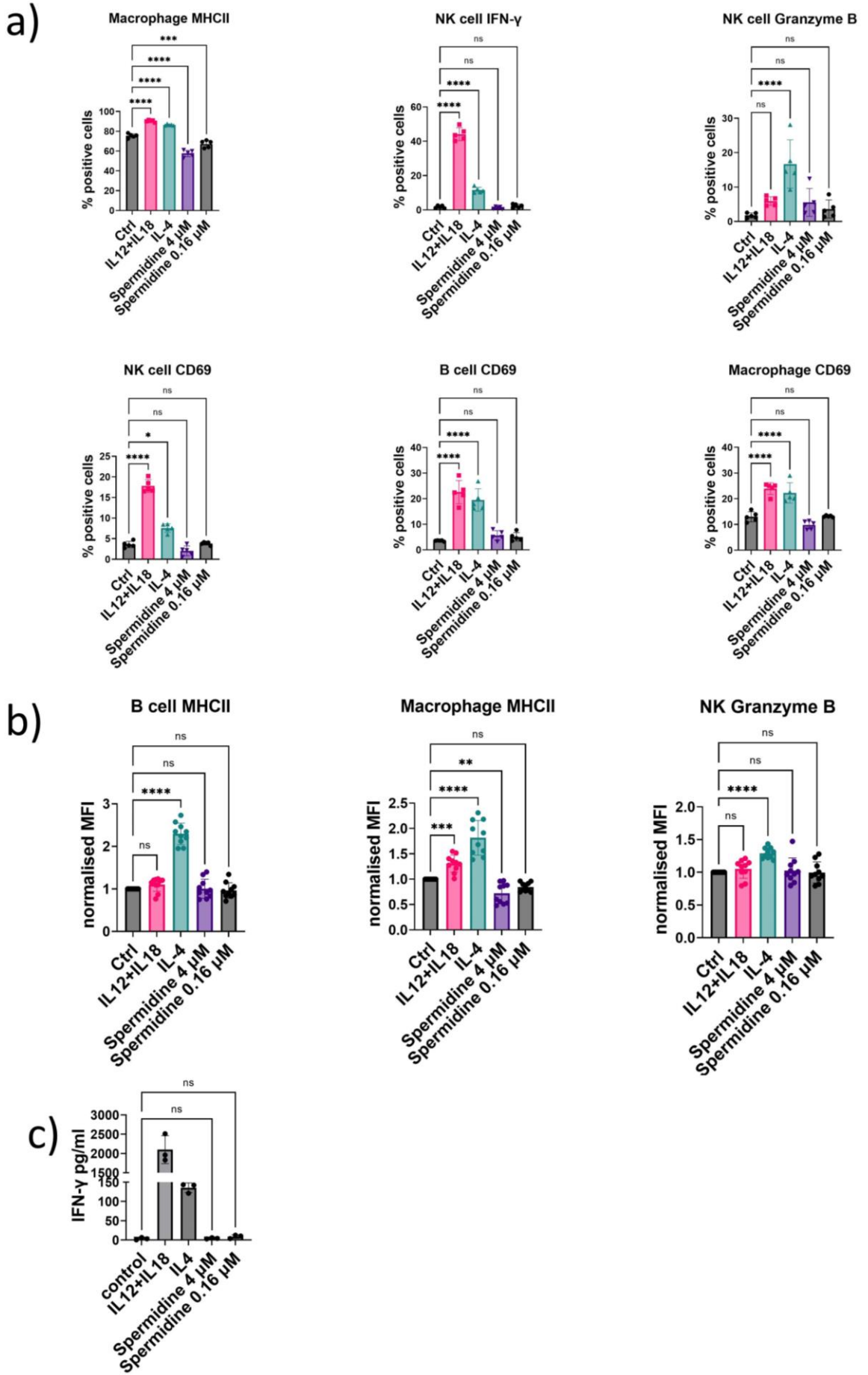
Figure 6.2.16 Flow cytometry and cytokine release analysis of splenic immune cells following stimulation with spermidine. Immune cells were isolated from spleen tissue and stimulated with 4 µM or 0.16 µM spermidine as well as IL12+IL-18 and IL-4 as positive controls. A) Percentage of immune cells (NK cells, B cells and macrophages) positively expressing specific peptides (MHCII, IFN-γ, Granzyme B and CD69). B) Mean fluorescence intensity (MFI) was normalised to control (no stimulation) and shows the relative amount of maker expressed within a positive population. A-B) One-way ANOVA was performed to compare stimulation versus the control condition (cells without treatment). C) ELISA was used to quantify the release of IFN-γ into immune cell supernatant and is shown as pg/ml. Unpaired T-test was performed to compared spermidine stimulated groups to control and did not include positive controls (cytokine stimulations). Data is shown as the mean of 3 biological replicates ± standard deviation (SD). *$p < 0.05$, **$p < 0.01$, ***$p < 0.001$, ****$p < 0.0001$ is considered statistically significant.

Following flow cytometry analysis, this study wanted to quantify the release of specific cytokines into the supernatant. A proteome profiler mouse cytokine array (8.1.18) indicated that IFN-γ was increased in the cell supernatant following treatment with spermidine compared to the control and was selected for quantification using ELISA. Figure 6.2.16c shows that treating cells with 4 µM or 0.16 µM spermidine did not significantly alter IFN-γ release compared to the control ($p = 0.9233$ and 0.1514, respectively).

6.2.5 Metabolic and cellular alterations in the lung associated with the microbiome

In the lung, ROC analysis found 7 peaks that could potentially discriminate between GF and SPF groups. Variation in the 7 molecules detected were analysed to examine the clustering of groups using multivariate statistical analysis including PLS-DA (M1) and PCA (M2). PCA score plots did show clear separation in the lung (parameters: R2X=0.7, Q2=0.509) (Figure 6.2.17). PLS-DA score plot (M1) was also able to separate the groups, as groups are above or below t[1]=0 line (parameters: R2X=0.699, R2Y=0.933, Q2=0.896).
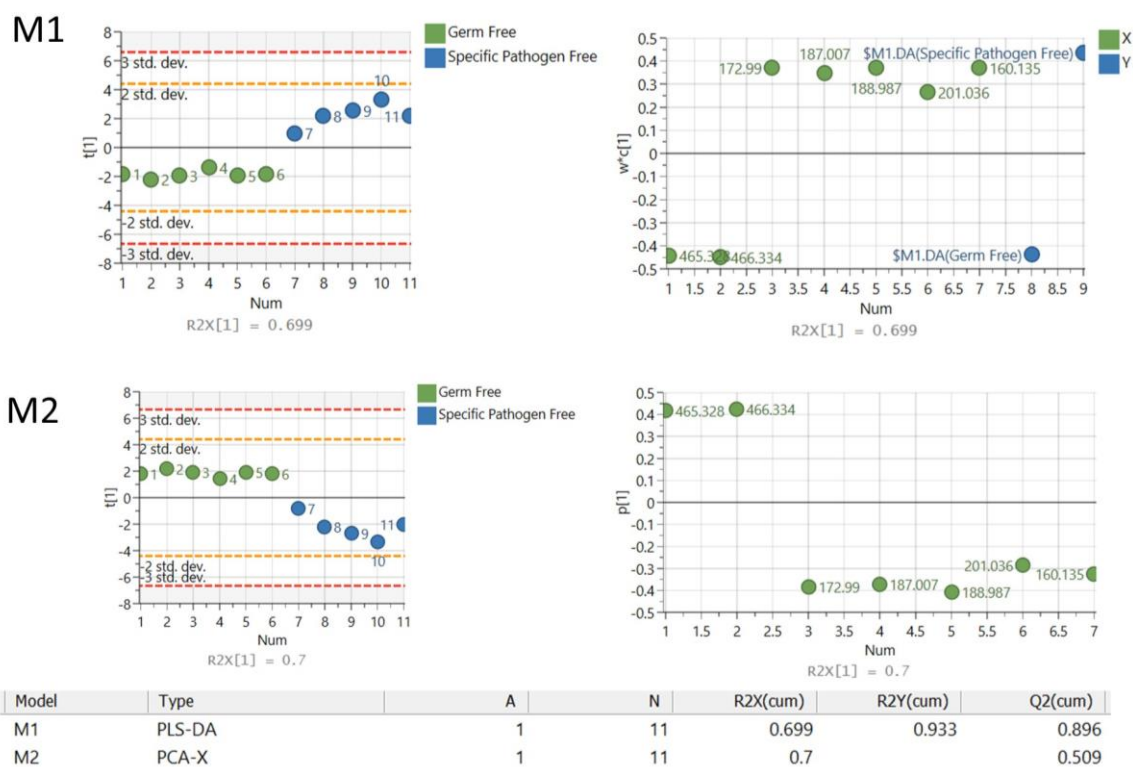
Figure 6.2.17 Unsupervised and supervised discriminant analysis
M1) Supervised PLS-DA analysis show the molecules in the lung of GF and SPF mice can discriminant between the groups (GF, green circles; SPF, blue circles). M2) Unsupervised PCA analysis was also able to discriminate between the groups using metabolite features. Analysis was performed using SIMCA 17 software. PLS-DA and PCA score plots consist of component 1 (t[1]).

The molecules *m/z* 465.3284 and 466.3339 were found to be significantly decreased 2.77-fold (*p*=0.000019) and 6.15-fold (*p*=0.000002), respectively, in the lung of SPF mice, compared to GF mice. The molecule with *m/z* 465.3284 was putatively identified as TetraHCA, whereas *m/z* 466.3339 could not be identified. However, TetraHCA was identified with the adduct M-H and both molecules have similar distribution patterns; thus, it is likely that *m/z* 466.3339 and 465.3284 are the same molecule. Four molecules were also found to be significantly increased in the lung of SPF mice, compared to GF mice and were putatively identified as follows: *m/z* 172.9904 (1055.48-fold, *p*=0.004204, phenol sulphate), 187.0066 (1289.82-fold, p=0.008928, p-cresol sulfate), 188.9867 (362.95-fold, p=0.00392, pyrocatechol sulfate) and 160.13547 (26.87-fold, p=0.0035, 5-AVAB) (Figure 6.2.18). This study attempted to perform pathway analysis using putative identities; however, enrichment was not possible (data not shown).
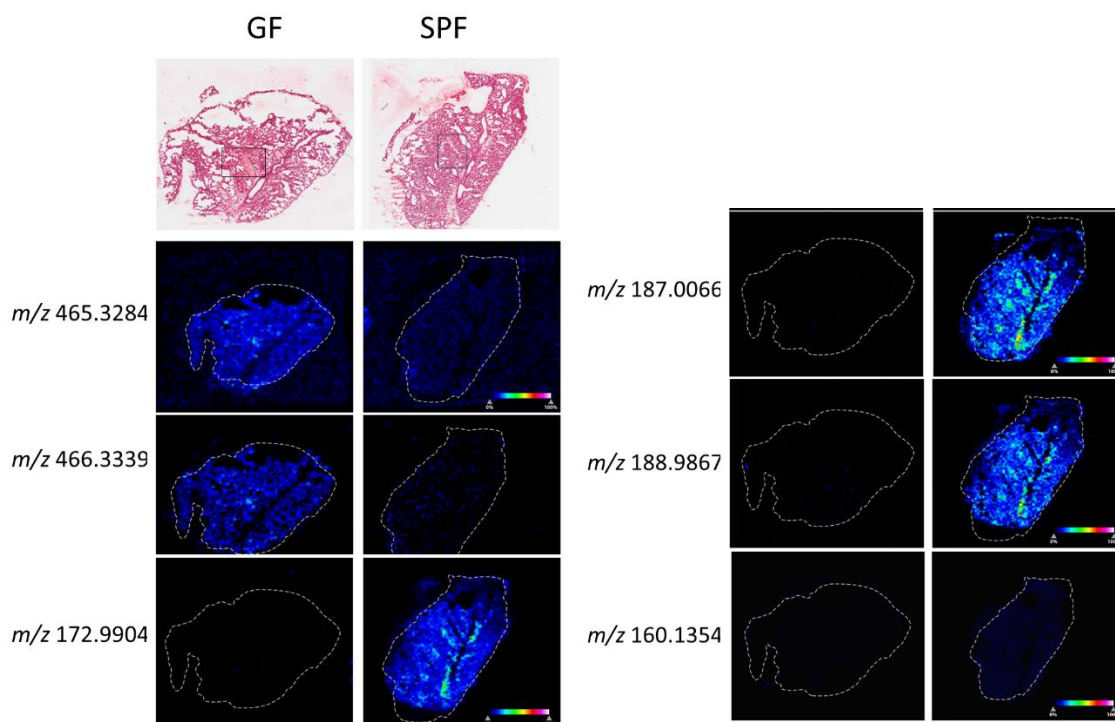
Figure 6.2.18 MSI image of m/z 465.3, 466.3,172.9, 187.0, 188.9 and 160.1 abundance in the lung.
From top to bottom: haematoxylin and eosin (H&E)-stained sections with rectangular boxes indicating region selected for IMC, MSI heatmap of m/z molecules (colour bar shows 0% to 100% relative abundance).

Unlike the liver, the lung did not have hundreds of metabolite changes between GF and SPF mice. However, this study used IMC to gain a better understanding of immunomodulation in systemic sites that may occur in the absence of substantial metabolomic alterations. Random forest machine learning tissue classifier module segmented the lung into tissue and vessel regions based on morphology and blood vessel cell marker, CD31. Figure 6.2.19 shows in the lung tissue, SPF mice had a significant decrease in the percentage of B220^{+} (1.46-fold; p=0.0050), Lyve1^{+} (1.33-fold; p=0.00211), CD19^{+} (2.91-fold; p=0.0319) and MHCII^{+} (2.13-fold; p=0.0186) expressing cells. The results also indicated that in the lung tissue of SPF mice, the percentage of cells with a phenotype indicative of M1 macrophages and dendritic cells were decreased 2.38-fold (p=0.0134) and 2.04-fold (p=0.0181), respectively, compared to GF mice. In lung vessels, the percentage of cells expressing ATPase was decreased 1.05-fold (p=0.0451) in SPF mice, compared to GF mice. However, the percentage of cells expressing Granzyme B increased 2.51-fold (p=0.0375) in SPF mice, compared to GF mice. Therefore, systemic immunomodulation does not depend on the number of

metabolites changed and it can be suggested that SPF mice have less activated immune cells in the lungs indicative of tolerance.
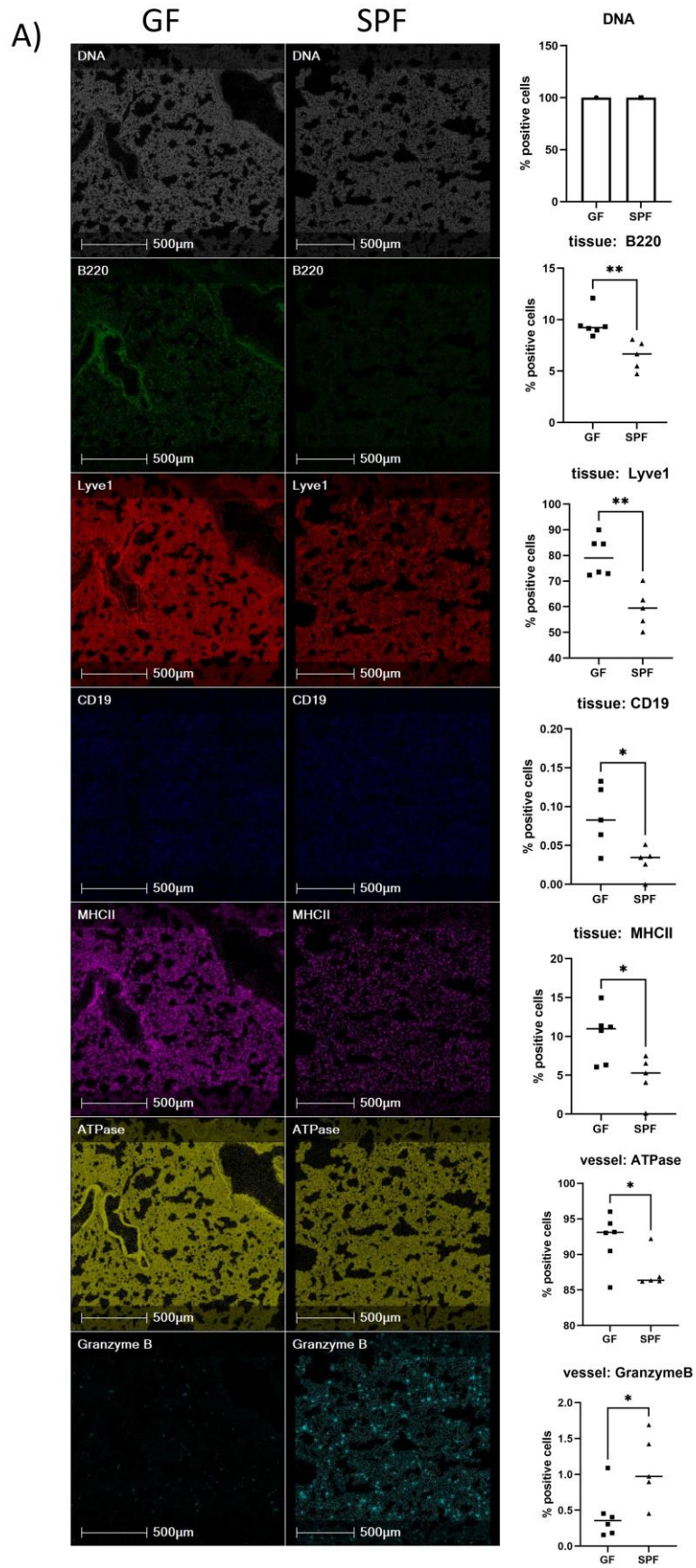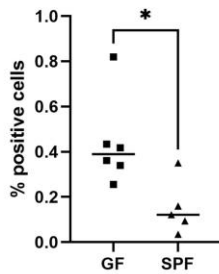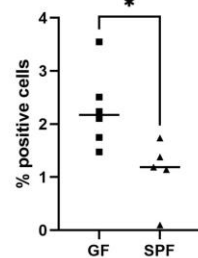
Figure 6.2.19 Representative IMC images of biological markers of cell function in the lung tissue and vessels.

Images shown are the region indicated in Fig 6.3.18 for GF and SPF groups. A) From top to bottom, DNA intercalator identified single cells within the tissue section, B220, Lyve1, CD19, MHCII, ATPase and granzyme B. B) Bar graph showing the percentage of cells with a phenotype indicative of M1 macrophages and dendritic cells. Percentage positive cells represented as bar graph showing five biological replicates. T-test performed to compare groups and *$p<0.05$, **$p<0.01$, ***$p<0.001$, ****$p<0.0001$ was considered statistically significant.

## 6.2.6 Metabolic alterations in the spleen associated with the microbiome

MSI was also used to discover metabolic changes in the spleen. ROC analysis found 6 peaks that could potentially discriminate between GF and SPF groups. Variation in the 6 molecules detected were analysed to examine the clustering of groups using multivariate statistical analysis including PCA (M1) and PLS-DA (M2). PCA score plots did show clear separation in the spleen (parameters: R2X=0.76, Q2=0.586) (Figure 6.2.20). PLS-DA score plot (M2) was also able to separate the groups (parameters: R2X=0.746, R2Y=0.911, Q2=0.889).
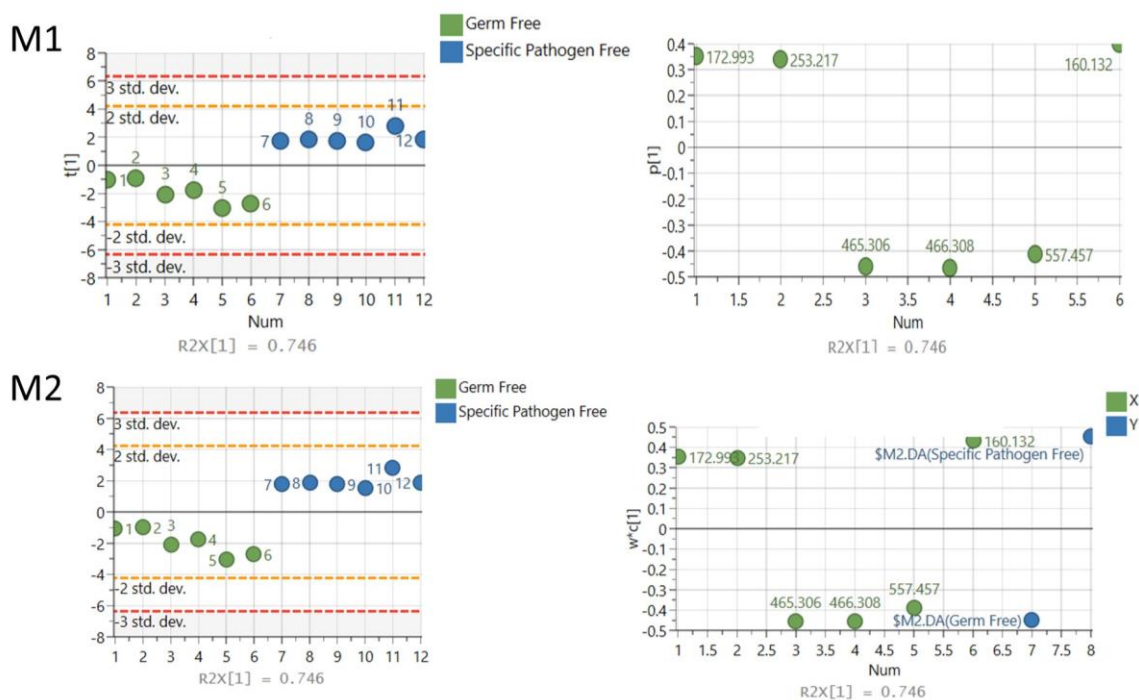
Figure 6.2.20 Unsupervised and supervised discriminant analysis
M1) Unsupervised PCA analysis was able to discriminate between the groups using metabolite features found in the spleen. M2) Supervised PLS-DA analysis also shows that the molecules in the spleen can discriminate between groups (GF, green circles; SPF, blue circles). Analysis was performed using SIMCA 17 software. PLS-DA and PCA score plots consist of component 1 (t [1]).
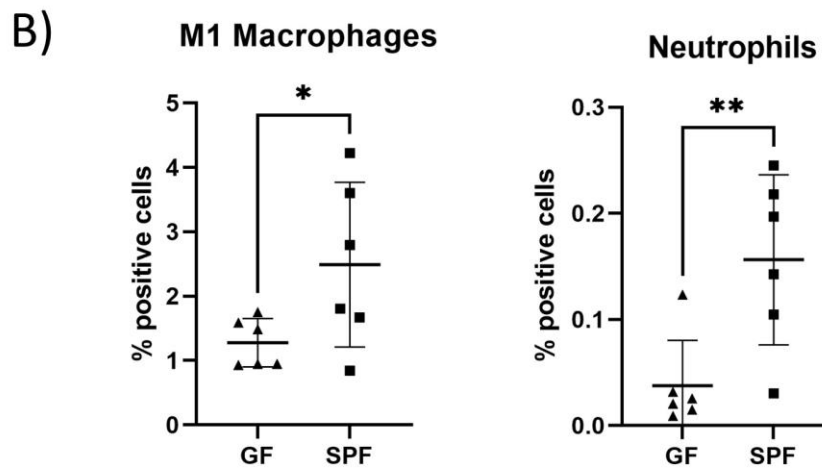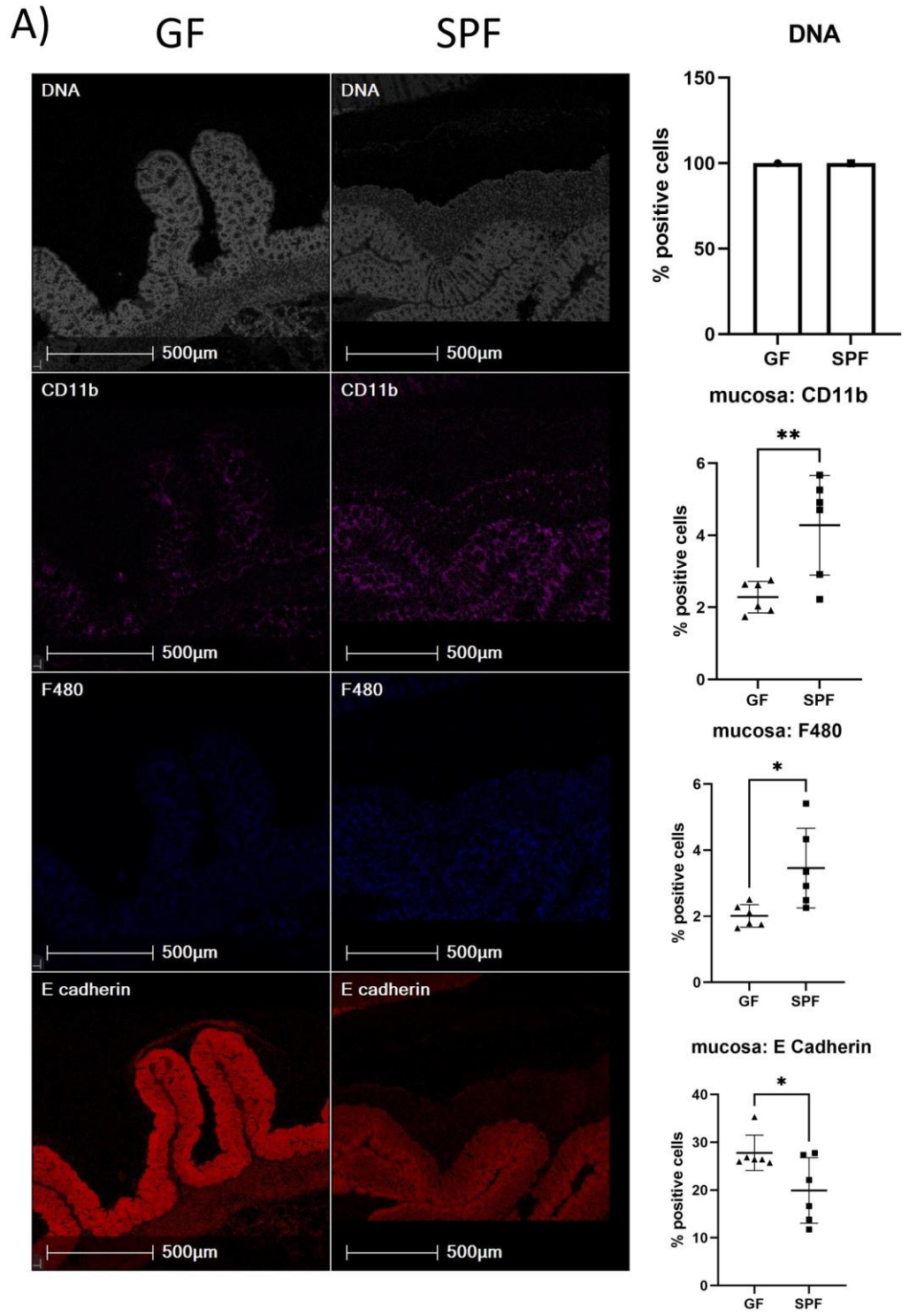
The molecule *m/z* 172.9926, putatively identified as phenol sulphate, was increased 988.16-fold ($p=0.0089$) in the spleen of SPF mice, compared to GF mice. Furthermore, the molecule *m/z* 160.1318, putatively identified as 5-AVAB, was increased 25.07-fold ($p=0.0002$) in the spleen of SPF mice compared to GF mice. The molecules *m/z* 465.3057 and 466.3084 were significantly decreased in the SPF spleen compared to GF mice by 2.82-fold ($p=0.000035$) and 4.03-fold ($p=0.000018$), respectively. The molecule with *m/z* 465.3057 was putatively identified as cholesterol sulphate (CS), whereas *m/z* 466.3339 could not be identified. However, CS was identified with the adduct M-H and both molecules have similar distribution patterns; thus, it is likely that *m/z* 466.3339 and 465.3284 are the same molecule. Lastly, *m/z* 557.4568 was decreased 1.71-fold ($p=0.0024$) in the spleen of SPF mice, compared to GF mice; however, the molecule could not be assigned a putative or confirmed identity (Figure 6.2.21). This study attempted to perform pathway analysis using putative identities; however, enrichment was not possible (data not shown).
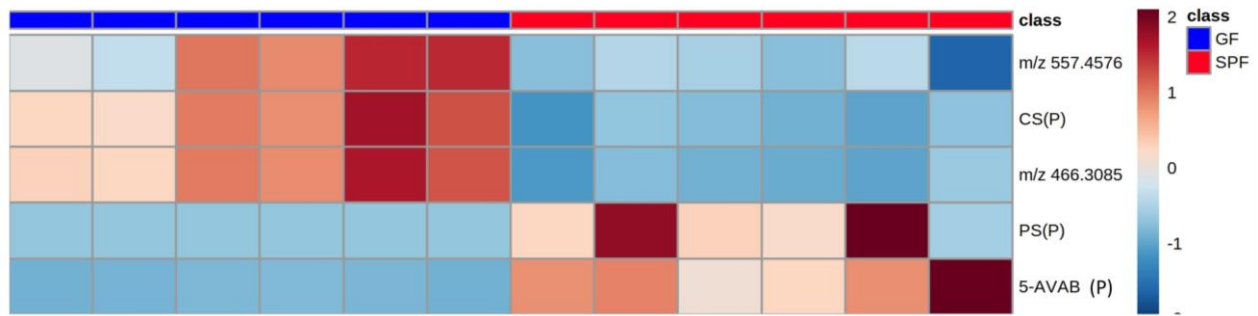
Figure 6.2.21 Molecules altered in spleen of GF and SPF mice
A) Heatmap shows *m/z* of molecules unable to be identified and putatively identified molecules (marked with a P). Heatmap was created using Metaboanalyst 5.0. The colour of each sample is proportional to the significance of change in metabolite abundance indicated by the colour bar (red, increased; blue, decreased). Rows correspond to metabolites and columns correspond to samples.

6.2.7 Metabolic alterations in the kidney associated with the microbiome

MSI was also used to discover metabolic changes in the kidney. ROC analysis found 5 peaks that could potentially discriminate between GF and SPF groups. Variation in the 5 molecules detected were analysed to examine the clustering of groups using multivariate statistical analysis including PCA (M1) and PLS-DA (M2). PCA score plots did show clear separation in the kidney (parameters: R2X=0.782, Q2=0.561) (Figure 6.2.22). PLS-DA score plot (M2) was also able to separate groups based on two significant components, resulting in the groups clustering within an ellipse (parameters: R2X=0.905, R2Y=0.916, Q2=0.851). As both plots had parameters above 0.5, the models are reliably predictive; thus, the metabolic profile in the kidney is able to distinguish SPF from GF group.
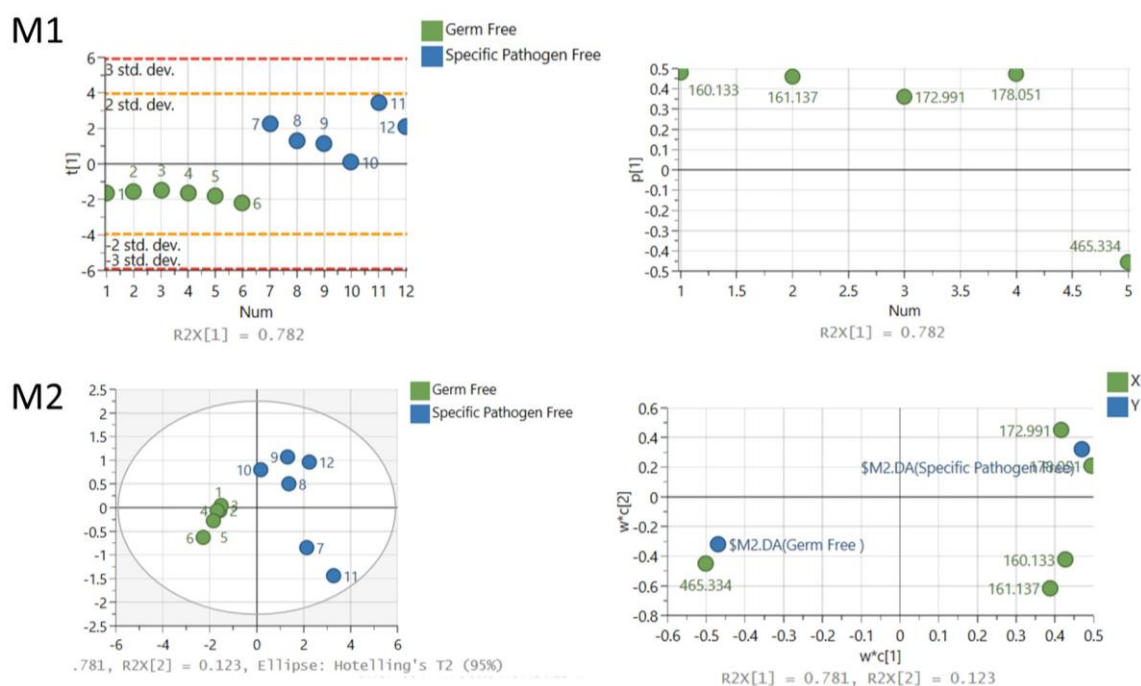
M1) Unsupervised PCA analysis was able to discriminate between the groups using metabolite features found in the kidney. M2) Supervised PLS-DA analysis shows that the molecules in the kidney can discriminate between groups and contribute to the separation (GF, green circles; SPF, blue circles). Analysis was performed using SIMCA 17 software. PLS-DA score plot consist of components 1 (t [1]) (x-axis) and 2 (t [2]) (y-axis). The ellipse represents the 95% confidence region for Hotelling's T2 statistic for the model.

Figure 6.2.23 shows that the molecule *m/z* 172.9906, putatively identified as Phenol sulphate, was increased 2361.54-fold (*p*=0.004068) in the kidney of SPF mice, compared to GF mice. Furthermore, the molecule *m/z* 160.1318, putatively identified as 5-AVAB, was increased 10.65-fold (*p*=0.002913) in the kidney of SPF mice compared to GF mice. The molecule *m/z* 161.1365 was also increased 177.21-fold (*p*=0.010701) in SPF compared to GF but could not be identified. The molecule m/z 178.0512, putatively identified as Hippuric acid was also increased 10.03-fold (*p*=0.000072) in the kidney of SPF mice, compared to GF mice. Whereas the molecule m/z 465.3335, putatively identified as vitamin K1 2,3-epoxide, was decreased 2.67-fold (*p*=0.000038) in the SPF kidney, compared to GF kidney. As this molecule has a similar *m/z* to the molecule found in the lung and spleen, it is possible that they are the same molecule. This study attempted to perform pathway analysis using putative identities; however,

enrichment was not possible (data not shown). Therefore, the only molecules shared between the intestine and systemic tissue are phenol sulphate which was increased in the SPF colon, liver, lung, spleen, and kidney, and 5-AVAB which was increased in the SPF ileum, lung, spleen, and kidney.
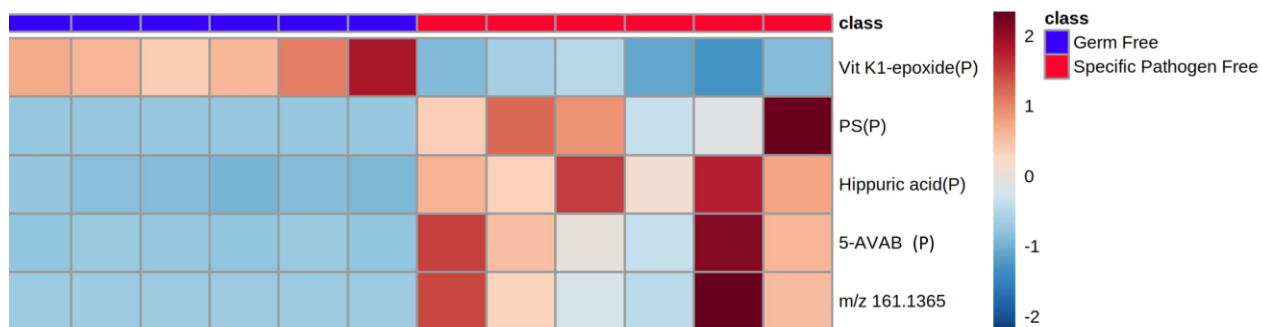
Figure 6.2.23 Molecules altered in kidney of GF and SPF mice
A) Heatmap shows m/z of molecules unable to be identified and putatively identified molecules (marked with a P). Heatmap was created using Metaboanalyst 5.0. The colour of each sample is proportional to the significance of change in metabolite abundance indicated by the colour bar (red, increased; blue, decreased). Rows correspond to metabolites and columns correspond to samples.

6.3 Discussion

Metabolomic and immunological changes in the ileum

Microbial metabolites are found in a variety of biological tissue such as faeces and urine and have a profound effect on host physiology [924]. The previous chapters have investigated changes in the metabolome that might contribute to disease progression after infection, the onset of intestinal colitis or CIA. Specific metabolite changes in the models were linked to the gut microbiome. This chapter set out to investigate the possible contribution of intestinal gut microbiota in the synthesis of systemic molecules that may influence immunomodulation and host physiology. The study found the molecule with m/z 160.13, putatively identified as 5-AVAB, was increased in the ileum, lung, spleen, and kidney of SPF mice compared to GF mice. As previously described, 5-AVAB is metabolically important as it can inhibit β-oxidation of fatty acids and is associated with specific members of the gut microbiome [393,395]. Therefore, it is not unsurprising that the molecule is increased in the ileum of SPF mice, compared to GF mice lacking a microbiome. Moreover, 5-AVAB was previously found to be decreased in the colon of mice infected with *E. coli* LF82 and 3% DSS colitis mice. Therefore, this study expected to find higher levels of 5-AVAB in the colon instead of the ileum. Bacterial catabolism of lysine derived from host diet has been described as one of the main sources of intestinal 5-AVAB [925]. Studies have found that absorption and digestion of dietary amino acids, including lysine, is reduced in the large intestine compared to the ileum [926]. It can be suggested that increased levels in the ileum of SPF mice is dependent on the presence of microbes and nutrient availability; thus, the decrease observed in the colon of infected and colitis mice is linked to poor nutrient availability as well as bacterial dysbiosis [925,926].

This study did not investigate the direct role 5-AVAB has on host physiology; however, IMC was applied to gain an overview of cell function in the ileum of GF and SPF mice. In the ileal mucosa, the percentage of cells expressing sodium/potassium-transporting ATPase decreased in SPF compared to GF mice. This ATPase is an integral protein located on the basolateral membrane of IECs [927]. The protein provides an intracellular gradient to promote all sodium dependent transport processes including the absorption of macronutrients

(glucose, amino acids), vitamins and nucleic acids [927,928]. Studies have shown that IBD patients have down-regulated sodium-potassium-ATPase activity and our DSS study also concluded that ATPase was decreased in the colon of mice with colitis; however, the molecular mechanism involved in this downregulation is not known [927,929]. Moreover, several studies have described a decreased activity of sodium-potassium-ATPase during acute and transient infectious enteritis resulting in impaired glucose, alanine, glutamine, taurocholate, and adenosine transport [930,931]. Therefore, this study suggests that microbes or microbially derived products such as 5-AVAB may be involved in the molecular mechanism that down-regulates sodium-potassium-ATPase activity [928,930,931]. Furthermore, the percentage of cells expressing the marker for cell proliferation (Ki67) was increased in the ileum of SPF mice compared to GF mice. A decrease in cellular proliferation is a hallmark of intestinal physiology in GF and microbial depleted mice; thus, IMC results in this study are more likely to be accurate and reliable [932]. Furthermore, F4/80^{+} and CD163^{+} cells are described as having a phenotype indicative of M2c macrophages and were found to be decreased in the ileum of SPF mice, compared to GF mice. Macrophages are converted into the anti-inflammatory M2c subtype after stimulation with IL-10 before entering apoptosis [933]. Studies have found that eliminating the innate immune response enhances M2c macrophage differentiation and efficacy [933,934]. Therefore, it can be suggested that the higher levels of M2c macrophages in GF mice is an adaptation to maintain homeostasis in the intestine in the absence of microbes and a primed immune response. Furthermore, the main function of M2c macrophages is to limit the duration and intensity of immune and inflammatory reactions in diseases such as acute lung injury and systemic lupus [934,935]. As the microbiome has been implicated in the development of inflammatory conditions including IBD, it can be suggested that a microbiome reduces M2c macrophage differentiation, resulting in less controlled pro-inflammatory responses [936]. Therefore, microbial induced immunomodulation involved in human diseases may include the impairment of M2c macrophages [933,934,936].

This study also wanted to assess differences in immune profile in the muscularis, as well as the mucosa. In the ileal muscularis, the percentage of cells that were granzyme B[+] increased in SPF mice, compared to GF mice. Granzyme B is a serine protease produced by a variety of immune and non-immune cells and has

been shown to induce inflammation by stimulating cytokine release and signalling extracellular matrix remodelling [937,938]. Studies have also suggested that inflammation associated with commensal and pathogenic bacterial exposure, triggers granzyme B expression in the gut [939]. Our DSS colitis study also found that granzyme B was increased in the inflamed colon, compared to the uninflamed control. Therefore, it can be suggested that the presence of specific bacteria in the gut, enhances granzyme B expression which might be a mechanism that is exacerbated during inflammatory conditions [938,939]. However, phosphorylated serine/threonine-protein kinase (pAkt+) expressing cells were decreased in the ileal muscularis of SPF mice, compared to GF mice. This protein is a major downstream effector of the phosphatidylinositide 3-kinase (PI3K) pathway and participates in inducing oxidative stress which is linked to the development of human cancers [940]. Furthermore, studies have shown that treating mice with specific bifidobacteria decreases the hyperphosphorylation of pAkt in signalling pathways [941,942]. Therefore, it can be suggested that a gut microbiome provides a protective affect against oxidative stress and PI3K pathway associated cancer development by reducing pAkt expression. Therefore, the addition of a gut microbiome results in immunomodulation in the ileal mucosa and muscularis which may be implicated in health and disease.

Metabolomic alterations in the colon important for human health

To assess whether molecular changes were similar throughout the intestine, MSI was used to investigate alterations within the colon. Phenol sulphate was found to be increased in the colon as well as liver, lung, spleen, and kidney of SPF mice compared to GF mice. Phenol sulphate is a microbially derived gut metabolite that is synthesised via bacterial enzyme tyrosine phenol-lyase activity during the production of phenol from dietary tyrosine [943]. Studies have indicated that increasing levels of microbial phenol sulphate induces ROS production, resulting in the progression of diabetes and associated kidney albuminuria in rats [943,944]. Thus, the molecule has been described as a potential biomarker and therapeutic target in diabetic kidney disease despite the biological activity not being fully understood [943,945]. As the molecule was increased in the gut and systemic organs in SPF mice, it may have a role in microbiome related disease conditions. However, our research did not identify

the molecule during *E. coli* LF82 infection, DSS induced colitis or CIA; thus, this study cannot suggest the molecule has a role in those inflammatory conditions. The molecule putatively identified as dodecanedioic acid (DODA) was also increased in the colon of SPF mice, compared to GF mice. DODA is a twelve-carbon dicarboxylic acid (DAs) that is derived from the β-oxidation of longer chain DAs [946]. DODA can enter the mitochondria and undergo oxidative metabolism to generate acetyl-CoA and succinyl-CoA within the Krebs cycle [947,948]. This mechanism allows DODA to be used as a carbon substate and has been found to improve energy deficiency and mitochondrial dysfunction in diabetic patients [946,949]. Furthermore, the production of DODA has been positively associated with specific bacteria such as *Clostridium butyricum,* which resulted in enhanced fatty acid oxidation in piglets [950]. Therefore, this study supports evidence that a gut microbiome enhances the production of DODA, which may be a useful therapeutic in mitochondrial dysfunction diseases [947,949,950].

A molecule putatively identified as uridine, and its isomer pseudouridine, were also increased in the colon of SPF mice compared to GF mice [951]. These molecules play an important role in biochemical and physiological processes including the synthesis of DNA, RNA, and glycosylation [952]. Due to this function, uridine and pseudouridine have been used as precursors in anti-tumour and anti-viral drugs including the Covid-19 mRNA vaccine [951,953]. *Bacillus subtilis* has been found to synthesis uridine 5'monophosphate (UMP) through *de novo* pyrimidine biosynthesis and has attracted attention as a biological strategy for enhancing uridine production for therapeutics [954]. In addition, studies have found uremic patients have an increase in pseudouridine producing enzymes in the microbiome; thus, bacteria and the molecule may play a role in kidney disease [955]. Our study found that infection with *E. coli* LF82 decreased pseudouridine in the colon, compared to uninfected controls. Therefore, our studies can suggest that the microbiome is important for uridine and pseudouridine production and infection may outcompete the bacteria involved in their synthesis.

The study also revealed that the molecule putatively identified as L-threonine was decreased in the colon of SPF mice compared to GF mice. Threonine is an amino acid obtained from the diet and is involved in lipid metabolism and

protein synthesis [956]. Studies have shown that threonine deficiency may induce hepatic glyceride accumulation as a protective mechanism to provide the mitochondria with substates for energy production [957,958]. Our study can support this as an increase in hepatic glycerides was observed in SPF mice, which is negatively correlated with threonine in the colon. Threonine can be degraded by certain commensal *Clostridium* species, resulting in the production of fatty acids such as acetic acid and butyric acid, which are required for maintaining intestinal function and priming immune responses [956,959]. Therefore, a decrease in the colon of SPF mice might represent an increase in microbial degradation to support gut health [959]. Threonine can also improve intestinal barrier function and immune function by modulating the expression of inflammatory cytokines [960]. In piglets and chickens, supplementation with threonine resulted in the upregulation of IL-6 genes and down regulation of IFN-γ, IL-12 and TNF-α [960,961]. Our IMC data indicated that cells with a phenotype indicative of M1 macrophages were increased in the colonic mucosa of SPF mice compared to GF mice. Therefore, it is possible that a decrease in threonine results the overproduction of pro-inflammatory cytokines, which encourages macrophages to undergo M1 activation [962]. *Cellular phenotype and functional changes within the colon*

Cells with a phenotype indicative of neutrophils were also increased in the colonic mucosa of SPF mice compared to GF mice. Previous studies have suggested that the reduction or absence of microbes and their products, significantly decreased the number of neutrophils in neonates and adult mice [963]. This depletion could be rescued following administration with heat-killed *E. coli* or LPS, suggesting microbial component derivates mediate neutrophil activation and recruitment [964,965]. This is because innate lymphoid cells in the intestine can recognise microbial ligands such as LPS and peptidoglycan, stimulating the production of IL-17 via the TLR4/Myd88 pathway [966]. This pathway results in the production of granulocyte colony-stimulating factor (G-CSF), which is a regulator of neutrophil differentiation [964,966]. Therefore, it was expected that neutrophil-like cells would be increased in the colon of SPF mice, indicating that IMC is accurately reflecting tissue immunology. To the best of our knowledge, there is limited information available detailing the effect of molecules identified in this study on neutrophil function. Therefore, the increase in neutrophils is likely to be a consequence of bacteria presence and we cannot determine the role of

molecules identified in this study. IMC also revealed that cells expressing E-cadherin were reduced in the colonic mucosa of SPF mice, compared to GF mice. E-cadherin forms the core of a signalling hub called adherens junction (AJ) which play a key role in controlling cell-cell adhesion [967]. Dysfunctional or reduced levels of E-cadherin have been associated with the development of IBD, our own DSS colitis model showed a decrease in E-cadherin in the inflamed colon and can result in luminal cells undergoing apoptosis and clearance [967,968]. Studies have suggested that pathogenic bacteria such as *Helicobacter pylori* can synthesis proteins that cleave E-cadherin to disrupt the epithelial barrier as a virulence mechanism [969]. Therefore, it can be suggested that microbes in the colon of SPF and DSS colitis mice have the ability to disrupt E-cadherin, similarly to pathogenic bacteria [968,969]. Thus, this bacterial mechanism might be involved in IBD and warrants further investigation as to what commensals, if any, are contributing to E-cadherin disruption.

Metabolomic pathways involved in liver physiology

Many studies have linked the progression of liver diseases such as NAFLD to alterations in the gut microbiome due to impaired immune regulation [970]. Patients with cirrhosis have an altered gut-liver axis associated with damage to the gut barrier and changes in bacterial composition and function [971,972]. Microbial functional changes observed in liver disease patients include increased release of endotoxins and a decrease in the production of secondary bile acids, affecting host physiology [970,973]. Furthermore, dysregulated lipid metabolism in the liver is a key factor in various metabolic diseases and has been associated with perturbations in the gut microbiome [974]. For example, NAFLD patients with a reduced intestinal microbial diversity and an overgrowth of bacteria such as *Escherichia* and *Peptoniphilus*, show accelerated rates of hepatic lipid metabolism dysfunction [975,976]. This affect has been largely attributed to microbial metabolites including SCFAs, bile acids and amino-acid derived molecules that play an important role in modulating host lipids via pathways related to lipid absorption, synthesis, and clearance [977]. Our study shows that SPF mice have significant changes in lipid metabolism in the liver compared to GF mice as different lipids including diglycerides, triglycerides, ceramides, and sphingomyelins are significantly changed. Therefore, identifying microbial and

host derived molecules and pathways that may influence this metabolomic shift could highlight new biomarkers of gut-liver axis dysbiosis and disease [977,978].

Our study showed that the arachidonic acid (AA) metabolism pathway was significantly enriched in the model. As previously described, AA pathway involves the multiple enzymatic pathways (LOX and COX) which results in the production of biologically active molecules such as hydroperoxyeicosatetraenoic acids (HPETEs), prostaglandin and leukotrienes [979]. The pathway in our study involves putatively identified prostaglandin G2 (PGG2), which is decreased in the liver of SPF mice compared to GF mice. PGG2 has been described as playing a pivotal role in acute inflammation by stimulating platelet aggregation and activating COX activity in inflammatory cells; thus, a decrease in this molecule suggests the addition of a gut microbiome provides an anti-inflammatory effect [980,981]. However, the pathway also involves an increase in putatively identified LTB4 in the liver of SPF mice compared to GF mice. This molecule is known to be a potent lipid mediator involved in the recruitment and activation of neutrophils, leading to tissue injury and inflammation [982]. Furthermore, AA has been described as an early biomarker of inflammation during the onset of NAFLD [983]. Therefore, this study suggests that the AA pathway in the liver can be modulated by the gut microbiome and may contribute towards immunomodulation and disease; thus, elucidating which microbes contribute to the pathway in the liver may provide insight into lipid metabolism and inflammation [979,982,983]. Furthermore, Amino sugar and nucleotide sugar metabolism was significantly enriched in the liver of the model and molecules such as putatively identified fructose-6 phosphate were increased in SPF mice compared to GF mice. This pathway involves D-fructose being phosphorylated to produced Beta-D-fructose-6-phosphate which reacts with glucosamine 6-phosphate synthase, resulting in the release of glucosamine 6-phosphate [984]. Nucleotide sugars act as building blocks for numerous glycoproteins, glycolipids, and glycosylphosphatidylinositol anchors, which play an important role in biological processes including cell signalling [984,985]. Studies have shown that disruptions in this pathway are involved in various human diseases including cancer and neurodegenerative conditions [986]. Furthermore, it has been reported that elevated levels of glucosamine occur in the liver of rats with type 2 diabetes mellitus (T2DM), whilst fructose is decreased [987]. This imbalance is thought to contribute to disease onset by

inducing bacterial dysbiosis, macrophage activation and proinflammatory cytokine release as well as reducing insulin sensitivity and fatty acid oxidation [988,989]. As putatively identified fructose-6 phosphate, a derivative of fructose, is increased in the liver of SPF mice, it can be suggested that microbes and their metabolites contribute to reactions within the pathway and in turn protect against the development of diseases [988,990].

The effect of spermine and spermidine on cell phenotype and function

MSMS was able to confirm the identity of spermidine and spermine in the liver, and both molecules were decreased in SPF mice compared to GF mice. These molecules are naturally occurring polyamines (PAs), a family of molecules that are derived from dietary ornithine through decarboxylation processes [991]. These molecules are critical for cellular homeostasis by enhancing DNA and RNA stabilization, enzymatic modulation and regulating translation [992]. In addition to dietary derived spermidine and spermine, the gut microbiota has been described as a major source of PAs in the colon, and PAs gain access to the bloodstream via the mucosa [993]. Therefore, it would have been reasonable expect an increase in systemic PAs following the addition of a gut microbiome and understanding why a reduction was observed may highlight new microbial-host metabolic interactions [993-995]. Interestingly, spermidine levels decline with ageing and a possible connection between reduced spermidine concentration and age-related deterioration has been suggested [996]. This correlation has been attributed to spermidines role in inducing autophagy in the liver, heart, and muscles by regulating the transcription factor elF5A and inhibiting several acetyltransferases, resulting in broad health promoting effects and longevity [997]. Furthermore, studies have shown that GF mice exhibit less age-related inflammation and on average live longer than conventional mice [998]. Therefore, it can be suggested that the introduction of a microbiome results in decreased spermidine levels, leading to impaired autophagy and ageing [993,997,998].

Due to the large number of molecular differences in the liver of SPF mice compared to GF mice, it was hypothesised that there would be significant alterations in immune cell phenotypes and function. However, IMC indicated that the only difference in immune profile was an increase in the percentage of cells expressing CD45 in SPF mice compared to GF mice. CD45 expression

increases during B- and T-cell differentiation and maturation; thus, it can be suggested that the gut microbiome is supporting the normal function of the immune system [999]. Moreover, studies have shown that the addition of spermidine to mice with psoriasis resulted in the reduction of CD45^{+} immune cells including neutrophils and DC, resulting in dampened autoimmunity[1000]. Therefore, it can be hypothesised that spermidine and CD45 expression are negatively correlated and may be an important mechanism in microbial mediated immunomodulation [997,1000,1001]. Furthermore, spermidine and spermine have also been shown to exert other anti-inflammatory and antioxidant properties, enhance mitochondrial metabolic function and improve proteostasis [994,995]. Studies have also revealed that oral supplementation with spermidine can reduce liver fibrosis and hepatocellular carcinoma by stabilising the microtubule-associated protein, MAP1S, to increase autophagy signalling [1002].

Due to spermidine and spermines role in inflammatory processes and liver function, we wanted to assess the effect different molecular concentrations have on liver cell function *in vitro*. Our study indicated that caspase-3/7 release was significantly reduced when HepG2 cells were exposed to 50 µM of spermidine and spermine, suggesting the molecules can prevent liver cells undergoing apoptosis. Studies have shown that the addition of 10 µM spermidine can suppress hydrogen peroxide induced cytotoxicity, apoptosis, and cell cycle arrest in retinal pigment epithelial cells by protecting against oxidative stress and downregulating extrinsic caspase-8 activity [1003]. However, exposing HeLa cells to 120-180 µM spermidine increased the release of caspase-3 and pro-apoptotic BAX protein, suggesting the intrinsic mitochondrial apoptosis pathway had been triggered [1004]. Our data also shows that increasing the concentration to 100 µM spermidine and spermine does not have the same suppressive effect on caspase-3/7 release compared to the lower concentration. Therefore, it can be suggested that a lower concentration of spermidine and spermine will be more affective at preventing apoptosis, whilst a higher concentration might trigger apoptosis; thus, a reduction in the SPF liver might be a protective affect against cell death [1002-1004]. As caspase-3/7 release was more inhibited after supplementation with 50 µM spermidine or spermine compared to 100 µM, it was expected that the lower concentration would be less cytotoxic. However, our results show that supplementation with 50 µM spermidine and spermine had

more of a cytotoxic effect than exposure to 100 μM. Studies have shown that both PAs have a dose-dependent cytotoxic effect on IECs caused by the induction of necrosis and not apoptosis [1005]. However, PAs concentration below 5 mM showed minimal LDH release; thus, it can be suggested that the cytotoxic effect of the PAs tested are cell specific and are likely to involve necrosis [1004,1005]. As previously described, spermidine supplementation can reduce fibrosis in mice, hence studies have suggested dietary supplementation as an approach to delay the progression [1002,1006]. However, this study suggests that both PAs have the potential to induce cytotoxic effects in a dose-dependent manner; thus, careful consideration is needed if spermidine is to be used as a therapeutic.

This study also wanted to evaluate whether the PAs could influence the production of inflammatory mediators in epithelial-like HepG2 cells. Spermidine and spermine at the tested concentrations did not have any significant effect on the release of IL-8 and TNF-α. However, other studies have shown that LPS stimulated macrophages treated with spermidine have reduced levels of TNF-α secretion, inhibiting inflammatory pathways [1007]. However, inducing inflammation before PA treatment might alter results and warrants further investigation to fully elucidate their role in liver cell inflammation. This study did find that higher concentrations of spermidine significantly increased the secretion of IL-6, whereas spermine had no effect. This study also found supplementation with 50 μM spermidine and spermine decreased the secretion of IL-15, whereas increasing spermine to 100 μM increased IL-15 secretion. Therefore, it can be suggested that higher levels of spermidine and spermine increase the release of specific cytokines which may have health implications[1008]. However, the data presented in this study shows a degree of variability and repeating the experiment is necessary to ensure the effect is reproducible.

This study also wanted to evaluate how spermidine affected the function of immune cells. Supplementing splenic immune cells with spermidine reduced the percentage of macrophages expressing MHCII in a dose dependent manner. Intestinal macrophages expression of MHCII has been linked to microbial stimuli exposure as GF and antibiotic treated mice have downregulated MHCII expression [1009]. Furthermore, macrophages deficient in the transcription factor

NFAT5 have defective expression of MCHII which in turn has been found to reduce the activation of CD4^{+} T lymphocytes [1010]. Therefore, studies have concluded that macrophage MHCII expression involves exposure to microbes and provides a signal for regulating gut CD4^{+} T cells [1009,1010]. As macrophage MHCII expression was inhibited at higher spermidine concentrations, it can be suggested that higher levels in GF mice have the potential to cause immune dysfunction [1011]. Therefore, the reduction in spermidine in the liver of SPF mice could be a microbial adaptation that ensures macrophages express MHCII which in turn supports the development and homeostasis of the adaptive immune response [1010-1012].

Metabolomic alterations in the lung

There were specific molecular changes in the lung of SPF mice compared to GF mice, such as an increase in microbially derived 5-AVAB and phenol sulphate that have been previously described. This study also found the molecule putatively identified as p-cresol sulphate (pCS) to be increased in the lung of SPF mice compared to GF mice. At least 55 bacteria strains present in the intestinal microbiota are able to produce p-cresol, predominantly in the colon, via enzymatic reactions with aromatic amino acids such as tyrosine and phenylalanine obtained from the diet [1013]. In the colon and liver, p-cresol is sulphated into pCS, which enters circulation, binds plasma albumin, and is filtered in the glomerulus before being excreted in urine [1014,1015]. Studies have shown that patients with chronic kidney disease (CKD) have an accumulation of pCS in the kidneys, which has been associated with worsening outcomes and the development of cardiovascular complications; thus, pCS has been described as a protein-bound uremic toxin [1014,1016]. Furthermore, pCS has been linked to the developed of central nervous system (CNS) diseases in CKD rodent models as it is elevated in systemic circulation and in the brain [1017,1018]. Within the kidney and the brain, pCS has been found to contribute to inflammation by exacerbating cell death, increasing oxidative stress, impairing mitochondrial function and causing vascular disruption [1018-1020]. This proinflammatory effect has also been observed in lung tissue as pCS can promote alveolar cell death and injury by triggering intracellular ROS, prostaglandin pathways, release of chemoattractants and leukocyte activation [1021,1022]. In contrast to the

inflammatory effects described the administration of pCS in mice with primary biliary cholangitis (PBC) significantly reduced inflammatory markers in the liver and macrophages were polarized towards an M2 phenotype [1023]. Our IMC data showed that the percentage of cells with a phenotype indicative of M1 macrophages were decreased in the lung of SPF mice, compared to GF mice. Thus, it can be suggested that the microbiota present in the SPF produce pCS to a level that supports an anti-inflammatory environment. Therefore, gaining a better understanding of the pCS toxicity level and effect on different tissue types might highlight a new therapeutic strategy for controlling inflammation via microbial modulation [1016,1020,1021].

Immunological changes in the lung

IMC of lung tissue also found that SPF mice have a decrease in the percentage of cells expressing B220 and CD19 mature, resting B cell markers as well as the APC marker, MHCII [1024,1025]. Furthermore, the percentage of cells with a phenotype indicative of dendritic cells were reduced in the lung of SPF mice, compared to GF mice. This suggests that the microenvironment of the SPF lung is having an immunosuppressive effect, which might lead to functional impairment of the immune system, increasing susceptibility to infection and disease [1026]. For example, patients with chronic obstructive pulmonary disease (COPD) have a significant decrease in the number of B cell subsets with a reduced ability to produce anti-inflammatory IL-10, worsening the condition [1027]. On the contrary, studies have demonstrated that reducing B cells and dendritic cells in the lung, protect the organ from CD4$^+$ T cell-induced inflammation [1027-1029]. To our knowledge, most GF studies do not report a difference in B cell and dendritic cell number but do report a change in function [1030]. Therefore, this study is proposing that IMC can reveal changes in immune cell number between GF and SPF mice and that the addition of a gut microbiome might prevent inflammation caused by an activated immune response by reducing the cells responsible for T cell priming [1027,1029]. Thus, further investigation into confirming the identity of the molecules in the lung and assessing their role in immunomodulation might highlight a new mechanism for controlling inflammation. Furthermore, the percentage of cells in lung vessels expressing ATPase marker was reduced, whilst granzyme B expression was increase in SPF mice, compared to the control. As

previously described, the reduction in ATPase might be linked to the gut microbiome and results in impaired nutrient availability, causing reduce cellular energy [930]. Furthermore, granzyme B can be released into the extracellular environment and cleave extracellular matrix proteins, contributing to the development of COPD and an emphysematous phenotype in the lung [1031]. Therefore, the addition of a gut microbiome might alter lung function by reducing airflow and energy supply.

Systemic metabolomic alterations in the spleen and kidney

This study also aimed to investigate whether the gut microbiome can affect the metabolome in the spleen and kidney in a manner that might affect organ function. The study found that molecules putatively identified as phenol sulphate and 5-AVAB are significantly increased in the spleen and kidney of SPF mice, compared to GF mice. These molecules may alter organ function and immune cell profiles as previously described. The molecules m/z 465.3057, putatively identified as cholesterol sulphate (CS), and m/z 466.3084, unidentified, were significantly decreased in the spleen of SPF mice, compared to GF mice. In the kidney, the molecule m/z 465.3335, putatively identified as vitamin K1 2,3-epoxide, was decreased in SPF group compared to GF group. Moreover, the molecules m/z 465.3284, putatively identified as TetraHCA, and 466.3339, unidentified, were decreased in the lung of SPF mice compared to GF mice. As both CS and TetraHCA were identified with the adduct M-H, it is likely that the unidentified molecule with m/z 466.3 is the same molecule plus hydrogen [1032]. As MSI requires a three-dimensional tissue sample, variations in height can occur leading to inhomogeneity in the acceleration field, resulting in lower mass resolution and mass accuracy [1033]. Furthermore, we were unable to confirm the identity of these molecules using MSMS as fragmentation patterns could not be matched with spectra available online (HBDB and mzCloud). As SPF mice had a decrease in the molecule m/z 465.3 across the spleen, kidney, and lung, it is possible that it is the same molecule and that MSI limitations have hindered accuracy. TetraHCA belongs to the class bile acid and has been negatively correlated with the severity of atherosclerosis; however, the mechanism underpinning this effect is unknown [1034]. Furthermore, CS can be produced via microbial metabolism of dietary cholesterol and has emerged as an

important regulatory molecule for stabilising cell membranes and supporting platelet adhesion; thus, a decrease in CS may have detrimental effects [1035,1036]. Lastly, Vitamin K1 2,3-epoxide is the inactive form of vitamin K and intestinal bacteria are a major source of vitamin K in the body [1037]. Vitamin K has drawn growing interest in recent years as it plays an important role in blood coagulation as well as anti-inflammatory, immunomodulatory and anti-tumorigenesis effects in the intestine [1038]. Our previous results also showed that the molecule m/z 465.3, putatively identified as CS, was significantly decreased in the ileum of 3% DSS colitis mice, compared to the control. Therefore, confirming the identity of this molecule across the tissue types is warranted as the putative identities indicate that changes in molecular abundance is linked to microbial presence and could have an impact on immune and organ function [1034,1035,1037].

Furthermore, the molecule putatively identified as Hippuric acid was increased in the kidney of SPF mice, compared to GF mice. Hippuric acid is produced via the conjugation of benzoate with glycine due to the formation of benzoyl CoA, in the mitochondria of the liver and kidney [1039]. Animal studies have shown that the excretion of hippuric acid in urine if modulated by the composition of intestinal microbiota [1040]. This is because benzoate is produced in the intestine from the microbial degradation of dietary aromatic compounds, leading to higher levels of hippuric acid [1041,1042]. Patients with CD have been shown to have reduced levels of hippuric acid excretion, which has been linked to altered gut microbial metabolism of dietary benzoate [1042,1043]. Therefore, it is not unsurprising that hippuric acid is increased in the kidney when a microbiome is present. Our previous study also indicated that a molecule was a very similar m/z (m/z 178.01) was decreased in the liver of 3% DSS colitis mice, compared to controls; thus, it can be speculated that this molecule is possibly hippuric acid and a reduction is due to microbial dysbiosis [1040,1043]. Additionally, the accumulation of hippuric acid has been positively correlated with the progression of CKD by increasing ROS accumulation and promoting the development of renal fibrosis [1044]. Therefore, hippuric acid could be a useful biomarker of CD and other microbiome related diseases; thus, gaining a better understanding of the molecular role in inflammatory processes as well as controlling levels via microbial manipulation could highlight new intervention

therapies [1044,1045]. Lasty, the molecule *m/z* 557.4568 was decreased in the spleen of SPF compared to GF mice but could not be assigned a putatively identity. Our research did not find this molecule in other tissue types or animal models. Therefore, it is unlikely that this molecule is involved in immunomodulation that drives inflammatory conditions such as IBD and RA [1046,1047].

In conclusion, this chapter shows that DESI MSI can be employed to discover molecules derived by the host and microbiota. Specific microbial metabolites such as 5-AVAB and phenol sulphate were putatively identified and increased in SPF mice. These molecules were found in numerous tissue types including gut, liver, lung, spleen, and kidney and may have specific outcomes for immunomodulation and host physiology. Moreover, this study used IMC to investigate immune changes in the gut and systemic organs in GF mice compared to SPF mice. This study highlighted specific immunological changes within the intestinal mucosa and muscularis that might contribute to organ function. Furthermore, specific alterations were also highlighted in the lung and liver which could be linked to the presence of specific microbial associated molecules within the tissue. For example, spermidine was decreased in the liver of SPF mice compared to GF mice and was negatively correlated with CD45 expression. This study also investigated the role spermidine and spermine have on liver and immune cell function *in vitro*. We found that the PAs have a cell specific effect and can induce cell death, cytokine signalling and MHCII macrophage expression. Therefore, PAs such as spermidine might play a direct role in immunomodulation and host physiology. Hence, further investigation is needed to fully confirm the identity of microbially derived molecules and elucidate their mechanistic potential.

Chapter 7 Final conclusions and future work

MSI is an established analytical tool capable of determining the spatial distribution of molecules within complex tissue. Furthermore, IMC accurately assesses complex phenotypes and immune spatial interactions within the tissue microenvironment. These technologies have been used separately to investigate clinical and pharmaceutical biological questions, especially in relation to cancer research and drug development. However, very few studies have been able to use both technologies simultaneously as a systems biology approach to gain a broader understanding of how the immune system is interconnected with biomolecular pathways and processes [1048]. Therefore, this study aimed to combine these powerful imaging techniques to characterise key metabolomic and immunological differences between diseased and healthy tissue. The studies revealed specific changes in immune cell number and phenotype occurred in microenvironments in which specific molecules were altered depending on

disease state. This information was then used to design *in vitro* experiments to highlight specific metabolic mechanisms involved in immune cell phenotype and function in relation to inflammation. The main conclusions of this research have been described in each chapter, but a brief summary will be discussed here.

This study began by applying MSI to investigate metabolomic changes in the intestine and systemic organs (liver and eye) of mice, following infection with an IBD-associated pathobiont, AIEC LF82 and propionic acid supplementation. Various molecules were found to be significantly changed in the tissue of infected vs non-infected mice. Many of these molecules were host derived, suggesting that infection is able to disrupt cellular metabolic processes which may lead to inflammation and tissue damage. In particular, a molecule *m/z* 160.13 was decreased in the colon and eye of infected mice compared to uninfected mice. This molecule was putatively identified as 5-AVAB; however, this identity has been disputed and may be in fact two microbe-derived compounds, 3M,4-TMAB and 4-TMAP [209]. These molecules have been implicated in the impaired ß-oxidation of fatty acids; thus, their role in the infection model warrants further investigation. Due to resource limitations, this study had only one time point (14 days post infection) and one bacterial load. Therefore, it would be interesting to establish a time-dependent and bacterial load dependent effect on metabolic changes e.g. are metabolomic changes more pronounced before day 14 and what implications do they have for inflammation and disease onset [1049].

In addition to the model above, we aimed to establish intestinal and systemic metabolic changes in a well-established model of IBD. The DSS colitis model was selected as it reflects the complex interactions between the epithelial barrier, intestinal microbiota, and the host immune response. The study found that numerous molecules were significantly changed between DSS colitis mice and healthy controls. The molecules changed in the colon, ileum, liver, kidney, and spleen were able to clearly separate the diseased group from the control group using multivariate analysis, suggesting that the molecules could be important factors in disease onset or progression. This study also showed that various molecules were similarly changed in different tissue. For example, gamma-Linolenic acid was decreased in the liver, kidney, ileum, and colon of DSS colitis

mice compared to the control and was suggested to be a substate for arachidonic acid production, which may support a proinflammatory environment [648,650]. Therefore, molecules that are altered in different tissues may be involved in systemic inflammation and warrant further investigation. The study was also able to confirm the identity of docosahexaenoic acid (DHA) and creatine (increased in ileum of DSS colitis mice) as well as 1-methylnicotinamide (increased in colon of DSS colitis mice); all three molecules identified as playing a role in multivariate clustering of groups. IMC revealed specific immunological markers and cell phenotypes were either up- or down- regulated depending on the microenvironment. For example, helper T cells (CD3$^+$, CD4$^+$) and dendritic cells (CD11c$^+$, MHCII$^+$) were decreased in the ileum of DSS colitis mice, suggesting that the model might be in a state of anti-inflammatory remission. *In vitro* modelling then revealed that DHA can reduce the secretion of IL-8, which is known to signal the activation and accumulation of T-cells in the mucosa. Therefore, it can be suggested that in the context of IBD, an increase in DHA may dampen IL-8 signalling to reduce immune cell infiltration and activation, resulting in less inflammation.

As rheumatoid arthritis (RA) has been linked to IBD and also has systemic complications following local inflammation, we decided to apply MSI and IMC to a collagen induced arthritis (CIA) model. We found molecular changes in the kidney, liver, spleen, and lung; some molecular changes were also able to cluster the disease group separately from controls, indicating that they could be biomarkers of disease. However, the focus of this chapter was on the only molecule increased in the lung of CIA mice compared to control mice: identified by MSMS as lysophosphatidylcholine (18:0) (LysoPC (18:0)). LysoPC (18:0) was speculatively accumulated at one end of the CIA lung tissue, hence this area was selected as the region of interest (ROI) for IMC analysis. IMC revealed changes in immune cell marker expression and phenotype, e.g. CD19$^+$ and B220$^+$ B cells were increased in the lung of the CIA group compared to naïve controls. Our *in vitro* analysis using splenic immune cells then found treatment with LysoPC (18:0) increased the relative expression of MHCII on B cells: MHCII molecules have been found to play a role in RA by interacting with CD4+ T-cells, resulting in the production of pro-inflammatory cytokines and autoantibodies [700,701,785]. Therefore, LysoPC (18:0) in the CIA lung may promote the recruitment of B cells

and enhance their expression of MHCII, causing or perpetuating an inflammatory environment. As RA patients often experience lung complications that are hard to diagnose, LysoPC (18:0) may be a useful biomarker and target for new therapeutics. Therefore, these studies are proof of concept that MSI and IMC can be used together in order to reveal potential mechanisms of immune homeostasis and disease that may be harnessed to develop new intervention therapies.

IBD and RA studies have implicated the microbiome as an important factor in disease pathology and involves the production of bacterial molecules. Therefore, this study applied MSI and IMC to germ-free (GF) and specific pathogen free mice (SPF), to elucidate how the microbiome is involved in host health and identify any molecules that may drive inflammatory conditions. MSI found metabolomic changes in the ileum, colon, liver, kidney, and spleen that were able to separate GF and SPF groups using multivariate analysis. Molecules such as 5-AVAB were increased in the ileum, lung, spleen, and kidney of SPF mice compared to GF mice: this molecule was decreased in AIEC infection model and DSS colitis mice, hence this molecule is likely to be of microbial origin and play a role in inflammatory processes. Moreover, the liver had the most pronounced molecular difference between the two groups, suggesting that the microbiome is important for normal liver metabolism and function. This study was able to confirm the identity of two polyamine molecules, spermine and spermidine, that were decreased in the SPF liver compared to the GF liver. These molecules can be produced by the gut microbiota as well as the host; thus, a decrease in the SPF liver was unexpected. IMC analysis revealed that despite huge alterations in molecules detected, the only marker for which differential expression was measured was CD45 (increased expression in SPF mice compared to GF mice). However, *in vitro* analysis using splenic immune cells revealed that spermidine supplementation reduced the percentage of macrophages expressing MHCII in a dose dependent manner. Therefore, higher levels of spermidine in GF mice might impair macrophage MHCII driven CD4$^+$ T cells activation, resulting in immune dysregulation [1009,1010]. Hence, the reduction of spermidine in the liver of SPF mice could be a microbial adaptation that ensures macrophages express MHCII at a level that supports the development and homeostasis of the adaptive immune response [1010-1012]. Therefore, this study shows that MSI and IMC can be

used together in order to reveal potential mechanisms of microbe-host interactions that may lead to immune homeostasis or dysregulation.

However, this study does have some limitations that need to be overcome in order to fully understand the information available within these datasets. Firstly, spatial segmentation partitions MSI data into distinct regions of interest (ROI), such as different anatomical or pathological areas, for downstream statistical analysis [1050]. This allows studies to gain a better understanding of molecular signatures in relation to the tissue landscape [1051]. This study attempted to segment intestinal tissue using unsupervised spatial segmentation, which is a popular approach to automate ROI definitions: this approach clusters pixels based of their spectral similarity using k-means algorithms [1052]. However, this segmentation was unsuccessful at defining distinct anatomical regions (e.g. mucosa, muscularis). The reason as to why segmentation was unsuccessful is not fully known but may include the following: the algorithm can segment tissue on the basis of instrument noise or acquisition artifacts and produce ROIs that are not biologically accurate, intestinal tissue size and preparation (swiss roll) resulted in delocalisation of molecules making it difficult for algorithm to classify based on spectra [1053]. The study also attempted to define ROIs by co-registering the MSI image with the histological H&E image and performing classification steps on SCiLS. However, after classifying the tissue (muscularis, mucosa), there were no significant difference between the regions. Therefore, this study decided to focus on molecular differences between control and diseased organs rather than spatial differences within the tissue. As the technology and software for analysis are continuously improving, different segmentation algorithms and methods have been developed to improve ROI selection; thus, more in depth spatial analysis could be performed in the future using the datasets generated in this study to highlight spatial differences [1051,1053].

At the beginning of the project, we aimed to use human tissue biopsied from IBD patients. Due to the pandemic, access to human tissue was not feasible and we used animal models instead, avoiding substantial delays in research. Animal models can be useful when investigating disease mechanisms and the models selected in this project were based on reliability, reproducibility, and similarity to human disease. However, animal models do not fully represent the human

situation [469,480]. For example, only 17% of metabolomic changes that can differentiate between IBD, and controls are shared between human and animal studies [1054]. This means that the majority of metabolite changes that occur during human disease will not be observed in animal models and *vice versa*; thus, metabolomic adaptations and mechanisms observed in this study might not fully reflect clinical disease. Therefore, future work might involve confirming the presence of molecules implicated in animal disease mechanisms in human patients. Moreover, using human tissue might allow for clearer segmentation between anatomical regions and improve our spatial understanding of molecules in relation to disease outcomes. However, many of the pathways (e.g. Arachidonic acid), molecules and microbiome changes observed throughout this study have already been identified in human studies, suggesting that some of the observed mechanisms of immunological function may be applicable in humans [1054].

A key limiting factor in this study was the identification of molecules. The majority of significantly changed molecules throughout this study were either unidentified or characterised using accurate mass only (MSMS could confirm the identity of very few). This is a known limitation in untargeted metabolomic approaches as on average only 10% of molecules in these studies can be annotated. This low annotation rate makes it hard for researchers to interpret biochemical changes, reducing the ability to draw meaningful comparisons and conclusions [1055]. The majority of studies rely on manually matching annotations to reference spectral libraries; however, there is a distinct bias as most matches are related to medicine and drugs, while there are much fewer matches to microbial metabolites [1055,1056]. Moreover, spectral libraries account for a small proportion of known molecules, estimated to cover only 1% of molecules [1056,1057]. Therefore, a significant amount of information in this study has been missed due to the inability to identify molecules, especially those of a microbial origin; thus, conclusions about the importance of specific pathways may be incomplete. Furthermore, follow up *in vitro* experiments tested the immunological and functional impact of MSMS confirmed molecules, which overlooks the important role other molecules in the study may play in disease pathogenesis.

[1055][1055,1056][1056,1057]However, due to the expansion of metabolomic research, spectral libraries are growing in size and resulting in improving matches rates by scoring the confidence estimation of potential matches, automated and semi-automated annotation [1057]. Therefore, revisiting this dataset periodically to match molecules using spectral libraries may produce new and important molecules of interest. Furthermore, it would be interesting to confirm the identity of molecules that could not be assigned a putative identity, especially those that were significantly changed in multiple tissues. This could be achieved by employing nuclear magnetic resonance (NMR): a powerful analytical technique used to identify and characterise molecules, including novel ones. NMR works by exploiting the magnetic properties of certain atomic nuclei, particularly hydrogen (protons) and carbon-13 (^{13}C) [1058]. A magnetic field and radiofrequency energy allows the NMR instrument to detect emitted signals, containing information about the chemical environment and interactions of the nuclei within the molecule [1059]. Chemists can then use software and databases to interpret the generated NMR spectrum by comparing it to known spectra to identify molecular structure and confirm its novelty [1058,1060]. If successful, the newly identified molecules can then be assessed *in vitro* to characterise their role in cellular phenotype and function; thus, highlighting novel molecular mechanisms in human health.

Overall, this study has demonstrated the capabilities of combining metabolomic and immunological imaging techniques to investigate the role host and microbial metabolic signals play in cellular phenotype and function. DESI-MSI allowed us to image the abundance of molecules in the intestine during AIEC infection, DSS induced colitis and microbially adapted mice. Moreover, DESI-MSI revealed key metabolic changes in systemic sites that frequently experience extraintestinal disease manifestations (i.e. liver, lung, kidney, and spleen) in the same models as well as a CIA mouse model. IMC then revealed distinct cellular profiles between disease and control mice within specific ROIs (selected based on molecular abundance). These techniques revealed specific metabolic and cellular changes and provided information needed for further analysis (e.g., what molecule to test on specific cell lines/ immune cells). Therefore, new molecular mechanisms of cellular regulation were identified and may improve our understanding of inflammation and disease pathology.

References

Bibliography not presented in a single format (e.g., differences in journal title naming, DOIs and dates of access). References were automatically generated in Mendeley and changing settings did not address the problem.

1. Qiu, P. *et al.* The Gut Microbiota in Inflammatory Bowel Disease. *Front Cell Infect Microbiol* **12**, 733992 (2022).
2. Ulcerative Colitis and Crohn's Disease - PMC. https://www.ncbi.nlm.nih.gov/pmc/articles/PMC4123809/.
3. Bradley, C. A. IBD: Tofacitinib effective in ulcerative colitis. *Nat Rev Gastroenterol Hepatol* **14**, 388 (2017).
4. Cominelli, F., Arseneau, K. O., Rodriguez-Palacios, A. & Pizarro, T. T. Uncovering Pathogenic Mechanisms of Inflammatory Bowel Disease Using Mouse Models of Crohn's Disease–Like Ileitis: What is the Right Model? *Cell Mol Gastroenterol Hepatol* **4**, 19–32 (2017).
5. Zhang, Y. Z. & Li, Y. Y. Inflammatory bowel disease: Pathogenesis. *World Journal of Gastroenterology : WJG* **20**, 91 (2014).
6. Wang, R., Li, Z., Liu, S. & Zhang, D. Global, regional and national burden of inflammatory bowel disease in 204 countries and territories from 1990 to 2019: a systematic analysis based on the Global Burden of Disease Study 2019. *BMJ Open* **13**, e065186 (2023).
7. Kaplan, G. G. The global burden of IBD: from 2015 to 2025. *Nature Reviews Gastroenterology & Hepatology 2015 12:12* **12**, 720–727 (2015).
8. Mak, W. Y., Zhao, M., Ng, S. C. & Burisch, J. The epidemiology of inflammatory bowel disease: East meets west. *Journal of Gastroenterology and Hepatology (Australia)* **35**, 380–389 (2020).
9. Piovani, D., Danese, S., Peyrin-Biroulet, L. & Bonovas, S. Inflammatory bowel disease: estimates from the global burden of disease 2017 study. *Aliment Pharmacol Ther* **51**, 261–270 (2020).
10. Molodecky, N. A. *et al.* Increasing incidence and prevalence of the inflammatory bowel diseases with time, based on systematic review. *Gastroenterology* **142**, 46–54 (2012).
11. Ananthakrishnan, A. N. Epidemiology and risk factors for IBD. *Nat Rev Gastroenterol Hepatol* **12**, 205–217 (2015).
12. Mulder, D. J., Noble, A. J., Justinich, C. J. & Duffin, J. M. A tale of two diseases: the history of inflammatory bowel disease. *J. Crohns Colitis* **8**, 341–348 (2014).
13. Piovani, D., Danese, S., Peyrin-Biroulet, L. & Bonovas, S. Inflammatory bowel disease: estimates from the global burden of disease 2017 study. *Aliment Pharmacol Ther* **51**, 261–270 (2020).
14. Inflammatory Bowel Disease. *Jones' Clinical Paediatric Surgery* 147–152 (2014) doi:10.1002/9781118777305.CH24.
15. Çekin, A. H. A microbial signature for Crohn's disease. *Turkish Journal of Gastroenterology* **28**, 237–238 (2017).
16. Caruso, R., Lo, B. C. & Núñez, G. Host–microbiota interactions in inflammatory bowel disease. *Nat Rev Immunol* **20**, 411–426 (2020).
17. Duerr, R. H. Genetics of inflammatory bowel disease. *Inflamm Bowel Dis* **2**, 48–60 (1996).

18. Duerr, R. H. Genome-Wide Association Studies Herald a New Era of Rapid Discoveries in Inflammatory Bowel Disease Research. *Gastroenterology* **132**, 2045–2049 (2007).

19. Cooney, R. *et al.* NOD2 stimulation induces autophagy in dendritic cells influencing bacterial handling and antigen presentation. *Nature Medicine 2009 16:1* **16**, 90–97 (2009).

20. Cooney, R. *et al.* NOD2 stimulation induces autophagy in dendritic cells influencing bacterial handling and antigen presentation. *Nature Medicine 2009 16:1* **16**, 90–97 (2009).

21. Ogura, Y. *et al.* A frameshift mutation in NOD2 associated with susceptibility to Crohn's disease. *Nature* **411**, 603–606 (2001).

22. Levine, B. & Kroemer, G. Autophagy in the pathogenesis of disease. *Cell* **132**, 27–42 (2008).

23. Cummings, J. R. F. *et al.* Confirmation of the role of ATG16L1 as a Crohn's disease susceptibility gene. *Inflamm. Bowel Dis.* **13**, 941–946 (2007).

24. Hampe, J. *et al.* A genome-wide association scan of nonsynonymous SNPs identifies a susceptibility variant for Crohn disease in ATG16L1. *Nat. Genet.* **39**, 207–211 (2007).

25. Hugot, J. P. *et al.* Association of NOD2 leucine-rich repeat variants with susceptibility to Crohn's disease. *Nature* **411**, 599–603 (2001).

26. Prescott, N. J. *et al.* A nonsynonymous SNP in ATG16L1 predisposes to ileal Crohn's disease and is independent of CARD15 and IBD5. *Gastroenterology* **132**, 1665–1671 (2007).

27. Rioux, J. D. *et al.* Genome-wide association study identifies new susceptibility loci for Crohn disease and implicates autophagy in disease pathogenesis. *Nat. Genet.* **39**, 596–604 (2007).

28. Duerr, R. H. *et al.* A genome-wide association study identifies IL23R as an inflammatory bowel disease gene. *Science (1979)* **314**, 1461–1463 (2006).

29. Tremelling, M. *et al.* IL23R Variation Determines Susceptibility But Not Disease Phenotype in Inflammatory Bowel Disease. *Gastroenterology* **132**, 1657–1664 (2007).

30. Bengtson, M. B. *et al.* Familial aggregation in Crohn's disease and ulcerative colitis in a Norwegian population-based cohort followed for ten years. *J. Crohns Colitis* **3**, 92–99 (2009).

31. Brant, S. R. Update on the heritability of inflammatory bowel disease: the importance of twin studies. *Inflamm. Bowel Dis.* **17**, 1–5 (2011).

32. Halme, L. *et al.* Family and twin studies in inflammatory bowel disease. *World Journal of Gastroenterology : WJG* **12**, 3668 (2006).

33. Rivas, M. A. *et al.* Deep resequencing of GWAS loci identifies independent rare variants associated with inflammatory bowel disease. *Nature Genetics 2011 43:11* **43**, 1066–1073 (2011).

34. Piovani, D. *et al.* Environmental Risk Factors for Inflammatory Bowel Diseases: An Umbrella Review of Meta-analyses. *Gastroenterology* **157**, 647-659.e4 (2019).

35. Malik, T. A. Inflammatory Bowel Disease. Historical Perspective, Epidemiology, and Risk Factors. *Surgical Clinics of North America* **95**, 1105–1122 (2015).

36. Reif, S., Klein, I., Arber, N. & Gilat, T. Lack of association between smoking and inflammatory bowel disease in Jewish patients in Israel. *Gastroenterology* **108**, 1683–1687 (1995).

37. Narula, N. *et al.* Associations of Antibiotics, Hormonal Therapies, Oral Contraceptives, and Long-Term NSAIDS With Inflammatory Bowel Disease: Results From the Prospective Urban Rural Epidemiology (PURE) Study. *Clinical Gastroenterology and Hepatology* (2023) doi:10.1016/j.cgh.2022.11.037.

38. Lautenschlager, S. A. *et al.* Lifestyle factors associated with inflammatory bowel disease: data from the Swiss IBD cohort study. *BMC Gastroenterol* **23**, (2023).

39. Steensberg, A. *et al.* Strenuous exercise decreases the percentage of type 1 T cells in the circulation. *J Appl Physiol* **91**, 1708–1712 (2001).

40. Mawdsley, J. E. & Rampton, D. S. The role of psychological stress in inflammatory bowel disease. *Neuroimmunomodulation* **13**, 327–336 (2006).

41. Goodhand, J. R. *et al.* Do Antidepressants Influence the Disease Course in Inflammatory Bowel Disease? A Retrospective Case-Matched Observational Study. *Inflamm Bowel Dis* **18**, 1232–1239 (2012).

42. Mawdsley, J. E. & Rampton, D. S. Psychological stress in IBD: New insights into pathogenic and therapeutic implications. *Gut* **54**, 1481–1491 (2005).

43. Ananthakrishnan, A. N., McGinley, E. L., Binion, D. G. & Saeian, K. Ambient air pollution correlates with hospitalizations for inflammatory bowel diseaseAn ecologic analysis. *Inflamm Bowel Dis* **17**, 1138–1145 (2011).

44. Loftus, E. V. Clinical epidemiology of inflammatory bowel disease: incidence, prevalence, and environmental influences. *Gastroenterology* **126**, 1504–1517 (2004).

45. Levine, A., Sigall Boneh, R. & Wine, E. Evolving role of diet in the pathogenesis and treatment of inflammatory bowel diseases. *Gut* **67**, 1726–1738 (2018).

46. Pigneur, B. *et al.* Mucosal Healing and Bacterial Composition in Response to Enteral Nutrition Vs Steroid-based Induction Therapy—A Randomised Prospective Clinical Trial in Children With Crohn's Disease. *J Crohns Colitis* **13**, 846–855 (2019).

47. Vancamelbeke, M. & Vermeire, S. The intestinal barrier: a fundamental role in health and disease. *Expert Rev Gastroenterol Hepatol* **11**, 821 (2017).

48. Muniz, L. R., Knosp, C. & Yeretssian, G. Intestinal antimicrobial peptides during homeostasis, infection, and disease. *Front Immunol* **3**, 32484 (2012).

49. Artis, D. Epithelial-cell recognition of commensal bacteria and maintenance of immune homeostasis in the gut. *Nature Rev. Immunol.* **8**, 411–420 (2008).

50. Turner, J. R. Intestinal mucosal barrier function in health and disease. *Nature Reviews Immunology 2009 9:11* **9**, 799–809 (2009).

51. Bjarnason, I., Macpherson, A. & Hollander, D. Intestinal permeability: An overview. *Gastroenterology* **108**, 1566–1581 (1995).

52. Pearson, A. D. J., Eastham, E. J., Laker, M. F., Craft, A. W. & Nelson, R. Intestinal permeability in children with Crohn's disease and coeliac disease. *Br Med J* **285**, 20–21 (1982).

53. Groschwitz, K. R. & Hogan, S. P. Intestinal barrier function: Molecular regulation and disease pathogenesis. *Journal of Allergy and Clinical Immunology* **124**, 3–20 (2009).

54. Salim, S. Y. & Söderholm, J. D. Importance of disrupted intestinal barrier in inflammatory bowel diseases. *Inflamm Bowel Dis* **17**, 362–381 (2011).

55. Hooper, L., Immunology, A. M.-N. R. & 2010, undefined. Immune adaptations that maintain homeostasis with the intestinal microbiota. *nature.comLV Hooper, AJ MacphersonNature Reviews Immunology, 2010•nature.com*.

56. Artis, D. Epithelial-cell recognition of commensal bacteria and maintenance of immune homeostasis in the gut. *Nature Reviews Immunology 2008 8:6* **8**, 411–420 (2008).

57. Kiuchi-Saishin, Y. *et al.* Differential expression patterns of claudins, tight junction membrane proteins, in mouse nephron segments. *J. Am. Soc. Nephrol.* **13**, 875–886 (2002).

58. Medzhitov, R. & Janeway, C. A. Decoding the Patterns of Self and Nonself by the Innate Immune System. *Science (1979)* **296**, 298–300 (2002).

59. Ukabam, S. O., Clamp, J. R. & Cooper, B. T. Abnormal small intestinal permeability to sugars in patients with crohn's disease of the terminal ileum and colon. *Digestion* **27**, 70–74 (1983).

60. Zhang, M. *et al.* Interactions between Intestinal Microbiota and Host Immune Response in Inflammatory Bowel Disease. *Front Immunol* **8**, (2017).

61. Antoni, L., Nuding, S., Wehkamp, J. & Stange, E. F. Intestinal barrier in inflammatory bowel disease. *World Journal of Gastroenterology : WJG* **20**, 1165 (2014).

62. Wells, J. M., Rossia, O., Meijerink, M. & Van Baarlen, P. Epithelial crosstalk at the microbiota-mucosal interface. *Proc Natl Acad Sci U S A* **108**, 4607–4614 (2011).

63. Salim, S., diseases, J. S.-I. bowel & 2011, undefined. Importance of disrupted intestinal barrier in inflammatory bowel diseases. *academic.oup.comSY Salim, JD SöderholmInflammatory bowel diseases, 2011•academic.oup.com*.

64. Silva, F. A. R., Rodrigues, B. L., Ayrizono, M. D. L. S. & Leal, R. F. The Immunological Basis of Inflammatory Bowel Disease. *Gastroenterol Res Pract* **2016**, (2016).

65. Imam, T., Park, S., Kaplan, M. H. & Olson, M. R. Effector T Helper Cell Subsets in Inflammatory Bowel Diseases. *Front Immunol* **9**, 1 (2018).

66. Emmrich, J., Seyfarth, M., Fleig, W. E. & Emmrich, F. Treatment of inflammatory bowel disease with anti-CD4 monoclonal antibody. *The Lancet* **338**, 570–571 (1991).

67. Hsieh, C. S. *et al.* Development of TH1 CD4+ T cells through IL-12 produced by Listeria-induced macrophages. *Science (1979)* **260**, 547–549 (1993).

68. Powrie, F. *et al.* Inhibition of Thl responses prevents inflammatory bowel disease in scid mice reconstituted with CD45RBhi CD4+ T cells. *Immunity* **1**, 553–562 (1994).

69. Thieu, V. T. *et al.* Signal transducer and activator of transcription 4 is required for the transcription factor T-bet to promote T helper 1 cell-fate determination. *cell.comVT Thieu, Q Yu, HC Chang, N Yeh, ET Nguyen, S Sehra, MH KaplanImmunity, 2008•cell.com* **29**, 679–690 (2008).

70. Nava, P. *et al.* Interferon-γ Regulates Intestinal Epithelial Homeostasis through Converging β-Catenin Signaling Pathways. *Immunity* **32**, 392–402 (2010).

71. Lawson, M. M., Thomas, A. G. & Akobeng, A. K. Tumour necrosis factor alpha blocking agents for induction of remission in ulcerative colitis. *Cochrane Database of Systematic Reviews* (2009) doi:10.1002/14651858.CD005112.PUB2/MEDIA/CDSR/CD005112/IMAGE_N/N CD005112-CMP-003-01.PNG.

72. Hsieh, C. S. *et al.* Development of TH1 CD4+ T cells through IL-12 produced by Listeria-induced macrophages. *Science (1979)* **260**, 547–549 (1993).

73. Stronkhorst, A. *et al.* CD4 antibody treatment in patients with active Crohn's disease: A phase 1 dose finding study. *Gut* **40**, 320–327 (1997).

74. Thelemann, C. *et al.* Interferon-γ induces expression of MHC class II on intestinal epithelial cells and protects mice from colitis. *PLoS One* **9**, (2014).

75. Soderquest, K. *et al.* Genetic variants alter T-bet binding and gene expression in mucosal inflammatory disease. *PLoS Genet* **13**, (2017).

76. Weaver, C. T., Elson, C. O., Fouser, L. A. & Kolls, J. K. The Th17 pathway and inflammatory diseases of the intestines, lungs, and skin. *Annual Review of Pathology: Mechanisms of Disease* **8**, 477–512 (2013).

77. Meitei, H., Jadhav, N., reviews, G. L.-A. & 2021, undefined. CCR6-CCL20 axis as a therapeutic target for autoimmune diseases. *Elsevier*.

78. Matsunaga, Y., Clark, T., Wanek, A., … J. B.-T. J. of & 2021, undefined. Intestinal IL-17R signaling controls secretory IgA and oxidase balance in Citrobacter rodentium infection. *journals.aai.orgY Matsunaga, T Clark, AG Wanek, JP Bitoun, Q Gong, M Good, JK KollsThe Journal of Immunology, 2021•journals.aai.org*.

79. Chen, J. *et al.* IL-17 inhibits CXCL9/10-mediated recruitment of CD8+ cytotoxic T cells and regulatory T cells to colorectal tumors. *J Immunother Cancer* **7**, (2019).

80. Ueno, A. *et al.* Th17 plasticity and its relevance to inflammatory bowel disease. *J Autoimmun* **87**, 38–49 (2018).

81. Chen, L. *et al.* The role of Th17 cells in inflammatory bowel disease and the research progress. *Front Immunol* **13**, 1055914 (2023).

82. Harrington, L. E. *et al.* Interleukin 17-producing CD4+ effector T cells develop via a lineage distinct from the T helper type 1 and 2 lineages. *Nat Immunol* **6**, 1123–1132 (2005).

83. Park, H. *et al.* A distinct lineage of CD4 T cells regulates tissue inflammation by producing interleukin 17. *Nat Immunol* **6**, 1133–1141 (2005).

84. Yang, J., Sundrud, M. S., Skepner, J. & Yamagata, T. Targeting Th17 cells in autoimmune diseases. *Trends Pharmacol Sci* **35**, 493–500 (2014).

85. Yan, J. Bin, Luo, M. M., Chen, Z. Y. & He, B. H. The Function and Role of the Th17/Treg Cell Balance in Inflammatory Bowel Disease. *J Immunol Res* **2020**, (2020).

86. Barbara, G. *et al.* Inflammatory and Microbiota-Related Regulation of the Intestinal Epithelial Barrier. *Front Nutr* **8**, 718356 (2021).

87. Steinbach, E. C. & Plevy, S. E. The role of macrophages and dendritic cells in the initiation of inflammation in IBD. *Inflamm Bowel Dis* **20**, 166 (2014).

88. Geremia, A., Biancheri, P., Allan, P., Corazza, G. R. & Di Sabatino, A. Innate and adaptive immunity in inflammatory bowel disease. *Autoimmun Rev* **13**, 3–10 (2014).

89. Mosser, D., immunology, J. E.-N. reviews & 2008, undefined. Exploring the full spectrum of macrophage activation. *nature.comDM Mosser, JP EdwardsNature reviews immunology, 2008•nature.com*.

90. Bijarchian, F., Taghiyar, L., Azhdari, Z. & Eslaminejad, M. B. M2c Macrophages enhance phalange regeneration of amputated mice digits in an organ co-culture system. *Iran J Basic Med Sci* **24**, 1602 (2021).

91. Dale, D. C., Boxer, L. & Conrad Liles, W. The phagocytes: neutrophils and monocytes. *Blood* **112**, 935–945 (2008).

92. Edwards, J., Zhang, X., … K. F.-J. of leukocyte & 2006, undefined. Biochemical and functional characterization of three activated macrophage populations. *academic.oup.comJP Edwards, X Zhang, KA Frauwirth, DM MosserJournal of leukocyte biology, 2006•academic.oup.com*.

93. Bettelli, E. *et al.* Reciprocal developmental pathways for the generation of pathogenic effector TH17 and regulatory T cells. *nature.comE Bettelli, Y Carrier, W Gao, T Korn, TB Strom, M Oukka, HL Weiner, VK KuchrooNature, 2006•nature.com*.

94. Langrish, C., Chen, Y., … W. B.-T. J. of & 2005, undefined. IL-23 drives a pathogenic T cell population that induces autoimmune inflammation. *rupress.orgCL Langrish, Y Chen, WM Blumenschein, J Mattson, B Basham, JD SedgwickThe Journal of experimental medicine, 2005•rupress.org*.

95. Bates, J. & Diehl, L. Dendritic cells in IBD pathogenesis: an area of therapeutic opportunity? *J Pathol* **232**, 112 (2014).

96. Maloy, K., immunology, M. K.-M. & 2008, undefined. IL-23 and Th17 cytokines in intestinal homeostasis. *Elsevier*.

97. Ahern, P. P. *et al.* Interleukin-23 drives intestinal inflammation through direct activity on T cells. *cell.comPP Ahern, C Schiering, S Buonocore, MJ McGeachy, DJ Cua, KJ Maloy, F PowrieImmunity, 2010•cell.com* doi:10.1016/j.immuni.2010.08.010.

98. Pidasheva, S. *et al.* Functional studies on the IBD susceptibility gene IL23R implicate reduced receptor function in the protective genetic variant R381Q. *PLoS One* **6**, (2011).

99.   Sarin, R., Wu, X. & Abraham, C. Inflammatory disease protective R381Q IL23 receptor polymorphism results in decreased primary CD4+ and CD8+ human T-cell functional responses. *Proc Natl Acad Sci U S A* **108**, 9560–9565 (2011).

100.   Nathan, C., Cell, A. D.- & 2010, undefined. Nonresolving inflammation. *cell.comC Nathan, A DingCell, 2010•cell.com*.

101.   Vong, L., Ferraz, J. G. P., Panaccione, R., Beck, P. L. & Wallace, J. L. A pro-resolution mediator, prostaglandin D2, is specifically up-regulated in individuals in long-term remission from ulcerative colitis. *Proc Natl Acad Sci U S A* **107**, 12023–12027 (2010).

102.   Wang, K. *et al.* A potential therapeutic approach for ulcerative colitis: targeted regulation of macrophage polarization through phytochemicals. *Front Immunol* **14**, 1155077 (2023).

103.   Mizoguchi, A. & Bhan, A. K. Immunobiology of B cells in inflammatory bowel disease. *Crohn's Disease and Ulcerative Colitis: From Epidemiology and Immunobiology to a Rational Diagnostic and Therapeutic Approach* 161–168 (2012) doi:10.1007/978-1-4614-0998-4_12.

104.   Brandtzaeg, P. & Johansen, F. E. Mucosal B cells: Phenotypic characteristics, transcriptional regulation, and homing properties. *Immunol Rev* **206**, 32–63 (2005).

105.   Brandtzaeg, P., Carlsen, H. S. & Halstensen, T. S. The B-cell system in inflammatory bowel disease. *Adv Exp Med Biol* **579**, 149–167 (2006).

106.   Uo, M. *et al.* Mucosal CXCR4+ IgG plasma cells contribute to the pathogenesis of human ulcerative colitis through FcγR-mediated CD14 macrophage activation. *gut.bmj.comM Uo, T Hisamatsu, J Miyoshi, D Kaito, K Yoneno, MT Kitazume, M Mori, A SugitaGut, 2013•gut.bmj.com* doi:10.1136/gutjnl-2012.

107.   Blair, P. A. *et al.* CD19+CD24hiCD38hi B Cells Exhibit Regulatory Capacity in Healthy Individuals but Are Functionally Impaired in Systemic Lupus Erythematosus Patients. *Immunity* **32**, 129–140 (2010).

108.   Kawamura, T., Kanai, T., … T. D.-T. J. of & 2004, undefined. Ectopic CD40 ligand expression on B cells triggers intestinal inflammation. *journals.aai.orgT Kawamura, T Kanai, T Dohi, K Uraushihara, T Totsuka, R Iiyama, C Taneda, M YamazakiThe Journal of Immunology, 2004•journals.aai.org*.

109.   Aziz, M., Holodick, N. E., Rothstein, T. L. & Wang, P. The role of B-1 cells in inflammation. *Immunol Res* **63**, 153–166 (2015).

110.   McPherson, M. *et al.* Colitis immunoregulation by CD8+ T cell requires T cell cytotoxicity and B cell peptide antigen presentation. *Am J Physiol Gastrointest Liver Physiol* **295**, (2008).

111.   Su, Y., Carey, G., Maric, M., Immunology, D. S.-T. J. of & 2008, undefined. B cells induce tolerance by presenting endogenous peptide-IgG on MHC class II molecules via an IFN-γ-inducible lysosomal thiol reductase-dependent pathway. *journals.aai.orgY Su, G Carey, M Maric, DW ScottThe Journal of Immunology, 2008•journals.aai.org*.

112.   Mizoguchi, A. & Bhan, A. K. Immunobiology of B cells in inflammatory bowel disease. *Crohn's Disease and Ulcerative Colitis: From Epidemiology and Immunobiology to a Rational Diagnostic and Therapeutic Approach: Second Edition* 111–116 (2017) doi:10.1007/978-3-319-33703-6_9/FIGURES/1.

113.   Noronha, A. M. *et al.* Hyperactivated B cells in human inflammatory bowel disease. *J Leukoc Biol* **86**, 1007–1016 (2009).

114.   Clemente, J. C., Manasson, J. & Scher, J. U. The role of the gut microbiome in systemic inflammatory disease. *BMJ* **360**, (2018).

115.   Jiang, W., Gong, L., Liu, F., Ren, Y. & Mu, J. Alteration of Gut Microbiome and Correlated Lipid Metabolism in Post-Stroke Depression. *Front Cell Infect Microbiol* **11**, (2021).

116. Shreiner, A. B., Kao, J. Y. & Young, V. B. The gut microbiome in health and in disease. *Curr Opin Gastroenterol* **31**, 69–75 (2015).

117. Greenblum, S., Turnbaugh, P. J. & Borenstein, E. Metagenomic systems biology of the human gut microbiome reveals topological shifts associated with obesity and inflammatory bowel disease. *Proc Natl Acad Sci U S A* **109**, 594–599 (2012).

118. Ko, Y. *et al.* Inflammatory Bowel Disease Environmental Risk Factors: A Population-Based Case-Control Study of Middle Eastern Migration to Australia. *Clinical Gastroenterology and Hepatology* **13**, 1453-1463.e1 (2015).

119. Qiu, P. *et al.* The Gut Microbiota in Inflammatory Bowel Disease. *Front Cell Infect Microbiol* **12**, 733992 (2022).

120. Caruso, R., Lo, B. C. & Núñez, G. Host–microbiota interactions in inflammatory bowel disease. *Nat Rev Immunol* **20**, 411–426 (2020).

121. Qiu, P. *et al.* The Gut Microbiota in Inflammatory Bowel Disease. *Front Cell Infect Microbiol* **12**, 733992 (2022).

122. Alexeev, E. E. *et al.* Microbiota-Derived Indole Metabolites Promote Human and Murine Intestinal Homeostasis through Regulation of Interleukin-10 Receptor. *American Journal of Pathology* **188**, 1183–1194 (2018).

123. Allen-Vercoe, E. & Coburn, B. A Microbiota-Derived Metabolite Augments Cancer Immunotherapy Responses in Mice. *Cancer Cell* **38**, 452–453 (2020).

124. Santana, P. T., Rosas, S. L. B., Ribeiro, B. E., Marinho, Y. & de Souza, H. S. P. Dysbiosis in Inflammatory Bowel Disease: Pathogenic Role and Potential Therapeutic Targets. *Int J Mol Sci* **23**, (2022).

125. Vich Vila, A. *et al.* Gut microbiota composition and functional changes in inflammatory bowel disease and irritable bowel syndrome. *Sci Transl Med* **10**, (2018).

126. Kaakoush, N. O. *et al.* Microbial dysbiosis in pediatric patients with Crohn's disease. *J Clin Microbiol* **50**, 3258–3266 (2012).

127. Imhann, F. *et al.* Interplay of host genetics and gut microbiota underlying the onset and clinical presentation of inflammatory bowel disease. *Gut* **67**, 108–119 (2018).

128. Halfvarson, J. *et al.* Dynamics of the human gut microbiome in inflammatory bowel disease. *Nature Microbiology 2017 2:5* **2**, 1–7 (2017).

129. Sokol, H. *et al.* Faecalibacterium prausnitzii is an anti-inflammatory commensal bacterium identified by gut microbiota analysis of Crohn disease patients. *Proc Natl Acad Sci U S A* **105**, 16731–16736 (2008).

130. Bischoff, S. C. *et al.* Intestinal permeability - a new target for disease prevention and therapy. *BMC Gastroenterol* **14**, (2014).

131. Michielan, A. & D'Incà, R. Intestinal Permeability in Inflammatory Bowel Disease: Pathogenesis, Clinical Evaluation, and Therapy of Leaky Gut. *Mediators Inflamm* **2015**, (2015).

132. Merga, Y., Campbell, B., diseases, J. R.-D. & 2014, undefined. Mucosal barrier, bacteria and inflammatory bowel disease: possibilities for therapy. *karger.comY Merga, BJ Campbell, JM RhodesDigestive diseases, 2014•karger.com*.

133. Vindigni, S. M., Zisman, T. L., Suskind, D. L. & Damman, C. J. The intestinal microbiome, barrier function, and immune system in inflammatory bowel disease: a tripartite pathophysiological circuit with implications for new therapeutic directions. *Therap Adv Gastroenterol* **9**, 606 (2016).

134. Png, C., Lindén, S., … K. G.-O. journal of the & 2010, undefined. Mucolytic bacteria with increased prevalence in IBD mucosa augmentin vitroutilization of mucin by other bacteria. *journals.lww.comCW Png, SK Lindén, KS Gilshenan, EG Zoetendal, CS McSweeney, LI Sly, MA McGuckinOfficial journal of the American College of Gastroenterology| ACG, 2010•journals.lww.com*.

135. Berkes, J., Viswanathan, V. K., Savkovic, S. D. & Hecht, G. Intestinal epithelial responses to enteric pathogens: effects on the tight junction barrier, ion transport, and inflammation. *Gut* **52**, 439–451 (2003).

136. Hooper, L. V. *et al.* Molecular Analysis of Commensal Host-Microbial Relationships in the Intestine. *Science (1979)* **291**, 881–884 (2001).

137. Zareie, M. *et al.* Novel effects of the prototype translocating Escherichia coli, strain C25 on intestinal epithelial structure and barrier function. *Cell Microbiol* **7**, 1782–1797 (2005).

138. Khaloian, S. *et al.* Mitochondrial impairment drives intestinal stem cell transition into dysfunctional Paneth cells predicting Crohn's disease recurrence. *Gut* **69**, 1939–1951 (2020).

139. Goethel, A., Croitoru, K. & Philpott, D. J. The interplay between microbes and the immune response in inflammatory bowel disease. *J Physiol* **596**, 3869 (2018).

140. Kawai, T. & Akira, S. Review Toll-like Receptors and Their Crosstalk with Other Innate Receptors in Infection and Immunity. *Immunity* **34**, 637–650 (2011).

141. Hisamatsu, T. *et al.* Immune aspects of the pathogenesis of inflammatory bowel disease. *Pharmacol Ther* **137**, 283–297 (2013).

142. Korta, A., Kula, J. & Gomułka, K. The Role of IL-23 in the Pathogenesis and Therapy of Inflammatory Bowel Disease. *Int J Mol Sci* **24**, 10172 (2023).

143. Goethel, A., Croitoru, K. & Philpott, D. J. The interplay between microbes and the immune response in inflammatory bowel disease. *J Physiol* **596**, 3869 (2018).

144. Moayyedi, P. *et al.* Fecal microbiota transplantation induces remission in patients with active ulcerative colitis in a randomized controlled trial. *Elsevier*.

145. Viladomiu, M. *et al.* IgA-coated E. Coli enriched in Crohn's disease spondyloarthritis promote TH17-dependent inflammation. *Sci Transl Med* **9**, (2017).

146. Simpson, S. J. *et al.* T cell-mediated pathology in two models of experimental colitis depends predominantly on the interleukin 12/signal transducer and activator of transcription (Stat)-4 pathway, but is not conditional on interferon γ expression by T cells. *Journal of Experimental Medicine* **187**, 1225–1234 (1998).

147. Jin, Y., Lin, Y., Lin, L. & Zheng, C. IL-17/IFN-γ interactions regulate intestinal inflammation in TNBS-induced acute colitis. *Journal of Interferon and Cytokine Research* **32**, 548–556 (2012).

148. Fujii, M. *et al.* Expression of Interleukin-26 is upregulated in inflammatory bowel disease. *World J Gastroenterol* **23**, 5519 (2017).

149. Alexander, M. *et al.* Human gut bacterial metabolism drives Th17 activation and colitis. *Cell Host Microbe* **30**, 17-30.e9 (2022).

150. Devkota, S., Wang, Y., Musch, M., Nature, V. L.- & 2012, undefined. Dietary-fat-induced taurocholic acid promotes pathobiont expansion and colitis in Il10−/− mice. *nature.comS Devkota, Y Wang, MW Musch, V Leone, H Fehlner-Peach, A Nadimpalli, DA AntonopoulosNature, 2012•nature.com*.

151. Dalal, S. R. & Chang, E. B. The microbial basis of inflammatory bowel diseases. *J Clin Invest* **124**, 4190 (2014).

152. Uzzan, M., Colombel, J. F., Cerutti, A., Treton, X. & Mehandru, S. B Cell-Activating Factor (BAFF)-Targeted B Cell Therapies in Inflammatory Bowel Diseases. *Dig Dis Sci* **61**, 3407–3424 (2016).

153. Mizoguchi, A. *et al.* Cytokine imbalance and autoantibody production in T cell receptor-alpha mutant mice with inflammatory bowel disease. *rupress.orgA Mizoguchi, E Mizoguchi, C Chiba, GM Spiekermann, S Tonegawa, C Nagler-AndersonThe Journal of experimental medicine, 1996•rupress.org*.

154. Ferreira-Gomes, M. *et al.* B Cell Recognition of Candida albicans Hyphae via TLR 2 Promotes IgG1 and IL-6 Secretion for TH17 Differentiation. *Front Immunol* **12**, (2021).

155. Sartor, R., Gastroenterology, G. W.- & 2017, undefined. Roles for intestinal bacteria, viruses, and fungi in pathogenesis of inflammatory bowel diseases and therapeutic approaches. *Elsevier*.

156. Scaldaferri, F., Gerardi, V., … F. M.-W. journal of & 2016, undefined. Role and mechanisms of action of Escherichia coli Nissle 1917 in the maintenance of remission in ulcerative colitis patients: an update. *ncbi.nlm.nih.govF Scaldaferri, V Gerardi, F Mangiola, LR Lopetuso, M Pizzoferrato, V Petito, A PapaWorld journal of gastroenterology, 2016•ncbi.nlm.nih.gov*.

157. Praveschotinunt, P. *et al.* Engineered E. coli Nissle 1917 for the delivery of matrix-tethered therapeutic domains to the gut. *Nature Communications 2019 10:1* **10**, 1–14 (2019).

158. Nishida, A. *et al.* Can control of gut microbiota be a future therapeutic option for inflammatory bowel disease? *World J Gastroenterol* **27**, 3317–3326 (2021).

159. Saha, S., Mara, K., Pardi, D. S. & Khanna, S. Long-term Safety of Fecal Microbiota Transplantation for Recurrent Clostridioides difficile Infection. *Gastroenterology* **160**, 1961-1969.e3 (2021).

160. Moayyedi, P. *et al.* Fecal microbiota transplantation induces remission in patients with active ulcerative colitis in a randomized controlled trial. *Elsevier*.

161. Bajaj, J. S. *et al.* Fecal microbiota transplant from a rational stool donor improves hepatic encephalopathy: A randomized clinical trial. *Hepatology* **66**, 1727–1738 (2017).

162. Nicholson, J. K. & Lindon, J. C. Systems biology: Metabonomics. *Nature* **455**, 1054–1056 (2008).

163. Lin, H. M., Helsby, N. A., Rowan, D. D. & Ferguson, L. R. Using metabolomic analysis to understand inflammatory bowel diseases. *Inflamm Bowel Dis* **17**, 1021–1029 (2011).

164. Kaddurah-Daouk, R., Kristal, B. S. & Weinshilboum, R. M. Metabolomics: A global biochemical approach to drug response and disease. *Annu Rev Pharmacol Toxicol* **48**, 653–683 (2008).

165. Worley, B., metabolomics, R. P.-C. & 2013, undefined. Multivariate analysis in metabolomics. *ingentaconnect.comB Worley, R PowersCurrent metabolomics, 2013•ingentaconnect.com*.

166. Nyamundanda, G., Brennan, L. & Gormley, I. C. Probabilistic principal component analysis for metabolomic data. *BMC Bioinformatics* **11**, 1–11 (2010).

167. Gromski, P. S. *et al.* A tutorial review: Metabolomics and partial least squares-discriminant analysis--a marriage of convenience or a shotgun wedding. *Anal Chim Acta* **879**, 10–23 (2015).

168. Gallagher, K., Catesson, A., Griffin, J. L., Holmes, E. & Williams, H. R. T. Metabolomic Analysis in Inflammatory Bowel Disease: A Systematic Review. *J Crohns Colitis* **15**, 813–826 (2021).

169. Marczyk, M., Drazek, G., Pietrowska, M., … P. W.-P. C. & 2015, undefined. Modeling of imaging mass spectrometry data and testing by permutation for biomarkers discovery in tissues. *Elsevier*.

170. Carreira, R. J. *et al.* Large-scale mass spectrometry imaging investigation of consequences of cortical spreading depression in a transgenic mouse model of migraine. *J Am Soc Mass Spectrom* **26**, 853–861 (2015).

171. Oetjen, J. *et al.* An approach to optimize sample preparation for MALDI imaging MS of FFPE sections using fractional factorial design of experiments. *Anal Bioanal Chem* **408**, 6729–6740 (2016).

172. Buchberger, A. R., DeLaney, K., Johnson, J. & Li, L. Mass Spectrometry Imaging: A Review of Emerging Advancements and Future Insights. *Anal Chem* **90**, 240 (2018).

173. Shen, A., Jiang, H., Fu, H. & He, K. False Discovery Rate Control in Cancer Biomarker Selection Using Knockoffs. *Cancers (Basel)* **11**, (2019).

174. Gilbert, J. A. *et al.* Microbiome-wide association studies link dynamic microbial consortia to disease. *Nature* **535**, 94–103 (2016).

175. Soret, R. *et al.* Short-chain fatty acids regulate the enteric neurons and control gastrointestinal motility in rats. *Gastroenterology* **138**, (2010).

176. Maurice, C. F., Haiser, H. J. & Turnbaugh, P. J. Xenobiotics shape the physiology and gene expression of the active human gut microbiome. *Cell* **152**, 39–50 (2013).

177. Quinn, R. A. *et al.* Microbial, host and xenobiotic diversity in the cystic fibrosis sputum metabolome. *ISME J* **10**, 1483–1498 (2015).

178. Brestoff, J. R. & Artis, D. Commensal bacteria at the interface of host metabolism and the immune system. *Nat Immunol* **14**, 676–684 (2013).

179. Bishai, J. D. & Palm, N. W. Small Molecule Metabolites at the Host–Microbiota Interface. *The Journal of Immunology* **207**, 1725–1733 (2021).

180. Zheng, L., Wen, X.-L. & Duan, S.-L. Role of metabolites derived from gut microbiota in inflammatory bowel disease. *World J Clin Cases* **10**, 2660–2677 (2022).

181. Funabashi, M. *et al.* A metabolic pathway for bile acid dehydroxylation by the gut microbiome. *Nature* **582**, 566–570 (2020).

182. Ocvirk, S. & O'Keefe, S. J. D. Dietary fat, bile acid metabolism and colorectal cancer. *Semin Cancer Biol* **73**, 347–355 (2021).

183. Guzior, D. V & Quinn, R. A. Review: microbial transformations of human bile acids. *Microbiome* **9**, 140 (2021).

184. Xiao, H. & Kang, S. The Role of the Gut Microbiome in Energy Balance With a Focus on the Gut-Adipose Tissue Axis. *Front Genet* **11**, 297 (2020).

185. Barra, M., Danino, T. & Garrido, D. Engineered Probiotics for Detection and Treatment of Inflammatory Intestinal Diseases. *Front Bioeng Biotechnol* **8**, 265 (2020).

186. Pavlidis, P. *et al.* Systematic review: bile acids and intestinal inflammation-luminal aggressors or regulators of mucosal defence? *Aliment Pharmacol Ther* **42**, 802–817 (2015).

187. Thomas, J. P., Modos, D., Rushbrook, S. M., Powell, N. & Korcsmaros, T. The Emerging Role of Bile Acids in the Pathogenesis of Inflammatory Bowel Disease . *Frontiers in Immunology* vol. 13 Preprint at https://www.frontiersin.org/articles/10.3389/fimmu.2022.829525 (2022).

188. Jaworska, K. *et al.* Inflammatory bowel disease is associated with increased gut-to-blood penetration of short-chain fatty acids: A new, non-invasive marker of a functional intestinal lesion. *Exp Physiol* **104**, 1226–1236 (2019).

189. Zhang, Z. *et al.* Regulatory role of short-chain fatty acids in inflammatory bowel disease. *Cell Communication and Signaling* **20**, 64 (2022).

190. Peng, L., He, Z., Chen, W., Holzman, I. R. & Lin, J. Effects of Butyrate on Intestinal Barrier Function in a Caco-2 Cell Monolayer Model of Intestinal Barrier. *Pediatr Res* **61**, 37–41 (2007).

191. Gasaly, N., Hermoso, M. A. & Gotteland, M. Butyrate and the Fine-Tuning of Colonic Homeostasis: Implication for Inflammatory Bowel Diseases. *Int J Mol Sci* **22**, 3061 (2021).

192. Wojciech, L., Tan, K. S. W. & Gascoigne, N. R. J. Taming the Sentinels: Microbiome-Derived Metabolites and Polarization of T Cells. *Int J Mol Sci* **21**, 7740 (2020).

193. Chang, P. V, Hao, L., Offermanns, S. & Medzhitov, R. The microbial metabolite butyrate regulates intestinal macrophage function via histone deacetylase inhibition. *Proc Natl Acad Sci U S A* **111**, 2247–2252 (2014).

194. Chen, J. & Vitetta, L. The Role of Butyrate in Attenuating Pathobiont-Induced Hyperinflammation. *Immune Netw* **20**, e15–e15 (2020).

195. Upadhyay, K. G., Desai, D. C., Ashavaid, T. F. & Dherai, A. J. Microbiome and metabolome in inflammatory bowel disease. *J Gastroenterol Hepatol* **38**, 34–43 (2023).

196. Chen, L.-M. *et al.* Tryptophan-kynurenine metabolism: a link between the gut and brain for depression in inflammatory bowel disease. *J Neuroinflammation* **18**, 135 (2021).

197. Haq, S., Grondin, J. A. & Khan, W. I. Tryptophan-derived serotonin-kynurenine balance in immune activation and intestinal inflammation. *FASEB J* **35**, e21888–e21888 (2021).

198. Alexeev, E. E. *et al.* Microbiota-Derived Indole Metabolites Promote Human and Murine Intestinal Homeostasis through Regulation of Interleukin-10 Receptor. *Am J Pathol* **188**, 1183–1194 (2018).

199. Scott, S. A., Fu, J. & Chang, P. V. Microbial tryptophan metabolites regulate gut barrier function via the aryl hydrocarbon receptor. *Proceedings of the National Academy of Sciences* **117**, 19376–19387 (2020).

200. Li, X., Zhang, B., Hu, Y. & Zhao, Y. New Insights Into Gut-Bacteria-Derived Indole and Its Derivatives in Intestinal and Liver Diseases . *Frontiers in Pharmacology* vol. 12 Preprint at https://www.frontiersin.org/articles/10.3389/fphar.2021.769501 (2021).

201. Jalandra, R., Makharia, G. K., Sharma, M. & Kumar, A. Inflammatory and deleterious role of gut microbiota-derived trimethylamine on colon cells. *Front Immunol* **13**, 8161 (2023).

202. Rath, S., Heidrich, B., Pieper, D. H. & Vital, M. Uncovering the trimethylamine-producing bacteria of the human gut microbiota. *Microbiome* **5**, (2017).

203. Fennema, D., Phillips, I. R. & Shephard, E. A. Trimethylamine and trimethylamine N-oxide, a Flavin-Containing Monooxygenase 3 (FMO3)-mediated host-microbiome metabolic axis implicated in health and disease. *Drug Metabolism and Disposition* **44**, 1839–1850 (2016).

204. Wilson, A. *et al.* Trimethylamine-N-oxide: A Novel Biomarker for the Identification of Inflammatory Bowel Disease. *Dig Dis Sci* **60**, 3620–3630 (2015).

205. Wang, Q. *et al.* Gut microbiota-dependent trimethylamine n-oxide pathway contributes to the bidirectional relationship between intestinal inflammation and periodontitis. *Front Cell Infect Microbiol* **12**, (2023).

206. El-Deeb, O. S. *et al.* Moderating Gut Microbiome/Mitochondrial Axis in Oxazolone Induced Ulcerative Colitis: The Evolving Role of β-Glucan and/or, Aldose Reductase Inhibitor, Fidarestat. *International Journal of Molecular Sciences 2023, Vol. 24, Page 2711* **24**, 2711 (2023).

207. Yue, C. *et al.* Trimethylamine N-oxide prime NLRP3 inflammasome via inhibiting ATG16L1-induced autophagy in colonic epithelial cells. *Biochem Biophys Res Commun* **490**, 541–551 (2017).

208. Jaworska, K. *et al.* TMA, A Forgotten Uremic Toxin, but Not TMAO, Is Involved in Cardiovascular Pathology. *Toxins (Basel)* **11**, (2019).

209. Hulme, H. *et al.* Microbiome-derived carnitine mimics as previously unknown mediators of gut-brain axis communication. *Sci Adv* **6**, (2020).

210. Tars, K. *et al.* Targeting carnitine biosynthesis: Discovery of new inhibitors against γ-butyrobetaine hydroxylase. *J Med Chem* **57**, 2213–2236 (2014).

211. Williams, H. R. T. *et al.* Differences in gut microbial metabolism are responsible for reduced hippurate synthesis in Crohn's disease. *BMC Gastroenterol* **10**, 108 (2010).

212. Jarmakiewicz-Czaja, S., Piątek, D. & Filip, R. The impact of selected food additives on the gastrointestinal tract in the example of nonspecific inflammatory bowel diseases. *Archives of Medical Science* **18**, 1286–1296 (2022).

213. Walczak-Nowicka, Ł. J. & Herbet, M. Sodium Benzoate—Harmfulness and Potential Use in Therapies for Disorders Related to the Nervous System: A Review. *Nutrients* **14**, (2022).

214. Oshima, Y. *et al.* Sodium benzoate attenuates 2,8-dihydroxyadenine nephropathy by inhibiting monocyte/macrophage TNF-α expression. *Sci Rep* **13**, 3331 (2023).

215. Gevers, D. *et al.* Cell Host & Microbe The Treatment-Naive Microbiome in New-Onset Crohn's Disease. *Cell Host Microbe* **15**, 382–392 (2014).

216. Campbell, H. E. *et al.* Review article: cinnamon- and benzoate-free diet as a primary treatment for orofacial granulomatosis. *Aliment Pharmacol Ther* **34**, 687–701 (2011).

217. Kamada, N., Seo, S. U., Chen, G. Y. & Núñez, G. Role of the gut microbiota in immunity and inflammatory disease. *Nat Rev Immunol* **13**, 321–335 (2013).

218. Fernandes, J., Su, W., Rahat-Rozenbloom, S., Wolever, T. M. S. & Comelli, E. M. Adiposity, gut microbiota and faecal short chain fatty acids are linked in adult humans. *Nutr Diabetes* **4**, (2014).

219. Mafra, D. *et al.* Role of altered intestinal microbiota in systemic inflammation and cardiovascular disease in chronic kidney disease. *Future Microbiol* **9**, 399–410 (2014).

220. Vavricka, S. R. *et al.* Extraintestinal Manifestations of Inflammatory Bowel Disease. *Inflamm Bowel Dis* **21**, 1982–1992 (2015).

221. Gaspar, R., Macedo, G. & Branco, C. C. Liver manifestations and complications in inflammatory bowel disease: A review. *World J Hepatol* **13**, 1956 (2021).

222. Navaneethan, U. & Shen, B. Hepatopancreatobiliary manifestations and complications associated with inflammatory bowel disease. *Inflamm Bowel Dis* **16**, 1598–1619 (2010).

223. Loftus, E. V., Sandborn, W. J., Lindor, K. D. & LaRusso, N. F. Interactions Between Chronic Liver Disease and Inflammatory Bowel Disease. *Inflamm Bowel Dis* **3**, 288–302 (1997).

224. Yaccob, A. & Mari, A. Review: Practical clinical approach to the evaluation of hepatobiliary disorders in inflammatory bowel disease. *Frontline Gastroenterol* **10**, 309 (2019).

225. Yarur, A. J., Czul, F. & Levy, C. Hepatobiliary manifestations of inflammatory bowel disease. *Inflamm Bowel Dis* **20**, 1655–1667 (2014).

226. Bessissow, T. *et al.* Incidence and Predictors of Nonalcoholic Fatty Liver Disease by Serum Biomarkers in Patients with Inflammatory Bowel Disease. *Inflamm Bowel Dis* **22**, 1937–1944 (2016).

227. Saubermann, L. J. *et al.* Hepatic issues and complications associated with inflammatory bowel disease: A clinical report from the naspghan inflammatory bowel disease and hepatology committees. *J Pediatr Gastroenterol Nutr* **64**, 639–652 (2017).

228. Chen, J. & Vitetta, L. Gut Microbiota Metabolites in NAFLD Pathogenesis and Therapeutic Implications. *Int J Mol Sci* **21**, 1–19 (2020).

229. Rodríguez-Reyna, T. S., Martínez-Reyes, C. & Yamamoto-Furusho, J. K. Rheumatic manifestations of inflammatory bowel disease. *World J Gastroenterol* **15**, 5517–5524 (2009).

230. Arvikar, S. L. & Fisher, M. C. Inflammatory bowel disease associated arthropathy. *Curr Rev Musculoskelet Med* **4**, 123 (2011).

231. Tautog, J. D. *et al.* The germfree state prevents development of gut and joint inflammatory disease in HLA-B27 transgenic rats. *Journal of Experimental Medicine* **180**, 2359–2364 (1994).

232. Orchard, T. R., Wordsworth, B. P. & Jewell, D. P. Peripheral arthropathies in inflammatory bowel disease: Their articular distribution and natural history. *Gut* **42**, 387–391 (1998).

233. Haslock, I. Arthritis and Crohn's disease. A family study. *Ann Rheum Dis* **32**, 479–486 (1973).

234. Calin, A., Porta, J., Fries, J. F. & Schurman, D. J. The clinical history as a screening test for ankylosing spondylitis. *Rhumatologie - Revue International de Rhumatologie* **6**, 445–449 (1976).

235. Meisinger, C. & Freuer, D. Rheumatoid arthritis and inflammatory bowel disease: A bidirectional two-sample Mendelian randomization study. *Semin Arthritis Rheum* **55**, 151992 (2022).

236. Halling, M. L., Kjeldsen, J., Knudsen, T., Nielsen, J. & Hansen, L. K. Patients with inflammatory bowel disease have increased risk of autoimmune and inflammatory diseases. *World J Gastroenterol* **23**, 6137–6146 (2017).

237. Wen, Y.-P. & Yu, Z.-G. Identifying shared genetic loci and common risk genes of rheumatoid arthritis associated with three autoimmune diseases based on large-scale cross-trait genome-wide association studies. *Front Immunol* **14**, (2023).

238. Attalla, M. G., Singh, S. B., Khalid, R., Umair, M. & Djonga Emmanuel, E. Relationship between Ulcerative Colitis and Rheumatoid Arthritis: A Review. *Cureus* **11**, (2019).

239. Zippi, M. *et al.* Extraintestinal manifestations in a large series of Italian inflammatory bowel disease patients. *World J Gastroenterol* **20**, 17463–17467 (2014).

240. Wu, H. J. & Wu, E. The role of gut microbiota in immune homeostasis and autoimmunity. *Gut Microbes* **3**, (2012).

241. Grigg, J. B. & Sonnenberg, G. F. Host-Microbiota Interactions Shape Local and Systemic Inflammatory Diseases. *J Immunol* **198**, 564–571 (2017).

242. Teng, F. *et al.* Gut Microbiota Drive Autoimmune Arthritis by Promoting Differentiation and Migration of Peyer's Patch T Follicular Helper Cells. *Immunity* **44**, 875–888 (2016).

243. Campisi, L. *et al.* Apoptosis in response to microbial infection induces autoreactive TH17 cells. *Nat Immunol* **17**, 1084–1092 (2016).

244. Horai, R. *et al.* Microbiota-Dependent Activation of an Autoreactive T Cell Receptor Provokes Autoimmunity in an Immunologically Privileged Site. *Immunity* **43**, 343–353 (2015).

245. Palm, N. W. *et al.* Immunoglobulin A coating identifies colitogenic bacteria in inflammatory bowel disease. *Cell* **158**, 1000–1010 (2014).

246. Halling, M. L., Kjeldsen, J., Knudsen, T., Nielsen, J. & Hansen, L. K. Patients with inflammatory bowel disease have increased risk of autoimmune and inflammatory diseases. *World J Gastroenterol* **23**, 6137–6146 (2017).

247. Zhu, X., Xu, T., Peng, C. & Wu, S. Advances in MALDI Mass Spectrometry Imaging Single Cell and Tissues. *Front Chem* **9**, (2022).

248. Cobice, D. F. *et al.* Future technology insight: Mass spectrometry imaging as a tool in drug research and development. *Br J Pharmacol* **172**, 3266–3283 (2015).

249. Tuck, M., Grélard, F., Blanc, L. & Desbenoit, N. MALDI-MSI Towards Multimodal Imaging: Challenges and Perspectives. *Front Chem* **10**, (2022).

250. Buck, A., Aichler, M., Huber, K. & Walch, A. In Situ Metabolomics in Cancer by Mass Spectrometry Imaging. *Adv Cancer Res* **134**, 117–132 (2017).

251. Carter, C. L., Jones, J. W., Farese, A. M., Macvittie, T. J. & Kane, M. A. Inflation-Fixation Method for Lipidomic Mapping of Lung Biopsies by Matrix Assisted Laser Desorption/Ionization-Mass Spectrometry Imaging. *Anal Chem* **88**, 4788–4794 (2016).

252. O'Rourke, M. B., Raymond, B. B. A., Djordjevic, S. P. & Padula, M. P. A versatile cost-effective method for the analysis of fresh frozen tissue sections via matrix-assisted laser desorption/ionisation imaging mass spectrometry. *Rapid Communications in Mass Spectrometry* **29**, 637–644 (2015).

253. Holzlechner, M., Reitschmidt, S., Gruber, S., Zeilinger, S. & Marchetti-Deschmann, M. Visualizing fungal metabolites during mycoparasitic interaction by MALDI mass spectrometry imaging. *Wiley Online LibraryM Holzlechner, S Reitschmidt, S Gruber, S Zeilinger, M Marchetti-DeschmannProteomics, 2016•Wiley Online Library* **16**, 1742–1746 (2016).

254. Bergman, H., Lundin, E., Andersson, M., Analyst, I. L.- & 2016, undefined. Quantitative mass spectrometry imaging of small-molecule neurotransmitters in rat brain tissue sections using nanospray desorption electrospray ionization. *pubs.rsc.orgHM Bergman, E Lundin, M Andersson, I LanekoffAnalyst, 2016•pubs.rsc.org*.

255. Zhang, Y., Buchberger, A., Muthuvel, G. & Li, L. Expression and distribution of neuropeptides in the nervous system of the crab Carcinus maenas and their roles in environmental stress. *Proteomics* **15**, 3969–3979 (2015).

256. Andersen, M. K. *et al.* Spatial differentiation of metabolism in prostate cancer tissue by MALDI-TOF MSI. *Cancer Metab* **9**, (2021).

257. Zhu, X., Xu, T., Peng, C. & Wu, S. Advances in MALDI Mass Spectrometry Imaging Single Cell and Tissues. *Front Chem* **9**, 782432 (2022).

258. Bai, J., Liu, Y. H., Cain, T. C. & Lubman, D. M. Matrix-Assisted Laser Desorption/Ionization Using an Active Perfluorosulfonated Ionomer Film Substrate. *Anal Chem* **66**, 3423–3430 (1994).

259. Avery, J. L., McEwen, A., Flinders, B., Francese, S. & Clench, M. R. Matrix-assisted laser desorption mass spectrometry imaging for the examination of imipramine absorption by Straticell-RHE-EPI/001 an artificial model of the human epidermis. *Xenobiotica* **41**, 735–742 (2011).

260. He, M. J. *et al.* Comparing DESI-MSI and MALDI-MSI Mediated Spatial Metabolomics and Their Applications in Cancer Studies. *Front Oncol* **12**, 891018 (2022).

261. Ekelöf, M., McMurtrie, E. K., Nazari, M., Johanningsmeier, S. D. & Muddiman, D. C. Direct Analysis of Triterpenes from High-Salt Fermented Cucumbers Using Infrared Matrix-Assisted Laser Desorption Electrospray Ionization (IR-MALDESI). *J Am Soc Mass Spectrom* **28**, 370–375 (2017).

262. Krijnen, K. *et al.* A Multimodal SIMS/MALDI Mass Spectrometry Imaging Source with Secondary Electron Imaging Capabilities for Use with timsTOF Instruments. *J Am Soc Mass Spectrom* **34**, 720–727 (2023).

263. Agüi-Gonzalez, P., Jähne, S. & Phan, N. T. N. SIMS imaging in neurobiology and cell biology. *J Anal At Spectrom* **34**, 1355–1368 (2019).

264. Claude, E., Jones, E. A. & Pringle, S. D. DESI Mass Spectrometry Imaging (MSI). *Methods Mol Biol* **1618**, 65–75 (2017).

265. Eberlin, L. S., Ferreira, C. R., Dill, A. L., Ifa, D. R. & Cooks, R. G. Desorption electrospray ionization mass spectrometry for lipid characterization and biological tissue imaging. *Biochim Biophys Acta Mol Cell Biol Lipids* **1811**, 946–960 (2011).

266. Towers, M. W., Karancsi, T., Jones, E. A., Pringle, S. D. & Claude, E. Optimised Desorption Electrospray Ionisation Mass Spectrometry Imaging (DESI-MSI) for the Analysis of Proteins/Peptides Directly from Tissue Sections on a Travelling Wave Ion Mobility Q-ToF. *J Am Soc Mass Spectrom* **29**, 2456–2466 (2018).

267. Liu, C., Qi, F. & Pan, Y. Imaging of Polar and Nonpolar Lipids Using Desorption Electrospray Ionization/Post-photoionization Mass Spectrometry. *Methods in Molecular Biology* **2306**, 285–298 (2021).

268. Qi, K., Wu, L., Liu, C. & Pan, Y. Recent Advances of Ambient Mass Spectrometry Imaging and Its Applications in Lipid and Metabolite Analysis. *Metabolites 2021, Vol. 11, Page 780* **11**, 780 (2021).

269. Lee, Y. J., Perdian, D. C., Song, Z., Yeung, E. S. & Nikolau, B. J. Use of mass spectrometry for imaging metabolites in plant. *Plant J.* **70**, 81–95 (2012).

270. Shon, H. K., Yoon, S., Moon, J. H. & Lee, T. G. Improved mass resolution and mass accuracy in TOF–SIMS spectra and images using argon gas cluster ion beams. *Biointerphases* **11**, 02A321 (2016).

271. Bich, C., Touboul, D. & Brunelle, A. Cluster TOF–SIMS imaging as a tool for micrometric histology of lipids in tissue. *Mass Spec. Rev.* **33**, 442–451 (2014).

272. Yoon, S. & Lee, T. G. Biological tissue sample preparation for time-of-flight secondary ion mass spectrometry (ToF–SIMS) imaging. *Nano Converg* **5**, 1–13 (2018).

273. Singhal, N., Kumar, M., Kanaujia, P. K. & Virdi, J. S. MALDI-TOF mass spectrometry: an emerging technology for microbial identification and diagnosis. *Front Microbiol* **6**, (2015).

274. Angelakis, E., Million, M., Henry, M. & Raoult, D. Rapid and Accurate Bacterial Identification in Probiotics and Yoghurts by MALDI-TOF Mass Spectrometry. *J Food Sci* **76**, (2011).

275. Sipe, S. N., Sanders, J. D., Reinecke, T., Clowers, B. H. & Brodbelt, J. S. Separation and Collision Cross Section Measurements of Protein Complexes Afforded by a Modular Drift Tube Coupled to an Orbitrap Mass Spectrometer. *Anal Chem* **94**, 9434–9441 (2022).

276. Henry, H. *et al.* Comparison between a high-resolution single-stage Orbitrap and a triple quadrupole mass spectrometer for quantitative analyses of drugs. *Rapid Communications in Mass Spectrometry* **26**, 499–509 (2012).

277. Perry, R. H., Cooks, R. G. & Noll, R. J. Orbitrap mass spectrometry: Instrumentation, ion motion and applications. *Mass Spectrom Rev* **27**, 661–699 (2008).

278. Bourmaud, A., Gallien, S. & Domon, B. Parallel reaction monitoring using quadrupole-Orbitrap mass spectrometer: Principle and applications. *Proteomics* **16**, 2146–2159 (2016).

279. Lesur, A. & Domon, B. Advances in high-resolution accurate mass spectrometry application to targeted proteomics. *Proteomics* **15**, 880–890 (2015).

280. Luu, G. T., Condren, A. R., Kahl, L. J., Dietrich, L. E. P. & Sanchez, L. M. Evaluation of data analysis platforms and compatibility with MALDI-TOF imaging mass spectrometry data sets. *J Am Soc Mass Spectrom* **31**, 1313 (2020).

281. Bond, N. J., Koulman, A., Griffin, J. L. & Hall, Z. massPix: an R package for annotation and interpretation of mass spectrometry imaging data for lipidomics. *Metabolomics* **13**, (2017).

282. McDonnell, L. A., Angel, P. M., Lou, S. & Drake, R. R. Mass Spectrometry Imaging in Cancer Research: Future Perspectives. *Adv Cancer Res* **134**, 283–290 (2017).

283. Arentz, G. *et al.* Applications of Mass Spectrometry Imaging to Cancer. *Adv Cancer Res* **134**, 27–66 (2017).

284. Eberlin, L. S. *et al.* Molecular assessment of surgical-resection margins of gastric cancer by mass-spectrometric imaging. *Proc Natl Acad Sci U S A* **111**, 2436–2441 (2014).

285. Buck, A., Aichler, M., Huber, K. & Walch, A. In Situ Metabolomics in Cancer by Mass Spectrometry Imaging. *Adv Cancer Res* **134**, 117–132 (2017).

286. Heijs, B. *et al.* Histology-Guided High-Resolution Matrix-Assisted Laser Desorption Ionization Mass Spectrometry Imaging. *Anal Chem* **87**, 11978–11983 (2015).

287. Hufsky, F. & Böcker, S. Mining molecular structure databases: Identification of small molecules based on fragmentation mass spectrometry data. *Mass Spectrom Rev* **36**, 624–633 (2017).

288. Büyükköroğlu, G., Dora, D. D., Özdemir, F. & Hizel, C. Techniques for protein analysis. *Omics Technologies and Bio-engineering: Towards Improving Quality of Life* **1**, 317–351 (2018).

289. Dass, C. Mass spectrometry: Structure determination of proteins and peptides. *Comprehensive Natural Products II: Chemistry and Biology* **9**, 457–496 (2010).

290. Neagu, A. N. *et al.* Applications of Tandem Mass Spectrometry (MS/MS) in Protein Analysis for Biomedical Research. *Molecules* **27**, (2022).

291. Mittal, R. D. Tandem Mass Spectroscopy in Diagnosis and Clinical Research. *Indian Journal of Clinical Biochemistry* **30**, 121–123 (2015).

292. Gomez-Caudillo, L. *et al.* Principal component analysis on LC-MS/MS and 2DE-MALDI-TOF in glioblastoma cell lines reveals that mitochondria act as organelle sensors of the metabolic state in glioblastoma. *Oncol Rep* **44**, 661–673 (2020).

293. Wang, M. F., Joignant, A. N., Sohn, A. L., Garrard, K. P. & Muddiman, D. C. Time of acquisition and high spatial resolution mass spectrometry imaging. *Journal of Mass Spectrometry* **58**, e4911 (2023).

294. Tu, A. & Muddiman, D. C. Systematic Evaluation of Repeatability of IR-MALDESI-MS and Normalization Strategies for Correcting the Analytical Variation and Improving Image Quality. *Anal Bioanal Chem* **411**, 5729 (2019).

295. Meuleman, W. *et al.* Comparison of normalisation methods for surface-enhanced laser desorption and ionisation (SELDI) time-of-flight (TOF) mass spectrometry data. *BMC Bioinformatics* **9**, (2008).

296. Norris, J. L. *et al.* Processing MALDI Mass Spectra to Improve Mass Spectral Direct Tissue Analysis. *Int J Mass Spectrom* **260**, 212 (2007).

297. Tobias, F., Pathmasiri, K. C. & Cologna, S. M. Mass spectrometry imaging reveals ganglioside and ceramide localization patterns during cerebellar degeneration in the Npc1-/- mouse model. *Anal Bioanal Chem* **411**, 5659–5668 (2019).

298. Rzagalinski, I., (BBA)-Proteins, D. V.-B. et B. A. & 2017, undefined. Quantification of low molecular weight compounds by MALDI imaging mass spectrometry–A tutorial review. *Elsevier*.

299. Deininger, S. O. *et al.* Normalization in MALDI-TOF imaging datasets of proteins: practical considerations. *Anal Bioanal Chem* **401**, 167 (2011).

300. Wehrli, P. M., Michno, W., Blennow, K., Zetterberg, H. & Hanrieder, J. Chemometric Strategies for Sensitive Annotation and Validation of Anatomical Regions of Interest in Complex Imaging Mass Spectrometry Data. *J Am Soc Mass Spectrom* **30**, 2278–2288 (2019).

301. Hamm, G., Bonnel, D., Legouffe, R., … F. P.-J. of & 2012, undefined. Quantitative mass spectrometry imaging of propranolol and olanzapine using tissue extinction calculation as normalization factor. *Elsevier*.

302. Grund, B., AIDS, C. S.-C. O. in H. and & 2010, undefined. Analysis of biomarker data: logs, odds ratios and ROC curves. *ncbi.nlm.nih.govB Grund, C SabinCurrent Opinion in HIV and AIDS, 2010•ncbi.nlm.nih.gov*.

303. Scheipers, U., Perrey, C., Siebers, S., Hansen, C. & Ermert, H. A tutorial on the use of ROC analysis for computer-aided diagnostic systems. *Ultrason Imaging* **27**, 181–198 (2005).

304. Bianchi, L. *et al.* Evaluating the predictive accuracy and the clinical benefit of a nomogram aimed to predict survival in node-positive prostate cancer patients: External validation on a multi-institutional database. *International Journal of Urology* **25**, 574–581 (2018).

305. Wang, M. C. & Li, S. ROC analysis for multiple markers with tree-based classification. *Lifetime Data Anal* **19**, 257–277 (2013).

306. Schlecht, A. *et al.* Imaging mass cytometry for high-dimensional tissue profiling in the eye. *BMC Ophthalmol* **21**, 1–9 (2021).

307. Baharlou, H., Canete, N. P., Cunningham, A. L., Harman, A. N. & Patrick, E. Mass Cytometry Imaging for the Study of Human Diseases—Applications and Data Analysis Strategies. *Front Immunol* **10**, 469030 (2019).

308. Veenstra, J. *et al.* Research Techniques Made Simple: Use of Imaging Mass Cytometry for Dermatological Research and Clinical Applications. *J Invest Dermatol* **141**, 705 (2021).

309. Giesen, C., Wang, H., Schapiro, D., … N. Z.-N. & 2014, undefined. Highly multiplexed imaging of tumor tissues with subcellular resolution by mass cytometry. *nature.comC Giesen, HAO Wang, D Schapiro, N Zivanovic, A Jacobs, B Hattendorf, PJ SchüfflerNature methods, 2014•nature.com*.

310. Kuett, L. *et al.* Three-dimensional imaging mass cytometry for highly multiplexed molecular and cellular mapping of tissues and the tumor microenvironment. *Nature Cancer 2021 3:1* **3**, 122–133 (2021).

311. Le Rochais, M., Hemon, P., Pers, J. O. & Uguen, A. Application of High-Throughput Imaging Mass Cytometry Hyperion in Cancer Research. *Front Immunol* **13**, 859414 (2022).

312. Brábek, J., Mierke, C. T., Rösel, D., Veselý, P. & Fabry, B. The role of the tissue microenvironment in the regulation of cancer cell motility and invasion. *Cell Communication and Signaling* **8**, (2010).

313. Sachs, P. C., Mollica, P. A. & Bruno, R. D. Tissue specific microenvironments: A key tool for tissue engineering and regenerative medicine. *J Biol Eng* **11**, (2017).

314. Xiao, X. *et al.* Multiplexed imaging mass cytometry reveals distinct tumor-immune microenvironments linked to immunotherapy responses in melanoma. *Communications Medicine 2022 2:1* **2**, 1–14 (2022).

315. Palma, M. De, Biziato, D., Cancer, T. P.-N. R. & 2017, undefined. Microenvironmental regulation of tumour angiogenesis. *nature.comM De Palma, D Biziato, TV PetrovaNature Reviews Cancer, 2017•nature.com*.

316. Milosevic, V. Different approaches to Imaging Mass Cytometry data analysis. *Bioinformatics Advances* **3**, (2023).

317. Gassen, S. Van *et al.* FlowSOM: Using self-organizing maps for visualization and interpretation of cytometry data. *Wiley Online LibraryS Van Gassen, B Callebaut, MJ Van Helden, BN Lambrecht, P Demeester, T DhaeneCytometry Part A, 2015•Wiley Online Library* **87**, 636–645 (2015).

318. Hoch, T. *et al.* Multiplexed imaging mass cytometry of the chemokine milieus in melanoma characterizes features of the response to immunotherapy. *Sci Immunol* **7**, 1692 (2022).

319. Caicedo: Evaluation of Deep Learning Strategies for... - Google Scholar. https://scholar.google.com/scholar_lookup?author=JC.+Caicedo&author=J.+Roth&author=A.+Goodman&author=T.+Becker&author=KW.+Karhohs&author=M.+Broisin+&publication_year=2019&title=Evaluation+of+deep+learning+strategies+for+nucleus+segmentation+in+fluorescence+images&journal=bioRxiv&pages=335216.

320. Wang, Y. J. *et al.* Multiplexed In Situ Imaging Mass Cytometry Analysis of the Human Endocrine Pancreas and Immune System in Type 1 Diabetes. *Cell Metab* **29**, 769-783.e4 (2019).

321. Liu, Z. *et al.* Imaging mass cytometry: High-dimensional and single-cell perspectives on the microenvironment of solid tumours. *Prog Biophys Mol Biol* **175**, 140–146 (2022).

322. Thirumal, S., Jamzad, A., Cotechini, T., Siemens, D. R. & Mousavi, P. Automated Cell Phenotyping for Imaging Mass Cytometry. *Annu Int Conf IEEE Eng Med Biol Soc* **2022**, 426–429 (2022).

323. Bhate, S. S., Barlow, G. L., Schürch, C. M. & Nolan, G. P. Tissue schematics map the specialization of immune tissue motifs and their appropriation by tumors. *Cell Syst* **13**, 109-130.e6 (2022).

324. Schürch, C. M. *et al.* Coordinated Cellular Neighborhoods Orchestrate Antitumoral Immunity at the Colorectal Cancer Invasive Front. *Cell* **182**, 1341-1359.e19 (2020).

325. Jackson, H. W. *et al.* The single-cell pathology landscape of breast cancer. *Nature 2020 578:7796* **578**, 615–620 (2020).

326. Zamani, M., Alizadeh-Tabari, S., Chitkara, P., Singh, S. & Loomba, R. Prevalence of Nonalcoholic Fatty Liver Disease in Patients With Rheumatoid Arthritis: A Systematic Review and Meta-Analysis. *Clin Gastroenterol Hepatol* (2023) doi:10.1016/J.CGH.2023.02.021.

327. Pang, Z., Chong, J., Li, S. & Xia, J. MetaboAnalystR 3.0: Toward an Optimized Workflow for Global Metabolomics. *Metabolites* **10**, (2020).

328. Martinson, J. N. V & Walk, S. T. Escherichia coli Residency in the Gut of Healthy Human Adults. *EcoSal Plus* **9**, 10.1128/ecosalplus.ESP-0003–2020 (2020).

329. Escribano-Vazquez, U. *et al.* The commensal Escherichia coli CEC15 reinforces intestinal defences in gnotobiotic mice and is protective in a chronic colitis mouse model. *Sci Rep* **9**, 11431 (2019).

330. Ramos, S. *et al.* Escherichia coli as Commensal and Pathogenic Bacteria Among Food-Producing Animals: Health Implications of Extended Spectrum β-lactamase (ESBL) Production. *Animals (Basel)* **10**, 2239 (2020).

331. Tenaillon, O., Skurnik, D., Picard, B. & Denamur, E. The population genetics of commensal Escherichia coli. *Nat Rev Microbiol* **8**, 207–217 (2010).

332. Desvaux, M. *et al.* Pathogenicity Factors of Genomic Islands in Intestinal and Extraintestinal Escherichia coli . *Frontiers in Microbiology* vol. 11 Preprint at https://www.frontiersin.org/articles/10.3389/fmicb.2020.02065 (2020).

333. Kaper, J. B., Nataro, J. P. & Mobley, H. L. T. Pathogenic Escherichia coli. *Nat Rev Microbiol* **2**, 123–140 (2004).

334. Martinez-Medina, M., Garcia-Gil, J., Barnich, N., Wieler, L. H. & Ewers, C. Adherent-invasive Escherichia coli phenotype displayed by intestinal pathogenic E. coli strains from cats, dogs, and swine. *Appl Environ Microbiol* **77**, 5813–5817 (2011).

335. Prudent, V. *et al.* The Crohn's disease-related bacterial strain LF82 assembles biofilm-like communities to protect itself from phagolysosomal attack. *Commun Biol* **4**, 627 (2021).

336. Miquel, S. *et al.* Complete genome sequence of Crohn's disease-associated adherent-invasive E. coli strain LF82. *PLoS One* **5**, e12714 (2010).

337. Small, C.-L. N., Reid-Yu, S. A., McPhee, J. B. & Coombes, B. K. Persistent infection with Crohn's disease-associated adherent-invasive Escherichia coli leads to chronic inflammation and intestinal fibrosis. *Nat Commun* **4**, 1957 (2013).

338. Chokr, D. *et al.* Adherent invasive Escherichia coli (AIEC) strain LF82, but not Candida albicans, plays a profibrogenic role in the intestine. *Gut Pathog* **13**, 5 (2021).

339. Bretin, A. *et al.* AIEC infection triggers modification of gut microbiota composition in genetically predisposed mice, contributing to intestinal inflammation. *Sci Rep* **8**, 12301 (2018).

340. Pastorelli, L., De Salvo, C., Mercado, J., Vecchi, M. & Pizarro, T. Central Role of the Gut Epithelial Barrier in the Pathogenesis of Chronic Intestinal Inflammation: Lessons Learned from Animal Models and Human Genetics . *Frontiers in Immunology* vol. 4 Preprint at https://www.frontiersin.org/articles/10.3389/fimmu.2013.00280 (2013).

341. Coskun, M. Intestinal epithelium in inflammatory bowel disease. *Front Med (Lausanne)* **1**, 24 (2014).

342. Shawki, A. & McCole, D. F. Mechanisms of Intestinal Epithelial Barrier Dysfunction by Adherent-Invasive Escherichia coli. *Cell Mol Gastroenterol Hepatol* **3**, 41–50 (2017).

343. Keita, Å. V *et al.* Enhanced E. coli LF82 Translocation through the Follicle-associated Epithelium in Crohn's Disease is Dependent on Long Polar Fimbriae and CEACAM6 expression, and Increases Paracellular Permeability. *J Crohns Colitis* **14**, 216–229 (2020).

344. Zheng, L., Duan, S.-L., Dai, Y.-C. & Wu, S.-C. Role of adherent invasive Escherichia coli in pathogenesis of inflammatory bowel disease. *World J Clin Cases* **10**, 11671–11689 (2022).

345. Burgueño, J. F. & Abreu, M. T. Epithelial Toll-like receptors and their role in gut homeostasis and disease. *Nat Rev Gastroenterol Hepatol* **17**, 263–278 (2020).

346. Mahapatro, M., Erkert, L. & Becker, C. Cytokine-Mediated Crosstalk between Immune Cells and Epithelial Cells in the Gut. *Cells* vol. 10 Preprint at https://doi.org/10.3390/cells10010111 (2021).

347. Han, X., Ding, S., Jiang, H. & Liu, G. Roles of Macrophages in the Development and Treatment of Gut Inflammation . *Frontiers in Cell and Developmental Biology* vol. 9 Preprint at https://www.frontiersin.org/articles/10.3389/fcell.2021.625423 (2021).

348. Tawfik, A., Flanagan, P. K. & Campbell, B. J. Escherichia coli-host macrophage interactions in the pathogenesis of inflammatory bowel disease. *World J Gastroenterol* **20**, 8751–8763 (2014).

349. Meconi, S. *et al.* Adherent-invasive Escherichia coli isolated from Crohn's disease patients induce granulomas in vitro. *Cell Microbiol* **9**, 1252–1261 (2007).

350. Bringer, M.-A., Billard, E., Glasser, A.-L., Colombel, J.-F. & Darfeuille-Michaud, A. Replication of Crohn's disease-associated AIEC within macrophages is dependent on TNF-α secretion. *Laboratory Investigation* **92**, 411–419 (2012).

351. Buisson, A. *et al.* Macrophages Inability to Mediate Adherent-Invasive E. coli Replication is Linked to Autophagy in Crohn's Disease Patients. *Cells* **8**, 1394 (2019).

352. Dharmasiri, S. *et al.* Human Intestinal Macrophages Are Involved in the Pathology of Both Ulcerative Colitis and Crohn Disease. *Inflamm Bowel Dis* **27**, 1641–1652 (2021).

353. Kamali Dolatabadi, R., Feizi, A., Halaji, M., Fazeli, H. & Adibi, P. The Prevalence of Adherent-Invasive Escherichia coli and Its Association With Inflammatory Bowel Diseases: A Systematic Review and Meta-Analysis . *Frontiers in Medicine* vol. 8 Preprint at https://www.frontiersin.org/articles/10.3389/fmed.2021.730243 (2021).

354. Adegbola, S. O., Sahnan, K., Warusavitarne, J., Hart, A. & Tozer, P. Anti-TNF Therapy in Crohn's Disease. *Int J Mol Sci* **19**, 2244 (2018).

355. Veca, R. *et al.* A Comparative Study of the Adherent-Invasive Escherichia coli Population and Gut Microbiota of Healthy Vegans versus Omnivores. *Microorganisms* **8**, 1165 (2020).

356. López-Siles, M. *et al.* Prevalence, Abundance, and Virulence of Adherent-Invasive Escherichia coli in Ulcerative Colitis, Colorectal Cancer, and Coeliac Disease. *Front Immunol* **13**, 748839 (2022).

357. Zhang, S. *et al.* Mucosal metabolites fuel the growth and virulence of E. coli linked to Crohn's disease. *JCI Insight* **7**, (2022).

358. Ormsby, M. J. *et al.* Inflammation associated ethanolamine facilitates infection by Crohn's disease-linked adherent-invasive Escherichia coli. *EBioMedicine* **43**, 325–332 (2019).

359. Chervy, M., Barnich, N. & Denizot, J. Adherent-Invasive E. coli: Update on the Lifestyle of a Troublemaker in Crohn's Disease. *International Journal of Molecular Sciences* vol. 21 Preprint at https://doi.org/10.3390/ijms21103734 (2020).

360. Pobeguts, O. V *et al.* Propionate Induces Virulent Properties of Crohn's Disease-Associated Escherichia coli . *Frontiers in Microbiology* vol. 11 Preprint at https://www.frontiersin.org/articles/10.3389/fmicb.2020.01460 (2020).

361. Ormsby, M. J. *et al.* Propionic Acid Promotes the Virulent Phenotype of Crohn's Disease-Associated Adherent-Invasive Escherichia coli. *Cell Rep* **30**, 2297-2305.e5 (2020).

362. Agus, A. *et al.* Propionate catabolism by CD-associated adherent-invasive E. coli counteracts its anti-inflammatory effect. *Gut Microbes* **13**, 1839318 (2021).

363. Zhilu, X. *et al.* Association of Adherent-invasive Escherichia coli with severe Gut Mucosal dysbiosis in Hong Kong Chinese population with Crohn's disease. *Gut Microbes* **13**, 1994833 (2021).

364. Baydi, Z. *et al.* An Update of Research Animal Models of Inflammatory Bowel Disease. *ScientificWorldJournal* **2021**, 7479540 (2021).

365. Nag, D., Farr, D., Raychaudhuri, S. & Withey, J. H. An adult zebrafish model for adherent-invasive Escherichia coli indicates protection from AIEC infection by probiotic E. coli Nissle. *iScience* **25**, 104572 (2022).

366. Perše, M. & Cerar, A. Dextran sodium sulphate colitis mouse model: traps and tricks. *J Biomed Biotechnol* **2012**, 718617 (2012).

367. Carvalho, F. A. *et al.* Crohn's disease adherent-invasive Escherichia coli colonize and induce strong gut inflammation in transgenic mice expressing human CEACAM. *J Exp Med* **206**, 2179–2189 (2009).

368. Wikoff, W. R. *et al.* Metabolomics analysis reveals large effects of gut microflora on mammalian blood metabolites. *Proc Natl Acad Sci U S A* **106**, 3698–3703 (2009).

369. Aldars-García, L., Gisbert, J. P. & Chaparro, M. Metabolomics insights into inflammatory bowel disease: A comprehensive review. *Pharmaceuticals* **14**, 1190 (2021).

370. Silpe, J. E. & Balskus, E. P. Deciphering Human Microbiota-Host Chemical Interactions. *ACS Cent Sci* **7**, 20–29 (2021).

371. Kaja, S., Payne, A. J., Naumchuk, Y., Koulen, P. & Protoc Toxicol Author manuscript, C. Quantification of lactate dehydrogenase for cell viability testing using cell lines and primary cultured astrocytes KEY REFERENCE 1. Detailed description of primary neuronal culture for plate reader-based assays: HHS Public Access Author manuscript. *Curr Protoc Toxicol* (2018) doi:10.1002/cptx.21.

372. Hedlund, G. L., Longo, N. & Pasquali, M. Glutaric acidemia type 1. *Am J Med Genet C Semin Med Genet* **142C**, 86–94 (2006).

373. N2-Succinyl-L-glutamic acid 5-semialdehyde | C9H13NO6 - PubChem. https://pubchem.ncbi.nlm.nih.gov/compound/N2-Succinyl-L-glutamic-acid-5-semialdehyde.

374. Zhang, Z. *et al.* Identification of lysine succinylation as a new post-translational modification. *Nat Chem Biol* **7**, 58–63 (2011).

375. Dai, X., Zhou, Y., Han, F. & Li, J. Succinylation and redox status in cancer cells. *Front Oncol* **12**, 6920 (2022).

376. Alleyn, M., Breitzig, M., Lockey, R. & Kolliputi, N. Cell-to-Cell Communication and Signaling Pathways: The dawn of succinylation: a posttranslational modification. *Am J Physiol Cell Physiol* **314**, C228 (2018).

377. Tretter, L., Patocs, A. & Chinopoulos, C. Succinate, an intermediate in metabolism, signal transduction, ROS, hypoxia, and tumorigenesis. *Biochim Biophys Acta Bioenerg* **1857**, 1086–1101 (2016).

378. Dey, S. *et al.* Multifaceted entrancing role of glucose and its analogue, 2-deoxy-D-glucose in cancer cell proliferation, inflammation, and virus infection. *Biomedicine & Pharmacotherapy* **156**, 113801 (2022).

379. Zatorski, H. *et al.* Colonic inflammation induces changes in glucose levels through modulation of incretin system. *Pharmacological Reports* **73**, 1670–1679 (2021).

380. Stone, L. Effect of high glucose on E. coli. *Nature Reviews Urology 2022 20:1* **20**, 7–7 (2022).

381. Mohanty, S. *et al.* Diabetes downregulates the antimicrobial peptide psoriasin and increases E. coli burden in the urinary bladder. *Nat Commun* **13**, (2022).

382. Sang, M.-M., Sun, Z.-L. & Wu, T.-Z. Inflammatory bowel disease and diabetes: Is there a link between them? *World J Diabetes* **13**, 126 (2022).

383. Zong, H. *et al.* AMP kinase is required for mitochondrial biogenesis in skeletal muscle in response to chronic energy deprivation. *Proc Natl Acad Sci U S A* **99**, 15983 (2002).

384. Gureev, A. P., Shaforostova, E. A., Starkov, A. A. & Popov, V. N. β-Guanidinopropionic Acid Stimulates Brain Mitochondria Biogenesis and Alters Cognitive Behavior in Nondiseased Mid-Age Mice. *J Exp Neurosci* **12**, (2018).

385. Antihyperglycemic action of guanidinoalkanoic acids: 3-guanidinopropionic acid ameliorates hyperglycemia in diabetic KKAy and C57BL6Job/ob mice and increases glucose disappearance in rhesus monkeys - PubMed. https://pubmed.ncbi.nlm.nih.gov/8371149/.

386. Cui, L. *et al.* RNA modifications: importance in immune cell biology and related diseases. *Signal Transduction and Targeted Therapy 2022 7:1* **7**, 1–26 (2022).

387. Nombela, P., Miguel-López, B. & Blanco, S. The role of m6A, m5C and Ψ RNA modifications in cancer: Novel therapeutic opportunities. *Molecular Cancer 2020 20:1* **20**, 1–30 (2021).

388. Barbieri, I. & Kouzarides, T. Role of RNA modifications in cancer. *Nat. Rev. Cancer* **20**, 303–322 (2020).

389. Jana, S., Hsieh, A. C. & Gupta, R. Reciprocal amplification of caspase-3 activity by nuclear export of a putative human RNA-modifying protein, PUS10 during TRAIL-induced apoptosis. *Cell Death Dis* **8**, e3093 (2017).

390. D-Mannonic acid | C6H12O7 - PubChem. https://pubchem.ncbi.nlm.nih.gov/compound/D-Mannonic-acid.

391. Badia, J. *et al.* L-lyxose metabolism employs the L-rhamnose pathway in mutant cells of Escherichia coli adapted to grow on L-lyxose. *J Bacteriol* **173**, 5144–5150 (1991).

392. Alves, A., Bassot, A., Bulteau, A. L., Pirola, L. & Morio, B. Glycine Metabolism and Its Alterations in Obesity and Metabolic Diseases. *Nutrients* **11**, (2019).

393. Haikonen, R., Kärkkäinen, O., Koistinen, V. & Hanhineva, K. Diet- and microbiota-related metabolite, 5-aminovaleric acid betaine (5-AVAB), in health and disease. *Trends in Endocrinology & Metabolism* **33**, 463–480 (2022).

394. Vuong, H. E. *et al.* The maternal microbiome modulates fetal neurodevelopment in mice. *Nature 2020 586:7828* **586**, 281–286 (2020).

395. Carracedo, A., Cantley, L. C. & Pandolfi, P. P. Cancer metabolism: fatty acid oxidation in the limelight. *Nature Reviews Cancer 2013 13:4* **13**, 227–232 (2013).

396. Kärkkäinen, O. *et al.* Whole grain intake associated molecule 5-aminovaleric acid betaine decreases β-oxidation of fatty acids in mouse cardiomyocytes. *Sci Rep* **8**, 13036 (2018).

397. Liepinsh, E. *et al.* Inhibition of L-carnitine biosynthesis and transport by methyl-γ-butyrobetaine decreases fatty acid oxidation and protects against myocardial infarction. *Br J Pharmacol* **172**, 1319–1332 (2015).

398. D'Onofrio, N. *et al.* Antioxidant and Anti-Inflammatory Activities of Buffalo Milk Î-Valerobetaine. *J Agric Food Chem* **67**, 1702–1710 (2019).

399. Rui, W. S. *et al.* Metformin Effect on Nontargeted Metabolite Profiles in Patients With Type 2 Diabetes and in Multiple Murine Tissues. *Diabetes* **65**, 3776–3785 (2016).

400. Bruce, S. J., Guy, P. A., Rezzi, S. & Ross, A. B. Quantitative measurement of betaine and free choline in plasma, cereals and cereal products by isotope dilution LC-MS/MS. *J Agric Food Chem* **58**, 2055–2061 (2010).

401. Ghersin, I. *et al.* Comorbidities in adolescents with inflammatory bowel disease: findings from a population-based cohort study. *Pediatric Research 2019 87:7* **87**, 1256–1262 (2019).

402. Gaspar, R., Macedo, G. & Branco, C. C. Liver manifestations and complications in inflammatory bowel disease: A review. *World J Hepatol* **13**, 1956 (2021).

403. Llorente, C. & Schnabl, B. The Gut Microbiota and Liver Disease. *Cell Mol Gastroenterol Hepatol* **1**, 275–284 (2015).

404. Zhu, L. *et al.* Multi-Omics Analysis of the Gut-Liver Axis Reveals the Mechanism of Liver Injury in Colitis Mice. *Front Immunol* **12**, 5756 (2022).

405. Liver manifestations and complications in inflammatory bowel disease: A review - PMC. https://www.ncbi.nlm.nih.gov/pmc/articles/PMC8727205/.

406. Hesketh, G. G. & Dennis, J. W. N-acetylglucosamine: more than a silent partner in insulin resistance. *Glycobiology* **27**, 595–598 (2017).

407. Iljazovic, A. *et al.* Perturbation of the gut microbiome by Prevotella spp. enhances host susceptibility to mucosal inflammation. *Mucosal Immunol* **14**, 113–124 (2021).

408. Drago, L. Prevotella Copri and Microbiota in Rheumatoid Arthritis: Fully Convincing Evidence? *J Clin Med* **8**, 1837 (2019).

409. Battista, N., Bari, M. & Bisogno, T. N-Acyl Amino Acids: Metabolism, Molecular Targets, and Role in Biological Processes. *Biomolecules* **9**, (2019).

410. Tan, B. *et al.* Identification of endogenous acyl amino acids based on a targeted lipidomics approach. *J Lipid Res* **51**, 112–119 (2010).

411. Grill, M. *et al.* Members of the endocannabinoid system are distinctly regulated in inflammatory bowel disease and colorectal cancer. *Sci Rep* **9**, 2358 (2019).

412. Mintz, R., Feller, E. R., Bahr, R. L. & Shah, S. A. Ocular manifestations of inflammatory bowel disease. *Inflamm Bowel Dis* **10**, 135–139 (2004).

413. Horai, R. *et al.* Microbiota-Dependent Activation of an Autoreactive T Cell Receptor Provokes Autoimmunity in an Immunologically Privileged Site. *Immunity* **43**, 343–353 (2015).

414. Yilmaz, S., Aydemir, E., Maden, A. & Unsal, B. The prevalence of ocular involvement in patients with inflammatory bowel disease. *Int J Colorectal Dis* **22**, 1027–1030 (2007).

415. Taleban, S. *et al.* Ocular manifestations in inflammatory bowel disease are associated with other extra-intestinal manifestations, gender, and genes implicated in other immune-related traits. *J Crohns Colitis* **10**, 43–49 (2016).

416. Roomets, E., Kivelä, T. & Tyni, T. Carnitine Palmitoyltransferase i and Acyl-CoA Dehydrogenase 9 in Retina: Insights of Retinopathy in Mitochondrial Trifunctional Protein Defects. *Invest Ophthalmol Vis Sci* **49**, 1660–1664 (2008).

417. Tyni, T., Paetau, A., Strauss, A. W., Middleton, B. & Kivelä, T. Mitochondrial fatty acid beta-oxidation in the human eye and brain: implications for the retinopathy of long-chain 3-hydroxyacyl-CoA dehydrogenase deficiency. *Pediatr Res* **56**, 744–750 (2004).

418. Fu, Z., Kern, T. S., Hellström, A. & Smith, L. E. H. Fatty acid oxidation and photoreceptor metabolic needs. *J Lipid Res* **62**, 100035 (2021).

419. Ge, X., Huang, S., Ren, C. & Zhao, L. Taurocholic Acid and Glycocholic Acid Inhibit Inflammation and Activate Farnesoid X Receptor Expression in LPS-Stimulated Zebrafish and Macrophages. *Molecules* **28**, (2023).

420. Zhang, Y. L., Li, Z. J., Gou, H. Z., Song, X. J. & Zhang, L. The gut microbiota–bile acid axis: A potential therapeutic target for liver fibrosis. *Front Cell Infect Microbiol* **12**, 1416 (2022).

421. Pi, Y. *et al.* Gut microbiota-derived ursodeoxycholic acid alleviates low birth weight-induced colonic inflammation by enhancing M2 macrophage polarization. *Microbiome 2023 11:1* **11**, 1–21 (2023).

422. Delmas, J. *et al.* Metabolic adaptation of adherent-invasive Escherichia coli to exposure to bile salts. *Sci Rep* **9**, (2019).

423. Chen, J. & Vitetta, L. The Role of Butyrate in Attenuating Pathobiont-Induced Hyperinflammation. *Immune Netw* **20**, (2020).

424. Oshima, Y. *et al.* Sodium benzoate attenuates 2,8-dihydroxyadenine nephropathy by inhibiting monocyte/macrophage TNF-α expression. *Sci Rep* **13**, 3331 (2023).

425. Viola, A., Munari, F., Sánchez-Rodríguez, R., Scolaro, T. & Castegna, A. The metabolic signature of macrophage responses. *Front Immunol* **10**, (2019).

426. Batista-Gonzalez, A., Vidal, R., Criollo, A. & Carreño, L. J. New Insights on the Role of Lipid Metabolism in the Metabolic Reprogramming of Macrophages. *Front Immunol* **10**, 2993 (2020).

427. Qing, J., Zhang, Z., Novák, P., Zhao, G. & Yin, K. Mitochondrial metabolism in regulating macrophage polarization: an emerging regulator of metabolic inflammatory diseases. *Acta Biochim Biophys Sin (Shanghai)* **52**, 917–926 (2020).

428. Jergens, A. E., Parvinroo, S., Kopper, J. & Wannemuehler, M. J. Rules of Engagement: Epithelial-Microbe Interactions and Inflammatory Bowel Disease. *Front Med (Lausanne)* **8**, 669913 (2021).

429. Nunes, T., Bernardazzi, C. & de Souza, H. S. Cell Death and Inflammatory Bowel Diseases: Apoptosis, Necrosis, and Autophagy in the Intestinal Epithelium. *Biomed Res Int* **2014**, (2014).

430. Cell Death and Inflammatory Bowel Diseases: Apoptosis, Necrosis, and Autophagy in the Intestinal Epithelium - PMC. https://www.ncbi.nlm.nih.gov/pmc/articles/PMC4121991/.

431. Ruemmele, F. M. *et al.* Butyrate induced Caco-2 cell apoptosis is mediated via the mitochondrial pathway. *Gut* **52**, 94–100 (2003).

432. Pant, K. *et al.* Butyrate induces ROS-mediated apoptosis by modulating miR-22/SIRT-1 pathway in hepatic cancer cells. *Redox Biol* **12**, 340–349 (2017).

433. Zamaraeva, M. V. *et al.* Cells die with increased cytosolic ATP during apoptosis: a bioluminescence study with intracellular luciferase. *Cell Death & Differentiation 2005 12:11* **12**, 1390–1397 (2005).

434. Guerbette, T., Boudry, G. & Lan, A. Mitochondrial function in intestinal epithelium homeostasis and modulation in diet-induced obesity. *Mol Metab* **63**, 101546 (2022).

435. Stolfi, C., Maresca, C., Monteleone, G. & Laudisi, F. Implication of Intestinal Barrier Dysfunction in Gut Dysbiosis and Diseases. *Biomedicines* vol. 10 Preprint at https://doi.org/10.3390/biomedicines10020289 (2022).

436. Wine, E., Ossa, J. C., Gray-Owen, S. D. & Sherman, P. M. Adherent-invasive Escherichia coli target the epithelial barrier. *Gut Microbes* **1**, 80 (2010).

437. Calzadilla, N. *et al.* Bile acids as inflammatory mediators and modulators of intestinal permeability. *Front Immunol* **13**, (2022).

438. Shi, X. *et al.* Antibacterial Properties of TMA against Escherichia coli and Effect of Temperature and Storage Duration on TMA Content, Lysozyme Activity and Content in Eggs. *Foods* **11**, (2022).

439. Chen, H. & Zhong, Q. Antibacterial activity of acidified sodium benzoate against Escherichia coli O157:H7, Salmonella enterica, and Listeria monocytogenes in tryptic soy broth and on cherry tomatoes. *Int J Food Microbiol* **274**, 38–44 (2018).

440. Lin, M. H. & Khnykin, D. Fatty acid transporters in skin development, function and disease. *Biochim Biophys Acta* **1841**, 362 (2014).

441. Deng, J. *et al.* Expression of Aquaporin 4 and Breakdown of the Blood-Brain Barrier after Hypoglycemia-Induced Brain Edema in Rats. *PLoS One* **9**, (2014).

442. Oshima, T., Koseki, J., Chen, X., Matsumoto, T. & Miwa, H. Acid modulates the squamous epithelial barrier function by modulating the localization of claudins in the superficial layers. *Laboratory Investigation 2012 92:1* **92**, 22–31 (2011).

443. Zheng, L. *et al.* Microbial-derived Butyrate Promotes Epithelial Barrier Function Through IL-10 Receptor-dependent Repression of Claudin-2. *J Immunol* **199**, 2976 (2017).

444. Bhat, M. I., Sowmya, K., Kapila, S. & Kapila, R. Escherichia coli K12: An evolving opportunistic commensal gut microbe distorts barrier integrity in human intestinal cells. *Microb Pathog* **133**, 103545 (2019).

445. Baumgartner, M. *et al.* Atypical enteropathogenic E. coli are associated with disease activity in ulcerative colitis. *Gut Microbes* **14**, (2022).

446. Bhat, M. I., Sowmya, K., Kapila, S. & Kapila, R. Escherichia coli K12: An evolving opportunistic commensal gut microbe distorts barrier integrity in human intestinal cells. *Microb Pathog* **133**, 103545 (2019).

447. Tapia, R., Kralicek, S. E. & Hecht, G. A. Modulation of epithelial cell polarity by bacterial pathogens. *Ann N Y Acad Sci* **1405**, 16 (2017).

448. Bugda Gwilt, K. & Thiagarajah, J. R. Membrane Lipids in Epithelial Polarity: Sorting out the PIPs. *Front Cell Dev Biol* **10**, 1124 (2022).

449. Stoops, E. H. & Caplan, M. J. Trafficking to the Apical and Basolateral Membranes in Polarized Epithelial Cells. *J Am Soc Nephrol* **25**, 1375 (2014).

450. Andrews, C., McLean, M. H. & Durum, S. K. Cytokine Tuning of Intestinal Epithelial Function . *Frontiers in Immunology* vol. 9 Preprint at https://www.frontiersin.org/articles/10.3389/fimmu.2018.01270 (2018).

451. Huang, D. B., DuPont, H. L., Jiang, Z.-D., Carlin, L. & Okhuysen, P. C. Interleukin-8 response in an intestinal HCT-8 cell line infected with enteroaggregative and enterotoxigenic Escherichia coli. *Clin Diagn Lab Immunol* **11**, 548–551 (2004).

452. Healy, L. L., Cronin, J. G. & Sheldon, I. M. Polarized epithelial cells secrete interleukin 6 apically in the bovine endometrium. *Biol Reprod* **92**, (2015).

453. Mirsepasi-Lauridsen, H. C., Vallance, B. A., Krogfelt, K. A. & Petersen, A. M. Escherichia coli pathobionts associated with inflammatory bowel disease. *Clin Microbiol Rev* **32**, (2019).

454. Russo, T. A. & Johnson, J. R. Proposal for a New Inclusive Designation for Extraintestinal Pathogenic Isolates of Escherichia coli: ExPEC. *J Infect Dis* **181**, 1753–1754 (2000).

455. Hernandes, R. T., Elias, W. P., Vieira, M. A. M. & Gomes, T. A. T. An overview of atypical enteropathogenic Escherichia coli. *FEMS Microbiol Lett* **297**, 137–149 (2009).

456. Cai, Y. *et al.* In Vivo Characterization of Alveolar and Interstitial Lung Macrophages in Rhesus Macaques: Implications for Understanding Lung Disease in Humans. *The Journal of Immunology* **192**, 2821–2829 (2014).

457. Ebert, E. C. IL-15 converts human intestinal intraepithelial lymphocytes to CD94+ producers of IFN-γ and IL-10, the latter promoting Fas ligand-mediated cytotoxicity. *Immunology* **115**, 118 (2005).

458. Mention, J. J. *et al.* Interleukin 15: A key to disrupted intraepithelial lymphocyte homeostasis and lymphomagenesis in celiac disease. *Gastroenterology* **125**, 730–745 (2003).

459. Mottawea, W. *et al.* Altered intestinal microbiota–host mitochondria crosstalk in new onset Crohn's disease. *Nat Commun* **7**, 13419 (2016).

460. Jackson, D. N. *et al.* Mitochondrial dysfunction during loss of prohibitin 1 triggers Paneth cell defects and ileitis. *Gut* **69**, 1928 LP – 1938 (2020).

461. Nicholls, D. G. Mitochondrial membrane potential and aging. *Aging Cell* **3**, 35–40 (2004).

462. Li, Y. *et al.* Mitochondria as novel mediators linking gut microbiota to atherosclerosis that is ameliorated by herbal medicine: A review. *Front Pharmacol* **14**, 52 (2023).

463. Nguyen, D., Samson, S. L., Reddy, V. T., Gonzalez, E. V. & Sekhar, R. V. Impaired mitochondrial fatty acid oxidation and insulin resistance in aging: novel protective role of glutathione. *Aging Cell* **12**, 415–425 (2013).

464. Mikó, E. *et al.* Lithocholic acid, a bacterial metabolite reduces breast cancer cell proliferation and aggressiveness. *Biochimica et Biophysica Acta (BBA) - Bioenergetics* **1859**, 958–974 (2018).

465. Kuipers, F., Bloks, V. W. & Groen, A. K. Beyond intestinal soap—bile acids in metabolic control. *Nature Reviews Endocrinology 2014 10:8* **10**, 488–498 (2014).

466. Xu, W. *et al.* Sodium benzoate attenuates secondary brain injury by inhibiting neuronal apoptosis and reducing mitochondria-mediated oxidative stress in a rat model of intracerebral hemorrhage: Possible involvement of DJ-1/Akt/IKK/NFκB pathway. *Front Mol Neurosci* **12**, 105 (2019).

467. Chassaing, B., Aitken, J. D., Malleshappa, M. & Vijay-Kumar, M. Dextran Sulfate Sodium (DSS)-Induced Colitis in Mice. *Current protocols in immunology / edited by John E. Coligan ... [et al.]* **104**, Unit (2014).

468. Taghipour, N. *et al.* An experimental model of colitis induced by dextran sulfate sodium from acute progresses to chronicity in C57BL/6: correlation between conditions of mice and the environment. *Gastroenterol Hepatol Bed Bench* **9**, 45 (2016).

469. Baydi, Z. *et al.* An Update of Research Animal Models of Inflammatory Bowel Disease. *The Scientific World Journal* **2021**, (2021).

470. Mizoguchi, A. & Mizoguchi, E. Animal models of IBD: linkage to human disease. *Curr Opin Pharmacol* **10**, 578 (2010).

471. Jurjus, A. R., Khoury, N. N. & Reimund, J. M. Animal models of inflammatory bowel disease. *J Pharmacol Toxicol Methods* **50**, 81–92 (2004).

472. Kühn, R., Löhler, J., Rennick, D., Rajewsky, K. & Müller, W. Interleukin-10-deficient mice develop chronic enterocolitis. *Cell* **75**, 263–274 (1993).

473. Glocker, E.-O. *et al.* Inflammatory Bowel Disease and Mutations Affecting the Interleukin-10 Receptor. *New England Journal of Medicine* **361**, 2033–2045 (2009).

474. Khor, B., Gardet, A. & Xavier, R. J. Genetics and pathogenesis of inflammatory bowel disease. *Nature 2011 474:7351* **474**, 307–317 (2011).

475. Berg, D. J. *et al.* Enterocolitis and colon cancer in interleukin-10-deficient mice are associated with aberrant cytokine production and CD4(+) TH1-like responses. *J Clin Invest* **98**, 1010–1020 (1996).

476. Mizoguchi, A., Takeuchi, T., Himuro, H., Okada, T. & Mizoguchi, E. Genetically Engineered Mouse Models for Studying Inflammatory Bowel Disease. *J Pathol* **238**, 205 (2016).

477. Kosiewicz, M. M. *et al.* Th1-type responses mediate spontaneous ileitis in a novel murine model of Crohn's disease. *J Clin Invest* **107**, 695–702 (2001).

478. Matsumoto, S. *et al.* Inflammatory bowel disease-like enteritis and caecitis in a senescence accelerated mouse P1/Yit strain. *Gut* **43**, 71–78 (1998).

479. Genetically Engineered Mouse Models for Studying Inflammatory Bowel Disease - PMC. https://www.ncbi.nlm.nih.gov/pmc/articles/PMC4689626/.

480. Baydi, Z. *et al.* An Update of Research Animal Models of Inflammatory Bowel Disease. *Scientific World Journal* **2021**, (2021).

481. Powrie, F., Leach, M. W., Mauze, S., Caddie, L. B. & Coffman, R. L. Phenotypically distinct subsets of CD4+ T cells induce or protect from chronic intestinal inflammation in C. B-17 scid mice. *Int Immunol* **5**, 1461–1471 (1993).

482. Powrie, F. *et al.* Inhibition of Thl responses prevents inflammatory bowel disease in scid mice reconstituted with CD45RBhi CD4+ T cells. *Immunity* **1**, 553–562 (1994).

483. Okayasu, I. *et al.* A novel method in the induction of reliable experimental acute and chronic ulcerative colitis in mice. *Gastroenterology* **98**, 694–702 (1990).

484. Kim, S. H. *et al.* Inflammatory responses of C57BL/6NKorl mice to dextran sulfate sodium-induced colitis: comparison between three C57BL/6 N sub-strains. *Lab Anim Res* **37**, (2021).

485. Wirtz, S. *et al.* Chemically induced mouse models of acute and chronic intestinal inflammation. *Nat. Protoc.* **12**, 1295 (2017).

486. Chen, Y. *et al.* Induction of experimental acute ulcerative colitis in rats by administration of dextran sulfate sodium at low concentration followed by intracolonic administration of 30% ethanol. *J Zhejiang Univ Sci B* **8**, 632–637 (2007).

487. Okayasu, I. *et al.* A novel method in the induction of reliable experimental acute and chronic ulcerative colitis in mice. *Gastroenterology* **98**, 694–702 (1990).

488. Axelsson, L. G., Landström, E., Goldschmidt, T. J., Grönberg, A. & Bylund-Fellenius, A. C. Dextran sulfate sodium (DSS) induced experimental colitis in immunodeficient mice: effects in CD4(+) -cell depleted, athymic and NK-cell depleted SCID mice. *Inflamm Res* **45**, 181–191 (1996).

489. Yazbeck, R., Howarth, G. S., Butler, R. N., Geier, M. S. & Abbott, C. A. Biochemical and histological changes in the small intestine of mice with dextran sulfate sodium colitis. *J Cell Physiol* **226**, 3219–3224 (2011).

490. Chassaing, B., Aitken, J. D., Malleshappa, M. & Vijay-Kumar, M. Dextran Sulfate Sodium (DSS)-Induced Colitis in Mice. *Curr Protoc Immunol* **104**, 15.25.1-15.25.14 (2014).

491. Kwon, J., Lee, C., Heo, S., Kim, B. & Hyun, C. K. DSS-induced colitis is associated with adipose tissue dysfunction and disrupted hepatic lipid metabolism leading to hepatosteatosis and dyslipidemia in mice. *Scientific Reports 2021 11:1* **11**, 1–16 (2021).

492. Hudcovic, T. *et al.* Protective effect of Clostridium tyrobutyricum in acute dextran sodium sulphate-induced colitis: Differential regulation of tumour necrosis factor-α and interleukin-18 in BALB/c and severe combined immunodeficiency mice. *Clin Exp Immunol* **167**, 356–365 (2012).

493. Guan, Q. A Comprehensive Review and Update on the Pathogenesis of Inflammatory Bowel Disease. *J Immunol Res* **2019**, (2019).

494. Dieleman, L. A. *et al.* Dextran sulfate sodium-induced colitis occurs in severe combined immunodeficient mice. *Gastroenterology* **107**, 1643–1652 (1994).

495. Kiesler, P., Fuss, I. J. & Strober, W. Experimental Models of Inflammatory Bowel Diseases. *Cell Mol Gastroenterol Hepatol* **1**, 154–170 (2015).

496. Dieleman, L. A. *et al.* Chronic experimental colitis induced by dextran sulphate sodium (DSS) is characterized by Th1 and Th2 cytokines. *Clin Exp Immunol* **114**, 385 (1998).

497. Kim, T. W. *et al.* Involvement of lymphocytes in dextran sulfate sodium-induced experimental colitis. *World Journal of Gastroenterology : WJG* **12**, 302 (2006).

498. Hernández-Chirlaque, C. *et al.* Germ-free and Antibiotic-treated Mice are Highly Susceptible to Epithelial Injury in DSS Colitis. *J Crohns Colitis* **10**, 1324–1335 (2016).

499. Hold, G. L. *et al.* Role of the gut microbiota in inflammatory bowel disease pathogenesis: What have we learnt in the past 10 years? *World J Gastroenterol* **20**, 1192–1210 (2014).

500. Park, H., Yeo, S., Kang, S. & Huh, C. S. Longitudinal Microbiome Analysis in a Dextran Sulfate Sodium-Induced Colitis Mouse Model. *Microorganisms* **9**, 1–18 (2021).

501. Yeo, S. *et al.* Anti-Inflammatory and Gut Microbiota Modulatory Effect of Lactobacillus rhamnosus Strain LDTM 7511 in a Dextran Sulfate Sodium-Induced Colitis Murine Model. *Microorganisms 2020, Vol. 8, Page 845* **8**, 845 (2020).

502. Bian, X. *et al.* Administration of Akkermansia muciniphila Ameliorates Dextran Sulfate Sodium-Induced Ulcerative Colitis in Mice. *Front Microbiol* **10**, 2259 (2019).

503. Bian, X. *et al.* Administration of Akkermansia muciniphila Ameliorates Dextran Sulfate Sodium-Induced Ulcerative Colitis in Mice. *Front Microbiol* **10**, 2259 (2019).

504. Elinav, E. *et al.* NLRP6 Inflammasome Regulates Colonic Microbial Ecology and Risk for Colitis. *Cell* **145**, 745–757 (2011).

505. Kiesler, P., Fuss, I. J. & Strober, W. Experimental Models of Inflammatory Bowel Diseases. *Cell Mol Gastroenterol Hepatol* **1**, 154–170 (2015).

506. Zeng, M. Y., Inohara, N. & Nuñez, G. Mechanisms of inflammation-driven bacterial dysbiosis in the gut. *Mucosal Immunol* **10**, 18–26 (2017).

507. Singh, V. *et al.* Interplay between enterobactin, myeloperoxidase and lipocalin 2 regulates E. coli survival in the inflamed gut. *Nature Communications 2015 6:1* **6**, 1–11 (2015).

508. Eichele, D. D. & Kharbanda, K. K. Dextran sodium sulfate colitis murine model: An indispensable tool for advancing our understanding of inflammatory bowel diseases pathogenesis. *World J Gastroenterol* **23**, 6016–6029 (2017).

509. Zheng, L., Wen, X. L. & Duan, S. L. Role of metabolites derived from gut microbiota in inflammatory bowel disease. *World J Clin Cases* **10**, 2660 (2022).

510. Schmalle, V. & Lorentz, A. Role of the microbiota in circadian rhythms of the host. *Chronobiol Int* **37**, 301–310 (2020).

511. Cani, P. D. *et al.* Microbial regulation of organismal energy homeostasis. *Nature Metabolism 2019 1:1* **1**, 34–46 (2019).

512. Ji, Y., Gao, Y., Chen, H., Yin, Y. & Zhang, W. Indole-3-Acetic Acid Alleviates Nonalcoholic Fatty Liver Disease in Mice via Attenuation of Hepatic Lipogenesis, and Oxidative and Inflammatory Stress. *Nutrients 2019, Vol. 11, Page 2062* **11**, 2062 (2019).

513. Davenport, M. *et al.* Metabolic alterations to the mucosal microbiota in inflammatory bowel disease. *Inflamm Bowel Dis* **20**, 723–731 (2014).

514. Mukhopadhyay, S. *et al.* Differential colitis susceptibility of Th1- and Th2-biased mice: A multi-omics approach. *PLoS One* **17**, e0264400 (2022).

515. Ding, S. *et al.* Lactobacillus brevis Alleviates DSS-Induced Colitis by Reprograming Intestinal Microbiota and Influencing Serum Metabolome in Murine Model. *Front Physiol* **10**, (2019).

516. Shiomi, Y. *et al.* GCMS-based metabolomic study in mice with colitis induced by dextran sulfate sodium. *Inflamm Bowel Dis* **17**, 2261–2274 (2011).

517. Zhao, L. P. *et al.* DSS-induced acute colitis causes dysregulated tryptophan metabolism in brain: an involvement of gut microbiota. *J Nutr Biochem* **115**, 109282 (2023).

518. Wu, W. *et al.* Expression of Tryptophan 2,3-Dioxygenase and Production of Kynurenine Pathway Metabolites in Triple Transgenic Mice and Human Alzheimer's Disease Brain. *PLoS One* **8**, e59749 (2013).

519. Sundaram, G. *et al.* Kynurenine pathway modulation reverses the experimental autoimmune encephalomyelitis mouse disease progression. *J Neuroinflammation* **17**, 1–14 (2020).

520. Wang, L., Jiang, D., Jiang, X., Cao, L. & Wu, H. Investigation on the impact of thermal-kernel effect of lithium hydride on the reactivity of nuclear propulsion particle bed reactor. *Ann Nucl Energy* **128**, 24–32 (2019).

521. Luzoro, A., Sabat, P., Guzmán, L. & Frias, F. Extraintestinal Manifestations of Inflammatory Bowel Disease. *Gastroenterol Hepatol (N Y)* **7**, 235 (2011).
522. Adawi, D., Molin, G. & Jeppsson, B. Gut–liver axis. *HPB* **1**, 173–186 (1999).
523. Laffineur, G. *et al.* [Bacterial translocation in Crohn disease]. *Gastroenterol Clin Biol* **16**, 777–781 (1992).
524. Sartini, A. *et al.* Non-alcoholic fatty liver disease phenotypes in patients with inflammatory bowel disease. *Cell Death & Disease 2018 9:2* **9**, 1–8 (2018).
525. Bosch, D. E. & Yeh, M. M. Primary sclerosing cholangitis is protective against nonalcoholic fatty liver disease in inflammatory bowel disease. *Hum Pathol* **69**, 55–62 (2017).
526. Kim, S. H. *et al.* Metabolomic Analysis of the Liver of a Dextran Sodium Sulfate-Induced Acute Colitis Mouse Model: Implications of the Gut–Liver Connection. *Cells* **9**, (2020).
527. Keles, U., Ow, J. R., Kuentzel, K. B., Zhao, L. N. & Kaldis, P. Liver-derived metabolites as signaling molecules in fatty liver disease. *Cellular and Molecular Life Sciences 2022 80:1* **80**, 1–14 (2022).
528. Massafra, V. *et al.* Splenic dendritic cell involvement in FXR-mediated amelioration of DSS colitis. *Biochimica et Biophysica Acta (BBA) - Molecular Basis of Disease* **1862**, 166–173 (2016).
529. Xie, D. *et al.* Systematic Metabolic Profiling of Mice with Dextran Sulfate Sodium-Induced Colitis. *J Inflamm Res* **14**, 2941 (2021).
530. Zhang, R. *et al.* Dextran sulphate sodium increases splenic Gr1+CD11b+ cells which accelerate recovery from colitis following intravenous transplantation. *Clin Exp Immunol* **164**, 417 (2011).
531. Raftery, A. L., O'Brien, C. A., Harris, N. L., Tsantikos, E. & Hibbs, M. L. Development of severe colitis is associated with lung inflammation and pathology. *Front Immunol* **14**, 1125260 (2023).
532. Tallima, H. & El Ridi, R. Arachidonic acid: Physiological roles and potential health benefits – A review. *J Adv Res* **11**, 33 (2018).
533. Sala, A., Proschak, E., Steinhilber, D. & Rovati, G. E. Two-pronged approach to anti-inflammatory therapy through the modulation of the arachidonic acid cascade. *Biochem Pharmacol* **158**, 161–173 (2018).
534. Wang, B. *et al.* Metabolism pathways of arachidonic acids: mechanisms and potential therapeutic targets. *Signal Transduction and Targeted Therapy 2021 6:1* **6**, 1–30 (2021).
535. Yarla, N. S. *et al.* Targeting arachidonic acid pathway by natural products for cancer prevention and therapy. *Semin Cancer Biol* **40–41**, 48–81 (2016).
536. Sheng, J. *et al.* The Role of Cyclooxygenase-2 in Colorectal Cancer. *Int J Med Sci* **2020**, 1095–1101 (2020).
537. Patrono, C. & Rocca, B. Measurement of thromboxane biosynthesis in health and disease. *Front Pharmacol* **10**, 1244 (2019).
538. Ye, J. *et al.* Metabolomics-Guided Hypothesis Generation for Mechanisms of Intestinal Protection by Live Biotherapeutic Products. *Biomolecules 2021, Vol. 11, Page 738* **11**, 738 (2021).
539. Wallace, J. L. Prostaglandins, NSAIDs, and gastric mucosal protection: Why doesn't the stomach digest itself? *Physiol Rev* **88**, 1547–1565 (2008).
540. Sharon, P. & Stenson, W. F. Enhanced Synthesis of Leukotriene B4 by Colonic Mucosa in Inflammatory Bowel Disease. *Gastroenterology* **86**, 453–460 (1984).
541. Piotrowska, M., Binienda, A. & Fichna, J. The role of fatty acids in Crohn's disease pathophysiology – An overview. *Mol Cell Endocrinol* **538**, 111448 (2021).
542. Spector, A. A., Fang, X., Snyder, G. D. & Weintraub, N. L. Epoxyeicosatrienoic acids (EETs): Metabolism and biochemical function. *Prog Lipid Res* **43**, 55–90 (2004).

543. Calder, P. C. Omega-3 Fatty Acids and Inflammatory Processes. *Nutrients* **2**, 355 (2010).

544. Middel, P., Raddatz, D., Gunawan, B., Haller, F. & Radzun, H. J. Increased number of mature dendritic cells in Crohn's disease: evidence for a chemokine mediated retention mechanism. *Gut* **55**, 220 (2006).

545. Imam, T., Park, S., Kaplan, M. H. & Olson, M. R. Effector T Helper Cell Subsets in Inflammatory Bowel Diseases. *Front Immunol* **9**, 1 (2018).

546. Zhang, Y. *et al.* Arachidonic acid inhibits inflammatory responses by binding to myeloid differentiation factor-2 (MD2) and preventing MD2/toll-like receptor 4 signaling activation. *Biochimica et Biophysica Acta (BBA) - Molecular Basis of Disease* **1866**, 165683 (2020).

547. Serhan, C. N. Pro-resolving lipid mediators are leads for resolution physiology. *Nature* **510**, 92–101 (2014).

548. Serhan, C. N. & Levy, B. D. Resolvins in inflammation: emergence of the pro-resolving superfamily of mediators. *J Clin Invest* **128**, 2657 (2018).

549. De Mattos, B. R. R. *et al.* Inflammatory Bowel Disease: An Overview of Immune Mechanisms and Biological Treatments. *Mediators Inflamm* **2015**, (2015).

550. Zaiatz Bittencourt, V., Jones, F., Tosetto, M., Doherty, G. A. & Ryan, E. J. Dysregulation of Metabolic Pathways in Circulating Natural Killer Cells Isolated from Inflammatory Bowel Disease Patients. *J Crohns Colitis* **15**, 1316–1325 (2021).

551. Stagg, A. J., Hart, A. L., Knight, S. C. & Kamm, M. A. The dendritic cell: its role in intestinal inflammation and relationship with gut bacteria. *Gut* **52**, 1522–1529 (2003).

552. Saravia, J., Raynor, J. L., Chapman, N. M., Lim, S. A. & Chi, H. Signaling networks in immunometabolism. *Cell Research 2020 30:4* **30**, 328–342 (2020).

553. Bittleman, D. B. & Casale, T. B. 5-Hydroxyeicosatetraenoic acid (HETE)-induced neutrophil transcellular migration is dependent upon enantiomeric structure. *Am J Respir Cell Mol Biol* **12**, 260–267 (1995).

554. Clark, S. R. *et al.* Esterified eicosanoids are acutely generated by 5-lipoxygenase in primary human neutrophils and in human and murine infection. *Blood* **117**, 2033 (2011).

555. Viryasova, G. M., Galkina, S. I., Gaponova, T. V., Romanova, J. M. & Sud'Ina, G. F. Regulation of 5-oxo-ETE synthesis by nitric oxide in human polymorphonuclear leucocytes upon their interaction with zymosan and Salmonella typhimurium. *Biosci Rep* **34**, 207–216 (2014).

556. He, Y. Bacterial Whole-Genome Determination and Applications. *Molecular Medical Microbiology* 357–368 (2014) doi:10.1016/B978-0-12-397169-2.00020-2.

557. Nichols, R. C. & Vanderhoek, J. Y. 5-Hydroxyeicosanoids selectively stimulate the human neutrophil 15- lipoxygenase to use endogenous substrate. *J Exp Med* **171**, 367 (1990).

558. Mendelski, M. N. *et al.* Steroids originating from bacterial bile acid degradation affect Caenorhabditis elegans and indicate potential risks for the fauna of manured soils. *Sci Rep* **9**, 11120 (2019).

559. Bah, S. Y., Dickinson, P., Forster, T., Kampmann, B. & Ghazal, P. Immune oxysterols: Role in mycobacterial infection and inflammation. *J Steroid Biochem Mol Biol* **169**, 152–163 (2017).

560. Diczfalusy, U. *et al.* Marked upregulation of cholesterol 25-hydroxylase expression by lipopolysaccharide. *J Lipid Res* **50**, 2258–2264 (2009).

561. de Freitas, F. A. *et al.* Effects of Oxysterols on Immune Cells and Related Diseases. *Cells* **11**, (2022).

562. Reboldi, A. *et al.* 25-hydroxycholesterol suppresses interleukin-1-driven inflammation downstream of type I interferon. *Science (1979)* **345**, 679–684 (2014).

563. Shimano, H. Sterol regulatory element-binding proteins (SREBPs): Transcriptional regulators of lipid synthetic genes. *Prog Lipid Res* **40**, 439–452 (2001).

564. Rider, P. *et al.* IL-1α and IL-1β Recruit Different Myeloid Cells and Promote Different Stages of Sterile Inflammation. *The Journal of Immunology* **187**, 4835–4843 (2011).

565. Small molecule antagonism of oxysterol-induced Epstein–Barr virus induced gene 2 (EBI2) activation - Benned-Jensen - 2013 - FEBS Open Bio - Wiley Online Library. https://febs.onlinelibrary.wiley.com/doi/full/10.1016/j.fob.2013.02.003.

566. Chalmin, F. *et al.* Oxysterols regulate encephalitogenic CD4+ T cell trafficking during central nervous system autoimmunity. *J Autoimmun* **56**, 45–55 (2015).

567. Liu, C. *et al.* Oxysterols direct B-cell migration through EBI2. *Nature 2011 475:7357* **475**, 519–523 (2011).

568. Griffiths, W. J. *et al.* Additional pathways of sterol metabolism: Evidence from analysis of Cyp27a1-/- mouse brain and plasma. *Biochim Biophys Acta Mol Cell Biol Lipids* **1864**, 191–211 (2019).

569. Wang, Y., Yutuc, E. & Griffiths, W. J. Neuro-oxysterols and neuro-sterols as ligands to nuclear receptors, GPCRs, ligand-gated ion channels and other protein receptors. *Br J Pharmacol* **178**, 3176–3193 (2021).

570. Marion-Letellier, R., Savoye, G., Beck, P. L., Panaccione, R. & Ghosh, S. Polyunsaturated Fatty Acids in Inflammatory Bowel DiseasesA Reappraisal of Effects and Therapeutic Approaches. *Inflamm Bowel Dis* **19**, 650–661 (2013).

571. Tabbaa, M., Golubic, M., Roizen, M. F. & Bernstein, A. M. Docosahexaenoic Acid, Inflammation, and Bacterial Dysbiosis in Relation to Periodontal Disease, Inflammatory Bowel Disease, and the Metabolic Syndrome. *Nutrients* **5**, 3299 (2013).

572. Kwon, Y. Immuno-Resolving Ability of Resolvins, Protectins, and Maresins Derived from Omega-3 Fatty Acids in Metabolic Syndrome. *Mol Nutr Food Res* **64**, 1900824 (2020).

573. Ferreira, I., Falcato, F., Bandarra, N. & Rauter, A. P. Resolvins, Protectins, and Maresins: DHA-Derived Specialized Pro-Resolving Mediators, Biosynthetic Pathways, Synthetic Approaches, and Their Role in Inflammation. *Molecules* **27**, (2022).

574. Serhan, C. N. & Levy, B. D. Resolvins in inflammation: emergence of the pro-resolving superfamily of mediators. *J Clin Invest* **128**, 2657 (2018).

575. Levy, B. D. *et al.* Protectin D1 Is Generated in Asthma and Dampens Airway Inflammation and Hyperresponsiveness. *The Journal of Immunology* **178**, 496–502 (2007).

576. Ariel, A. *et al.* The docosatriene protectin D1 is produced by TH2 skewing promotes human T cell via lipid raft clustering. *Journal of Biological Chemistry* **280**, 43079–43086 (2005).

577. Liu, Y. *et al.* Fish Oil Enhances Intestinal Integrity and Inhibits TLR4 and NOD2 Signaling Pathways in Weaned Pigs after LPS Challenge, 3. *J Nutr* **142**, 2017–2024 (2012).

578. Kong, W., Yen, J. H. & Ganea, D. Docosahexaenoic acid prevents dendritic cell maturation, inhibits antigen-specific Th1/Th17 differentiation and suppresses experimental autoimmune encephalomyelitis. *Brain Behav Immun* **25**, 872–882 (2011).

579. Calder, P. C. Omega-3 Fatty Acids and Inflammatory Processes. *Nutrients* **2**, 355 (2010).

580. Balestrieri, P. *et al.* Nutritional Aspects in Inflammatory Bowel Diseases. *Nutrients* **12**, (2020).

581. Wall, R. *et al.* Contrasting effects of Bifidobacterium breve NCIMB 702258 and Bifidobacterium breve DPC 6330 on the composition of murine brain fatty acids and gut microbiota. *Am J Clin Nutr* **95**, 1278–1287 (2012).

582. Levy, B. D. Resolvins and Protectins: Natural Pharmacophores For Resolution Biology. *Prostaglandins Leukot Essent Fatty Acids* **82**, 327 (2010).

583. Serhan, C. N. & Levy, B. D. Resolvins in inflammation: emergence of the pro-resolving superfamily of mediators. *J Clin Invest* **128**, 2657 (2018).

584. Jeong, S. *et al.* Docosahexaenoic acid-induced apoptosis is mediated by activation of mitogen-activated protein kinases in human cancer cells. *BMC Cancer* **14**, 1–11 (2014).

585. Silke, J. & Meier, P. Inhibitor of Apoptosis (IAP) Proteins–Modulators of Cell Death and Inflammation. *Cold Spring Harb Perspect Biol* **5**, (2013).

586. Pan, J. *et al.* Acrolein-derived DNA adduct formation in human colon cancer cells: Its role in apoptosis induction by docosahexaenoic acid. *Chem Res Toxicol* **22**, 798–806 (2009).

587. Burgueño, J. F. *et al.* Intestinal Epithelial Cells Respond to Chronic Inflammation and Dysbiosis by Synthesizing H2O2. *Front Physiol* **10**, 1484 (2019).

588. Song, E. A. & Kim, H. Docosahexaenoic Acid Induces Oxidative DNA Damage and Apoptosis, and Enhances the Chemosensitivity of Cancer Cells. *Int J Mol Sci* **17**, (2016).

589. Gurzell, E. A. *et al.* DHA-enriched fish oil targets B cell lipid microdomains and enhances ex vivo and in vivo B cell function. *J Leukoc Biol* **93**, 463–470 (2013).

590. Andrews, C., McLean, M. H. & Durum, S. K. Cytokine tuning of intestinal epithelial function. *Front Immunol* **9**, 1270 (2018).

591. Storey, A., McArdle, F., Friedmann, P. S., Jackson, M. J. & Rhodes, L. E. Eicosapentaenoic Acid and Docosahexaenoic Acid Reduce UVB- and TNF-α-induced IL-8 Secretion in Keratinocytes and UVB-induced IL-8 in Fibroblasts. *Journal of Investigative Dermatology* **124**, 248–255 (2005).

592. Donnelly, M. A. & Steiner, T. S. Two nonadjacent regions in enteroaggregative Escherichia coli flagellin are required for activation of toll-like receptor 5. *Journal of Biological Chemistry* **277**, 40456–40461 (2002).

593. Pagliari, D. *et al.* The role of IL-15 in gastrointestinal diseases: A bridge between innate and adaptive immune response. *Cytokine Growth Factor Rev* **24**, 455–466 (2013).

594. Yoshihara, K., Yajima, T., Kubo, C. & Yoshikai, Y. Role of interleukin 15 in colitis induced by dextran sulphate sodium in mice. *Gut* **55**, 334 (2006).

595. Alspach, E., Lussier, D. M. & Schreiber, R. D. Interferon γ and Its Important Roles in Promoting and Inhibiting Spontaneous and Therapeutic Cancer Immunity. *Cold Spring Harb Perspect Biol* **11**, (2019).

596. Negishi, H., Taniguchi, T. & Yanai, H. The interferon (IFN) class of cytokines and the IFN regulatory factor (IRF) transcription factor family. *Cold Spring Harb Perspect Biol* **10**, (2018).

597. Wyss, M. & Kaddurah-Daouk, R. Creatine and creatinine metabolism. *Physiol. Rev.* **80**, 1107–1213 (2000).

598. Antonio, J. *et al.* Common questions and misconceptions about creatine supplementation: what does the scientific evidence really show? *Journal of the International Society of Sports Nutrition 2021 18:1* **18**, 1–17 (2021).

599. Marshall, R. P., Droste, J. N., Giessing, J. & Kreider, R. B. Role of Creatine Supplementation in Conditions Involving Mitochondrial Dysfunction: A Narrative Review. *Nutrients 2022, Vol. 14, Page 529* **14**, 529 (2022).

600. Harris, R. C., Soderlund, K. & Hultman, E. Elevation of creatine in resting and exercised muscle of normal subjects by creatine supplementation. *Clin Sci* **83**, 367–374 (1992).

601. Bonilla, D. A. *et al.* Metabolic basis of creatine in health and disease: A bioinformatics-assisted review. *Nutrients* **13**, (2021).

602. Wallimann, T., Tokarska-Schlattner, M. & Schlattner, U. The creatine kinase system and pleiotropic effects of creatine. *Amino Acids* **40**, 1271–1296 (2011).

603. Turer, E. *et al.* Creatine maintains intestinal homeostasis and protects against colitis. *Proc Natl Acad Sci U S A* **114**, E1273–E1281 (2017).

604. Glover, L. E. *et al.* Control of creatine metabolism by HIF is an endogenous mechanism of barrier regulation in colitis. *Proc Natl Acad Sci U S A* **110**, 19820–19825 (2013).

605. Wallimann, T., Riek, U. & Möddel, M. Intradialytic creatine supplementation: A scientific rationale for improving the health and quality of life of dialysis patients. *Med Hypotheses* **99**, 1–14 (2017).

606. Fairman, C. M. *et al.* The potential therapeutic effects of creatine supplementation on body composition and muscle function in cancer. *Crit Rev Oncol Hematol* **133**, 46–57 (2019).

607. Riesberg, L. A. *et al.* Creatinine downregulates TNF-α in macrophage and T cell lines. *Cytokine* **110**, 29–38 (2018).

608. Huang, D. B., DuPont, H. L., Jiang, Z. D., Carlin, L. & Okhuysen, P. C. Interleukin-8 Response in an Intestinal HCT-8 Cell Line Infected with Enteroaggregative and Enterotoxigenic Escherichia coli. *Clin Diagn Lab Immunol* **11**, 548 (2004).

609. Lee, J. S., Wang, R. X., Alexeev, E. E. & Colgan, S. P. Intestinal Inflammation as a Dysbiosis of Energy Procurement: New Insights into an Old Topic. (2021) doi:10.1080/19490976.2021.1880241.

610. Borrego, F., Robertson, M. J., Ritz, J., Peña, J. & Solana, R. CD69 is a stimulatory receptor for natural killer cell and its cytotoxic effect is blocked by CD94 inhibitory receptor. *Immunology* **97**, 159 (1999).

611. González-Amaro, R., Cortés, J. R., Sánchez-Madrid, F. & Martín, P. Is CD69 an effective brake to control inflammatory diseases? *Trends Mol Med* **19**, 625–632 (2013).

612. Sancho, D. *et al.* Functional Analysis of Ligand-Binding and Signal Transduction Domains of CD69 and CD23 C-Type Lectin Leukocyte Receptors. *The Journal of Immunology* **165**, 3868–3875 (2000).

613. Mcinnes, I. B., Leung, B. P., Sturrock, R. D., Field, M. & Liew, F. Y. Interleukin-15 mediates T cell-dependent regulation of tumor necrosis factor-α production in rheumatoid arthritis. *Nature Medicine 1997 3:2* **3**, 189–195 (1997).

614. Hasegawa, A. *et al.* Crucial Role for CD69 in the Pathogenesis of Dextran Sulphate Sodium-Induced Colitis. *PLoS One* **8**, e65494 (2013).

615. Radulovic, K. & Niess, J. H. CD69 Is the Crucial Regulator of Intestinal Inflammation: A New Target Molecule for IBD Treatment? *J Immunol Res* **2015**, (2015).

616. Radulovic, K. *et al.* CD69 Regulates Type I IFN-Induced Tolerogenic Signals to Mucosal CD4 T Cells That Attenuate Their Colitogenic Potential. *The Journal of Immunology* **188**, 2001–2013 (2012).

617. Jeong, S. P., Kang, J. A. & Park, S. G. Intestinal intraepithelial TCRγδ+ T cells are activated by normal commensal bacteria. *Journal of Microbiology* **50**, 837–841 (2012).

618. Campos-Ferraz, P. L. *et al.* Exploratory studies of the potential anti-cancer effects of creatine. *Amino Acids* **48**, 1993–2001 (2016).

619. Blazejczyk, A. *et al.* 1-methylnicotinamide and its structural analog 1,4-dimethylpyridine for the prevention of cancer metastasis. *Journal of Experimental and Clinical Cancer Research* **35**, 1–13 (2016).

620. Jakubowski, A. *et al.* 1-Methylnicotinamide protects against liver injury induced by concanavalin A via a prostacyclin-dependent mechanism: A possible involvement of IL-4 and TNF-α. *Int Immunopharmacol* **31**, 98–104 (2016).

621. Sternak, M. *et al.* Differential involvement of IL-6 in the early and late phase of 1-methylnicotinamide (MNA) release in Concanavalin A-induced hepatitis. *Int Immunopharmacol* **28**, 105–114 (2015).

622. Sternak, M. *et al.* Nicotinamide N-methyltransferase (NNMT) and 1-methylnicotinamide (MNA) in experimental hepatitis induced by concanavalin A in the mouse. *Pharmacol Rep* **62**, 483–493 (2010).

623. Lau, K. E. & Lui, F. Physiology, Prostaglandin I2. *StatPearls* (2022).

624. Sternak, M. *et al.* Nicotinamide N-methyltransferase (NNMT) and 1-methylnicotinamide (MNA) in experimental hepatitis induced by concanavalin A in the mouse Abbreviations: ALT-alanine aminotransaminase, INFg-inter-feron-g, Met-2PY-1-methyl-2-pyridone-5-carboxamide, Met-4PY-1-methyl-4-pyridone-5-carboxamide, MNA-1-methyl-nicotinamide, NA-nicotinamide, NNMT-nicotinamide N-methyltransferase, TNFa-tumor necrosis factor-a. *Pharmacological Reports* **62**, 483–493 (2010).

625. Zhang, J., Wang, Y., Li, G., Yu, H. & Xie, X. Down-Regulation of Nicotinamide N-methyltransferase Induces Apoptosis in Human Breast Cancer Cells via the Mitochondria-Mediated Pathway. *PLoS One* **9**, e89202 (2014).

626. Pozzi, V. *et al.* RNA-mediated gene silencing of nicotinamide N-methyltransferase is associated with decreased tumorigenicity in human oral carcinoma cells. *PLoS One* **8**, (2013).

627. Kilgour, M. K. *et al.* 1-Methylnicotinamide is an immune regulatory metabolite in human ovarian cancer. *Sci Adv* **7**, (2021).

628. Liu, Z. G. Molecular mechanism of TNF signaling and beyond. *Cell Research 2005 15:1* **15**, 24–27 (2005).

629. Mezouar, S. & Mege, J. L. Changing the paradigm of IFN-γ at the interface between innate and adaptive immunity: Macrophage-derived IFN-γ. *J Leukoc Biol* **108**, 419–426 (2020).

630. Green, A. M., DiFazio, R. & Flynn, J. L. IFN-γ from CD4 T cells is essential for host survival and enhances CD8 T cell function during Mycobacterium tuberculosis infection. *J Immunol* **190**, 270 (2013).

631. Bergheim, I. *et al.* Antibiotics protect against fructose-induced hepatic lipid accumulation in mice: Role of endotoxin. *J Hepatol* **48**, 983–992 (2008).

632. Wang, R. *et al.* Gut microbiome, liver immunology, and liver diseases. *Cell Mol Immunol* **18**, 4 (2021).

633. Chopyk, D. M. & Grakoui, A. Contribution of the Intestinal Microbiome and Gut Barrier to Hepatic Disorders. *Gastroenterology* **159**, 849–863 (2020).

634. Wang, R. *et al.* Gut microbiome, liver immunology, and liver diseases. *Cell Mol Immunol* **18**, 4 (2021).

635. Duparc, T. *et al.* Hepatocyte MyD88 affects bile acids, gut microbiota and metabolome contributing to regulate glucose and lipid metabolism. *Gut* **66**, 620–632 (2017).

636. Sørensen, M. *et al.* Hepatic uptake and metabolism of galactose can be quantified in vivo by 2-[18F]fluoro-2-deoxygalactose positron emission tomography. *Am J Physiol Gastrointest Liver Physiol* **295**, G27 (2008).

637. Azman, K. F., Safdar, A. & Zakaria, R. D-galactose-induced liver aging model: Its underlying mechanisms and potential therapeutic interventions. *Exp Gerontol* **150**, 111372 (2021).

638. Meireles, P. *et al.* GLUT1-mediated glucose uptake plays a crucial role during Plasmodium hepatic infection. *Cell Microbiol* **19**, e12646 (2017).

639. Zatorski, H. *et al.* Colonic inflammation induces changes in glucose levels through modulation of incretin system. *Pharmacological Reports* **73**, 1670 (2021).

640. Boström, P. J. *et al.* Hypoxia Marker GLUT-1 (Glucose Transporter 1) is an Independent Prognostic Factor for Survival in Bladder Cancer Patients Treated with Radical Cystectomy. *Bladder Cancer* **2**, 101 (2016).

641. Suzuki, T., Shinjo, S., Arai, T., Kanai, M. & Goda, N. Hypoxia and fatty liver. *World Journal of Gastroenterology : WJG* **20**, 15087 (2014).

642. Rankin, E. B. *et al.* Hypoxia-Inducible Factor 2 Regulates Hepatic Lipid Metabolism. *Mol Cell Biol* **29**, 4527 (2009).

643. Nath, B. *et al.* Hepatocyte-specific hypoxia-inducible factor-1α is a determinant of lipid accumulation and liver injury in alcohol-induced steatosis in mice. *Hepatology* **53**, 1526–1537 (2011).

644. Junior, Lai, Y. S., Nguyen, H. T., Salmanida, F. P. & Chang, K. T. MERTK+/hi M2c Macrophages Induced by Baicalin Alleviate Non-Alcoholic Fatty Liver Disease. *Int J Mol Sci* **22**, (2021).

645. Yao, Y., Xu, X. H. & Jin, L. Macrophage Polarization in Physiological and Pathological Pregnancy. *Front Immunol* **10**, 792 (2019).

646. Rengachar, P. *et al.* Gamma-Linolenic Acid (GLA) Protects against Ionizing Radiation-Induced Damage: An In Vitro and In Vivo Study. *Biomolecules 2022, Vol. 12, Page 797* **12**, 797 (2022).

647. Sergeant, S., Rahbar, E. & Chilton, F. H. Gamma-linolenic acid, Dihommo-gamma linolenic, Eicosanoids and Inflammatory Processes. *Eur J Pharmacol* **785**, 77 (2016).

648. Lee, T. C. *et al.* The impact of polyunsaturated fatty acid-based dietary supplements on disease biomarkers in a metabolic syndrome/diabetes population. *Lipids Health Dis* **13**, 1–11 (2014).

649. Amagai, Y. *et al.* Dihomo-γ-linolenic acid prevents the development of atopic dermatitis through prostaglandin D1 production in NC/Tnd mice. *J Dermatol Sci* **79**, 30–37 (2015).

650. Sergeant, S., Rahbar, E. & Chilton, F. H. Gamma-linolenic acid, Dihommo-gamma linolenic, Eicosanoids and Inflammatory Processes. *Eur J Pharmacol* **785**, 77–86 (2016).

651. Chilton-Lopez, C.-L. *et al.* Metabolism of gammalinolenic acid in human neutrophils. *The Journal of Immunology* **156**, 2941–2947 (1996).

652. Barham, J. B. *et al.* Addition of eicosapentaenoic acid to gamma-linolenic acid-supplemented diets prevents serum arachidonic acid accumulation in humans. *J Nutr* **130**, 1925–1931 (2000).

653. Hester, A. G. *et al.* Relationship between a Common Variant in the Fatty Acid Desaturase (FADS) Cluster and Eicosanoid Generation in Humans. *J Biol Chem* **289**, 22482 (2014).

654. Queck, A. *et al.* Pathophysiological role of prostanoids in coagulation of the portal venous system in liver cirrhosis. *PLoS One* **14**, e0222840 (2019).

655. Milosevic, I. *et al.* Gut-Liver Axis, Gut Microbiota, and Its Modulation in the Management of Liver Diseases: A Review of the Literature. *International Journal of Molecular Sciences 2019, Vol. 20, Page 395* **20**, 395 (2019).

656. Salviati, L., Trevisson, E., Doimo, M. & Navas, P. Primary Coenzyme Q10 Deficiency. *GeneReviews®* (2017).

657. Dallner, G. & Sindelar, P. J. Regulation of ubiquinone metabolism. *Free Radic Biol Med* **29**, 285–294 (2000).

658. Barros, M. H. *et al.* The Saccharomyces cerevisiae COQ10 gene encodes a START domain protein required for function of coenzyme Q in respiration. *Journal of Biological Chemistry* **280**, 42627–42635 (2005).

659. Mantle, D., Lopez-Lluch, G. & Hargreaves, I. P. Coenzyme Q10 Metabolism: A Review of Unresolved Issues. *International Journal of Molecular Sciences 2023, Vol. 24, Page 2585* **24**, 2585 (2023).

660. Dragan, S. *et al.* Benefits of multiple micronutrient supplementation in heart failure: A comprehensive review. *https://doi.org/10.1080/10408398.2018.1540398* **59**, 965–981 (2018).

661. Olivieri, F. *et al.* Anti-inflammatory effect of ubiquinol-10 on young and senescent endothelial cells via miR-146a modulation. *Free Radic Biol Med* **63**, 410–420 (2013).

662. Olivieri, F. *et al.* Anti-inflammatory effect of ubiquinol-10 on young and senescent endothelial cells via miR-146a modulation. *Free Radic Biol Med* **63**, 410–420 (2013).

663. Moura, F. A., de Andrade, K. Q., dos Santos, J. C. F., Araújo, O. R. P. & Goulart, M. O. F. Antioxidant therapy for treatment of inflammatory bowel disease: Does it work? *Redox Biol* **6**, 617–639 (2015).

664. Cominelli, F. & Pizarro, T. T. Interleukin-1 and interleukin-1 receptor antagonist in inflammatory bowel disease. *Aliment Pharmacol Ther* **10 Suppl 2**, 49–53 (1996).

665. Farsi, F. *et al.* Effects of coenzyme Q10 on health-related quality of life, clinical disease activity and blood pressure in patients with mild to moderate ulcerative colitis: a randomized clinical trial. *Med J Islam Repub Iran* **35**, 3 (2021).

666. Cinelli, M. A. & Lee, K. S. S. Asymmetric Total Synthesis of 19,20-Epoxydocosapentaenoic Acid, a Bioactive Metabolite of Docosahexaenoic Acid. *Journal of Organic Chemistry* **84**, 15362–15372 (2019).

667. Capozzi, M. E. & Penn, J. S. Epoxydocosapentaenoic acid (EDP) and epoxyeicosatrienoic acid (EET) affect TNFα production and leukocyte adhesion in diabetic retinopathy. *Invest Ophthalmol Vis Sci* **57**, (2016).

668. Molfino, A. *et al.* DHA Oral Supplementation Modulates Serum Epoxydocosapentaenoic Acid (EDP) Levels in Breast Cancer Patients. *Oxid Med Cell Longev* **2019**, (2019).

669. Dalli, J. *et al.* Human Sepsis Eicosanoid and Proresolving Lipid Mediator Temporal Profiles: Correlations with Survival and Clinical Outcomes. *Crit Care Med* **45**, 58–68 (2017).

670. Zhang, G. *et al.* Epoxy metabolites of docosahexaenoic acid (DHA) inhibit angiogenesis, tumor growth, and metastasis. *Proc Natl Acad Sci U S A* **110**, 6530–6535 (2013).

671. Guo, Q. *et al.* Rheumatoid arthritis: pathological mechanisms and modern pharmacologic therapies. *Bone Res* **6**, (2018).

672. Silman, A. J. & Pearson, J. E. Epidemiology and genetics of rheumatoid arthritis. *Arthritis Res* **4 Suppl 3**, S265–S272 (2002).

673. Jang, S., Kwon, E. J. & Lee, J. J. Rheumatoid Arthritis: Pathogenic Roles of Diverse Immune Cells. *Int J Mol Sci* **23**, (2022).

674. Tracy, A., Buckley, C. D. & Raza, K. Pre-symptomatic autoimmunity in rheumatoid arthritis: when does the disease start? *Seminars in Immunopathology 2017 39:4* **39**, 423–435 (2017).

675. Bowman, S. J. & Guest, L. The national clinical audit for rheumatoid and early inflammatory arthritis. *Clinical Medicine* **16**, 500 (2016).

676. Hsieh, P. H., Geue, C., Wu, O., McIntosh, E. & Siebert, S. How do multiple long-term conditions impact on the cost-of-illness in early rheumatoid arthritis? *RMD Open* **8**, e002454 (2022).

677. Characterizing the quantitative genetic contribution to rheumatoid arthritis using data from twins - MacGregor - 2000 - Arthritis & Rheumatism - Wiley Online Library. https://onlinelibrary.wiley.com/doi/10.1002/1529-0131(200001)43:1%3C30::AID-ANR5%3E3.0.CO;2-B.

678. Westra, H. J. *et al.* Fine-mapping and functional studies highlight potential causal variants for rheumatoid arthritis and type 1 diabetes. *Nat Genet* **50**, 1366–1374 (2018).

679. Stahl, E. A. *et al.* Genome-wide association study meta-analysis identifies seven new rheumatoid arthritis risk loci. *Nature Genetics 2010 42:6* **42**, 508–514 (2010).

680. Ernst, M. & Jenkins, B. J. Acquiring signalling specificity from the cytokine receptor gp130. *Trends in Genetics* **20**, 23–32 (2004).

681. Characterizing the quantitative genetic contribution to rheumatoid arthritis using data from twins - MacGregor - 2000 - Arthritis & Rheumatism - Wiley Online Library. https://onlinelibrary.wiley.com/doi/10.1002/1529-0131(200001)43:1%3C30::AID-ANR5%3E3.0.CO;2-B.

682. Mitchell, D. M. *et al.* Survival, prognosis, and causes of death in rheumatoid arthritis. *Arthritis Rheum* **29**, 706–714 (1986).

683. Aletaha, D. *et al.* 2010 Rheumatoid arthritis classification criteria: An American College of Rheumatology/European League Against Rheumatism collaborative initiative. *Arthritis Rheum* **62**, 2569–2581 (2010).

684. Cho, S. K. *et al.* Factors associated with time to diagnosis from symptom onset in patients with early rheumatoid arthritis. *Korean J Intern Med* **34**, 910 (2019).

685. Alamanos, Y. & Drosos, A. A. Epidemiology of adult rheumatoid arthritis. *Autoimmun Rev* **4**, 130–136 (2005).

686. Rönnelid, J., Turesson, C. & Kastbom, A. Autoantibodies in Rheumatoid Arthritis – Laboratory and Clinical Perspectives. *Front Immunol* **12**, 1 (2021).

687. Majithia, V. & Geraci, S. A. Rheumatoid Arthritis: Diagnosis and Management. *Am J Med* **120**, 936–939 (2007).

688. Naeem, F., Khan, S. E. A., Saeed, M. A. & Farman, S. Diagnostic and therapeutic delay in Rheumatoid Arthritis patients: Impact on disease outcome. *Pak J Med Sci* **37**, 1001 (2021).

689. van Oosterhout, M. *et al.* Differences in synovial tissue infiltrates between anti-cyclic citrullinated peptide-positive rheumatoid arthritis and anti-cyclic citrullinated peptide-negative rheumatoid arthritis. *Arthritis Rheum* **58**, 53–60 (2008).

690. Dolhain, R. J. E. M., van der Heiden, A. N., ter Haar, N. T., Breedveld, F. C. & Miltenburg, A. M. M. Shift toward T lymphocytes with a T helper 1 cytokine-secretion profile in the joints of patients with rheumatoid arthritis. *Arthritis Rheum* **12**, 1961–1969 (1996).

691. Cope, A. P. T cells in rheumatoid arthritis. *Arthritis Res Ther* **10**, 1–10 (2008).

692. Yap, H. Y. *et al.* Pathogenic Role of Immune Cells in Rheumatoid Arthritis: Implications in Clinical Treatment and Biomarker Development. *Cells* **7**, (2018).

693. Podojil, J. R. & Miller, S. D. Molecular mechanisms of T-cell receptor and costimulatory molecule ligation/blockade in autoimmune disease therapy. *Immunol Rev* **229**, 337–355 (2009).

694. Williams, M. A. & Bevan, M. J. Effector and Memory CTL Differentiation. *https://doi.org/10.1146/annurev.immunol.25.022106.141548* **25**, 171–192 (2007).

695. Meednu, N. *et al.* Production of RANKL by Memory B Cells: A Link between B Cells and Bone Erosion in Rheumatoid Arthritis. *Arthritis and Rheumatology* **68**, 805–816 (2016).

696. Scott, D. L. *et al.* The links between joint damage and disability in rheumatoid arthritis. *Rheumatology* **39**, 122–132 (2000).

697. Al-Saadany, H. M., Hussein, M. S., Gaber, R. A. & Zaytoun, H. A. Th-17 cells and serum IL-17 in rheumatoid arthritis patients: Correlation with disease activity and severity. *The Egyptian Rheumatologist* **38**, 1–7 (2016).

698. Alunno, A. *et al.* Altered immunoregulation in rheumatoid arthritis: The role of regulatory T cells and proinflammatory Th17 cells and therapeutic implications. *Mediators Inflamm* **2015**, (2015).

699. Schulze-Koops, H. & Kalden, J. R. The balance of Th1/Th2 cytokines in rheumatoid arthritis. *Best Pract Res Clin Rheumatol* **15**, 677–691 (2001).

700. Ueno, H., Banchereau, J. & Vinuesa, C. G. Pathophysiology of T follicular helper cells in humans and mice. *Nature Immunology 2014 16:2* **16**, 142–152 (2015).

701. Shoda, H. *et al.* Increased serum concentrations of IL-1 beta, IL-21 and Th17 cells in overweight patients with rheumatoid arthritis. *Arthritis Res Ther* **19**, 1–9 (2017).

702. Rönnelid, J., Turesson, C. & Kastbom, A. Autoantibodies in Rheumatoid Arthritis – Laboratory and Clinical Perspectives. *Front Immunol* **12**, 1619 (2021).

703. Laurent, L. *et al.* IgM rheumatoid factor amplifies the inflammatory response of macrophages induced by the rheumatoid arthritis-specific immune complexes containing anticitrullinated protein antibodies. *Ann Rheum Dis* **74**, 1425–1431 (2015).

704. Harre, U. *et al.* Glycosylation of immunoglobulin G determines osteoclast differentiation and bone loss. *Nature Communications 2015 6:1* **6**, 1–11 (2015).

705. Kinne, R. W., Bräuer, R., Stuhlmüller, B., Palombo-Kinne, E. & Burmester, G. R. Macrophages in rheumatoid arthritis. *Arthritis Res* **2**, 189–202 (2000).

706. Bondeson, J., Wainwright, S. D., Lauder, S., Amos, N. & Hughes, C. E. The role of synovial macrophages and macrophage-produced cytokines in driving aggrecanases, matrix metalloproteinases, and other destructive and inflammatory responses in osteoarthritis. *Arthritis Res Ther* **8**, 1–12 (2006).

707. Kinne, R. W., Bräuer, R., Stuhlmüller, B., Palombo-Kinne, E. & Burmester, G. R. Macrophages in rheumatoid arthritis. *Arthritis Res* **2**, 189–202 (2000).

708. Schlegel, P. M., Steiert, I., Kötter, I. & Müller, C. A. B Cells Contribute to Heterogeneity of IL-17 Producing Cells in Rheumatoid Arthritis and Healthy Controls. *PLoS One* **8**, e82580 (2013).

709. Koetz, K. *et al.* T cell homeostasis in patients with rheumatoid arthritis. *Proc Natl Acad Sci USA* **97**, 9203–9208 (2000).

710. Chen, J. *et al.* An expansion of rare lineage intestinal microbes characterizes rheumatoid arthritis. *Genome Med* **8**, 1–14 (2016).

711. Zhou, L. *et al.* Faecalibacterium prausnitzii Produces Butyrate to Maintain Th17/Treg Balance and to Ameliorate Colorectal Colitis by Inhibiting Histone Deacetylase 1. *Inflamm Bowel Dis* **24**, 1926–1940 (2018).

712. Zhang, X., Chen, B. di, Zhao, L. dan & Li, H. The Gut Microbiota: Emerging Evidence in Autoimmune Diseases. *Trends Mol Med* **26**, 862–873 (2020).

713. Pacifici, R. T cells, osteoblasts, and osteocytes: interacting lineages key for the bone anabolic and catabolic activities of parathyroid hormone. *Ann N Y Acad Sci* **1364**, 11–24 (2016).

714. Afrasiabi, S., Chiniforush, N., Partoazar, A. & Goudarzi, R. The role of bacterial infections in rheumatoid arthritis development and novel therapeutic interventions: Focus on oral infections. *J Clin Lab Anal* e24897 (2023) doi:10.1002/JCLA.24897.

715. Moten, D., Teneva, I., Apostolova, D., Batsalova, T. & Dzhambazov, B. Molecular Mimicry of the Rheumatoid Arthritis-Related Immunodominant T-Cell Epitope within Type II Collagen (CII260-270) by the Bacterial L-Asparaginase. *International Journal of Molecular Sciences 2022, Vol. 23, Page 9149* **23**, 9149 (2022).

716. Chriswell, M. E. & Kuhn, K. A. Microbiota-mediated mucosal inflammation in arthritis. *Best Pract Res Clin Rheumatol* **33**, (2019).

717. Repac, J. *et al.* Mining the capacity of human-associated microorganisms to trigger rheumatoid arthritis—A systematic immunoinformatics analysis of T cell epitopes. *PLoS One* **16**, e0253918 (2021).

718. Pianta, A. *et al.* Two rheumatoid arthritis–specific autoantigens correlate microbial immunity with autoimmune responses in joints. *J Clin Invest* **127**, 2946 (2017).

719. Stoll, M. L. Genetics, Prevotella, and the pathogenesis of rheumatoid arthritis. *Lancet Rheumatol* **2**, e375–e376 (2020).
720. Xu, X. *et al.* The bridge of the gut–joint axis: Gut microbial metabolites in rheumatoid arthritis. *Front Immunol* **13**, (2022).
721. Zaiss, M. M., Joyce Wu, H. J., Mauro, D., Schett, G. & Ciccia, F. The gut–joint axis in rheumatoid arthritis. *Nat Rev Rheumatol* **17**, 224–237 (2021).
722. Ahmad, O., Nogueira, J., Heubi, J. E., Setchell, K. D. R. & Ashraf, A. P. Bile Acid Synthesis Disorder Masquerading as Intractable Vitamin D-Deficiency Rickets. *J Endocr Soc* **3**, 397–402 (2019).
723. He, J. *et al.* Intestinal butyrate-metabolizing species contribute to autoantibody production and bone erosion in rheumatoid arthritis. *Sci Adv* **8**, 1511 (2022).
724. Yoshitake, F., Itoh, S., Narita, H., Ishihara, K. & Ebisu, S. Interleukin-6 directly inhibits osteoclast differentiation by suppressing receptor activator of NF-κB signaling pathways. *Journal of Biological Chemistry* **283**, 11535–11540 (2008).
725. Salmon, M. *et al.* Inhibition of T cell apoptosis in the rheumatoid synovium. *J Clin Invest* **99**, 439–446 (1997).
726. Cho, C., Nguyen, A., Bryant, K. J., O'Neill, S. G. & McNeil, H. P. Prostaglandin D2 metabolites as a biomarker of in vivo mast cell activation in systemic mastocytosis and rheumatoid arthritis. *Immun Inflamm Dis* **4**, 64–69 (2016).
727. Cheng, Q., Wu, H. & Du, Y. The roles of small-molecule inflammatory mediators in rheumatoid arthritis. *Scand J Immunol* **93**, e12982 (2021).
728. Giles, J. T. Extra-articular Manifestations and Comorbidity in Rheumatoid Arthritis: Potential Impact of Pre–Rheumatoid Arthritis Prevention. *Clin Ther* **41**, 1246–1255 (2019).
729. Kelly, C. A. *et al.* Rheumatoid arthritis-related interstitial lung disease: associations, prognostic factors and physiological and radiological characteristics – a large multicentre UK study. *Rheumatology (Oxford)* **53**, 1676–1682 (2014).
730. Bongartz, T. *et al.* Incidence and mortality of interstitial lung disease in rheumatoid arthritis - A population-based study. *Arthritis Rheum* **62**, 1583–1591 (2010).
731. Schurgers, E. *et al.* Pulmonary inflammation in mice with collagen-induced arthritis is conditioned by complete Freund's adjuvant and regulated by endogenous IFN-γ. *Eur J Immunol* **42**, 3223–3234 (2012).
732. Yunt, Z. X. & Solomon, J. J. Lung Disease in Rheumatoid Arthritis. *Rheum Dis Clin North Am* **41**, 225 (2015).
733. Xiong, L., Xiong, L., Ye, H. & Ma, W. L. Animal models of rheumatoid arthritis-associated interstitial lung disease. *Immun Inflamm Dis* **9**, 37 (2021).
734. Matsuoka, T. *et al.* Induction of Pulmonary Thromboembolism by Neutrophil Elastase in Collagen-Induced Arthritis Mice and Effect of Recombinant Human Soluble Thrombomodulin. *Pathobiology* **75**, 295–305 (2008).
735. Bilgici, A. *et al.* Pulmonary involvement in rheumatoid arthritis. *Rheumatol Int* **25**, 429–435 (2005).
736. Assayag, D. *et al.* Predictors of mortality in rheumatoid arthritis-related interstitial lung disease. *Respirology* **19**, 493–500 (2014).
737. Lewis, B. J. B. & Branch, D. R. Mouse Models of Rheumatoid Arthritis for Studies on Immunopathogenesis and Preclinical Testing of Fc Receptor-Targeting Biologics. *Pharmacology* **105**, 618–629 (2020).
738. Vincent, T. L. *et al.* Mapping pathogenesis of arthritis through small animal models. *Rheumatology (United Kingdom)* **51**, 1931–1941 (2012).
739. Geboes, L. *et al.* Freund's complete adjuvant induces arthritis in mice lacking a functional interferon-γ receptor by triggering tumor necrosis factor α-driven osteoclastogenesis. *Arthritis Rheum* **56**, 2595–2607 (2007).
740. Chen, J. *et al.* Biomarkers of Rheumatoid Arthritis–Associated Interstitial Lung Disease. *Arthritis Rheumatol* **67**, 28 (2015).

741. Radovanović-Dinić, B., Tešić-Rajković, S., Zivkovic, V. & Grgov, S. Clinical connection between rheumatoid arthritis and liver damage. *Rheumatol Int* **38**, 715–724 (2018).

742. Shimoda, S., Chong, Y., Akahoshi, M., Niiro, H. & Tsukamoto, H. Hepatic and gastrointestinal manifestations in rheumatic and connective tissue diseases. *J Gen Fam Med* **17**, 132–137 (2016).

743. Ebert, E. C. & Hagspiel, K. D. Gastrointestinal and hepatic manifestations of rheumatoid arthritis. *Dig Dis Sci* **56**, 295–302 (2011).

744. Haroon, M., Adeeb, F., Devlin, J., O'Gradaigh, D. & Walker, F. A comparative study of renal dysfunction in patients with inflammatory arthropathies: Strong association with cardiovascular diseases and not with anti-rheumatic therapies, inflammatory markers or duration of arthritis. *Int J Rheum Dis* **14**, 255–260 (2011).

745. Chiu, H. Y. *et al.* Increased Risk of Chronic Kidney Disease in Rheumatoid Arthritis Associated with Cardiovascular Complications – A National Population-Based Cohort Study. *PLoS One* **10**, (2015).

746. Nishiya, K., Hisakawa, N., Hosokawa, T. & Hashimoto, K. Enlarged spleen detected by abdominal ultrasonography in patients with RA. *Ann Rheum Dis* **59**, 750–750 (2000).

747. Fishman, D. & Isenberg, D. A. Splenic involvement in rheumatic diseases. *Semin Arthritis Rheum* **27**, 141–155 (1997).

748. Felty's syndrome - Symptoms, diagnosis and treatment | BMJ Best Practice. https://bestpractice.bmj.com/topics/en-gb/361.

749. Kronzer, V. L., Crowson, C. S., Sparks, J. A., Myasoedova, E. & Davis, J. M. Comorbidities As Risk Factors for Rheumatoid Arthritis and Their Accrual After Diagnosis. *Mayo Clin Proc* **94**, 2488–2498 (2019).

750. Meisinger, C. & Freuer, D. Rheumatoid arthritis and inflammatory bowel disease: A bidirectional two-sample Mendelian randomization study. *Semin Arthritis Rheum* **55**, 151992 (2022).

751. Weng, X., Liu, L., Barcellos, L. F., Allison, J. E. & Herrinton, L. J. Clustering of inflammatory bowel disease with immune mediated diseases among members of a northern California-managed care organization. *Am J Gastroenterol* **102**, 1429–1435 (2007).

752. Cohen, R. *et al.* Autoimmune disease concomitance among inflammatory bowel disease patients in the United States, 2001-2002. *Inflamm Bowel Dis* **14**, 738–743 (2008).

753. Chen, Y. *et al.* The risk of rheumatoid arthritis among patients with inflammatory bowel disease: A systematic review and meta-analysis. *BMC Gastroenterol* **20**, 1–11 (2020).

754. Esposito, A. J., Chu, S. G., Madan, R., Doyle, T. J. & Dellaripa, P. F. Thoracic Manifestations of Rheumatoid Arthritis. *Clin Chest Med* **40**, 545–560 (2019).

755. Das, P. & David, C. S. Rheumatoid Arthritis, Animal Models. in (ed. Delves, P. J. B. T.-E. of I. (Second E.) 2106–2110 (Elsevier, Oxford, 1998). doi:https://doi.org/10.1006/rwei.1999.0532.

756. Asquith, D. L., Miller, A. M., McInnes, I. B. & Liew, F. Y. Animal models of rheumatoid arthritis. *Eur J Immunol* **39**, 2040–2044 (2009).

757. Kannan, K., Ortmann, R. A. & Kimpel, D. Animal models of rheumatoid arthritis and their relevance to human disease. *Pathophysiology* **12**, 167–181 (2005).

758. Hashida, R. *et al.* New studies of pathogenesis of rheumatoid arthritis with collagen-induced and collagen antibody-induced arthritis models: New insight involving bacteria flora. *Autoimmune Dis* **2021**, (2021).

759. Marinova-Mutafchieva, L. *et al.* Dynamics of proinflammatory cytokine expression in the joints of mice with collagen-induced arthritis (CIA). *Clin Exp Immunol* **107**, 507–512 (1997).

760. Teixeira, J. H. *et al.* The Systemic Immune Response to Collagen-Induced Arthritis and the Impact of Bone Injury in Inflammatory Conditions. *Int J Mol Sci* **20**, (2019).

761. Gao, B. *et al.* Upregulation of chemokine CXCL10 enhances chronic pulmonary inflammation in tree shrew collagen-induced arthritis. *Scientific Reports 2018 8:1* **8**, 1–9 (2018).

762. Lung Disease in Rheumatoid Arthritis - PMC. https://www.ncbi.nlm.nih.gov/pmc/articles/PMC4415514/.

763. Shi, Y. *et al.* Analysis of Hepatic Lipid Metabolism and Immune Function During the Development of Collagen-Induced Arthritis. *Front Immunol* **13**, (2022).

764. Trentham, D. E., Townes, A. S. & Kang, A. H. Autoimmunity to type II collagen: An experimental model of arthritis*. *Journal of Experimental Medicine* **146**, 857–868 (1977).

765. Teixeira, J. H. *et al.* The Systemic Immune Response to Collagen-Induced Arthritis and the Impact of Bone Injury in Inflammatory Conditions. *Int J Mol Sci* **20**, (2019).

766. Gauster, M. *et al.* Endothelial lipase releases saturated and unsaturated fatty acids of high density lipoprotein phosphatidylcholine. *J Lipid Res* **46**, 1517–1525 (2005).

767. Chen, X., Hyatt, B. A., Mucenski, M. L., Mason, R. J. & Shannon, J. M. Identification and characterization of a lysophosphatidylcholine acyltransferase in alveolar II cells. *Proc Natl Acad Sci U S A* **103**, 11724–11729 (2006).

768. Law, S. H. *et al.* An Updated Review of Lysophosphatidylcholine Metabolism in Human Diseases. *Int J Mol Sci* **20**, (2019).

769. Zhao, Y. *et al.* Identification and characterization of a major liver lysophosphatidylcholine acyltransferase. *Journal of Biological Chemistry* **283**, 8258–8265 (2008).

770. Sasagawa, T., Suzuki, K., Shiota, T., Kondo, T. & Okita, M. The Significance of Plasma Lysophospholipids in Patients with Renal Failure on Hemodialysis. *J Nutr Sci Vitaminol (Tokyo)* **44**, 809–818 (1998).

771. Cao, X., van Putten, J. P. M. & Wösten, M. M. S. M. Biological functions of bacterial lysophospholipids. *Adv Microb Physiol* **82**, 129–154 (2023).

772. Gao, Y. *et al.* Integrated metabolomics and network analysis reveal changes in lipid metabolisms of tripterygium glycosides tablets in rats with collagen-induced arthritis. *Comput Struct Biotechnol J* **21**, 1828–1842 (2023).

773. Ferreira, H. B., Melo, T., Paiva, A. & Domingues, M. D. R. Insights in the Role of Lipids, Oxidative Stress and Inflammation in Rheumatoid Arthritis Unveiled by New Trends in Lipidomic Investigations. *Antioxidants* **10**, 1–21 (2021).

774. Yoder, M. *et al.* Bioactive Lysophosphatidylcholine 16:0 and 18:0 Are Elevated in Lungs of Asthmatic Subjects. *Allergy Asthma Immunol Res* **6**, 61 (2014).

775. Spangelo"' An11, B. L. & Jarvis, W. D. Lysophosphatidylcholine stimulates interleukin-6 release from rat anterior pituitary cells in vitro. *Endocrinology* **137**, 4419–4426 (1996).

776. Zhu, X. *et al.* Regulation of Eosinophil Adhesion by Lysophosphatidylcholine via a Non–Store-Operated Ca2+ Channel. *https://doi.org/10.1165/rcmb.2006-0391OC* **36**, 585–593 (2012).

777. Liu, P. *et al.* The mechanisms of lysophosphatidylcholine in the development of diseases. *Life Sci* **247**, 117443 (2020).

778. Shotland, A. M., Fontenot, A. P. & McKee, A. S. Pulmonary macrophage cell death in lung health and disease. *Am J Respir Cell Mol Biol* **64**, 547–556 (2021).

779. Bach, G. *et al.* Single lysophosphatidylcholine components exhibit adjuvant activities in vitro and in vivo. *Clinical and Vaccine Immunology* **17**, 429–438 (2010).

780. Aiyar, N. *et al.* Lysophosphatidylcholine induces inflammatory activation of human coronary artery smooth muscle cells. *Molecular and Cellular Biochemistry 2006 295:1* **295**, 113–120 (2006).

781. Radu, C. G., Yang, L. V., Riedinger, M., Au, M. & Witte, O. N. T cell chemotaxis to lysophosphatidylcholine through the G2A receptor. *Proc Natl Acad Sci U S A* **101**, 245–250 (2004).

782. Nishi, E. *et al.* Lysophosphatidylcholine enhances cytokine-induced interferon gamma expression in human T lymphocytes. *Circ Res* **83**, 508–515 (1998).

783. Olofsson, K. E., Andersson, L., Nilsson, J. & Björkbacka, H. Nanomolar concentrations of lysophosphatidylcholine recruit monocytes and induce pro-inflammatory cytokine production in macrophages. *Biochem Biophys Res Commun* **370**, 348–352 (2008).

784. Qin, X., Qiu, C. & Zhao, L. Lysophosphatidylcholine perpetuates macrophage polarization toward classically activated phenotype in inflammation. *Cell Immunol* **289**, 185–190 (2014).

785. Yap, H. Y. *et al.* Pathogenic Role of Immune Cells in Rheumatoid Arthritis: Implications in Clinical Treatment and Biomarker Development. *Cells* **7**, (2018).

786. Koh, J. H. *et al.* Factors associated with the composition of the gut microbiome in patients with established rheumatoid arthritis and its value for predicting treatment responses. *Arthritis Res Ther* **25**, 1–14 (2023).

787. Hong, M. *et al.* Fusobacterium nucleatum aggravates rheumatoid arthritis through FadA-containing outer membrane vesicles. *Cell Host Microbe* **31**, (2023).

788. Picchianti-Diamanti, A. *et al.* Analysis of Gut Microbiota in Rheumatoid Arthritis Patients: Disease-Related Dysbiosis and Modifications Induced by Etanercept. *Int J Mol Sci* **19**, (2018).

789. Hillmann, F., Argentini, M. & Buddelmeijer, N. Kinetics and phospholipid specificity of apolipoprotein N-acyltransferase. *Journal of Biological Chemistry* **286**, 27936–27946 (2011).

790. Cao, X., van Putten, J. P. M. & Wösten, M. M. S. M. Biological functions of bacterial lysophospholipids. *Adv Microb Physiol* **82**, 129–154 (2023).

791. Sohlenkamp, C. & Geiger, O. Bacterial membrane lipids: diversity in structures and pathways. *FEMS Microbiol Rev* **40**, 133–159 (2016).

792. Rokitskaya, T. I. *et al.* Single channel activity of OmpF-like porin from Yersinia pseudotuberculosis. *Biochimica et Biophysica Acta (BBA) - Biomembranes* **1858**, 883–891 (2016).

793. Pride, A. C., Herrera, C. M., Guan, Z., Giles, D. K. & Trent, M. S. The outer surface lipoprotein VolA mediates utilization of exogenous lipids by Vibrio cholerae. *mBio* **4**, (2013).

794. Zheng, L., Lin, Y., Lu, S., Zhang, J. & Bogdanov, M. Biogenesis, transport and remodeling of lysophospholipids in Gram-negative bacteria. *Biochim Biophys Acta Mol Cell Biol Lipids* **1862**, 1404–1413 (2017).

795. Cao, X. *et al.* The Unique Phospholipidome of the Enteric Pathogen Campylobacter jejuni: Lysophosholipids Are Required for Motility at Low Oxygen Availability. *J Mol Biol* **432**, 5244–5258 (2020).

796. Tang, X. X. *et al.* Origin, regulation, and fitness effect of chromosomal rearrangements in the yeast saccharomyces cerevisiae. *Int J Mol Sci* **22**, 1–17 (2021).

797. Yadav, J., Ismaeel, S. & Qadri, A. Lysophosphatidylcholine Potentiates Antibacterial Activity of Polymyxin B. *Antimicrob Agents Chemother* **64**, (2020).

798. Miyazaki, H. *et al.* Antimicrobial effects of lysophosphatidylcholine on methicillin-resistant Staphylococcus aureus. *Ther Adv Infect Dis* **4**, 89–94 (2017).

799. Zhang, X. *et al.* Dietary ε-Polylysine Affects on Gut Microbiota and Plasma Metabolites Profiling in Mice. *Front Nutr* **9**, 842686 (2022).

800. Attur, M., Scher, J. U., Abramson, S. B. & Attur, M. Role of Intestinal Dysbiosis and Nutrition in Rheumatoid Arthritis. *Cells 2022, Vol. 11, Page 2436* **11**, 2436 (2022).

801. Natelson, S. & Sherwin, J. E. Proposed mechanism for urea nitrogen re-utilization: relationship between urea and proposed guanidine cycles. *Clin Chem* **25**, 1343–1344 (1979).

802. Biodegradation of Guanidinium Ion in Aerobic Soil Samples. https://apps.dtic.mil/sti/citations/ADA199145.

803. Kanamori, T., Kanou, N., Atomi, H. & Imanaka, T. Enzymatic Characterization of a Prokaryotic Urea Carboxylase. *J Bacteriol* **186**, 2532–2539 (2004).

804. Barrick, J. E. *et al.* New RNA motifs suggest an expanded scope for riboswitches in bacterial genetic control. *Proc Natl Acad Sci U S A* **101**, 6421–6426 (2004).

805. Meyer, M. M. *et al.* Challenges of ligand identification for riboswitch candidates. *http://dx.doi.org/10.4161/rna.8.1.13865* **8**, 5–10 (2011).

806. Weinberg, Z. *et al.* Comparative genomics reveals 104 candidate structured RNAs from bacteria, archaea, and their metagenomes. *Genome Biol* **11**, 1–17 (2010).

807. Nelson, J. W., Atilho, R. M., Sherlock, M. E., Stockbridge, R. B. & Breaker, R. R. Metabolism of Free Guanidine in Bacteria Is Regulated by a Widespread Riboswitch Class. *Mol Cell* **65**, 220–230 (2017).

808. Zyzak, D. V., Richardson, J. M., Thorpe, S. R. & Baynes, J. W. Formation of Reactive Intermediates from Amadori Compounds under Physiological Conditions. *Arch Biochem Biophys* **316**, 547–554 (1995).

809. Mehler, J. *et al.* Identification of Pseudomonas asiatica subsp. bavariensis str. JM1 as the first Nε-carboxy(m)ethyllysine-degrading soil bacterium. *Environ Microbiol* **24**, 3229–3241 (2022).

810. Graf von Armansperg, B. *et al.* Transcriptional regulation of the Nε-fructoselysine metabolism in Escherichia coli by global and substrate-specific cues. *Mol Microbiol* **115**, 175–190 (2021).

811. Souliotis, V. L., Vlachogiannis, N. I., Pappa, M., Argyriou, A. & Sfikakis, P. P. DNA damage accumulation, defective chromatin organization and deficient DNA repair capacity in patients with rheumatoid arthritis. *Clinical Immunology* **203**, 28–36 (2019).

812. Shao, L. *et al.* Deficiency of the DNA repair enzyme ATM in rheumatoid arthritis. *Journal of Experimental Medicine* **206**, 1435–1449 (2009).

813. Weyand, C. M. & Goronzy, J. J. T-cell-targeted therapies in rheumatoid arthritis. *Nat Clin Pract Rheumatol* **2**, 201–210 (2006).

814. Reha-Krantz, L. J. Mutagens. *Brenner's Encyclopedia of Genetics: Second Edition* 528–532 (2013) doi:10.1016/B978-0-12-374984-0.00996-7.

815. Kundu, S., Schaible, M. J., McKee, A. D. & Orlando, T. M. Direct Damage of Deoxyadenosine Monophosphate by Low-Energy Electrons Probed by X-ray Photoelectron Spectroscopy. *Journal of Physical Chemistry B* **124**, 1585–1591 (2020).

816. Aoshiba, K., Zhou, F., Tsuji, T. & Nagai, A. DNA damage as a molecular link in the pathogenesis of COPD in smokers. *European Respiratory Journal* **39**, 1368–1376 (2012).

817. Shao, L. DNA Damage Response Signals Transduce Stress From Rheumatoid Arthritis Risk Factors Into T Cell Dysfunction. *Front Immunol* **9**, 3055 (2018).

818. Hannun, Y. A. & Obeid, L. M. Sphingolipids and their metabolism in physiology and disease. *Nat Rev Mol Cell Biol* **19**, 175–191 (2018).

819. Choi, R. H., Tatum, S. M., Symons, J. D., Summers, S. A. & Holland, W. L. Ceramides and other sphingolipids as drivers of cardiovascular disease. *Nature Reviews Cardiology 2021 18:10* **18**, 701–711 (2021).

820. Gaggini, M., Ndreu, R., Michelucci, E., Rocchiccioli, S. & Vassalle, C. Ceramides as Mediators of Oxidative Stress and Inflammation in Cardiometabolic Disease. *Int J Mol Sci* **23**, (2022).

821. Gaggini, M., Pingitore, A. & Vassalle, C. Plasma ceramides pathophysiology, measurements, challenges, and opportunities. *Metabolites* **11**, (2021).

822. Choi, R. H., Tatum, S. M., Symons, J. D., Summers, S. A. & Holland, W. L. Ceramides and other sphingolipids as drivers of cardiovascular disease. *Nat Rev Cardiol* **18**, 701–711 (2021).

823. Alexandropoulou, I. *et al.* Ceramides in Autoimmune Rheumatic Diseases: Existing Evidence and Therapeutic Considerations for Diet as an Anticeramide Treatment. *Nutrients* **15**, (2023).

824. Mizushima, N., Kohsaka, H. & Miyasaka, N. Ceramide, a mediator of interleukin 1, tumour necrosis factor α, as well as Fas receptor signalling, induces apoptosis of rheumatoid arthritis synovial cells. *Ann Rheum Dis* **57**, 495–499 (1998).

825. Schoeler, M. & Caesar, R. Dietary lipids, gut microbiota and lipid metabolism. *Rev Endocr Metab Disord* **20**, 461–472 (2019).

826. Zhang, X. *et al.* Gut Microbiome and Metabolome Were Altered and Strongly Associated With Platelet Count in Adult Patients With Primary Immune Thrombocytopenia. *Front Microbiol* **11**, 1550 (2020).

827. Johnson, E. L. *et al.* Sphingolipids produced by gut bacteria enter host metabolic pathways impacting ceramide levels. *Nature Communications 2020 11:1* **11**, 1–11 (2020).

828. Brown, E. M. *et al.* Bacteroides-Derived Sphingolipids Are Critical for Maintaining Intestinal Homeostasis and Symbiosis. *Cell Host Microbe* **25**, 668-680.e7 (2019).

829. Donaldson, G. P. *et al.* Gut microbiota utilize immunoglobulin A for mucosal colonization. *Science (1979)* **360**, 795 LP – 800 (2018).

830. di Rienzi, S. C. *et al.* The microbiome affects liver sphingolipids and plasma fatty acids in a murine model of the Western diet based on soybean oil. *bioRxiv* 2020.09.03.281626 (2020) doi:10.1101/2020.09.03.281626.

831. Wang, X., Xia, J. & Jiang, C. Role of gut microbiota in the development of non-alcoholic fatty liver disease. *Liver Res* **3**, 25–30 (2019).

832. Lewinska, M. *et al.* The altered serum lipidome and its diagnostic potential for Non-Alcoholic Fatty Liver (NAFL)-associated hepatocellular carcinoma. (2021) doi:10.1016/j.ebiom.2021.103661.

833. Doi, K. *et al.* Reduced Production of Creatinine Limits Its Use as Marker of Kidney Injury in Sepsis. *J Am Soc Nephrol* **20**, 1217 (2009).

834. Jäger, R. *et al.* The effects of creatine pyruvate and creatine citrate on performance during high intensity exercise. *J Int Soc Sports Nutr* **5**, 4 (2008).

835. Gianella, F. G. *et al.* Spot urinary citrate-to-creatinine ratio is a marker for acid-base status in chronic kidney disease. *Kidney Int* **99**, 208–217 (2021).

836. Stanimirova, I. *et al.* Serum metabolomics approach to monitor the changes in metabolite profiles following renal transplantation. *Scientific Reports 2020 10:1* **10**, 1–14 (2020).

837. Ostermann, M., Kashani, K. & Forni, L. G. The two sides of creatinine: both as bad as each other? *J Thorac Dis* **8**, E628 (2016).

838. Cartin-Ceba, R., Afessa, B. & Gajic, O. Low baseline serum creatinine concentration predicts mortality in critically ill patients independent of body mass index. *Crit Care Med* **35**, 2420–2423 (2007).

839. Hein, T. R. *et al.* The effect of disease-modifying anti-rheumatic drugs on skeletal muscle mass in rheumatoid arthritis patients: a systematic review with meta-analysis. *Arthritis Res Ther* **24**, 1–14 (2022).

840. Wysham, K. D., Shoback, D. M., Imboden, J. B. & Katz, P. P. Association of High Anti–Cyclic Citrullinated Peptide Seropositivity and Lean Mass Index With Low Bone Mineral Density in Rheumatoid Arthritis. *Arthritis Care Res (Hoboken)* **70**, 961–969 (2018).

841. Isaacs, J. D. *et al.* Changes in serum creatinine in patients with active rheumatoid arthritis treated with tofacitinib: Results from clinical trials. *Arthritis Res Ther* **16**, 1–12 (2014).

842. Meyer, D. M. *et al.* Anti-inflammatory activity and neutrophil reductions mediated by the JAK1/JAK3 inhibitor, CP-690,550, in rat adjuvant-induced arthritis. *J Inflamm* **7**, 1–12 (2010).

843. de Jonge, N. F. *et al.* Good practices and recommendations for using and benchmarking computational metabolomics metabolite annotation tools. *Metabolomics* **18**, (2022).

844. de Jonge, N. F. *et al.* Good practices and recommendations for using and benchmarking computational metabolomics metabolite annotation tools. *Metabolomics* **18**, (2022).

845. Chen, L. Q., Cheung, L. S., Feng, L., Tanner, W. & Frommer, W. B. Transport of Sugars. *https://doi.org/10.1146/annurev-biochem-060614-033904* **84**, 865–894 (2015).

846. Zhang, J. Z., Behrooz, A. & Ismail-Beigi, F. Regulation of glucose transport by hypoxia. *Am J Kidney Dis* **34**, 189–202 (1999).

847. Zezina, E., Sercan-Alp, O., Herrmann, M. & Biesemann, N. Glucose transporter 1 in rheumatoid arthritis and autoimmunity. *Wiley Interdiscip Rev Syst Biol Med* **12**, (2020).

848. Cho, S. J., Moon, J. S., Lee, C. M., Choi, A. M. K. & Stout-Delgado, H. W. Glucose transporter 1-dependent glycolysis is increased during aging-related lung fibrosis, and phloretin inhibits lung fibrosis. *Am J Respir Cell Mol Biol* **56**, 521–531 (2017).

849. Cho, S. J. *et al.* GLUT1-dependent glycolysis regulates exacerbation of fibrosis via AIM2 inflammasome activation. *Thorax* **75**, 227–236 (2020).

850. Chen, C. *et al.* Metabolomics reveals metabolite changes of patients with pulmonary arterial hypertension in China. *J Cell Mol Med* **24**, 2484–2496 (2020).

851. MacLean, M. R., Herve, P., Eddahibi, S. & Adnot, S. 5-hydroxytryptamine and the pulmonary circulation: receptors, transporters and relevance to pulmonary arterial hypertension. *Br J Pharmacol* **131**, 161–168 (2000).

852. Quiñonez-Flores, C. M., González-Chávez, S. A. & Pacheco-Tena, C. Hypoxia and its implications in rheumatoid arthritis. *J Biomed Sci* **23**, (2016).

853. Waypa, G. B. & Schumacker, P. T. HYPOXIA-INDUCED CHANGES IN PULMONARY AND SYSTEMIC VASCULAR RESISTANCE: WHERE IS THE O2 SENSOR? *Respir Physiol Neurobiol* **174**, 201 (2010).

854. Perito, E. R. *et al.* Hepatic steatosis after pediatric liver transplant. *Liver Transplantation* **23**, 957–967 (2017).

855. Browning, J. D. *et al.* Prevalence of hepatic steatosis in an urban population in the United States: Impact of ethnicity. *Hepatology* **40**, 1387–1395 (2004).

856. Alves-Bezerra, M. & Cohen, D. E. Triglyceride metabolism in the liver. *Compr Physiol* **8**, 1 (2017).

857. Buqué, X. *et al.* A subset of dysregulated metabolic and survival genes is associated with severity of hepatic steatosis in obese Zucker rats. *J Lipid Res* **51**, 500–513 (2010).

858. Jensen-Urstad, A. P. L. & Semenkovich, C. F. Fatty acid synthase and liver triglyceride metabolism: housekeeper or messenger? *Biochim Biophys Acta* **1821**, 747 (2012).

859. Turi, K. N. *et al.* Using urine metabolomics to understand the pathogenesis of infant respiratory syncytial virus (RSV) infection and its role in childhood wheezing. *Metabolomics* **14**, 1–13 (2018).

860. Chlopicki, S. *et al.* 1-Methylnicotinamide (MNA), a primary metabolite of nicotinamide, exerts anti-thrombotic activity mediated by a cyclooxygenase-2/prostacyclin pathway. *Br J Pharmacol* **152**, 230–239 (2007).

861. Sidor, K., Jeznach, A., Hoser, G. & Skirecki, T. 1-Methylnicotinamide (1-MNA) inhibits the activation of the NLRP3 inflammasome in human macrophages. *Int Immunopharmacol* **121**, 110445 (2023).

862. Man, S. M., Karki, R. & Kanneganti, T. D. Molecular mechanisms and functions of pyroptosis, inflammatory caspases and inflammasomes in infectious diseases. *Immunol Rev* **277**, 61 (2017).

863. Noor, M. T. & Manoria, P. Immune Dysfunction in Cirrhosis. *J Clin Transl Hepatol* **5**, 50 (2017).

864. Petin, K. *et al.* NAD metabolites interfere with proliferation and functional properties of THP-1 cells. doi:10.1177/1753425919844587.

865. Quaranta, A., Revol-Cavalier, J. & Wheelock, C. E. The octadecanoids: an emerging class of lipid mediators. *Biochem Soc Trans* **50**, 1569–1582 (2022).

866. Takatori, T. *et al.* Dynamics of Subcellular Localization of Leukotoxin (9:10-epoxy-12-octadecenoic acid) in Lungs of Rats as Revealed by Immunoelectron Microscopy. *Acta Medicinæ Legalis Vol. XLIV 1994* 321–323 (1995) doi:10.1007/978-3-642-79523-7_107.

867. Levan, S. R. *et al.* Elevated faecal 12,13-diHOME concentration in neonates at high risk for asthma is produced by gut bacteria and impedes immune tolerance. *Nature Microbiology 2019 4:11* **4**, 1851–1861 (2019).

868. Jang, W. H. *et al.* Low level of lead can induce phosphatidylserine exposure and erythrophagocytosis: a new mechanism underlying lead-associated anemia. *Toxicol Sci* **122**, 177–184 (2011).

869. Wong, K. *et al.* Phosphatidylserine receptor Tim-4 is essential for the maintenance of the homeostatic state of resident peritoneal macrophages. *Proc Natl Acad Sci U S A* **107**, 8712–8717 (2010).

870. Glassman, F. Y. *et al.* Phosphatidylserine is not just a cleanup crew but also a well-meaning teacher. *J Pharm Sci* **107**, 2048 (2018).

871. Chen, X., Doffek, K., Sugg, S. L. & Shilyansky, J. Phosphatidylserine Regulates the Maturation of Human Dendritic Cells. *The Journal of Immunology* **173**, 2985–2994 (2004).

872. Gaitonde, P., Peng, A., Straubinger, R. M., Bankert, R. B. & Balu-Iyer, S. V. Phosphatidylserine reduces immune response against human recombinant Factor VIII in Hemophilia A mice by regulation of dendritic cell function. *Clinical Immunology* **138**, 135–145 (2011).

873. Ravichandran, K. S. & Lorenz, U. Engulfment of apoptotic cells: signals for a good meal. *Nature Reviews Immunology 2007 7:12* **7**, 964–974 (2007).

874. Belkaid, Y. & Hand, T. W. Role of the Microbiota in Immunity and inflammation. *Cell* **157**, 121 (2014).

875. Wernroth, M. L. *et al.* Development of gut microbiota during the first 2 years of life. *Scientific Reports 2022 12:1* **12**, 1–13 (2022).

876. Rackaityte, E. *et al.* Viable bacterial colonization is highly limited in the human intestine in utero. *Nat. Med.* **26**, 599–607 (2020).

877. Tanaka, M. & Nakayama, J. Development of the gut microbiota in infancy and its impact on health in later life. *Allergology International* **66**, 515–522 (2017).

878. Roswall, J. *et al.* Developmental trajectory of the healthy human gut microbiota during the first 5 years of life. *Cell Host Microbe* **29**, 765-776.e763 (2021).

879. Vallès, Y. *et al.* Microbial Succession in the Gut: Directional Trends of Taxonomic and Functional Change in a Birth Cohort of Spanish Infants. *PLoS Genet* **10**, e1004406 (2014).

880. Wernroth, M. L. *et al.* Development of gut microbiota during the first 2 years of life. *Scientific Reports 2022 12:1* **12**, 1–13 (2022).

881. Wang, Y. *et al.* Oral microbiome alterations associated with early childhood caries highlight the importance of carbohydrate metabolic activities. *mSystems* **4**, e00450-19 (2019).

882. Vaishampayan, P. A. *et al.* Comparative Metagenomics and Population Dynamics of the Gut Microbiota in Mother and Infant. *Genome Biol Evol* **2**, 53–66 (2010).

883. Niu, J. *et al.* Evolution of the Gut Microbiome in Early Childhood: A Cross-Sectional Study of Chinese Children. *Front Microbiol* **11**, 475213 (2020).

884. Yatsunenko, T. *et al.* Human gut microbiome viewed across age and geography. *Nature* **486**, 222–227 (2012).

885. Francino, M. P. Early Development of the Gut Microbiota and Immune Health. *Pathogens 2014, Vol. 3, Pages 769-790* **3**, 769–790 (2014).

886. Platt, A. M. & Mowat, A. M. I. Mucosal macrophages and the regulation of immune responses in the intestine. *Immunol Lett* **119**, 22–31 (2008).

887. Erturk-Hasdemir, D. *et al.* Symbionts exploit complex signaling to educate the immune system. *Proc Natl Acad Sci U S A* **116**, 26157–26166 (2019).

888. Janeway, C. A. & Medzhitov, R. Innate Immune Recognition. *https://doi.org/10.1146/annurev.immunol.20.083001.084359* **20**, 197–216 (2003).

889. Zheng, D., Liwinski, T. & Elinav, E. Interaction between microbiota and immunity in health and disease. *Cell Research 2020 30:6* **30**, 492–506 (2020).

890. Wen, L. *et al.* Innate immunity and intestinal microbiota in the development of Type 1 diabetes. *Nature* **455**, 1109–1113 (2008).

891. Hayashi, A. *et al.* A Single Strain of Clostridium butyricum Induces Intestinal IL-10-Producing Macrophages to Suppress Acute Experimental Colitis in Mice. *CHOM* **13**, 711–722 (2013).

892. Sims, M. C. *et al.* Novel manifestations of immune dysregulation and granule defects in gray platelet syndrome. *Blood* **136**, 1956 (2020).

893. Romagnani, S. Regulation of the T cell response. *Clinical & Experimental Allergy* **36**, 1357–1366 (2006).

894. Akdis, M. Healthy immune response to allergens: T regulatory cells and more. *Curr Opin Immunol* **18**, 738–744 (2006).

895. Slocum, C., Kramer, C. & Genco, C. A. Immune dysregulation mediated by the oral microbiome: Potential link to chronic inflammation and atherosclerosis. *J. Intern. Med.* **280**, 114–128 (2016).

896. Strauch, U. G. *et al.* Influence of intestinal bacteria on induction of regulatory T cells: lessons from a transfer model of colitis. *Gut* **54**, 1546–1552 (2005).

897. Ivanov, I. I. *et al.* Induction of Intestinal Th17 Cells by Segmented Filamentous Bacteria. *Cell* **139**, 485–498 (2009).

898. Tan, T. G. *et al.* Identifying species of symbiont bacteria from the human gut that, alone, can induce intestinal Th17 cells in mice. *Proc Natl Acad Sci U S A* **113**, E8141–E8150 (2016).

899. Hachimura, S., Totsuka, M. & Hosono, A. Immunomodulation by food: impact on gut immunity and immune cell function. *Biosci Biotechnol Biochem* **82**, 584–599 (2018).

900. Tezuka, H. & Ohteki, T. Regulation of IgA production by intestinal dendritic cells and related cells. *Front Immunol* **10**, 462850 (2019).

901. Tezuka, H. & Ohteki, T. Regulation of IgA production by intestinal dendritic cells and related cells. *Front Immunol* **10**, 462850 (2019).

902. Sellon, R. K. *et al.* Resident enteric bacteria are necessary for development of spontaneous colitis and immune system activation in interleukin-10-deficient mice. *Infect Immun* **66**, 5224–5231 (1998).

903. Hu, K. A., Gubatan, J. & John Gubatan, C. Gut microbiome–based therapeutics in inflammatory bowel disease. *Clinical and Translational Discovery* **3**, e182 (2023).

904. Albillos, A., de Gottardi, A. & Rescigno, M. The gut-liver axis in liver disease: Pathophysiological basis for therapy. *J Hepatol* **72**, 558–577 (2020).

905. Chen, B. *et al.* Presence of segmented filamentous bacteria in human children and its potential role in the modulation of human gut immunity. *Front Microbiol* **9**, 1403 (2018).

906. Albillos, A., de Gottardi, A. & Rescigno, M. The gut-liver axis in liver disease: Pathophysiological basis for therapy. *J Hepatol* **72**, 558–577 (2020).

907. Blacher, E., Levy, M., Tatirovsky, E. & Elinav, E. Microbiome-modulated metabolites at the interface of host immunity. *J Immunol* **198**, 572–580 (2017).

908. Atarashi, K. *et al.* Th17 cell induction by adhesion of microbes to intestinal epithelial cells. *Cell* **163**, 367–380 (2015).

909. Spadoni, I., Fornasa, G. & Rescigno, M. Organ-specific protection mediated by cooperation between vascular and epithelial barriers. *Nature Reviews Immunology 2017 17:12* **17**, 761–773 (2017).

910. Levy, M., Blacher, E. & Elinav, E. Microbiome, metabolites and host immunity. *Curr Opin Microbiol* **35**, 8–15 (2017).

911. Han, H. *et al.* Depletion of Gut Microbiota Inhibits Hepatic Lipid Accumulation in High-Fat Diet-Fed Mice. *Int J Mol Sci* **23**, (2022).

912. Han, H. *et al.* Intestinal dysbiosis in nonalcoholic fatty liver disease (NAFLD): focusing on the gut–liver axis. *Crit Rev Food Sci Nutr* **63**, 1689–1706 (2023).

913. Adams, L. A. *et al.* Bile acids associate with specific gut microbiota, low-level alcohol consumption and liver fibrosis in patients with non-alcoholic fatty liver disease. *Liver International* **40**, 1356–1365 (2020).

914. Xia, Y. *et al.* Gut microbiome and microbial metabolites in NAFLD and after bariatric surgery: Correlation and causality. *Front Microbiol* **13**, 1003755 (2022).

915. Al-Asmakh, M. & Zadjali, F. Use of germ-free animal models in microbiota-related research. *J Microbiol Biotechnol* **25**, 1583–1588 (2015).

916. Bayer, F., Ascher, S., Pontarollo, G. & Reinhardt, C. Antibiotic Treatment Protocols and Germ-Free Mouse Models in Vascular Research. *Front Immunol* **10**, (2019).

917. Smith, K., McCoy, K. D. & Macpherson, A. J. Use of axenic animals in studying the adaptation of mammals to their commensal intestinal microbiota. *Semin Immunol* **19**, 59–69 (2007).

918. Uzbay, T. Germ-free animal experiments in the gut microbiota studies. *Curr Opin Pharmacol* **49**, 6–10 (2019).

919. Eberl, C. *et al.* Reproducible Colonization of Germ-Free Mice With the Oligo-Mouse-Microbiota in Different Animal Facilities. *Front Microbiol* **10**, (2020).

920. Kennedy, E. A., King, K. Y. & Baldridge, M. T. Mouse microbiota models: Comparing germ-free mice and antibiotics treatment as tools for modifying gut bacteria. *Front Physiol* **9**, 417794 (2018).

921. Schoeb, T. R. & Rahija, R. J. Chapter 26 - Gnotobiotics. *Laboratory Animal Medicine: Third Edition* 1263–1296 (2015) doi:10.1016/B978-0-12-409527-4.00026-2.

922. Meier, K. H. U. *et al.* Metabolic landscape of the male mouse gut identifies different niches determined by microbial activities. *Nature Metabolism 2023 5:6* **5**, 968–980 (2023).

923. Tadepally, H. D. Role of microbial metabolites in regulating host immunity. *Recent Developments in Applied Microbiology and Biochemistry: Volume 2* 29–33 (2020) doi:10.1016/B978-0-12-821406-0.00004-7.

924. Zheng, L., Wen, X. L. & Duan, S. L. Role of metabolites derived from gut microbiota in inflammatory bowel disease. *World J Clin Cases* **10**, 2660 (2022).

925. Zarei, I. *et al.* Tissue-wide metabolomics reveals wide impact of gut microbiota on mice metabolite composition. *Scientific Reports 2022 12:1* **12**, 1–20 (2022).

926. van der Wielen, N., Moughan, P. J. & Mensink, M. Amino Acid Absorption in the Large Intestine of Humans and Porcine Models. *J Nutr* **147**, 1493–1498 (2017).

927. Clausen, M. V., Hilbers, F. & Poulsen, H. The structure and function of the Na,K-ATPase isoforms in health and disease. *Front Physiol* **8**, 257141 (2017).

928. Saha, P. *et al.* Molecular mechanism of regulation of villus cell Na-K-ATPase in the chronically inflamed mammalian small intestine. *Biochim Biophys Acta* **1848**, 702–711 (2015).

929. Arthur, S., Saha, P., Sundaram, S., Kekuda, R. & Sundaram, U. Regulation of Sodium-glutamine Cotransport in Villus and Crypt Cells by Glucocorticoids During Chronic Enteritis. *Inflamm Bowel Dis* **18**, 2149–2157 (2012).

930. Sundaram, U., Wisel, S., Rajendren, V. M. & West, A. B. Mechanism of inhibition of Na+-glucose cotransport in the chronically inflamed rabbit ileum. *Am J Physiol Gastrointest Liver Physiol* **273**, (1997).

931. Ejderhamn, J., Finkel, Y. & Strandvik, B. Na, K-ATPase Activity in Rectal Mucosa of Children with Ulcerative Colitis and Crohn's Disease. *http://dx.doi.org/10.3109/00365528909089265* **24**, 1121–1125 (2009).

932. Kennedy, E. A., King, K. Y. & Baldridge, M. T. Mouse microbiota models: Comparing germ-free mice and antibiotics treatment as tools for modifying gut bacteria. *Front Physiol* **9**, 417794 (2018).

933. Bijarchian, F., Taghiyar, L., Azhdari, Z. & Eslaminejad, M. B. M2c Macrophages enhance phalange regeneration of amputed mice digits in an organ co-culture system. *Iran J Basic Med Sci* **24**, 1602 (2021).

934. Rojas, J. *et al.* Macrophage Heterogeneity and Plasticity: Impact of Macrophage Biomarkers on Atherosclerosis. *Scientifica (Cairo)* **2015**, 1–17 (2015).

935. Hilliard, B. A. *et al.* Increased expression of Mer tyrosine kinase in circulating dendritic cells and monocytes of lupus patients: correlations with plasma interferon activity and steroid therapy. *Arthritis Res Ther* **16**, R76 (2014).

936. Yang, R. *et al.* Exosomes Derived From M2b Macrophages Attenuate DSS-Induced Colitis. *Front Immunol* **10**, 476632 (2019).

937. Velotti, F., Barchetta, I., Cimini, F. A. & Cavallo, M. G. Granzyme B in Inflammatory Diseases: Apoptosis, Inflammation, Extracellular Matrix Remodeling, Epithelial-to-Mesenchymal Transition and Fibrosis. *Front Immunol* **11**, 587581 (2020).

938. Trapani, J. A. & Sutton, V. R. Granzyme B: Pro-apoptotic, antiviral and antitumor functions. *Curr Opin Immunol* **15**, 533–543 (2003).

939. Castleman, M. J. *et al.* Gut Bacteria Induce Granzyme B Expression in Human Colonic ILC3s In Vitro in an IL-15-Dependent Manner. *J Immunol* **206**, 3043–3052 (2021).

940. Zhou, L. *et al.* Expression of pAkt is associated with a poor prognosis in chinese women with invasive ductal breast cancer. *Oncol Lett* **15**, 4859–4866 (2018).

941. Oroojzadeh, P., Bostanabad, S. Y. & Lotfi, H. Psychobiotics: the Influence of Gut Microbiota on the Gut-Brain Axis in Neurological Disorders. *Journal of Molecular Neuroscience 2022 72:9* **72**, 1952–1964 (2022).

942. Bonfili, L. *et al.* Gut microbiota manipulation through probiotics oral administration restores glucose homeostasis in a mouse model of Alzheimer's disease. *Neurobiol Aging* **87**, 35–43 (2020).

943. Kikuchi, K. *et al.* Gut microbiome-derived phenyl sulfate contributes to albuminuria in diabetic kidney disease. *Nat Commun* **10**, (2019).

944. Marhuenda-Muñoz, M. *et al.* Microbial Phenolic Metabolites: Which Molecules Actually Have an Effect on Human Health? *Nutrients* **11**, (2019).

945. Kikuchi, K. *et al.* Metabolomic analysis of uremic toxins by liquid chromatography/electrospray ionization-tandem mass spectrometry. *Journal of Chromatography B* **878**, 1662–1668 (2010).

946. Radzikh, I. *et al.* Metabolic Outcomes of Anaplerotic Dodecanedioic Acid Supplementation in Very Long Chain Acyl-CoA Dehydrogenase (VLCAD) Deficient Fibroblasts. *Metabolites* **11**, (2021).

947. Bharathi, S. S., Zhang, Y., Gong, Z., Muzumdar, R. & Goetzman, E. S. Role of mitochondrial acyl-CoA dehydrogenases in the metabolism of dicarboxylic fatty acids. *Biochem Biophys Res Commun* **527**, 162–166 (2020).

948. Ranea-Robles, P. & Houten, S. M. The biochemistry and physiology of long-chain dicarboxylic acid metabolism. *Biochemical Journal* **480**, 607–627 (2023).

949. Salinari, S. *et al.* Dodecanedioic acid overcomes metabolic inflexibility in type 2 diabetic subjects. *Am J Physiol Endocrinol Metab* **291**, 1051–1058 (2006).

950. Liang, J. *et al.* Effects of Clostridium butyricum on growth performance, metabonomics and intestinal microbial differences of weaned piglets. *BMC Microbiology 2021 21:1* **21**, 1–16 (2021).

951. Morais, P., Adachi, H. & Yu, Y. T. The Critical Contribution of Pseudouridine to mRNA COVID-19 Vaccines. *Front Cell Dev Biol* **9**, (2021).

952. Dobolyi, A., Juhasz, G., Kovacs, Z. & Kardos, J. Uridine Function in the Central Nervous System. *Curr Top Med Chem* **11**, 1058–1067 (2011).

953. Cheng, K. G. *et al.* Conjugation of Uridine with Oleanolic Acid Derivatives as Potential Antitumor Agents. *Chem Biol Drug Des* **88**, 329–340 (2016).

954. Fan, X. *et al.* Improvement of uridine production of Bacillus subtilis by atmospheric and room temperature plasma mutagenesis and high-throughput screening. *PLoS One* **12**, (2017).

955. Popkov, V. A. *et al.* Gut microbiota as a source of uremic toxins. *Int J Mol Sci* **23**, 483 (2022).

956. Tang, Q., Tan, P., Ma, N. & Ma, X. Physiological Functions of Threonine in Animals: Beyond Nutrition Metabolism. *Nutrients* **13**, (2021).

957. Aon, M. A., Bhatt, N. & Cortassa, S. Mitochondrial and cellular mechanisms for managing lipid excess. *Front Physiol* **5**, (2014).

958. Ross-Inta, C. M., Zhang, Y. F., Almendares, A. & Giulivi, C. Threonine-deficient diets induced changes in hepatic bioenergetics. *Am J Physiol Gastrointest Liver Physiol* **296**, 1130–1139 (2009).

959. Neis, E. P. J. G., Dejong, C. H. C. & Rensen, S. S. The Role of Microbial Amino Acid Metabolism in Host Metabolism. *Nutrients 2015, Vol. 7, Pages 2930-2946* **7**, 2930–2946 (2015).

960. Zhang, H. *et al.* l-Threonine improves intestinal mucin synthesis and immune function of intrauterine growth–retarded weanling piglets. *Nutrition* **59**, 182–187 (2019).

961. Wils-Plotz, E. L., Jenkins, M. C. & Dilger, R. N. Modulation of the intestinal environment, innate immune response, and barrier function by dietary threonine and purified fiber during a coccidiosis challenge in broiler chicks. *Poult Sci* **92**, 735–745 (2013).

962. Lu, H. L. *et al.* Activation of M1 macrophages plays a critical role in the initiation of acute lung injury. *Biosci Rep* **38**, 20171555 (2018).

963. Zhang, D. & Frenette, P. S. Cross talk between neutrophils and the microbiota. *Blood* **133**, 2168 (2019).

964. Deshmukh, H. S. *et al.* The microbiota regulates neutrophil homeostasis and host resistance to Escherichia coli K1 sepsis in neonatal mice. *Nature Medicine 2014 20:5* **20**, 524–530 (2014).

965. Khosravi, A. *et al.* Gut Microbiota Promote Hematopoiesis to Control Bacterial Infection. *Cell Host Microbe* **15**, 374–381 (2014).

966. Mei, J. *et al.* Cxcr2 and Cxcl5 regulate the IL-17/G-CSF axis and neutrophil homeostasis in mice. *J Clin Invest* **122**, 974–986 (2012).

967. Derksen, P. W. B. *et al.* Mammary-specific inactivation of E-cadherin and p53 impairs functional gland development and leads to pleomorphic invasive lobular carcinoma in mice. *Dis Model Mech* **4**, 347–358 (2011).

968. Bruner, H. C. & Derksen, P. W. B. Loss of E-Cadherin-Dependent Cell–Cell Adhesion and the Development and Progression of Cancer. *Cold Spring Harb Perspect Biol* **10**, (2018).

969. Hoy, B. *et al.* Distinct Roles of Secreted HtrA Proteases from Gram-negative Pathogens in Cleaving the Junctional Protein and Tumor Suppressor E-cadherin. *Journal of Biological Chemistry* **287**, 10115–10120 (2012).

970. Lee, N. Y. & Suk, K. T. The Role of the Gut Microbiome in Liver Cirrhosis Treatment. *Int J Mol Sci* **22**, 1–16 (2021).

971. Bajaj, J. S. *et al.* Salivary microbiota reflects changes in gut microbiota in cirrhosis with hepatic encephalopathy. *Hepatology* **62**, 1260–1271 (2015).

972. Bajaj, J. S. Altered Microbiota in Cirrhosis and Its Relationship to the Development of Infection. *Clin Liver Dis (Hoboken)* **14**, 107–111 (2019).

973. Acharya, C. & Bajaj, J. S. Altered Microbiome in Patients With Cirrhosis and Complications. *Clinical Gastroenterology and Hepatology* **17**, 307–321 (2019).

974. Han, H. *et al.* Depletion of Gut Microbiota Inhibits Hepatic Lipid Accumulation in High-Fat Diet-Fed Mice. *Int J Mol Sci* **23**, (2022).

975. Asnicar, F. *et al.* Microbiome connections with host metabolism and habitual diet from 1,098 deeply phenotyped individuals. *Nat Med* **27**, 321–332 (2021).

976. Schwimmer, J. B. *et al.* Microbiome Signatures Associated With Steatohepatitis and Moderate to Severe Fibrosis in Children With Nonalcoholic Fatty Liver Disease. *Gastroenterology* **157**, 1109–1122 (2019).

977. Han, H. *et al.* Intestinal dysbiosis in nonalcoholic fatty liver disease (NAFLD): focusing on the gut–liver axis. *Crit Rev Food Sci Nutr* **63**, 1689–1706 (2023).

978. Jardon, K. M., Canfora, E. E., Goossens, G. H. & Blaak, E. E. Dietary macronutrients and the gut microbiome: a precision nutrition approach to improve cardiometabolic health. *Gut* (2022) doi:10.1136/GUTJNL-2020-323715.

979. Wang, B. *et al.* Metabolism pathways of arachidonic acids: mechanisms and potential therapeutic targets. *Signal Transduction and Targeted Therapy 2021 6:1* **6**, 1–30 (2021).

980. Kuehl, F. A. *et al.* Role of prostaglandin endoperoxide PGG2 in inflammatory processes. *Nature 1977 265:5590* **265**, 170–173 (1977).

981. Hunt, J. A. Inflammation. *Encyclopedia of Materials: Science and Technology* 4069–4075 (2001) doi:10.1016/B0-08-043152-6/00714-2.

982. Asahara, M. *et al.* Role of leukotriene B4 (LTB4)-LTB4 receptor 1 signaling in post-incisional nociceptive sensitization and local inflammation in mice. *PLoS One* **17**, e0276135 (2022).

983. Sztolsztener, K., Chabowski, A., Harasim-Symbor, E., Bielawiec, P. & Konstantynowicz-Nowicka, K. Arachidonic Acid as an Early Indicator of Inflammation during Non-Alcoholic Fatty Liver Disease Development. *Biomolecules* **10**, 1–15 (2020).

984. Van Scherpenzeel, M. *et al.* Dynamic tracing of sugar metabolism reveals the mechanisms of action of synthetic sugar analogs. *Glycobiology* **32**, 239–250 (2022).

985. Frenkel-Pinter, M. *et al.* Interplay between protein glycosylation pathways in Alzheimer's disease. *Sci Adv* **3**, (2017).

986. Moriwaki, K. *et al.* Deficiency of GMDS Leads to Escape from NK Cell-Mediated Tumor Surveillance Through Modulation of TRAIL Signaling. *Gastroenterology* **137**, 188-198.e2 (2009).

987. Yu, Y. *et al.* Serum untargeted metabolomics analysis of the mechanisms of evodiamine on type 2 diabetes mellitus model rats. *Food Funct* **13**, 6623–6635 (2022).

988. He, R. *et al.* L-Fucose ameliorates DSS-induced acute colitis via inhibiting macrophage M1 polarization and inhibiting NLRP3 inflammasome and NF-kB activation. *Int Immunopharmacol* **73**, 379–388 (2019).

989. Achari, A. E. & Jain, S. K. Adiponectin, a Therapeutic Target for Obesity, Diabetes, and Endothelial Dysfunction. *International Journal of Molecular Sciences 2017, Vol. 18, Page 1321* **18**, 1321 (2017).

990. Richards, N. G. J., Humkey, R. N., Li, K., Meyer, M. E. & Córdova de Sintjago, T. C. Tunnels and intermediates in the glutamine-dependent amidotransferases. *Comprehensive Natural Products II: Chemistry and Biology* **8**, 161–230 (2010).

991. Pucciarelli, S. *et al.* Spermidine and spermine are enriched in whole blood of nona/centenarians. *Rejuvenation Res* **15**, 590–595 (2012).

992. Pegg, A. E. Functions of Polyamines in Mammals *. *Journal of Biological Chemistry* **291**, 14904–14912 (2016).

993. Tofalo, R., Cocchi, S. & Suzzi, G. Polyamines and gut microbiota. *Front Nutr* **6**, 439682 (2019).

994. Madeo, F., Eisenberg, T., Pietrocola, F. & Kroemer, G. Spermidine in health and disease. *Science (1979)* **359**, (2018).

995. Madeo, F., Bauer, M. A., Carmona-Gutierrez, D. & Kroemer, G. Spermidine: a physiological autophagy inducer acting as an anti-aging vitamin in humans? *Autophagy* **15**, 165 (2019).

996. Madeo, F., Bauer, M. A., Carmona-Gutierrez, D. & Kroemer, G. Spermidine: a physiological autophagy inducer acting as an anti-aging vitamin in humans? *Autophagy* **15**, 165 (2019).

997. Eisenberg, T. *et al.* Induction of autophagy by spermidine promotes longevity. *Nature Cell Biology 2009 11:11* **11**, 1305–1314 (2009).

998. Fransen, F. *et al.* Aged gut microbiota contributes to systemical inflammaging after transfer to germ-free mice. *Front Immunol* **8**, 293898 (2017).

999. Hendrickx, A. & Bossuyt, X. Quantification of the leukocyte common antigen (CD45) in mature B-cell malignancies. *Cytometry* **46**, 336–339 (2001).

1000. Li, G. *et al.* Spermidine Suppresses Inflammatory DC Function by Activating the FOXO3 Pathway and Counteracts Autoimmunity. *iScience* **23**, (2020).

1001. Hofer, S. J. *et al.* Mechanisms of spermidine-induced autophagy and geroprotection. *Nature Aging 2022 2:12* **2**, 1112–1129 (2022).

1002. Yue, F. *et al.* Spermidine prolongs lifespan and prevents liver fibrosis and hepatocellular carcinoma by activating MAP1S-mediated autophagy. *Cancer Res* **77**, 2938–2951 (2017).

1003. Kim, D. H. *et al.* Spermidine Attenuates Oxidative Stress-Induced Apoptosis via Blocking Ca2+ Overload in Retinal Pigment Epithelial Cells Independently of ROS. *Int J Mol Sci* **22**, 1–16 (2021).

1004. Chen, Y., Zhuang, H., Chen, X., Zheqi, S. H. I. & Wang, X. Spermidine-induced growth inhibition and apoptosis via autophagic activation in cervical cancer. *Oncol Rep* **39**, 2845–2854 (2018).

1005. del Rio, B. *et al.* Spermine and spermidine are cytotoxic towards intestinal cell cultures, but are they a health hazard at concentrations found in foods? *Food Chem* **269**, 321–326 (2018).

1006. Campreciós, G. *et al.* Spermidine supplementation protects the liver endothelium from liver damage in mice. *Nutrients* **13**, (2021).

1007. Jeong, J. W. *et al.* Spermidine Protects against Oxidative Stress in Inflammation Models Using Macrophages and Zebrafish. *Biomol Ther (Seoul)* **26**, 146 (2018).

1008. Zhu, S. *et al.* Spermine Protects Mice Against Lethal Sepsis Partly by Attenuating Surrogate Inflammatory Markers. *Molecular Medicine* **15**, 275 (2009).

1009. Guillaume, J., Leufgen, A., Hager, F. T., Pabst, O. & Cerovic, V. MHCII expression on gut macrophages supports T cell homeostasis and is regulated by microbiota and ontogeny. *Scientific Reports 2023 13:1* **13**, 1–13 (2023).

1010. Buxadé, M. *et al.* Macrophage-specific MHCII expression is regulated by a remote Ciita enhancer controlled by NFAT5. *Journal of Experimental Medicine* **215**, 2901–2918 (2018).

1011. Lee, N. & Kim, W. U. Microbiota in T-cell homeostasis and inflammatory diseases. *Experimental & Molecular Medicine 2017 49:5* **49**, e340–e340 (2017).

1012. Xu, T. T. *et al.* Spermidine and spermine delay brain aging by inducing autophagy in SAMP8 mice. *Aging (Albany NY)* **12**, 6401 (2020).

1013. Bermudez-Martin, P. *et al.* The microbial metabolite p-Cresol induces autistic-like behaviors in mice by remodeling the gut microbiota. *Microbiome* **9**, 1–23 (2021).

1014. Gryp, T., Vanholder, R., Vaneechoutte, M. & Glorieux, G. p-Cresyl Sulfate. *Toxins (Basel)* **9**, (2017).

1015. Meyer, T. W. & Hostetter, T. H. Uremic solutes from colon microbes. *Kidney Int* **81**, 949–954 (2012).

1016. Bao, M. *et al.* Altered gut microbiota and gut-derived p-cresyl sulfate serum levels in peritoneal dialysis patients. *Front Cell Infect Microbiol* **12**, 639624 (2022).

1017. Liu, W. C., Tomino, Y. & Lu, K. C. Impacts of Indoxyl Sulfate and p-Cresol Sulfate on Chronic Kidney Disease and Mitigating Effects of AST-120. *Toxins 2018, Vol. 10, Page 367* **10**, 367 (2018).

1018. Sun, C. Y. *et al.* p-Cresol Sulfate Caused Behavior Disorders and Neurodegeneration in Mice with Unilateral Nephrectomy Involving Oxidative Stress and Neuroinflammation. *Int J Mol Sci* **21**, 1–16 (2020).

1019. Park, J. S. *et al.* Alpha-lipoic acid attenuates p-cresyl sulfate-induced renal tubular injury through suppression of apoptosis and autophagy in human proximal tubular epithelial cells. *Biomedicine & Pharmacotherapy* **112**, 108679 (2019).

1020. Azevedo, M. L. V. *et al.* p-Cresyl sulfate affects the oxidative burst, phagocytosis process, and antigen presentation of monocyte-derived macrophages. *Toxicol Lett* **263**, 1–5 (2016).

1021. Chang, J. F. *et al.* Translational Medicine in Pulmonary-Renal Crosstalk: Therapeutic Targeting of p-Cresyl Sulfate Triggered Nonspecific ROS and Chemoattractants in Dyspneic Patients with Uremic Lung Injury. *J Clin Med* **7**, 266 (2018).

1022. Campillo, S. *et al.* Indoxyl sulfate- and P-cresol-induced monocyte adhesion and migration is mediated by integrin-linked kinase-dependent podosome formation. *Experimental & Molecular Medicine 2022 54:3* **54**, 226–238 (2022).

1023. Fu, H. Y. *et al.* The Clostridium Metabolite P-Cresol Sulfate Relieves Inflammation of Primary Biliary Cholangitis by Regulating Kupffer Cells. *Cells* **11**, (2022).

1024. Rodig, S. J., Shahsafaei, A., Li, B. & Dorfman, D. M. The CD45 isoform B220 identifies select subsets of human B cells and B-cell lymphoproliferative disorders. *Hum Pathol* **36**, 51–57 (2005).

1025. Wosen, J. E., Mukhopadhyay, D., MacAubas, C. & Mellins, E. D. Epithelial MHC class II expression and its role in antigen presentation in the gastrointestinal and respiratory tracts. *Front Immunol* **9**, 408694 (2018).

1026. Nouri-Shirazi, M. & Guinet, E. Evidence for the immunosuppressive role of nicotine on human dendritic cell functions. *Immunology* **109**, 365 (2003).

1027. Courtemanche, O. *et al.* Co-modulation of T cells and B cells enhances the inhibition of inflammation in experimental hypersensitivity pneumonitis. *Respir Res* **23**, 1–12 (2022).

1028. Jacobs, M. *et al.* IL-10 producing regulatory B cells are decreased in blood from smokers and COPD patients. *Respir Res* **23**, 1–12 (2022).

1029. Chougnet, C. A. *et al.* Loss of Phagocytic and Antigen Cross-Presenting Capacity in Aging Dendritic Cells Is Associated with Mitochondrial Dysfunction. *The Journal of Immunology* **195**, 2624–2632 (2015).

1030. Kennedy, E. A., King, K. Y. & Baldridge, M. T. Mouse microbiota models: Comparing germ-free mice and antibiotics treatment as tools for modifying gut bacteria. *Front Physiol* **9**, 417794 (2018).

1031. Ngan, D. A., Vickerman, S. V, Granville, D. J., Paul Man, S. F. & Sin, D. D. The possible role of granzyme B in the pathogenesis of chronic obstructive pulmonary disease. doi:10.1177/1753465809341965.

1032. Zhu, J. & Cole, R. B. Formation and decompositions of chloride adduct ions, [M + Cl]−, in negative ion electrospray ionization mass spectrometry. *J Am Soc Mass Spectrom* **11**, 932–941 (2000).

1033. Römpp, A. & Spengler, B. Mass spectrometry imaging with high resolution in mass and space. *Histochem Cell Biol* **139**, 759 (2013).

1034. Hu, X. *et al.* Impacts of Cigarette Smoking Status on Metabolomic and Gut Microbiota Profile in Male Patients With Coronary Artery Disease: A Multi-Omics Study. *Front Cardiovasc Med* **8**, 766739 (2021).

1035. Strott, C. A. & Higashi, Y. Cholesterol sulfate in human physiology: what's it all about? *J Lipid Res* **44**, 1268–1278 (2003).

1036. Hanyu, O. *et al.* Cholesterol sulfate induces expression of the skin barrier protein filaggrin in normal human epidermal keratinocytes through induction of RORα. *Biochem Biophys Res Commun* **428**, 99–104 (2012).

1037. Yan, H. *et al.* The Relationship Among Intestinal Bacteria, Vitamin K and Response of Vitamin K Antagonist: A Review of Evidence and Potential Mechanism. *Front Med (Lausanne)* **9**, (2022).

1038. Lai, Y., Masatoshi, H., Ma, Y., Guo, Y. & Zhang, B. Role of Vitamin K in Intestinal Health. *Front Immunol* **12**, 791565 (2022).

1039. Caldwell, J., Moffatt, J. R. & Smith, R. L. Post-mortem Survival of Hippuric Acid Formation in Rat and Human Cadaver Tissue Samples. *http://dx.doi.org/10.3109/00498257609151639* **6**, 275–280 (2009).

1040. Nicholls, A. W., Mortishire-Smith, R. J. & Nicholson, J. K. NMR Spectroscopic-Based Metabonomic Studies of Urinary Metabolite Variation in Acclimatizing Germ-Free Rats. *Chem Res Toxicol* **16**, 1395–1404 (2003).

1041. Rechner, A. R. *et al.* The metabolic fate of dietary polyphenols in humans. *Free Radic Biol Med* **33**, 220–235 (2002).

1042. Williams, H. R. T. *et al.* Differences in gut microbial metabolism are responsible for reduced hippurate synthesis in Crohn's disease. *BMC Gastroenterol* **10**, 108 (2010).

1043. Wu, X. *et al.* Biomarkers of Metabolomics in Inflammatory Bowel Disease and Damp-Heat Syndrome: A Preliminary Study. *Evidence-based Complementary and Alternative Medicine* **2022**, (2022).

1044. Sun, B. *et al.* Hippuric Acid Promotes Renal Fibrosis by Disrupting Redox Homeostasis via Facilitation of NRF2–KEAP1–CUL3 Interactions in Chronic Kidney Disease. *Antioxidants 2020, Vol. 9, Page 783* **9**, 783 (2020).

1045. Ziessman, H. A., O'Malley, J. P. & Thrall, J. H. Genitourinary System. *Nuclear Medicine* 215–262 (2006) doi:10.1016/B978-0-323-02946-9.50013-1.

1046. Microbial metabolites in health and disease: Navigating the unknown in search of function - PMC. https://www.ncbi.nlm.nih.gov/pmc/articles/PMC5448084/.

1047. Martinez, K. B., Leone, V. & Chang, E. B. Microbial metabolites in health and disease: Navigating the unknown in search of function. *J Biol Chem* **292**, 8553 (2017).

1048. Dhillon, B. K., Smith, M., Baghela, A., Lee, A. H. Y. & Hancock, R. E. W. Systems Biology Approaches to Understanding the Human Immune System. *Front Immunol* **11**, 542199 (2020).

1049. Savkovic, S. D., Villanueva, J., Turner, J. R., Matkowskyj, K. A. & Hecht, G. Mouse Model of Enteropathogenic Escherichia coli Infection. *Infect Immun* **73**, 1161 (2005).

1050. Hu, H., Yin, R., Brown, H. M. & Laskin, J. Spatial Segmentation of Mass Spectrometry Imaging Data by Combining Multivariate Clustering and Univariate Thresholding. *Anal Chem* **93**, 3477 (2021).

1051. Alexandrov, T. *et al.* Spatial segmentation of imaging mass spectrometry data with edge-preserving image denoising and clustering. *ACS Publications* **9**, 6535–6546 (2010).

1052. Verbeeck, N., … R. C.-M. spectrometry & 2020, undefined. Unsupervised machine learning for exploratory data analysis in imaging mass spectrometry. *Wiley Online LibraryN Verbeeck, RM Caprioli, R Van de PlasMass spectrometry reviews, 2020•Wiley Online Library* **39**, 245–291 (2020).

1053. Guo, A., Chen, Z., Li, F. & Luo, Q. Delineating regions of interest for mass spectrometry imaging by multimodally corroborated spatial segmentation. *Gigascience* **12**, 1–10 (2022).

1054. Knudsen, L. A. *et al.* Translational Potential of Metabolomics on Animal Models of Inflammatory Bowel Disease—A Systematic Critical Review. *Int J Mol Sci* **21**, (2020).

1055. de Jonge, N. F. *et al.* Good practices and recommendations for using and benchmarking computational metabolomics metabolite annotation tools. *Metabolomics* **18**, (2022).

1056. Bittremieux, W., Wang, M. & Dorrestein, P. C. The critical role that spectral libraries play in capturing the metabolomics community knowledge. *Metabolomics 2022 18:12* **18**, 1–16 (2022).

1057. Judge, M. T. & Ebbels, T. M. D. Problems, principles and progress in computational annotation of NMR metabolomics data. *Metabolomics* **18**, 1–15 (2022).

1058. Li, Q. & Kang, C. B. A Practical Perspective on the Roles of Solution NMR Spectroscopy in Drug Discovery. *Molecules* **25**, (2020).

1059. Markwick, P. R. L., Malliavin, T. & Nilges, M. Structural biology by NMR: Structure, dynamics, and interactions. *PLoS Comput Biol* **4**, (2008).

1060. Sugiki, T., Furuita, K., Fujiwara, T. & Kojima, C. Current NMR techniques for structure-based drug discovery. *Molecules* **23**, (2018).

Chapter 8 Appendix

8.1.1 Appendix 1

Growth curve of AIEC LF82 over a 24 h period. Bacteria were cultured in LB and supplemented with 0, 250 or 500 nM GCA and grown at 37°C in a shaken incubator. Results shown as mean of three biological replicates. Two-way ANOVA did not show any significant changes in growth between control condition (0 nM) and the two GCA supplemented conditions.
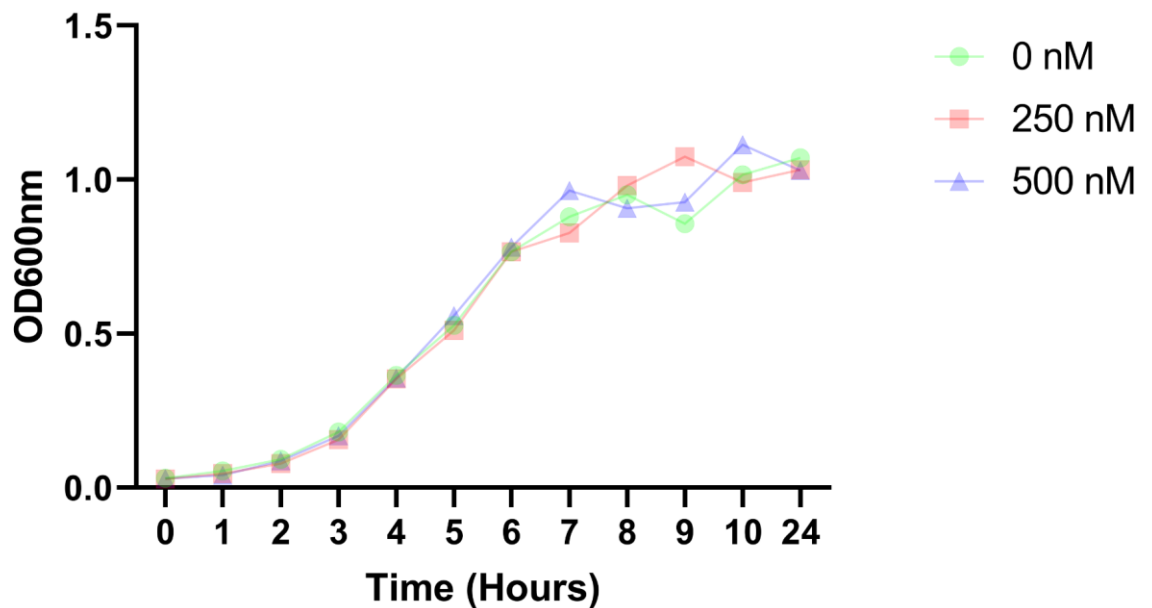
8.1.2 Appendix 2

TNF-α production was quantified by homogenising small tissue sections and performing an ELISA. Results were normalised to protein concentrations that were quantified using BCA and shown as mean of three biological replicates. T-tests showed that A) AIEC LF82 infection increased TNF-α production (p=0.0418) in colon only when water was supplemented with PA. B) Infection with AIEC LF82 increased TNF-α production in the ileum with and without PA supplementation (p=0.0156 and p=0.0315).
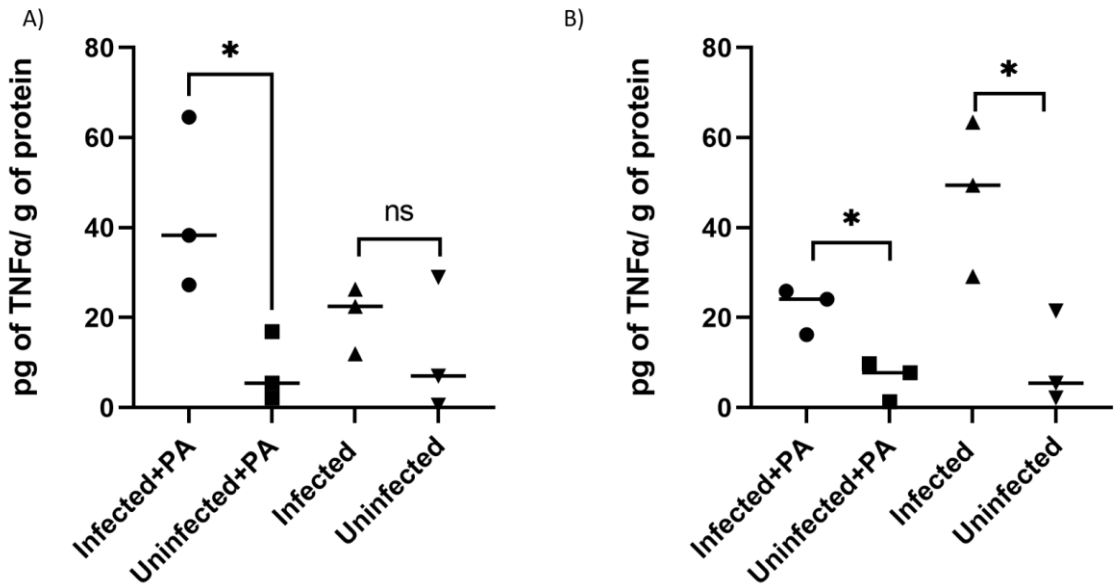
8.1.3 Appendix 3

DSS induced colitis resulted in a drop in body weight % (a), significantly reduced the length of the colon (b) and colitis was initiated after 5 days of DSS treatment shown as disease activity index (DAI) (c). At the end of the experiment (day 7), mice had significantly higher DAI, indicating that severe colitis had been induced. Ordinary one-way ANOVA was performed on colon lengths and 2way ANOVA was used for DAI (*$p<0.05$, **$p<0.01$, ***$p<0.001$, ****$p<0.0001$).
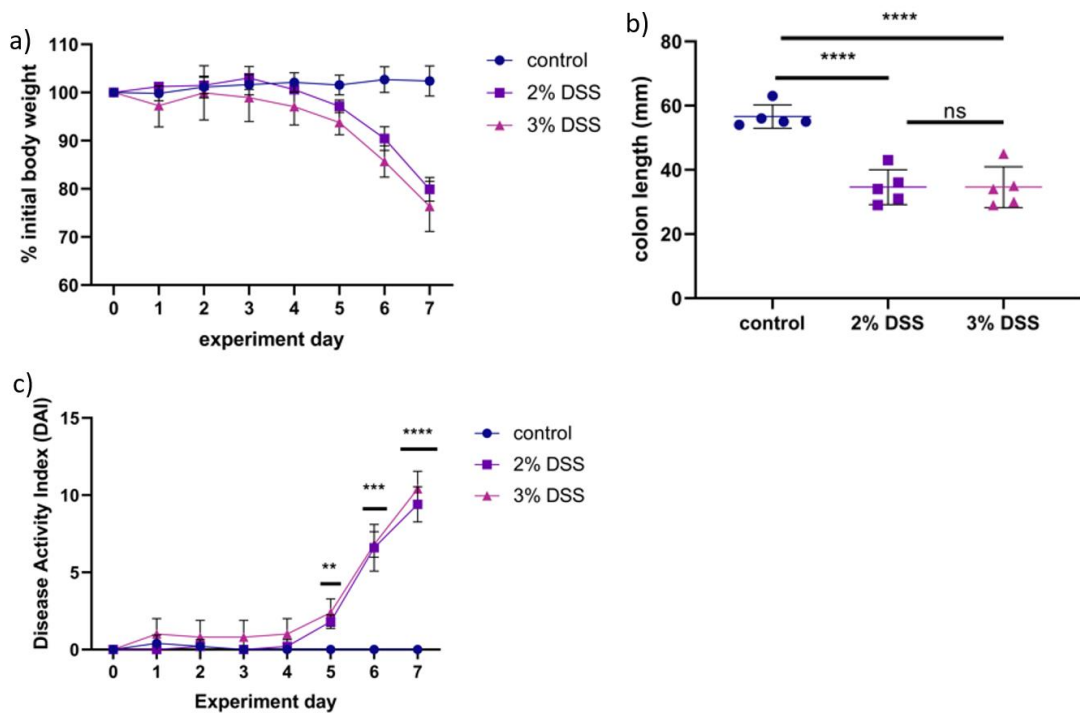
8.1.4 Appendix 4

Table shows the *m/z*, abbreviated names shown in heatmap (Figure 4.3.3) and full compound name for molecules found to be significantly changed in the ileum of DSS colitis model. Table includes the mean relative abundance value for each molecule within the groups. P-values highlighted in grey are for molecules down regulated in 3% group compared to control group and p-values not highlighted show molecules upregulated in 3% group compared to the control.

m/z	Heatmap ID	compound_name	adduct	ppm	Mean 0%	Mean 3%	p-value
131.035	Glutaric acid(P)	Glutaric acid	M-H	10	18.51141	39.78651	0.001903
132.0771	Creatine	Creatine	M+H	6	26.6331	61.16262	0.005447
162.1126	L-carnitine	L-carnitine	M+H	6	77.24398	121.6827	0.009899
167.1078	m/z 167.1078				22.19504	45.44605	0.001747
193.1234	m/z 193.1234				15.4677	27.59501	0.001903
195.1027	m/z 195.1027				29.71642	67.00769	0.001903
211.0975	m/z 211.0975				18.15224	34.83791	0.001903
221.1183	m/z 221.1183				12.98418	29.31121	0.001903
235.1339	m/z 235.1339				52.56577	115.0212	0.001845
251.2016	m/z 251.2016				43.0718	92.0656	0.001314
253.2174	m/z 253.2174				1918.392	656.5393	0.001903
254.2207	m/z 254.2207				489.9919	167.8958	0.001903
259.1518	m/z 259.1518				67.3124	156.7913	0.009899
277.2173	GLA (P)	gamma-Linolenic acid	M-H	0	858.6101	406.1114	0.001227
278.2207	m/z 278.2207				108.4817	50.61569	0.001227
285.1249	m/z 285.1249				9.299744	24.01997	0.001903
301.1658	Hydroxy steroid(P)	11b-Hydroxyandrost-4-ene-3,17-dione	M-H	5	3.26949	15.59533	0.001903
303.233	Arachidonic acid	Arachidonic acid	M-H	4	2488.715	4830.248	0.001903
304.2364	m/z 304.2364				799.7057	1556.888	0.001903
305.2485	m/z 305.2485				56.22055	110.3871	0.001903
317.1759	Ubiquinone-2(P)	Ubiquinone-2	M-H	5	16.0724	49.1914	0.001227
317.2126	Leukotriene A4	Leukotriene A4	M-H	7	48.1168	121.7857	0.002981
319.2281	5,6-EET(P)	5,6-Epoxy-8,11,14-eicosatrienoic acid	M-H	2	141.8269	336.1047	0.003894
327.233	DHA	Docosahexaenoic acid	M-H	5	814.25	2169.011	0.001974
328.2364	m/z 328.2364				128.3666	342.4678	0.001943
343.2201	EDPA	Epoxydocosapentaenoic acid	M-H	4	19.77427	67.14966	0.003894
349.1975	12-Oxo-LTB4(P)	12-Oxo-20-hydroxy-leukotriene B4	M-H	8	22.06216	63.45958	0.002909
351.2173	Lipoxin A4	Lipoxin A4	M-H	1	55.84294	116.4331	0.003457
357.2406	m/z 357.2406				30.05336	61.45339	0.009899
363.2105	m/z 327.23471				17.24567	57.95692	0.001747
367.2442	PGG2(P)	Prostaglandin G2	M-H	1	15.26352	45.37761	0.001314
369.277	m/z 369.277				11.44372	41.41741	0.009899
391.2122	14-Hydro-neuro(P)	14-Hydroperoxy-H4-neuroprostane	M-H	5	6.858846	30.54859	0.001903
395.3138	m/z 395.3138				24.91365	64.43831	0.009899

m/z	Name	Full Name	Adduct	n	Val1	Val2	Val3
395.3502	m/z 395.3502				13.67504	45.53829	0.005447
425.3394	20α-OHC(P)	20alpha-hydroxy cholesterol	M+Na	2	38.54771	69.84752	0.009899
437.3397	m/z 437.3397				10.34558	32.61636	0.009899
441.3336	20a,22b-DOHC(P)	20a,22b-Dihydroxycholesterol	M+Na	2	19.46659	41.79346	0.009933
463.3036	m/z 463.3036				43.04457	5.886998	0.009899
465.1743	PGH2(P)	Prostaglandin H2 2-glyceryl Ester	M+K	2	12.78091	38.20404	0.004235
465.3045	CS(P)	Cholesterol sulfate	M-H	1	33.2425	4.233776	0.000998
465.3192	m/z 465.3192				96.64857	218.7687	0.004235
466.3078	m/z 466.3078				27.57423	63.99506	0.000998
508.3044	m/z 508.3044				10.09489	29.71496	0.003614
509.4576	FAHFA(16:0)(P)	FAHFA(16:0/6-O-16:0)	M-H	2	53.5792	13.78694	0.001903
510.4609	m/z 510.4609				26.14738	5.056658	0.001903
511.4732	m/z 511.4732				175.7986	88.69382	0.001903
512.4764	m/z 512.4764				40.79809	18.6329	0.001903
546.354	LycoPC(20:3)	LysoPC(20:3(8Z,11Z,14Z)/0:0)	M+H	3	55.5838	102.0115	0.004235
557.4561	m/z 557.4561				49.9586	19.31112	0.001227
567.5356	m/z 567.5356				22.93004	64.37812	0.001277
568.5387	m/z 568.5387				3.96036	14.91338	0.001903
583.4942	m/z 583.4942				45.28996	8.891721	0.001903
584.4978	m/z 584.4978				10.26839	1.554362	0.001943
587.5028	m/z 587.5028				20.31425	35.32787	0.014693
594.3413	PC(20:1)(P)	PC(18:1(12Z)-2OH(9,10)/2:0)	M-H	2	110.1503	29.7129	0.001903
605.4545	DG(32:1)(P)	DG(14:0/18:1(9Z)/0:0)	M+K	2	78.64177	25.3103	0.010204
607.4734	m/z 607.4734				8.390444	31.04291	0.002871
607.4943	DG(34:1) (P)	DG(16:0/18:1(12Z)-O(9S,10R)/0:0)	M-H	1	43.57882	13.68875	0.002337
629.455	DG(16:0) (P)	DG(14:0/20:3(8Z,11Z,14Z)/0:0)	M+K	2	209.8574	38.52766	0.009933
631.4899	DG(36:4) (P)	DG(20:4(5Z,7E,11Z,14Z)-OH(9)/0:0/i-16:0)	M-H	9	36.97692	7.677196	0.003829
701.5625	PA(36:2) (P)	PA(20:2(11Z,14Z)/16:0)	M+H	2	82.98722	9.306941	0.009933
702.5005	PE-NMe(32:2) (P)	PE-NMe(18:2(9Z,12Z)/14:0)	M+H	14	36.02354	3.804072	0.009933
703.5279	PA(36:1) (P)	PA(22:1(13Z)/14:0)	M+H	0	68.36887	9.47622	0.009899
704.5315	PC(30:1) (P)	PC(16:1(9Z)/14:0)	M+H	14	20.69057	2.720816	0.009899
841.6671	PA (46:2) (P)	PA(24:1(15Z)/22:1(13Z))	M+H	1	54.33888	13.32923	0.009899
843.6834	PA (46:1) (P)	PA(24:1(15Z)/22:0)	M+H	1	73.93822	20.10841	0.009899
847.7393	m/z 847.7393				23.56876	3.401429	0.003831
854.73	m/z 854.73				128.6605	21.60667	0.009899
855.7419	TG(32:2) P)	TG(15:0/20:1(11Z)/15:0)	M+Na	0	143.3241	28.17171	0.009899
856.7457	m/z 856.7457				73.97373	14.58817	0.009899
865.5019	PG(38:4)(P)	PG(18:0/20:4(6Z,8E,10E,14Z)-2OH(5S,12R))	M+Cl	2	7.877709	35.65681	0.002871
867.6741	PA(46:0)(P)	PA(22:0/24:0)	M+Na	0	111.6849	24.31171	0.009899
868.6808	PE-NMe(44:3)(P)	PE-NMe(24:1(15Z)/20:2(11Z,14Z))	M+H	7	65.14419	14.15516	0.009899
869.6996	PA(44:2)(P)	PA(24:1(15Z)/24:1(15Z))	M+H	2	226.1649	56.43565	0.009899
870.7031	PC(46:2)(P)	PC(24:1(15Z)/18:1(11Z))	M+H	7	126.6299	32.11966	0.009899
871.7151	PA(48:1)(P)	PA(24:1(15Z)/24:0)	M+H	2	136.7504	39.93581	0.009899
881.7571	TG(54:5)(P)	TG(14:0/18:0/22:5(4Z,7Z,10Z,13Z,16Z))	M+H	2	198.736	41.89184	0.004733
882.7615	m/z 882.7615				105.5943	22.51055	0.004733
893.7012	TG(52:4)(P)	TG(16:1(9Z)/14:1(9Z)/22:2(13Z,16Z))	M+K	1	124.2978	25.89853	0.004838
894.7032	PC(44:4)(P)	PC(24:1(15Z)/20:3(5Z,8Z,11Z))	M+H	9	71.4225	14.86303	0.004975
895.7146	TG(52:3)(P)	TG(16:0/22:2(13Z,16Z)/14:1(9Z))	M+K	0	197.9684	52.55442	0.004983
896.7183	PC(44:3)(P)	PC(24:1(15Z)/20:2(11Z,14Z))	M+H	9	105.9555	28.17985	0.005399

341.2457	MA(P)	Methyl Arachidonate	M+Na	1	9.578257	32.72954	0.005401
367.3187	m/z 367.3187				20.14158	54.79385	0.009899

8.1.5 Appendix 5

PLS-DA generated VIP>1 list of molecules in the ileum that contribute towards group separation in the DSS induced colitis model.

mz	VIP list
162.1130066	1.306210041
466.3070068	1.305969954
465.3049927	1.3046
546.3540039	1.259809971
587.5029907	1.235599995
317.177002	1.191900015
367.2120056	1.190739989
567.5339966	1.17723
256.0589905	1.172199965
391.2109985	1.167940021
363.2099915	1.16779995
277.2170105	1.151690006
278.2219849	1.151550055
343.2290039	1.139610052
568.5390015	1.134230018
557.4559937	1.130779982
865.5020142	1.130169988
251.128006	1.126889944
465.2260132	1.11748004
317.2099915	1.115929961
193.1230011	1.114580035

344.2319946	1.111469984
320.2309875	1.110579967
319.2290039	1.110360026
301.1789856	1.110200047
235.1360016	1.105029941
349.1990051	1.104580045
385.2720032	1.104089975
221.1190033	1.099099994
167.1080017	1.099009991
351.2179871	1.095260024
594.34198	1.090180039
395.3510132	1.086809993
195.1000061	1.067849994
211.095993	1.06475997
372.276001	1.062000036
328.2369995	1.060909986
461.2309875	1.059649944
327.2319946	1.057909966
511.4729919	1.05637002
253.2169952	1.053130031
254.2169952	1.052770019
583.4940186	1.052250028
305.2409973	1.051090002
132.076004	1.050529957
512.4780273	1.049790025
285.1289978	1.049319983

8.1.6 Appendix 6

Table shows the m/z, abbreviated names shown in heatmap (Figure 4.3.6) and full compound name for molecules found to be significantly changed in the colon of DSS colitis model. Table includes the mean relative abundance value for each molecule within the groups. P-values highlighted in grey are for molecules down regulated in 3% group compared to control group and p-values not highlighted show molecules upregulated in 3% group compared to the control.

m/z	Heatmap ID	compound_name	adduct	ppm	mean 0%	mean 3%	p-value

Mz	Name	Compound	Adduct	Col	Val1	Val2	p-value
137.071	1-MNA(P)	1-Methylnicotinamide	M+H	12	33.89	88.04	0.001162
140.0682	L-Valine(P)	L-Valine	M+Na	7	165.8	405.4	0.011395
159.0664	Pimelic acid(P)	Pimelic acid	M-H	4	19.29	34.46	0.03815
160.133	5-AVAB(P)	5-amino valeric acid betaine	M+H	6	741	406.4	0.02202
167.018	Uric acid(P)	Uric acid	M-H	12	28.57	93.51	0.021785
193.1234	m/z 193.1227				9.994	23.22	0.023974
221.1183	m/z 221.1183				10.11	27.89	0.03815
235.1339	m/z 235.1339				43.17	87.87	0.040343
261.1493	m/z 261.1493				6.989	27.22	0.023974
263.1652	m/z 263.1652				7.707	25.11	0.023974
273.1861	ODT acid	(10Z,14E,16E)-10,14,16-Octadecatrien-12-ynoic acid	M-H	6	17.56	35.71	0.040343
277.2172	GLA	gamma-Linolenic acid	M-H	3	415.5	202.1	0.045769
278.2207	m/z 278.2207				78.49	37.38	0.045769
300.0397	N-AGLANS	N-Acetylglucosamine 6-sulfate	M-H	3	0.09121	11.7	0.006095
301.1808	Hydroxy steroid (P)	11b-Hydroxyandrost-4-ene-3,17-dione	M-H	6	1.192	18.85	0.037431
317.1759	Ubiquinone-2(P)	Ubiquinone-2	M-H	2	7.63	60.24	0.02292
319.228	5-HETE(P)	5-HETE	M-H	2	145	296	0.040343
320.2312	19(S)-HETE(P)	19-Hydroxyeicosatetraenoic acid	M-H	2	29.83	62.71	0.040343
331.2643	EA(P)	Ethyl Arachidonate	M-H	4	125.4	552.9	0.043938
332.2676	m/z 332.2676				29.2	131	0.043938
333.2709	m/z 333.2709				1.288	13.13	0.043938
343.228	EDPA (P)	Epoxydocosapentaenoic acid	M-H	1	8.95	62.92	0.021785
344.2312	m/z 344.2312				1.016	26.92	0.021785
345.2436	DHT propionate(P)	Dihydrotestosterone propionate	M-H	2	5.341	31.91	0.023974
347.2593	CTXA2(P)	Carbocyclic thromboxane A2	M-H	0	4.247	31.24	0.021785
359.223	Resolvin D5(P)	Resolvin D5	M-H	2	1.069	20.29	0.021785
359.2957	m/z 359.2957				5.139	41.88	0.03815
375.2177	Resolvin D1(P)	Resolvin D1	M-H	1	0.6427	12.25	0.023974
391.2126	14-Hydro-neuro(P)	14-Hydroperoxy-H4-neuroprostane	M-H	5	1.981	25.04	0.023974

8.1.7 Appendix 7

PLS-DA generated VIP>1 list of molecules in the colon that contribute towards group separation in the DSS induced colitis model.

Mz	VIP list
140.069	1.66642
137.070007	1.60515
160.132004	1.48317
300.039001	1.2944
167.018997	1.22168
188.985001	1.03454
278.218994	1.00477
277.21701	1.00427

8.1.8 Appendix 8

Table shows the *m/z*, abbreviated names used in Figure 4.3.17 Enrichment of pathways in the liver of DSS colitis model and full compound name for molecules found to be significantly changed in the liver of DSS colitis model. Table includes the mean relative abundance value for each molecule within the groups. P-values highlighted in grey are for molecules decreased in 3% group compared to control group and p-values not highlighted show molecules increased in 3% group compared to the control.

m/z	Heatmap ID	Compound name	ppm	Mean 0%	Mean 3%	p-value
128.03638	pyroglut acid(P)	Pyroglutamic acid	8	31.21	53.63	0.00076
132.03081				15.34	36.96	0.002047
151.02595	L-Aspartic acid(P)	L-Aspartic acid	4	253	407.7	0.001693
161.04562				59.78	39.12	0.000995
178.01636				14.14	39.73	0.002318
179.05575				278.6	164.5	0.000313
180.05995	D-Galactose(P)	D-Galactose	2	17.13	6.792	0.000039
253.2166				4031	916.5	0.00003
253.34612	Palmitelaidic acid(P)	Palmitelaidic acid	3		0.04633	0.001032
254.22081				683.6	155.6	0.00003
254.55981				11.25	4.667	0.001724
265.21749				19.59	7.815	0.000464
267.19552	HDD acid(P)	10Z-Heptadecenoic acid	4	131.5	33.13	0.000712
267.2339	9Z-HDD acid(P)	9Z-Heptadecenoic acid	4	143.7	67.7	0.000058
268.19972				19.99	1.228	0.000442
268.2365				25.02	7.803	0.000111
275.20038	Stearidonic acid(P)	Stearidonic acid	5	89.57	37.59	0.000173
276.20458				16.16	2.995	0.00003
277.21838	GLA(P)	gamma-Linolenic acid	4	1026	631.6	0.00162
278.21939				194.8	119.8	0.001713
279.23319	Linoelaidic acid(P)	Linoelaidic acid	1	8050	11345	0.000435
280.23739				1547	2188	0.000435
280.46925	petroselinate(P)	petroselinate	12	13.79	2.159	0.000176
281.09928				20.67	12.52	0.000195
281.24799				17096	10374	0.000071
281.3999				19.81	10.28	0.000195
282.2522				2205	1335	0.000071

283.2564				304.5	173.8	0.000132
284.25901				18.27	4.106	0.000195
300.04006				0.1048	15.65	0.00003
309.27938				295.1	140	0.000071
310.28359				62.7	28.72	0.000084
315.20867	Linoleic acid(P)	Linoleic acid	3	31.41	83.05	0.000208
316.21287	3-hydroxycarnitine(P)	3-hydroxynonanoyl carnitine	0	3.112	14.41	0.000097
317.1755	Ubiquinone-2(P)	Ubiquinone-2	1	33.33	91.29	0.001089
318.17971				3.414	16.07	0.001089
325.2747				18.18	3.543	0.00156
337.31077				33.79	8.324	0.000852
339.21205	AA	Arachidonic acid	7	15.55	47.46	0.000422
351.18415				12.93	37.57	0.000843
363.23141	MG(16:1)(P)	MG(16:1(9Z)/0:0/0:0)	2	112.6	17.71	0.000011
364.23402				34.82	1.388	0.000011
391.21224	14-Hydro-neuro(P)	14-Hydroperoxy-H4-neuroprostane	3	34.17	83.25	0.001891
393.26322				222.2	164.9	0.002594
403.18854	PGG2(P)	Prostaglandin G2	2	1.523	15.28	0.001926
417.28578	Palmitoyl(P)	Palmitoyl glucuronide	0	11.07	0.08066	0.000588
433.28111				112.2	8.95	0.000014
434.28371				16.31	0.1557	0.000045
435.29591				405.8	190.4	0.000058
436.30012				97.99	44.33	0.000051
441.27797				0.9505	16.74	0.000309
457.28128				30.06	12.02	0.001425
461.3125				528.9	189.9	0.000019
462.3151				93.72	32.94	0.000019
477.22627	PGG2-2-glyc(P)	Prostaglandin G2 2-glyceryl Ester	0	11.62	33.7	0.001143
477.30622				28.77	2.28	0.000073
480.30924				25.87	53.13	0.002573
485.31267	Vitamin K1(P)	Vitamin K1	13	19.33	3.964	0.00006
489.34389				20.43	0.6295	0.000018
497.34874				48.14	14.19	0.00102
507.44196				43.06	9.682	0.000309
508.30225				39.53	71.85	0.002243
508.44457				7.65	0.6146	0.001089
509.45837	FAHFA(32:0)(P)	FAHFA(16:0/10-O-16:0)	2	151.6	45.06	0.000014
510.46097				79.23	18.48	0.000014
511.47317				252.6	167.8	0.000435

512.47578				89.3	58.42	0.000405
525.31937				12.81	2.507	0.000468
526.38274				28.34	9.224	0.002635
531.44054				19.31	3.284	0.000222
533.45535				147.3	69.37	0.000048
534.45955				53.96	21.56	0.000071
537.48976	FAHFA(34:0)(P)	FAHFA(16:0/6-O-18:0)	2	373.3	207.1	0.00003
538.49236				211.7	117.6	0.00003
545.36189				17.04	1.903	0.000286
552.29698				12.21	29.3	0.001455
558.33341	LysoPC(18:0)(P)	LysoPC(0:0/18:0)	0	7.585	35.18	0.000017
559.47193				181.6	320	0.000442
560.47614				70.89	125	0.000488
563.50474				321.4	204.2	0.000309
564.50735	Octadecadiene(P)	N-(2R-Hydroxyhexadecanoyl)-2S-amino-9-methyl-4E,8E-octadecadiene-1,3R-diol	13	85.31	54.37	0.000309
572.48182	Cer(d35:1)(P)	Cer(d18:1/16:0)	1	11.5	124.7	0.000164
573.48443				1.133	29.7	0.000248
574.47904	Cer(d36:4)(P)	Cer(d16:1/20:3(6,8,11)-OH(5))	9	0.3994	20.14	0.000588
581.47809	TG(32:0)(P)	TG(16:0/8:0/8:0)	1	36.06	6.427	0.000731
582.4823				10.71	0.6303	0.001891
583.47371				32.9	106	0.000902
583.4945				71.64	8.063	0.000019
584.47632	Cer(d37:6)(P)	Cer(d17:1/20:5(6E,8Z,11Z,14Z,17Z)-OH(5))	13	7.452	28.05	0.001612
584.4971				40.29	1.491	0.000018
591.53613				14.2	1.305	0.000018
592.32607				30.81	65.89	0.001891
594.34087				63.66	138.6	0.002356
595.34508	DG(30:6)(P)	DG(22:6(4Z,7Z,11E,13Z,15E,19Z)-2OH(10S,17)/0:0/8:0)	7	18.37	42.62	0.00202
601.46145				8.282	0.09036	0.000246
607.49468				148.7	33.91	0.000071
608.49728	Cer(d16:1/PGF1alpha)(P)	Cer(d16:1/PGF1alpha)	13	30.26	88.49	0.007231
611.52589				277.3	115	0.000031
612.52849				169.3	69.76	0.000035
613.5359				16.76	3.646	0.000062
625.46483	DG(34:3)(P)	DG(20:3(8Z,11Z,14Z)/14:0/0:0)	1	9.643	1.155	0.000953
626.53619				3.029	36.16	0.000435
629.49284	DG(34:1)(P)	DG(14:1(9Z)/20:0/0:0)	2	39.4	9.589	0.000843
630.49545				20.2	2.804	0.000132
631.49166	DG(36:3)(P)	DG(i-16:0/20:3(8Z,11Z,14Z)-O(5,6)/0:0)	4	33.35	11.46	0.001511

632.49586				11.99	2.376	0.001877
637.54087	DG(36:0)(P)	TG(18:0/10:0/8:0)	1	315.7	147.9	0.00004
638.33081				9.962	44.13	0.001454
638.54508	Cer(t36:1)(P)	Cer(d18:0/PGF1alpha)	13	134.1	61.48	0.000045
639.48532	DG(35:3)(P)	DG(15:0/20:3(5Z,8Z,11Z)/0:0)	14	13.38	0.5345	0.000248
641.50013	DG(35:2n6)(P)	DG(15:0/0:0/20:2n6)	13	50.44	20.78	0.001425
642.50433	Cer(d20:1/PGJ2)(P)	Cer(d20:1/PGJ2)	9	17.77	3.468	0.001939
648.35047				15.79	44.4	0.00202
655.50783	DG(36:2)(P)	DG(14:0/22:2(13Z,16Z)/0:0)	1	36.26	6.024	0.00006
656.51203	Cer(t38:3)(P)	Cer(t18:0/20:3(6,8,11)-OH(5))	14	17.28	1.879	0.000022
657.4139	DG(PGE2)(P)	DG(13:0/PGE2/0:0)	0	3.86	25.56	0.00033
662.36776				25.52	62.64	0.002591
682.59258	Cer(d42:2)(P)	Cer(d18:1/24:1(15Z))	2	28.7	73.8	0.000878
683.59359				16.94	43.56	0.000883
702.39684	azahexane(P)	1-(4-Biphenylyl)-4(S)-hydroxy-5(S)-2,5-bis((N-(methoxycarbonyl-)-L-tert-leucinyl)amino)-6-phenyl-2-azahexane	14	8.762	22.31	0.000435
773.53389				6.33	50.69	0.000111
790.50304				13.91	59.56	0.000712
791.50564				2.714	16.58	0.001345
792.52904				12.39	26.28	0.002318
794.53745	PC(PGJ2/P-16:0)(P)	PC(PGJ2/P-16:0)	0	21.33	56.5	0.000309
795.53845	SM(d36:2)(P)	SM(d18:1/18:1)-2OH(9,10))	5	12.25	35.06	0.001239
810.52957	PE(P-40:6)(P)	PE(22:5(4Z,7Z,10Z,13Z,16Z)/P-18:1(11Z))	11	19.26	90.77	0.000071
811.53218	PA(i-39:1)(P)	PA(18:1(12Z)-2OH(9,10)/i-21:0)	7	4.074	28.44	0.000069
826.48811	PC(36:7)(P)	PC(14:1(9Z)/22:6(5Z,7Z,10Z,13Z,16Z,19Z)-OH(4))	10	11.35	36.41	0.000309
834.52655	PS(40:6)(P)	PS(20:4(8Z,11Z,14Z,17Z)/20:2(11Z,14Z))	3	6.631	21.69	0.00104
842.52341				4.119	11.37	0.000132
847.73952				12.09	0.9954	0.001349
858.51714	PC(DiMe/22:5)(P)	PC(22:5(4Z,7Z,10Z,13Z,19Z)-O(16,17)/DiMe(9,3))	14	10.28	25.35	0.000712
873.75291	PC(24:4)(P)			18.07	2.219	0.000931
885.55072	PI(38:4)(P)	PI(18:1(9Z)/20:3(5Z,8Z,11Z))	1	106.5	273.7	0.000246
886.55172	PC(DiMe/22:6)(P)	PC(DiMe(9,5)/22:5(4Z,7Z,10Z,13Z,19Z)-O(16,17))	10	54.38	143.5	0.000208
162.11389	L-carnitine	L-Carnitine	9	259	968.9	0.003349
163.11851				1.159	17.64	0.003564
184.09451	L-Carnitine(P)	L-Carnitine	1	37.8	213	0.003964
200.06846				67.52	275.3	0.003564
218.14107	Propionylcarnitine(P)	Propionylcarnitine	11	64.06	300.6	0.003388
221.18648				158.4	429.4	0.004688

351.25031	5a-Tetrahydrocorticosterone(P)	5a-Tetrahydrocorticosterone	8	328.6	17.36	0.002451
367.22426	MG(16:1)(P)	MG(16:1(9Z)/0:0/0:0)	1	350.6	33.89	0.002347
379.28231	MG(20:4)(P)	MG(20:4(8Z,11Z,14Z,17Z)/0:0/0:0)	5	592.3	209.7	0.002451
380.27904	LTB4 ethanolamide(P)	Leukotriene B4 ethanolamide	11	87.62	25.73	0.002451
391.22464	MG(18:3)(P)	MG(18:3(9Z,12Z,15Z)/0:0/0:0)	0	29.87	8.094	0.002451
395.25626	LysoPA(P-16:0)(P)	LysoPA(P-16:0/0:0)	2	763.8	299.3	0.002474
396.25562				173.2	64.48	0.002474
397.25498				36.37	6.782	0.002451
411.25125	DG(18:0)(P)	DG(8:0/10:0/0:0)	1	58.03	16.56	0.002451
415.20924				145.7	7.112	0.002474
439.20961				143.8	30.38	0.002451
441.22674				237.6	133.4	0.005634
443.24123				392.4	135.7	0.003044
444.24322				174.4	42.44	0.002451
521.32529				359.4	5.185	0.004147
522.32728				48.03	0.1579	0.006701
523.33979	PA(23:0)(P)	PA(10:0/13:0)	1	1172	193.5	0.002451
533.38071				319.9	16.39	0.003564
549.35992				351.7	37.16	0.002755
550.35928				343.8	19.65	0.002474
560.31078	LysoPC(18:1)(P)	PC(18:1(6Z)/0:0)	1	100.4	21.11	0.002451
565.35228				60.93	6.034	0.002451
575.37216				35.63	1.92	0.004916
589.48152	DG(34:4)(P)	DG(14:0/0:0/20:4n6)	2	130.9	0.6817	0.008035
597.33963				253.2	23.12	0.002451
603.44361	DG(32:2)(P)	DG(16:1n7/0:0/16:1n7)	8	92.45	6.827	0.009217
613.4819	DG(36:6)(P)	DG(16:1n7/0:0/20:5n3)	1	167.5	6.163	0.003964
617.51352	DG(34:3)(P)	DG(14:0/20:3(5Z,8Z,11Z)/0:0)	3	229.1	24.94	0.002345
618.51551	Cer(t18:0/20:5)(P)	Cer(t18:0/20:5(6E,8Z,11Z,14Z,17Z)-OH(5))	10	178.1	10.2	0.002203
629.45585	DG(34:3n11)(P)	DG(14:1n5/0:0/20:2n6)	3	612.6	35.94	0.002474
630.45784	Cer(d16:1/20:3)(P)	Cer(d16:1/20:3(8Z,11Z,14Z)-2OH(5,6))	13	121.6	4.223	0.002474
633.48747	DG(34:1)(P)	DG(18:0/0:0/16:1n7)	3	747.8	107	0.002203
634.48946	LysoPC(26:1)(P)	LysoPC(26:1(5Z)/0:0)	14	595.1	67.62	0.002203
635.49408	DG(35:4)(P)	DG(20:4(8Z,11Z,14Z,17Z)-2OH(5S,6R)/0:0/i-15:0)	1	27.82	3.367	0.002203
643.42845	DG(i-34:4)(P)	DG(i-14:0/0:0/20:4(5Z,7E,11Z,14Z)-OH(9))	8	27.94	0.5011	0.006621
643.52839	DG(38:5)(P)	DG(20:2n6/0:0/18:3n3)	2	171.1	22.3	0.002347
644.53038	Cer(t40:5)(P)	Cer(t18:0/22:5(4Z,7Z,10Z,13Z,19Z)-O(16,17))	9	131.1	9.777	0.002345
645.45084	DG(i-34:3)(P)	DG(18:3(9,11,15)-OH(13)/0:0/i-16:0)	3	493.8	46.54	0.003564
646.45283	Cer(d16:1)(P)	Cer(d16:1/PGD1)	13	97.01	6.799	0.003564

647.46534	DG(i-34:1)(P)	DG(18:1(9Z)-O(12,13)/0:0/i-16:0)	1	390.7	48.57	0.003964
648.46995				142.8	12.19	0.003964
657.48522	DG(36:3)(P)	DG(16:0/20:3(11Z,14Z,17Z)/0:0)	0	1709	459.1	0.002474
658.40568				27.73	6.539	0.002474
658.48983	Cer(t18:0/20:4)(P)	Cer(t18:0/20:4(5Z,7E,11Z,14Z)-OH(9))	14	726	183.7	0.002474
659.50234	DG(36:2)(P)	DG(18:1n9/0:0/18:1n9)	2	584.9	97.86	0.002203
660.50696				245.7	33.41	0.002203
661.4432	DG(i-34:3)(P)	DG(20:3(8Z,11Z,14Z)-2OH(5,6)/0:0/i-14:0)	1	112.8	4.947	0.004147
661.50895	DG(36:1)(P)	DG(22:0/0:0/14:1n5)	12	33.63	2.176	0.002203
662.44782	Cer(d40:8)(P)	Cer(d18:2(4E,14Z)/22:5(4Z,7Z,10Z,13Z,19Z)-O(16,17))	10	37.82	0.6588	0.006576
673.48021	DG(i-36:3)(P)	DG(18:3(9,11,15)-OH(13)/0:0/i-18:0)	0	417	48.68	0.003279
674.37963				125.3	32.56	0.003249
674.48482	Cer(t38:4)(P)	Cer(t18:0/20:4(8Z,11Z,14Z,17Z)-2OH(5S,6R))	14	161.9	12.41	0.003249
679.45532	PA(i-32:1)(P)	PA(18:1(12Z)-2OH(9,10)/i-14:0)	1	516.2	51.75	0.002451
680.45993	Cer(d40:7)(P)	Cer(d18:1/22:6(4Z,7Z,11E,13Z,15E,19Z)-2OH(10S,17))	8	205.1	15.8	0.002451
681.46455	PG(i-29:0)(P)	PG(i-14:0/i-15:0)	8	205.6	17.24	0.002203
682.47443	Cer(t40:6)(P)	Cer(t18:0/22:5(4Z,7Z,10Z,13Z,19Z)-O(16,17))	9	392	16.11	0.002203
683.47379				34.64	0.4178	0.002451
705.46493	DG(i-16:0/0:0/PGD1)(P)	DG(5-iso PGF2VI/0:0/i-18:0)	3	447.9	68.34	0.002451
706.47218	PS(30:1)(P)	PS(16:1(9Z)/14:0)	13	283.7	36	0.002451
707.48994	DG(PGF1alpha/0:0/i-16:0)(P)	DG(PGF1alpha/0:0/i-16:0)	6	319.5	30.81	0.002203
708.49193	Cer(d20:1/22:6)	Cer(d20:1/22:6(4Z,7Z,11E,13Z,15E,19Z)-2OH(10S,17))	6	195.9	9.771	0.002203
709.49655	PG(i-14:0/i-17:0)(P)	PG(i-14:0/i-17:0)	7	23	0.7987	0.002451
719.45331	PG(i-31:3)(P)	PG(18:3(9,11,15)-OH(13)/i-13:0)	5	61.21	5.565	0.006969
754.53604	PE-NMe2(35:4)(P)	PE-NMe2(20:4(8Z,11Z,14Z,17Z)/15:0)	3	186.7	17.41	0.002451
755.54066	SM(d35:1)(P)	SM(d19:1/16:0)	8	72.84	2.346	0.002474
759.57491	DG(PGD1/0:0/i-21:0)(P)	DG(PGD1/0:0/i-21:0)	0	6.355	49.33	0.004688
770.51	PE-NMe2(33:1)(P)	PE-NMe2(18:1(9Z)/15:0)	0	378.8	52.84	0.003249
771.51461	DG(41:5)(P)	DG(20:5(7Z,9Z,11E,13E,17Z)-3OH(5,6,15)/0:0/i-21:0)	4	167.2	14.16	0.002735
786.60229	PC(36:2)	PC(18:1(9Z)-O(12,13)/P-18:0)	2	13.51	112.5	0.006722
802.52628	PS(36:2)(P)	PS(18:1(9Z)-O(12,13)/18:1(9Z))	4	28.55	1.329	0.002347
818.50023	DG(LTE4/0:0/i-18:0)(P)	DG(LTE4/0:0/18:0)	1	78.96	14.09	0.002451
831.55493	PG(i-37:0)(P)	PG(i-13:0/i-24:0)	4	95.13	37.37	0.003044
861.66987				63.42	138.4	0.00735
871.71342	TG(50:1)(P)	TG(14:0/18:1(9Z)/18:0)	2	290.1	19.67	0.002451
872.71804	PC(42:1)(P)	PC(24:1(15Z)/18:0)	9	139.9	6.056	0.002451
897.72829	TG(52:2)(P)	TG(14:0/18:1(9Z)/20:1(11Z))	0	768.6	91.46	0.002474

| 898.73291 | PE-NMe(46:2)(P) | PE-NMe(24:1(15Z)/22:1(13Z)) | 10 | 416.5 | 41.96 | 0.002451 |
| 899.73753 | TG(52:1)(P) | TG(14:0/24:0/14:1(9Z)) | 11 | 166.5 | 13.2 | 0.002451 |

8.1.9 Appendix 9

PLS-DA generated VIP>1 list of molecules in the liver that contribute towards group separation in the DSS induced colitis model

m/z	VIP list
656.5120239	1.208789945
489.3439941	1.190179944
842.5189819	1.18987
364.2340088	1.189360023
558.3330078	1.188580036
363.2309875	1.186579943
655.5079956	1.185269952
591.5360107	1.184820056
509.4580078	1.181589961
510.4609985	1.181229949
433.2810059	1.180879951
300.0400085	1.178550005
462.3150024	1.176789999
461.3129883	1.176280022
584.4970093	1.17445004
485.3129883	1.17227006
276.2049866	1.171900034
611.526001	1.171239972
583.4949951	1.171090007
810.5300293	1.170300007
180.0599976	1.170050025
811.5319824	1.169929981
612.5289917	1.16989994
365.2269897	1.169819951
533.4550171	1.165969968
537.4899902	1.165949941
538.4920044	1.165410042
436.2999878	1.165019989
254.220993	1.164790034
253.2169952	1.164330006
826.4879761	1.164319992
630.4949951	1.16407001
435.29599	1.163190007
637.5410156	1.160719991
309.2789917	1.160339952
638.5449829	1.158370018
773.5339966	1.155329943
434.2839966	1.155169964
310.2839966	1.154590011
267.2340088	1.152150035
534.460022	1.151170015
316.2130127	1.150329947
552.2969971	1.149690032
337.3110046	1.149279952
607.4949951	1.148560047
477.3059998	1.147539973
613.5360107	1.147359967
886.552002	1.144719958
281.2479858	1.144649982
282.2520142	1.144119978
608.4970093	1.143650055
702.3969727	1.141000032
794.5339966	1.14064002
885.5510254	1.140020013
572.4819946	1.134539962
268.2349854	1.13409996
275.2000122	1.133659959
858.5170288	1.130879998
283.256012	1.129999995
657.4140015	1.127689958
634.4890137	1.127339959
633.4869995	1.125460029
771.5180054	1.12451005
531.440979	1.124500036
315.2090149	1.122720003
280.4689941	1.122689962
708.4920044	1.122099996
179.0559998	1.121639967
774.5360107	1.121209979
707.4899902	1.120239973
281.098999	1.118800044
281.3999939	1.11864996
284.2590027	1.118350029
573.4840088	1.118070006
545.3619995	1.115869999
635.4940186	1.113720059
601.4609985	1.113649964
512.4769897	1.113309979
639.4849854	1.112759948
441.2780151	1.112040043

280.2369995	1.110820055	709.4970093	1.069370031
279.2330017	1.110739946	267.1960144	1.068809986
511.4729919	1.109990001	581.4780273	1.06851995
681.4650269	1.109109998	560.3109741	1.067569971
618.5159912	1.106960058	630.4580078	1.06704998
660.507019	1.104900002	397.2550049	1.067029953
790.5029907	1.103520036	595.3449707	1.066359997
563.5050049	1.103170037	648.3499756	1.066249967
564.507019	1.102710009	549.3599854	1.065389991
525.3189697	1.101979971	128.0359955	1.065250039
507.4419861	1.101600051	791.5059814	1.065029979
659.5020142	1.101140022	629.4559937	1.064450026
661.5089722	1.10089004	444.2430115	1.064059973
682.473999	1.099670053	873.7529907	1.063189983
644.5300293	1.09849	411.2510071	1.062909961
617.5139771	1.097959995	871.7130127	1.062849998
795.5380249	1.097309947	379.2820129	1.062070012
559.4719849	1.096490026	351.1820068	1.061429977
367.223999	1.095010042	683.5939941	1.060950041
560.4760132	1.092620015	583.473999	1.06020999
629.492981	1.092370033		
643.5280151	1.09205997		
626.5360107	1.092000008		
339.2120056	1.09149003		
802.526001	1.091429949		
592.3259888	1.090680003		
834.5269775	1.088619947		
513.4799805	1.087520003		
268.2000122	1.08739996		
706.4719849	1.087170005		
417.2860107	1.087069988		
265.2170105	1.08573997		
705.4650269	1.084959984		
351.25	1.084939957		
831.5549927	1.083950043		
597.3400269	1.083539963		
574.4790039	1.081650019		
524.3439941	1.081590056		
899.7379761	1.077250004		
818.5	1.076810002		
638.3309937	1.076629996		
754.5360107	1.076390028		
161.0460052	1.07565999		
391.2250061	1.07562995		
523.3400269	1.07506001		
380.2789917	1.074820042		
680.460022	1.073089957		
872.7180176	1.072639942		
550.3590088	1.071429968		
565.3519897	1.071179986		
679.4550171	1.071099997		
439.2099915	1.070899963		
415.2090149	1.069949985		
682.5930176	1.069910049		

8.1.10   Appendix 10

Table shows the m/z, abbreviated names shown in heatmap (Figure 4.3.22 Molecules and pathways altered in spleen of DSS colitis model and full compound name for molecules found to be significantly changed in the spleen of DSS colitis model. Table includes the mean relative abundance value for each molecule within the groups. P-values highlighted in grey are for molecules down regulated in 3% group compared to control group and p-values not highlighted show molecules increased in 3% group compared to control group.

m/z	Heatmap ID	compound_name	adduct	ppm	Mean 0%	Mean 3%	p-value
117.0558	5-HPA(P)	5-Hydroxypentanoic acid	M-H	10	76.95	154	0.0118
118.08744	Betaine(P)	Betaine	M+H	5	124.5	247.1	0.0036
124.0152	m/z 124.0152				4220	3031	0.0499
134.0473	m/z 134.0473				88.11	166.9	0.0795
156.04378	3-AMBA	3-Amino-3-methylbutanoic acid	M+K	11	1235	2173	0.0002
157.04563	m/z 157.0456				45.43	103	7E-05
158.04035	2-DHBA(P)	(+)-threo-2-Amino-3,4-dihydroxybutanoic acid	M+Na	13	39.42	75.59	0.0001
160.13189	5-AVAB(P)	5-amino valeric acid betaine	M+H	8	1775	1083	0.0287
161.13849	m/z 161.1384				143.7	82.82	0.0299
166.018	Quinolinic acid(P)	Quinolinic acid	M-H	11	656.3	431.6	0.0503
174.0409	NFLGA(P)	N-Formyl-L-glutamic acid	M-H	1	217.9	118.5	0.0369
183.1391	m/z 183.1391				126.9	200.7	0.0051
187.0976	m/z 187.0976				375.3	550.1	0.0665
188.05581	NALGA(P)	N-Acetyl-L-glutamic acid	M-H	3	0.3565	19.28	0.0251
211.134	m/z 211.134				171.9	245.4	0.0046
221.18775	m/z 221.18775				294.1	783.7	0.0001
222.1896	m/z 222.1896				13.99	70.27	0.0002
227.129	m/z 227.129				112.5	178	0.0129
229.1962	m/z 229.1962				17.8	32.71	5E-05
249.1859	m/z 249.1859				11	26.1	0.029
251.2016	m/z 251.2016				36.05	56.97	0.0091
254.2207	m/z 254.2207				300.8	192.9	0.0276
256.0595	N-AMA(P)	N-Acetylmannosamine	M+Cl	0	5.014	33.23	0.011
263.0408	m/z 263.0408				112.4	52.39	0.0131

273.1861	ODT acid(P)	(10Z,14E,16E)-10,14,16-Octadecatrien-12-ynoic acid	M-H	3	201.2	311.4	0.0003
274.1896	m/z 274.1896				30.6	55.33	7E-05
277.0597	m/z 277.0597				41.15	95.22	0.0122
279.0562	Biotin(P)	Biotin	M+Cl	7	7.915	28.21	0.0101
279.233	DHL acid(P)	Dihomolinoleic acid	M-H	0	6841	8970	0.0351
280.2363	Petroselinate(P)	petroselinate	M-H	12	876.3	1151	0.0348
281.0536	m/z 281.0536				50.53	22.8	0.0223
301.1811	Hydroxy steroid (P)	11b-Hydroxyandrost-4-ene-3,17-dione	M-H	1	8.653	40.3	0.0491
317.1759	Ubiquinone-2(P)	Ubiquinone-2	M-H	1	30.77	103.8	0.0055
318.1737	m/z 318.1737				1.079	15.98	0.0198
327.2331	DHA(P)	Docosahexaenoicacid(DHA)	M-H	1	1236	3224	0.0704
328.2364	m/z 328.2364				290.7	763.3	0.0391
329.2335	9,10,13-TriHOME(P)	9,10,13-TriHOME	M-H	9	20.58	59.11	0.0744
332.2267	m/z 332.2267				38.38	12.67	0.0126
341.2139	14-oxo-DoHE(1-)(P)	14-oxo-DoHE(1-)	M-H	5	7.892	73.42	0.0618
343.228	EDP acid(P)	Epoxydocosapentaenoic acid	M-H	1	89.45	212	0.0016
344.2302	m/z 344.2302				22.08	71.88	0.0016
359.223	Resolvin D5(P)	Resolvin D5	M-H	1	32.96	75.22	0.0058
363.2099	m/z 363.2099				56.1	142.1	0.0156
363.2309	MG(16:1)	MG(16:1(9Z)/0:0/0:0)	M+Cl	2	54.54	15.94	0.0085
365.2097	9,12,13-TriHOME(P)	9,12,13-TriHOME	M+Cl	1	11.24	42.09	0.0089
373.2019	m/z 373.2019				17.21	82.12	0.0324
375.2171	Resolvin D1(P)	Resolvin D1	M-H	1	27.97	63.26	0.0062
413.2464	Nor-DCA(P)	Nordeoxycholic acid	M+Cl	0	444.4	200.6	0.0444
414.2498	m/z 414.2498				111.5	49.1	0.0435
415.2339	MG(20:3)(P)	MG(20:3(8Z,11Z,14Z)/0:0/0:0)	M+Cl	0	211.4	102.2	0.0505
415.2711	m/z 415.2711				42.05	15.19	0.0341
416.2374	m/z 416.2374				34.01	13.04	0.0425
439.2626	MG(22:5)(P)	MG(22:5(4Z,7Z,10Z,13Z,16Z)/0:0/0:0)	M+Cl	1	75.25	29.07	0.0448
467.2988	m/z 467.2988				70.7	27.08	0.02
558.3332	LysoPC(18:0)(P)	LysoPC(0:0/18:0)	M+Cl	1	25.31	52.76	0.016
611.5255	m/z 611.5255				112.5	70.13	0.0179
736.6459	m/z 736.6459				189.5	110.5	0.0423
737.6491	m/z 737.6491				90.76	51.31	0.0406
742.57217	PC(O-34:3)(P)	PC(O-16:1(9Z)/18:2(9Z,12Z))	M+H	3	141.7	61.65	0.0057
750.5431	PE(P-38:4)(P)	PE(P-18:1(9Z)/20:3(5Z,8Z,11Z))	M-H	4	161.7	96.69	0.0441
758.54479	m/z 758.5448				269.3	100.9	0.0075
768.58703	PC(P-34:0)(P)	PC(P-18:0/16:0)	M+Na	1	71.58	37.78	0.0107
784.55964	PC(O-34:1)(P)	PC(O-18:1(9Z)/16:0)	M+K	3	210.3	113.4	0.0067
788.5455	PS(36:1)(P)	PS(22:1(13Z)/14:0)	M-H	1	136	56.33	0.0105
789.5492	SM(d40:6)(P)	SM(d18:1/22:5(4Z,7Z,10Z,13Z,19Z)-O(16,17))	M-H	7	83.55	28	0.004

8.1.11 Appendix 11

PLS-DA generated VIP>1 list of molecules in the spleen that contribute towards group separation in the DSS induced colitis model

m/z	VIP list
273.1870117	1.278789997
274.1889954	1.276319981
157.0460052	1.264089942
229.197998	1.253790021
158.0399933	1.252120018
156.0440063	1.244019985
221.1880035	1.221740007
222.1900024	1.205440044
558.3330078	1.138569951
343.2279968	1.112179995
758.5449829	1.111770034
344.230011	1.111410022
784.5599976	1.087800026
742.5720215	1.077800035
183.1390076	1.074849963
789.5490112	1.067000031
118.086998	1.057729959
359.2219849	1.044929981
611.526001	1.042279959
317.1759949	1.041479945
227.128006	1.039909959
211.1329956	1.039870024
251.201004	1.027750015
277.0610046	1.023830056
788.5449829	1.023040056
375.2170105	1.020480037
279.0559998	1.016469955
215.072998	1.013659954
768.5869751	1.008110046
332.2260132	1.004760027
365.2099915	1.003100038

8.1.12 Appendix 12

Table shows the m/z, abbreviated names shown in heatmap (Figure 4.3.25) and full compound name for molecules found to be significantly changed in the kidney of DSS colitis model. Table includes the mean relative abundance value for each molecule within the groups. P-values highlighted in grey are for molecules decreased in 3% group compared to control group and p-values not highlighted show molecules increased in 3% group compared to the control.

m/z	Heatmap ID	compound_name	adduct	ppm	Mean 0%	Mean 3%	p-value
257.176	TDA(P)	Tetradecanedioic acid	M-H	1	99.36	10.26	0.018893
277.217	GLA(P)	gamma-Linolenic acid	M-H	5	699.4	344.5	0.016252
278.21					129.2	57.14	0.015677
305.249	DGLA(P)	Dihomo-gamma-linolenic acid	M-H	4	620	362.7	0.010765
306.243	m/z 306.2433				130.8	72.03	0.007959
317.183	m/z 317.183				24.04	87.71	0.042873
363.248	m/z 363.2475				104.7	19.77	0.003618
367.27	m/z 367.2697				199.1	111.3	0.01858
603.477	DG(32:0)(P)	DG(19:0/13:0/0:0)	M+Cl	5	49.23	9.139	0.001994
754.537	PC(34:4)(P)	PC(20:4(8Z,11Z,14Z,17Z)/14:0)	M+H	0	49.34	26.78	0.00601
770.512	PC(32:1)(P)	PC(18:1(9Z)/14:0)	M+K	4	81.58	47.07	0.025015
771.516	PG(36:4)(P)	PG(20:4(5Z,8Z,11Z,14Z)/16:0)	M+H	2	34.46	16.62	0.009635
772.528	PE(35:0)(P)	PE(20:0/15:0)	M+K	4	1123	721	0.110219
773.531	PG(36:3)(P)	PG(18:3(9Z,12Z,15Z)/18:0)	M+H	3	495.8	318.6	0.107909
817.501	PG(40:8)(P)	PG(20:4(8Z,11Z,14Z,17Z)/20:4(8Z,11Z,14Z,17Z))	M-H	1	16.03	149.8	0.081714
865.502	PG(38:4)(P)	PG(20:4(6Z,8E,10E,14Z)-2OH(5S,12R)/18:0)	M+Cl	0	42.29	615.5	0.025988

8.1.13   Appendix 13

PLS-DA generated VIP>1 list of molecules in the kidney that contribute towards group separation in the DSS induced colitis model.

m/z	VIP list
754.5380249	1.343119979
771.5150146	1.293339968
770.5130005	1.258380055
772.5280151	1.05061996
773.5310059	1.049360037

8.1.14   Appendix 14

MSMS fragmentation pattern (m/z plotted against relative abundance) using NCE 10 shown in m/zCloud, colon tissue and 1-MNA purchased standard. Peaks at 137.07, 110.06, and 94.06 are of similar abundance in all three fragmentation patterns; thus, 137.07 in colon tissue is most likely to be 1-MNA.

NCE 10 m/zCloud

NCE 10 Colon tissue
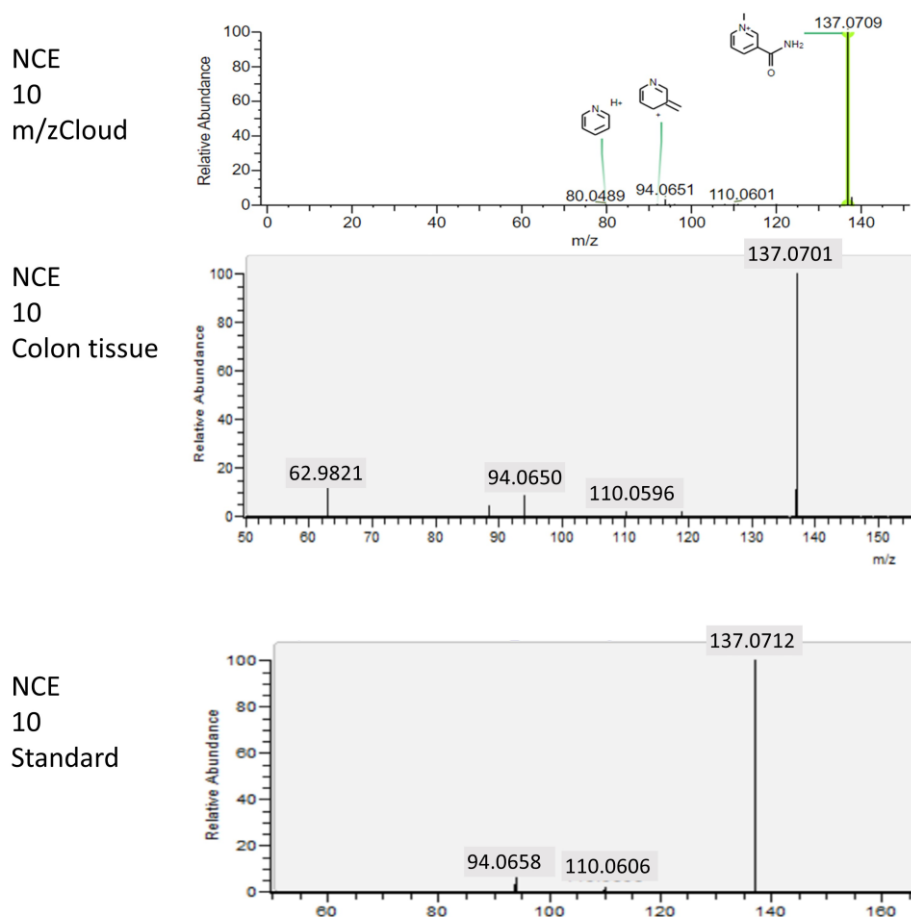
NCE 10 Standard

8.1.15 Appendix 15

MSMS fragmentation pattern (m/z plotted against relative abundance) using NCE 10 shown in m/zCloud, ileum tissue and a Creatine purchased standard. Peaks at 132.07 and 90.05 are of similar abundance in all three fragmentation patterns; thus, 132.07 in ileum is most likely to be Creatine.
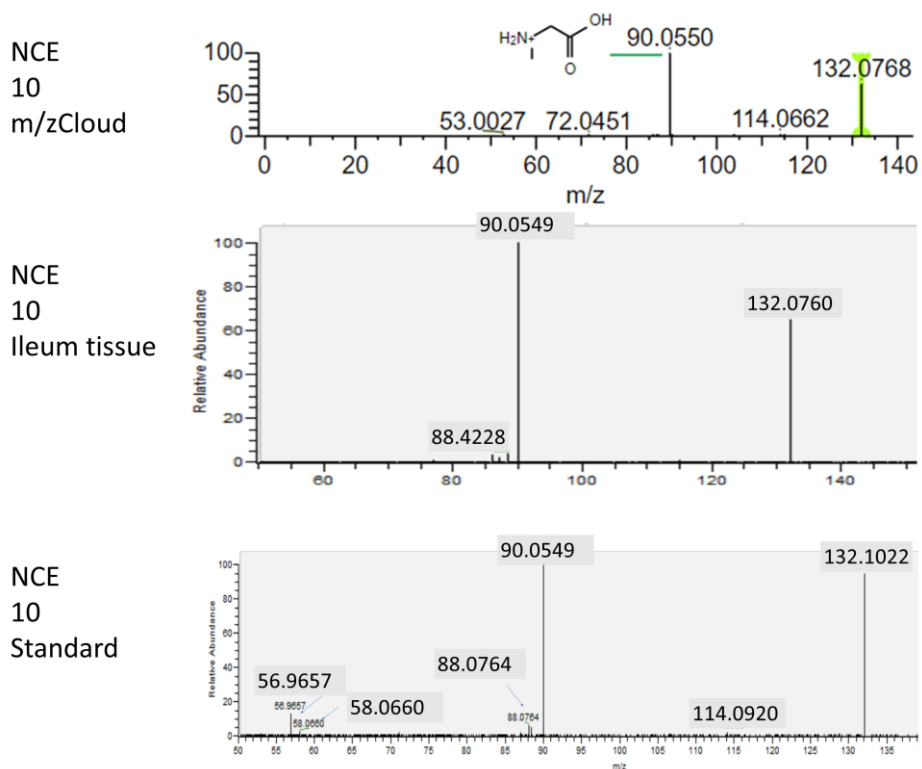
8.1.16 Appendix 16

MSMS fragmentation pattern (m/z plotted against relative abundance) using NCE 10 shown in m/z cloud, ileum tissue and a DHA purchased standard. Peaks at 327.23, 283.24, 249.18, 229.19 and 177.16 are of similar abundance in mzCloud and ileum fragmentation patterns; thus, the molecule was putatively identified as DHA. However, the DHA standard only matches the 327.23 and 283.24, suggesting that the molecule might not be the same as the one found in the ileum.
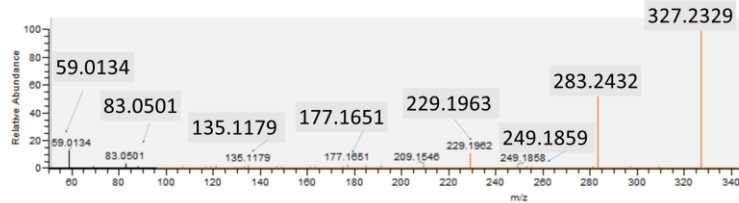
8.1.17 Appendix 17

For flow cytometry analysis across chapters 4-6, cells were gated on FCS-A vs H to exclude duplets, among singlets dead cells were excluded based on viability staining. Among live cells CD45+ hematopoietic cells were used for analysis. CD45+ cells were split into lymphocytes and myeloid cells based on size (FSC) and granularity (SSC). Lymphocytes were further divided into NK cells (NK1.1+CD3-) and B cells (CD19+CD3-). Macrophages were identified based on F4/80 expression out of Myeloid cells. CD69 activation marker were used as a readout of putative activation on both myeloid and lymphoid cells. The figure shows the overlay of actual signal vs isotype control (background) stain (in grey). IFN-γ and Granzyme B levels were assessed in NK cells with positivity being considered based on isotype control staining (overlayed in grey/black). MHCII expression levels were quantified on macrophages and B cells based on isotype control stains for background levels (negative vs positive signal). Percentages of positive or MFI (mean fluorescence intensity) levels were extracted and used to graph results and perform statistical analysis.
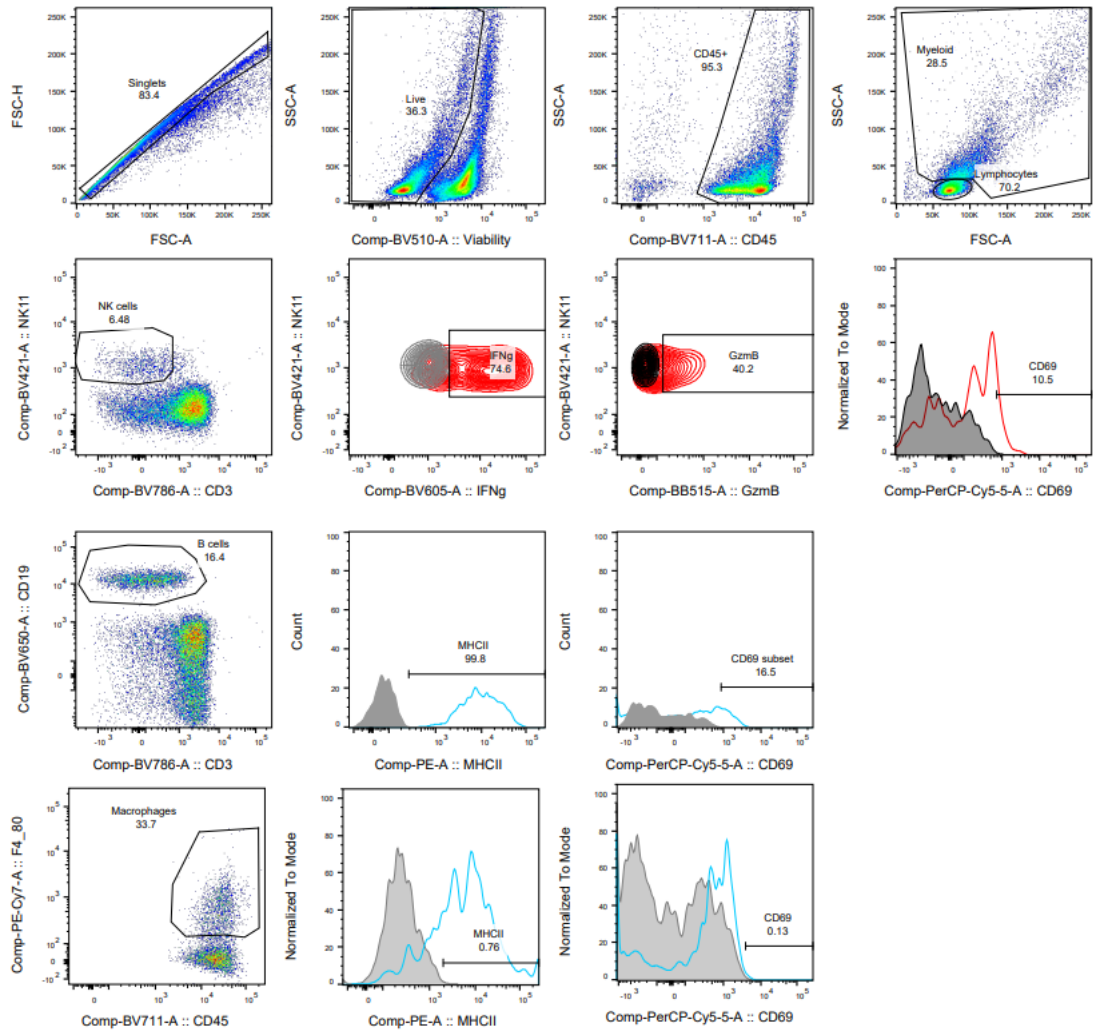
8.1.18   Appendix 18

Proteome Profiler Mouse Cytokine Array Kit, Panel A (ARY006, R&D systems) was used following manufacturers protocol to determine cytokine changes in splenic immune cells following stimulation with molecules and flow cytometry analysis. Results obtained are from one biological replicate and based on evidence IFN-γ was selected for quantification using ELISA.
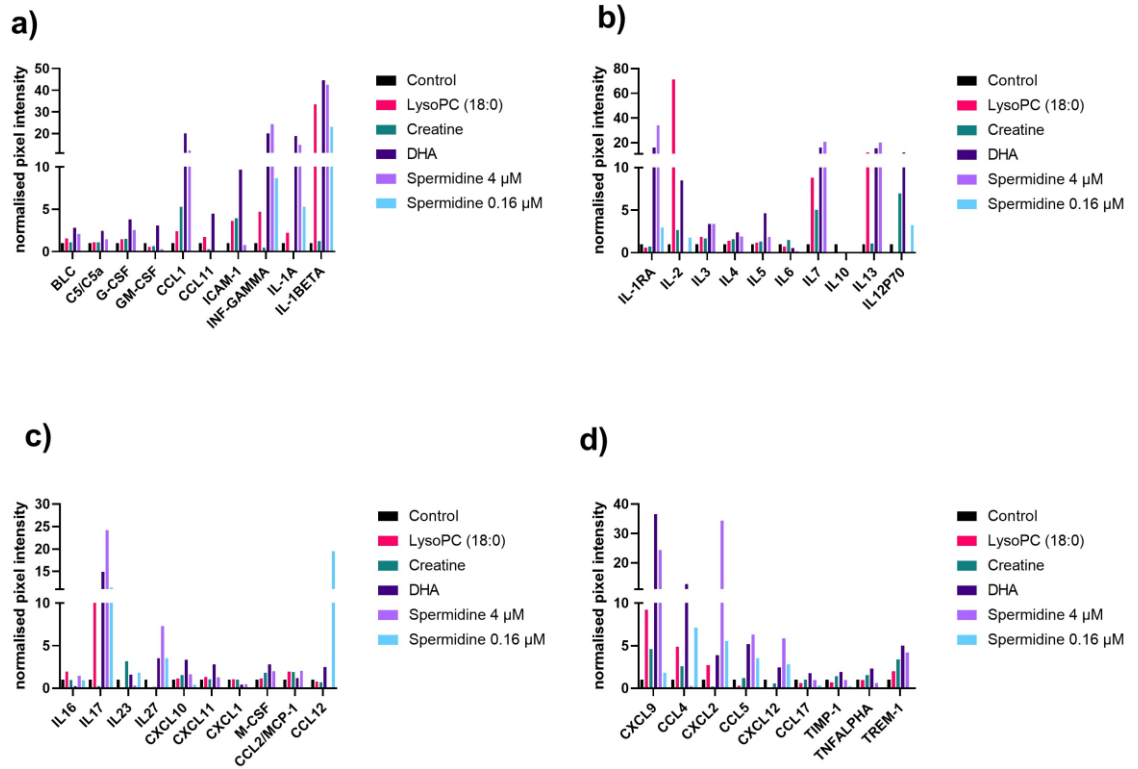
8.1.19   Appendix 19

CIA mice had a significant increase in DAI (a), significantly increased paw width (b), and length of colon and small intestine was not significantly changed (c). Ordinary one-way ANOVA was performed for DAI, paw width and intestinal length (*p<0.05, **p<0.01, ***p<0.001, ****p<0.0001).
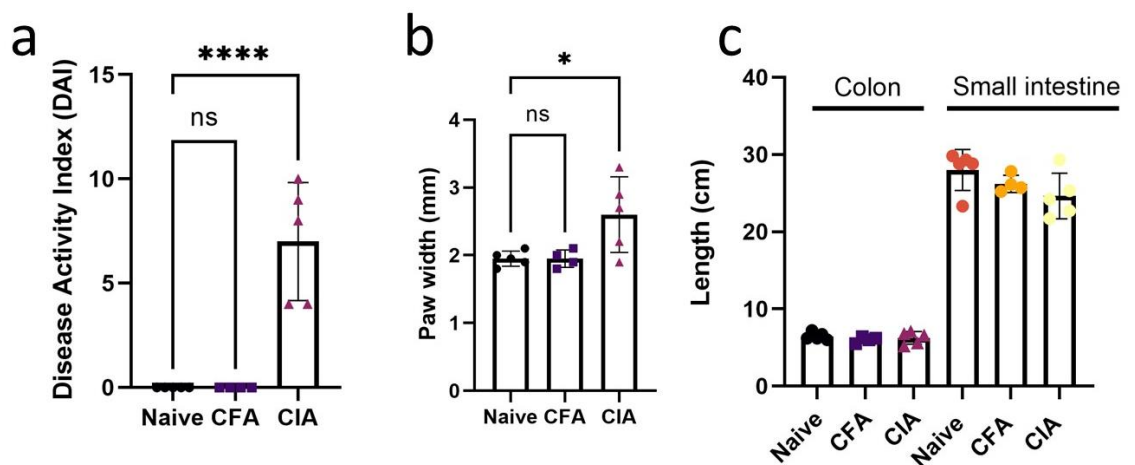
8.1.20   Appendix 20

Table shows the *m/z*, abbreviated names shown in heatmap Figure 5.3.11 Heatmap of increased and decreased molecules in lung of CIA model and full compound name for molecules found to be significantly changed in the lung of CIA model. Table includes the mean relative abundance value for each molecule within the groups. P-values highlighted in grey are for molecules decreased in CIA group compared to control group and p-values not highlighted show molecules increased in CIA group compared to the control.

m/z	Heatmap ID	compound name	ppm	Mean naïve	Mean CFA	Mean CIA	Adjusted P value
266.0391	Guanidine(P)	Guanidine, (4-chloro-3-methoxy-1-oxo-1H-2-benzopyran-7-yl)-	14	67.55	35.06	5.358	0.0001
272.0503	Fructoseglycine(P)	Fructoseglycine	15	73.34	67.03	23.82	0.0243
282.035	m/z 282.035			69.09	38.09	3.314	0.0005
330.0628	dAMP(P)	2'-Deoxyadenosine 3'-monophosphate	11	75.61	36.76	8.82	0.0034
367.3105	m/z 367.3105			34.72	11.31	3.741	0.0063
629.4926	DG(34:1)(P)	DG(18:1(11Z)/16:0/0:0)	3	819.2	633.2	507.5	0.0187
630.4956	Cer(t36:1)(P)	Cer(t18:0/18:1(9Z)-O(12,13))	15	340	262.9	210.9	0.014
298.0294	Creatinine citrate(P)	Creatinine citrate	5	159	84.54	22.73	0.004
562.3272	LysoPC(0:0/18:0)	LysoPC(0:0/18:0)	0	54.31	48.29	135.9	0.0275

8.1.21   Appendix 21

Table shows the m/z, abbreviated names shown in heatmap Figure 5.3.3 of increased and decreased molecules in lung of CIA model and full compound name for molecules found to be significantly changed in the lung of CIA model. Table includes the mean relative abundance value for each molecule within the groups. P-values highlighted in grey are for molecules decreased in CIA group compared to control group and p-values not highlighted show molecules increased in CIA group compared to the control.

m/z	Heatmap ID	compound_name	adduct	ppm	Mean naïve	Mean CFA	Mean CIA	Adjusted p-value
295.2264	9,10-EOA(P)	9,10-Epoxy-12-octadecenoic acid	M-H	0	964	992.1	557.6	0.0126
296.2306	18-hydroxyoleate(P)	18-hydroxyoleate	M-H	14	184.9	189.8	104.4	0.0111
266.0292	m/z 266.0292				11.54	14.39	0.2655	0.0066
297.2435	10-OxoODE(P)	10-Oxooctadecanoic acid	M-H	4	446.2	458.6	325.3	0.0284
298.2469	m/z 298.2469				55.64	56.67	39.36	0.0264
293.2123	13-OxoODE(P)	13-OxoODE	M-H	1	594	518	268.4	0.003

m/z	Heatmap ID	compound_name	adduct	ppm	Mean naïve	Mean CFA	Mean CIA	Adjusted p-value
294.2155	18-oxo-oleate(P)	18-oxo-oleate	M-H	13	75.79	65.38	31.25	0.0025
312.2263	m/z 312.2263				54.45	51.2	32	0.0086
806.498	PS(38:6)(P)	PS(20:2(11Z,14Z)/18:4(6Z,9Z,12Z,15Z))	M-H	0	17.5	27.01	38.36	0.0085
285.1115	m/z 285.11146				189.5	167.8	89.82	0.0004
377.2674	MG(18:2)(P)	MG(0:0/18:2(9Z,12Z)/0:0)	M+Na	3	218.4	191.8	78.2	0.0362
393.24	cPA(16:0)(P)	CPA(16:0/0:0)	M+H	0	450.1	390.1	189.2	0.0077
409.2364	MG(18:1)(P)	MG(0:0/18:1(9Z)-O(12,13)/0:0)	M+K	3	99.57	83.1	23.08	0.0017
425.2303	PA(8:0/8:0)(P)	PA(8:0/8:0)	M+H	1	56.96	46.01	12.37	0.0017
443.2423	m/z 443.24227				180.2	145	81.48	0.0038
758.5469	m/z 758.54685				370.9	340	256.5	0.0062

8.1.22   Appendix 22

Table shows the m/z, abbreviated names shown in heatmap Figure 5.3.5. Heatmap of increased and decreased molecules in kidney of CIA model and full compound name for molecules found to be significantly changed in the lung of CIA model. Table includes the mean relative abundance value for each molecule within the groups. P-values highlighted in grey are for molecules decreased in CIAgroup compared to control group and p-values not highlighted show molecules increased in CIA group compared to the control.

m/z	Heatmap ID	compound_name	adduct	ppm	Mean naïve	Mean CFA	Mean CIA	Adjusted p-value
272.0509	Fructoseglycine(P)	Fructoseglycine	M+Cl	12	434.1	408.1	112.4	0.0246
282.0328	m/z 282.03276				39.63	33.22	0.9577	0.0296
298.0289	Creatinine citrate(P)	Creatinine citrate	M-H	9	105.5	88.43	21.57	0.0097

8.1.23   Appendix 23

Table shows the m/z, abbreviated names of molecules in Figure 5.3.7. Molecules increased and decreased molecules in liver of CIA model and full compound name for molecules found to be significantly changed in the lung of CIA model. Table includes the mean relative abundance value for each molecule within the groups. P-values highlighted in grey are for molecules decreased in CIA group compared to control group

and p-values not highlighted show molecules increased in CIA group compared to the control.

m/z	Heatmap ID	compound_name	adduct	ppm	Mean naïve	Mean CFA	Mean CIA	Adjusted p-value
877.7253	TG(54:7)(P)	TG(16:0/16:1(9Z)/22:6(4Z,7Z,10Z,13Z,16Z,19Z))	M+H	0	25.79	43.91	87.17	0.0375
137.072	1-MNA(P)	1-Methylnicotinamide	M+H	4	69.78	43.69	19.75	0.0229

8.1.24   Appendix 24

Table shows the m/z, abbreviated names of molecules in Figure 6.3.1. Molecule increased in ileum of SFP group. Table includes the mean relative abundance value for each molecule within the groups.

m/z	heatmap ID	compound_name	adduct	ppm	Mean GF	Mean SPF	p-value
160.1333	5-AVAB	5-amino valeric acid betaine	M+H	3	7.12	104.9	<0.0001

8.1.25   Appendix 25

Table shows the m/z, abbreviated names of molecules in Figure 6.3.4. Table includes the mean relative abundance value for each molecule within the groups. P-values highlighted in grey are for molecules decreased in SPF group compared to GF group and p-values not highlighted show molecules increased in SPF group compared to the GF group.

m/z	Heatmap ID	compound_name	adduct	ppm	Mean GF	Mean SPF	p-value
172.9915	Phenol sulphate(P)	Phenol sulphate	M-H	3	0.06879	19.32	0.000373
206.0493	2,4 DOBA(P)	4-(2-Aminophenyl)-2,4-dioxobutanoic acid	M-H	5	10.12	61.23	0.006214
215.1283	m/z 215.1283				106.6	173.7	0.000929
229.1445	Dodecanedioic acid(P)	Dodecanedioic acid	M-H	1	51.62	90.28	0.002363
243.0623	Pseudouridine(P)	Pseudouridine	M-H	7	69.79	110.6	0.041662
279.039	Uridine(P)	Uridine	M+Cl	2	125.2	254.9	0.007065
281.0359	m/z 281.0359				38.14	80.02	0.008065

m/z	Heatmap ID	compound_name	adduct	delta(ppm),	Mean GF	Mean SPF	p-value
407.2806	Cholic acid(P)	Cholic acid	M-H	1	2.275	51.02	0.000179
118.051	L-Threonine(P)	L-Threonine	M-H	11	26.07	8.582	0.000061

8.1.26   Appendix 26

Table shows the m/z, abbreviated names of molecules in Figure 6.3.4. Table includes the mean relative abundance value for each molecule within the groups identified in the lung. P-values highlighted in grey are for molecules decreased in SPF group compared to GF group and p-values not highlighted show molecules increased in SPF group compared to the GF group.

m/z	Heatmap ID	compound_name	adduct	delta(ppm),	Mean GF	Mean SPF	p-value
465.3284	TetraHCA(P)	TetraHCA	M-H	13	68.92	24.8	0.000019
466.33395		466.33395			34.45	5.601	0.000002
172.9904	Phenol sulphate(P)	Phenol sulphate	M-H	6	0.146	154.1	0.004203
187.0066	p-Cresol sulfate(P)	p-Cresol sulfate	M-H	2	0.0344	44.37	0.008928
188.9868	Pyrocatechol sulfate(P)	Pyrocatechol sulfate	M-H	2	0.09679	35.13	0.00392
160.1355	5-AVAB	5-amino valeric acid betaine	M+H	14	17.12	460.1	0.0035

8.1.27   Appendix 27

Table shows the m/z, abbreviated names of molecules in Figure 6.3.4. Table includes the mean relative abundance value for each molecule within the groups (identified in the spleen). P-values highlighted in grey are for molecules decreased in SPF group compared to GF group and p-values not highlighted show molecules increased in SPF group compared to the GF group.

m/z	Heatmap ID	compound_name	adduct	delta(ppm),	Mean GF	Mean SPF	p-value
172.99269	PS(P)	Phenol sulphate	M-H	7	0.0169	16.7	0.008994
465.30576	CS(P)	Cholesterol sulfate(P)	M-H	1	204.4	72.69	0.000035
466.3084	466.3085	m/z 466.3085			38.57	9.567	0.000018

m/z	Heatmap ID	compound_name	adduct	delta(ppm)	Mean GF	Mean SPF	p-value
557.45685	m/z 557.4576	m/z 557.4576			55.8	32.6	0.002453
160.13189	5-AVAB	5-AVAB	M+H	8	11.88	297.9	0.0002

8.1.28 Appendix 28

Table shows the m/z, abbreviated names of molecules in Figure 6.3.23. Table includes the mean relative abundance value for each molecule within the groups (identified in kidney). P-values highlighted in grey are for molecules decreased in SPF group compared to GF group and p-values not highlighted show molecules increased in SPF group compared to the GF group.

m/z	Heatmap ID	compound_name	adduct	delta(ppm),	Mean GF	Mean SPF	p-value
172.9906	PS(P)	Phenol sulphate	M-H	4	0.08956	211.5	0.004068
178.0512	Hippuric acid(P)	Hippuric acid	M-H	1	7.376	73.98	0.000072
465.3335	Vit K1-epoxide(P)	Vitamin K1 2,3-epoxide	M-H	8	213	79.72	0.000038
160.1341	5-AVAB(P)	5-amino valeric acid betaine	M+H	6	17.87	190.3	0.002913
161.1365	m/z 161.1365				0.06907	12.24	0.010701

8.1.29 Appendix 29

Table shows the m/z, abbreviated names of molecules in Figure 6.3.23 (liver negative mode MSI). Table includes the mean relative abundance value for each molecule within the groups and *p-value* (GFvsSPF).

m/z	Heatmap ID	compound_name	adduct	ppm	Mean GF	Mean SPF	p-value
108.04502	m/z 108.04502	108.04502			26.7310136	16.95855697	0.001192
122.03513	m/z 122.03513	122.03513			96.7424021	70.14389582	0.000082
124.99178	m/z 124.99178	124.99178			54.8394267	30.50889614	0.012562
144.04609	3-Iald(P)	Indole-3-carboxaldehyde(P)	M-H	4	330.949509	256.8541229	0.002148
152.0297	CSA(P)	Cysteine sulfinic acid(P)	M-H	4	549.311864	337.0226776	0.000138

m/z	Abbrev	Name	Adduct				
155.10833	m/z 155.10833	155.10833			182.198693	130.2513439	0.00011
159.10277	HO acid(P)	Hydroxyoctanoic acid(P)	M-H	1	76.9515199	57.39878215	0.000468
165.04005	m/z 165.04005	165.04005			156.889301	75.35421185	0.00005
169.12243	m/z 169.12243	169.12243			89.5673455	56.34480405	0.000049
172.10626	m/z 172.10626	172.10626			508.322054	404.1658083	0.000181
172.99214	PS(P)	Phenol sulphate	M-H	4	2.26269578	19.23909726	0.015829
173.08168	2-PGA(P)	2-Propylglutaric acid(P)			115.607782	70.62198345	0.000048
173.11686	m/z 173.11686	173.11686			123.693323	90.02598881	0.000488
178.01956	m/z 178.01956	178.01956			58.538383	36.84165752	0.000087
183.13973	CLA(P)	Cyclopropaneoctanoic acid(p)	M-H	1	1833.5312974	1050.83509	0.000077
184.14571	m/z 184.14571	184.14571			213.000315	121.2547822	0.000089
187.09898	m/z 187.09898	187.09898			6469.16491	4856.903552	0.000097
188.09999	m/z 188.09999	188.09999			1869.38967	1398.872046	0.00285
211.13274	m/z 211.13274	211.13274			1974.49454	1330.480738	0.001357
212.13694	m/z 212.13694	212.13694			251.352614	169.1438518	0.00139
227.12966	m/z 227.12966	227.12966			2322.18395	1343.955501	0.000093
228.13067	m/z 228.13067	228.13067			297.662571	171.5608568	0.000091
229.14447	DDDA(P)	Dodecanedioic acid(P)	M-H	0	67.0868013	50.18754018	0.002533
242.0808	m/z 242.0808	242.0808			4.36083634	20.02769979	0.000005
253.2166	Palmitoleic acid(P)	Palmitoleic acid(P)	M-H	3	1174.89619	1686.681299	0.005695
254.22081	m/z 254.22081	254.22081			199.691216	287.6254964	0.005391
254.24959	Palmitic amide(P)	Palmitic amide(P)	M-H	3	60.5640233	28.10258966	0.000191
259.02116	G6P(P)	Glucose 6-phosphate(P)	M-H	5	26.7043361	11.41634049	0.000323
267.19552	m/z 267.19552	267.19552			165.26901	221.2582814	0.009919
278.10745	m/z 278.10745	278.10745			28.8215483	16.46527141	0.000309
283.2628	Stearic acid(P)	Stearic acid(P)	M-H	5	2104.75404	1577.554997	0.000242
284.267	m/z 284.267	284.267			405.233249	303.6744303	0.000175

m/z	Abbreviation	Name	Adduct				
287.15009	9,10-EODA(P)	9,10-Epoxystearic acid (EODA)(P)	M-H	5	93.8840551	54.36973763	0.000041
297.24491	9-oxoODE(P)	9-Oxooctadecanoic acid(P)	M-H	5	1606.73416	2183.248796	0.001092
298.24592	m/z 298.24592	298.24592			465.169546	632.573798	0.000029
315.14471	DHSA(P)	Dihydroxystearic acid(P)	M-H	2	49.8026648	30.93288322	0.001438
315.25344	Glucosyl-HE(P)	Glucosyl (E)-2,6-Dimethyl-2,5-heptadienoate (P)	M-H	1	38.8823556	55.02659333	0.000082
321.20831	DiAcSpm(P)	N1,N12-Diacetylspermine (DiAcSpm)(P)	M+Cl	6	20.9822565	6.569893342	0.000068
326.27091	N-SPN(P)	n-methylsphingosine(P)	M-H	3	1.4331706	14.00918962	0.000038
335.22241	LTB4(P)	Leukotriene B4(P)	M-H	1	166.701703	116.4722549	0.01663
349.20133	TXA3(P)	Thromboxane A3(P)	M-H	2	172.645098	121.4401972	0.023324
349.21412	9,10-EOA(P)	9,10-Epoxyoctadecanoic acid(P)	M+Cl	3	11.3358129	27.81798803	0.000069
363.23141	MG(16:1)(P)	MG(16:1)(P)	M+Cl	2	17.8031925	39.39216564	0.000628
365.23343	PGE2-ME(P)	Prostaglandin E2 methyl ester(P)	M-H	0	71.1759282	31.70156269	0.000018
368.07654	m/z 368.07654	368.07654			19.9320307	6.816286875	0.000058
381.23035	Calcium caprate(P)	Calcium caprate(P)	M-H	5	35.9822757	17.48406757	0.000083
391.2628	MG(18:1)(P)	MG(18:1)(P)	M+Cl	2	305.87185	550.6880941	0.00012
392.26541	m/z 392.26541	392.26541			104.688074	190.7735378	0.000111
393.25842	m/z 393.25842	393.25842			98.6917253	183.7028647	0.003637
394.26423	PGD2-EA(P)	PGD2 ethanolamide(P)	M-H	11	25.6753276	62.88588833	0.000075
399.23888	MG(isoPGF2/0:0)(P)	MG(5-iso PGF2VI/0:0/0:0)(P)	M-H	0	208.823825	104.6458486	0.000151
400.24308	m/z 400.24308	400.24308			44.9762173	20.4991309	0.000185
407.25653	MG(18:1(P))(P)	MG(0:0/18:1(12Z)-2OH(9,10)/0:0)(P)	M+Cl	1	45.2443389	70.7223389	0.000056
423.25185	DG(18:0)(P)	DG(18:0)(P)	M+Cl	1	32.3808303	63.80207672	0.00001
427.34222	DG(22:0)(P)	DG(22:0)(P)	M+Cl	0	72.6678949	43.06420197	0.000011
445.31717	m/z 445.31717	445.31717			27.4062928	53.9597042	0.000051
461.3125	m/z 461.3125	461.3125			285.272709	437.2800304	0.000004
462.3151	m/z 462.3151	462.3151			49.5563314	77.56837294	0.000003
465.30533	CS(P)	Cholesterol sulfate(P)	M-H	2	94.9404605	37.02222307	0.000044

m/z							
466.30794	m/z	466.30794			36.8372024	8.969892901	0.000156
477.30782	m/z	477.30782			43.9959274	62.59708471	0.000016
481.29905	25HC3S(P)	5-Cholesten-3beta-25-diol-3-sulfate(P) 25HC3S	M-H	1	23.4634013	8.407767086	0.000134
497.34874	m/z	497.34874			79.1347669	119.9497978	0.000185
498.35135	m/z	498.35135			8.86932466	22.167893	0.000007
501.37995	m/z	501.37995			42.7581113	14.86227604	0.000029
509.25209	PA(20:1)(P)	PA(18:1(12Z)-2OH(9,10)/2:0)(P)	M-H	0	39.0448432	19.65908552	0.000114
525.37853	m/z	525.37853			251.960301	379.2928255	0.00014
526.38274	m/z	526.38274			82.7239153	125.0732158	0.000136
539.50456	m/z	539.50456			70.1073626	42.37873535	0.000112
545.36189	m/z	545.36189			30.5134503	74.86405334	0.000252
561.35722	m/z	561.35722			37.0028357	66.01346021	0.000526
564.29467	LysoPE(22:4)(P)	LysoPE(22:4(7Z,10Z,13Z,16Z)/0:0)(P)	M+Cl	15	81.9305511	28.81203957	0.000133
609.30321	PA(26:3)(P)	PA(18:3(9,11,15)-OH(13)/8:0)(P)	M+Cl	11	38.3525632	19.4158427	0.000122
613.39518	m/z	613.39518			144.737104	100.5729431	0.016424
627.47923	DG(34:2)(P)	DG(34:2)(P)	M+Cl	5	9.63384904	22.05829734	0.000015
651.51979	m/z	651.51979			32.530681	58.07003365	0.000076
653.49142	DG(36:3)(P)	DG(36:3)(P)	M-H	13	4.71885253	28.63085904	0.000012
667.51511	DG(PGFa/i-16:0)(P)	DG(PGF1alpha/0:0/i-16:0)(P)	M-H	0	16.4871767	33.96806502	0.000007
678.39826	m/z	678.39826			77.7923275	25.87527313	0.000064
679.40087	PA(22:5/i-12:0)(P)	PA(22:5(4Z,7Z,10Z,13Z,19Z)-O(16,17)/i-12:0)(P)	M-H	4	35.849637	6.984637564	0.000046
685.48047	PA(35:2)(P)	PA(35:2)(P)	M-H	1	4.35827666	32.02100258	0.000003
685.52524	SM(d33:2)(P)	SM(d33:2)(P)	M-H	5	76.6743151	119.8753452	0.000171
686.52945	m/z	686.52945			23.114832	48.86649628	0.000063
701.47739	DG(PGD1/16:0)(P)	DG(PGD1/16:0)(P)	M+Cl	1	4.17786898	26.36613865	0.000003
763.60857	DG(isoPGF2/a25:0)(P)	DG(5-iso PGF2VI/0:0/a-25:0)(P)	M+Cl	10	3.81842715	17.43567731	0.00012

8.1.30   Appendix 30

Table shows the m/z, abbreviated names of molecules in Figure 6.3.8 (liver positive mode MSI). Table includes the mean relative abundance value for each molecule within the groups and *p-value* (GFvsSPF).

m/z	Heatmap ID	Compound name	adduct	delta (ppm)	Mean GF	Mean SPF	p-value
104.13534	m/z 104.13534	104.13534			99.697773	144.0953598	0.002573
123.05476	Isonicotinamide	Isonicotinamide(P)	M+H	4	82.941981	28.00788002	0.001352
129.14033	m/z 129.14033	129.14033			92.0433502	28.12771721	0.00061
130.16073	m/z 130.16073	130.16073			97.8130163	52.91099319	0.0003222
146.16624	Spermidine	Spermidine	M+H	7	860.546539	359.2022461	0.00121
195.09534	m/z 195.09534	195.09534			321.478799	166.145175	0.00111
203.22433	Spermine	Spermine	M+H	6	516.141113	252.9964355	0.0006733
211.09296	Methylsuberic acid(P)	3-Methylsuberic acid(P)	M+Na	5	181.889674	83.41132126	0.0020223
216.06345	GPEA(P)	Glycerylphosphorylethanolamine(P)	M+H	1	84.9140307	26.94120026	0.0012997
241.10526	IDHP(P)	Isopropyl 3-(3,4-dihydroxyphenyl)-2-hydroxypropanoate	M+H	7	70.3277156	24.60460358	0.00019
255.11995	NPA(P)	n-propyl-l-arginine(P)	M+H	11	59.2819047	27.85450516	0.0000944
265.0846	Methionyl-Aspartate(P)	Methionyl-Aspartate(P)	M+H	3	99.4329211	34.57464867	0.0005784
267.0991	m/z 267.0991	267.0991			86.68448	29.02466335	0.0015911

m/z	Name	Full Name	Adduct	n			
269.13463	3-HODE	3-Hydroxydodecanedioic acid(P)	M+Na	5	2220.8571	1033.781738	0.0000057
270.13925	m/z	270.13925			282.37568	124.2152725	0.0000046
271.0939	m/z	271.0939			35.509475	10.42233459	0.0000636
285.10858	PG(P)	Phosphatidylglycerol(P)	M+H	12	1863.49874	836.5843872	0.0001059
286.1132	Threonyllysine(P)	Threonyllysine(P)	M+K	11	236.37485	96.53646393	0.0000891
287.10993	Glucopyranoside(P)	(Z)-2-Methyl-2-butene-1,4-diol 4-O-beta-D-Glucopyranoside(P)	M+H	9	55.9483969	15.83471959	0.0000555
299.14693	10-oxoODE(P)	10-(2,3-Dihydroxypropoxy)-10-oxodecanoic acid(P)	M+H	7	109.509472	63.02425537	0.0000398
299.18375	3-oxo-carnitine(P)	3-oxododecanoylcarnitine(P)	M+H	5	64.878287	18.35188122	0.0000002
300.26464	m/z	300.26464			41.9846687	12.31247439	0.0000071
301.10357	m/z	301.10357			479.193609	235.069873	0.0003499
308.22005	Myristoylglycine(P)	Myristoylglycine(P)	M+H	6	412.42654	161.3627075	0.0000018
309.16682	Fructose-lysine(P)	Fructose-lysine(P)	M+H	4	163.124036	72.01422958	0.0000045
315.12089	m/z	315.12089			116.664323	68.21658249	0.0003556
315.1577	Valerenolic acid(P)	Acetylvalerenolic acid(P)	M+Na	3	125.412328	56.01547089	0.0000332
317.11434	m/z	317.11434			325.0193613	150.6461823	0.0000736
320.21761	Dec-l-carnitine(P)	Decadienyl-l-carnitine(P)	M+Na	6	160.2632269	62.87987518	0.0001061
323.14731	m/z	323.14731			160.3299051	66.62998276	0.0000033
325.10395	indole-3-acty-glut(P)	indole-3-acetyl-glutamine(P)	M+Na	0	124.364891	60.63520432	0.0001294

m/z	Name	Full name	Adduct				
325.14077	DHAP(10:0)(P)	DHAP(10:0) Dihydroxyacetone phosphate(P)	M+ Na	2	188.26804	84.26820221	0.000665
325.16181	m/z 325.16181	325.16181			215.722898	102.4395805	0.0001188
329.20921	11-oxyandrosterone(P)	11-Hydroxyandrosterone(P)	M+ Na	2	721.578551	400.7113265	0.00197
329.35911	m/z 329.35911	329.35911			159.651549	93.85009613	0.001961
330.21119	m/z 330.21119	330.21119			243.475517	131.1488602	0.001845
339.12126	m/z 339.12126	339.12126			283.781657	139.6382584	0.000852
341.13576	2-oxoenterodiol(P)	2-Hydroxyenterodiol(P)	M+ Na	1	222.57797	92.45417862	0.000792
354.04326	m/z 354.04326	354.04326			417.322922	164.0631378	0.000262
356.04197	m/z 356.04197	356.04197			166.217635	46.18260117	0.000135
364.96256	m/z 364.96256	364.96256			115.040527	27.89951897	0.000338
365.03647	melatonin sulfate(P)	6-Hydroxymelatonin sulfate(P)	M+ Na	13	50.0505455	17.49173165	0.000662
365.27815	m/z 365.27815	365.27815			164.747794	60.49773102	0.000065
376.21849	m/z 376.21849	376.21849			138.87182	80.10278015	0.00233
377.2757	m/z 377.2757	377.2757			93.8420219	39.71828156	0.001819
385.15485	m/z 385.15485	385.15485			178.632668	83.83159637	0.000145
397.27339	3b-oxoCholenoic (P)	3b-Hydroxy-5-cholenoic acid(P)	M+ Na	5	212.53739	100.165538	0.000289
401.12881	m/z 401.12881	401.12881			474.051865	253.7756042	0.002128
402.13342	m/z 402.13342	402.13342			84.5830898	28.96754379	0.001663

m/z	Abbreviation	Name	Adduct				
407.18281					121.714729	70.15003204	0.002577
	PGG2(P)	Prostaglandin G2	M+K	1			
421.20013	m/z	421.20013			322.246157	124.2822006	0.000745
423.23566	MG(0:0/5isoPGF2)(P)	MG(0:0/5-iso PGF2VI)(P)	M+Na	1	244.376676	176.8496185	0.002386
426.29159	m/z	426.29159			201.933711	140.0929993	0.000408
437.20564	m/z	437.20564			170.80132	92.20862732	0.001517
439.23065	m/z	439.23065			109.880015	48.21114273	0.002006
453.16907	m/z	453.16907			142.931001	47.24500504	0.000073
455.2046	455.2046	455.2046			273.449471	153.7395706	0.000252
505.35134	m/z	505.35134			21.5166697 7	86.38057785	0.000544
521.32529	m/z	521.32529			133.476672	286.4905975	0.000978
522.32728	m/z	522.32728			7.78474034	36.68663559	0.000193
533.38071	m/z	533.38071			295.873484	597.3532349	0.002721
534.38533	m/z	534.38533			77.2905661	189.697876	0.001809
549.35466	m/z	549.35466			715.95018	1602.947217	0.000954
550.35928	m/z	550.35928			252.465874	531.402948	0.001161
575.36953	3-11oxo-12UO(P)	3-Benzoyloxy-11-oxo-12-ursen-28-oic acid(P)	M+H	6	13.5644568	57.39898911	0.000809
618.33667	PC(22:4)(P)	PC(22:4)(P)	M+H	6	42.6300481	16.81428868	0.000448
629.47689	DG(36:5)(P)	DG(36:5)(P)	M+Na	3	86.7387428	174.7018982	0.001082

631.49401	DG(i-34:1)(P)	DG(i-34:1)(P)	M+H	1	12.0914819	39.50968575	0.004723
632.35399	m/z 632.35399	632.35399			289.0073577	167.599176	0.003621
632.47496	m/z 632.47496	632.47496			95.12890344	217.7920288	0.003348
633.48747	DG(34:1)(P)	DG(34:1)(P)	M+K	3	151.5868433	343.661874	0.003366
634.48946	LysoPC(26:1)(P)	LysoPC(26:1)(P)	M+H	14	107.3882611	274.2298859	0.011108
646.45283	Cer(d16:1/PGD1)(P)	Cer(d16:1/PGD1)(P)	M+K	13	37.81057844	88.21597242	0.001009
647.46534	DG(i-34:1)(P)	DG(i-34:1)(P)	M+K	1	135.9662533	298.8584869	0.000419
648.46995	m/z 648.46995	648.46995			31.38454299	109.3189346	0.0000072
649.48246	PA(i-32:0)(P)	PA(i-32:0)(P)	M+H	1	18.12877744	61.55374527	0.0003
653.43782	PG(i-14:0/i-13:0)(P)	PG(i-14:0/i-13:0)(P)	M+H	3	74.44873899	144.6614156	0.001875
654.44243	Cer(d18:1/PGJ2)(P)	Cer(d18:1/PGJ2)(P)	M+H	3	14.97047446	49.63173771	0.000498
655.49439	DG(i-36:4)(P)	DG(i-36:4)(P)	M+H	6	23.14110088	81.65991745	0.000394
657.48522	PA(P-34:2)(P)	PA(P-34:2)(P)	M+H	1	189.290824	467.6228943	0.002612
657.50888	DG(i-36:5)(P)	DG(i-36:5)(P)	M+H	1	8.817578922	38.36619167	0.000851
658.40568	m/z 658.40568	658.40568			36.32569622	17.28784475	0.000099
658.48983	Cer(t38:4)(P)	Cer(t38:4)(P)	M+K	14	66.562466	193.4840271	0.001921
659.50234	DG(36:2)(P)	DG(36:2)(P)	M+H	2	63.991531	239.546233	0.001293
660.50696	m/z 660.50696	660.50696			19.60066711	99.0341918	0.000876

No.	Name	Name	Adduct				
661.4432	PA(i-32:1)(P)	PA(i-32:1)(P)	M+H	1	29.295546	80.16031036	0.000135
663.46033	m/z 663.46033	663.46033			67.2950215	109.7353143	0.000853
664.46494	Cer(d40:6)(P)	Cer(d40:6)(P)	M+K	1	18.6666657	40.67474486	0.000143
665.49586	DG(36:4)(P)	DG(36:4)(P)	M+H	4	278.960899	468.6719482	0.001122
666.50048	Cer(d20:1/PGJ2)(P)	Cer(d20:1/PGJ2)(P)	M+Na	9	109.118623	207.2179871	0.000529
671.46571	PA(P-34:3)(P)	PA(P-34:3)(P)	M+H	2	182.234239	496.3943909	0.000035
672.47033	m/z 672.47033	672.47033			22.3381994	69.42514598	0.004013
673.4251	PA(i-31:0)(P)	PA(i-31:0)(P)	M+K	7	96.4835741	54.27828617	0.002426
673.48021	PA(P-34:1)(P)	PA(P-34:1)(P)	M+H	0	120.666068	368.8839813	0.000236
673.50388	DG(i-38:6)(P)	DG(i-38:6)(P)	M+H	0	6.58755849	35.64799347	0.000158
674.48301	PE-NMe(30:2)(P)	PE-NMe(30:2)(P)	M+H	11	11.1364245	49.7275191	0.000078
675.49679	PA(34:1)(P)	PA(34:1)(P)	M+H	1	7.2073516	49.11284489	0.000263
679.45532	PA(i-32:1)(P)	PA(i-32:1)(P)	M+K	1	338.806239	556.3595286	0.002162
680.45993	Cer(d40:7)(P)	Cer(d40:7)(P)	M+K	8	134.740774	222.6716709	0.002306
681.46981	PG(i-29:0)(P)	PG(i-29:0)(P)	M+H	0	1215.67352	2201.691235	0.000225
682.47443	Cer(t40:6)(P)	Cer(t40:6)(P)	M+K	9	530.389109	924.5782471	0.000282
683.47379	PA(35:4)(P)	PA(35:4)(P)	M+H	13	50.1390191	92.68077021	0.000148
688.42065	m/z 688.42065	688.42065			300.640557	130.6336288	0.000105

m/z	Name	Name	Adduct	n	Value 1	Value 2	Value 3
689.4226	PA(36:8)(P)	PA(36:8)(P)	M+H	7	104.532502	30.78954223	0.000058
689.47282	PA(i-34:1)(P)	PA(i-34:1)(P)	M+Na	11	46.3442411	168.0916298	0.000048
690.37462	m/z	690.37462	M+		92.2074432	31.47920418	0.003571
690.47682	Cer(d18:1/TXB2)(P)	Cer(d18:1/TXB2)(P)	M+K	9	5.21185199	32.55756487	0.000022
691.51296	DG(i-38:5)(P)	DG(i-38:5)(P)	M+Na	1	43.722031	112.7115824	0.002304
692.51731	PE(32:0)(P)	PE(32:0)(P)	M+H	7	10.9501584	45.27275182	0.001145
701.43857	PA(i-34:4)(P)	PA(i-34:4)(P)	M+H	0	6.92455311	52.21939983	0.000107
705.47019	PG(i-31:2)(P)	PG(i-31:2)(P)	M+K	0	818.378545	1673.977563	0.00101
706.47481	PS(30:1)(P)	PS(30:1)(P)	M+K	0	348.148664	715.1582275	0.001046
707.48773	PA(i-34:1)(P)	PA(i-34:1)(P)	M+H	3	381.371404	812.9483337	0.000803
708.4893	PS(30:0)(P)	PS(30:0)(P)	M+H	12	287.215851	651.2325623	0.000737
717.4546	PA(38:8)(P)	PA(38:8)(P)	M+H	8	64.0580724	8.558537656	0.000309
719.45068	PG(i-31:3)(P)	PG(i-31:3)(P)	M+H	2	190.171691	487.2664307	0.000612
720.4553	PE(33:4)(P)	PE(33:4)(P)	M+Na	3	64.6423512	177.7855484	0.00042
721.46518	PG(i-33:3)(P)	PG(i-33:3)(P)	M+H	0	135.297125	332.2385498	0.00041
722.4698	PE-NMe(34:6)(P)	PE-NMe(34:6)(P)	M+H	8	32.6094522	124.4697983	0.00012
731.48512	PA(i-36:3)(P)	PA(i-36:3)(P)	M+H	1	6.20684434	28.49794487	0.000087
735.44357	PA(TXB2/14:0)(P)	PA(TXB2/14:0)(P)	M+H	1	43.0885328	89.81517696	0.002315

No.				n			
737.45754	PA(P-36:3)(P)	PA(P-36:3)(P)	M+K	8	20.2140644	64.82093697	0.000371
755.47254	PA(PGF1a/P-16:0)(P)	PA(PGF1alpha/P-16:0)(P)	M+K	13	293.694154	542.3330261	0.002297
756.4767	PE(PGJ2/15:0)(P)	PE(PGJ2/15:0)(P)	M+H	6	135.197529	243.065303	0.003579
758.57072	PC(P-34:1)(P)	PC(P-34:1)(P)	M+H	2	27.3501132	2.131328898	0.000066
759.55387	PA(i-39:1)(P)	PA(i-39:1)(P)	M+H	1	29.0421205	194.5824615	0.000352
760.55586	PC(33:1)(P)	PC(33:1)(P)	M+H	9	14.5843632	144.6959137	0.000438
769.59479	SM(d38:4)(P)	SM(d38:4)(P)	M+H	12	46.0466396	186.8852276	0.002726
770.59941	PC(O-36:3)(P)	PC(O-36:3)(P)	M+H	8	16.2593872	90.80287094	0.00225
771.55143	PA(i-40:3)(P)	PA(i-40:3)(P)	M+H	3	2.76447978	30.98089215	0.000001
773.56856	DG(i-42:3)(P)	DG(i-42:3)(P)	M+H	1	21.3383011	155.4455109	0.000009
774.57318	PC(34:1)(P)	PC(34:1)(P)	M+H	11	4.78038124	58.35001221	0.000074
780.55354	PC(P-36:5)(P)	PC(P-36:5)(P)	M+H	12	2084.77513	1165.255615	0.003032
785.574	SM(d38:4)(P)	SM(d38:4)(P)	M+H	8	95.0268011	333.9081357	0.000334
786.57336	PC(35:3)(P)	PC(35:3)(P)	M+H	11	81.2888707	330.8655617	0.000277
787.58587	SM(d38:3)(P)	SM(d38:3)(P)	M+H	13	614.982814	2759.911377	0.002799
788.59049	PC(35:1)(P)	PC(35:1)(P)	M+H	13	250.267431	1345.185999	0.002607
795.61229	SM(d40:5)(P)	SM(d40:5)(P)	M+H	14	24.2990139	139.1868347	0.001819
801.56151	PA(i-41:3)(P)	PA(i-41:3)(P)	M+H	3	43.6319999	129.2115036	0.000394

No.	Name	Name	Adduct		Val1	Val2	Val3
802.56572	PC(35:3)(P)	PC(35:3)(P)	M+H	8	19.0292372	127.2014526	0.000186
803.57823	SM(d39:5)(P)	SM(d39:5)(P)	M+Na	14	46.625168	190.0718517	0.001124
804.58548	PE(PGF1a/P-18:0)(P)	PE(PGF1alpha/P-18:0)(P)	M+H	13	11.3174088	132.5296478	0.001193
811.58373	SM(d38:2)(P)	SM(d38:2)(P)	M+K	1	56.3475025	244.0824944	0.000166
812.58826	PC(37:4)(P)	PC(37:4)(P)	M+H	10	20.9062702	117.1517693	0.000104
813.60074	PA(a-43:3)(P)	PA(a-43:3)(P)	M+H	0	184.098703	830.5365723	0.000559
814.60536	PC(37:3)(P)	PC(37:3)(P)	M+H	12	67.6325874	353.9644043	0.000152
815.5416	PG(i-38:4)(P)	PG(i-38:4)(P)	M+H	2	10.5528087	45.51022151	0.000262
817.5561	PG(i-38:3)(P)	PG(i-38:3)(P)	M+H	3	10.2392958	82.32054888	0.000112
818.56334	PE(TXB2/P-18:0)(P)	PE(TXB2/P-18:0)(P)	M+H	11	6.22458309	54.89474049	0.000135
827.57829	PG(40:4)(P)	PG(40:4)(P)	M+K	2	65.8702539	173.9228897	0.001674
827.61542	PA(i-44:3)(P)	PA(i-44:3)(P)	M+H	1	6.1166035	64.37721043	0.003079
828.51222	PE(42:10)(P)	PE(42:10)(P)	M+H	12	115.896738	18.20180597	0.001631
833.55372	PG(i-38:3)(P)	PG(i-38:3)(P)	M+H	0	172.505774	618.6510544	0.003095
834.5557	PE(42:7)(P)	PE(42:7)(P)	M+H	10	123.293949	408.1079224	0.002369
841.59592	PA(i-44:4)(P)	PA(i-44:4)(P)	M+H	1	11.8294836	98.04649162	0.000055
842.59791	PC(PGD1/P-18:1)(P)	PC(PGD1/P-18:1)(P)	M+H	9	9.54242271	91.14537506	0.000045
843.5736	PG(i-40:4)(P)	PG(i-40:4)(P)	M+H	1	6.19621087	69.94719372	0.000345

m/z	Name	Name	Adduct				
856.54421	PE(44:9)(P)	PE(44:9)(P)	M+H	5	63.1970773	13.68138546	0.0036636
856.57577	PC(38:5)(P)	PC(38:5)(P)	M+H	7	38.2648784	89.03742596	0.0014133
859.56859	PG(i-42:6)(P)	PG(i-42:6)(P)	M+H	1	70.7258218	263.7389046	0.0011299
860.57321	PE(44:7)(P)	PE(44:7)(P)	M+H	8	25.7906678	129.0635769	0.0009555
875.56369	PG(i-40:4)(P)	PG(i-40:4)(P)	M+H	1	46.0356054	130.3954765	0.0026733
879.74247	TG(54:6)(P)	TG(54:6)(P)	M+H	1	73.4748068	316.0178528	0.0024911
880.74456	m/z 880.74456	880.74456			18.7633893	89.54716873	0.0033392
881.53869	PGP(38:3)(P)	PGP(38:3)(P)	M+K	9	13.3887208	122.1130632	0.0022225
895.71526	PA(48:0)(P)	PA(48:0)(P)	M+K	0	202.116804	484.0904953	0.0021833
896.71841	PE-NMe(46:3)(P)	PE-NMe(46:3)(P)	M+H	9	114.462101	288.1557953	0.0019488
897.73092	TG(52:2)(P)	TG(52:2)(P)	M+K	0	301.235798	1109.404492	0.0007266
898.73554	PC(44:2)(P)	PC(44:2)(P)	M+H	11	142.116919	610.8799805	0.0006888
899.73753	TG(52:1)(P)	TG(52:1)(P)	M+K	10	26.392685	123.4938026	0.0012133

8.1.31 Appendix 31

PLS-DA generated VIP>1 list of molecules in the liver (positive and negative mode) that contribute towards group separation in the GF vs SPF model.

m/z	VIP
771.5510254	1.182350039
701.4769897	1.176280022
462.3150024	1.174520016
685.4799805	1.173789978
461.3129883	1.171569943
242.0809937	1.167670012
498.3510132	1.164440036
667.5150146	1.164319992
773.5689697	1.160549998
423.2520142	1.159229994
427.3420105	1.157179952
653.4910278	1.156380057
627.4790039	1.152529955
477.3080139	1.151219964
365.2330017	1.149880052
690.4769897	1.146520019
439.2309875	1.142879963
501.3800049	1.141250014
298.2460022	1.141109943
297.2449951	1.140400052
323.1470032	1.138730049
326.2709961	1.135929942
287.1499939	1.134539962
465.3049927	1.132730007
309.1669922	1.132629991
842.5980225	1.132509947
679.401001	1.13191998
270.1390076	1.131850004
173.0820007	1.131189942
689.4730225	1.131039977
689.4699707	1.131039977
169.121994	1.130470037
165.0399933	1.130460024
445.3169861	1.129819989
841.5960083	1.128059983
407.2569885	1.127940059
269.1350098	1.127429962
368.0769958	1.12717998
689.4229736	1.127099991
686.5289917	1.125040054
678.3980103	1.124840021
365.2780151	1.124340057
758.5709839	1.123970032

674.4849854	1.123800039
321.2080078	1.123469949
349.2139893	1.123070002
300.2650146	1.122470021
171.0670013	1.122159958
648.4699707	1.122050047
453.1690063	1.121649981
774.572998	1.121479988
394.2640076	1.12116003
651.5200195	1.120869994
183.1399994	1.120399952
674.4829712	1.120280027
121.0289993	1.119989991
223.0299988	1.119449973
315.2529907	1.119120002
122.0350037	1.119099975
381.230011	1.118600011
178.0200043	1.117599964
731.4849854	1.117509961
188.1000061	1.117190003
184.1459961	1.117050052
228.1309967	1.116559982
209.1549988	1.116119981
227.1300049	1.115890026
255.1199951	1.11559999
187.098999	1.114879966
658.4060059	1.114490032
812.5880127	1.113080025
688.4210205	1.113000035
701.4390259	1.112339973
393.2579956	1.112310052
155.1080017	1.111680031
392.2650146	1.111430049
817.5560303	1.11116004
539.5050049	1.11116004
509.2520142	1.110900044
253.1450043	1.110659957
279.1610107	1.110360026
325.1619873	1.109830022
391.2630005	1.109539986
763.6090088	1.109519958
722.4699707	1.109419942
609.3029785	1.109120011
281.3999939	1.108440042
127.0770035	1.107560039
564.2949829	1.106739998
481.2990112	1.106570005
356.0419922	1.106410027
661.4429932	1.106389999
818.5629883	1.106259942

526.3829956	1.106220007
155.0700073	1.105839968
152.003006	1.105739951
525.3790283	1.105419993
664.4650269	1.104689956
353.1990051	1.104660034
385.1549988	1.104339957
683.473999	1.10374999
351.1809998	1.103690028
399.2390137	1.103279948
814.6049805	1.103139997
466.3080139	1.102380037
673.5040283	1.102010012
149.0099945	1.101729989
811.5839844	1.10055995
638.3309937	1.100139976
207.1380005	1.100010037
283.2630005	1.099799991
145.0500031	1.099760056
685.5250244	1.09968996
284.2669983	1.099130034
654.4959717	1.098590016
308.2200012	1.098340034
172.1060028	1.098109961
581.2930298	1.0977
271.1180115	1.097579956
400.2430115	1.097550035
497.348999	1.097530007
802.565979	1.097280025
115.0390015	1.09702003
241.1049957	1.096729994
254.25	1.096539974
522.3270264	1.096269965
273.1860046	1.096109986
299.1839905	1.095129967
285.1340027	1.094849944
580.2880249	1.094709992
171.102005	1.091799974
681.4699707	1.091689944
189.9550018	1.091199994
673.4799805	1.090149999
283.256012	1.089450002
188.951004	1.089169979
225.1130066	1.08912003
545.3619995	1.088199973
638.5449829	1.088150024
216.0549927	1.08810997
190.9490051	1.088080049
144.9609985	1.087649941
191.9519958	1.087499976

273.1340027	1.087350011
167.1080017	1.087170005
815.5419922	1.086959958
146.9600067	1.086910009
192.9450073	1.086889982
354.0429993	1.086869955
675.4970093	1.086770058
325.1659851	1.086240053
215.0500031	1.085409999
786.572998	1.085199952
125.0970001	1.084810019
682.473999	1.084560037
397.2730103	1.083770037
131.0359955	1.083709955
126.1019974	1.082640052
649.4819946	1.082559943
278.1069946	1.081599951
717.4550171	1.081590056
449.3259888	1.080340028
108.0449982	1.080340028
251.128006	1.080240011
130.1609955	1.080189943
259.0209961	1.080160022
135.0469971	1.07960999
247.1179962	1.079439998
211.0980072	1.079380035
315.1579895	1.079220057
785.5739746	1.078989983
364.9630127	1.078639984
843.5739746	1.077870011
160.9579926	1.077649951
671.4660034	1.077419996
211.1710052	1.077329993
759.5540161	1.077229977
624.34198	1.07693994
737.4580078	1.075479984
672.4699707	1.074470043
191.1799927	1.074110031
157.0879974	1.073760033
655.4940186	1.07336998
801.5620117	1.07336998
299.1470032	1.073029995
153.0939941	1.072639942
426.2919922	1.072149992
721.4650269	1.07198
252.1320038	1.071969986
647.4650269	1.071179986
720.4550171	1.071079969
129.0570068	1.070989966
359.2399902	1.070420027

239.1289978	1.070299983
623.3400269	1.069859982
760.5560303	1.069579959
425.2869873	1.069180012
159.029007	1.068950057
618.3369751	1.068799973
650.3300171	1.068539977
622.3369751	1.06851995
166.052002	1.068449974
281.2479858	1.067849994
313.1650085	1.067559958
282.2520142	1.06735003
159.1029968	1.067229986
173.1170044	1.065719962
213.1860046	1.065639973
185.1190033	1.065179944
636.5289917	1.064949989
654.4420166	1.064939976
285.1300049	1.064239979
270.2130127	1.063850045
631.4940186	1.063320041
635.5239868	1.063259959
561.3569946	1.062890053
236.173996	1.062849998
666.5	1.06269002
637.5419922	1.062150002
195.1390076	1.062059999
307.07901	1.061750054
505.3510132	1.06159997
137.0249939	1.061570048
393.2969971	1.061529994
301.1659851	1.061380029
287.1099854	1.060860038
813.6010132	1.060570002
259.118988	1.060400009
165.128006	1.059700012
302.1700134	1.059620023
608.3200073	1.059110045
265.0849915	1.058949947
301.1400146	1.057430029
235.1699982	1.057389975
129.1399994	1.057250023
171.0980072	1.057170033
719.4509888	1.057090044
329.196991	1.056990027
116.9199982	1.056929946
151.0399933	1.056200027
233.1549988	1.056120038
363.2309875	1.056110024
87.0463028	1.056010008

629.492981	1.055899978
271.0939941	1.055619955
365.0360107	1.054059982
325.1409912	1.053830028
340.2019958	1.053580046
235.1300049	1.053419948
203.223999	1.053380013
636.315979	1.053339958
326.20401	1.052729964
898.7360229	1.052489996
115.9219971	1.052240014
150.0010071	1.051779985
592.3259888	1.050799966
897.7310181	1.050349951
317.1140137	1.04974997
708.4890137	1.04974997
306.0780029	1.049710035
421.2000122	1.049289942
325.2030029	1.048509955
197.0820007	1.048169971
606.3400269	1.047960043
269.2080078	1.047629952
213.1119995	1.046910048
285.1820068	1.046880007
341.1359863	1.046769977
707.4879761	1.04618001
575.3699951	1.045869946
199.1719971	1.045699954
243.1230011	1.045459986
226.1159973	1.044970036
657.5089722	1.043769956
339.1210022	1.043730021
255.1609955	1.043679953
663.460022	1.043670058
612.4920044	1.043380022
173.0809937	1.043359995
185.0809937	1.043089986
115.0039978	1.043009996
651.3699951	1.042629957
660.507019	1.042549968
126.0019989	1.042449951
339.2009888	1.042240024
113.9260025	1.041949987
286.1130066	1.041839957
668.3049927	1.041579962
146.1190033	1.041309953
115.0780029	1.040809989
313.2330017	1.040750027
578.309021	1.040470004
124.0070038	1.04042995

549.3549805	1.038890004
860.572998	1.038830042
314.2369995	1.038290024
325.1839905	1.037899971
326.1879883	1.037889957
521.3250122	1.037819982
123.0110016	1.037029982
311.1690063	1.036960006
267.2340088	1.036800027
705.4650269	1.03647995
646.4530029	1.036440015
705.4699707	1.036389947
312.1719971	1.036149979
255.0619965	1.035519958
298.1560059	1.034929991
706.4749756	1.034839988
595.3079834	1.034360051
285.1090088	1.034289956
320.2179871	1.03421998
629.4769897	1.033329964
241.1089935	1.033169985
297.1520081	1.032909989
138.0209961	1.032539964
195.0950012	1.032179952
251.125	1.032119989
235.0630035	1.031949997
665.4959717	1.031690001
803.5780029	1.031640053
859.5689697	1.031419992
594.3060303	1.031399965
650.367981	1.030799985
692.5170288	1.030789971
550.3590088	1.030169964
181.1230011	1.030060053
299.1489868	1.029659986
299.1480103	1.029659986
133.0160065	1.029530048
103.0049973	1.02895999
804.5859985	1.028929949
261.1350098	1.028499961
146.1660004	1.028270006
899.7379761	1.028149962
262.1359863	1.027999997
429.3009949	1.027799964
319.1919861	1.02760005
191.1080017	1.026890039
434.3359985	1.026080012
187.0930023	1.02560997
313.1619873	1.025249958
659.5020142	1.025200009

301.1610107	1.025189996
325.1040039	1.025149941
433.3320007	1.025069952
216.0630035	1.02504003
563.5050049	1.024260044
564.507019	1.02402997
123.0550003	1.023100019
211.1329956	1.022930026
181.9920044	1.021980047
212.1369934	1.021790028
317.1600037	1.021690011
620.3209839	1.021450043
856.5759888	1.020990014
441.2980042	1.020930052
315.144989	1.02015996
302.1659851	1.019729972
183.1029968	1.018749952
357.2619934	1.018669963
110.973999	1.017770052
437.2059937	1.017580032
317.2250061	1.01722002
180.0659943	1.01602006
267.098999	1.015239954
579.3309937	1.014500022
828.5120239	1.014009953
612.5289917	1.014000058
402.1329956	1.01304996
827.5780029	1.012719989
213.151001	1.012069941
297.1690063	1.010429978
534.3850098	1.008810043
795.6119995	1.008520007
377.276001	1.008509994
125.0080032	1.008239985
330.2109985	1.007789969
233.1040039	1.007329941
653.4379883	1.006979942
611.526001	1.006829977
152.0350037	1.00672996
233.1179962	1.005949974
658.4899902	1.005730033
201.1100006	1.00545001
896.7180176	1.004999995
329.3590088	1.00466001
329.2090149	1.004420042
274.1679993	1.003900051
211.0930023	1.003039956
273.1690063	1.002689958

315.1789856   1.001850009
585.5089722   1.000800014
401.1289978   1.000380039
655.5079956   1.000139952

8.1.32   Appendix 32

Proteowizard settings for MSConvert were as follows:

PeakPicking-values for picker type set to 'vendor', MS levels set to 1, minimum signal to noise ratio 0.1, minimum peak spacing 0.1.